

Supporting Documents for Quantitative Metric 3.3.1

**3.3.1 Number of research papers published per
teacher in the Journals notified on UGC website
during the last five years**

ACADEMIC YEAR 2020-2021



Submitted to

NAAC

By

**Mohamed Sathak Engineering College(MSEC)
Kilakarai -Ramanathapuram**



MOHAMED SATHAK ENGINEERING COLLEGE

KILAKARAI, RAMANATHAPURAM DIST.
Approved by AICTE, COA NewDelhi , DGS Mumbai, Affiliated to Anna University, Chennai.
(Sponsored by Mohamed Sathak Trust, Chennai - 06.)



3.3.1 Number of research papers published per teacher in the Journals notified on UGC website

S.No	Title of paper	Name of the author/s	Department of the teacher	Name of journal	Year of publication	ISSN number	Link to the recognition in UGC enlistment of the Journal /Digital Object Identifier (doi) number		
							Link to website of the Journal	Link to article / paper / abstract of the article	Is it listed in UGC Care list/Scopus/ Web of Science/other, mention
1.	Evaluation of groundwater quality in Ramanathapuram district, using water quality index (WQI)	Sathees Kumar, Vidya Rajesh, Nazeer Khan	Civil	Modeling Earth Systems and Environment	2020-2021	2363-6211	https://link.springer.com	https://doi.org/10.1007/s40808-020-01025-z	Scopus
2.	Elimination of nickel (II) ions using various natural/modified clay minerals: A review	Abdul Gafoor, Dhanasekar, Sathees Kumar, Sankaran, Sivaranjani, Sabeena Begum, Zunaithur Rahman	Civil	Materials Today Proceedings (Elsevier)	2020-2021	2214-7853	Materials Today: Proceedings Journal ScienceDirect .com by Elsevier	https://doi.org/10.1016/j.matpr.2020.07.500	Yes



B. Sathak
PRINCIPAL
MOHAMED SATHAK ENGINEERING COLLEGE
KILAKARAI - 623 806.

3.	Strength and Ductility behaviour of FRC beams strengthenend with externally bonded GFRP Laminates	Jagadheeswari, Sivarethinamohan, Muthumari, Ramalakshmi, Ilayaraja	Civil	Materials Today Proceedings (Elsevier)	2020-2021	2214-7853	Materials Today: Proceedings Journal ScienceDirect .com by Elsevier	https://doi.org/10.1016/j.matpr.2020.08.491	Yes
4.	Application of remote sensing and GIS in land resource management	Sathees Kumar, Nazeer Khan	Civil	Journal of geography and cartography	2020-2021	2578-1979.	Journal of Geography and Cartography (enpress-publisher.com)	http://dx.doi.org/10.24294/jgc.v4i2.437	Scopus
5.	Applicability and new trends of electrocoagulation on mitigation of industrial effluent: A review	Sivaranjani, Abdul Gafoor, Nasar Ali, Sathees Kumar, Ramalakshmi, Sabeena Begum, Zunaithur Rahman	Civil	Materials Today Proceedings (Elsevier)	2020-2021	2214-7853	Materials Today: Proceedings Journal ScienceDirect .com by Elsevier	https://doi.org/10.1016/j.matpr.2020.05.379	Yes
6.	Advancement And Execution Of Quality Assurance In Bored Cast In-Situ Piles	D. Zunaithur Rahman, K. Sirajudeen, R. Nasar Ali, G. Muthumari, G. Alagumurugan, E. Vani,P. Sathees Kumar, S.	Civil	Materials Today Proceedings (Elsevier)	2020-2021	2214-7853	Materials Today: Proceedings Journal ScienceDirect .com by Elsevier	https://doi.org/10.1016/j.matpr.2020.07.517	Yes



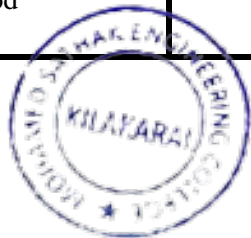

 PRINCIPAL
 PRINCIPAL
 MOHAMED SATHAK ENGINEERING COLLEGE
 KILAKARAI - 623 806.

7.	ANFIS – Based Accurate Estimation of the confinement effect for Concrete – Filled steel tubular (CFST)	S.Balasubramanian, J.Jegan & M. C. Sundararaja	Civil	International Journal of Fuzzy System	2020-2021	1562-2479	https://link.springer.com/	https://doi.org/10.1007/s40815-020-00902-0	Yes
8.	Cloud based secured log retrieval using Fully Homomorphic Encryption	B. Rasina Begum and P.Chithra	CSE	Asian Journal of Engineering and applied technology	2020-2021	2249-068X	https://ojs.trp.org.in/index.php/ajeat	https://www.trp.org.in/issues/cloud-based-secured-log-retrieval-using-fully-homomorphic-encryption	Yes
9.	ECC-CRT: An Elliptical Curve Cryptographic Encryption and Chinese Remainder Theorem based Deduplication in Cloud	B. Rasina Begum and P.Chithra	CSE	Wireless Personal Communications – Springer	2020-2021	DOI: 10.1007/s11277-020-07756-7	https://www.springer.com/journal/11277/	https://link.springer.com/article/10.1007/s11277-020-07756-7	Yes
10.	A Novel Fuzzy Knowledge Based Glaucoma System for Diabetic Retinopathy using Vessel Extraction from Fundus Images	R Karthikeyan Mr. V.R.Sathish Kumar Dr.V. Balamurugan Ms. M. ShanmugaPriya	CSE	European Journal of Molecular & Clinical Medicine	2020-2021	ISSN 2515-8260	https://ejmcm.com/	https://ejmcm.com/article_4583.html	SCI Annexure-1




PRINCIPAL
PRINCIPAL
 MOHAMED SATHAK ENGINEERING COLLEGE
 KILAKARAI - 623 806.

11.	Energy-aware and SLA-guaranteed optimal virtual machine swap and migrate system in cloud-Internet of	Dr.R.Karthikeyan Dr.V.Balamurugan	CSE	Concurrency and Computation: Practice and Experience, Wiley	2020-2021	ISSN 1532-0634	https://onlinelibrary.wiley.com/toc/15320634/2022/34/22	https://onlinelibrary.wiley.com/doi/abs/10.1002/cpe.6171	Yes
12.	Enhanced security in IOT environment using Blockchain: A survey	S.Ramamoorthi,B. Muthu Kumar, M.Mohamed Sithik, T.Thinesh Kumar, J.Ragaventhiran, M.Islabudeenb	CSE	Materials Today Proceedings - Elsevier	2020-2021	ISSN 2214-7853	https://www.sciencedirect.com/journal/materials-today-proceedings	https://www.sciencedirect.com/science/article/pii/S2214785321023981	Yes
13.	Effective adaptive routing for Lossy networks using enhanced RPL in the heterogeneous network	MMohamed Sithik, B.Muthu Kumar, S.Ramamoorthi, R.Karthikeyan, J.Ragaventhiran, M.Islabudeen	CSE	Materials Today Proceedings - Elsevier	2020-2021	ISSN 2214-7853	https://www.sciencedirect.com/journal/materials-today-proceedings	https://www.sciencedirect.com/science/article/pii/S2214785321024020	Yes
14.	SEEDDUP: A Three – Tier Secure Data Deduplication Architecture based Storage and Retrieval for Cross-Domains Over Clod	B. Rasina Begum and P.Chithra	CSE	IETE Journal of Research , taylor & francis publication	2020-2021	https://doi.org/10.1080/03772063.2021.1886882	https://www.tandfonline.com/journals/tijr	https://www.tandfonline.com/doi/abs/10.1080/03772063.2021.1886882	Yes



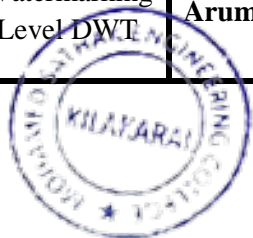

PRINCIPAL
PRINCIPAL
 MOHAMMED SATHAK ENGINEERING COLLEGE
 KILAKARAI - 623 806.

15.	Electrokinetic remediation: An innovation for heavy metal contamination in the soil environment	ZunaithurRahman , Jagadheeswari, ArunMohana, TharinicSelvendran , ShanmugaPriya	Chemical	Materials Today: Proceedings	2020-2021		https://www.sciencedirect.com/journal/materials-today-proceedings	https://doi.org/10.1016/j.matpr.2020.08.541	Yes
16.	Biodecolorization of Reactive Red 120 in batch and packed bed column using biochar derived from Ulva reticulata	Madhu Kumar, Ravindiran Gokulan, Sivarethinamohan Sujatha, Siva Pathanjali Shanmuga Priya , Saravanan Praveen,	Chemical	Biomass Conversion and Biorefinery	2020-2021	2190-6823,2190-6815	https://www.springer.com/journal/13399/	https://link.springer.com/article/10.1007/s13399-020-01268-x	Yes
17.	Impact of air pollution in health and socio-economic aspects: Review on future approach	R.Sivarethinamohan, S.Sujatha, ShanmugaPriya, Sankaran, AbdulGafoore, ZunaithurRahman	Chemical	Materials Today: Proceedings	2020-2021	2214-7853	https://www.sciencedirect.com/journal/materials-today-proceedings	https://doi.org/10.1016/j.matpr.2020.08.540	Yes
18.	Automatic Detection of Covid 19 And Viral Pneumonia Using X-Ray Images And Deep Convolutional Neural Network	A RIZHA UL HAQ , A MOHAMED IFTHIKAR ALI , I SHEIK ARAFAT	ECE	Proceedings of the Suraj Punj Journal For Multi Disciplinary Research	2020-2021	2394-2886	http://www.spjmr.com	http://www.spjmr.com/gallery/18.spjmr%201387.pdf	Yes




 PRINCIPAL
 PRINCIPAL
 MOHAMED SATHAK ENGINEERING COLLEGE
 KILAKARAI - 623 806.

19.	Comparative Performance Analysis of Pre-Processing Techniques in CT Angiogram Images	Dr.C.Priya, Dr.I.Sheik Arafat, S.Vengateshkumar, Dr.R.Premkumar, Dr.A.Shyamala	ECE	International Journal for Modern Trends in Science and Technology	2020-2021	2455-3778	http://www.ijmtst.com	http://www.ijmtst.com/volume7/issue04/29.IJMTS T0704074.pdf	Others
20.	Tracking the Nanoparticles using Multi Tracking Method in Human Crowds	Dr.A.Shyamala, S.Vengatesh Kumar , Dr.C.Priya, Dr.I.Sheik Arafat	ECE	International Journal of P2P Network Trends and Technology	2020-2021	2249 – 2615	https://ijptjournal.org/	http://www.ijmtst.com/volume7/issue04/28.IJMTS T0704079.pdf	Others
21.	Internet of Things (IoT) Based Smart Plant Monitoring System	Dr.M.Vidhyalakshmi, H.Peer oli, N.Hemakumari S.Bismillah Khan, Dr.C.Priya	ECE	1. Internet of Things (IoT) Based Smart Plant Monitoring System	2020-2021	2455-3778	http://www.ijmtst.com	http://www.ijmtst.com/volume7/issue05/24.IJMTS T0704082.pdf	Others
22.	Automatic Segmentation of Brain Tissues Using CNN in Functional MRI	Nandhini.S, A.Muthuvel	ECE	Suraj Punj Journal For Multidisciplinary Research	2020-2021	2394-2886	http://www.spirjmr.COM	http://www.spirjmr.com/gallery/21.spirjmr%201390.pdf	Others
23.	An Effective Optimization and High Authenticate Feature Extraction in Digital Watermarking Using 2-Level DWT	Dr.A.Lakshmi, N.Bhuvaneshwary, .S.Jeevitha, .Muthuvel Arumugam	ECE	Journal of Critical Reviews	2020-2021	2394-5125	https://www.jcreview.com/	https://www.jcreview.com/admin/Uploads/Files/61b386246aea59.92548904.pdf	Others




PRINCIPAL
PRINCIPAL

MOHAMED SATHAK ENGINEERING COLLEGE
KILAKARAI - 623 806.

24.	Ship Detection In Medium Resolution SAR Image Via VGG NET	Madhanmani R, Mr.K.M.Alaudeen	ECE	International Journal of P2P Network Trends and Technology	2020-2021	2249 – 2615	https://ijptjournal.org/asserts/year/2021/volume-11-issue-2/IJPTT-V11I2P401.pdf	https://ijptjournal.org/archives/ijptt-v11i2p401	Others
25.	Joint intensity transformer network for gait recognition robust against clothing and carrying status	M.Amanulla Khan S.M.H.Sithi Shameem Fathimab B.Arockia Stepnila A.Mohamed Ifthikar Ali	ECE	Materials today Proceedings	2020-2021	2214-7853	https://www.sciencedirect.com/	https://www.sciencedirect.com/science/article/pii/S2214785320319489?via%3Dihub	Yes
26.	Three Ways Chip to Chip Communication via a Single Photonic Structure: A Future Paragon of 3D Photonics to Optical VLSI	Dr.S.Boobalan,P. Venkatesh Kumar,K.Vinoth Kumar,G.Palai	EEE	IETE Journal of Research	2020-2021	0377-2063	https://www.tandfonline.com/doi/abs/10.1080/03772063.2021.1908179?journalCode=tj20	https://doi.org/10.1080/03772063.2021.1908179	Yes
27.	Automatic Uninterrupt Power Control System for Remotely Operated Communication System	P.Sujidha,T.ShanmugaPriya,P.Radhya,A.Usha,Dr.M.Sarojini devi	EEE	International Journal of Advanced Research in Science, Communication and Technology	2020-2021	2581-9429	https://ijarsct.co.in/	https://ijarsct.co.in/A821.pdf	Others




 PRINCIPAL
 PRINCIPAL
 MOHAMED SATHAK ENGINEERING COLLEGE
 KILAYARA

28.	Optimized FOPID controller for power quality enhancement between feeders using interline dynamic voltage restorer	M.Sarojini Devi, Dr. V. SueshKumar	EEE	Materials Today: Proceedings	2020-2021	0303-6286	https://www.scinapse.io/papers/3135700924	https://doi.org/10.1016/j.matpr.2020.11.137	Yes
29.	IOT Based Home Automation Using NodeMCU and Blynk Application	Dr.M.Sarojini devi, P.Sujidha, P.Radha, T.ShanmugaPriya, A.Usha	EEE	International Journal for Modern Trends in Science and Technology,	2020-2021	2455-3778	http://www.ijmtst.com/vol7issue03.html	https://doi.org/10.46501/IJMTST0703027	Web of Science
30.	Studies on Prosopis Julifera Methyl Ester Production and its Effect on DI Diesel Engine	M Rajeshwaran,, P Marimuthub, V Mayilvelnathana & R Parthasarathic	Mechanical engineering	Indian Journal of Geo Marine Sciences	2020-2021	1286 – 1292	http://op.nisca.ir.res.in/index.php/IJMS	http://14.139.47.15/bitstream/123456789/55087/1/IJMS%2049%287%29%201286-1292.pdf	Scopus
31.	Experimental investigation on thermal behavior of graphene dispersed erythritol PCM in a shell and helical tube latent energy storage system	MayilvelnathanV. Valan ArasuA.	Mechanical engineering	International Journal of Thermal Sciences	2020-2021	106446	https://www.sciencedirect.com/journal/international-journal-of-thermal-sciences	https://doi.org/10.1016/j.ijthermalsci.2020.106446	Yes



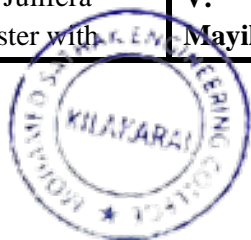

PRINCIPAL
PRINCIPAL
 MOHAMED SATHAK ENGINEERING COLLEGE
 KILAKARAI - 623 806.

32.	Performance investigation of shell and helical tube heat energy storage system with graphene dispersed erythritol PCM	Mayilvelnathan V, Valan Arasu A	Mechanical engineering	Energy storage	2020-2021	2578-4862	https://online.library.wiley.com/journal/25784862	https://doi.org/10.1002/est2.198	Yes
33.	Effect of Mechanical properties of banana fiber macro particle reinforced with epoxy composites	Chinnapalanichamy Jayaseelana* , Palani Padmanabhanb , Ayyanar Athijayamanic & Kalimuthu Ramanathand	Mechanical engineering	Indian Journal of Engineering and materials sciences	2020-2021	0975-1017	https://www.scimagojr.com/journalsearch.php?q=29812&tip=sid&clean=0	http://nopr.niscares.in/bitstream/123456789/55246/1/IJEMS%2027%283%29%20643-648.pdf	Yes
34.	Experimental Investigations on Microstructure, Properties and Workability Behavior of Zinc Oxide Reinforced Al-Si-Mg Matrix Composites	RM. Sakthi Sadhasivam, K. Ramanathan, M. Ravichandran & C. Jayaseelan	Mechanical engineering	Springer Netherlands	2020-2021	2175-2187	https://link.springer.com/	https://doi.org/10.1007/s12633-021-01012-8	Scopus




 PRINCIPAL
 PRINCIPAL
 MOHAMMED SATHAK ENGINEERING COLLEGE
 KILAKARAI - 623 806.

35.	A multi-variant approach to optimize process parameters for oil extraction from non edible feedstock: Acacia nilotica	M.Rajeshwaran R.Parthasarathi J.Ganeshkumar A.Ponshanmugakumar	Mechanical engineering	Materials Today : Proceedings	2020-2021	4671-4676	https://www.sciencedirect.com/journal/materials-today-proceedings	https://doi.org/10.1016/j.matpr.2020.08.314	Yes
36.	A critical evaluation of oil extraction and fatty acid composition of Prosopis Julifera	M.Rajeshwaran S.Ramasamy R.Parthasarathi A.Ponshanmugakumar	Mechanical engineering	Materials Today : Proceedings	2020-2021	4630-4634	https://www.sciencedirect.com/journal/materials-today-proceedings	https://doi.org/10.1016/j.matpr.2020.08.291	Yes
37.	Investigations of performance and emission characteristics in diesel engine fueled with Hemp oil methyl ester	N.Bhanu Teja M.Mohamed Abdul Hafeez G.Surendran M.Rajeshwaran N.Alagumurthi	Mechanical engineering	Materials Today : Proceedings	2020-2021	5631-5651	https://www.sciencedirect.com/journal/materials-today-proceedings	https://doi.org/10.1016/j.matpr.2020.11.110	Yes
38.	Enzymatic Production of Biodiesel from Acacia nilotica oil Using NaOCH ₃ as a Catalyst	M. Rajeshwaran, K. Niraikulasekaran, V. Mayilvelnathan, J. Ganeshkumar	Mechanical engineering	International Journal of All Research Education and Scientific Methods	2020-2021	2455-6211	http://www.ijaresm.com/	http://www.ijaresm.com/uploaded_files/document_file/M._Rajeshwaran_bRIM.pdf	Scopus
39.	Environmental Effect of CRDI Diesel Engine Using Prosopis Julifera methyl ester with	M. Rajeshwaran, K. Niraikulasekaran V. Mayilvelnathan' J.	Mechanical engineering	International Journal of All Research Education and Scientific	2020-2021	2455-6211	http://www.ijaresm.com/	http://www.ijaresm.com/uploaded_files/document_file/M._Rajeshwaran,_K._Nirai	Scopus



PRINCIPAL
PRINCIPAL
MOHAMMED SATHAK ENGINEERING COLLEGE
KILAKARAI - 623 806.

	Doped Nano Additives	Ganeshkumar		Methods				kulasekaran, V . Mayilvelnathan, J . Ganeshkumar quXI.pdf	
40.	Experimental analysis of solar wiper and its power estimates	A.Arjun P. UmarAhamed K. ShahulHameed M.P.M. MohamedIbraheem J. MohammedAzharudeen A. MuhammadSaleh	Mechanical engineering	Materials Today: Proceedings	2020-2021	2059-2062	https://www.sciencedirect.com/journal/materials-today-proceedings	https://doi.org/10.1016/j.matpr.2020.09.589	Yes
41.	Optimizing the process parameters for powder metallurgy electrode in electrical discharge machining	J.Mohammed Azarudeen R.Kaja Bantha Navas G.Vikas Reddy b R.S.Gowsik Saranb S.PrakashbA.Ander sonb	Mechanical engineering	Materials Today: Proceedings	2020-2021	9372-9377	https://www.sciencedirect.com/journal/materials-today-proceedings	https://doi.org/10.1016/j.matpr.2020.02.920	Yes
42.	Structural and Optical Behavior of CuO/Ag and CuO/Ag/Au Nanocatalysts Synthesized Via a Novel Two Step Synthesis Approach for Enhancement of Catalytic Activity	A. Sankaran, K. Kumaraguru & B. Balraj	Marine Engineering	Journal of Inorganic and Organometallic Polymers and Materials	2020-2021	10904-01655	https://link.springer.com/	https://link.springer.com/article/10.1007/s10904-020-01655-x	Yes




 PRINCIPAL
 PRINCIPAL
 MOHAMED SATHAK ENGINEERING COLLEGE
 KILAKARAI - 623 806.

43.	Investigation on catalytic activity of CuO/La ₂ O ₃ , CuO/Gd ₂ O ₃ and CuO/La ₂ O ₃ /Gd ₂ O ₃ nanocatalysts prepared via novel two step approach	A. Sankaran K. Kumaraguru B.Balraj A.Sridevi R.Magesh	Marine Engineering	Materials Science and Engineering B (MSEB)	2020-2021	263-114836	https://www.sciencedirect.com/	https://www.sciencedirect.com/science/article/abs/pii/S0921510720303433	Yes
44.	The novel two step synthesis of CuO/ZnO and CuO/CdO nanocatalysts for enhancement of catalytic activity	A.Sankaran, K.Kumaraguru	Marine Engineering	Journal of Molecular Structure	2020-2021	1221-128772	https://www.sciencedirect.com/	https://www.sciencedirect.com/science/article/abs/pii/S0022286020310978#!	Yes
45.	Entrepreneurship for Innovation and Sustainability and Business Reengineering	Dr.N.Shankar, Dr.A.Abdul Brosekhan, M.Mohamed Naimudeen	MBA	Journal of Interdisciplinary Cycle Research	2020-2021	022-1945	http://www.jicrjournal.com/	https://drive.google.com/file/d/1jahiPn_0og5s88vMW3jofhLSAcNr7sb/view	Others
46.	Biodiesel from Scenedesmus species: Engine performance, emission characteristics, corrosion inhibition and bioanalysis	ArivalaganPugazhendhi, SundaramArvindnarayan, SuthaShoban, Jeyaprakash Dharmarajad, ManokaranVadiv	S & H-Chemistry	Fuel	2020-2021	0016-2361	Fuel Journal ScienceDirect .com by Elsevier	https://www.sciencedirect.com/science/article/abs/pii/S001623612031070X	Yes




 PRINCIPAL
 PRINCIPAL
 MOHAMED SATHAK ENGINEERING COLLEGE
 KILAKARAI - 623 806.

47.	Water soluble Cu (II) and Zn (II) complexes of bidentate-morpholine based ligand: synthesis, spectral, DFT calculation, biological activities and molecular docking studies	Gurusamy Sankararaj Senthilkumar, Murugesan Sankarganesh, Jeyaraj Dhaveethu Raja , Paul Raj Adwin Jose, Arumugam Sakthivel, Thayalaraj Christopher Jeyakumar, Radhakrishnan Nandini Asha	S & H- Chemistry	Journal of Biomolecular Structure and Dynamics	2020-2021	0739- 1102	https://www.tandfonline.com/journals/tbsd20	https://www.tandfonline.com/doi/abs/10.1080/07391102.2020.1821783	Yes
48.	Fabrication and modeling of prototype bike silencer using hybrid glass and chicken feather fiber/hydroxyapatite reinforced epoxy composites	D. DucNguyenab, ManokaranVadivel , SuthaShobana, SundaramArvindnarayan, JeyaprakashDharmaraja, Rathnam KrishnaPriya, PhuongNguyen-Trig, GopalakrishnanKumar, Soon WoongChang	S & H- Chemistry	Progress In Organic Coatings	2020-2021	0300-9440	https://www.sciencedirect.com/journal/progress-in-organic-coatings	https://www.sciencedirect.com/science/article/pii/S0300944020307724?via%3Dihub	Yes




PRINCIPAL
PRINCIPAL
 MOHAMED SATHAK ENGINEERING COLLEGE
 KILAKARAI - 623 806.



Evaluation of groundwater quality in Ramanathapuram district, using water quality index (WQI)

Sathees Kumar¹ · Vidya Rajesh² · Nazeer Khan¹

Received: 9 May 2020 / Accepted: 17 October 2020
© Springer Nature Switzerland AG 2020

Abstract

In Ramanathapuram area, the fundamental hotspot for drinking and different purposes, for the most part, relies upon groundwater since the surface water is least and the stream water additionally not accessible during the storm season. The primary point of the work is to find the water quality index (WQI) in Ramanathapuram area by utilizing Geographical Information System (GIS). Around forty-six water specimens were gathered from the wells and examined to evaluate the groundwater quality in the investigation region. Water quality examinations of similar specimens were done for pH, total dissolved solids (TDS), fluoride (F^-), Fe, ammonia (NH_3), phosphate (PO), nitrate (NO_3^-), nitrite (NO_2^-), alkalinity and chloride (Cl^-). The water quality map for the study area was generated based on the results of forty-six observation wells. Based on the results, the study area is classified into five different categories as excellent, good, poor, very poor and water unsuitable for consumption. In this manner, continual checking of groundwater is important to save the groundwater in the future.

Keywords Groundwater pollution · Geoinformatics · Ramanathapuram · Water quality index

Introduction

Groundwater is a vital source used by millions of peoples in the country for irrigation and drinking water purposes. The necessity of groundwater is rising due to the demand for drinking and irrigation purpose and insufficiency of existing surface water (Sivasubramanian et al. 2013). Groundwater is affected by several factors. Groundwater contamination in coastal area occurs due to saline water interference, wind driven sea spray and aerosols of marine deposited on the topsoil (Sanford et al. 2007). On other hands, due to anthropogenic activities such as industrialization, agricultural fertilizers, wastewater, sewer effluent and landfill are other major reason of water quality contamination (Sivasubramanian et al. 2013).

Uncontrolled urban development is the fundamental explanation behind groundwater contamination in the vast majority of the evolving nations like India. The quality of groundwater is influenced by urban sprawl and business exercises, due to extreme growth of the population. Groundwater defilements make a hazard for people well-being and vast effect on the nature (Pattnaik and Reddy 2009). Defilements on groundwater make dangerous effects on individuals, for the most part where improper urban development happens (Maiti and Agrawal 2005). These problems should be addressed as a result of the tremendous requirement for groundwater because of lacking accessibility of other water resources (Rao and Jugran 2003). Groundwater quality investigation creates systems to reduce water contamination.

Water quality index is a mathematical technique created by Horton (1965). WQI gives a complete details about the quality of groundwater in the study region (Deepa and Venkateswaran 2018; Deshmukh et al. 2016; Judran and Kumar 2020; Kadam et al. 2019; Kathiravan et al. 2019; Sakizadeh 2015). Numerous analysts are broadly utilizing the Geospatial strategies for evaluation of groundwater quality (Abbasnia et al. 2019; El-Zeiny and Elbeih 2019; Isiyaka et al. 2018; Kumar and Sangeetha 2020; Mehrjardi et al. 2008; Ramadan et al. 2019; Taghizadeh et al. 2008; Ugochukwu et al. 2019). Kriging and inverse distance weighting (IDW)

✉ Sathees Kumar
geosat08@gmail.com; Satheeskumar@msec.org.in

Vidya Rajesh
vidya@civil.sastra.edu

¹ Department of Civil Engineering, Mohamed Sathak Engineering College, Kilakarai, Ramanathapuram, Tamil Nadu 623806, India

² School of Civil Engineering, SASTRA University, Thanjavur, Tamil Nadu, India



have been utilized for different groundwater contamination studies. Panhalkar and Jarag (2016) were stated that the IDW is the most opted technique for groundwater interpolation analysis (Gorai and Kumar 2013; Paul et al. 2019; Setianto and Triandini 2013; Weber and Englund 1992). The assessment of groundwater contamination in the Ramanathapuram district has been considered by utilizing parameter examination, water quality index and spatial analysis. The investigation likewise uncovers that the coordination of field information and its spatial analysis utilizing geoinformatics systems is an advanced technique for the assessment of quality of groundwater in the Ramanathapuram district.

Study area

The Ramanathapuram district, Tamil Nadu, is a well-known district in India (Fig. 1). The geographical extension of the study area is from 9°05' to 9°52' North latitude and 78°10' to 79°27' East longitude, and it has an average elevation of 2 m. Ramanathapuram district limit was 4175 km². The

population of the district is 13.53 lakhs (as per 2011 census) (NIC). It comprises of two revenue divisions which are additionally subdivided into 9 Taluks with 429 Panchayats which incorporates 400 revenue villages towns and 236 hamlet villages. The atmosphere wins with a base temperature of 22.6 °C in winter and a limit of 34.9 °C in summer. During the storm season, the normal precipitation of the study region is recorded to be 500 mm.

Methodology

Thematic map using GIS

In Ramanathapuram region, forty-six groundwater specimens were gathered and the areas are recorded by utilizing handheld GPS equipment. Figure 2 shows the forty-six observation wells utilized in the analysis. Groundwater specimens were tested by utilizing standard testing strategies (TWAD). The investigation results of water tests are listed in Table 1. The water quality parameters exceeding the

Fig. 1 Study area map

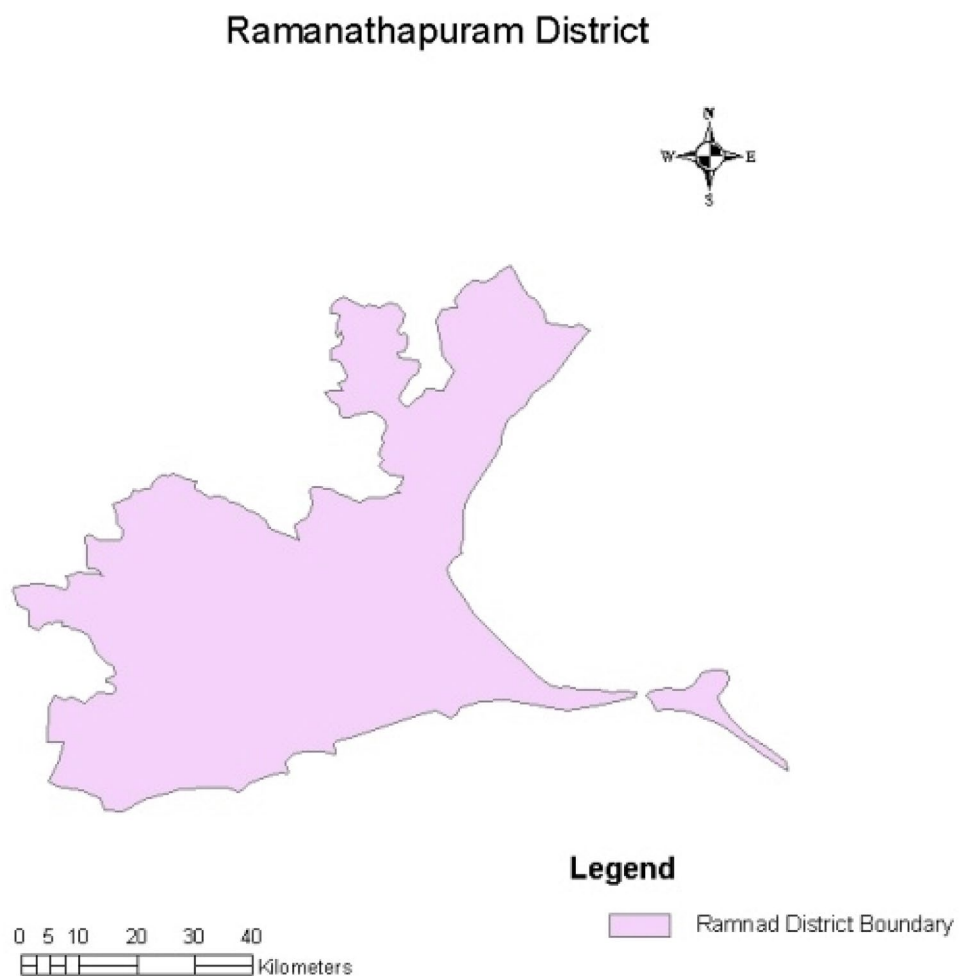
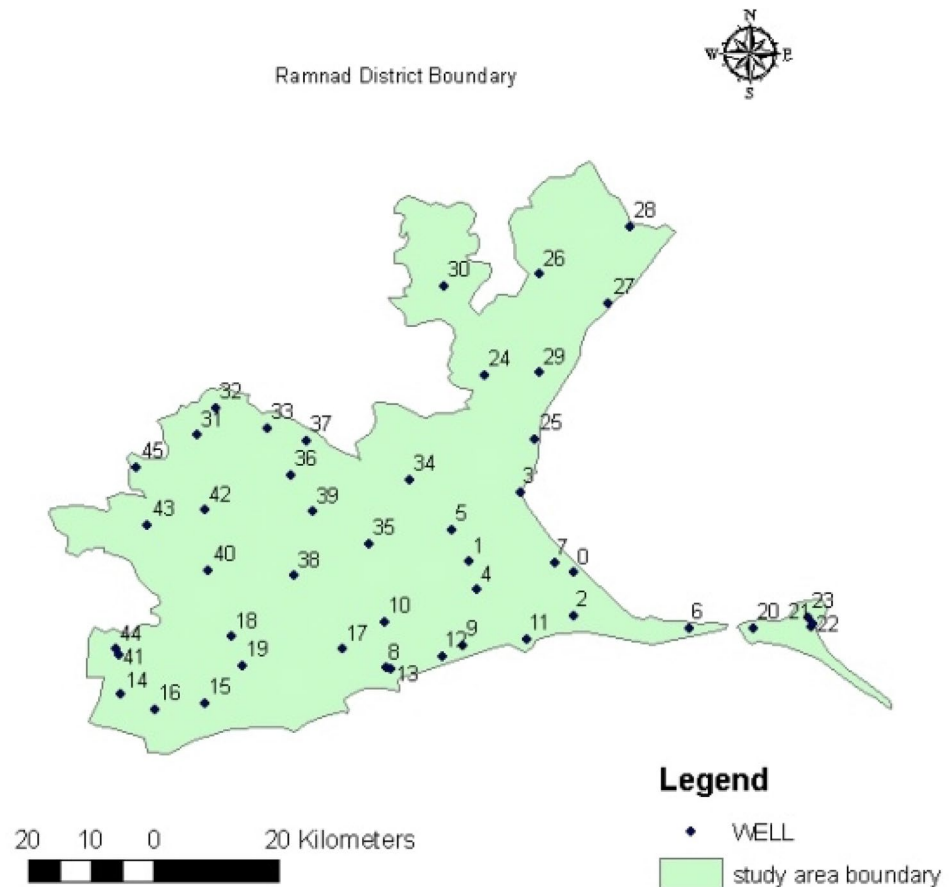


Fig. 2 Groundwater sampling location map



permissible and desired limit prescribed by Bureau of Indian standards (BIS 2012) are presented in Table 2; Figure 3. The thematic maps were prepared by utilizing IDW method in GIS Software and shown in Figs. 4, 5, 6, 7, 8, 9, 10, 11, 12, and 13; (Boufekane and Saighi 2018; Dhanasekarapandian et al. 2016; Kumar and Sangeetha 2020; Muzenda et al. 2019; Panhalkar and Jarag 2016; Shakerkhatibi et al. 2019; Talebiniya et al. 2019). Figure 3 shows the methodology adopted for this study.

Computation of WQI

It is a valuable technique to assess the nature of groundwater for consumption. The parameters like alkalinity, ammonia, pH, Cl^- , iron, CaCO_3 , PO, NO_2 , NO_3^- , fluoride and TDS were utilized for estimating the WQI in the study area. It depends on the comparative weighted strategy (Acharya and Sharma 2018; Boufekane and Saighi 2019; Deshmukh et al. 2016; Horton 1965; Kumar and Sangeetha 2020; Misaghi et al. 2017). Ravikumar et al. (2013) inferred a method for the WQI estimation is applied in this study.

Based on the importance of parameters, the weight (w_i) was assigned. The parameter NO_3 and TDS assigned to value 5 for its high effect on the quality of groundwater,

and the values 3 and 2 were allocated to other parameters for its low effect on the quality of groundwater. Equation 1 is utilized to find the relative weight (W_i) of each parameter. The values are shown in Table 3.

$$W_i = \frac{w_i}{\sum_{n=1}^n w_i} \quad (1)$$

where w_i is the weight of each parameter and n is no. of parameters.

A quality rating scale (q_i) for every parameter is figured by partitioning its fixation in each groundwater test by its specific standard as per the technique which is given by BIS and afterwards, the outcome was multiplied by hundred utilizing Eq. 2.

$$q_i = \frac{C_i}{S_i} \times 100 \quad (2)$$

where C_i is the concentration in mg/L. S_i is the parameter value based on BIS standard in mg/L excluding for pH (BIS 2012).

Equation 3 is used to find the water quality sub-index (SI_i) for each parameter,

Table 1 Water quality analyses of different samples

Well no.	pH	NO ₃ ⁻	PO	Cl ⁻	Nitrite (NO ₂)	CaCO ₃	Fluoride	Alkalinity	Fe	Ammonia (NH ₃)	TDS
W1	7	45	1	380	0	500	0.5	340	0	0	1464
W2	7.5	45	0.5	110	0	450	1	620	0	0	1428
W3	7.5	45	3	1000	1	650	1	700	0	0	2100
W4	7.5	45	0.5	850	2	200	1.5	650	0	0	1848
W5	7	0	2	360	0	250	1.5	330	0	0.5	1128
W6	6.5	0	0	370	0	390	0	270	0	0	1236
W7	7.5	45	1	1000	0	640	1.5	670	0	0.5	2200
W8	7.5	45	0.5	1000	1	660	1	480	0	0.5	2100
W9	7	45	0	1000	0.2	670	1.5	350	0	1	2100
W10	7	45	0	1000	0	660	1.5	280	0	0.5	2200
W11	6.5	0	0.5	50	0	80	1	130	0	0.5	312
W12	7	45	0.5	140	0	400	1	280	0	0	984
W13	7.5	45	1	1000	0.2	690	1.5	280	0	0	2100
W14	7.5	50	0.5	1100	2	700	3	700	0	0.5	2100
W15	7	45	2	1000	0	690	1	400	0	0	2210
W16	7.5	45	0.5	1000	0.5	680	1.5	660	0	0.5	2150
W17	7	45	1	80	0	300	1.5	180	0	0	672
W18	7.5	45	0.5	1000	0.2	680	1.5	370	0	0.5	2100
W19	7	75	1	100	0	200	1	180	0	0	576
W20	7.5	45	3	770	1	500	1.5	680	0	1	1864
W21	7	45	0	120	0.2	350	0.5	250	0	0	864
W22	7	45	2	200	0.2	400	1	300	0	0.5	1080
W23	7.5	45	2	700	0.2	690	1	430	0	0	2130
W24	7	45	2	320	0	690	1.5	330	0	0.5	2120
W25	7.5	45	0.5	1100	0.5	680	1	690	0	0.5	2200
W26	7.5	45	0.5	720	0.2	300	1.5	530	0	2	1860
W27	7	45	0	520	0	300	1.5	330	0	2	1380
W28	7	45	3	410	0.2	640	0.5	360	0	0.5	1644
W29	7.5	0	2	340	0	370	1	610	0	2	1584
W30	7.5	29	0	570	0.2	230	1.5	540	0	0	1618
W31	7	45	0.5	250	0	130	1.5	320	0	0.5	840
W32	7.5	45	1	1200	0	650	1	580	0	0	2115
W33	7.5	45	2	420	0	670	1.5	540	0	0	1872
W34	7	0	1	300	0	200	2	310	0	0	972
W35	7.5	0	0.5	600	0	250	1.5	520	0	2	1644
W36	7.5	45	2	1100	0.2	330	2	700	0	1	2100
W37	7	0	2	700	0	400	1	450	0	0.5	2100
W38	7.5	0	0	100	0	570	1	500	0	0	1404
W39	7	45	2	1250	0.2	650	1	630	0	0.5	2110
W40	7.5	0	0.5	700	0	450	1.5	330	0	2	2215
W41	7.5	45	1	950	0.2	60	1	700	0	0.5	2100
W42	7	0	0.5	140	0	260	1.5	250	0	0	780
W43	7	45	1	600	0	500	1	400	0	0.5	1800
W44	7.5	45	2	450	0	550	2	700	0	2	2150
W45	7.5	0	0	650	0	400	1.5	370	0	0.5	1704
W46	7	45	0	950	0	680	1	500	0	2	2050

Table 2 Water quality data exceeding the permissible and desirable limits

Sl. no.	Parameters	BIS (10,500:2012)		Value range of samples		Values exceeding permissible limits (%)	Values exceeding desirable limits (%)
		Desirable limit	Permissible limit	Min	Max		
1	pH	6.5–8.5	No relaxation	6.5	7.5	–	–
2	NO ₃ ⁻ (mg/L)	45	No relaxation	0	75	–	2
3	PO (mg/L)	–	–	0	3	–	–
4	Cl ⁻ (mg/L)	250	1000	50	1250	5	36
5	NO ₂ (mg/L)	0.1	No relaxation	0	2	–	19
6	CaCO ₃ (mg/L)	200	600	60	700	18	40
7	F ⁻ (mg/L)	1	1.5			4	24
8	Alkalinity(mg/L)	200	600	130	700	13	43
9	Fe(mg/L)	0.3	No relaxation	–	–	–	–
10	Ammonia(mg/L)	0.5	No relaxation	0	2	–	10
11	TDS (mg/L)	500	2000	312	2215	21	45

$$SI = W_i q_i \quad (3)$$

Finally, the WQI is derived by using SI values.

$$WQI = \sum_{i=1}^n SI_i \quad (4)$$

Preparation of WQI map using GIS

ArcGIS software is utilized to create the WQI map by using the geospatial technique. The WQI map for Ramanathapuram district is shown in Fig. 14. It is an important map for groundwater assessment studies. By using WQI thematic map, the study area is divided into five categories.

Results and discussion

Examination of water quality parameters

In Ramanathapuram region, water quality investigations of various samples are given in Table 1. From the investigation, the estimation of pH in the samples was satisfied by the norms of BIS (Table 2). The higher estimation of Cl in water sample means that contamination and used to observing for groundwater contamination (Loizidou and Kapetanios 1992). It shows that the Cl in the study region is surpassing the BIS standards (Table 2). The result shows that five groundwater samples surpass permissible limit of BIS.

The TDS value in 54% of groundwater samples in the study region was come under the recommended range of BIS. Total alkalinity in 72% of the samples and total

hardness in 61% were recorded within the permissible limit of BIS. The fluoride content in 91% of the samples was registered within the BIS permissible limit. The minimum and maximum fluoride recorded in the study region was 0.5 and 1.5 mg/l, respectively. The value of NO₃, PO, and Fe in the samples was within the limit of BIS (Table 2).

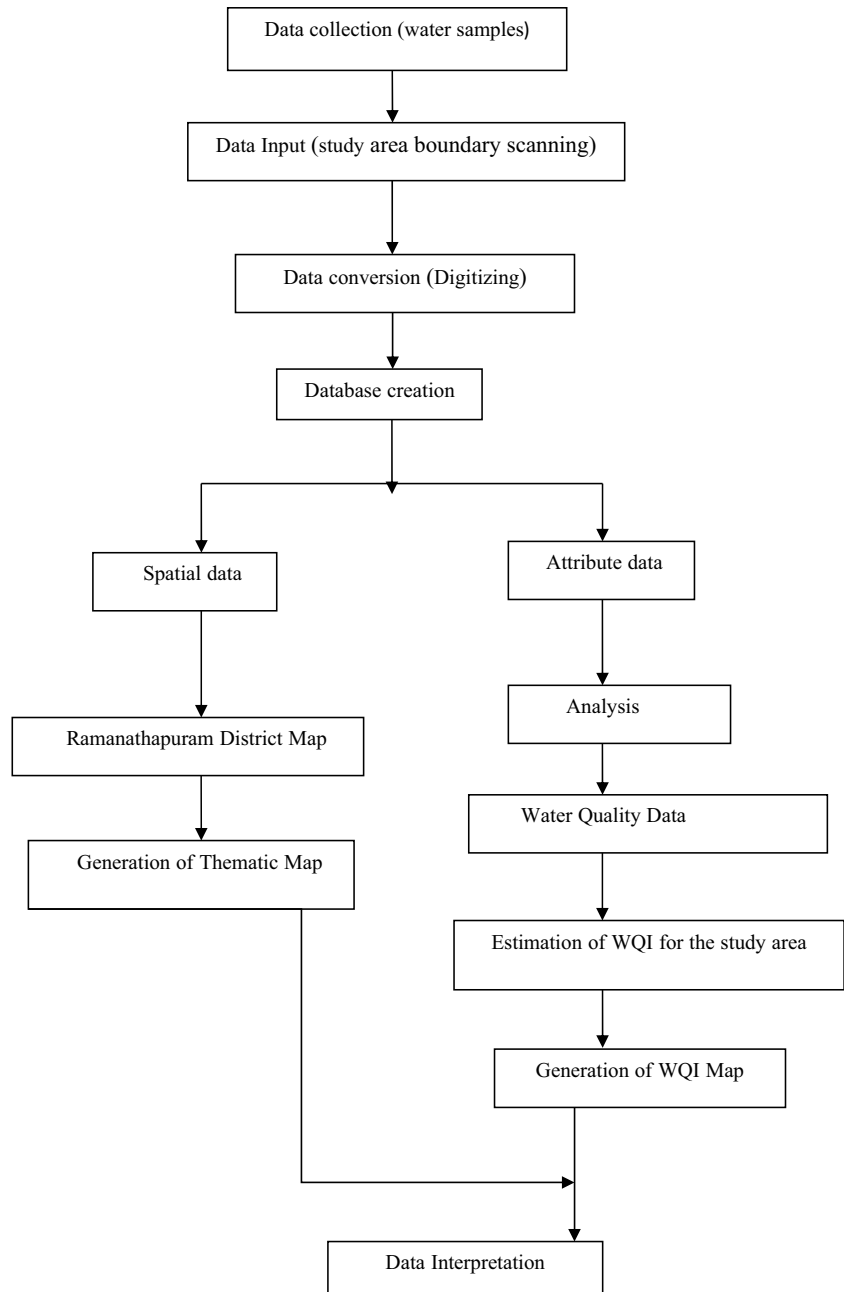
Correlation matrix

Correlation matrix (Pearson's matrix) is used to find the relationship between two or more variables (Swan and Sandilands 1995). The matrices between 11 parameters were calculated and are given in Table 4. In the matrix, pH is positively correlated with TDS, F, Fe, NH₃, PO, NO₃, NO₂, alkalinity and Cl. The fluoride was positively correlated with all elements expect PO and RC. There was a strong significant correlation between TDS and Cl. It also illustrates that CaCO₃ shows positive correlation with all the elements. The values of chloride with TDS and other parameters are found significant in the water samples. The values prove the excess of calcium-rich minerals such as gypsum and limestone in the study area. TDS were positively correlated with all physicochemical parameters expect RC. NH₃ was negatively correlated with TH, NO₂, PO, RC and NO₃.

Assessment of groundwater quality

The WQI values in the South-East part of the investigation region are seen as higher when compared to other areas (Fig. 14). The estimation of WQI is high in the sample W18 because of conceivable high scope of Ca, Mg, pH and TH. The WQI range determined for the examination region is from 55 to 243. At that point, groundwater quality in the study region ranged into five different categories. The outcome shows that 15.22% groundwater tests fall

Fig. 3 Methodology



unsatisfactory class and it is not prescribed for drinking purposes. The water quality assessment values are given in Table 5.

The quality of groundwater is commonly examined by various parameters. It is imperative to proceed with monitoring of groundwater which is important to control the groundwater contamination. The investigation has shown the estimating

quality of groundwater by utilizing water quality index with the assistance of GIS (Chande and Mayo 2019; Paul et al. 2019). The outcomes which are computed from this analysis will be useful to the administrative authorities and the groundwater management policies.

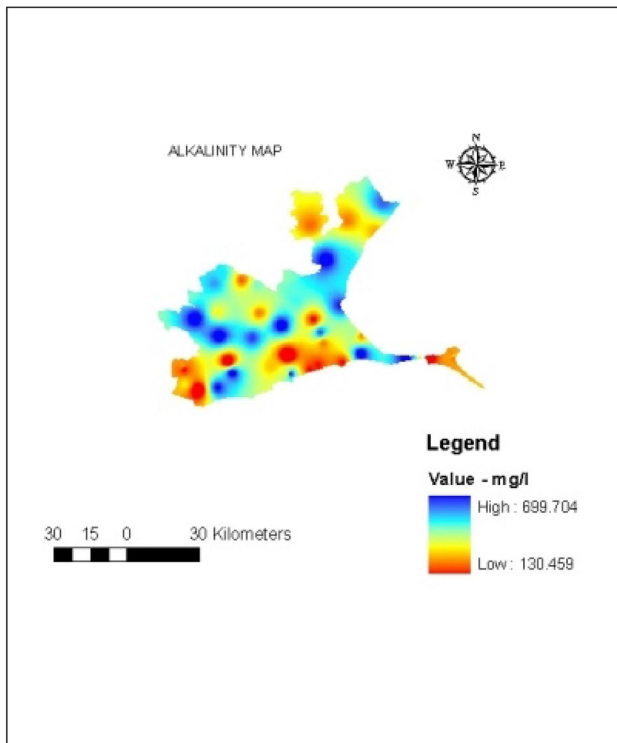


Fig. 4 Spatial distribution of Alkalinity

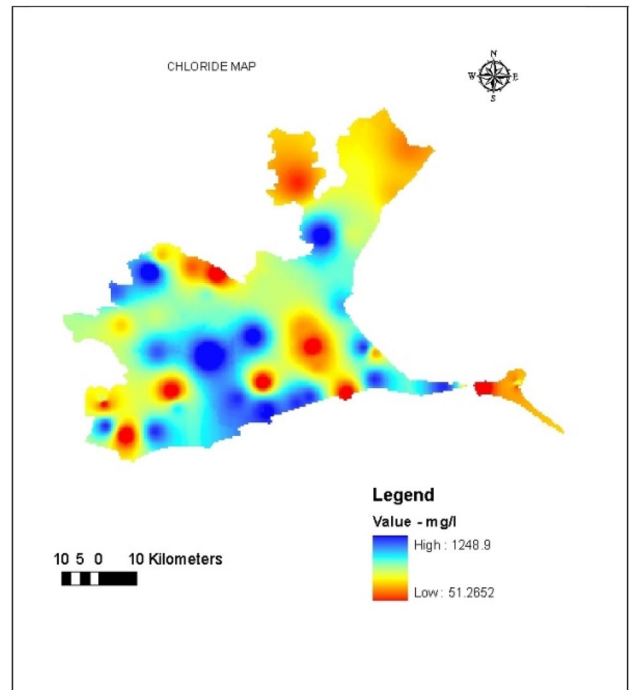


Fig. 6 Spatial distribution of Cl⁻

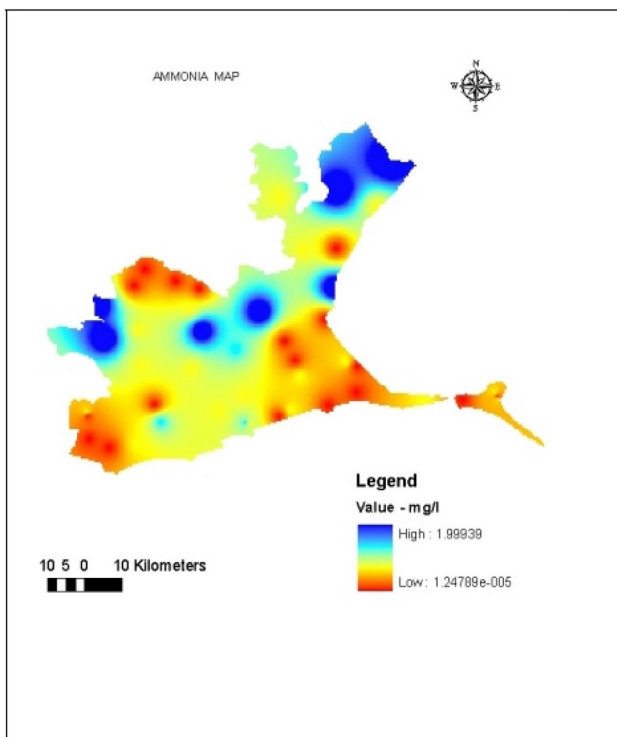


Fig. 5 Spatial distribution of NH₃

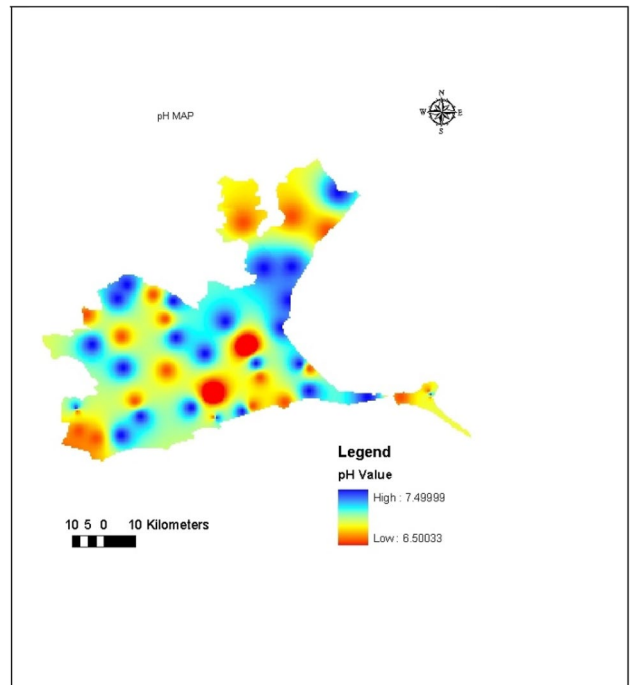


Fig. 7 Spatial distribution of pH

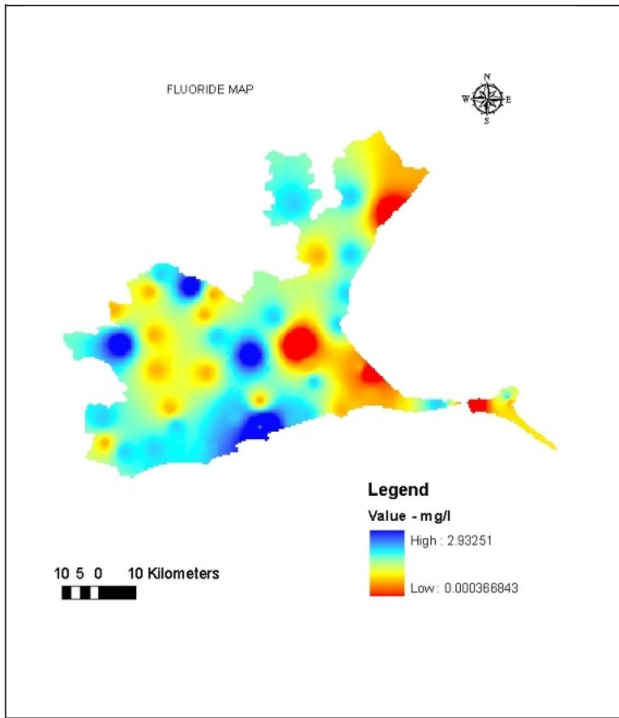


Fig. 8 Spatial distribution of F^-

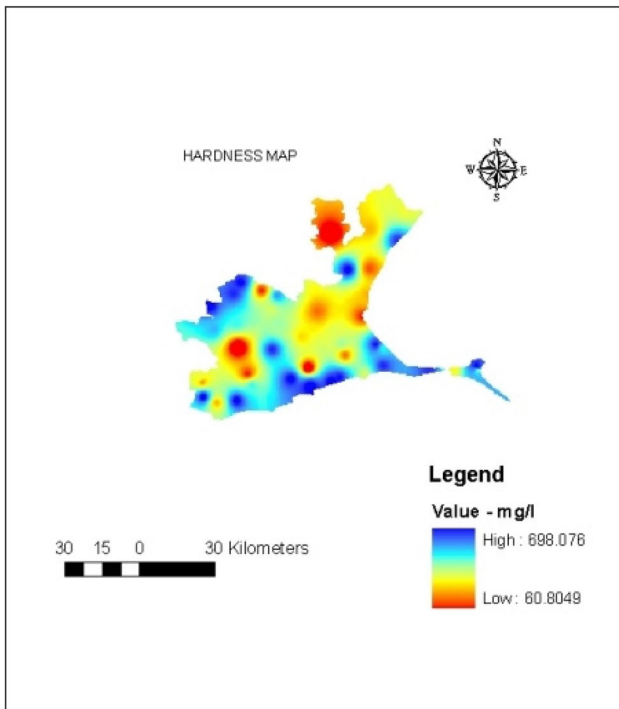


Fig. 9 Spatial distribution of $CaCO_3$

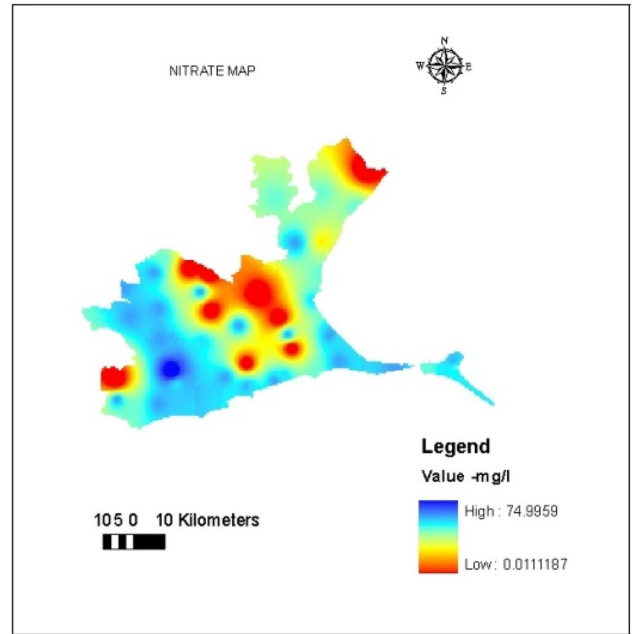


Fig. 10 Spatial distribution of NO_3^-

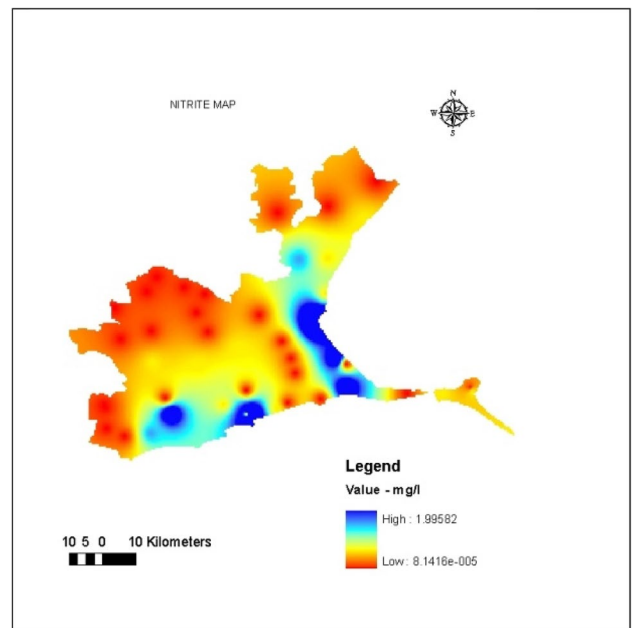


Fig. 11 Spatial distribution of NO_2

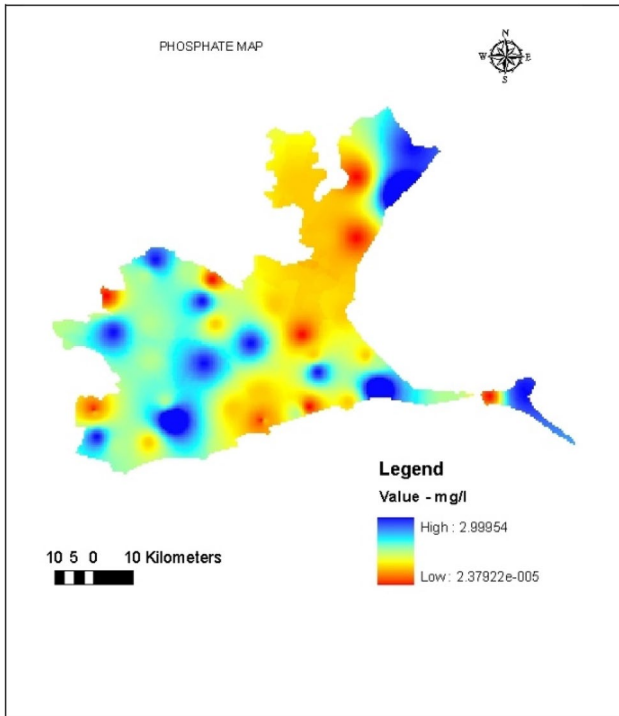


Fig. 12 Spatial distribution of PO

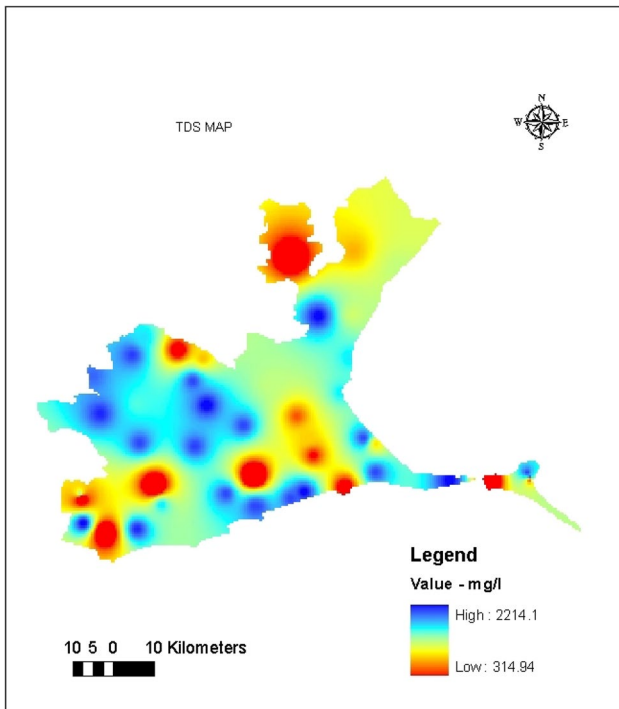


Fig. 13 Spatial distribution of TDS

Table 3 Weight assignment for water quality index calculation

Sl. no.	Parameter	Weight (w_i)	Relative weight (W_i)
1	pH	3	0.091
2	Alkalinity	2	0.061
3	Hardness	3	0.091
4	Cl ⁻	3	0.091
5	F ⁻	2	0.061
6	Fe	2	0.061
7	Ammonia	2	0.061
8	NO ₂	2	0.061
9	NO ₃	5	0.152
10	PO	2	0.061
11	Residual chloride	2	0.061
12	TDS	5	0.152

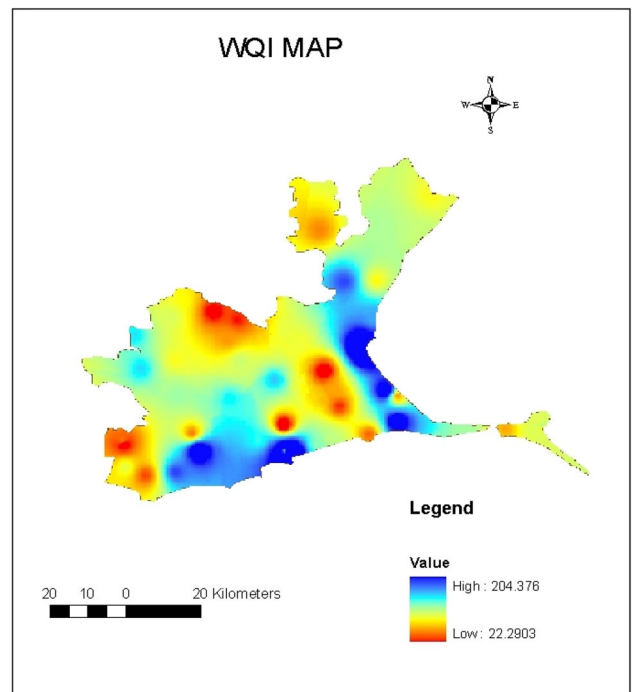


Fig. 14 WQI to the study area

Table 4 Pearson's correlation matrix for groundwater quality parameters

	pH	CaCO ₃	TH	Cl ⁻	F	NH ₃	NO ₂	PO	RC	TDS	NO ₃
pH	1										
CaCO ₃	0.72	1									
TH	0.26	0.27	1								
Cl ⁻	0.44	0.58	0.53	1							
F	0.40	0.27	0.00	0.24	1						
NH ₃	0.17	0.22	-0.06	0.15	0.25	1					
NO ₂	0.36	0.46	0.14	0.40	0.34	-0.11	1				
PO	0.09	0.26	0.20	0.06	-0.04	-0.03	0.06	1			
RC	-0.24	0.00	-0.06	0.01	-0.14	-0.16	0.34	-0.22	1		
TDS	0.58	0.65	0.68	0.84	0.21	0.25	0.27	0.20	-0.05	1	
NO ₃	0.15	0.20	0.36	0.30	0.04	-0.14	0.27	0.14	-0.16	0.25	1

Table 5 Groundwater quality assessment using WQI

Sl. no.	WQI range	Water quality	Percentage of samples
1	<25	Excellent water	2.17
2	26–50	Good water	26.09
3	51–75	Poor water	30.43
4	76–100	Very poor water	26.09
5	>100	Unsuitable for drinking	15.22

Conclusions

The current work summarizes the changes in water quality around Ramanathapuram district. The water quality index derived around the Ramanathapuram region is extremely valuable to evaluate the quality of groundwater and also to locate the good quality of groundwater in the Ramanathapuram district. GIS methods were utilized efficiently for assessing WQI value. WQI map is to be utilized as a monitoring device to highlight and for site-explicit investigation. Out of forty-six examples, four surpassed the allowable limit of BIS. The WQI value was high at W3, W4, W8, W14, W16, W20 and W25 shown the groundwater contamination in Ramanathapuram region. Groundwater quality map and GIS tool are used to know the quality of groundwater in Ramanathapuram district. The authorities of administrative as well as the common people should take effort to minimize the contamination range in the study region. This research work finds the viability of the GIS techniques in groundwater study.

References

Abbasnia A, Yousefi N, Mahvi AH, Nabizadeh R, Radfard M, Yousefi M, Alimohammadi M (2019) Evaluation of groundwater quality

using water quality index and its suitability for assessing water for drinking and irrigation purposes: case study of Sistan and Baluchistan province (Iran). *Appl Water Sci*. <https://doi.org/10.1007/s13201-018-0888-2>

Acharya SK, Sharma SV (2018) Assessment of groundwater quality by water quality indices for irrigation and drinking in South West Delhi, India. *Data Brief* 18:2019–2028. <https://doi.org/10.1016/j.dib.2018.04.120>

Boufekane A, Saighi O (2018) Application of groundwater vulnerability overlay and index methods to the Jijel plain (Algeria). *Groundwater* 56:143–156

Boufekane A, Saighi O (2019) Assessing groundwater quality for irrigation using geostatistical method—case of wadi Nil Plain (North-East Algeria). *Groundw Sustain Dev* 8:179–186

Bureau of Indian Standards –BIS (2012) Drinking water specifications. IS:10500

Chande MM, Mayo AW (2019) Assessment of groundwater vulnerability and water quality of Ngwerere sub-catchment urban aquifers in Lusaka, Zambia. *Phys Chem Earth*. <https://doi.org/10.1016/j.pce.2019.03.004>

Deepa S, Venkateswaran S (2018) Appraisal of groundwater quality in upper Manimuktha sub basin, Vellar river, Tamil Nadu, India by using water quality index (WQI) and multivariate statistical techniques. *Model Earth Syst Environ* 4(3):1165–1180. <https://doi.org/10.1007/s40808-018-0468-3>

Deshmukh KK, Aher SP (2016) Assessment of the impact of municipal solid waste on groundwater quality near the Sangamner city using GIS approach. *Water Resour Manag*. <https://doi.org/10.1007/s11269-016-1299-5>

Dhanasekarapandian M, Chandran S, Devi S, Kumar DV (2016) Spatial and temporal variation of groundwater quality and its suitability for irrigation and drinking purpose using GIS and WQI in an urban fringe. *J Afr Earth Sci* 124:270–288. <https://doi.org/10.1016/j.jafrearsci.2016.08.015>

El Zeiny AM, Elbeih SF (2019) GIS based evaluation of groundwater quality and suitability in Dakhla Oases, Egypt. *Earth Syst Environ*. <https://doi.org/10.1007/s41748-019-00112-1>

Gorai AK, Kumar S (2013) Spatial distribution analysis of groundwater quality index using GIS: a case study of Ranchi municipal corporation area. *Geoinform Geostat Overview* 1:1–11

Horton RK (1965) An index number system for rating water quality. *J Water Pollut Control Fed* 37:300–305

Isiyaka HA, Mustapha A, Juahir H, Phil-Eze P (2018) Water quality modelling using artificial neural network and multivariate statistical techniques. *Model Earth Syst Environ* 5(2):583–593. <https://doi.org/10.1007/s40808-018-0551-9>

- Judran NH, Kumar A (2020) Evaluation of water quality of Al-Gharraf River using the water quality index (WQI). *Model Earth Syst Environ* 6(3):1581–1588. <https://doi.org/10.1007/s40808-020-00775-0>
- Kadam AK, Wagh VM, Muley AA, Umrikar BN, Sankhua RN (2019) Prediction of water quality index using artificial neural network and multiple linear regression modelling approach in Shivganga River basin, India. *Model Earth Syst Environ* 5(3):951–962. <https://doi.org/10.1007/s40808-019-00581-3>
- Kathiravan K, Natesan U, Vishnunath R (2019) Developing GIS based coastal water quality index for Rameswaram Island, India positioned in Gulf of Mannar marine biosphere reserve. *Model Earth Syst Environ* 5(4):1519–1528. <https://doi.org/10.1007/s40808-019-00656-1>
- Kumar S, Sangeetha B (2020) Assessment of ground water quality in Madurai city by using geospatial techniques. *Groundw Sustain Dev* 10:100297. <https://doi.org/10.1016/j.gsd.2019.100297>
- Loizidou M, Kapetanos EG (1992) Study on the gaseous emissions from a landfill. *Sci Total Environ* 127(3):201–210. [https://doi.org/10.1016/0048-9697\(92\)90503-k](https://doi.org/10.1016/0048-9697(92)90503-k)
- Maiti S, Agrawal PK (2005) Environmental degradation in the context of growing urbanization: a focus on the metropolitan cities in India. *J Hum Ecol* 17:277–287
- Mehrjardi TR, Jahromi ZM, Mahmodi S, Heidari A (2008) Spatial distribution of groundwater quality with geostatistics, case study: Yazd-Ardakan Plain. *World Appl Sci J* 4:9–17
- Misaghi F, Delgosha F, Razzaghmanesh M, Myers B (2017) Introducing a water quality index for assessing water for irrigation purposes: a case study of the Ghezel Ozan River. *Sci Total Environ* 589:107–116
- Muzenda F, Masocha M, Misi SN (2019) Groundwater quality assessment using a water quality index and GIS: a case of Ushewokunze Settlement, Harare, Zimbabwe. *Phys Chem Earth*. <https://doi.org/10.1016/j.pce.2019.02.011>
- Panhalkar SS, Jarag AP (2016) Assessment of spatial interpolation techniques for river bathymetry generation of Panchganga river basin using geoinformatic techniques. *Asian J Geoinform* 15: 9–15. <https://www.geoinfo.ait.ac.th/ajg/index.php/journal/article/view/240>.
- Pattnaik S, Reddy MV (2009) Bioconversion of municipal (organic) solid waste into nutrient rich vermicompost by earthworms (*Eudriluseugeniae*, *Eisenia fetida* and *Perionyx excavatus*). *Dyn Soil Dyn Plant* 3:122–128
- Paul R, Brindha K, Gowrisankar G, Tan ML, Mahesh Kumar Singh MK (2019) Identification of hydrogeochemical processes controlling groundwater quality in Tripura, Northeast India using evaluation indices, GIS, and multivariate statistical methods. *Environ Earth Sci* 78:470. <https://doi.org/10.1007/s12665-019-8479-6>
- Ramadan EM, Fahmy MR, Nosair AMM, Badr AM (2019) Using geographic information system (GIS) modeling in evaluation of canals water quality in Sharkia Governorate, East Nile Delta. *Egypt Model Earth Syst Environ* 5(4):1925–1939. <https://doi.org/10.1007/s40808-019-00618-7>
- Rao YS, Jugran DK (2003) Delineation of groundwater potential zones and zones of groundwater quality suitable for domestic purposes using remote sensing and GIS. *Hydrol Sci J* 48:821–833. <https://doi.org/10.1623/hysj.48.5.821.51452>
- Ravikumar P, Mehmood MA, Somashekar RK (2013) Water quality index to determine the surface water quality of Sankey tank and Mallathahalli lake, Bangalore urban district, Karnataka, India. *Appl Water Sci* 3:247–261. <https://doi.org/10.1007/s13201-013-0077-2>
- Sanford W, Langevin C, Polemio M, Povinec P (2007) A new focus on groundwater-seawater interactions, vol 312. IAHS Publications. ISBN 978-1-901502-04-6
- Sakizadeh M (2015) Artificial intelligence for the prediction of water quality index in groundwater systems. *Model Earth Syst Environ* 2(1):8. <https://doi.org/10.1007/s40808-015-0063-9>
- Setianto A, Triandini T (2013) Comparison of kriging and inverse distance weighted (IDW) interpolation methods in lineament extraction and analysis. *J Appl Geol* 5(1):21–29. <https://doi.org/10.22146/jag.7204>
- Shakerkhatibi M, Mosafer M, Pourakbar MM, Safavi N, Banitorab F (2019) Comprehensive investigation of groundwater quality in the North-west of Iran: physicochemical and heavy metal analysis. *Groundw Sustain Dev* 8:156–168
- Sivasubramanian P, Balasubramanian N, Soundranayagam JP, Chandrasekar N (2013) Hydrochemical characteristics of coastal aquifers of Kadaladi, Ramanathapuram district, Tamilnadu, India. *Appl Water Sci* 3(3):603–612. <https://doi.org/10.1007/s13201-013-0108-z>
- Swan ARH, Sandilands M (1995) Introduction to Geological Data Analysis. Blackwell, Oxford
- Taghizadeh RF, Zare'ian M, Mahmoudi S, Heidari A, Sarmadian F (2008) Evaluation of spatial interpolation methods for determining spatial changes in groundwater quality, Rafsanjan plain. *Iran Water Sci Eng* 2:941–932
- Talebiniya M, Khosravi H, Zohrabi S (2019) Assessing the ground water quality for pressurized irrigation systems in Kerman Province, Iran using GIS. *Sustain Water Resour Manag* 5(3):1335–1344. <https://doi.org/10.1007/s40899-019-00318-1>
- Ugochukwu UC, Onuora OH, Onuora AL (2019) Water quality evaluation of Ekulu river using water quality index (WQI). *J Environ Stud* 4(1):4
- Weber D, Englund E (1992) Evaluation and comparison of spatial interpolators. *Math Geol* 24(4):381–391. <https://doi.org/10.1007/bf00891270>

Publisher's Note Springer Nature remains neutral with regard to jurisdictional claims in published maps and institutional affiliations.



Elimination of nickel (II) ions using various natural/modified clay minerals: A review

Abdul Gafoor^a, Dhanasekar^b, Sathees Kumar^a, Sankaran^c, Sivaranjani^d, Sabeena Begum^c, Zunaithur Rahman^{f,*}

^a Department of Civil Engineering, Mohamed Sathak Engineering College, Kilakarai 623 806, Tamil Nadu, India

^b Department of Civil Engineering, SRM Institute of Science and Technology, Chennai 603 203, Tamilnadu, India

^c Department of Marine Engineering, Mohamed Sathak Engineering College, Kilakarai 623 806, Tamil Nadu, India

^d Department of Civil Engineering, Vel Tech Rangarajan Dr.Saguntala R&D Institute of Science and Technology, Chennai 600 062, Tamilnadu, India

^e Department of Physics, Sethu Institute of Technology, Kariapatti 626 115, Tamil Nadu, India

^f Department of Civil Engineering, Sethu Institute of Technology, Kariapatti 626 115, Tamil Nadu, India

ARTICLE INFO

Article history:

Received 2 July 2020

Accepted 20 July 2020

Available online xxxxx

Keywords:

Wastewater

Adsorption

Nickel

Clay minerals

Natural/modified

ABSTRACT

Adsorption has proved the strongest water treatment process because of its significant advantages. Clay minerals have been used widely as adsorption to extract harmful heavy metals from the water for decades and are plentiful and inexpensive products. As addressed thoroughly in this analysis, clays and their minerals in both their normal and modified types extract nickel ions from the aqueous solution. Throughout this systematic analysis, comprehensive literature is collected from recent work over the past years and the results from adsorption experiments that clay minerals used as adsorbent. This study paper summarized the preparation of adsorbents, optimum conditions, sorbent capacity, and efficiency and desorption efficiency of many clay minerals and identified their mechanisms of adsorption behavior. The analysis demonstrates the excellent viability of both normal and modified clay minerals in extracting different harmful metal contaminants. The synthesis and the application of novel clay materials to adsorb specific contaminants, to enhance pollution protection, remains to be modified and further research.

© 2020 Elsevier Ltd. All rights reserved.

Selection and peer-review under responsibility of the scientific committee of the International Conference on Newer Trends and Innovation in Mechanical Engineering: Materials Science.

1. Introduction

Water consumption today is growing steadily due to population growth and urbanization. The measurements of used water rise exponentially with the growth of industrialization. Chemical practices contaminate the freshwater properties, and it is impossible to discover freshwater every day due to insane use. A major issue in this regard is the use of freshwater by industries and the discharge of resulting wastewaters into the environment without treatment. Also, water pollution, as well as the raw materials used and converted into waste products in these sectors, are critical environmental and economic concerns. So it needs a better care method. They are toxic to humans and other living beings in limited amounts, too [1].

The separation of radioactive metals from aqueous solutions needs many methods of treatment. Such processes may be divided into three human, mechanical, and biological assemblies. Numerous researchers have examined chemical precipitation [2], ion exchange [3], adsorption [4], membrane filtration [5], liquid membrane [6], coagulation and flocculation [7], flotation [8] and electrochemical treatment [9] among the types of expulsion Fig. 1. Alternatively, some of these recovery approaches have been implemented in real-scale applications [10,11]. The mechanisms of removal and absorption, ion exchange and adsorption are a power to be dealt with as the most common means of expelling heavy metals from wastewater [12].

Each of these approaches alluded to above have its features and provides different beneficial advantages and drawbacks. Heavy metal contaminants and degradation are the most significant environmental problems because they are extremely detrimental to life forms and not biodegradable [7]. For eg, a few industries, metal plating, clothing, cloth industry, pesticides and fertilizers, battery

* Corresponding author.

E-mail address: zunaithur@gmail.com (Z. Rahman).

<https://doi.org/10.1016/j.matpr.2020.07.500>

2214-7853/© 2020 Elsevier Ltd. All rights reserved.

Selection and peer-review under responsibility of the scientific committee of the International Conference on Newer Trends and Innovation in Mechanical Engineering: Materials Science.

Please cite this article as: A. Gafoor, Dhanasekar, S. Kumar et al., Elimination of nickel (II) ions using various natural/modified clay minerals: A review, Materials Today: Proceedings, <https://doi.org/10.1016/j.matpr.2020.07.500>



PRINCIPAL
MOHAMED SATHAK ENGINEERING COLLEGE
KILAKARAI 623 806

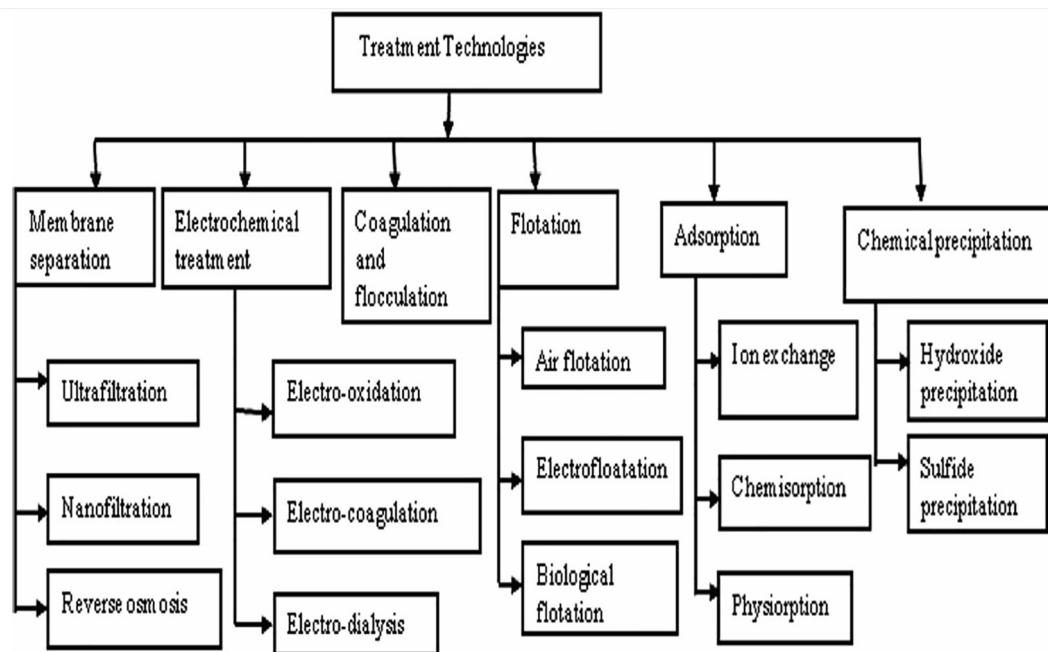


Fig. 1. Various wastewater treatment methods.

manufacturing, paint and pigment manufacturing, electrical appliances and chemical industry, and so on, manufacture wastewater including different heavy metals and even discharge their effluents into the atmosphere. Many of these utilizations, raw resources run dry, and wastewaters comprising these products by disrupting the environment contribute to basic ecological issues. For starters, heavy metals such as Pb, Hg, Cu, Cd, Ni, and Cr are the most toxic contaminants contained in wastewaters [13]. The removal and recovery of heavy metals are significant economic and ecological focal points [14].

Among such contaminants, nickel is a silver-white hue of significant carbon. It is solid, malevolent and the richest portion in the crust of the earth. The Ni(II) oxidation condition of nickel in aqueous solutions is the most significant one. Nickel increases the resilience and safety of multiple metals 'corrosion at a high temperature as it alloys with them. That is one of the nickel's most significant highlights. Nickel, its mixtures and composites are used in many new, industry applications [15]. Nickel usually exists in the sulfide, nitrate, and oxide groups in the atmosphere, rock, and ocean salts. The water level is 3 to 10 mg/L [16]. In their operations, nickel electroplating, leather tanning, battery processing, paint manufacturing, printing, power plants, ceramics, enameling, and aircraft industries use nickel [17–19]. Exorbitant application of nickel-containing goods causes severe pollution concerns. If people are subjected to environmentally polluted media with high levels of nickel, various pathological effects can occur on human safety. Such symptoms include dermatitis of touch, lung fibrosis, obesity, cardiovascular disease, and kidney disease [15]. For human usage as a standard, nickel fixation in waters should be up to 0.02 mg/L. USEPA [20] has defined the most extreme concentration of nickel in drinking waters as 0.5 mg/L. Nickel recovery and reuse is important to the recycling cycle. Ecological risks may be minimized by storing nickel. Both techniques have both benefits and limitations when researching the methods of removing nickel from water and wastewater. The emergence of certain modern experimental treatments is likely, since traditional and innovative forms of care have a few disadvantages. Adsorption one of these complementary approaches brings into account as a procedure of therapy which is traditional and environmentally sustainable.

Many adsorbents are used to remove heavy metals from soil and wastewater. In biosorption; algae, fungi, bacteria, tree and so on are used efficiently as dead-biomass for various types of heavy metal expulsion [21,22]. If the basic goal is to remove the metal particles by the usage of sorbents, biomasses will be healthy enough during the process to survive ridiculous working environments. Specific considerations, for example, the cost of supplies and care, demand, and permanent supply, play an important role in sorbent selection. A good sorbent should be convincing in large ranges of pH and temperature, should not produce secondary contaminants, and should have great solidity. Also, it will pose a reasonable take-up cap concerning specific ions, economically, without pretreatment, adjustments, device configuration, successively extract metal particles and should have easy desorption and reuse. Biomasses present in nature cannot handle such requirements. The sorbents will consequently be custom-made to satisfy the required technological requirements [23].

The object of this review is to examine the removal by adsorption of nickel ions from water and wastewater which is an important, efficient and realistic treatment method. The findings of other adsorption study studies were analyzed in this experiment to provide insight into more adsorption thoughts. Additionally, the sorption part, pH impacts, initial metal concentration, sorbent mass, equilibrium duration, and temperature were analyzed.

The quantity of metal ions sorbed by adsorbent was calculated using the following equation from the variations between the original quantity of metal ions added and the quantity remaining in the supernatant:

$$\text{Adsorbent capacity } (Q) = V (C_o - C_f) / M \quad (1)$$

$$\text{Adsorbent efficiency}(\%) = [(C_o - C_f) / C_o] * 100 \quad (2)$$

Where Q is the uptake of metal ions (mg/g), C_o and C_f are the original and final concentrations of metal ions in the solution (mg/L), V is the volume of metal solution (L) respectively, and M is the weight of added sorbent (g).

2. Adsorption of Ni(II) by various natural/modified clay

Typical natural/modified sorbent can be derived from two sources from different works of literature as follows, (i) Natural clay minerals, (ii) Modified clay minerals.

2.1. Clay minerals

Several inorganic and organic adsorbents, including zeolites, montmorillonites, clay rocks, trivalent, and tetravalent metal phosphates, have also been used for adsorption [24–37].

2.2. Natural clay minerals

Clay is a small substance that can usually be found on earth's surface, primarily made up of silica, alumina, water and weathered rock [38]. The usage of clay for more than a decade in aqueous solutions as an important adsorbent to control the poisonous metal ions is a significant reason for concern [39]. There are three primary clay groups: kaolinite, montmorillonite-smectite and mica. Montmorillonite has the largest cation exchange capacity and provides an average 20 times cheaper than activated carbon with the current selling price. Their heavy metal removal efficiency is lower than that of zeolites, but their simple availability and economical properties render them less expensive [40–42]. The usage of clay as an adsorbent in terms of cost-effectiveness, high efficiency, a very precise surface region, outstanding adsorption properties, non-toxicity and strong ion exchange capability [43]. The absorption of heavy metals by clay minerals requires other complicated processes for adsorption, including primary binding of cations of metal to the surface of clay minerals, complexation of surfaces as well as the interaction of ions [44]. For some studies the adsorption ability of clay is improved by pretreating, thus increasing metal absorption [45]. Such pre-treatment raises the surface region, the amount of pore and the number of acidic sites found on the soil [46]. In this portion, we discussed the varieties of natural minerals such as montmorillonite [47], montmorillonite and kaolinite [48], smectite [49], kaolinite [50], kaolinite and bentonite [51], bentonite [52], clinoptilolite [53,54], sericite [55], sepiolite [56], palygorskite [57], hectorite [58] and their efficiency and characteristics are described in Table 1.

Analytical grade of **montmorillonite** (MMT) has been obtained from Aldrich Chemicals. The fraction of clay passing to a 150 μm sieve was utilized as a collected, unwashed mud. The area of clay surface was estimated to be 699 m^2/g . Nickel and copper were tested as a sorbate for aqueous solutions for the surface properties of MMT as well as their adsorption functions for heavy metals. The results of heavy metal concentration, pH, MMT dose, reaction time

and temperature for Cu^{2+} and Ni^{2+} absorption have been observed in the investigation of MMT remediation potentials as a sorbent for heavy metals tainted water. The sorption of the metal ions by MMT was pH based and could well be adapted to the pseudo-second-order rate model, the sorption rate observed by adsorption kinetics. The findings based on mass transfer and intraparticle diffusion models verified the diffusion of solutes in the clay particles as a rate control step and are more important than external mass transfer for the adsorption process. Adsorption isotherms demonstrated that the absorption of Ni(II) (12.89 mg/g) and Cu(II) (7.62 mg/g) in a low pH, 0.1 g/l MMT, 100 mg/l Ni(II), and balance at 180 mins in the Langmuir model, and the positive Delta G values at different temperatures suggest that the sorption of the two metal ions can be described. Increases in enthalpy (ΔH) for Ni(II) and Cu(II) were 28.9 and 13.27 kJ / mol, respectively, resulting in an endothermic diffusion cycle, as ion absorption improved with a rise in temperature. At the sorbent/sorbate system, Delta S values indicated low randomness during both Ni(II) and Cu(II) absorption by MMT. Montmorillonite has a significant ability to extract heavy metal cationic compounds from aqueous fluid and wastewater [47]. Smectite, the same as MMT clay mineral used in this analysis by another scientist, registered a metal adsorption potential of 6.68 mg/g at a low pH of 3 to 4 [48].

Kaolinite (KT) and **Montmorillonite** (MMT), both clays were calcined at 773 K for 10 h before being used as adsorbents. The present research explores the immobilization by process of adsorption (metal ion concentration, clay volume, pH and the temperature of the interaction) of Ni(II) and Cd(II) on clays (CT and MMT), utilizing a variable selection methods. Improved pH enables the metal ions to be removed until precipitation as hydroxides becomes insoluble. The absorption is fast and the maximal adsorption is observed for Ni(II) and Cd(II) within 180 min. The kinetics and immobilization mechanism was evaluated by several functional models, including Lagergren's PFO, PSO and Elovich equation, liquid film and intraparticle diffusion. The experimental findings were well-placed by two isothermal equations credited to Langmuir and Freundlich. KT and MMT have a broad Langmuir monolayer capacity with 4–5.2 mg/g (KT) and 21.6–21.7 mg/g (MMT) for Cd(II) and Ni(II). The thermodynamic immobilization processes have Ni(II), also Cd (II) thermology of exothermic characteristics. Ni(II) interactions are distinguished by a decrease in entropy and Gibbs energy, while increased entropy and substantial reductions in Gibbs energy contribute to endothermic immovability in Cd(II). The findings demonstrated a strong ability for KT and MMT to extract heavy metals such as Cd(II) and Ni(II) from the aqueous medium by adsorption-mediated immobilization [49].

Kaolinite clay (KT) was parched at an 80 $^{\circ}\text{C}$ level of 3 h before being used as an adsorbent and measured to absorb 220 μm mesh.

Table 1
Sorption of Ni (II) by natural clay minerals.

Adsorbent	Optimum conditions (pH, dose, Ni (II) concentration, equilibrium time, temp)	Sorbent capacity (mg/g)	Adsorption efficiency (%)	Desorption efficiency (%)	References
Montmorillonite	pH 2.4, 0.1 g/l, 100 mg/l and 180 mins at 25 $^{\circ}\text{C}$	12.89	NA	NA	[47]
Montmorillonite and Kaolinite	pH 5.7, 2 g/l, 50 mg/l and 180 mins at 30 $^{\circ}\text{C}$	21.7 and 5.2	NA	NA	[48]
Smectite	pH 3–4 at 30 $^{\circ}\text{C}$	6.68	NA	NA	[49]
Kaolinite	pH 7, 25 g/l, 10 mg/l and 60 mins at 30 $^{\circ}\text{C}$	0.9	71	19.29	[50]
Kaolinite and Bentonite	pH 5, 2.5 g/l, 100 mg/l and 120 mins at 30 $^{\circ}\text{C}$	149.25 and 94.34	96.26 and 99	NA	[51]
Bentonite	pH 5.3, 0.1 g/l, 50 mg/l and 150 mins at 20 $^{\circ}\text{C}$	1.91	40	NA	[52]
Clinoptilolite	pH 7, 15 g/l, 25 mg/l and 45 mins at 20 $^{\circ}\text{C}$	1.61	93.6	96	[53]
Clinoptilolite	pH 6.2, 2.5 g/l and 20 mg/l and 30 mins	13.03	NA	NA	[54]
Sericite	pH 7.5, 10 g/l, 100 mg/l and 120 min at 30 $^{\circ}\text{C}$	44	93	100	[55]
Sepiolite	pH 7, 5 g/l, 10 mmol/l, and 24 hrs at 20–25 $^{\circ}\text{C}$	2.236	50	NA	[56]
Palygorskite	pH 7, 0.25 g/l and 20mins at 25 $^{\circ}\text{C}$	33.4	80	NA	[57]
Hectorite	pH 7–8, 2 g/l and 5 hrs at 30 $^{\circ}\text{C}$	62.24	95	NA	[58]

A power of 95 mmol/kg is given by Cation Exchange Capability (CEC). Kaolinite clay has a BET density of 3.7 m²/g. Kaolinite clay had a chemical composition of 53% SiO₂, 43.6% Al₂O₃, 2% Fe₂O₃, 0.2% MnO, 0.5% K₂O, and 0.1% TiO₂, respectively. The insulation of heavy metal ions from wastewater was tested for kaolinite clay. Thus, this analysis consists of adsorbing Ni(II) and Cu(II) in an aqueous solution to KT under special conditions (with varying metal ion concentration, clay volume, pH and time mixing) through the adsorption cycle. Higher pH allows metal ions to be ingested as insoluble hydroxides until it is precipitated. A maximal adsorption of Ni(II) (0.9 mg/g) and Cu(II) (0.5 mg/g) in a time period of 30 min is observed at 25 g/l KT, pH 7, 10 mg/l at 30 °C. Comparing the effects from the adsorption isotherm, this information might be more directly linked to the Freundlich equation than to the Langmuir equation. XRD findings have indicated that the predominant mixture of these two clays is this study of kaolinite clay. Analysis SEM pictures display peculiar morphology on the soil. Used to remove metal ions from actual wastewater, such as Ni (II), this kaolinite clay was then used, which reduced its concentration from 30 to 12 mg/L [50].

For wastewater extraction Mn(II) and Ni(II), low-cost adsorbents, such as **kaolinite** (KT) and **bentonite** (BT), were used. Effect on the removal of such metals was examined through various parameters including pH, adsorbent levels, contact length, initial concentration of the metal ion. Mn(II) and Ni(II) sorption is tested in batch mode for two water-soluble adsorbents: KT and BT. This studied the effect of pH, length of interaction, adsorbent dosage and initial metal ion concentration on adsorption. Mn(II) and Ni(II) with peak pH 5 and pH 6 values are closely sorted by adsorbents. Approximately 70% sorption was achieved for Mn(II) and Ni(II) within 20 min, with equilibrium reached at 90 min for Mn(II) and 120 min for Ni(II). The batch adsorption for Ni, 140.84 and 92.59 mg/g for Mn, which applied to KT or BT, was clarified by Freundlich and Langmuir statistical models. It was demonstrated that adsorption was efficient for all isotherms. The two metal ions adsorbed by an aqueous solution with two anticinematic adsorbents are pseudo-secondary kinetics [51].

Smectite clays are actually among the heavy metal removal clays of the most studied type of bentonite. Calcined to 500 °C for 24 h, the clay was prepared to improve mechanical strength and extract any impurities. Calcium, sodium and polycation type may be found in BT clay. The large region of BT clays (until 800 m²/g) shapes thixotropic gels. Such cations enable this drastic extension, such that a single cell may be separated into the crystal layers. The Na⁺ clay, which prevails as a cation, is known to swell in the presence of water, rising its original volume several times, as Na⁺ helps more water molecules to adsorb, increases the space between the layers, and thus eliminates each other's clay particles. The volume of adsorbed water is reduced for polycation or calcium clay, and through electrical and mass interactions the particles remain bound together. These features express special characteristics to BT that allow a large spectrum of applications across many fields. This study looks at the kinetics and dynamics of Bofe BT calcinated soil in nickel adsorption. Analysis of the clay was performed for EDX, surface area (BET) and XRD. The results of these parameters (pH, adsorbent size, temperature, and adsorbate concentration) are observed. Kinetic models for potential adsorption mechanisms have been identified. The Langmuir and Freundlich models were used for the study of the adsorption equilibrium. Thermodynamic parameters are measured as a process temperature function. The second-order approach explains the kinetic data better. The mechanism has had a major impact on the tested variables. Bofe clay consumes 1.91 mg metal/g (20 °C, pH 5.3, 0.1 g/L, and metal concentration 50 mg/l) combined adsorption capacity and thermodynamic studies have shown a spontaneous and

exothermic adsorption reaction. The Langmuir model is the perfect approach for isotherms of sorption [52].

Natural zeolites derived from the soils were obtained from **clinoptilolite** (CT). In line with the ASTM method, crushed particles were seven through a range of sieves, and this study only included particles that went through a 0.42 mm screen. Over about 15 min, the sieves were shaken and the different particles collected. Zeolite surfaces are formulated three times with filtered water such that residual salts in the equilibrium solution are not stored. The adsorbents were then cured in the oven at 85 °C for 2 h. This article discusses how Ni(II) ions are separated by CT from meal solutions. It was measured the effects of CT, touch period and pH. The concentrations of Ni(II) ions ranged from 0.1 to 100 mg/l have developed various isotherms. The second level of reaction kinetics is followed by the ion-exchange process against Langmuir's isotherm. It investigates thermodynamic parameters for ion exchange between Ni(II) and CT shows that the ion-exchange process is spontaneous and exothermic under natural conditions, including adaptations to the Gibbs free energy, entropy, and enthalpy. At 7 pH and 45 min the average removal output obtained stood at 93.6% (concentration of 25 mg/L and 15 g/L solid / liquid ratio) [53].

Approximately 75% of clinoptilolite was found in **clinoptilolite** (CT) rocks. The most widely found minerals are: granite, calcite, biotite, muscovite, chlorite, and montmorillonite. With the last one frequency, the exchange levels are Ca²⁺, Mg²⁺, Na⁺ and K⁺. Sorbent thermal equilibrium differs with steady water storage and relative humidity respectively between 923 and 973 K, with a consistent 9.03 and 10.19% capacity. Mesopores 37 and 120–230 Å in diameter are common. For raw zeolite, the total surface area was 13 m²/g. Work on sorption by single and multi-component aqueous solutions utilizing raw CT of heavy metals (Ni²⁺, Pb²⁺, and Cd²⁺) has been carried out. Sorption has an ion-exchange mechanism that consists of three stages, i.e. microcrystal surface adsorption, inversion rates which moderate microcrystal inside adsorption. Finer CT levels sorb low and low metal amounts owing to decreased zeolite enrichment. The slight variation between cadmium adsorption of the CT from one-component and multi-component systems can be shown by the different zeolite sorption centers of each drug. The reduction in the adsorption of nickel from multi-component solutions could be because of its vulnerability to other metals and its rivalries. At the first stages of 80 mg/L and 13.03 mg/g at 850 mg/L for Ni²⁺ the maximum Cd²⁺ sorption potential is 4.22 mg/g. In the versions, Langmuir and Freundlich the results of sorption are well balanced. The second is suitable for large-scale metal adsorption simulation [54].

Sericite (ST) sample was grinded and then screened with no additional care to produce a mesh of 14–16 using a mechanical sieve. BET surface area was to be 2.416 m²/g and 3.16 mequiv/100 g of ST were to be exchanged efficiency respectively. Ni(II) has been used for actual industrial wastewater. ST was used as a versatile adsorbent to remove Ni(II) from normal industrial wastewater at elevated rates of Na(I). Na(I) which generates ion intensity and maximum removal efficiency was about 93% at pH 7.5 need not have an impact on the elimination effectiveness of Ni(II). Na(I) The ST community of silanol (SiO₂) and aluminum (Al₂O₃) would possibly play a major role in the adsorption process. It took 120 min to full the full adsorption process and improved ST removal efficiency than the amberlite IR 120 plus resin. Temperature had a marginal impact on the removal output of Ni(II). HNO₃ will easily and completely explain the previously adsorbed Ni(II) to sericite. Table 1 sets out the optimal requirements and additional information [55].

This study provided a regular **sepiolite** (SP) sample. The content was used without any chemical alterations in its original state. Natural nanostructured clay adsorption potential (ST) has been

examined by batch method for inorganic organisms Ni(II) and As (V). The analysis and calculation of optimal experimental conditions included various parameters concerning sorption, such as adsorbing capacity, duration, and concentration of the sorbate and pH. In experimental results, Langmuir and Freundlich equations, which are commonly utilized to describe the equilibrium of sorption, were modeled. At pH 7, 10 mmol/l, 5 g/l, at 20–25 °C at 24 h, the average SP-to-Ni(II) and As(V) sorption was 2.236 mg/g and 0.006 mg/g. Various variables such as the ion charge and free hydration energy will explain the differences between sorption strength. This study finds that cationic sepiolite-adsorbing natural heavy metals and anionic metalloid organisms may have fascinating uses, such as recovery from polluted waters for the environment [56].

Palygorskite (PT), because of the excellent sorption properties, was used as an adsorbing agent in this research. To liquid absorption and heavy metal adsorption, PT porous and high-structure has advantages. By water, heavy metals may be contained as free ions or mixed with organic and inorganic ligands. A common element of heavy metal approaches measured the sensitivity of each PT product. Exploring the PT Deposit Investigation is the first to investigate potential uses of this tool for environmental cleaning up and remediation. The experimental use of PT clay as an adsorbent to remove ions from aqueous solutions including nickel and copper was studied. In this analysis, these metals have been tested with a room temperature batch method. The adsorption results were tested in both Langmuir and Freundlich models. A sufficient agreement between experimental results and the expected model values was described as the correlation coefficient (R^2). In contrast to the Freundlich method, the Langmuir model depicted a sorption loop, and a correlation coefficient (R^2) ranged from 0.953 to 0.994. Langmuir isothermic adsorption potential (Q_0) at a pH of 7.0 with a particle size of 125 μm at 25 °C was 33.4 mg Ni(II)/g and 30.7 mg Cu(II)/g. The degree of adsorption of metal ions was calculated through kinetic experiments. For different initial concentrations of metal ions, the first-order rate constants of Lagergren are calculated. The removal improved with a better time of touch, adsorbing volume, and pH solution in batch mode adsorption experiments. The findings of this study have demonstrated that the PT will efficiently adsorb aqueous solution metal cations in significant amounts. This opens up potential business and possible technology solutions in the PT industry [57].

The **Hectorite** (HT) is a crystalline surface form composed of the silica tetrahedron two layers and the smectite community with a centrally dioctahedral layer. It consists of two silica sheets with an octahedral core layer of Mg, 2:1 Smectitis Stone. The unfavorable charges are compensated by inorganic cations on the cement sheet. Throughout this analysis, experiments in the batch mode with HT were performed. This article discusses how Ni(II) is

recuperated by using HT clay from electroplating industry wastewater. Adsorption experiments in batch mode were performed and contact time effect, adsorbent dosage, pH, initial metal ion concentration and temperature were observed. Wastewaters of varying concentrations have been produced using nickel electroplating. The process of ion exchange observes kinetics of the second-order and Langmuir's isotherm. Including changes in Gibbs free energy, entropy and enthalpy for Ni(II) ion-exchange from electroplating wastewater on HT clay, this paper explores thermodynamic parameters and shows that the ion exchange process is spontaneous and exothermic at different temperature levels. The average adsorption potential was 62.24 mg/g at pH 7–8, and the contact periods were 5 h, for the optimum adsorbent dose and 2 g/l [58].

2.3. Modified clay minerals

Chitosan-functionalized cloisite 10A [59], bentonite [60], perlite [61–64], clinoptilolite [65], alumina [66,67], montmorillonite [68,69] and calcium alginate [70] were used for the sequestration of metals ions from wastewater. Organically modified clay nanocomposites or hierarchical porous polypyrrole nanoclusters act as a good sorbent for heavy metal ions [71–75]. Throughout this portion, we addressed varieties of changed clay minerals such as montmorillonite [76,77], bentonite [78–82], kaolinite and montmorillonite [83], kaolinite [84], and their output and characteristics are described throughout Table 2.

This study explains the kinetics of **Montmorillonite** (MMT) and Ca-exchanged heavy metal adsorption of single cation solutions and the equilibrium adsorption of Ca^{2+} cations. This study contributes to our understanding of the adsorption properties of MMT, the reactions and the effects of calcium in mineral adsorbed clay. This helps to determine the stability, action and the usage as a geochemical barrier to dangerous materials of heavy metals in the smectite environment. This research provides insights into soil metal emissions regulation and remediation. Adsorption of the Ba^{2+} , Ni^{2+} , Mn^{2+} , Cd^{2+} monocation-accompanied by second-order kinetics, Ca-montmorillonite for q_e removals higher than those of montmorillonite, Ni 73, Ba 68.15, Cd 20.03, Mn 16.32 mg/g. The Langmuir adsorption models of bimodal-metal Ca^{2+} solutions were followed by the Langmuir adsorption models with Ni 4.85, Mn 3.82 mg/g and Ca-montmorillonite with Ni 5.97 mg/g adsorbed by simple and hydroxyl cations, retaining the selectivity series $\text{Ni} > \text{Ba} > \text{Cd} > \text{Mn}$, adsorbed by clay [76].

Montmorillonite (MMT), known as parent clay, was examined without any prior examination. This clay was historically described, the surface region of the B.E.T. is 232 m^2/g . The following has been prepared for the adjusted 3-Mercaptopropyltrimethoxysilane (MMT/MPS). A sample of 7.0 g of industrial MMT clay was heated for 24 hrs for moisture extraction to 373 K under

Table 2
Sorption of Ni (II) by modified clay minerals.

Adsorbent	Modifying agent	Optimum conditions (pH, dose, Ni (II) concentration, equilibrium time, activated temp)	Sorbent capacity (mg/g)	Adsorption efficiency (%)	References
Montmorillonite	Calcium	pH 4, 2 hrs at 30 °C	73	100	[76]
Montmorillonite	3-mercaptopropyl trimethoxysilane	pH 6, 1 g/l, 100 mg/l and 15 mins at 30 °C	1.21 (MMT) and 2.18 (MMT/MPS)	NA	[77]
Bentonite	Sodium pyrophosphate	pH 6, 2 g/l, 50 mg/l and 120 mins	30.3	87.3	[78]
Bentonite	Sodium	pH 8, 5 g/l, 50 mg/l and 200 mins at 30 °C	13.96	80	[79]
Bentonite	Calcium and Sodium	pH 6, 10 g/l, 100 mg/l and 6 hrs at 22 °C	6.32 and 24.2	95	[80]
Bentonite	Chitosan	pH 4, 0.2 g/l, 200 mg/l and 60 mins at 25 °C	12.29	80	[81]
Bentonite	Crosslinked chitosan	pH 6, 0.1 g/l, 100 mg/l and 120mins at 25 °C	32.26	90	[82]
Kaolinite and Montmorillonite	Zirconium oxychloride	pH 8, 2 g/l, 150 mg/l and 40mins at 30 °C	8.8 and 22	NA	[83]
Kaolinite	tetrabutylammonium	pH 8, 2 g/l, 150 mg/l and 60 mins at 30 °C	15.23	NA	[84]

vacuum. 175 mL dry toluene and 7.0 mL MPS have been applied to the triggered mud using a three-neck ballon. To determine the effectiveness of this procedure, research was conducted on the metal retention capability of silylated modified clays. In batch removal processes MMT clay was updated with MPS. We studied the sorption cycle, the development of isotherms and adsorption kinetics and the pH effect, the desorption method and the recovery of metals. Adsorption and desorption (85%) were found to have strong retention and reasonable efficiency (2.18 mg/g) of the adjusted clay relative to raw MMT (1.21 mg/g) at pH 6. The usage of MMT/MPS as an adsorbent has seen to be more suitable in the final polishing of effluent after traditional treatment or when the initial concentration of Ni(II) in the effluent has small enough to enable for effective removal by conventional methods [77].

The normal powdered **bentonite** sample was cleaned with deionized water and dried at room temperature. The dried sample was treated with 0.01% sodium pyrophosphate solution for 24 h. The resulting NPP-bentonite was centrifuged and washed many times with deionized water, oven cleaned at 110 °C for 24 h, cooled and placed in an air-tight jar for further usage. Ni(II) adsorption from aqueous solution and electroplating wastewater was investigated from sodium pyrophosphoric (NPP-BT) based bentonite. The pH influence, adsorbent dosage, contact duration, and initial metal ion concentration were determined by the batch test. Ni(II) adsorption was achieved at pH 6 at 2 g/L, with 120 min of contact duration and 50 mg/L of initial metal ion concentration. The results of adsorption are well suited for Langmuir and Freundlich isotherm models with a 30.30 mg/g and 3.98 (mg/g)/(mg/L)^{1/n} of monolayer adsorption efficiency. The realistic application of NPP-BT as a potentially Ni(II) adsorber was demonstrated from wastewater electrical plating [78].

Sodium bentonite (Na-BT) was cured up to 24 h in the oven at 105 °C and then filtered before use by a 200 mesh sieve. The particles had a surface area of 1.5832 m²/g. The average pore volume and average pore diameter were up to 0.0091555 cm³/g and 2.3132 nm, respectively. The chemical structure of Na-bentonite is shown in Table 2. The elimination of copper and nickel from the aqueous Na-BT solution has been statistically checked. Owing

to pH, bentonite concentrations, time and temperature, tests were performed. The nickel adsorption time on the Na-BT requires 200 min. The pH-dependent adsorption of copper and nickel is 2–9 range. Best sorption was 13.96 mg/g (80%) at pH 8 and 5 g/l Na-BT at 50 mg/l metal concentration. The kinetic adsorption mechanism can be excellently represented by the kinetic equation of pseudo-second-order and the adsorbent isotherm can very well be used with regression analyses in the line of the Langmuir model [79].

Throughout this analysis, natural **Calcium bentonite** (Ca-BT) was converted from Ca-form to Na₂CO₃. The fractions < 0.1 mm of the particle size of such BTs were included. Ca-BT and Na-BT were tested for the batch sorption of Ni(II), Zn(II) for retention potentials for the type in wastewater in the galvanic industry of these metal cations. The Langmuir model described the sorption method well with a maximum sorption capacity of 6.32 mg Ni/g and 5.75 mg Zn/g for Ca-BT, 24.2 mg Ni/g and 23.1 mg Zn/g for Na-BT. Na-BT was successful in small and semi-industry experiments in wastewater purification from Ni and Acid-Zn electroplating processes. This shows that this approach is useful as an alternative to existing methods. Na-BT did not participate in Zn sorption for, on the other hand. In contrast, Na-BT was not involved in cyanide waste-water Zn sorption. Further descriptions are given in Table 2 [80].

Chitosan, small molecular weight and with 75–85% deacetylation. In 300 mL of 5% (v/v) of HCl, a magnetic plate was dissolved by stirring the 2 h solution to 300 rpm, about 5 g of chitosan. Applied gradually to the solution, bentonite (100 g) was mixed for another 3 h. Before neutralization, the solution was used with 1 N NaOH in a drop-wise process. The adsorbent has been washed with deionized water. It has been pulverized and tested in the oven at 65 °C for 24 h. Batch experiments were conducted with adsorbents in the sizes of 0.50 mm to 0.21 mm. The comparative and efficient adsorption of Ni(II) from aqueous solution utilizing bentonite immobilized chitosan (CH-BT) was examined. Adsorption results from single systems showed that the strongest matches, Ni(II) approaches Langmuir (12.29 mg/g-Ph 4 and 0.2 g/l CH-BT doses). Kinetic single-system experiments have demonstrated that

Table 3
A comparative review of Ni(II) sorption by clay minerals.

Adsorbent	Sorbent capacity (mg/g)	Efficiency (%)	References	Location of the study
Kaolinite	0.900	71	[50]	Brazil
Clinoptilolite	1.610	93.6	[53]	Turkey
Bentonite	1.910	40	[52]	Brazil
3-Mercaptopropyl trimethoxysilane modified Montmorillonite	2.180	NA	[77]	Brazil
Sepiolite	2.236	50	[56]	France
Kaolinite	5.200	NA	[48]	India
Calcium modified Bentonite	6.320	95	[80]	Spain
Smectite	6.680	NA	[49]	India
Zirconium oxychloride modified Kaolinite	8.800	NA	[83]	India
Chitosan modified Bentonite	12.290	80	[81]	Philippines
Montmorillonite	12.890	NA	[47]	Korea
Clinoptilolite	13.030	NA	[54]	Poland
Sodium modified Bentonite	13.960	80	[79]	China
Tetrabutylammonium modified Kaolinite	15.230	NA	[84]	India
Montmorillonite	21.700	NA	[48]	India
Zirconium oxychloride modified Montmorillonite	22.000	NA	[83]	India
Sodium modified Bentonite	24.200	95	[80]	Spain
Sodium pyrophosphate modified Bentonite	30.300	87.3	[78]	India
Crosslinked chitosan modified Bentonite	32.260	90	[82]	Turkey
Palygorskite	33.400	80	[57]	South Africa
Sericite	44.000	93	[55]	Korea
Hectorite	62.240	95	[58]	India
Calcium modified Montmorillonite	73.000	100	[76]	Mexico
Bentonite	94.340	99	[51]	India
Kaolinite	149.250	96.26	[51]	China

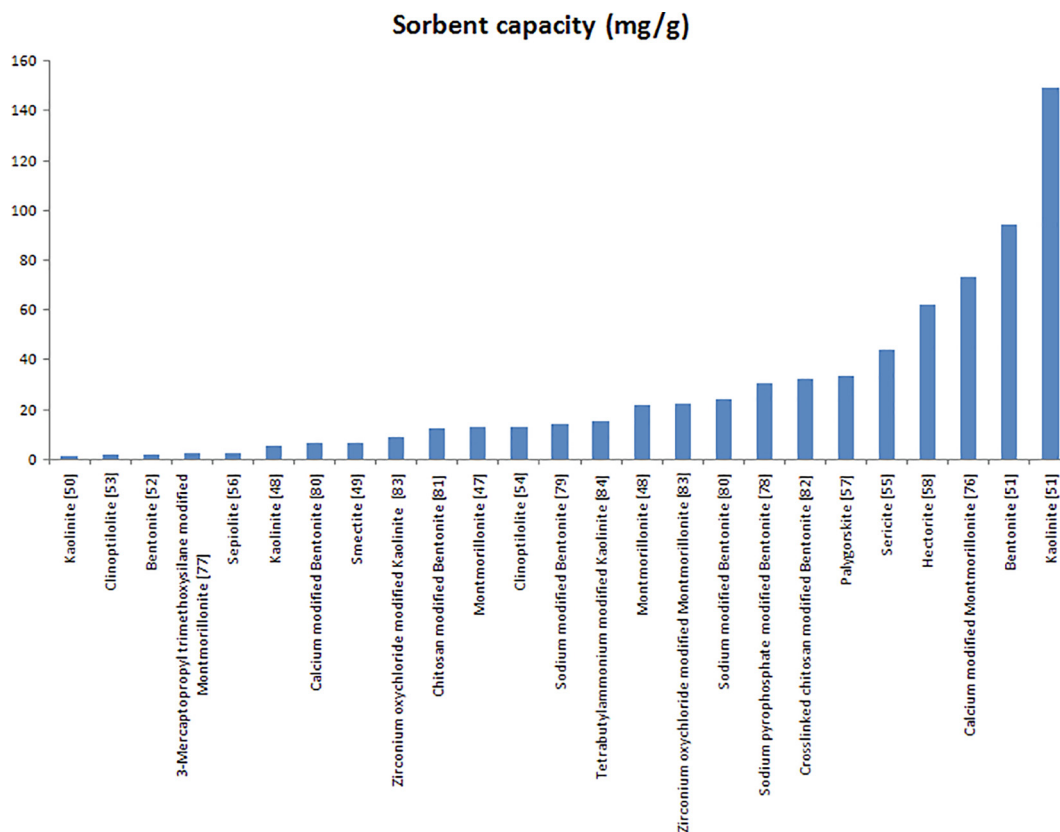


Fig. 2. A comparative review of Ni(II) sorption by clay minerals.

the pseudo-second-order is ideally matched to large correlation coefficients ($R^2 > 0.99$) and a small error magnitude of 0.13–0.46%. Thermodynamic experiments have demonstrated that CH-BT adsorption is exothermic and induces a reduction in entropy. Ni(II) adsorption is not random at 25–55 °C [81].

Chitosan, nano clay (hydrophilic bentonite, estimate particle scale 625 μm). The **epichlorohydrins crosslinked chitosan-clay** (CH-BT) were washed and rinsed with purified water and dried in the oven at 50 °C to continue their usage. The composite CH-BT beads had a particle size of 100–150 μm . In solutions indicating the contaminated substances including heavy metals, the removal of Ni(II) by adsorption of CH-BT composite beads was studied. Many essential parameters for the adsorption of Ni(II) ions were systematically tested by batch trials, such as contact duration, pH, temperature and metal concentration impact. Models of adsorption, Langmuir and Freundlich were used to define isotherm and constant adsorption. The results show that the Ni(II) equilibrium adsorption activity on the CH-BT beads can be extended to Langmuir and Freundlich. It has been estimated the absolute Ni(II) ion adsorption potential at pH 6 at 32.36 mg/g and at 120mins at 25 °C to be stabilized. The recovery of metal ions during adsorption and adsorbent regeneration was achieved using 0.1 M HNO_3 or 0.01 M EDTA in the primed beads [82].

Kaolinite clays are adjusted by treatment with zirconia oxychloride. ZrO-kaolinite (Z-KT) and ZrO-montmorillonite (Z-MMT) clay are calcinated at 773 K for 10 h before adsorbent used. This research investigates the reduction of metal ions like iron, cobalt, and nickel in aqueous solution in the form of zirconia oxychloride to the help of KT and MMT. In various environmental conditions, the research is conducted by comparing the pH, metal ion concentration, adsorbent volume, contact time and temperature. Adsorption is quick to a level of equilibrium within 300 min-Fe (III), Co(II)-240 min and Ni(II)-180 min. Second-order kinetics

provides an understanding of the rating process, and for all metal ions, Z-MMT has a greater adsorption rate than Z-KT. The monolayer potential of Langmuir also reveals significant variations between Z-KT and Z-MMT, the mean values for Z-KT and Z-MMT are 8.8 and 22.0 mg g⁻¹ for Ni(II) respectively at pH 8 and dose 2 g/l, the mean values for Ni ion concentration 50 mg/l and the equilibrium at 30 °C within 40 min. Z-KT communicates directly with Ni(II). The findings demonstrated a strong ability for ZrO-clays to be used as adsorbents for Ni(II) ions in aqueous media [83]. Another scientist researched modified kaolinite with tetrabutylammonium providing a strong adsorption potential (15.23 mg/g) for nickel removal in wastewater [84].

The Review briefly explained about the properties, removal characters of natural and modified clay minerals and comparative results are shown in Table 3 and Fig. 2.

3. Conclusion

Clay, a highly efficient adsorbent substance that is inexpensive, accessible locally, would undoubtedly offer many exciting benefits for the future. The enormous surface area and charge, strong adsorption ability, individuality, and physical and chemical properties of the clay minerals which can be seen in future investigations. Clay minerals have space within their layers and adsorb harmful metals found in water molecules. Most of the clay minerals can swell to accommodate both adsorbed water and the ionic species and increase the space between their layers. A variety of clay adsorbents were closely studied to reduce the usage of expensive adsorbents. In several of the papers, adsorption research was performed using batch studies which verified its applicability and selectivity and recorded maximum adsorption capacities about particular contaminants. Some of the clay products have demonstrated an impressive capacity to extract metal particles; however,

as mentioned in this study, their capacity to extract them is enhanced during certain experiments by other chemical modifications. The adsorption properties thus often depend on the degree to which the adsorbent is handled, enabled and changed. This review is ideally insightful enough to include innovations of clay minerals used as adsorbent. Furthermore, if suitable adsorbents and technologies are selected that are highly successful for the elimination of heavy metals and a safe environment, they will also lead to a healthy world and safeguard human safety, which ultimately leads to more promising approaches for a secure, clean future.

Declaration of Competing Interest

The authors declare that they have no known competing financial interests or personal relationships that could have appeared to influence the work reported in this paper.

Acknowledgement

The authors wish to acknowledge, Principal and Head of the Civil Engineering Department of Sethu Institute of Technology, Kariapatti, Tamilnadu, India and Mohamed Sathak Engineering College, Kilakarai, Tamilnadu, India for support and guide to prepare this research article successfully.

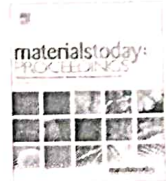
References

- [1] A.H. Abd, E. Hameed, W.E. Eweda, K.A.A. Abou-Taleb, H.I. Mira, *Ann. Agric. Sci.* 60 (2015) 1–7.
- [2] M.S. Oncel, A. Muhcu, E. Demirbas, M. Kobya, *J. Environ. Chem. Eng.* 1 (2013) 989–995.
- [3] M.A.P. Cechinel, D.A. Mayer, T.A. Pozdniakova, L.P. Mazur, R.A.R. Boaventura, A. A.U. de Souza, S.M.A.G.U. de Souza, V.J.P. Vilar, *Chem. Eng. J.* 286 (2016) 1–15.
- [4] L. Zhang, Y. Zeng, Z. Cheng, *J. Mol. Liq.* 214 (2016) 175–191.
- [5] Y. Huang, D. Wu, X. Wang, W. Huang, D. Lawless, *X. Feng, Sep. Purif. Technol.* 158 (2016) 124–136.
- [6] L. Gürel, L. Altaş, H. Büyükgüngör, *Environ. Eng. Sci.* 22 (2005) 411–420.
- [7] F. Fu, Q. Wang, *J. Environ. Manag.* 92 (2011) 407–418.
- [8] H. Al-Zoubi, K.A. Ibrahim, K.A. Abu-Sbeih, *J. Water Process Eng.* 8 (2015) 19–27.
- [9] J. Lu, Y. Li, M. Yin, X. Ma, S. Lin, *Chem. Eng. J.* 267 (2015) 86–92.
- [10] M. Arjomandzadegan, P. Rafiee, M.K. Moraveji, M. Tayebon, *Asian Pac. J. Trop. Med.* 7 (2014) S194–S198.
- [11] L.C. Shen, A. Lo, X.T. Nguyen, N.P. Hankins, *Sep. Purif. Technol.* 159 (2016) 169–176.
- [12] B. Fil, R. Boncukcuoğlu, A.E. Yılmaz, S. Bayar, 2012b. *Korean J. Chem. Eng.* 29, 1232–1238.
- [13] T. Bahadır, G. Bakan, L. Altaş, H. Buyukungor, *Enzyme Microb. Technol.* 41 (2007) 98–102.
- [14] M.M. Montazer-Rahmati, P. Rabbani, A. Abdolali, A.R. Keshtkar, *J. Hazard. Mater.* 185 (2011) 401–407.
- [15] V. Coman, B. Robotin, P. Ilea, *Resour. Conserv. Recycl.* 73 (2013) 229–238.
- [16] D. Prithviraj, K. Deboleena, N. Neelu, N. Noor, R. Aminur, K. Balasaheb, M. Abul, *Ecotoxicol. Environ. Saf.* 107 (2014) 260–268.
- [17] I. Aloma, M.A. Martin-Lara, I.L. Rodriguez, G. Blazquez, M. Calero, *J. Taiwan Inst. Chem. Eng.* 43 (2012) 275–281.
- [18] A. Bhatnagar, A.K. Minocha, *Colloids Surfaces B Biointerfaces* 76 (2010) 544–548.
- [19] R.M. Kulkarni, K.V. Shetty, G. Srinikethan, *J. Taiwan Inst. Chem. Eng.* 45 (2014) 1628–1635.
- [20] Y.F. Lam, L.Y. Lee, S.J. Chua, S.S. Lim, S. Gan, *Ecotoxicol. Environ. Saf.* 127 (2016) 61–70.
- [21] C.E. Borba, R. Guirardello, E.A. Silva, M.T. Veit, C.R.G. Tavares, *Biochem. Eng. J.* 30 (2006) 184–191.
- [22] W.C. Kao, C.C. Huang, J.S. Chang, *J. Hazard. Mater.* 158 (2008) 100–106.
- [23] K. Vijayaraghavan, R. Balasubramanian, *J. Environ. Manage.* 160 (2015) 283–296.
- [24] D. Mohan, C.U. Pittman, *J. Hazard. Mater.* 142 (2007) 1.
- [25] G.B. Samiey, C. Cheng, J. Wu, *Materials* 7 (2014) 673.
- [26] Z. Geng, Y. Lin, X. Yu, Q. Shen, L. Ma, Z. Li, N. Pan, X. Wang, *J. Mater. Chem* 22 (2012) 3527.
- [27] G. Crini, *Prog. Polym. Sci.* 30 (2005) 38.
- [28] P.X. Sheng, Y. Ting, J.P. Chen, L. Hong, *J. Colloid Interf. Sci.* 275 (2004) 131.
- [29] G. Abid, A. Jrad, K. Nahdi, M.T. Ayadi, *Desalination* 246 (2009) 595.
- [30] H. Tamai, T. Kakiy, Y. Hirota, T. Kumamoto, H. Yasuda, *Chem. Mater* 8 (1996) 454.
- [31] K. Mangold Weidlich, K. Juttner, *Electrochim. Acta* 47 (2001) 741.
- [32] M.M. Abdi, A. Kassim, H.N.M.E. Mahmud, W.M.M. Yunus, Z.A. Talib, A.R. Sadrolhosseini, *J. Mater. Sci.* 44 (2009) 3682.
- [33] H. Zhao, W. Price, P. Teasdale, G.G. Wallace, *React. Polym.* 23 (1994) 213.
- [34] T. Yao, C. Wang, J. Wu, Q. Lin, H. Lv, K. Zhang, et al., *J. Colloid Interf. Sci.* 338 (2009) 573.
- [35] H.T. Lee, Y.C. Liu, L.H. Lin, *J. Polym. Sci. Pol. Chem.* 44 (2006) 2724.
- [36] V. Truong, P. Lai, B. Moore, R. Muscat, M. Russo, *Synthetic Met.* 110 (2000) 7.
- [37] H.N.M.E. Mahmud, A. Kassim, Z. Zainal, W.M.M. Yunus, *J. Appl. Polym. Sci.* 100 (2005) 4107.
- [38] B.A. Kennedy, second ed., Port City Press, 1990.
- [39] B.M. Das, first ed., Cram101 Inc., Publication and services, 2012.
- [40] T. Vengris, R. Binkiene, A. Sveikauskaitė (2001) *Appl. Clay Sci.* 18:183–90.
- [41] M. Solenera, S. Tunalib, A.S. Özcan, A. Özcan, T. Gedikbey, *Desalination* 223 (2008) 308–322.
- [42] S.I. Abu-Eishah, *Appl. Clay Sci.* 42 (2008) 201–205.
- [43] G. Crini, P.-M. Badot, Presses Univ. Franche-Comté (2010).
- [44] G.J. Churchman, W.P. Gates, B.K.G. Theng, G. Yuan, in F. Bergaya, B.K.G. Theng, G. Lagaly (Eds.), *Development in Clay Science*, vol. 1, Elsevier Press, 2006.
- [45] D.W. O'Connell, C. Birkinshaw, T.F. O'Dwyer, *Bioresour. Technol.* 99 (2008) 6709–6724.
- [46] S. Ismadji, F.E. Soetaredjo, A. Ayucitra, *Clay Materials for Environmental Remediation*, in Springer Briefs in Green Chemistry for Sustainability, <http://dx.doi.org/10.1007/978-3-319-16712-1_1>.
- [47] C.O. Ijagbemi, M.H. Baek, D.S. Kim, *J. Hazard. Mater.* 166 (2009) 538–546.
- [48] J.K. Mbadcam, S. Dongmo, D.D. Ndaghu, *Int. J. Curr. Res.* 4 (2012) 162–167.
- [49] S.S. Gupta, K.G. Bhattacharyya, *J. Environ. Manage.* 87 (2008) 46–58.
- [50] M.Q. Jiang, X.Y. Jin, X.Q. Lu, Z.L. Chen, *Desalination* 252 (2010) 33–39.
- [51] B. Sathyanarayana, K. Sheshaiah, *Eur. J. Chem.* 8 (2011) 373–385.
- [52] M.G.A. Vieira, N.A.F. Almeida, M.L. de-Gimenes, M.G.C. Silva, *J. Hazard. Mater.* 177 (2010) 362–371.
- [53] M.E. Argun, *J. Hazard. Mater.* 150 (2008) 587–595.
- [54] M. Sprynskyy, B. Buszewski, A.P. Terzyk, J. Namiesnik, *J. Colloid Interface Sci.* 304 (2006) 21–28.
- [55] K. Taik-Nam, J. Choong, *J. Ind. Eng. Chem.* 19 (2013) 68–72.
- [56] S. Ansanay-Alex, C. Lomenech, C. Hurel, N. Marmier, *Int. J. Nanotechnol.* 9 (2012) 204–215.
- [57] H. Potgieter, S.S. Potgieter-Vermaak, P.D. Kalibantonga, *Miner. Eng.* 19 (2006) 463–470.
- [58] V. Ramamurthi, P.G. Priya, S. Saranya, C.A. Basha, *Mod. Appl. Sci.* 3 (2009) 37–51.
- [59] S. Pandey, S.B. Mishra, *J. Colloid Interface Sci.* 361 (2011) 509–520.
- [60] C.M. Futralan, W.-C. Tsai, S.-S. Lin, K.-J. Hsien, M.L. Dalida, M.-W. Wan, *Sustain. Environ. Res.* 22 (2012) 345–355.
- [61] S. Hasan, A. Krishnaiah, T.K. Ghosh, D.S. Viswanath, V.M. Boddu, E.D. Smith, *Sep. Sci. Technol.* 38 (2003) 3775–3793.
- [62] S. Kalyani, J.A. Priya, P.S. Rao, K. Abburi, *Sep. Sci. Technol.* 40 (2005) 1483–1495.
- [63] S. Hasan, A. Krishnaiah, T.K. Ghosh, D.S. Viswanath, V.M. Boddu, E.D. Smith, *Ind. Eng. Chem. Res.* 45 (2006) 5066–5077.
- [64] S. Hasan, T.K. Ghosh, D.S. Viswanath, V.M. Boddu, *J. Hazard. Mater.* 152 (2008) 826–837.
- [65] M.V. Dinu, E.S. Dragan, *Chem. Eng. J.* 160 (2010) 157–163.
- [66] M.R. Gandhi, N. Viswanathan, S. Meenakshi, *Int. J. Biol. Macromol.* 47 (2010) 146–154.
- [67] V.M. Boddu, K. Abburi, J.L. Talbott, E.D. Smith, *Environ. Sci. Technol.* 37 (2003) 4449–4456.
- [68] D. Fan, X. Zhu, M. Xu, J. Yan, *J. Biol. Sci.* 6 (2006) 941–945.
- [69] N. Bleiman, Y.G. Mishaal, *J. Hazard. Mater.* 183 (2010) 590–595.
- [70] Y. Vijaya, S.R. Popuri, V.M. Boddu, A. Krishnaiah, *Carbohydr. Polym.* 72 (2008) 261–271.
- [71] T. Yao, T. Cui, J. Wu, Q. Chen, S. Lu, K. Sun, *Polym. Chem.* 2 (2011) 2893.
- [72] H. Javadian, M. Taghavi, *Appl. Surf. Sci.* 289 (2014) 487.
- [73] U. Baig, R.A.K. Rao, A.A. Khan, M.M. Sanagi, M.A. Gondal, *Chem. Eng. J.* 280 (2015) 494.
- [74] C.W. Lim, K. Song, S.H. Kim, *J. Ind. Eng. Chem.* 18 (2012) 24.
- [75] M. Shafiabadi, A. Dashti, H.A. Tayebi, *Synthetic Met.* 212 (2016) 154.
- [76] L. De-Pablo, M.L. Chavez, M. Abatal, *Chem. Eng. J.* 171 (2011) 1276–1286.
- [77] W.A. Carvalho, C. Vignado, J. Fontana, *J. Hazard. Mater.* 153 (2008) 1240–1247.
- [78] B.N. Sandeep, S. Suresha, *Int. J. Environ. Sci.* 4 (2013) 113–122.
- [79] L. Zhi-Rong, Z. Shao-qi, *Proc. Saf. Environ. Protect.* 88 (2010) 62–66.
- [80] E. Alvarez-Ayuso, A. Garcia-Sanchez, *Clays Clay Miner.* 51 (2003) 475–480.
- [81] C.M. Futralan, C.C. Kan, M.L. Dalida, K.J. Hsien, C. Pascua, M.W. Wan, *Carbohydr. Polym.* 83 (2011) 528–536.
- [82] V.N. Tirtom, A. Dincer, S. Becerik, T. Aydemir, A. Celik, *Chem. Eng. J.* 197 (2012) 379–386.
- [83] K.G. Bhattacharyya, S.S. Gupta, *Colloids Surf. A* 317 (2008) 71–79.
- [84] K.G. Bhattacharyya, S.S. Gupta, *Appl. Clay Sci.* (2009) 46216–46221.



ELSEVIER

Materials Today: Proceedings

journal homepage: www.elsevier.com/locate/matpr

Strength and ductility behaviour of FRC beams strengthened with externally bonded GFRP laminates

Jagadheeswari ^a, Sivarethinamohan ^b, Muthumari ^c, Ramalakshmi ^c, Ilayaraja ^c, Zunaithur Rahman ^{d,*}^a Department of Civil Engineering, K.Ramakrishnan College of Technology, Trichy 621 112, Tamil Nadu, India^b Department of Professional Studies, CHRIST (Deemed to be University), Bangalore 560 029, Karnataka, India^c Department of Civil Engineering, Mohamed Sathak Engineering College, Kilakarai 623 806, Tamil Nadu, India^d Department of Civil Engineering, Sethu Institute of Technology, Kariapatti 626 115, Tamil Nadu, India

ARTICLE INFO

Article history:

Received 5 August 2020

Accepted 18 August 2020

Available online xxx

Keywords:

Fiber-reinforced polymer composites

Deflection

Ultimate load-carrying capacity

Ductility

GFRP Laminate

ABSTRACT

The repair and rehabilitation of structural members are perhaps one of the most crucial problems in civil engineering applications. One of the advanced techniques of strengthening the reinforced concrete members is done by fiber-reinforced polymer composites. FRP is very effective to repair and strengthen the structural members that have become structurally weak over their life span. FRP repair system provides an economically viable alternative to traditional repair systems and materials. This experimental study focuses on the flexural strengthening of fiber reinforced concrete beams externally bonded with FRP laminates of different thicknesses. Six beams were cast for the study and tested under a four-point bending system. Out of which two beams were served as a control beam, one beam was considered as a reinforced concrete beam and the other was fiber reinforced concrete beam. The fibers used in this investigation were steel fiber. The beams were strengthened with GFRP of 3 mm and 5 mm of woven roving type. The study parameters of this investigation included yield load, ultimate load, deflection, yield load deflection, ultimate load deflection, deflection ductility, energy ductility, and the beam was found to be very effective in the load-carrying capacity, deflection, and ductility when compared to the control specimen. The fiber-reinforced concrete beam exhibit an increase in ultimate deflection by 79.3% when compared to the control specimen. GFRP strengthened beams showed an increase in ultimate deflection by 18.75% to 94.06%. GFRP strengthened fiber reinforced concrete beams showed an increase in ultimate deflection by 7.8 to 13.125%. GFRP strengthened beams showed an increase in ultimate deflection by 54.7% to 81.88%. GFRP strengthened fiber reinforced concrete beams showed an increase in ultimate load-carrying capacity by 36.9% to 48.7%. The ductility for the specimens increases by 1.27% to 1.34%, compared to the controlled specimen.

© 2020 Elsevier Ltd. All rights reserved.

Selection and peer-review under responsibility of the scientific committee of the International Conference on Newer Trends and Innovation in Mechanical Engineering: Materials Science.

1. Introduction

Reinforced Concrete (RC) is considered as the foremost civil engineering materials due to the versatility of its applications, popularity of occurrence, and easy production technology [1,2]. With the growing demand for concrete, new challenges have been posed to concrete technologists the strong emphasis has been laid on "quality concrete" that has characteristics such as high early strength, high performance, and shorter construction in time [3].

The repair and rehabilitation of structural members are perhaps one of the most crucial problems in civil engineering applications. The structures designed constructed in the past were by the older design. Codes in a different part of the world are structurally unsafe according to the new design codes [4,5]. Infrastructure decay caused by the premature deterioration of buildings and structure has lead to the investigation of several processes for repairing or strengthening purposes [6]. One of the challenges in the strengthening of the concrete structure is the selection of a strengthening method that will enhance strength and serviceability of the structure while addressing limitations such as constructability, building operations, and budget structural

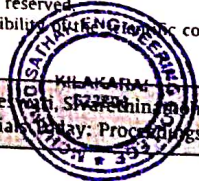
* Corresponding author.

E-mail address: zunaithur@gmail.com (Z. Rahman).<https://doi.org/10.1016/j.matpr.2020.08.491>

2214-7853/© 2020 Elsevier Ltd. All rights reserved.

Selection and peer-review under responsibility of the scientific committee of the International Conference on Newer Trends and Innovation in Mechanical Engineering: Materials Science.

Please cite this article as: Jagadheeswari, Sivarethinamohan, Muthumari et al., Strength and ductility behaviour of FRC beams strengthened with externally bonded GFRP laminates, Materials Today: Proceedings, <https://doi.org/10.1016/j.matpr.2020.08.491>



PRINCIPAL
MOHAMED SATHAK ENGINEERING COLLEGE
KILAKARAI 623 806

strengthening may be required due to many different situations [7,8].

The urgent need to strengthen concrete structures is on the rise. Various motivations lead to an increased demand for strengthening [9]. During the past two decades, the use of FRP as strengthening material on concrete structures has attracted world-wide interest in both practical applications and research. The use of Fiber Reinforced Polymers (FRP) as strengthening material has been gaining the interest of many researchers for the last two decades [10,11]. Various FRP materials are superior to steel in terms of resistance to electrochemical corrosion, strength to weight ratio, ease of handling, and fatigue resistance. The successful use of FRP in many industries like aerospace, sports, automobiles, and structural rehabilitation helped in decreasing the FRP cost [12]. This decrease in cost, combined with savings due to the elimination of future maintenance and repair costs, makes the application of FRP economically competitive with steel. Ductility is a structural design requirement in most design codes. In steel-reinforced concrete structures, ductility is defined as the ratio of ultimate deformation to yield deformation [13,14]. The most important aspect of ductility is a precaution of structural failure. A ductile structure can provide an advanced warning before failure.

The following objectives are followed in the experimental work,

- To assess the effect of FRP laminates as a retrofitting technique for the RCC beam and FRC beam.
- To evaluate the effect of FRP laminates on strengthened and Deflection of the strengthened beams.
- To examine the ductility of FRP strengthened beams.
- To understand the failure modes of strengthened and non Strengthened beams.

2. Material used

2.1. Cement

OPC 43 grade used in this investigation. The specific gravity of the cement is 3.15.

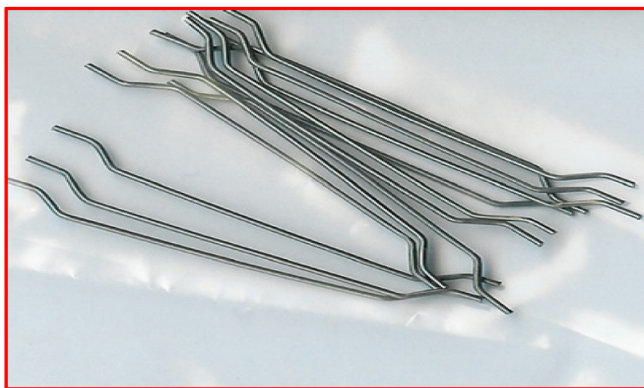


Fig. 1. Steel fiber.

Table 1
Properties of GFRP.

Type of GFRP	Thickness (mm)	Elasticity Modulus (MPa)	Ultimate Elongation (%)	Tensile Strength (MPa)
Chopped	3	7467.46	1.69	126.20
Strand Mat	5	11386.86	1.37	156
Uni-Directional	3	13965.63	3.02	446.90
Cloth	5	17365.30	2.60	451.50

2.2. Fine aggregate

Specific gravity of fine aggregate is 2.50 and Bulk Density of the aggregate 1302 Kg/m³.

2.3. Coarse aggregate

Maximum size of the coarse aggregate used is 20 mm and the specific gravity of the coarse aggregate is 2.66. Bulk Density of the coarse aggregate 1393Kg/m³.

2.4. Steel fiber

The size of the steel fiber is about 12 mm shown in Fig. 1. Yield strength is about 43.2 Mpa.

2.5. GFRB laminates

Glass Fiber Reinforced Polymer (GFRP) laminates were used for strengthening the beams. The soffit of the beam was well cleaned with a wire brush and roughened with a surface-grinding machine. Two-part epoxy adhesive consisting of epoxy resin and silica filler was used to bond the GFRP laminates. The adhesive was spread over the pasting surface with the help of a spread. The GFRP laminate was applied gently by pressing the sheet from one end of the beam to the other along the length of the beam [15,16]. The density of GFRP laminates ranges from 1200–2100 kg/m³ the coefficient of thermal expansion in longitudinal direction ranges from 6 to $10 \times 10^{-6}/c$ and in the transverse direction 19 to $23 \times 10^{-6}/c$. Table 1 showed the properties of GFRP laminates.

3. Mix design

Mix design is the most important aspect to achieve a specified strength on concrete. It is the process of determining the proportion of the ingredients to be used in the study. In this study, we use the M₃₀ grade of concrete.

3.1. Design stipulations

Mix proportioning is the process of determining the quantities of concrete ingredients that meet the mix design criteria. The mix proportion for M30 grade concrete for our requirement is as follows in Tables 2 and 3.

Table 2
Characteristics of a concrete mixture.

Grade of concrete	M ₃₀
Characteristic compressive Strength at 28 days	30 N/mm ²
Maximum size of aggregate	20 mm
Degree of workability	90 mm
Degree of control	Good
Type of exposure	Mild

Table 3
Mix proportion of concrete.

Water	Cement	Fine aggregate	Coarse aggregate	Super plasticizers
0.38	1	1.02	2.226	0.5%



Fig. 2. Reinforcement cage and Casted beam.

4. GFRP laminates

4.1. Reinforcement

The reinforced concrete beam specimens having a 150 mm × 300 mm cross-section and 2000 mm in length were cast for the study. The beams were reinforced with two bars of 10 mm diameter at the compression face and two bars of 12 mm diameter at the tension face. Shear reinforcement consists of 8 mm diameter stirrups at 150 mm spacing are shown in Fig. 2.

4.2. Strengthening of specimen

Glass fiber reinforced polymer was used to retrofit the beam in the tension region. The beam surface was made rough and cleaned. A primer was first applied on the concrete surface. An isophthalic polyester resin was applied to the concrete surface as a base coat and GFRP is bonded. The beam was strengthened by providing the 3 mm thickness and 5 mm thickness of the GFRP sheets. The wrapped beams were cured for 7 days. The strengthening of the test specimen is showing in Fig. 3.



Fig. 3. GFRP Laminate.

5. Results and discussion

5.1. Results at various stages of loading

A total number of six beams were cast and tested under a four-point bending test. The investigation is mainly focused on the strength, deflection, and ductility of the retrofitted beams. The performance of non-strengthened and strengthened beams was evaluated by considering the non-strengthened beam as reference. Typical failure modes of tested beam specimens were observed and presented.

The fiber-reinforced concrete beam V₂ exhibits an increase in ultimate load by 28% when compared to the control specimen V₁ showed in Table 4. GFRP strengthened beams showed an increase in ultimate load by 13% and 63% respectively for V₃ and V₄ when compared to the control beam V₁. GFRP strengthened fiber reinforced concrete beams showed an increase in ultimate load-carrying capacity by 35.5% and 95% respectively for V₅ and V₆.

Table 4
Test results on various loading.

Specimen	First Crack Load (KN)	Yield Load (KN)	Ultimate Load (KN)
V ₁	15	20.44	52.36
V ₂	12	27.44	67.06
V ₃	20	20.02	59.64
V ₄	28	47.32	85.82
V ₅	28.98	28.28	70.98
V ₆	20	42.56	102.48

GFRP strengthened beams showed an increase in ultimate load by 5% and 52% respectively for V₅ and V₆ when compared to the control beam V₂.

5.2. Deflection of beam

The fiber-reinforced concrete beam V₂ exhibits an increase in ultimate deflection by 79.3% when compared to the control specimen V₁, shown in Table 5. GFRP strengthened beams showed an increase in ultimate deflection by 18.75% and 94.06% respectively

Table 5
Test Results on Deflection.

Specimen	First Crack Deflection (mm)	Yield Load Deflection (mm)	Ultimate Load Deflection (mm)
V ₁	4.1	7.1	32.0
V ₂	2.3	10	57.4
V ₃	6.8	4.5	26.0
V ₄	5.6	10.7	62.1
V ₅	6.0	6.0	36.2
V ₆	3.6	5.1	29.5

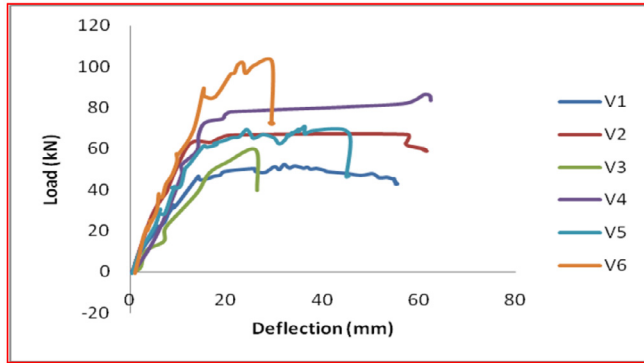


Fig. 4. Load vs Deflection for all beam.

for V₃ and V₄ when compared to the control beam V₁. GFRP strengthened fiber reinforced concrete beams showed an increase in ultimate deflection by 13.125% and 7.8% respectively for V₅ and V₆.

GFRP strengthened beams showed an increase in ultimate deflection by 54.7% and 81.88% respectively for V₃ and V₄ when compared to the control beam V₂. GFRP strengthened fiber reinforced concrete beams showed an increase in ultimate load-carrying capacity by 36.9% and 48.7% respectively for V₅ and V₆.

From above Fig. 4, it is found that Yield load of RCC control beam is 47KN and the maximum central deflection measured is 17.4 mm whereas 3 mm GFRP wrapped beam performs better than control RCC beam i.e. yield load is of about 48 KN with less maximum central deflection (16 mm) and 5 mm GFRP wrapped beam performs much better than RCC control beam and 3 mm GFRP wrapped beam, its yield load is about 72.5 KN and the central deflection measured is 15 mm. This reveals that GFRP wrapped beams are higher flexural capacity than that of control beam moreover slighter increase in the thickness of GFRP have a greater influence of increasing the flexural capacity of the beam.

There is an appreciable increase found in steel FRP added beam than control RCC beam, its yield load is of about 59 KN with 13 mm maximum central deflection. FRP added beams were compared

Table 6
Ductility of beam.

Specimen	Yield deflection (Δ_y)	Ultimate Deflection (Δ_u)	Deflection Ductility	Deflection ductility Ratio
V ₁	7.1	32	4.5	1
V ₂	10	57.4	5.74	1.27
V ₃	4.5	26	5.77	1.28
V ₄	10.7	62.1	5.80	1.28
V ₅	6	36.2	6.03	1.34
V ₆	5.1	29.5	5.78	1.28

with GFRP wrapped beam with varying thickness and it was found that steel FRP beam wrapped with 3 mm GFRP has a yield point of same that of steel FRP beam whereas 5 mm GFRP has a marginal increase in yield point (68 KN) than that of steel FRP beam but the ultimate load-carrying capacity is almost twofold. This exhibits that steel FRP with 5 mm wrapped beams performs higher flexural and loading carrying capacity than other beams.

5.3. Ductility of beam

Table 6 shows that the deflection ductility for the specimens V₂, V₃, V₄, V₅, V₆ increased by 1.27%, 1.28%, 1.28%, 1.34%, 1.28% compared to controlled specimen V₁. Table 6 shows that the deflection ductility for the specimens V₃, V₄, V₅, V₆ increased by 1.005%, 1.01%, 1.05%, 1.00% compare to controlled specimen V₂.

6. Conclusion

GFRP strengthened fiber reinforced concrete beam was found to be very effective in the load-carrying capacity, deflection, and ductility when compared to the control specimen. The GFRP strengthened fiber reinforced concrete beam V₆ showed an increase in ultimate load-carrying capacity by 95% compared to the control specimen. The retrofitted specimen V₆ exhibits an increase in ultimate deflection by 81.88% compared to the respective control specimen V₁. The GFRP strengthened fiber reinforced concrete beam exhibit a maximum increase of 6.03% in ductility. All the beams were failed due to the yielding of steel reinforcement. The rupture and debonding of FRP were observed on the strengthened beam.

Declaration of Competing Interest

The authors declare that they have no known competing financial interests or personal relationships that could have appeared to influence the work reported in this paper.

References

- [1] R.H.F. Souza, J. Appleton, Behaviour of shear-strengthened reinforced concrete beams, *J. Mater. Struct. Constr.* 30 (1997) 81–86.
- [2] F. Altun, An experimental study of the jacketed reinforced-concrete beams under bending, *J. Constr. Build. Mater.* 18 (2004) 611–618.
- [3] H.K. Cheong, N. MacAlevey, Experimental behavior of jacketed reinforced concrete beams, *J. Struct. Eng.* 126 (2000) 692–699.
- [4] H.A. Toutanji, W. Gómez, Durability characteristics of concrete beams externally bonded with FRP composite sheets, *J. Cem. Concr. Compos.* 19 (1997) 351–358.
- [5] O. Buyukozturk, B. Hearing, Failure behavior of precracked concrete beams retrofitted with FRP, *J. Compos. Constr.* 2 (1998) 138–144.
- [6] T. Triantafillou et al., Externally bonded FRP reinforcement for RC structures, *Int. Feder. Struct. Concr.* (2001) 75–95.
- [7] A. Naaman, H. Reinhardt, High performance fiber reinforced cement composites HPRC-4: International workshop Ann Arbor, Michigan, June 16–18, 2003, *J. Cem. Concr. Compos.* 26 (6) (2004) 757–759.
- [8] V.C. Li, H. Stang, H. Krenchel, Micromechanics of crack bridging in fibre-reinforced concrete, *J. Mater. Struct.* 26 (1993) 486–494.
- [9] A. Hemmati, A. Kheyroddin, M.K. Sharbatdar, Increasing the flexural capacity of RC beams using partially HPRC layers, *J. Comput. Concr.* 16 (2015) 545–568.
- [10] M.A. Abbaszadeh, M.K. Sharbatdar, A. Kheyroddin, Performance of two-way RC slabs retrofitted by different configurations of high performance fibre reinforced cementitious composite strips, *J. Open Civ. Eng. J.* 11 (2017) 650–663.
- [11] M.M. Fallah, M.K. Sharbatdar, A. Kheyroddin, Experimental strengthening of the twoway reinforced concrete slabs with high performance fiber reinforced cement composites (HPRC) prefabricated sheets, *J. Rehabil. Civ. Eng.* 7 (2019) 1–17.
- [12] A.E. Naaman, H.W. Reinhardt, Proposed classification of HPRC composites based on their tensile response, *J. Mater. Struct.* 39 (2007) 547–555.
- [13] V.J. Ferrari, J.B. De Hanai, R.A. De Souza, Flexural strengthening of reinforcement concrete beams using high performance fiber reinforcement cement-based composite (HPRC) and carbon fiber reinforced polymers (CFRP), *J. Constr. Build. Mater.* 48 (2013) 485–498.

- [14] A. Ilki, C. Demir, I. Bedirhanoglu, N. Kumbasar, Seismic retrofit of brittle and low strength RC columns using fiber reinforced polymer and cementitious composites, *J. Adv. Struct. Eng.* 12 (2009) 325–347.
- [15] I.H. Yang, C. Joh, B.S. Kim, Structural behavior of ultra high performance concrete beams subjected to bending, *J. Eng. Struct.* 32 (2010) 3478–3487.
- [16] J.M. Yang, K.H. Min, H.O. Shin, Y.S. Yoon, Effect of steel and synthetic fibers on flexural behavior of high-strength concrete beams reinforced with FRP bars, *J. Compos. Part B Eng.* 43 (2012) 1077–1086.

Further Reading

- [1] H.M. Tanarslan, Flexural strengthening of RC beams with prefabricated ultra high performance fibre reinforced concrete laminates, *J. Eng. Struct.* 151 (2017) 337–348.

Application of Remote Sensing and GIS in Land Resource Management

Sathees Kumar*, Nazeer Khan

Mohamed Sathak Engineering College/ Anna University, satheeskumar@msec.org.in

ABSTRACT

Land use Land cover (LU/LC) mapping serve as a basic information for land resource study. Detecting and analysing the quantitative changes along the earth's surface has become necessary and advantageous because it can result in proper planning which would ultimately result in improvement in infrastructure development, economic and industrial growth. The LU/LC pattern of Madurai city, Tamil Nadu, has undergone a significant change over past two decades due to accelerated urbanization. In this study, LU/LC change dynamics were investigated by the combined use of satellite remote sensing and geographical information system. To understand the LU/LC change in Madurai city, the different land use categories and their spatial as well as temporal variability has been studied over a period of seven years (1999-2006), from the analysis of LANDSAT images for the years 1999 and 2006 respectively, using ArcGIS 9.3 and ERDAS Imagine 9.1 software. This result shows that Geospatial technology is able to effectively capture the spatio-temporal trend in the landscape pattern associated with urbanization for this region.

Keywords: GIS; LANDSAT; Land Use; Land Cover; Remote Sensing

1. Introduction

Planning and development of urban areas with infrastructure, utilities, and services has its legitimate importance and requires extensive and accurate LU/LC classification. Information on changes in land resource classes, direction, area and pattern of LU/LC classes form a basis for future planning. It is also essential that this information on LU/LC be available in the form of maps and statistical data as they are very vital for spatial planning, management and utilization of land. However, LU/LC classification is a time consuming and expensive processes. In recent years, the significance of spatial data technologies, especially the application of remotely sensed data and geographic information systems (GIS) has greatly increased. Now-a-days, remote sensing technology is offering one of the quick and effective approaches to the classification and mapping of LU/LC changes over space and time. The satellite remote sensing data with their repetitive nature have proved to be quite useful in mapping LU/LC patterns and changes with time^[6,7,9,10].

Quantifying the anthropogenic or human activity that governs the LU/LC changes has become a key concept in the town planning profession. A major objective of planning analysis is to determine how much space and what kind of facilities a community will need for activities, in order to perform its functions. An inventory of land uses will show the kind and amount of space used by the urban system.

LU/LC study with the use of remote sensing technology is emerging as a new concept and has become a crucial item of basic tasks in order to carry through a series of important works, processes such as the prediction of land-use change, prevention and management of natural disaster, and protection of environment, etc and most importantly analysing the present development and future scope of development of the nation. In the recent years, with the enhancement of more advanced Remote Sensing technology and Geo-Analysis models, monitoring the status and dynamical change of LU/LC thoroughly using remotely sensed digital data has become one of the most rapid, credible and effectual methods.

The main aim of this paper is to assess the LU/LC changes, and to observe the growth of various urban classes

Copyright © 2018 Sathees Kumar *et al.*

doi:10.24294/jgc.v1i3.437

EnPress Publisher LLC. This work is licensed under the Creative Commons Attribution-NonCommercial 4.0 International License (CC BY-NC 4.0).

<http://creativecommons.org/licenses/by/4.0/>



Sathees Kumar
PRINCIPAL
MOHAMED SATHAK ENGINEERING COLLEGE
KILAKARAI 623 806

over a period of seven years along Madurai City, by using remote sensing and GIS technology. For this purpose, multi-spectral, multi-temporal LANDSAT images were downloaded from USGS Earth Resources Observation Systems data centre. The classification, identification and graphical representation of the changes detected in the classes defined for the study area were done using ERDAS Imagine 9.1 software and ArcGIS 9.2 software. The paper focuses on the analyses and discussions of the results including the pattern of changes in LU/LC studied from year 1999 to 2006.

2. Study area

The study area is Madurai city, Tamil Nadu (**Figure 1**), one of the famous historical and cultural cities in India. It is located in South Central Tamil Nadu, is the second largest city after Chennai and is the headquarters of Madurai District. In 2011, the jurisdiction of the Madurai Corporation was expanded from 72 wards to 100 wads covering area 151 Sq.Km, dividing into four regions Zone I, II, III, IV. There has been rapid growth in Madurai from 1967 and it has gradually increased over the years in Madurai and its surrounding areas. Most of the areas around Madurai are least developed and are in the transformation stage. It extended geographically from 9°50' North latitude to 10° North latitude and 78° 02' East longitude to 78°12' East longitude, and approximately 100 m above MSL. The terrain of the city is gradually sloped from the north to south and west to east.

The River Vaigai is the prominent physical feature which bisects the city into North and South zones with the north sloped towards Vaigai River and the south zone sloped away from the river. The city became municipality in 1867 and was upgraded as a corporation in 1971 after 104 years. The corporation limit was extended from 52.18 km² to 151 km² in 2011. As per 2011 census the population of the city is 15.35 lakhs^[4]. The area has been experiencing remarkable land cover changes due to urban expansion, population pressure and various economic activities in the recent years.

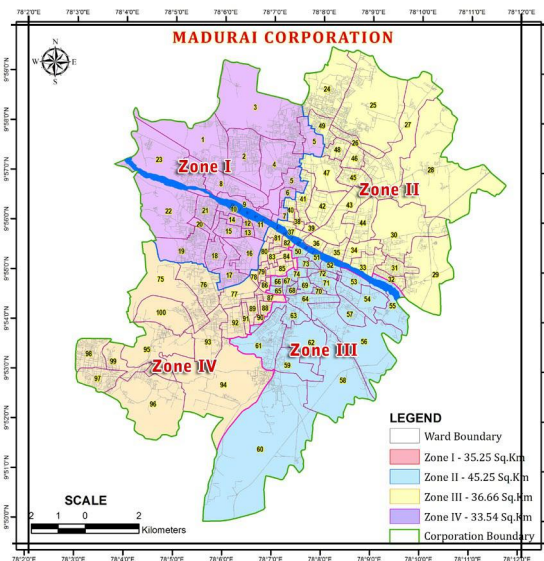


Figure 1; Study Area Location^[5].

3. Methodology

3.1 Data

For this study, Landsat ETM+ (path 143, row 53) images were used (**Table 1**). Landsat images were downloaded from USGS Earth Resources Observation Systems data centre^[2]. A base map of Madurai city was provided by Local Planning Authority of Madurai. The The Landsat ETM+ image data consists of eight spectral bands, with the same spatial resolution as the first five bands of the Landsat TM image. Its 6th and 8th (panchromatic) bands have resolutions of 60 m and 15 m, respectively. All visible and infrared bands (except the thermal infrared) were included in the analysis. Remote sensing image processing was performed using ERDAS Imagine 9.1 software. Landsat data of 1999, 2006, and SOI Toposheet were selected and used to find the spatial and temporal changes in the study area, during the period of study.

Sl.No	Data product	Imagery Date	Resolution (m)	Path/Row
1	LandsatETM+	04/12/1999	30	(143- 53)
2		21/01/2006	30	(143- 53)

Table 1. LANDSAT Satellite Data used in the study.

3.2 Image classification

In this study, totally, four LU/LC classes were considered as vegetation, Built-up land, waste land, and water area. The classes in the images were decided based on the LU/LC classification system devised by National Remote Sensing Agency (NRSA) for Indian conditions^[8]. The LU/LC classes are presented in **Table 2**. In the study area, a supervised classification of the image was performed using the signature files from the unsupervised classification. For the supervised classification a maximum likelihood rule was used for a parametric rule^[1,3]. The LU/LC classified maps for 1999 and 2006 were produced from Landsat images and are given in **Figure 2**.

Sl.No	LU/LC Classes
1	Vegetation
2	Built-up land
3	Waste land
4	Water area

Table 2. LU/LC Classification scheme considered for Madurai

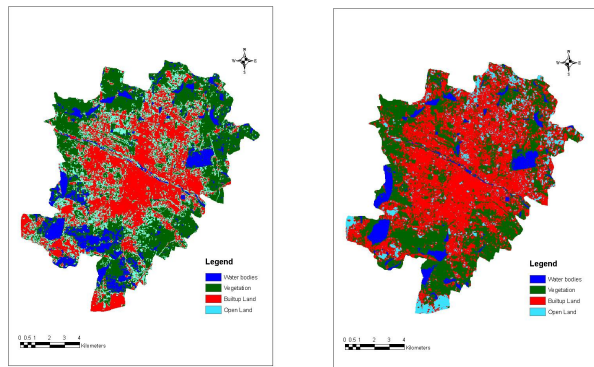


Figure 2; LU/LC Classified Images (a) 1999 (b) 2006.

4. Result and discussion

4.1 LULC change analysis

The LU/LC classification results are summarized from the year 1999 to 2006 in **Table 3**. From 1999 to 2006, built-up area increased by 17.09. On the other hand open land decreased by 11.82 % respectively. The fluctuations were observed in vegetation and water area due to seasonal variation found in the study area. All these land use change are closely related with the development of regional economy and the population growth in the city. The trend of LU/LC and urban change in the city is shown in the **Figure 3**.

LU/LC Class	Area (ha)	
	1999	2006
Built-up land	4533.57	7020.45
Open Land	2891.79	1170.45
Vegetation	5526.99	5411.79
Water bodies	1602.72	952.38
Total	14555.07	14555.07

Table 3. Summary of Areas for LU/LC Classes from 1999 to 2006

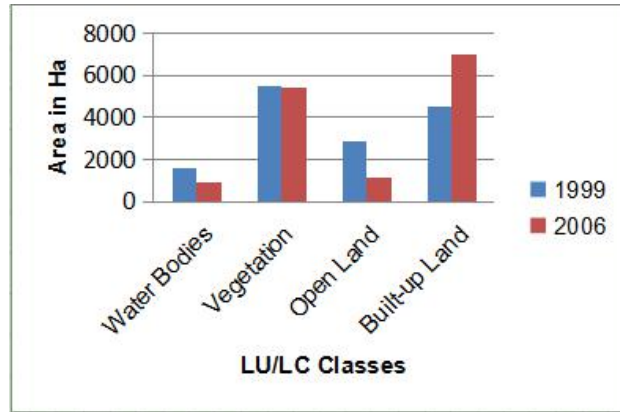


Figure 3; Comparison of LU/LC from 1999 to 2006.

5. Conclusion

This paper aims investigating LU/LC changes occurred in Madurai city between 1999 and 2006 using remote sensing and GIS. The areas of urban settlements and construction land in Madurai city increased by 17.09% from 1999 to 2006. The results of the study suggest that the analysis of sequential satellite data offers means of extraction of information on LU/LC. In fact, for shorter intervals satellite data are very helpful for the detection of LU/LC changes, due to repetitive coverage at very short intervals. In this study analysis has been done for period of seven years. This work shows that it is feasible to analyse and monitor LU/LC change based on remote sensing images and GIS applications. The results would be of great help to the land management department in quick decision making.

References

1. Coskun, G. H., Alganci, U., and Usta, G., (2008), Analysis of Land Use Change and Urbanization in the Kucukcekmece Water Basin (Istanbul, Turkey) with Temporal Satellite Data using Remote Sensing and GIS. Sensors, Vol.8, pp. 7213 - 7223.
2. Global Land Cover Network, United States Geological Survey, 2010, <http://www.glcen.org>.
3. Lillesand, T. M., and Kiefer, R. W., (2003), Remote Sensing and Image Interpretation, John Wiley and Sons, New York. 706 pages.
4. National Informatics Centre (NIC), Department of Information Technology, Government of India, 2010, <http://www.madurai.tn.nic.in/distprof.htm>.
5. National Informatics Centre (NIC), Tamil Nadu state centre, 2010, www.tnmaps.tn.nic.in.
6. Palaniyandi, M., and Nagarathinam, V., (1997), "Land Use/Land Cover Mapping and Change Detection Using Space Borne Data", Journal of the Indian Society of Remote Sensing, Vol. 25 (1), pp. 27 - 33.
7. Rahman, R., and Saha, S. K., (2008), "Multi-resolution Segmentation for Object-based Classification and Accuracy Assessment of Land Use/Land Cover Classification using Remotely Sensed Data", Journal of the Indian Society of Remote Sensing, Vol. 36, pp. 189-201.
8. Reddy, A. M., (2002), Text Book of Remote Sensing and Geographical Information Systems, B.S. Publications, Canada. 450 pages.
9. Roy, P.S., and Giriraj, A., (2008), "Land Use and Land Cover Analysis in Indian Context", Journal of Applied Scientific Information, V 8 (8), pp 1346-1353.
10. Sarma, V.V.L.N., Murali Krishna, G., Hema Malini, B., and Nageswara Rao, K (2001), "Landuse/Landcover Change Detection through Remote Sensing and its Climatic Implications in the Godavari Delta Region", Journal of the Indian Society of Remote Sensing, Vol. 29 (1&2), pp. 85 - 91.
11. Verbyla, D.L., (2005), Satellite Remote Sensing of Natural Resources, Lewis Publishers, New York. 198 pages.



Applicability and new trends of different electrode materials and its combinations in electro coagulation process: A brief review

Sivaranjani ^a, Abdul Gafoor ^b, Nasar Ali ^c, Sathees Kumar ^b, Ramalakshmi ^b, Sabeena Begum ^d, Zunaithur Rahman ^{c,*}

^a Department of Civil Engineering, Vel Tech Rangarajan Dr.Saguntala R&D Institute of Science and Technology, Chennai-600 062, Tamilnadu, India

^b Department of Civil Engineering, Mohamed Sathak Engineering College, Kilakarai-623 806, Tamil Nadu, India

^c Department of Civil Engineering, College of Engineering and Technology, Samara University, Afar-7260, Ethiopia

^d Department of Physics, Mohamed Sathak Engineering College, Kilakarai - 623 806, Tamil Nadu, India

^e Department of Physics, Mohamed Sathak Engineering College, Kilakarai 623 806, Tamil Nadu, India

ARTICLE INFO

Article history:

Received 7 May 2020

Accepted 13 May 2020

Available online xxx

Keywords:

Industrial effluent

Electrocoagulation

Direct current

Energy consumption and eco friendly

Eco friendly

ABSTRACT

Different technologies such as physical, chemical, biological, advanced oxidations and electro-chemical methods are involved in the treatment of industrial effluent. The widely followed biological treatment techniques are required more time, wide operational space and are not effective for wastewater contains heavy metal and hazardous elements. The advanced oxidation process needs tremendous operational cost and is usually procure high immaculate water. The chemical coagulation process is time delaying and brings about a huge volume of sludge. In the electrostatic coagulation process, the electrode plates are dissolved in the wastewater by a direct current source of metal electrodes immersed in the effluent. Electrocoagulation (EC) has a newly followed method used for treating industrial effluent due to its adaptability and cost-effective eco-friendly method. EC has been used for treating a wide range of industrial effluent. These metal ions combine with hydroxide ions to form metal hydroxide which acts as the coagulant for the destabilization of suspended as well as dissolved pollutants in the industrial wastewater. Therefore, the intention of this review paper is the possibility of EC for the treatment of industrial effluents as well as energy consumption in the EC.

© 2020 Elsevier Ltd. All rights reserved.

Selection and peer-review under responsibility of the scientific committee of the International Conference on Newer Trends and Innovation in Mechanical Engineering: Materials Science

1. Introduction

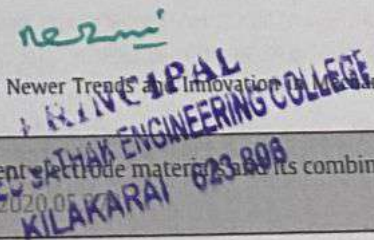
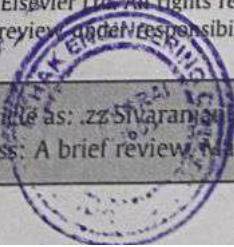
The textile wastewater fluctuation broadly depends on the composition of scum in fibers and the chemicals used in various stages. A large quantity of wastewater generated during the dyeing of cloths in the different stages like bleaching, dyeing, printing, and finishing. The primary contaminants in textile effluent are especially the organic and inorganic chemicals. Dyeing substance is the main pollutant in the textile wastewater and should be treated before releasing the wastewater into the water body. Untreated effluent produces an aesthetic issue, affects water transparency and aquatic life damage [1-7]. The metal plating industry is discharging a huge quantity of wastewaters into the ecosystem which

directly or indirectly increases metals and other hazardous substances to the environment [8]. Almost all the metals such as nickel, lead, and zinc are unsafe when they are freed without purification, due to that they are biologically inactive and lead to agglomerate in living organisms, and most of the heavy metal ions are harmful or destructive. Because of their huge toxicity, industrial effluents are rigorously monitored and have to be treated previously being released. Different methods were adopted for the removal of heavy metals, such as precipitation, adsorption ion-exchange and EC [9-17].

Wastes from oil and gas well drilling activities have hazardous characteristics and the ability to brunt the environment. Two main types of pollution from oils and gas industries is drilling fluids and cutting for the extraction process. In remedial measure for the drilled wastewater is an important thing in an aspect of huge volume in day to day life. The processing of drilled effluent remit by various approaches, but generally adopted are membran

* Corresponding author.

E-mail address: zunaithur@gmail.com (Z. Rahman).



processes (microfiltration and ultrafiltration) [18,19], chemical destabilization (conventional coagulation) and electrochemical destabilization (EC). The biological method was not adopted for the treatment of this well-drilled effluent because it contains biocide. The contamination due to the release of oil drilling effluent is now a day main reason for environmental pollution [20]. Oxidation of iron sulfide/ pyrite with water and oxygen formed as Acid mine drainage (AMD) emanates from coal mining both organic and inorganic reactions [10]. The acidic water will cause severe damage to the soil layer and coal deposits also act as a corrosive agent. Thus, AMD was with the following parameters low pH, high Sulphate, and many toxic metals [15]. After obtaining ethanol from the rice grain-based distillery industry the spent wash (SW) was released to the treatment unit which contains a high amount of organic pollutants. The spent wash after the biological digestion it's dark brown and called biodigester effluent (BDE) which contains high COD. The dark brown color of BDE was due to the presence of melanoidin. The eradication of color and COD from the BDE achieve huge value from the environmental perspective [21].

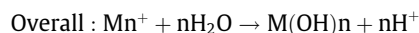
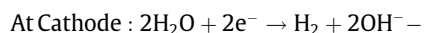
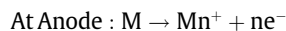
The Papermill industry creates a large volume of wastewater during the paper production. Wastewater from the paper mill industry consists of a huge quantity of toxic chemicals that come from raw materials. These contaminants can cause long-term toxic effects on animal life, such as respiratory stress, toxicity, mutagenicity and genotoxicity [3]. Landfilling is the natural and simple method of dumping solid waste. Municipal waste is generally disposed to the landfill. There are three types of products from landfills, they are air, liquid and solid. Leachates consist of organic pollutant in high quantity, and more amount of heavy metals [22]. Electrocoagulation (EC) has attracted the attention of the environmental sectors largely as an efficient way to treat different types of water and wastewater during the last two decades, and especially during the last few years. In this review paper, we propose the application of EC and electro-oxidation (EO) treatment for the various industrial effluents (Fig. 1).

2. Background of EC

EC is the technique of destabilizing suspended and dissolved substances in a liquid medium by inducing an electric field into the effluent. A variety of species of coagulants and hydroxides is produced to destabilize and coagulate suspended particles or to adsorb dissolved contaminants. The EC process takes place in three

stages. They are (i) production of coagulants by electro-oxidation (ii) Destabilization of the pollutants, (iii) gathering of the destabilized pollutant to form flocs [9]. Even with one anode and one cathode, we can set up an EC unit. Anode and cathode may be with the same electrode material or different material, an anode is usually called a sacrificial electrode. The destabilizing agent was generated during the EC process which neutralizes the charged substance available in the electrolyte. The bonding of charged substances will become a large floc and then settle fast. This technique has justified practically in removing pollutants from effluent and is identified by less sludge formation (Table 1).

General Equation in EC:



3. Effect of various operating parameters

- Material of the electrodes:** Most of the studies use Iron, Stainless steel and Aluminium electrode as well as few researches on the Copper and Nickel as the sacrificial electrode [23–26]. These electrodes are the multivalent valance metal electrode which form metal hydroxide coagulant during EC. As a review, Fe electrodes can obtain the same dye removal efficiency at fewer current than Al electrodes [22]. Preparation of the new Iron aluminium composite electrode was employed in the treatment of textile wastewater in the EC study [27]. In some of the research work will involve in the utilization of two different electrodes that is one type of material is used as anode another type of material was used as a cathode in the same EC process. Employing a steel wool cathode (591 cm²) for the mitigation of dye was 1.8–4.4 quicker than using an iron electrode [26].
- pH of the solution:** The effect of the initial pH on the EC process was related to the solubility of initially-formed aluminium hydroxide. It was found that almost all the studies that, the pH of the solution increases during the reaction phase, then stabilized at pH between 8 and 10.5 depends on the initial pH [28]. One of the benefits of treating the acid mine by the EC process

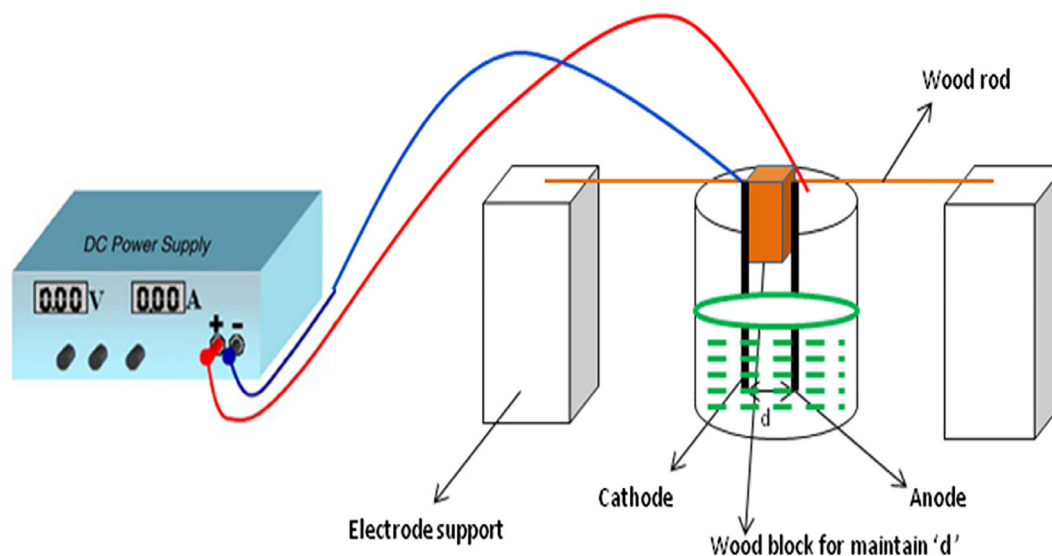


Fig 1. EC experimental set up [31].

Table 1
Removal of various pollutant using EC.

Pollutants	Electrode	Current (mA/cm ²)	Reactor	Energy consumption (kWh/m ³)	Efficiency	Reference
Color						
Textile dye	Al	4	Batch	4.66	99.99%	[25]
Reactive and dispersive dye	Fe, Al and stainless steel	4.45	Continuous	39 to 39.5	99.6%	[32]
Synthetic Dye	Fe nuts	6.5	Continuous	9.3×10^3	99%	[47]
Textile Dye	Fe and Al	10	Batch	50 and 80% of the total cost for Fe and Al	99%	[29]
Azo dye	Fe and Al	0.1	Batch	NA	98.32%	[4]
Methylene blue dye	Al	2.5	Batch	7×10^7	98%	[1]
Acid dye	Fe and Al	7.5	Batch	8.3×10^3	98%	[23]
Acid black and acid yellow dye	Al	4	Batch	0.95×10^3	92 and 97% for black and yellow dye	[6]
Textile dye	Fe	20	Continuous	69.1×10^3	96.88% in COD and colour	[19]
Blue reactive dye and Disperse Red dye	Fe and Al	3 to 4	Batch	1	>95%	[48]
Textile dye	Fe wool cathode	0.507	Batch	3.9×10^3	95%	[26]
Textile dye	Fe-Al composite	2	Batch	18	>90% in COD and colour	[27]
Textile dye wastewater	Al	31.25	Continuous	3.2×10^3	>85%	[49]
Crystal violet dye	Al	25	Batch	2.7	70%	[2]
Heavy metal						
Cr	Fe and Al	7.94	Batch	0.6	100%	[13]
Cu, Mn, Al, Fe and Zn	Fe, stainless steel and Al	70	Batch	NA	100, 89.17–99.96, 26.85, 97.52% for Cu, Fe, Al, Mn and Zn	[15]
Ni	Al	2.5 to 22.7	Continuous	NA	98%	[14]
Cr, Cu, Ni and Zn	Carbon steel electrodes of monopolar configuration	4	Batch	6.25	100, 99, 98 and 99%	[18]
Cr	Al or Stainless Steel	NA	Batch	NA	88.35%	[22]
Zn Cu and Ni	Carbon steel and Aluminum	0.006	Continuous	49	99% of Zn, 70% of Cu and Ni	[17]
Cr	Iron	1.12	Batch	$2 \text{ to } 7 \times 10^3$	100	[11]
Nutrient						
Nutrient	Al mesh	0.8	Continuous	0.4 to 22	74 to 93% and 44 to 76% for nitrogen and phosphorus	[18]
Comparison of electrode						
Dairy effluent	Al	0.065	Continuous	0.163	100, 98 and 80% for turbidity and suspended solids, total phosphate, COD	[31]
Comparison of Iron and Aluminium	Fe and Al	20	Continuous	NA	Al > Fe	[50]
Distillery effluent	Cu	8.93	Batch	11.42	83 and 73% of COD and colour	[21]
Drilling fluids wastewater	Al	3.4	Batch	NA	90	[20]

was the pH is modified to neutral during the reaction time [15]. The ionic properties of metal hydroxides and coloration molecules are determined in a solution and therefore have an important influence on the mechanism for color removal [28]. The solubility of metal hydroxide was lower between pH 5 and 8 [4]. Depending upon the type of metal in the electrode and the initial pH, the pH of medium tweaks during the process. In the meantime, EC displays a certain buffer capability, notably in the alkaline medium [29].

- **Treatment time:** EC time influences the treatment efficiency of the electrolytic process. During electrolysis, the anodic electro-dissolution led to the release of the coagulating species. The effectiveness of color removal explicitly relies on the metal ion concentration on electrodes used. Increasing the time of electrolysis leads to an increase in both the concentration of metal ions and the accumulation of hydroxide flocs [30]. Beyond some time there was no significant removal efficiency of pollutants from the EC process further reaction time will increase the reaction cost. Reaction time (time of electrolysis) determines the charge loading and thereby affects the performance of EC. The effect of electrolysis time on color and COD removal efficiency was investigated maintaining the optimum pH of 8 and keeping constant current density of 15 A/m². The CRE value is rising with increase electrolysis time up to a partic-

ular extend after that there was constant value was attained. The main reason for the constant CRE value was the formation of nascent electro-coagulant flocs [27].

- **Applied current:** Metal ions dissociations were increased with current density will depend on the Faraday's law [21] by racing, the applied current the hydrogen bubbles formation increase which causes the good mixing of the coagulant in the aqueous solution similarly increase the removal efficiency [26]. This is known that there is gradually a decrease in the volume of hydrogen bubbles and their size, resulting in the gradual reduction of contaminants and floc development with increased in applied current [31]. Applied current is a major influencing factor in the operational cost of the EC process [11]. Applied Current controls the coagulant generation and also the formation of a bubble, their size, and the flocs growth [1].
- **Concentration of the pollutant:** Adsorption of pollutant on to the metal hydroxide is the prime way for the pollutant removal [32]. There is no significant effect on the power consumption on the variation of initial dye concentration [28]. As applying steady current, there is a constant quantity of coagulating species was generated from the electrode. If the concentration of pollutant increases there was a constant coagulant species generated during EC which lead to remove the constant quantity of pollutant [30].

- **Inter electrode distance:** As the inter-electrode distance increases the resistance between electrode increases. Less contact between ions and hydroxide composites is anticipated with widening electrode distance [28]. Inter-electrode distance was the main parameter which influence on operational costs [32]. If the wastewater conductivity was very high then we have endorsed the increase of inter electro distance. Since the cathode is fixed and therefore increasing the distance between anodes leads to the decrease of distance between each anode and cathode. That color and COD removal efficiency is improved by decreasing the distance between the anodes and cathode (i.e., increasing the distance between two nodes). This can be attributed to the increase of electrical current associated with reducing the inter-electrode distance resulting in higher collisions of the ions that enhance the coagulation [11]. One of the author stated that beyond 3 cm there was not any considerable removal of pollutants during the EC process [13]. Inter electrode distance affects the following the energy consumption and mixing of the solution. For minimum inter-electrode distance, the floc formation was difficult and the accumulation of hydrogen bubbles on to the surface of electrode takes place which reduces the pollutant removal efficiency [2].
- **Type and Concentration of the electrolyte:** The conductivity of electrode immersed aqueous solution mainly dependent on the concentration and quantity of total dissolved solids [30]. The concentration of the electrolyte increases the conductivity which leads to reduce the resistance between two electrodes and hence removal efficiency depends on the conductivity directly [28]. It is noticeable that when the concentration of NaOH in solution increases, the solution conductivity increases. Also, there is a hike in evicton efficiency up to 80% when electrolyte concentration was 2–4 wt% [30]. They figured that with rising electric conductivity, the efficiency of elimination was greatly increased. The addition of any salts to rice the aqueous solution conductivity leads to increasing of pollutants in the aqueous solution. Higher the chloride ion concentration will tend to eliminate the passive oxide film which sticks onto the surface of the anode and reduce the metal hydroxide formation [20]. If the electrolyte concentration raised, the voltage drop-down and the solution conductivity hiked that ends in lower in electrical energy utilization [6,33].
- **Energy and electrode consumption:** Energy consumption and electrode consumption played a major role in the economic analysis of the EC process. Considering this factor energy and electrode consumption was estimated using these following equations

$$\text{Operating cost} = a \cdot C_{\text{energy}} + b \cdot C_{\text{electrode}} \quad (1)$$

$$C_{\text{energy}} = U \cdot I \cdot t / V \quad (2)$$

where C_{energy} , $C_{\text{electrode}}$, a, b, U, I, t and V represent energy consumption for each cubic meter of wastewater (kWh/m^3), electrode consumed for the treatment of one cubic meter of wastewater (kg/m^3), voltage (V), current (A), residence time (h) and volume of wastewater (L), respectively [25].

- **Effect of inflow rate:** Influent flowrate varies from 30 to 150 mL/min and EC reaction is monitored. the performance of the EC column is inversely proportional to the influent flow rate. For a constant initial concentration of 5 mg/L and inlet flow rate between 30 and 150 mL/min, the Removal of chromium is reduced from 93% to 43% for 30 mL/min to 150 mL/min for 1 min of reaction period. At higher the inflow rate there is fewer in the EC process and thus decreases the removal efficiency. This is due to the less contact time between the pollutant and

the metal hydroxide coagulant. Thus giving less time to adsorb the flocs which tends to slow down the rate of anodic reactions [34].

- **Effect of mixing:** The effect of air forces at the bottom of the EC column at different flow rates using a single air nozzle was investigated by author revealed that the gas-liquid interfacial contact is enhanced due to the speeding up of bubble formation and thus increasing the concentration of dissolved oxygen generated in the system. Huge air flow enhances the destabilizing rate of dissolved ions generating insoluble metal hydroxide and increasing coagulants growth size. Huge the airflow increase the turbulence is developed all over the liquid medium which increases the bubbles. Chromium removal was enhanced by up to 20% for the airflow of 2 l/min [34].
- **Type of reactor:** There are two main types of reactors used for the study of EC. In most of the studies, the batch mode reactor was used to treat the effluent from the industry or synthetic solution. The batch mode reactor was circular or rectangular in dimension. The batch mode reactor was more efficient and economic [7,35,36].

4. Advantages and disadvantages of EC

EC needs a simple apparatus and is a cinch to run. Sludge generates during the EC process was very less, easily dried and contains metal hydroxide that will recover from that sludge. Chemicals are not required for the EC process, so there was no risk of the generation of secondary pollution. The bubbles formed during electrolysis bring the pollutants to the surface of the solution where it has been isolate and collected easily. The maintenance required for the EC process was fewer due to its controlled electric potential with no moving apparatus. The EC can be suitably used with the help of other renewable sources of energy such as solar or wind in rural regions where power is not easily available [37–39].

Regular and timely replacement of sacrificial anode was required due to the oxidation of the electrode into the solution. There was a film developed on the surface of the electrode will reduce the efficiency. Highly conductive effluent was required to treat. Applying the electricity will lead to the expansion of the process. Sometimes there will be the possibility of dissolving of metal hydroxide takes place [11].

5. Applications

- **EC on textile wastewater:** The EC method was successfully established and obtained more than 90 percent COD and color destruction efficiency under optimized situations of pH 8, process time 80 min, current density 20 A/m² with a 3 cm range between electrodes. EC method obtained around 99 percent color reduction efficiency for actual textile wastewater and provided nearly colorless solutions even with a fewer treatment time of 60 min [10].
- **EC on tannery wastewater:** All over the world leather industry facing the problem of removing various kinds of contaminants due to the manufacturing process of leather. The recent research related the study of the performance of a hybrid EC/-electrodialysis process for the removal of COD, NH₃-N, Cr and color in tannery wastewater. The effects of current density and electrolysis time were analyzed to optimize the EC process with aluminium either iron electrodes. It is noticeable that the effluent treated with combined EC-ED techniques presents very similar values for the same parameter as the ones presented by normal feedwater [40].
- **EC on paper mill wastewater:** Biological treatment of debarking effluent was in effect due to the presence of tannins so the effluent contains toxic pollutants. Chemical coagulation

was also some problem with the destabilization of pollutants due to resin acids is weak water-soluble. So, EC was an emerging technique adopted to treat a wide range of toxic substances in effluents [3].

- **EC on drilling fluids wastewater:** The impurity created by freeing the oil drilling is also a cause of environmental deterioration and raises recently a special interest. EC techniques use the direct current (DC) electrolytic cell to remove petroleum content, such as diesel, from drilling fluid wastewater. [20].
- **EC on Dairy wastewater:** Dairy wastewaters are fatty, contain the nutrient, lactose (as well as detergents) with a high concentration of biologic oxygen demand (BOD), and generally contain sanitary agents. A different EC reactor with 20 aluminium electrodes in bipolar mode. The locations and directions of the electrodes are simple and efficient in electro flotation (shift to form an angle of 7 to the horizontal direction) [31].
- **EC on distillery wastewater:** The effluent from the rice grain-based distillery industry was consisting of large quantity organic pollutants. The effluent from the biodigester was dark in color also considering factors for the treatment. The EC was a prominent technique to degrade both organic and color from the wastewater [21].
- **EC on sewage wastewater:** EC technique was used as a better alternative method to treat the municipal wastewater instant of the chemical coagulation and the disinfection unit is coupled with the UV radiation. The economically low cost for the elimination of turbidity and e-coli from the municipal wastewater using the EC method [10]. Untreated laundry wastewater contains a large amount of COD which can be easily treated with the EC technique. The iron and Aluminium electrode was used to treat the laundry effluent, Aluminium shows the better removal of this wastewater. The Cl⁻ concentration in the laundry waste has a positive effect on the removal of COD. The betterment in the treatment was with the neutral pH [7].
- **EC on removal of nutrients:** The nutrient removal was also achieved by the EC process with considerable removal efficiency. In order to reduce the energy required for EC for nutrient removal, thermodynamically desiring active carbon air cathode and an aluminum sacrifice anode were used. Air cathode EC (ACEC) output was tested utilizing untreated wastes as well as a carbon-free synthetic solution for replicating nutrient removal in wastewater processed for the elimination in organic substances (nitrogen: 1:10 phosphorus ratio in deionised water). The final removal of 88% of nitrogen and Phosphorus was removed to a greater extent with 93% [18,41].
- **EC on removal of fluoride from Steel Industry wastewater:** Fluoride from the Steel industrial effluent was treated using the recent method of EC using the Aluminium electrode through the continuous flow method. There was a significant removal of fluoride achieved with 5 min of HRT with neutral pH. The second-order kinetics of adsorption was obeyed by the EC system [43].
- **EC on removal of COD from pharmaceutical wastewater:** The EC techniques are also applicable to the pharmaceutical industry to remove COD from the effluent with a good removal efficiency of 40 to 57% using an iron electrode for 60 min reaction time [44].
- **EC on mitigation of TOC from Cardboard Plant wastewater:** Cardboard plant effluent contains a huge amount TOC and COD which is removed by EC combined with Electro-oxidation using the boron-doped diamond electrode with a high removal efficiency of 83.7% TOC with a reaction time of 3 h [45].
- **EC on removal of petroleum hydrocarbon From groundwater:** The EC technique also plays a vital role in the treatment of Hydrocarbon contaminated groundwater using iron and steel electrode with high removal efficacy of 93.4% with a reaction time of 1 h [46].

- **EC on treatment of landfill leachate:** EC has a recent technique to eliminate the pollutant from the leachate which contains a large amount of organic pollutants and a huge quantity of heavy metal. The suspended and inorganic impurity from the leachate also treated by the EC technique [42].

6. Advance technology in EC

- **Wireless EC:** The wireless EC (WEC) suited for the bipolar electrochemistry to reduce the operation and electrode cost, the graphite was used as the driven electrode and Iron sheets act as the sacrificial anode. The iron substance generated during WEC was mainly based on the dimensional composition of BPE than electrochemical property. The different shapes of the sacrificial electrode were studied during the WEC in which the H shape electrode has low cost with the same removal efficiency. That is, the orientation of the Iron sheet parallel to the electric field could produce 84.6% of Metal dissociation more than any other way of Electrode placing [51].
- **EC with Alternate Current:** Batch mode EC is a study with the Alternate as well as Direct Current for the comparative study on the removal of pollutant and economic basis. The time of electrolysis in AC EC is also less when compared to the DC EC setup. The AC-EC is the best technique for the TOC and Dye removal when compared with DC using Aluminium Electrode [52].
- **Hybrid EC coupled with nanofiltration:** EC coupled with nanofiltration gives effective and good quality of treated effluent. The COD, Turbidity and color removal efficiency were examined after the treatment with various parameters as like Current density and reaction time. EC technique is one of the effective methods for the pre-treatment of the textile effluent when optimal parameters are achieved. The hybrid EC/NF method is satisfactory for generating reusable water aspects. Hybrid process combining EC and microfiltration was drawn up and verified in experiments. Adsorption of selenium over iron hydroxide is good in the EC process yet the settling was difficult because of the smaller size of sludge. Iron hydroxide fully eliminated from the effluent by using an integrated filtration of microfiltration ceramic membranes (mean pore size of 0.3 μm). So the EC is coupled with microfilter membrane to remove the selenium and other heavy metal up to 99% [53–55].
- **EC on Virus removal:** EC also investigated the removal of vulnerable pathogenic bacteria and viruses in the surface as well as groundwater using iron as the electrode coupled with Electro-oxidation (EO). EC performance better in groundwater than surface water [39].

7. Conclusions

Past research on EC has shown that it would be a good substitute to chemical coagulation which adds a chemical to the wastewater and biological treatment process which has some restriction as they need certain circumstances, thus have limitation in dealing with varied wastewaters with toxicity. This EC was further extended by integrated with capacitive deionization technology to achieve complete removal of all pollutants from the industry. EC is an electrochemical technique with many applications. Oily wastes can be removed from aqueous solutions by the EC process. The experimental results showed that Aluminium electrodes are more efficient than Iron electrodes. It may be because of the high adsorption capacity of hydrous Aluminium oxides for oil removal. Although all the studies in the EC are with positive results on the pollutant removal, move forward to the replacement of any one unit from the industry to EC.

EC is future development with the Alternate current for the removal pollutant other than dye. The fast-growing industries in the world are generating a huge volume of wastewater which is disposed to the natural water body harmful to the ecosystem. The quality of industrial effluents depends on the type of contaminants, concentrations of pollutant; treatment method and required disposal technique vary with the different of industry. In addition to that, the type of treatment technique for the industrial wastewater also depends on the type of pollutant in the effluent. EC is a recent technique for the treatment of wide varieties of industrial effluent, due to its simplicity, easy adaptability, less energy consumption, less maintenance and economically effective. Almost all the research study revealed at the lab level employing with artificially prepared wastewater. Efforts should be made to perform EC experiments at the pilot plant scale using real industrial effluent to explore the possibility of using EC for the treatment of real industrial effluent.

Declaration of Competing Interest

The authors declare that they have no known competing financial interests or personal relationships that could have appeared to influence the work reported in this paper.

References

- [1] H.P. De Carvalho, J. Huang, M. Zhao, G. Liu, L. Dong, X. Liu, Alexandria Eng. J. 54 (3) (2015) 777–786.
- [2] M.K. Mbacké, C. Kane, N.O. Diallo, C.M. Diop, F. Chauvet, M. Comtat, T.J. Tzedakis, Environ. Chem. Eng. 4 (4) (2016) 4001–4011.
- [3] M. Vepsäläinen, H. Kivisaari, M. Pulliainen, A. Oikari, M. Sillanpää, Sep. Purif. Technol. 81 (2) (2011) 141–150.
- [4] A.R. Amani-Ghadim, S. Aber, A. Olad, H. Ashassi-Sorkhabi, Chem. Eng. Process. 64 (2013) 68–78.
- [5] C. Weisbart, S. Raghavan, K. Muralidharan, B.G. Potter, Carbon 116 (2017) 318–324.
- [6] E. Pajootan, M. Arami, N.M.J. Mahmoodi, Taiwan Inst. Chem. Eng. 43 (2) (2012) 282–290.
- [7] C.-T. Wang, W.-L. Chou, Y.-M.J. Kuo, Hazard. Mater. 164 (1) (2009) 81–86.
- [8] M. Al-Shannag, Z. Al-Qodah, K. Bani-Melhem, M.R. Qtaishat, M. Alkasrawi, Chem. Eng. J. (Amsterdam, Neth.) 260 (2015) 749–756.
- [9] B. Al Aji, Y. Yavuz, A.S. Kopalal, Sep. Purif. Technol. 86 (2012) 248–254.
- [10] S. Cotillas, J. Llanos, O.G. Miranda, G.C. Díaz-Trujillo, P. Cañizares, M.A. Rodrigo, Electrochimica Acta 140 (2014) 396–403.
- [11] Y.A. El-Taweel, E.M. Nassef, I. Elkheriany, D. Sayed, Egypt. J. Pet 24 (2) (2015) 183–192.
- [12] S.M. Equeenuddin, S. Tripathy, P.K. Sahoo, M.K.J. Panigrahi, Geochem. Explor 105 (3) (2010) 75–82.
- [13] S.S. Hamdan, M.H. El-Naas, J. Ind. Eng. Chem 20 (5) (2014) 2775–2781.
- [14] J. Lu, Y. Li, M. Yin, X. Ma, S. Lin, Chem. Eng. J. 267 (2015) 86–92.
- [15] E. Nariyan, M. Sillanpää, C. Wolkersdorfer, Sep. Purif. Technol. 177 (2017) 363–373.
- [16] J.N. Hakizimana, B. Gourich, C. Vial, P. Drogui, A. Oumani, J. Naja, L. Hilali, Desalination 393 (2016) 90–101.
- [17] G.J. Rincón, E.J. La Motta, J. Environ. Manage 144 (2014) 42–50.
- [18] Y. Tian, W. He, X. Zhu, W. Yang, N. Ren, B.E. Logan, Chem. Eng. J. 292 (2016) 308–314.
- [19] U. Tezcan Un, E. Aytac, J. Environ. Manage 123 (2013) 113–119.
- [20] A.M.H. Lnenay, E. Nassef, G.F. Malash, M.H.A. Magid, J. Pet. 26 (1) (2017) 203–208.
- [21] A.K. Prajapati, P.K. Chaudhari, D. Pal, A. Chandrakar, R. Choudhary, J. Water Process Eng. 11 (2016) 1–7.
- [22] M.K.N. Mahmad, M.A.Z.M.R. Rozainy, I. Abustan, N. Baharun, Procedia Chem. 19 (2016) 681–686.
- [23] M. Chafi, B. Gourich, A.H. Essadki, C. Vial, A. Fabregat, Desalination 281 (2011) 285–292.
- [24] D. Kartikaningsih, Y.-H. Huang, Y.-J. Shih, Chemosphere 166 (2017) 184–191.
- [25] A.S. Naje, S. Chelliapan, Z. Zakaria, S.A. Abbas, J. Environ. Manage 176 (2016) 34–44.
- [26] M.-C. Wei, K.-S. Wang, C.-L. Huang, C.-W. Chiang, T.-J. Chang, S.-S. Lee, S.-H. Chang, Chem. Eng. J. 192 (2012) 37–44.
- [27] A.K. Verma, Journal of Water Process Engineering 20 (2017) 168–172.
- [28] B.K. Nandi, S. Patel, Arabian J. Chem. 10 (2017) S2961–S2968.
- [29] M. Bayramoglu, M. Koby, O.T. Can, M. Sozbir, Sep. Purif. Technol 37 (2) (2004) 117–125.
- [30] M.S. Mahmoud, J.Y. Farah, T.E. Farrag, Egypt. J. Pet 22 (1) (2013) 211–216.
- [31] H.D. Bassala, G. Kenne Dedzo, C.B. Njine Bememba, P.M. Tchekwage Seumo, J. Donkeng Dazie, C.P. Nansu-Njiki, E. Ngameni, Process Saf. Environ. Prot 111 (2017) 122–127.
- [32] T.-H. Kim, C. Park, E.-B. Shin, S. Kim, Desalination 150 (2) (2002) 165–175.
- [33] D.B. Wellner, S.J. Couperthwaite, G.J. Millar, J. Water Process Eng. 22 (2018) 13–26.
- [34] Shaima S. Hamdan, Muftah H. El-Naas, J. Water Process Eng. 4 (2014) 25–30.
- [35] S.Y. Lee, G.A. Gagnon, J. Water Process Eng. 10 (2016) 20–29.
- [36] Y. Yavuz, Ü.B. Ögütveren, J. Environ. Manage. 207 (2018) 151–158.
- [37] A Review of EC Process for Wastewater Treatment. International Journal of ChemTech Research. (2018)
- [38] M.M. Emamjomeh, M.J. Sivakumar, Environ. Manage 90 (5) (2009) 1663–1679.
- [39] R. Darvishi Cheshmeh Soltani, S. Jorfi, S. Alavi, P. Astereki, F. Momeni, Sep. Sci. Technol. 55 (5) (2019) 945–954.
- [40] A. Deghles, U. Kurt, Chem. Eng. Process 104 (2016) 43–50.
- [41] D. Franco, J. Lee, S. Arbelaez, N. Cohen, J.-Y. Kim, Ecol. Eng. 108 (2017) 589–596.
- [42] N. Huda, A.A.A. Raman, M.M. Bello, S. Ramesh, J. Environ. Manage. 204 (2017) 75–81.
- [43] V. Khatibikamal, A. Torabian, F. Janpoor, G.J. Hoshyaripour, Hazard. Mater 179 (1–3) (2010) 276–280.
- [44] S. Farhadi, B. Aminzadeh, A. Torabian, V. Khatibikamal, M. Alizadeh Fard, J. Hazard. Mater. 219–220 (2012) 35–42.
- [45] E. Gengec, Ecotoxicol. Environ. Saf 145 (2017) 184–192.
- [46] G. Moussavi, R. Khosravi, M. Farzadkia, Desalination 278 (1–3) (2011) 288–294.
- [47] C. Phalakornkule, T. Luanwuthi, P. Neragae, E.J. Moore, J. Taiwan Inst. Chem. Eng. 64 (2016) 124–133.
- [48] C. Phalakornkule, S. Polgumhang, W. Tongdaung, B. Karakat, T.J. Nuyut, Environ. Manage. 91 (4) (2010) 918–926.
- [49] B. Merzouk, B. Gourich, A. Sekki, K. Madani, C. Vial, M. Barkaoui, Chem. Eng. J. 149 (1–3) (2009) 207–214.
- [50] C. Jiménez, C. Sáez, F. Martínez, P. Cañizares, M.A. Rodrigo, Sep. Purif. Technol 98 (2012) 102–108.
- [51] Z. Qi, S. You, N. Ren, Electrochim. Acta 229 (2017) 96–101.
- [52] M. Eyvaz, M. Kirlaroglu, T.S. Aktas, E. Yuksel, Chem. Eng. J 153 (1–3) (2009) 16–22.
- [53] A. Aouni, C. Fersi, M. Ben-Sik-Ali, M. Dhahbi, J. Hazard. Mater 168 (2–3) (2009) 868–874.
- [54] V. Mavrov, S. Stamenov, E. Todorova, H. Chmiel, T. Erwe, Desalination 201 (1–3) (2006) 290–296.
- [55] D. Ghernaout, J. Environ. Sci. Allied Res. 02 (02) (2019) 37–43.



Advancement and execution of quality assurance in bored cast in-situ piles

D. Zunaithur Rahman^a, K. Sirajudeen^b, R. Nasar Ali^c, G. Muthumari^b, G. Alagumurugan^d, E. Vani^b, P. Sathees Kumar^b, S. Sivaranjani^{e,*}

^a Department of Civil Engineering, Sethu Institute of Technology, Kariapatti 626 115, Tamilnadu, India

^b Department of Civil Engineering, Mohamed Sathak Engineering College, Kilakarai 623 806, Tamil Nadu, India

^c Department of Civil Engineering, College of Engineering and Technology, Samara University, Afar 7260, Ethiopia

^d Department of Civil Engineering, Fatima Michael College of Engineering and Technology, Madurai 625 020, Tamil Nadu, India

^e Department of Civil Engineering, Vel Tech Rangarajan Dr.Saguntala R&D Institute of Science and Technology, Chennai 600 062, Tamilnadu, India

ARTICLE INFO

Article history:

Received 10 July 2020

Accepted 21 July 2020

Available online xxxxx

Keywords:

Concrete
Construction quality assessment
Pile test
CONQUAS score
Efficiency

ABSTRACT

This paper identifies the effect of working conditions and the developing nature of new lodging in the deal cost and capital development. To quantify development quality, the upside of a special circumstance in Singapore was recently finished private activities are evaluated freely on their workmanship under the Construction Quality Assessment System (CONQUAS). Despite the expansion of the action, the development of the board is certainly not a much-considered or arranged subject. There are still just pockets of greatness in an ocean of seat-of-the-pants. Most second-level development firms don't have efficient chronicle, recording, arranging and quality control methodology. The system named as CONQUAS has been utilized, which was vogue since the late eighties. Here the method has been introduced in the implementation of bored cast-in-situ concrete pile foundation. The Adoption of quality management should be a strategic decision of an organization. On the works carried out at site Piling work and construction of pile cap a CONQUAS score is going to be calculated.

© 2020 Elsevier Ltd. All rights reserved.

Selection and peer-review under responsibility of the scientific committee of the International Conference on Newer Trends and Innovation in Mechanical Engineering: Materials Science.

1. Introduction

CONQUAS has been propelled since 1989 (Building and Construction Authority, 2006). Today, CONQUAS is generally perceived and acknowledged globally as a benchmarking instrument for quality assessment. CONQUAS is currently an enrolled trademark, which has embraced in Singapore, Malaysia, China, Hong Kong, United Kingdom, Australia, South Africa and India, UK and Hong Kong development businesses [1–4]. A measure has been taken to introduce the quality assessment in India; it has been verified for checking the bored cast in situ piles. The points such as structural integrity, Mechanical and plumbing works are then summarized to give an all-out quality score called the CONQUAS Score for the structure project. CONQUAS covers most parts of the general structure works [5–7]. In creating CONQUAS, contemplates

and various preliminaries were led to calibrate its new test strategies and evaluation norms. Control of the scoring framework was completed alongside the preliminaries to guarantee its exactness and consistency [8].

1.1. Objective

- To have a perfect quality appraisal framework for development ventures.
- The quality measurements developed neutralizes working efficiency.
- To provide an economical way to reduce sensible expense and time.
- Calculate a CONQUAS score for the working pile and pile cap construction.

* Corresponding author.

E-mail address: sivaranjanishunmugam@gmail.com (S. Sivaranjani).

<https://doi.org/10.1016/j.matpr.2020.07.517>

2214-7853/© 2020 Elsevier Ltd. All rights reserved.

Selection and peer-review under responsibility of the scientific committee of the International Conference on Newer Trends and Innovation in Mechanical Engineering: Materials Science.



keemul
PRINCIPAL
MOHAMED SATHAK ENGINEERING COLLEGE
KILAKARAI 623 806

1.2. Software requirements

- OASYS pile
- AutoCAD

1.3. Components to be assessed

The CONQUAS Quality implementations are divided into three main components

- Check for Structural and architectural Integrity
- Mechanical and Electrical Works

1.4. Weightage for building category (CAT)

The nature of M&E Works is significant taking into account its inexorably significant expense extent and its effect on the exhibition of a structure. The appraisal covers Electrical Works, Air-molding and Mechanical Ventilation Works (ACMV), Fire Protection Works, Sanitary and Plumbing Works and essential M&E fittings [9,10]. The phases of the evaluation include a site review of introduced works before they are implanted/hidden, such things incorporate ACMV ventilation work, electrical conductors, and so forth [11].

The weights for Structural, Architectural and M&E works are allocated according to four categories of buildings as follows in Table 1 [12–14]:

Method of Installation of Bored Cast In-Situ Piles (Fig. 1)

1. The pile is going to be founded on competent strata with cut off levels.
2. The location of the pile will be marked using the total station with almost care.
3. The hydraulic rig will be centered over the designated pile location.
4. The pile hole will be bored continuously with regular draw out of drilled or cut soil
5. Upon reaching a certain depth, the temporary casing. This is done as a precautionary measure to provide adequate stability sides of boring walls to the free-standing.
6. The bore will be “flushed” to the bottom before concreting by using bentonite fluid for stabilizing the hole
7. Reinforcement cages will be lowered up to the full depth of the pile as per designed depth. Immediately after this process, Tromie pipes will be lowered up to 200–300 mm above the bottom of the borehole.
8. The bore will be “flushed” to the bottom before concreting by using bentonite slurry.
9. The density of the bentonite will be maintained as 1.03 g/cc to 1.10 g/cc during boring operation and < 1.12 g/cc before the concrete pour.
10. The temporary casing will be extracted after the concreting of the shaft. Necessary top-up concrete will be poured in the borehole.

11. The required quality of quarry dust will be filled into the empty bore from pile COL to working platform level

2. Experimental investigation

2.1. Compressive strength test

Compressive strength tests were performed in cubes and results at 28 days were absorbed. The summary of test reports must be enclosed by the project's structural QP (Qualified Person). The total Number of Cubes cast for 7 and 28 days is 42.

2.2. Non-destructive test

Ultra Pulse Velocity test for Concrete Uniformity (Fig. 2)

- To direct NDT utilizing ultrasonic heartbeat velocity (UPV) to check the level of consistency of solidified cement.
- 5 segments per set and 2 readings for each section.
- Assessment depends on the distinction between the 2UPV readings inside a segment that will not Surpass 0.05 Km/s [15].

Electro-Cover meter test:

To check the solidified solid spread for support bars in the wake of throwing: least 25 mm or higher as indicated by particular 5 basic examples per set including 3 for pieces off it@ 4 readings every, 1 for segment @2 readings each on both hub of the section, 1 for shaft @ 2 readings each on the soffit and one side of the bar. For each perusing inside a basic example, full point for ± 5 mm and half-point for ± 5 mm to ± 8 mm. Be that as it may, no focuses will be granted if any of the 4 readings inside the auxiliary example exceeds + 12 mm [16].

2.3. Routine compression pile load test

The routine compression load test has been carried out to locate the structural and geotechnical soundness of the pile and to ensure the settlement of the pile. To increase the load in stages on top of the pile head until the maximum test load (i.e., 1.5 \times of design load) is reached and then to unload until the rebound substantially finishes [17].

This method statement describes the procedure to be adopted for carrying out a routine compression load test on the installed working piles.

Diameter of the pile : 1000 m

Length of the pile : 18 m

Design load : 450 T

Test load (1.5 \times of design load) : 675 T

Kentledge load (1.25 times of test load) : 850 T

2.3.1. Kentledge arrangement

The purposed routine compression load test will be carried out using the kentledge system. There is shown in Fig. 3.

Table 1
Weightage for building category.

Components - Category	A	B	C	D
Identification of buildings	Commercial, Industrial, Institution& others	Private Housing	Public Housing	Landed Housing
Structural integrity checks	25%	30%	30%	35%
Architectural integrity checks	65%	55%	65%	60%
M&E Checks	45%	20%	5%	5%
CONQUAS Score	100%	100%	100%	100%

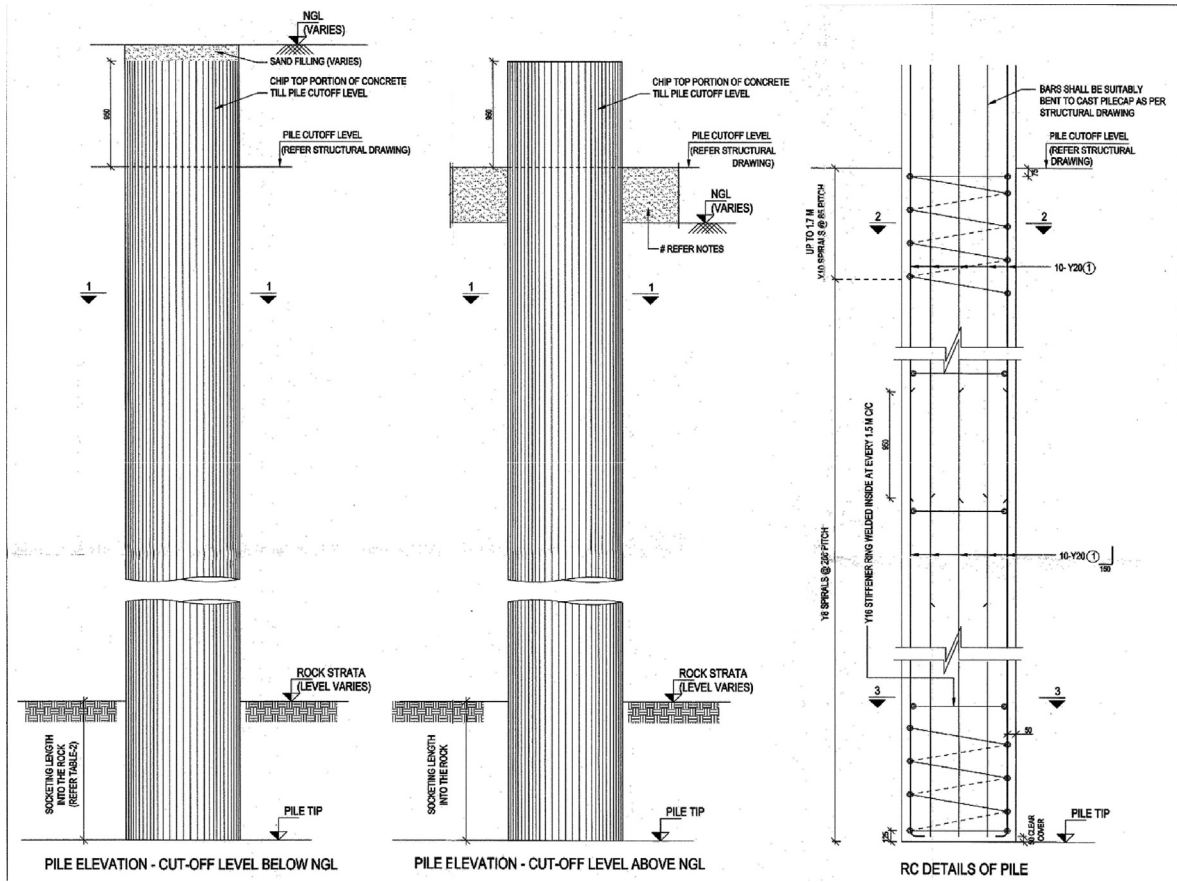


Fig. 1. Structural drawing of pile.



Fig. 2. Pile integrity test.

2.3.2. Loading procedure

As described above, the loading of the piles will be carried out using jacking the primary beam against the reaction. The increment of test load and monitoring measurement in each stage of loading will be as per the clause 702 of IS 2911 part-4-2013., i.e. the rate of settlement is equal to either 0.2 mm/h or until 2 h have elapsed, whatever is earlier subjected to a minimum of 1hr. The final test load will be maintained for 24 h after the stabilization of settlements the load increments are in the load chart.

2.3.3. Settlement measurement

Four calibrated dial gauges will be mounted and recorded independently in Fig. 4. For plotting purposes, the average of the recorded readings of the dial gauges will be taken. Readings will be recorded as per IS 2911 part-4-2013. The sample of the recording sheet is attached in Enclosure.

The loading and settlement monitoring records will be kept promptly throughout the testing period and duly signed by the supervising authorities. A copy of the same will be distributed to the super-



Fig. 3. Kentledge arrangements and loading/unloading hydraulic jack.

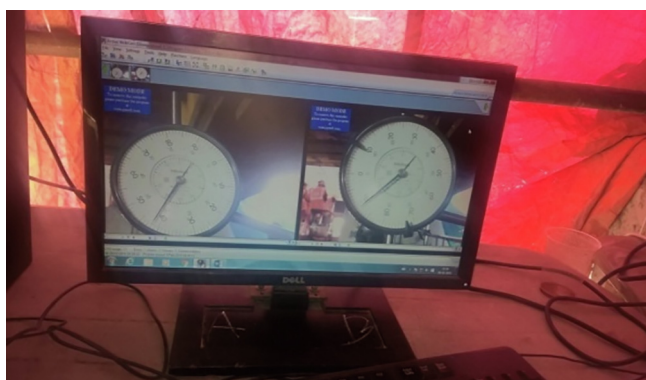


Fig. 4. Settlement dial gauges.

Table 2
Details of vertical load test.

Description	Details
Load test	Routine vertical load test
Finished diameter	1000 mm
Pile no	281
Date of installation	15.01.20
Type of pile	Bored cast-in-situ piles
Pile C.O.L/coordinated of the pile	8.925CD/NE
Pile length from C.O.L	10.07 M
Designed pile capacity	450MT
Test load required	675MT
Kentledge type	Concrete blocks
Kentledge load provided	843.75MT
Date of test	20.02.20
Capacity of jack	500 T
No of jack	2
Area of one jack	706.5 sq.cm
Make of jack	Mitutoyo
Pressure gauge	
Make & identification no	Baumer 0809PG140605
Calibration Date	14.01.20
Least count of pressure gauge	10 kg/cm ²
Maximum range	700 kg/cm ²
Dial gauge	
Least count	0.01 mm
No of dial gauges used	4 nos

vising authorities, on request the complete load-settlement records with necessary remarks will be provided in Table 2.

2.3.4. Displacement measurement

Two calibrated dial gauges of least count 0.01 mm will be placed and recorded independently. For plotting purposes, the

average of the recorded readings of the dial gauges will be taken. Reading will be recorded at 5 min, 10 min, 15 min, 30 min to satisfy clause 7.2, IS:2911 Part 4-2013.

2.3.5. Criteria for acceptance

The safe lateral load on the pile will be evaluated as per the clause 8.4.1, IS 2911 part 4-2013, as the least of the following. Final load at which the maximum deflection shall not exceed 5 mm.

3. Results and discussion

The tensile test has been carried out for different sizes of steel reinforcement bars are as follows: Tables 3-5.

3.1. Computerized pile testing

Because the establishments are covered far out, it doesn't imply that they can be overlooked: their plan is a key piece of structural building. How well a cushion, heap or pontoon acts and moves majorly affects the superstructure above, so it is vital to get it right (OASYS heap).

Pile gives the vertical limit of a heap over a scope of lengths through the dirt layers. It works with strong or empty heaps, round, square or H heaps, and heaps with and without under-reams. When clients have picked the heap length, they would then be able to ascertain the settlement at and around the heap utilizing Pile and compute the bowing minutes and avoidances from side-long loads in Fig. 5 [18].

4. Conclusion

- The final CONQUAS score for the construction of bored cast in suit pile is rated as 94.26. The architectural score is calculated only for completed construction works so it is not applicable for bored cast in suit pile. So the average of structural and M&E score is being added and the CONQUAS score for this project is rated as 94.26.
- Based on the score and rates got from the contextual investigation it very well may be inferred that CONQUAS is a viable device to gauge the nature of development works.
- Several implementation problems need to be addressed to harvest the full benefit from the application of quality assessment systems such as CONQUAS.



ANFIS-Based Accurate Estimation of the Confinement Effect for Concrete-Filled Steel Tubular (CFST)

S. Balasubramanian¹ · J. Jegan² · M. C. Sundarraja³

Received: 23 October 2018 / Revised: 11 March 2020 / Accepted: 31 May 2020
© Taiwan Fuzzy Systems Association 2020

Abstract This research is mainly focused on the accurate estimation of the confinement effect for the concrete-filled steel tubular (CFST) that makes it possible to evaluate the interaction between various parameters that affect the confinement effect. To do that, the CFST is analyzed with concrete and steel properties using ANFIS method. With respect to the shape of the CFST, both the circular and rectangle shapes are considered. Only then, the D/t ratio is increased and reduced the hoop stress, self-stress in the steel tube. To analyze the D/t ratio, the confinement effect and axial load capacity is determined. After that, the concrete strength is also analyzed according to their statistical measures like output target ratio (OTR), precision, efficiency, mean value (MV), mean square error (MSE), standard deviation (SD), etc. The proposed method is implemented in MATLAB platform and compared with the Artificial Neural Network (ANN) method. The proposed ANFIS method achieved a good prediction of the confinement effect and axial load capacity of the CFST.

Keywords Concrete-filled · ANFIS · CFST column · Short and long · D/t ratio · ANN · Load capacity · OTR · SD · MV

1 Introduction

Recent years, Concrete-filled steel tubular (CFST) is widely used in many large-span constructions. The mutual merits of concrete and steel materials with outstanding performance are documented using the member of concrete-filled steel tubular (CFST) [1]. Therefore, the girder steel and floor slabs contain the dependable relation in CFSTs and the architecture of side seismic load system resisting is included. The well suitable ductility production, more energy absorption, high axial load capacity, and low strength degradation become the main effect in mechanical performances [2–5]. Generally, the structural columns are most important due to the growing up of taller, lighter and well quick building up of structure. In the earliest lengthy civilization become dependent on the well-known columns because of the high load sustainability of masonry octagonal columns, such as high and big temples. The beam CFST columns are the key amalgamation application of concrete members and steel members individually. Increasing popularity gaining can be obtained from the various constructive space usage of CFST [6–9]. This is the most popular kind of constructive composites with more engineering compensation practices [10].

Similarly, the concrete core of confinement is obtained from the steel tube as well as the duplicity and strength has risen. Therefore, the possibility of steel wall local buckle can be reduced because of the concrete. The process of construction does not need any extra valuable merits. Enlargement development of structural CFSTs members with understanding of fire effect requirement is increased itself also which delivers the confinement type of post-fire repair [11–13]. The entire structure security background is basically attractive to solve the popular balance enhancement to the member protection and cost or expensive due to

✉ S. Balasubramanian
balasubramani.id@gmail.com

¹ Mohamed Sathak Engineering College, Kilakarai, India

² Faculty of Civil Engineering, University College of Engineering & Technology, Ramnad Campus, Ramanathapuram, India

³ Faculty of Civil Engineering, Thiagarajar College of Engineering, Madurai, India

M. C. Sundarraja



PRINCIPAL
MOHAMED SATHAK ENGINEERING COLLEGE
KILAKARAI 623808



ANFIS-Based Accurate Estimation of the Confinement Effect for Concrete-Filled Steel Tubular (CFST)

S. Balasubramanian¹ · J. Jegan² · M. C. Sundarraja³

Received: 23 October 2018/Revised: 11 March 2020/Accepted: 31 May 2020
© Taiwan Fuzzy Systems Association 2020

Abstract This research is mainly focused on the accurate estimation of the confinement effect for the concrete-filled steel tubular (CFST) that makes it possible to evaluate the interaction between various parameters that affect the confinement effect. To do that, the CFST is analyzed with concrete and steel properties using ANFIS method. With respect to the shape of the CFST, both the circular and rectangle shapes are considered. Only then, the D/t ratio is increased and reduced the hoop stress, self-stress in the steel tube. To analyze the D/t ratio, the confinement effect and axial load capacity is determined. After that, the concrete strength is also analyzed according to their statistical measures like output target ratio (OTR), precision, efficiency, mean value (MV), mean square error (MSE), standard deviation (SD), etc. The proposed method is implemented in MATLAB platform and compared with the Artificial Neural Network (ANN) method. The proposed ANFIS method achieved a good prediction of the confinement effect and axial load capacity of the CFST.

Keywords Concrete-filled · ANFIS · CFST column · Short and long · D/t ratio · ANN · Load capacity · OTR · SD · MV

1 Introduction

Recent years, Concrete-filled steel tubular (CFST) is widely used in many large-span constructions. The mutual merits of concrete and steel materials with outstanding performance are documented using the member of concrete-filled steel tubular (CFST) [1]. Therefore, the girder steel and floor slabs contain the dependable relation in CFSTs and the architecture of side seismic load system resisting is included. The well suitable ductility production, more energy absorption, high axial load capacity, and low strength degradation become the main effect in mechanical performances [2–5]. Generally, the structural columns are most important due to the growing up of taller, lighter and well quick building up of structure. In the earliest lengthy civilization become dependent on the well-known columns because of the high load sustainability of masonry octagonal columns, such as high and big temples. The beam CFST columns are the key amalgamation application of concrete members and steel members individually. Increasing popularity gaining can be obtained from the various constructive space usage of CFST [6–9]. This is the most popular kind of constructive composites with more engineering compensation practices [10].

Similarly, the concrete core of confinement is obtained from the steel tube as well as the duplicity and strength has risen. Therefore, the possibility of steel wall local buckle can be reduced because of the concrete. The process of construction does not need any extra valuable merits. Enlargement development of structural CFSTs members with understanding of fire effect requirement is increased itself also which delivers the confinement type of post-fire repair [11–13]. The entire structure security background is basically attractive to solve the popular balance enhancement to the member protection and cost or expensive due to

✉ S. Balasubramanian
balasubramani.id@gmail.com

¹ Mohamed Sathak Engineering College, Kilakarai, India

² Faculty of Civil Engineering, University College of Engineering & Technology, Ramnad Campus, Ramanathapuram, India

³ Faculty of Civil Engineering, Thiagarajar College of Engineering, Madurai, India

the designing architecture of complex members. Significantly, the procedure of CFST can be discussed with square shape, rectangular shape, rectangular and hollow shape which are dependent on the architectural design. When we compared to the steel hollow tube and the member of reinforced conventional concrete many more merits are gathered in the presence of circular CFST. Hence, capabilities of strength and strain concrete infill are raised with the compression of tri-axial state [14–17]. Eventually, the structural member resistance concerning protection features with the previous code structure required the quick corrected of much more experimental information that is applicable and enhanced the arithmetical methods are implemented. Additionally, the analysis of reliability with these variables must be analyzed depending upon the rationale statistical procedure [18–22].

In the paper, CFST columns are analyzed with the help of the proposed method and tested with the various loading conditions. Circular CFT columns obtain high load-bearing capacity because of the significant requirement impact by past exploratory and hypothetical investigations. CFST is built utilizing different tube shapes to acquire the most productive properties of concrete core and steel tube. The compressive strength of concrete is significantly expanded by the parallel limited steel tube in circular concrete. Extensive studies have been conducted on the CFST and empirical and theoretical formulas are recommended to predict the confinement effect. Nonetheless, the previously proposed equations vary significantly because of the nature of the complexity and uncertainty of the tri-axial stress state in the concrete infill. Therefore, ANFIS [23] is developed in this study to analyze the accuracy and influence compressive strength of the confined concrete on the capacity of CFST. The main aim of the study is to maximize the D/t ratio with the utilization of ANFIS method and to analyze the experimental data also. The detailed analysis of the proposed method with CFST is mentioned in the following section.

The organization of this paper is as follows. Section 1 presents a review of related works. The detailed process of the proposed ANFIS method is described in Sect. 3. Here, the short and long columns analysis is done for the circular and rectangular shape CFST. The main contribution of the paper is to improve the D/t ratio and reduce the corresponding losses. Moreover, statistical measures are analyzed and represented in the analysis Sect. 4. The rest of the document are as follows: Sect. 2 represents the literature review of recent analysis and Sect. 1 section mentions the general overview of the CFST analysis. The proposed method with the CFST analysis is mentioned in Sect. 3, 4 section. Finally, the concluding part of the paper is described in Sect. 5.

2 Literature Review: A Recent Analysis

Fundamentally, this section consists of many related works that are focused on the analyzing of CFST columns like long and short columns, loading circumstances and parametric based analysis which are discussed as follows:

Li et al. [20] introduced a finite element analysis (FEA) approach for stub columns CFDST of architectural character detection with the factor considered in effect of lengthy section. Yuan et al. [24] proposed productivity of concrete-filled double-skin composite tube columns (CFDSCT) beneath axially load compression with the usage of mathematical and exploratory analysis approaches. Yansheng et al. [25] carried out the Artificial Neural Network (ANN) design for the prediction of axial manner ability of rectangular columns CFST. In this process, the researchers have chosen 275 exploratory samples and trained them using the model of ANN. The combined model outcome data with the axial manner ability was obtained. Ahmadi et al. [26] proposed the integration method for predicting the steel-confined compressive strength of concrete using Artificial Neural Network (ANN).

Xu et al. [27] established the experimental analysis of single axial HSS–CFST compressive models. The axial compressive focused with 51 examples are analyzed. Therefore, the concrete strength, tube thickness, length-to-diameter and own pressure ranges of valuable factors were examined. Moon et al. [28] introduced the approach of Fuzzy Logic for confinement effect identification of the ability of axial stub CFST load and concrete infill. Han et al. [29] suggested a test sequence of the column with concrete-filled double-skin steel tubes (CFDST) for the limitation of the long-term sustained load. Two kinds of test procedures are added: they are ultimate strength test and long-term service test. Hassanein et al. [30] developed a method for diametric column determination with the usage of wide sequence thickness of (D/t) relation tends from 40 to 200 ranges and it mostly occupied with HSC up to 100 MPa. The experimental results of existing methods can be validated by the proposed approach and it predicts powerful outcomes. The HSCs used to fill the short CFST columns and strength effect with useful variables was debated.

Hua et al. [31] discussed the square part of CFST beam–columns with the amalgamation of both chloride corrosion and sustained the load. The entire 11 examples consist of CFST member of 7 and the reference of 4 hollow tubes designing were examined beneath 120 days of sustained load due to the increasing speed of chloride corrosion surroundings as well as the fault in load. The depth corrosion and load relationships are the most popular test

parameters. When they compared sustained load, full-range load–displacement relationship, ductility and the load–strain relationship of mode faults were compared and calculated.

3 Axial Strength Analysis of CFST Columns Using Adaptive Neuro-Fuzzy Inference System

Usually, the CFST columns with axial strengths are examined and it is denoted by using both circular and rectangular shapes. Based on the shapes, the various loading conditions are tested using CFST columns. Additionally, the column examination of short and long are obtained also the experimental data are analyzed with the usage of the suggested ANFIS concept. Therefore, the examination of circular CFST can be discussed as follows.

3.1 Circular CFST Long and Short Column Analysis

In this section, the Circular CFST (CCFST) with axial loading is accepted and experienced using the proposed concept. Basically, the ratio of Poisson’s are utilized from the axial loading of CCFST and it is a vital role of concrete steel exceeded with the absent of confinement property. In the case of incremental load, the ratio of Poisson in concrete arrived at the steel Poisson rates that may go beyond it. Significantly, vertical compression stress (σ) and horizontal hoop tensile stress are the appearances of steel tubes, because of the concrete confining pressure to rise up the stub column of compressive strength of concrete. The suitable network creation is the purpose of detecting the compressive length of concrete confined steel. Based on the limitation of axial loading from the column tube steel of filled circular concretes are extracted from the group of exploratory analysis. From data [32] that contains there are 268 trial outcomes. Experimental analysis of information criterion contains outer diameter (D) of columns in mm, wall thickness (t) of steel tube in mm, length (L) of columns in mm, compressive strength of unconfined concrete, tensile yield stress (F_y) of steel tube in MPa, KN with load axial ability of circular concrete-filled steel tube (P_{exp}). The analysis of short columns with the view of cross-sectional and modeling of CCFST is delineated in Fig. 1.

The reduction rate of vertical compressive stress received from the horizontal hoop tensile stress that produces the steel tube stress. The eventual load with the estimation of compressive vertical stress of steel tube can be given in Eq. (1):

$$\delta_v = 0.89\delta_{sy}. \tag{1}$$

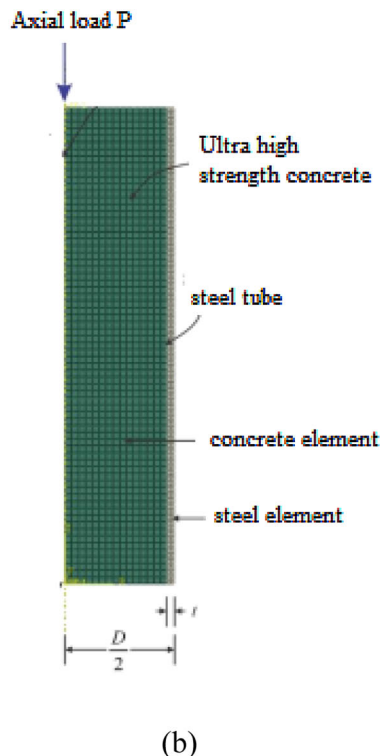
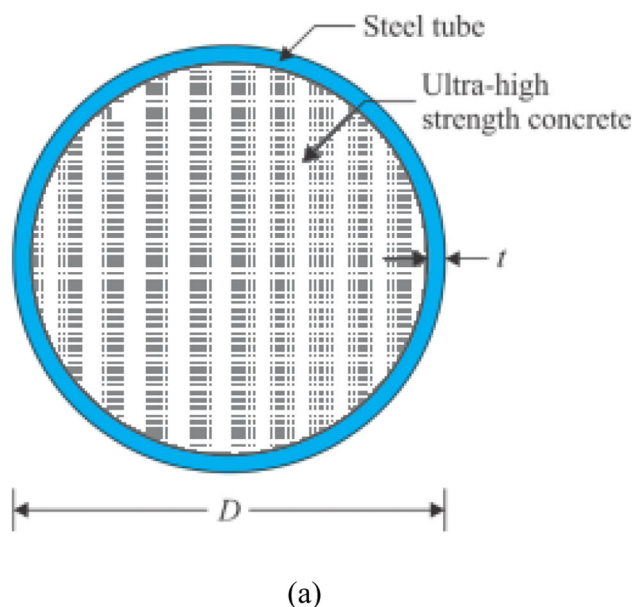


Fig. 1 View of (a) Cross-section and (b) modeling in CFST Columns

Therefore, the stub columns of circular filled concrete steel tube with the ability of axial loading is calculated from the Eq. (2):

$$P_{equ} = M_s\delta_v + M_c f'_{cc}. \tag{2}$$

Here, the concrete core with cross-sectional areas of the steel tube is denoted as M_s and M_c .

$$O_{4,i} = wt_i R_i, i = 1, 2 \tag{3}$$

However, the main focus of this paper is widespread experimental data implementation outcomes with the usage of the ANFIS controller concept and the suitable networks are formed. One of the popular Artificial Intelligence (AI) methods is the ANFIS controller and it is the amalgamation of the fuzzy and neural system. The entire concept of this paper is explained in the remaining sections.

3.2 Adaptive Neuro-Fuzzy Inference System (ANFIS)

The hybrid establishment of the ANFIS concept can mix the system interference of fuzzy which contains a high level of reasoning capabilities and that are created enlarge the amount of robustness with the usage of neural network with low-level computational power. The logical fuzzy consists of a multi-defined logic that describes the intermediate value among the true and false [33]. Therefore, this may be taken the ranges from low, very low, high, to very high based on the consideration of scales. Applying a number of fuzzy rules (IF–THEN), a knowledge-based fuzzy reasoning system has been formed [34–36].

Here, the input $p(\vec{x}_1), p(\vec{x}_2), \dots, p(\vec{x}_n)$ from the database can be fed through the well-known classifier of ANFIS for the detection of faults which contains there are five layers of nodes. Based on the five layers, the initial and the fourth layers notify the adaptive nodes everywhere; the fixed nodes are notified using the second, third and fifth layers. The structural design of the ANFIS is given in Fig. 2.

The specific rule origination of the ANFIS is given as follows:

If $p(\vec{x}_1)$ is $A_i, p(\vec{x}_2)$ is B_i , then C_i is.

$$R_i = a_i p(\vec{x}_1) + b_i p(\vec{x}_2) + c_i p(\vec{x}_n) + f_i. \tag{4}$$

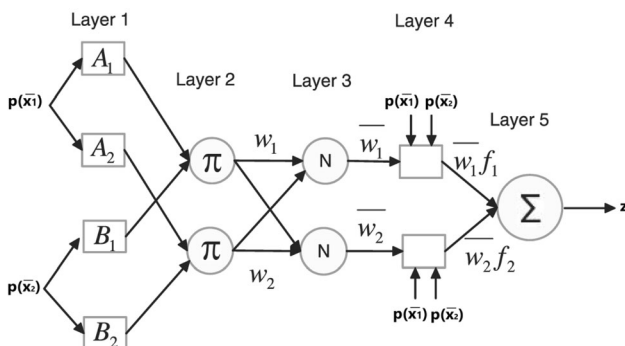


Fig. 2 Architecture of ANFIS

Here, the fuzzy set A_i, B_i and C_i with $p(\vec{x}_1), p(\vec{x}_2), \dots, p(\vec{x}_n)$ are the inputs, the output becomes R_i within the fuzzy region noted in the presence of fuzzy rule, similarly, the design parameters are a_i, b_i, c_i and f_i that are detected by the training process.

Layer-1 there is a node function in every node i and this layer is a square node.

$$O_{1,i} = \mu_{A_i} p(\vec{x}_1), O_{1,i} = \mu_{B_i} p(\vec{x}_2), O_{1,i} = \mu_{C_i} p(\vec{x}_n). \tag{5}$$

Frequently $\mu_{A_i} p(\vec{x}_1), \mu_{B_i} p(\vec{x}_2), \mu_{C_i} p(\vec{x}_n)$ are chosen as bell-shaped consideration with maximal equivalent to 1 and minimal equivalent to 0 which are described as follows:

$$\mu_{A_i} p(\vec{x}_1) = \mu_{B_i} p(\vec{x}_2) = \mu_{C_i} p(\vec{x}_n) = \left(\frac{1}{1 + \left(\frac{x - o_i}{p_i} \right)^{2q_i}} \right). \tag{6}$$

From the above equation, the parameter set is denoted as o_i, p_i, q_i . Based on the parameters, these layers are referred to as basic parameters.

Layer 2 In this layer, every node is labeled as a circle node which is the multiplications of incoming signals and sends the product out. For instance,

$$O_{2,i} = wt_i = \mu_{A_i} p(\vec{x}_1) \times \mu_{B_i} p(\vec{x}_2) \times \mu_{C_i} p(\vec{x}_n), i = 1, 2. \tag{7}$$

In every output, node denotes the strength firing of a rule.

Layer 3 In this layer, every node is denoted as a circular node. Therefore, the i th node estimates the ratio of the i th firing strength rules to the sum of the entire firing strengths rules:

$$O_{3,i} = wt_i = \frac{wt_i}{(wt_1 + wt_2)}, i = 1, 2. \tag{8}$$

Layer-4 In this layer, the entire node becomes mentioned as a square node with a node function

$$O_{4,i} = wt_i R_i, i = 1, 2, \tag{9}$$

where the output of layer-3 is described as wt_i and a_i, b_i, c_i and f_i are the parameter set. In this layer, the parametric values will be referred to as resultant parameters.

Layer 5 In this layer, the single node is denoted as a circle node and it computes the summation of all incoming signals with entire output [37].

$$O_{5,i} = \frac{\sum_i wt_i R_i}{\sum_i wt_i} \tag{10}$$

Based on the above analysis, system error has been detected. Because of the improvement of accuracy

prediction of ANFIS, the CCFST is examined. Before the analysis, the international standards of the proposed method with CFST are described in the following section.

3.3 International Standards for the Constructional Practice

The present designing concepts are the boundary to the strengths of the material for the designing of columns CFST. The international standardization of Eurocode 4 [38] and AS/NZS 5100.6 [39] are used for the checking of feasibility in short CFST columns of ultra-high strength.

3.3.1 As/nzs 5100.6

The concrete confinement's effects are also mentioned in AS/NZS 5100.6 [39], which is described in the following equation:

$$P_{u,AS} = \phi k_f A_s \eta_2 f_y + \phi A_r f_{ry} + \phi_c A_c f'_c \left(1 + \frac{\eta_1 t f_y}{d_o f'_c} \right). \quad (11)$$

From the above-mentioned equation, capacity reduction factor for steel is denoted as ϕ , the factor formation is k_f , A_s denotes the area of steel component, the area of the reinforcement is mentioned as A_r which is taken as zero, f_{ry} stands for the reinforcement yield strength, the capacity factor for concrete in compression becomes ϕ_c , A_c represents the area of concrete, d_o describes the diameter of column, in this study which is taken as D , the coefficients factors are η_1 and η_2 which are obtained from the following equations:

$$\eta_1 = 4.9 - 18.5\lambda_r + 17(\lambda_r)^2 (\eta_1 \geq 0), \quad (12)$$

$$\eta_2 = 0.25 (3 + 2\lambda_r) (\eta_2 \leq 1). \quad (13)$$

Therefore, the column slenderness is λ_r , this can be calculated by using below equations:

$$\lambda_r = \sqrt{\frac{N_{us}}{N_{cr}}}, \quad (14)$$

$$N_{us} = A_s f_y + A_c f'_c, \quad (15)$$

$$N_{cr} = \left(\frac{\pi^2 (EI)_e}{L_e^2} \right), \quad (16)$$

$$(EI)_e = EI_s + EI_r + E_c I_c. \quad (17)$$

From the equations, the cross-sectional maximum strength is described as N_{us} , the critical elastic load is N_{cr} with $(EI)_e$ standing for the successful flexural elastic stiffness, the effective length becomes L_e , elastic modulus are described as E for the steel and reinforcement, I_s indicates the secondary moment of steel area, and I_r describes the reinforcement area of secondary moment. From Eq. (16), the values such as ϕ , ϕ_c and k_f are considered as 1.0. The entire parameters interconnected to the reinforcement are also in use as zero.

3.3.2 Eurocode 4

The Eurocode 4 [40] can be regarded as the effect of concrete confinement in the following equations:

$$P_{u,EC4} = \eta_a A_s f_y + A_c f'_c \left[1 + \eta_c \frac{t f_y}{d f'_c} \right], \quad (18)$$

$$\eta_a = 0.25 (3 + 2\bar{\lambda}) \leq 1.0, \quad (19)$$

$$\eta_c = 4.9 - 18.5\bar{\lambda} + 17\bar{\lambda}^2 \geq 1, \quad (20)$$

Table 1 Experimental analysis of circular CFST short columns [42]

Specimen	D (mm)	L (mm)	t (mm)	D/t	f_u (MPa)	f'_c (MPa)	f_y (MPa)	$P_{u,exp}$ (kN)
C ₃	114.3	250	3.6	32	460	173.5	403	2422
C ₄						173.5	403	2340
C ₅						184.2	403	2497
C ₆						184.2	403	2314
C ₇			6.3	18	520	173.5	428	2610
C ₈						173.5	428	2633
C ₁₀	219.1	600	5.0	44	460	185.1	380	7837
C ₁₁						193.3	380	8664
C ₁₃			10.0	22		185.1	381	9085
C ₁₄						193.3	381	9187
C ₁₅			6.3	35	430	163.0	300	6915
C ₁₆						175.4	300	7407
C ₁₇						148.8	300	6838
C ₁₈						174.5	300	7569

Table 2 Parametric study of circular short CFST columns ($D = 600$ mm, $L/D = 3$) (column C_1 to C_{49})

Column	t (mm)	D/t	f_y (MPa)	f_u (MPa)	f'_c (MPa)	$P_{s,FE}$ (kN)
C ₁	30	20	380	460	190	21393
C ₂	20	30	380	460	190	14,009
C ₃	15	40	380	460	190	10,471
C ₄	12	50	380	460	190	8409
C ₅	30	20	420	500	60	23,551
C ₆	30	20	420	500	70	23,551
C ₇	30	20	420	500	80	23,551
C ₈	30	20	420	500	90	23,551
C ₉	30	20	420	500	100	23,551
C ₁₀	30	20	420	500	110	23,551
C ₁₁	30	20	420	500	120	23,551
C ₁₂	30	20	420	500	130	23,551
C ₁₃	30	20	420	500	140	23,551
C ₁₄	30	20	420	500	150	23,551
C ₁₅	30	20	420	500	160	23,551
C ₁₆	30	20	420	500	170	23,551
C ₁₇	30	20	420	500	180	23,551
C ₁₈	30	20	420	500	190	23,551
C ₁₉	20	30	420	500	60	15,472
C ₂₀	20	30	420	500	70	15,472
C ₂₁	20	30	420	500	80	15,472
C ₂₂	20	30	420	500	90	15,472
C ₂₃	20	30	420	500	100	15,472
C ₂₄	20	30	420	500	110	15,472
C ₂₅	20	30	420	500	120	15,472
C ₂₆	20	30	420	500	130	15,472
C ₂₇	20	30	420	500	140	15,472
C ₂₈	20	30	420	500	150	15,472
C ₂₉	20	30	420	500	160	15,472
C ₃₀	20	30	420	500	170	15,472
C ₃₁	20	30	420	500	180	15,472
C ₃₂	20	30	420	500	190	15,472
C ₃₃	15	40	420	500	60	11,616
C ₃₄	15	40	420	500	70	11,616
C ₃₅	15	40	420	500	80	11,616
C ₃₆	15	40	420	500	90	11,616
C ₃₇	15	40	420	500	100	11,616
C ₃₈	15	40	420	500	110	11,616
C ₃₉	15	40	420	500	120	11,616
C ₄₀	15	40	420	500	130	11,616
C ₄₁	15	40	420	500	140	11,616
C ₄₂	15	40	420	500	150	11,616
C ₄₃	15	40	420	500	160	11,616
C ₄₄	15	40	420	500	170	11,616
C ₄₅	15	40	420	500	180	11,616
C ₄₆	15	40	420	500	190	11,616
C ₄₇	12	50	420	500	60	9285

Table 2 continued

Column	t (mm)	D/t	f_y (MPa)	f_u (MPa)	f'_c (MPa)	$P_{s,FE}$ (kN)
C ₄₈	12	50	420	500	70	9285
C ₄₉	12	50	420	500	80	9285

$$\bar{\lambda} = \sqrt{\frac{N_{pl,Rk}}{N_{cr}}}, \quad (21)$$

$$N_{pl,Rk} = A_s f_y + A_c f'_c, \quad (22)$$

$$N_{cr} = \frac{\pi^2 (EI)_{eff}}{L^2}, \quad (23)$$

$$(EI)_{eff} = E_s I_s + 0.6 E_{cm} I_c. \quad (24)$$

Similarly, the effective flexural stiffness is denoted as $(EI)_{eff}$, η_a and η_c are the factors of concrete confining, $\bar{\lambda}$ describes the column slenderness, $N_{pl,Rk}$ is the plastic strength section and elastic critical normal force is described using N_{cr} .

3.3.3 American Code AISC

The enclosed equation of AISC [41] is mentioned as follows:

$$P_{u,AISC} = A_s f_y + C_2 f'_c A_c. \quad (25)$$

The safety factors are denoted as C_2 using the American code AISC [41], which is taken as 0.95. From this, the cross-sectional area of a CFST column is A_{sc} , f_{sc} notify the design strength of the compressive confining concrete in CFST column, influential factors of cross-sectional shapes on confinement effect are B and C . Similarly, the θ value stands for the factor of confinement. Based on the theoretical analysis, the calculations are performed and compared with the proposed method.

4 Results and Analysis

In the section, the long and short circular CFST columns are analyzed and implemented in MATLAB platform. The experimental data are tabulated in Table 1, which describe the circular CFST columns. The ultra-high-strength short circular CFST columns of peak loads are predicted by design codes that can be compared with the proposed analysis in Table 4. Based on the experimental analysis, the proposed ANFIS method is utilized and

Table 3 Parametric study of circular short CFST columns ($D = 600$ mm, $L/D = 3$) (column C₅₀ to C₉₉)

Column	t (mm)	D/t	f_y (MPa)	f_u (MPa)	f'_c (MPa)	$P_{s,FE}$ (kN)
C ₅₀	12	50	420	500	90	9285
C ₅₁	12	50	420	500	100	9285
C ₅₂	12	50	420	500	110	9285
C ₅₃	12	50	420	500	120	9285
C ₅₄	12	50	420	500	130	9285
C ₅₅	12	50	420	500	140	9285
C ₅₆	12	50	420	500	150	9285
C ₅₇	12	50	420	500	160	9285
C ₅₈	12	50	420	500	170	9285
C ₅₉	12	50	420	500	180	9285
C ₆₀	12	50	420	500	190	9285
C ₆₁	30	20	250	410	60	16,230
C ₆₂	30	20	260	410	60	16,490
C ₆₃	30	20	280	410	60	16,889
C ₆₄	30	20	300	430	60	17,868
C ₆₅	30	20	310	430	60	18,179
C ₆₆	30	20	320	430	60	18,608
C ₆₇	30	20	330	450	60	19,167
C ₆₈	30	20	340	450	60	19,535
C ₆₉	30	20	350	450	60	20,038
C ₇₀	30	20	360	450	60	20,438
C ₇₁	30	20	380	480	60	21,632
C ₇₂	30	20	400	480	60	22,455
C ₇₃	30	20	420	500	60	23,551
C ₇₄	30	20	250	410	120	16,230
C ₇₅	30	20	260	410	120	16,490
C ₇₆	30	20	280	410	120	16,889
C ₇₇	30	20	300	430	120	17,868
C ₇₈	30	20	310	430	120	18,179
C ₇₉	30	20	320	430	120	18,608
C ₈₀	30	20	330	450	120	19,167
C ₈₁	30	20	340	450	120	19,535
C ₈₂	30	20	350	450	120	20,038
C ₈₃	30	20	360	450	120	20,438
C ₈₄	30	20	380	480	120	21,632
C ₈₅	30	20	400	480	120	22,455
C ₈₆	30	20	420	500	120	23,551
C ₈₇	30	20	250	410	190	16,230
C ₈₈	30	20	260	410	190	16,490
C ₈₉	30	20	280	410	190	16,889
C ₉₀	30	20	300	430	190	17,868
C ₉₁	30	20	310	430	190	18,179
C ₉₂	30	20	320	430	190	18,608
C ₉₃	30	20	330	450	190	19,167
C ₉₄	30	20	340	450	190	19,535
C ₉₅	30	20	350	450	190	20,038
C ₉₆	30	20	360	450	190	20,438

Table 3 continued

Column	t (mm)	D/t	f_y (MPa)	f_u (MPa)	f'_c (MPa)	$P_{s,FE}$ (kN)
C ₉₇	30	20	380	480	190	21,632
C ₉₈	30	20	400	480	190	22,455
C ₉₉	30	20	420	500	190	23,551

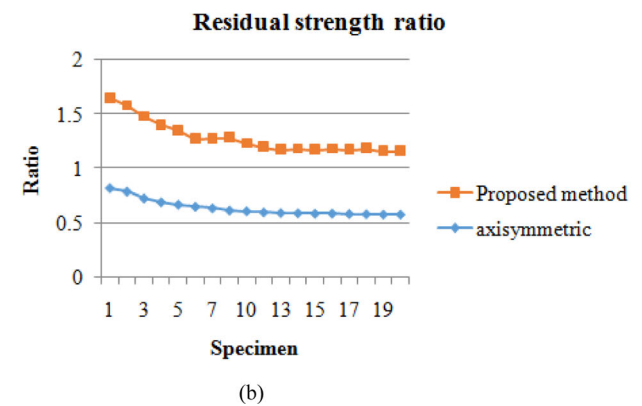
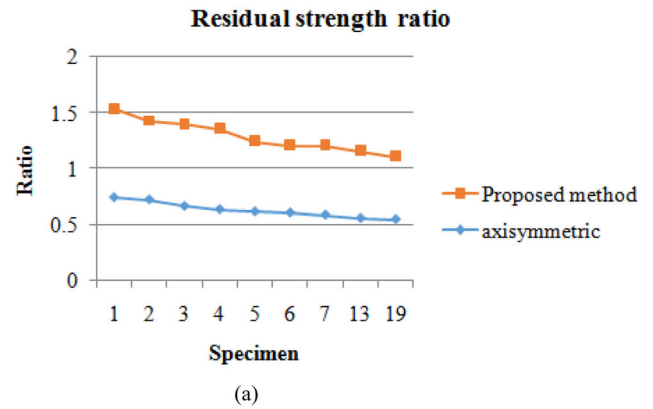


Fig. 3 Analysis of Residual Strength ratio in (a) 190Mpa and (b) 40 Mpa using proposed and axisymmetric method

analyzed their corresponding results also. Significantly, the AISC approach showed a conservative prediction of circular short CFST columns ultra-high-strength with a mean value of 0.88. The code prediction recommendations of CFST columns with ANFIS are also held up by the comparison between the test results which is labeled in Table 4. Further, it concluded that current ANFIS and Eurocode 4 can accurately predict the ultimate strength of ultra-high-strength circular short CFST.

Tables 2, 3 show the values of the parametric study analysis of the axisymmetric and proposed ANFIS method. These evaluated the effects of the material and geometric

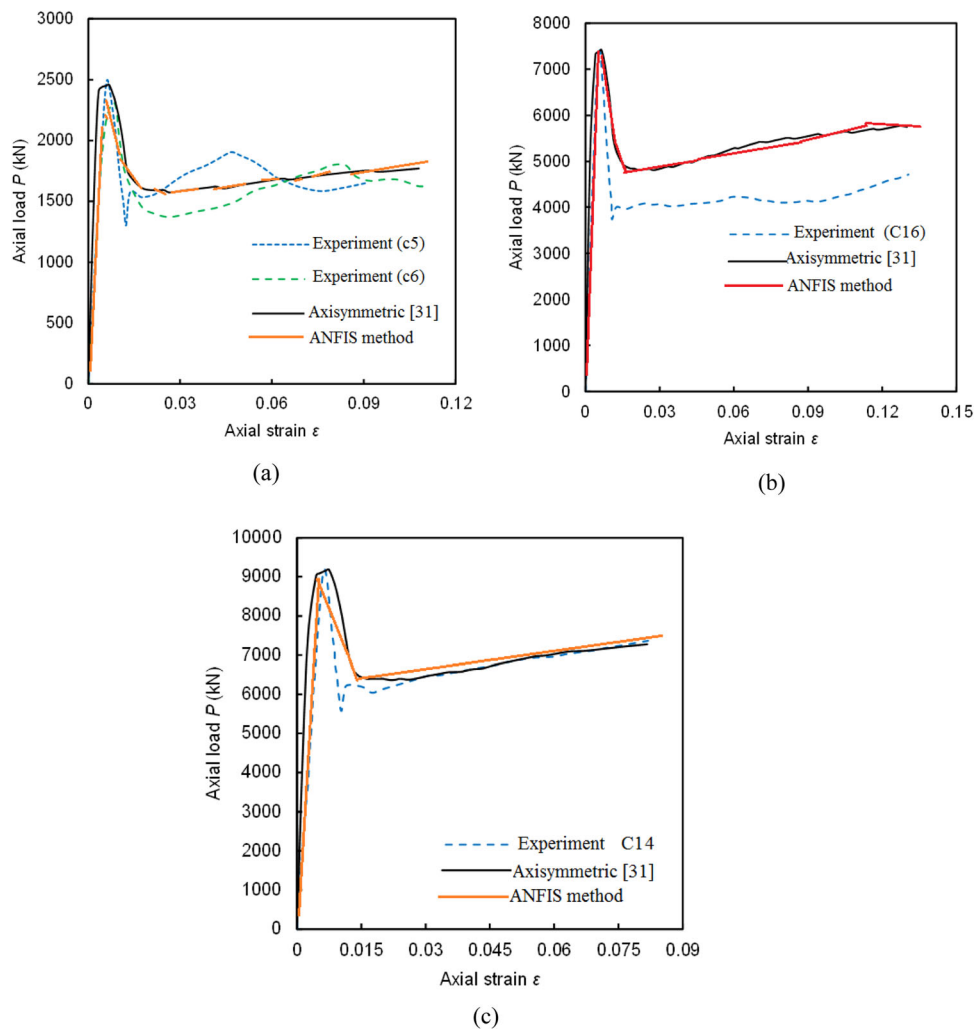


Fig. 4 Analysis of Axial Load Vs Axial Strain under various methods in different loads (a) 3000 (b) 8000 and (c) 10000

parameters like axial load–strain, ductility, residual strength ratio, column, etc. Under the short circuit, CFST columns are tested in 99 columns from [42] and the diameter is mentioned about 600 mm. The length of the columns is mentioned as the 1800 mm and the D/t ratio is varied from 20 to 50, after that the yield stress also varied. The corresponding outputs are illustrated in Figs. 3, 4, 5. Table 4 shows the residual strength ratio under various f_c .

Figure 3 mentions the residual strength ratio for the circular short CFST under axial loads. Normally, the residual strength ratio depends on the steel contribution ratio, concrete compressive strength and D/t ratio. The steel contribution ratio was determined by taking the ratio of steel tube strength ($P_{s,FE}$) to the maximum load ($P_{u,FE}$) of CFST columns [43]. Regarding this analysis, the f_c is analyzed in two conditions such as 190 MPa and 40 MPa. The average residual strength ratio of the proposed and axisymmetric method is 0.64477, 0.6611 and 0.63849, 0.6355 under 40 MPa and 190 MPa, respectively. Similarly,

other factors are tested and determined. Under the axial loads, the ductility of circular short CFST is determined with the help of residual strength ratio. Generally, for CFST columns, a smaller D/t ratio and a higher steel contribution ratio could lead to a sufficient ductility. This confirms the experimental observation reported by Liew and Xiong [32].

Under the various axial loading conditions, the yield stress and steel contributions are illustrated in Fig. 4. By utilizing the proposed method, the yield stress of the steel is evaluated and compared with the experimental methods. At a similar solid quality dimension, diminishing the D/t proportion, which compares to an expansion in the steel commitment proportion, can prompt a higher ductility. It tends to be seen that the residual strength increments with an expansion in the steel commitment proportion, yet it somewhat diminishes as the solid quality increments. Table 5 illustrates the comparison of the peak loads obtained from design codes and test [42].

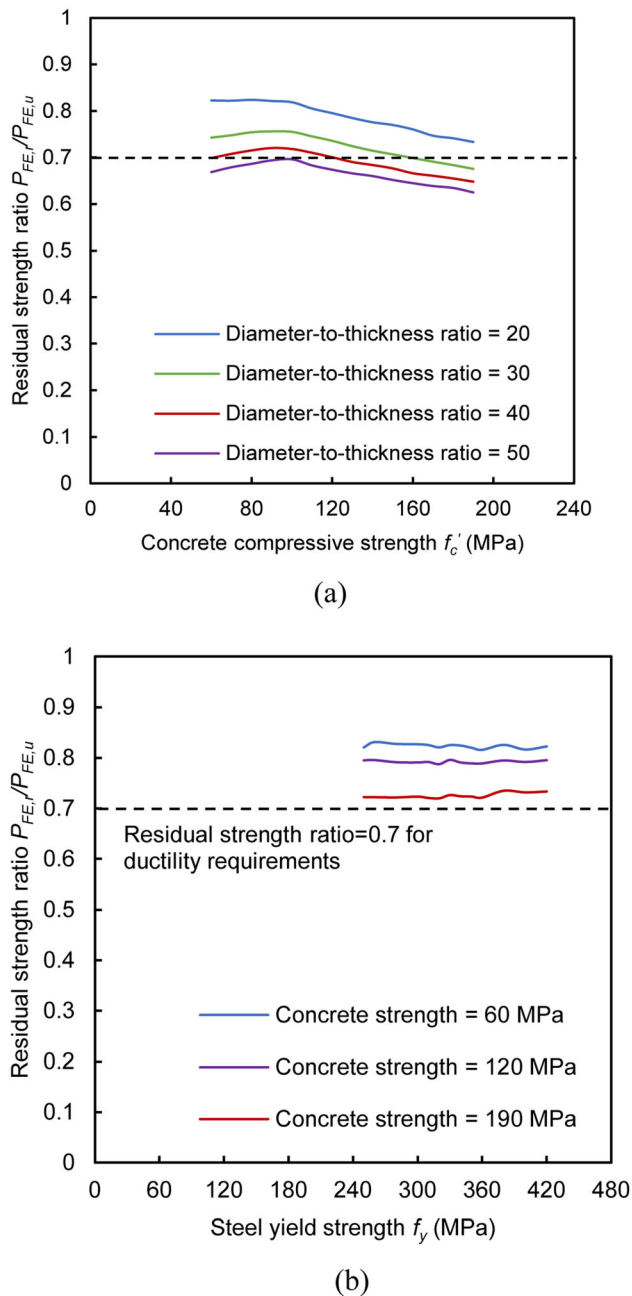


Fig. 5 Analysis of circular short CFST columns (a) compressive strength and (b) yield stress

Figure 5 illustrates the analysis of circular short CFST columns for compressive strength and yield stress. In the above section, the circular process is analyzed after that, a similar way of analysis of rectangular cross-sectional view is analyzed. For the analysis of rectangle cross-section, the following analysis is carried out. Table 6 mentions the D/t ratio and L/D ratio of the proposed method.

Table 4 Residual Strength ratio under various f_c

Specimen	Residual strength ratio (190 Mpa)	
	Axisymmetric	Proposed method
C ₁	0.75	0.79
C ₂	0.73	0.7
C ₃	0.67	0.73
C ₄	0.64	0.72
C ₅	0.62	0.63
C ₆	0.61	0.6
C ₇	0.59	0.62
C ₁₃	0.56	0.6
C ₁₉	0.55	0.56
Residual strength ratio (40 Mpa)		
C ₁	0.818541	0.83
C ₂	0.787564	0.79
C ₃	0.726337	0.75
C ₄	0.691568	0.71
C ₅	0.66976	0.68
C ₆	0.650638	0.62
C ₇	0.636481	0.64
C ₉	0.616535	0.67
C ₁₀	0.609967	0.62
C ₁₂	0.599548	0.6
C ₁₃	0.593744	0.58
C ₁₄	0.590863	0.59
C ₁₅	0.587395	0.586
C ₁₆	0.588055	0.59
C ₁₇	0.584974	0.59
C ₁₈	0.582734	0.6
C ₁₉	0.579031	0.58
C ₂₀	0.57921	0.58

Table 7 describes rectangle cross-section analysis of L/D ratio and D/t ratio. Under the various experimental methods, the performance measures functions are tabulated in Tables 1, 2, 3, 4, 5, 6, 7. When compared with the existing methods, the proposed technique provides better results. The proposed method provides suitable results while comparing it with existing methods. From the results, existing methods attained lower productivity, but our proposed EC4 presented better presentation, as well as the ANFIS also provides good performance results. For these reasons the proposed ANFIS works perfectly and it is applicable in many fields.

Table 5 Comparison of the peak loads obtained from design codes and test

Specimens	E_{cm} [44] (GPa)	$P_{u,exp}$ [44] (kN)	AS/NZS 5100.6 [39]		Eurocode 4 [38]		AISC [40]		ANFIS $P_{u,CAL}$ (kN)
			$P_{u,AS}$ (kN)	$\frac{P_{u,AS}}{P_{u,exp}}$	$P_{u,EC4}$ (kN)	$\frac{P_{u,EC4}}{P_{u,exp}}$	$P_{u,AISC}$ (kN)	$\frac{P_{u,AISC}}{P_{u,exp}}$	
C ₃	63	2422	2297	0.95	2277	0.94	1989	0.82	2423
C ₄	63	2340	2297	0.98	2277	0.97	1989	0.85	2423
C ₅	63	2497	2389	0.96	2369	0.95	2081	0.83	2437
C ₆	63	2314	2389	1.03	2369	1.02	2081	0.90	2437
C ₇	63	2610	2706	1.04	2685	1.03	2254	0.86	2905
C ₈	63	2633	2706	1.03	2685	1.02	2254	0.86	2905
C ₁₀	66	7837	8106	1.03	8030	1.02	7316	0.93	7752
C ₁₁	67	8664	8380	0.97	8303	0.96	7584	0.88	8142
C ₁₃	66	9085	9162	1.01	9080	1.00	7978	0.88	8848
C ₁₄	67	9187	9406	1.02	9323	1.01	8220	0.89	9105
C ₁₅	62	6915	7213	1.04	7152	1.03	6450	0.93	6897
C ₁₆	58	7407	7605	1.03	7545	1.02	6844	0.92	7567
C ₁₇	54	6838	6738	0.99	6682	0.98	5998	0.88	6662
C ₁₈	56	7569	7571	1.00	7512	0.99	6816	0.90	7312

Table 6 Circular Cross-section of L/D ratio and D/t ratio

Specimen	L/D ratio	Crippling load (KN)	D/t ratio	Crippling load
1	10.44	1589.01	25.44	192.04
2	11.52	1425.22	30.74	204.78
3	12.89	1253	38.01	213.11
4	15.14	730.52	42.11	306.74
5	16.32	562.41	47.84	420.48
6	17.85	406.08	51.52	591.55
7	16.85	291.51	55.66	769.28
8	18.55	203.44	60.45	1456.22
9	19.62	182.33	62.22	1548
10	21.75	169.36	73.52	1685

Table 7 Rectangle Cross section analysis of L/D ratio and D/t ratio

Specimen	L/D ratio	Crippling load (KN)	D/t ratio	Crippling load
1	11.58	1514.22	19.22	156.22
2	12.08	1469.78	24.45	222.52
3	12.84	1354	32.11	294
4	13	852.78	33	305
5	14.25	536	38.14	456.78
6	14.72	408.11	42.11	562.22
7	15.22	325.44	56.78	600.78
8	16.22	256.22	65.44	954.44
9	19.44	192.22	70.22	1354.44
10	20.41	157.44	73.22	1585.89

5 Conclusion

In this paper, the limitations of the axial loading of circular columns concrete steel tube with the group of experimental outcomes are analyzed. The proposed ANFIS controller

consists of a system with feedback-propagation. The inputs are taken for the examination strength of compressive unconfined concrete, length of the column, exterior diameter, tensile and thickness of the wall (t) may deliver the steel stress tube. Hence, the network of training stage can

be stopped by using the factor of regression and mean squared error (MSE). The various amounts of hidden neurons are used after a network training stage with N10-Tansig (number of hidden neurons is 50) can be chosen. The rectangular and circular short and long columns are analyzed and compared with the experimental methods also. The residual strength ratio is also analyzed according to the staining process. Then, the D/t ratio and L/D ratio is analyzed, and the various axial loading periods evaluated. The various compressive strengths of concrete are also analyzed. Hence, the practical equations dependence on the network of ANFIS is used for the analyzing stage. Ultimately, when compared to the existing methods the suggested concept can deliver the suitable results.

Conflict of interests The author(s) declared no potential conflicts of interest with respect to the research, authorship, and/or publication of this article.

References

- Tao, Z., Han, L.H.: Behaviour of fire-exposed concrete-filled steel tubular beam columns repaired with CFRP wraps. *Thin-Walled. Struct.* **45**, 63–76 (2007)
- Li, P., Zhang, T., Wang, C.: Behavior of concrete-filled steel tube columns subjected to axial compression. *Adv. Mater. Sci. Eng.* (2018). <https://doi.org/10.1155/2018/4059675>
- Esra Mete Güneş: Ayşegül Gültekin, and Kasım Mermerdas, ultimate capacity prediction of axially loaded CFST short columns. *Int. J. Steel. Struct.* **16**(1), 99–114 (2016)
- Shaat, A., Fam, A.: Axial loading tests on short and long hollow structural steel columns retrofitted using carbon fibre reinforced polymers. *Can. J. Civil. Eng.* **33**, 458–470 (2006)
- Kang, W.H., Uy, B., Tao, Z., Hicks, S.: Design strength of concrete-filled steel columns. *Adv. Steel. Construct.* **11**(2), 165–184 (2015)
- Pragna, M., Ganesan, P.: Analysis of concrete filled steel tubes using ansys. *Int. J. Latest. Eng. Res. Appl.* **1**(9), 71–78 (2016)
- Liu, X., Tao, J.F., Hajjar, J.F., Muxuan, T.: Comparison and analysis of design procedures for CFST-to-Steel girder connection panel zone shear strength.
- Huang, F., Xinmeng, Y., Chen, B.: The structural performance of axially loaded CFST columns under various loading conditions. *Steel. Compos. Struct.* **13**(5), 451–471 (2012)
- Han, L.H., Li, W., Bjorhovde, R.: Developments and advanced applications of concrete-filled steel tubular (CFST) structures: members. *J. Constr. Steel Res.* **100**, 211–228 (2014)
- Yang, C., Gao, P., Wu, X., Chen, Y.F., Li, Q., Li, Z.: Practical formula for predicting axial strength of circular-CFST columns considering size effect. *J. Constr. Steel Res.* **168**, 105979 (2020)
- Wang, K., Chen, Y., Wan, J., Han, S., Liao, L.: Compressive behavior of post-heated circular CFST short columns externally strengthened with CFRP sheets. *J. Adhes. Sci. Technol.* **32**, 833–853 (2018)
- Chen, Y., Wang, K., He, K., Wei, J., Wan, J.: Compressive behavior of CFRP-confined post heated square CFST stub columns. *Thin-Walled. Struct.* **127**, 434–445 (2018)
- Hou, C.C., Han, L.H.: Life-cycle performance of deteriorated concrete-filled steel tubular (CFST) structures subject to lateral impact. *Thin-Walled. Struct.* **132**, 362–374 (2018)
- Chen, J., Zeng, L.: Experiment on mechanical performance of axial compression of recycled concrete-filled steel tubular stub columns. *J. Lanzhou. Univ. Technol.* **39**, 112–116 (2013)
- Xu, Y., Chen, Q., Zhu, S.: Finite element analysis on 3D joints between composite CFST column and steel beam. *J. Shenyang. Jianzhu. Univ.* (2015).
- Yu Z, Ding F, Lin S. Researches on behavior of high-performance concrete filled tubular steel short columns, *J. Build. Struct.* (2002).
- Chen, B.C., Sheng, Y.: Research on load-carrying capacity of concrete-filled-steel tubular dumbbell-shaped long columns under axial loads. *Eng Mech.* 2008.
- Ma, D., Han, L.H., Li, W., Hou, C.: Behaviour of concrete-encased CFST stub columns subjected to long-term sustained loading. *J. Constr. Steel Res.* **151**, 58–69 (2018)
- Dey, P., Gupta, R.K., Laskar, A.I.: Numerical and experimental investigations of different cross-sectional configuration of plain concrete and CFST short columns under axial compression. *Int. J. Civil. Eng.* **17**, 1585–1601 (2019)
- Li, W., Han, L.H., Zhao, X.L.: Behavior of CFDST stub columns under preload, sustained load and chloride corrosion. *J. Constr. Steel Res.* **107**, 12–23 (2015)
- Reinhardt, H.W., Özkan, H., Mielich, O.: Creep of concrete as influenced by the rate of expansion due to alkali-silica reaction. *Struct. Concr.* **20**, 1781–1791 (2019)
- Sundararaj, V.: Optimised denoising scheme via opposition-based self-adaptive learning PSO algorithm for wavelet-based ECG signal noise reduction. *Int. J. Biomed. Eng. Technol.* **31**(4), 325 (2019)
- Jang, J.S.: ANFIS: adaptive-network-based fuzzy inference system. *IEEE. Transact. Syst. Man. Cybern.* **23**(3), 665–685 (1993)
- Yuan, W.B., Yang, J.J.: Experimental and numerical studies of short concrete-filled double skin composite tube columns under axially compressive loads. *J. Constr. Steel Res.* **80**, 23–31 (2013)
- Du, Y., Chen, Z., Zhang, C., Cao, X.: zhang and Xiaochun cao, Research on axial bearing capacity of rectangular concrete-filled steel tubular columns based on artificial neural networks. (2016).
- Ahmadi, M., Naderpour, H., Kheyroddin, A.: ANN model for predicting the compressive strength of circular steel-confined concrete. *Int. J. Civ. Eng.* **15**, 213–221 (2017)
- Xu, L., Zhou, P., Chi, Y., Huang, L., Ye, J., Yu, M.: Performance of the high-strength self-stressing and self-compacting concrete-filled steel tube columns subjected to the uniaxial compression. *Int. J. Civil. Eng.* **16**, 1069–1083 (2017)
- Moon, J., Kim, Jung J., Lee, Tae-Hyung, Lee, Hak-Eun: Prediction of axial load capacity of stub circular concrete-filled steel tube using fuzzy logic. *J. Constr. Steel Res.* **101**, 184–191 (2014)
- Han, L.H., Li, Y.J., Liao, F.Y.: Concrete-filled double skin steel tubular (CFDST) columns subjected to long-term sustained loading. *Thin-Walled. Struct.* **49**(12), 1534–1543 (2011)
- Hassanein, M.F., Patel, V.I., Elchalakani, M., Thai, H.T.: Finite element analysis of large diameter high strength octagonal CFST short columns. *Thin-Walled. Struct.* **123**, 467–482 (2018)
- Hua, Y.X., Han, L.H., Wang, Q.L., Hou, C.: Behaviour of square CFST beam-columns under combined sustained load and corrosion: experiments. *Thin-Walled. Struct.* **136**, 353–366 (2019)
- Liew, J.Y.R., Xiong, M.X., Xiong, D.X.: Design of concrete filled tubular beam-columns with high strength steel and concrete. *Structures* **8**, 213–226 (2016)
- Prakash, S., Sinha, S.K.: ALFC of hybrid multi-generation power system using UC and TCPS by ANFIS control technique. *Int J Electron.* **106**, 174–211 (2018)
- Sundararaj, V.: Optimal task assignment in mobile cloud computing by queue based ant-bee algorithm. *Wireless. Pers. Commun.* **104**(1), 173–197 (2019)

35. Sundararaj, V.: An efficient threshold prediction scheme for wavelet based ECG signal noise reduction using variable step size firefly algorithm. *Int. J. Intell. Eng. Syst.* **9**(3), 117–126 (2016)
36. Sundararaj, V., Muthukumar, S., Kumar, R.S.: An optimal cluster formation based energy efficient dynamic scheduling hybrid MAC protocol for heavy traffic load in wireless sensor networks. *Comput. Secur.* **77**, 277–288 (2018)
37. Truong, D.N., Tran, Q.C., Tran, P.N. Nguyen, Thi M.S.: ANFIS damping controller design for SSSC to improve dynamic stability of a grid connected wind power systems
38. EN 1994-1-1: Eurocode 4-design of composite steel and concrete structures, part 11 general rules and rules for building. British Standards Institution, London (2004)
39. AS/NZS 5100.6: Bridge design part 6: steel and composite construction. Standards Australia, Sydney (2017)
40. Portolés, J.M., Serra, E., Romero, M.L.: Influence of ultra-high strength infill in slender concrete-filled steel tubular columns. *J. Const. Steel. Res.* **86**, 107–114 (2013)
41. AISC 360-16: Specification for structural steel buildings. American Institute of Steel Construction, Chicago (2016)
42. Patel, V.I., Hassanein, M.F., Thai, H.T., Al Abadi, H., Elchalakani, M., Bai, Y.: Ultra-high strength circular short CFST columns: axisymmetric analysis, behaviour and design. *Eng Struct.* **179**, 268–283 (2019)
43. Liang, Q.Q., Fragomeni, S.: Nonlinear analysis of circular concrete-filled steel tubular short columns under axial loading. *J.Constr. Steel. Res.* **65**, 2186–2196 (2009)
44. Xiong, M.X., Xiong, D.X., Liew, J.Y.R.: Axial performance of short concrete filled steel tubes with high- and ultra-high- strength materials. *Eng. Struct.* **136**, 494–510 (2017)



S. Balasubramanian Research Scholar. Assistant Professor in Civil Engineering Department, Mohamed Sathak Engineering College, Kilakarai. He obtained Bachelor's degree (Civil Engineering) From Mohamed Sathak Engineering College, Kilakarai and Master's degree (Structural Engineering) from R.V.S College Engineering Technology, Dindugal, Tamil Nadu.



J. Jegan obtained his Bachelor's degree (Civil Engineering) and Master's degree (Environmental Engineering) from Bharathiyar University, Coimbatore, Tamil Nadu, and received Ph.D. degree from Anna University Chennai, India. His teaching experience spans over 20 years. Presently he is working as Dean and Professor, Department of Civil Engineering, Anna University, University College of Engineering Ramanathapuram. He has published 70+ international journals and 30+ national and international conferences in his professional career. He is a reviewer for various reputed international journals in Elsevier and Taylor & Francis. He is an editorial board member for the Journal of Environmental Biotechnology & Research. He holds the membership in various professional bodies like Indian Society for Technical Education, International Association of Civil Engineers, International Association for Hydro-Environment Engineering and Research, Asia-Pacific Chemical, Biological & Environmental Engineering Society, Institute of Public Health Engineers, Indian Water Works Association and The Institute of Engineers.



M. C. Sundarraja obtained his Bachelor's degree (Civil Engineering) From Thiagarajar College of Engineering, Madurai and Master's degree (Structural Engineering) from Thiagarajar College of Engineering, Madurai, Tamil Nadu, and received Ph.D. degree from Anna University Chennai, India. And Post Doctoral Fellowship (Structural Engineering) from Queensland University of Technology, Australia.



Cloud Based Secured Log Retrieval Using Fully Homomorphic Encryption

B. Rasina Begum¹ and P.Chithra²

¹Research Scholar, Department of Computer Science and Engineering, Mohamed Sathak Engineering College, Kilakarai, Ramanathapuram, Tamil Nadu, India

²Professor, Department of Computer Science and Engineering, Thiagarajar College of Engineering, Madurai, Tamil Nadu India

E-mail: rasinayousuf@gmail.com, pccse@tce.edu

Abstract - Cloud computing provides a scalable platform for growing amount of data and processes that work on various applications and services by means of on-demand service providing. The storage services offered by clouds have become a new profit growth by providing a comparably cheapest, scalable, location-independent platform for managing users' data. Client uses the cloud storage and enjoys the high-quality applications and services from a shared pool of configurable computing resources using cloud services. It reduces the trouble of local data storage and maintenance. But it gives severe security threats toward users' outsourced data. Maintaining the log record securely over extended period is very crucial to the proper functioning of any organization. Log holds the record of system events specially user activities. It is the main target for malicious attackers. An attacker, breaking into a system would not try to leave traces of his or her activities behind. This proposed work mainly concentrates on the problem of log security in cloud computing system and using fully homomorphism encryption algorithm in the cloud computing log data.

Keywords: Cloud Security; Logging; Fully Homomorphic Encryption; Decipherment

I. INTRODUCTION

Organization need to rapidly increase their businesses, which may enforce them to enlarge the IT infrastructure by adding storage devices, new servers, network bandwidth, etc. Mission Critical business data must be protected, and it should be available to the intended user, which in turn requires data security and disaster infrastructure. As the capital expenditure rises to fulfill the requirements, the risk associated with the investment also increases. For small and medium sized businesses, this may be a big problem, which eventually affect their business to grow. As an individual, it may not be affordable every time to purchase new applications if they are required only for a short period. Instead of purchasing needed resources, Cloud resources are hired based on pay-per-use without involving any CAPEX. CSP provide on-demand network access configurable computing resources such as servers, network, storage and applications. Users can scale up or scale down the demand of computing resources with minimal management effort or CSP interaction. Users can influence cloud service provider's expertise to store, process, protect, backup and replicate the data empowered by the most advanced

technology, which otherwise would cost more. Although the cloud computing has become a good service model, and have a large commercial, cloud computing is still facing many issues. It brings a lot of security threats to the outsourced data. As a result, the correctness of the information within the cloud is place with risks. The threats in cloud side occurs from time to time. The remedy to preserve the data is to encrypt the data before uploading the data to the cloud and user must send only the encrypted query for retrieval.

Log is a record of all system events [1]. For example, Log files in web server have all requests submitted to the server. With the help of this tool, it is possible to identify the outsiders who used the system and all their activities. When system has severe security issues, Log files are used to identify the critical incidents, policy violation, unauthorized activities, and all operational problems. This kind of tools are highly helpful for auditing and all forms of forensic analysis, preparing baselines and find long term security problems. Log files have many types namely Request Log file, Manager Log file and internal concurrent manager log file. Again, there are two types called event log and transaction log. Event log records all events during the execution to provide audit trail. This audit trail helps to understand the system activities for diagnosing the problems. Database system must maintain the transaction log. This is the history of actions executed by Database Management system to check the ACID properties.

Originally logs were used mainly for troubleshooting problems[7], but logs now serves many applications in many organizations, such as optimizing the system and network performance, recording the actions of the users, and providing the data useful for investigating malicious activity. Due to advancements in security, nowadays log contains information related to many different types of events related to networks and systems. Within an business enterprise, many logs used to have records related to system security; common examples of these computer security logs are audit logs that contains user authentication attempts and security device logs that record possible attacks. Basic problem with log management that occurs in many organizations is effectively balancing a limited quantity of

log management resources with providing the log data continuously. Generation of logs and storing them became complicated by following factors, including a higher number of log sources; inconsistent content of log, formats, and timestamps among sources; and increasingly large volume of log data.

Organizations need to protect their logs. Many logs have maximum size as holding the thousands of most recent events or keeping hundred megabytes of log data. When the threshold is reached, the log might overwrite the old data with the new data or stop logging altogether, both of which would cause a loss of log data availability. To satisfy data retention requirements, organization are required need to keep copies of log files for the longer period than the original log sources can support, which necessitates establishing log storing system. Because of the increase in size and number of logs, it will be preferable in some cases to reduce the logs by filtering out the entities that are not required to archived. The confidentiality and Integrity of the archived log file need to be protected by storing the log in encrypted form.

II. THE THREAT MODEL

A log entry consists of a date (time) and description of events. A well experienced attacker will try to compromise log data pertaining to the past during breaking into the system: he wishes to alter, or erase, any entries pertaining to his current or past login attempts. In many of the real-world applications, the log files are used to generated and stored on an untrusted machine which is not physically secure enough to guarantee that it cannot be compromised. Most of the system component responsible for logging-is not totally error-free, which is unfortunately always the case. In systems using remote logging, if the server is unavailable, then the log has to be buffered and stored temporarily at the local machine once an attacker obtains the current secret key of the log machine, he can modify the post-compromise data at will, in this case, the favourable step is to forward integrity: how to ensure that pre-compromise data cannot be modified. That is, even if the attacker obtains the current secret key, he must be unable to modify the audit data generated before intrusion. An attacker who gains access to the system naturally wishes to remove the trace of his presence to hide attack details or frame from innocent users.

In fact, first target of the well experienced attacker would often be the logging system. To make the log secure, one must prevent the attacker from modifying log data. Secure versions of log should be designed to defend against tampering.

The capabilities of attackers [3] are

1. He can intercept any messages sent over the internet.
2. He can synthesize, replicate, and replay messages in his possession.
3. He can be the legitimate participant of the network or can try to impersonate legitimate hosts.

III. SYSTEM ARCHITECTURE

The architecture of the cloud based secure log management system [4] is shown in fig. 1.

There are four major functional components namely

A. Log Generators

It is used for generation of the log data. Every organization that uses the cloud-based log management service has a few log generators. These generators are built with logging capability. The log files generated by the host are not stored locally, but they are pushed to the logging client.

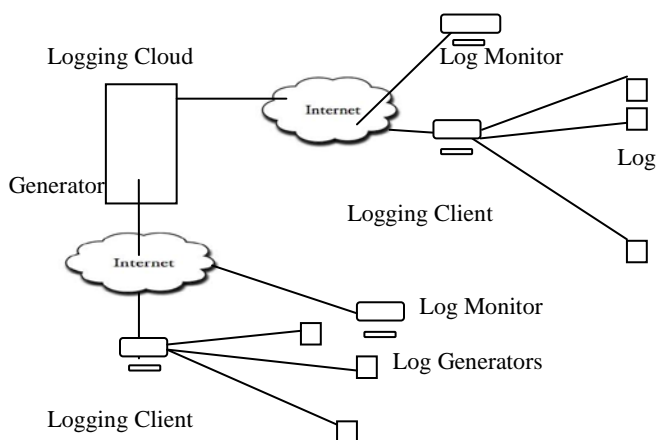


Fig 1 System architecture for cloud based secure logging

B. Logging Client or Logging Relay

The logging client is a collector that receives set of log records generated by one or more number of log generators, and produces the log data so that it could be pushed to the cloud for storing them for a long term. The log data is transferred from the generators to the client in batches, either on schedule, or as and when needed depending on the amount of log data waiting to be transferred.

C. Logging Cloud

The logging cloud provides the long-term storage and maintenance service to the log data received from different logging clients belongs to several organizations. The logging cloud is maintained by a cloud service provider. The organizations that have subscribed to the logging cloud services can upload their log data to the cloud. The cloud, on request from an organization can also delete log data and perform log rotation. logging cloud requires a proof from the requester that the latter is authorized to make such a request as a previous step to deleting or rotating log data. The logging client generates such a proof. However, the proof can be given by logging client to any that it wants to authorize.

D. Log Monitor

Log monitor is used to monitor and review log data. It is used to generate queries to retrieve log data from the cloud. Based on the log data retrieved, these will perform further analysis as needed. It will also query the log cloud to delete log data permanently, or to rotate logs.

IV. PROPERTIES OF SECURE LOG

The following are the properties hold by secure log [4].

A. Verifiability

It ensures that the content of log has not been modified by unauthorized way and available as it is. All entries must have the sufficient information for its verification.

B. Confidentiality

Log records usually hold sensitive information. It is essential to prevent sensitive information from reaching the wrong people, while making sure that the right people can in fact get it: Access must be restricted to those authorized to view the data.

C. Tamper Resistance

A secure log should be tampering resistant in such a way that no valid entries can be introduced by anyone other than the creator. In addition, once those entries are created, they cannot be manipulated without detection. No one can prevent an attacker, who has compromised the logging system from altering what that system will put in future log entries.

D. Correctness

Log record should reflect the true history of the system rather than wrong information. Once the log record is stored in storage, it will not be edited or modified by the attackers.

E. Privacy

Log records should not be casually traceable or linkable to other sources during transmission and in storage.

V. PROPOSED SCHEME

A. Privacy Protection

User transmits and save their log to the cloud by encrypted form. Both ensure the security of log data in process of transmission and ensure safe storage of data. Although the cloud computing service provider handle, they can't easily obtain information of plain text.

B. Data Processing

Fully Homomorphic encryption mechanism enables users or the trusted third-party process cipher text data directly, instead of the original log data. Users can obtain arithmetic results to decrypt to get good data.

C. The Cipher Text Retrieval

Fully Homomorphic encryption technology based on cipher text retrieval method can search directly on the cipher text data. It is not only ensuring the query privacy and improve the efficiency of retrieval, the retrieval data can be added and multiply without changing the corresponding plaintext.

VI. HOMOMORPHIC ENCRYPTION

In both private and public cloud, data should be encrypted to ensure security [5]. Data can be transmitted from local machine to cloud data store through secured way. The stored data being encrypted and secured key exchange is also possible. But performing computations, the data stored in the cloud should be decrypted first. This makes the sensitive data available to the Cloud service provider. To achieve the security completely, it is necessary for the crypto system which is based on Homomorphic Encryption.

Homomorphic encryption is one of the theoretical advancements in science to keep secrets in data. It is a cryptosystem that compute data without decrypting it. It allows complex mathematical operations to be performed on cipher text without decryption. This Homomorphic encryption plays crucial role in cloud computing that allows companies to store the encrypted data in a public Cloud. It has two types namely Fully homomorphic encryption (FHE) and Somewhat Homomorphic Encryption (SHE).

Fully Homomorphic encryption [2] is an encryption scheme that allows arbitrarily complex programs on cipher text. It allows one to perform arbitrary computation over encrypted data. This scheme can perform addition and multiplication on cipher text. But Somewhat Homomorphic Encryption (SHE) supports one of the two operation.

There are two types of fully homomorphic encryption algorithm namely multiplicative homomorphic encryption algorithm and additive homomorphic encryption algorithm. Additive Homomorphic encryption algorithm supports only addition homomorphism and multiplicative homomorphic encryption supports multiplication homomorphism only. This paper suggests fully homomorphic algorithm to find an encryption, which can be any number of addition algorithm and multiplication algorithm in the encrypted information.

For example, Cloud user wants to store the encrypted form of data in cloud storage. So, Cloud user has to do the following for enforcing security.

1. User has very important data set ABCD that consists of the numbers 10 and 20. For encrypting the data, Cloud user must simply multiply the data by 2. After multiplication, the new data set numbers are 20 and 40.
 2. Now send the cipher text to the cloud storage. Now the data are available in cloud storage in encrypted form.
 3. After some months, Cloud user requests the Cloud provider to perform the addition and multiplication of those two data. Cloud service provider performs the addition and multiplication of encrypted data 20 and 40 without the knowledge of original data 10 and 20.
 4. Cloud service provider sends the addition result 60 and multiplication result of 800 to the user. Now he performs decryption on 60 and 800 and gets the result 30 and 200.
- This kind of processing is called blind processing because the cloud provider does not know about original data.

A. Encryption and Decryption Algorithm

1. Encryption Algorithm

Consider the encryption parameters p, q and s, where p is positive odd number, q is large positive integer, p and q determined in the generation phase, p is an encryption key, and s is a random number encrypted when selected. For the text M, calculation

$$C=M+2s+pq$$

Then you can get the cipher text.

2. Decipherment Algorithm

To plain text,

$$M= (C \text{ mod } p) \text{ mod } 2$$

Because the $p \times q$ is much less than $2s+M$, then

$$(C \text{ mod } p) \text{ mod } 2= (2s+M) \text{ mod } 2=M$$

B. Homomorphism Verification

1) The Homomorphism Addictive Property Verification

Suppose there are two groups of the plain text M1 and M2, to encrypt them become the cipher text,

$$C_1=M_1+2s_1+pq_1$$

$$C_2=M_2+2s_2+pq_2$$

To plaintext

$$M_3=M_1+M_2$$

Due to $C_3=C_1+C_2 = (M_1+M_2) + 2(s_1+s_2) + p (q_1+q_2)$

As long as

$$(M_1+M_2) + 2(s_1+s_2) \text{ is much less than } p,$$

$$C_3= (C_1+C_2) \text{ mod } p= (M_1+M_2) + 2(s_1+s_2)$$

This algorithm satisfies the additive homomorphism conditions.

2) The Homomorphic Multiplicative Property Verification

To plaintext $M_4=M_1 \times M_2$

Due to

$$C_4=C_1 \times C_2 = (M_1+2s_1+pq_1) \times (M_2+2s_2+pq_2) =$$

$$M_1M_2+2s_2M_1+M_1pq_2+2M_2s_1+4s_1s_2+2s_1pq_2+M_2pq_1+2pq_1s_2+p^2q_1q_2=M_1M_2+2(2s_1s_2+s_1M_2+s_2M_1) +$$

$$p^2q_1q_2+q_2(M_1p+2s_1p)+ q_1(M_2p+2s_2p)$$

$$= M_1M_2+2(2s_1s_2+s_1M_2+s_2M_1) + p[pq_1q_2+q_2(M_1+2s_1)+$$

$$q_1(M_2+2s_2)]$$

As long as $M_1M_2+2(2s_1s_2+s_1M_2+s_2M_1)$ is less than p

Then,

$$C_4 = (C_1 \times C_2) \text{ mod } p= M_1M_2+2(2s_1s_2+s_1M_2+s_2M_1)$$

This algorithm satisfies the multiplicative homomorphism conditions.

C. Log Retrieval Using Fully Homomorphic Encryption

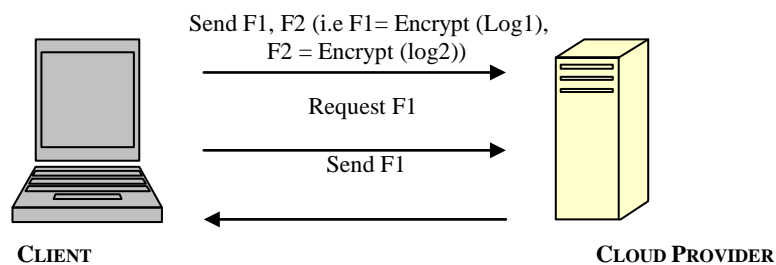


Fig.2 Secured log transmission between client and cloud provider

The log transmission using fully homomorphic encryption [6] is depicted in Fig.2. Instead of storing the original data

Log1 and log2, Client has to encrypt the log data and transmit it to Cloud. When the client wants to retrieve the

data, he must send the query in encrypted form and the cloud provider has to transmit the required data in encrypted form. Client will decrypt it and get the original log.

VII. CONCLUSION AND FUTURE WORK

Cloud computing does not process the data on the user's computer, but in the cloud. So, the data has to be encrypted first and then uploaded to the cloud for process. This Fully Homomorphic encryption algorithm helps to attain confidentiality because of the calculations done in encrypted form without knowing the original form. It is very important for the data safety of the cloud computing platform because the data is invisible to the third party and can be processed by the cloud itself.

This paper suggests the fully homomorphic encryption mechanism for processing log data to propose a cloud computing data security scheme. This scheme ensures the transmission of log between cloud and the user safely. Even in cloud storage, their data is safe. At present, fully homomorphic encryption scheme has high computational problem. Future work will be eliminated that overhead.

REFERENCES

- [1] K. Kent and M. Souppaya, "Guide to Computer Security Log Management", NIST Special Publication.
- [2] Feng Zhao, Chao Li and Chun Feng Liu, "A cloud computing security solution based on Fully homomorphic encryption", *ICACT2014*, February 2014
- [3] V. Varadharajan and U.Tupakula, "Security as a Service Model for Cloud Environment", *IEEE transactions on Network and Service Management*, Vol. 11, No 1, March 2014
- [4] Indrajit Ray, Kirill Belyaev, Mikhail Strizhov, Dieudonne Mulamba, and Mariappan Rajaram, "Secure Logging as a Service-Delegating Log Management to the Cloud", *IEEE Systems Journal*, Vol. 7, No. 2, June 2013
- [5] Shahank Bajjal and Padmija Srivastava, "A Fully Homomorphic Encryption Implementation on cloud Computing", *International Journal of Information & Computation Technology*, Vol. 4, No. 8, 2014
- [6] Maha Tebaa, Saïd El Hajji and Abdellatif El Ghazi, "Homomorphic Encryption Applied to the Cloud Computing Security", *World Congress on Engineering*, 2012
- [7] Badugu Rajeswari and Badugu Suneel Kumar, "CLASS: Cloud Log Assuring Soundness and Secrecy scheme for cloud Forensics", *International Journal of Engineering Technology Science and Research*, Vol. 6, No. 7, July 2019.

Published: 07 September 2020

ECC-CRT: An Elliptical Curve Cryptographic Encryption and Chinese Remainder Theorem based Deduplication in Cloud

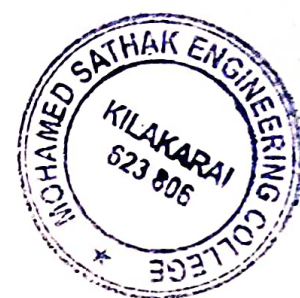
B. Rasina Begum  & P. Chitra

Wireless Personal Communications **116**, 1683–1702 (2021)

311 Accesses | **2** Citations | [Metrics](#)

Abstract

Cloud computing provides the data storage facility for the maintenance, management and remote backup of the data. The storage cost and data retrieving time has increased. To encrypt, the Elliptical Curve Cryptographic and to generate key the Chinese Remainder Theorem (ECC-CRT) based deduplication scheme is proposed. Data deduplication is the process of eliminating the repeated data in cloud storage. Cloud service provider receives the encrypted data and checks for duplication. Deduplication is performed by using cosine similarity checking. The advantage of the method is, it avoids malicious upload and downloads in storage space. The performance is compared with existing methods.





ECC-CRT: An Elliptical Curve Cryptographic Encryption and Chinese Remainder Theorem based Deduplication in Cloud

B. Rasina Begum¹ · P. Chitra²

© Springer Science+Business Media, LLC, part of Springer Nature 2020

Abstract

Cloud computing provides the data storage facility for the maintenance, management and remote backup of the data. The storage cost and data retrieving time has increased. To encrypt, the Elliptical Curve Cryptographic and to generate key the Chinese Remainder Theorem (ECC-CRT) based deduplication scheme is proposed. Data deduplication is the process of eliminating the repeated data in cloud storage. Cloud service provider receives the encrypted data and checks for duplication. Deduplication is performed by using cosine similarity checking. The advantage of the method is, it avoids malicious upload and downloads in storage space. The performance is compared with existing methods.

Keywords Chinese Remainder Theorem (CRT) · Elliptical Curve Cryptography (ECC) · Key generation · Deduplication and Cosine similarity

1 Introduction

Cloud computing is an emerging technology because of their ability to offer the cost efficient and on demand use of huge storage. Cloud is the terminology, which is commonly utilized to refer a bunch of components. Cloud computation is the practice of delivering computational services like servers, storages, data bases, networking, and applications. The groups that provide those services are termed as Cloud Service Provider (CSP). Cloud computing is a model for enabling convenient, on demand network access to shared pool of configurable computing resources. The service models of cloud computing was categorized into three such as Infrastructure as a Service (IaaS), [1] Platform as a Service (PaaS), and Software as a Service (SaaS). The cloud offers many benefits such as, fast deployment, pay for use, lower cast, scalability, rapid provisioning, rapid elasticity, ubiquitous network access, greater resiliency, hypervisor protection against network attacks, low cost

✉ B. Rasina Begum
rasinabegumphd@yahoo.com

¹ Department of Computer Science and Engineering, Mohamed Sathak Engineering College, Keelakarai, Tamil Nadu 623806, India

² Department of Computer Science and Engineering, Thiyagarajar College of Engineering, Madurai, Tamil Nadu 625 015, India

disaster recovery and data storage solutions, on demand security controls, real time detection of system tempering and rapid re-constitution of services. In cloud computing, it categorized into four, such as private cloud, public cloud, hybrid cloud and community cloud. Data deduplication is the process of reducing the storage space. It identifies the redundant data by using hash values and compares the data chunks and generates the logical values to other copies instead of storing other authentic copies of redundant data. Deduplication reduces the data volume so the disk space and network bandwidth are reduced, so it reduces the cost and energy consumption for running storage system. Data duplication is considered as a way to reduce or eliminate the redundant files, bytes or data blocks and ensures the unique data copy stored via duplicate data detection. It is used to control the data functionality and reduces the demands for capacity during the data protection. Single Instance Storage (SIS) merges the duplicate files into shared storage space. The duplicate files are replaced with file links. These links are operated like an original files. It saves the disk space occupied by duplicate files [2] and maximizes the use of current storage resources. Deduplication includes three methods, such as,

File level deduplication: it identify the files with different names and same content. These types of files are eliminated and stored with link or numerical values.

Block level deduplication [3] groups the data stream into fixed length or variable length data blocks and then matched with their stored data blocks to detect or identify the same data blocks. **Byte level deduplication [4]** compares the data stream with stored data stream byte by byte. It uses a cache disk to back up the data temporarily, before byte level data deduplication. So this process may be limited to set of backup data streams rather than entire backup.

In deduplication process, the different methods are used to evaluate the efficient method. The existing methods are RSA (RSA stands for Rivest Shamir Adleman considered as first public key cryptosystems used for data transmission in secure way), Elgamal, convergent encryption (CE), leakage resilient (LR) deduplication, Randomized Convergent Encryption (RCE). The cloud services have the ability to provide data backup. The users store their confidential data, which could be individual or business oriented. The user can retrieve their information from the cloud, after recovering from their calamity conditions. They can smoothly continue their regular process without any further delay. The existing techniques utilized the Elliptic Curve Cryptography (ECC) for encrypting the data. The scheme is formulated on the basis of algebraic structure of elliptic curve. In RSA scheme [5], the encrypting time is higher and it is not applicable to single user environment. Convergent Encryption (CE) is utilized to convert encrypted key from hash of plain text. In ByCE technique, the same encryption key is applied for two identical plain text to obtain same ciphertext. So the CSP is able to perform deduplication on ciphertext. CE offers data privacy in deduplication process. The secure CE is for efficient encryption and it considering the key management and block level deduplication.

Leakage resilient (LR) deduplication scheme: it is applied to solve the data integrity problems. LR enables the use of randomly selected key to encrypt the data, then the data encrypted key is encrypted under a KEK-(stands for Key Encryption Key which states as a key encrypts other key used for storage or transmission) which is derived from the data and distributed among the data holders after the Proof-of ownership (PoW) process. Data integrity is checked by using the data encryption key with same KEK.

The CRT generates the key to encrypt the data by using ECC and these data are stored in server at that time, the cosine similarity is used to identify the similar data. If the data are similar, then the similar data are required to generate the hash value by using hash function. If the data are not similar it will be stored in cloud. Then the data are stored in

cloud. So the data storage space is reduced in cloud. In this work, the novelty is implemented in key generation, encryption and decryption process for improving the security. It includes some limitations; secure proof of ownership (PoW) scheme in the standard model is an open problem and lack of dynamic ownership management between the data holders.

The remaining section of the paper are organized as follows: Section 2 presents a brief review of the existing research works related to the cloud security, and deduplication of cloud storage. Section 3 shows the detailed description of proposed work. Section 4 illustrates the performance analysis and comparative analysis of proposed work. Section 5 involves the short discussion of conclusion and future work.

2 Related Works

This section presents some of the existing works based on key distribution, attributed based encryption algorithm for cloud security. Ryan [6] surveyed the security issues in cloud computing. The safety and problems related to privacy in cloud systems kept on growing. Kshetri [7] framed a strategy to resolve the confidentiality and safety problems in cloud computing. The issues were categorized into technology based issues, human intrusion issues and corrupted data storing in cloud. Advanced research has been performed to explore the past history of a cloud organization before deploying them in cloud. Compatibility, complexness, observability and trialability had to be analyzed. Previous techniques were focused on security issues in data storage. Wei et al. [8] aimed to solve the computation security. A novel auditing algorithm termed Sec-Cloud was framed to bridge storage security and computational security. Different requirements of various users were controlled by batch verification method. The development process was to implement the algorithm in linear computation and data mining. Real cloud platforms such as EC2 and open stack were also planned for implementation. Sujithra et al. [9] gave a cryptographic tactic to preserve the information in cloud and also maintained performance level. Previously the cryptographic technique was implemented to individual system. Throughput required to be enhanced. Liu et al. [10] designed a novel security scheme for cloud system. In this scheme, the data sender encrypts the data with the identity parameter of the receiver and transmitted it to the cloud. The user was provided with a private key and a security device to access cloud. The user executed the same encryption algorithm to decrypt the data in cloud. If the security device was lost, the CSP would execute an algorithm that changed the decryption code so that the unauthorized use of the device was prevented. The improvement of the scheme was to enhance the efficiency of the algorithm. Cloud computing paved the path to data. The insurance process depended on the cloud system for their smooth operation. The exchanged data faced security issues. The Patient Health Record (PHR) management was the significant consideration of the scheme proposed by Li et al. [11], in which a patient-centric model was designed. Attribute Based Encryption (ABE) was executed to encrypt the PHR. It reduced the complexity in managing the key. The PHR owner decided to permit access rights to other agents over their data. The scheme required enhancement in managing trust of external users who request the access of PHR. Rapid improvement in cloud computation led to data privacy in addition to duplication of user identity. Jung et al. [12] proposed an anonymity control algorithm to completely prevent the user identity leakage and an efficient revocation of user to reduce network traffic in cloud. The accumulation of encrypted data in cloud increased rapidly. This slowed down the query process in cloud computation. Li et al. [13] developed a Key word Search

Function (KSF) and reduced the computational cost at both the owner and other trusted authorities. Future process was intended to frame the KSF for standard model which would be CCA secured. The Proxy Re-Encryption (PRE) was executed by the user to cancel the permission rights of any other user from accessing the private cloud data. Numerous PRE schemes were formulated. Liang et al. [14] made an enhancement to the PRE scheme, termed as Cypher text Policy Attribute Based PRE (CPB-PRE). It enhanced the CCA secure process of storing, forwarding and sharing data in cloud servers. The cloud provided a central data storage facility which was globally accessed by the users. Internet services costs was higher for the users to access their data in cloud. To reduce the cost, Tysowski and Hasan [15] offered, an improved encryption technique on attribute basis. The cloud service provider re-encrypted the data to eliminate revocation cost to users and in addition it provided data security. This scheme reduced computational complexity and network traffic. Security to data in cloud computation was accomplished by control of data access. Cipher text Policy Attribute Based Encryption (CP-ABE) technique gave the data owners to directly control their data accessibility in cloud. Yang and Jia [16] proposed, a revocable multi authority CP-ABE scheme to revoke attributes in addition to providing security to the data. The scheme was secure in random oracle model. Development works were to implement the model in complex remote storage system and social networks. The cloud network faced numerous safety and confidentiality problems. Cloud data accessing by individual users was surpassed by data sharing among organizations, both internal and external. Fabian et al. [17] developed, an attribute based data encryption technique, to share data among different cloud servers. The model contained individual cloud providers grouped under one cloud environment. Inter—organizational medical big data of patients was shared securely among these clouds. Next level of improvement was to manage the private and public keys of the cloud users to enhance security while sharing data. The online data sharing practice grew with the invention of cloud computing. Optimum security to online data was the key to successful cloud computing. Patranabis et al. [18] combined Chosen Plain text Attacks (CPA) and Chosen Cipher Attacks (CCA) to construct, Key Aggregate Cryptosystem (KAC) to solve the security issues in online sharing of license of any product and other online data sharing criticalities. The scheme utilized lower overhead cipher texts and key aggregates along with asymmetrical bilinear paring. The succeeding phase of the work was to enhance the scheme's scalability.

Jia et al. [19] imposed the Chinese Remainder Theorem in their study for generating secret reconstruction and share generation validity. This kind of strategy used for computational security. For recovery lesser difficulty and size of sharing also lesser which have been exhibited in this proposed study. The secret recovery computational complexity termed as $O(t)$ related to the previous $O(\log_2 t)$. Prasetyo et al. [20] exhibited the Chinese Remainder Theorem CRT and Boolean X-OR process to generate n number of shared images from the n number of secret images. By this proposed approach the security increased by shared color imaged merged into 2-D matrix representation. Yan et al. [21] designed a Chinese Remainder Theorem based on 2-in-1 image secret sharing with visual previewing capability, lossless recovery and grayscale stacking recovery decoding options. The CRT theorem encoded the grayscale secret image. Further it has been decoded through linear congruence set equations.

Wang et al. [22] The data reduction techniques for the storage and savings of I/O through duplicate removal content has considered as compression and De-duplication techniques and however for index management they also incur significant memory. To overcome this problem Auster-cache- a new flash caching method used for indexing the memory efficient when preserving the deduplication and compression benefits. This proposed

method focused on the Austerccache management and various core methods proposed for cache replacement and data organization and implement the lightweight in memory index structures by eliminates the much indexing metadata. This proposed flash caching design supported the compression and deduplication and maintains the read hit ratio and write reduction ration and high I/O throughput obtained at the end. Yan et al. [23] The privacy of data holders preserved and the in cloud the data have stored in encrypted form. Yet the new challenges introduced by the encrypted data for the cloud data deduplication and it becomes important for cloud processing and big data storage. On encrypted data conventional deduplication schemes have not employed. Security weakness suffered by encrypted data deduplication's traditional solutions. The revocation and data access control cannot be flexibly supported. In this study, deduplicate encrypted data scheme proposed for cloud based storage on proxy re-encryption and ownership challenge. Cloud data deduplication with access control integrated. Based on computer simulations and extensive analysis the performance evaluated. For big data deduplication in storage of cloud the efficiency resulted. In this study, [24] for bipolar and bipolar neutrosophic set of interval-valued the weighted cosine similarity measures and cosine similarity measure proposed. These similarity measures ratios have been examined and based on proposed measures the two multi attribute decision making methods focused. The feasibility of proposed study made and found the bipolar disorder similarity using cosine similarity technique. [25] Among picture fuzzy set based cosine function the eight similarity measures presented by positive membership degree, neutral membership degree, refusal membership degree and negative membership degree have been considering in this study. For strategic decision making these similarity measures of weighted cosine function applied. For strategic decision making issues these similarity measures efficiency have been demonstrated.

3 Propose Work

In this section, the detailed description of proposed CRT-ECC based cloud architecture is explained for secure data sharing and reducing the storage space by using deduplication process. Figure 1 shows the overall flow of proposed work. Initially, the user generates the key using Chinese remainder theorem and the data are encrypted by using elliptical curve cryptography. Then the encrypted data are stored in the server. When the data are stored in the server then, the cosine similarity is used to check the similarity of the data. If the data are similar then the hash function is generated for the particular data otherwise the data are stored in the cloud. This method is used for reducing the storage space in cloud.

3.1 Key Generation Using CRT

The user selects the input data and service provider send the control information to Chinese remainder theorem for generating the secret key. The novelty is presented in this section. The CRT generates the key using control information for each user. The advantage of Chinese remainder theorem reduces the complexity of key generation in cryptography system. Let m_1, m_2, \dots, m_3 are the collection of pairwise relatively prime integers and consider a_1, a_2, \dots, a_m are the arbitrary integers. Based on this, the CRT illustrates the congruence system as follows,

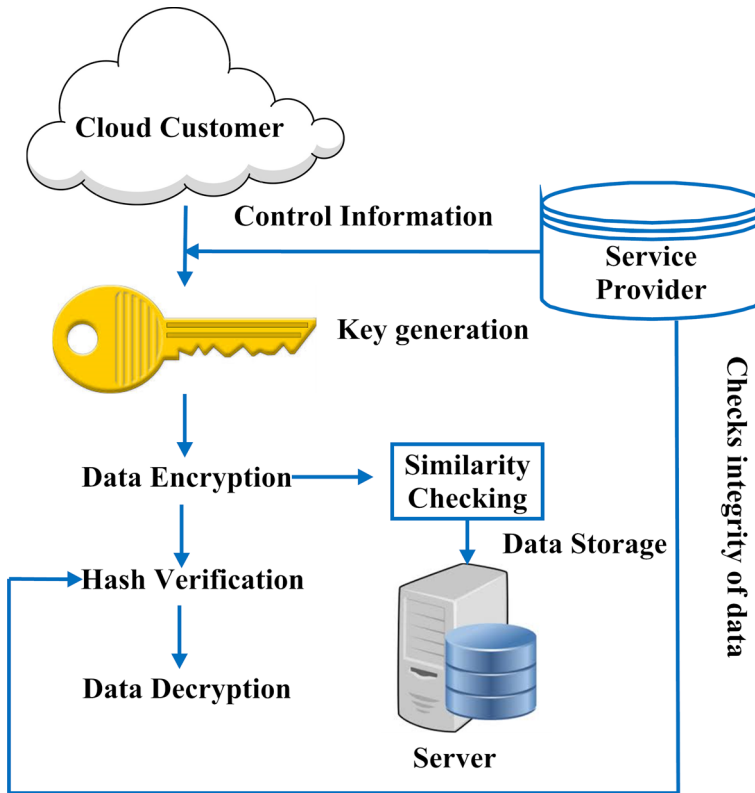


Fig. 1 Overall flow diagram of proposed work

$$\begin{aligned}
 Y &\equiv a_1 \pmod{m_1} \\
 Y &\equiv a_m \pmod{m_n}
 \end{aligned}
 \tag{1}$$

Here, the service provider provides the secret information based on their factorized value. Then the control information offers different information for each user. Finally, the CSP checks their factorized value to secret key.

Algorithm I: Chinese Remainder Theorem Based Key Generation

$CRTK \leftarrow$ Chinese remainder theorem key

Given $(X_1, Y_1), (X_2, Y_2), (X_3, Y_3)$

If the secret is valid, then the CRT-based key generation is expressed as,

$$N = Y_1 * Y_2 * \dots * Y_n$$

$$CRTK \equiv X_1 * N_1 * N_1^{-1} + \dots + X_n * N_n * N_n^{-1} \pmod{N}$$

Where, $N_i = \frac{N}{y_i}, N_i^{-1} = N_i \text{ mod } y_i$

3.2 ECC Encryption

Elliptical curve cryptography is used to encrypt the data then the encrypted data are stored in the cloud. The algebraic construction of an ellipse is basis behind formation of the technique. The equation for an ellipse given by

$$y^2 = x^3 + ax + b \tag{3}$$

Suppose if a user needs to exchange data with another, then they must know a secret key. The private key being d which is an integer, selected on a random basis within the interval $[1, n-1]$. The public key Q is also employed which is given by

$$Q = dG \tag{4}$$

d -Private key

G -base point

The sender's key be $(d_A Q_A)$ and the key of receiver be $(d_B Q_B)$. It is required that each users must possess the public key of the other user in order to exchange the data.

The sender of the data computes,

$$k = d_A Q_B \tag{5}$$

The receiver compute,

$$k = d_B Q_A \tag{6}$$

The above values are calculated by both sender and receiver are equal since,

$$d_A Q_B = d_A d_B G = d_B d_A G = d_B Q_A \quad (7)$$

This curve includes numerous value, characters and finite number of elements. The elliptical curve is derived by arithmetic (addition, subtraction, multiplication and division) operations for both encryption and decryption. ECC provides high security to the data with minimum cost.

Algorithm II: Modified ECC Encryption

Input: CRTK, Raw Data

Output: encrypted data

$Sd \leftarrow$ select data

$Ed \leftarrow$ encrypted data

$Pu \leftarrow$ public key

$k =$ constant

Generate the CRT

\parallel Set CRTK as secret key

$Pr =$ CRTK

Initialize P as point on curve

Initialize K as random number generated between (1 to $n-1$)

Generate the public key

$Pu = Pr * p$

Encrypted data by below steps,

while $Sd.data$

$Ed = Sd.data + (k * Pu)$ (8)

end while

Transfer Ed from consumer to service provider

The encrypted data (E_d) is fully protected for secure cloud sharing. Authenticated users of the network can access E_d . The private key is generated by using Chinese remainder theorem. k represents the constant value and P_u represents public key. The encrypted data calculates by using Eq. (8). Then the encrypted data is transferred from consumer to service provider.

3.3 Deduplication

In deduplication process, the similarity checking is the main process. It is used to match the stored encrypted data. If the data are same, then it will generate the hash value. Otherwise the encrypted data are stored in cloud. If the cosine similarity value is less than 0.9, then the data are stored in cloud. If the cosine similarity value is greater than 0.9, then it is duplicate data so these data are not stored in cloud. But it generates the hash value. So the storage space of cloud is reduced. This is represented in Fig. 2. The cosine similarity of two non-zero vectors are derived by using Euclidean dot products,

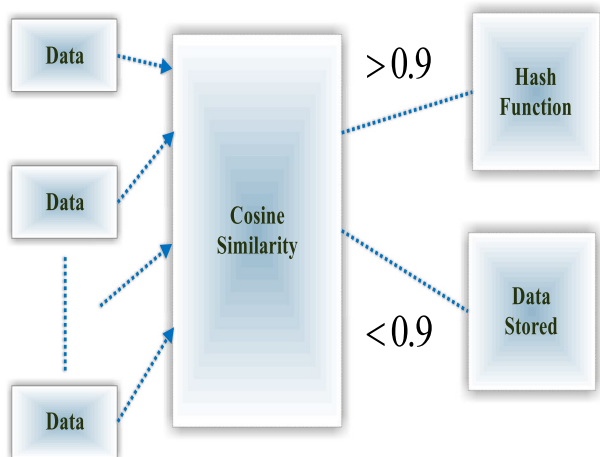
The dot product of two vectors A_k and B_k is represented as,

$$A_k \cdot B_k = A_k B_k \cos \theta$$

Here, θ is the measure of angle between A_k and B_k

The dot product is defined as the sum of product of each vector as,

Fig. 2 Similarity matching



Algorithm III: Similarity Checking

$Cs \leftarrow$ cosine similarity

$Exd \leftarrow$ existing data

For $i=0: Sd$

do

for $j=0: Exd$

do

 Cosine similarity is calculated by using equation (10)

end for

end for

if $Cs_{ij} > 0.9$ **then**

 Duplicate data

else

 New data

end if

$$A_k \cdot B_k = A_{k1} \cdot B_{k1} + A_{k2} \cdot B_{k2} + A_{k3} \cdot B_{k3} + \dots \quad (9)$$

$$Cs_{ij} = \frac{\sum_{k=1}^n A_k B_k}{\sqrt{\sum_{k=1}^n A_k^2} \sqrt{\sum_{k=1}^n B_k^2}} \tag{10}$$

$A_k B_k$ – term frequency vector document

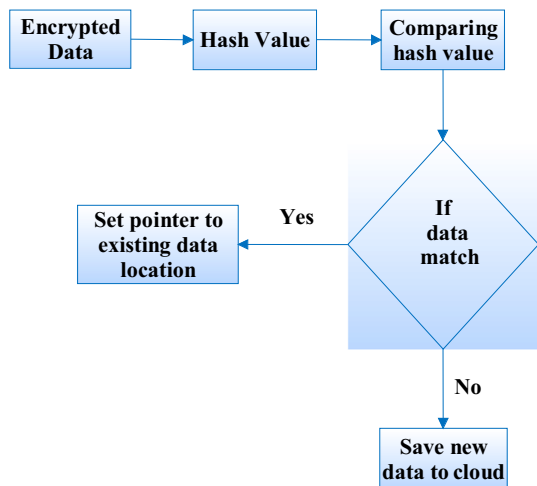
The above algorithm III represents the detail explanation of similarity checking. It is used to check the similarity of data and similarity data are termed as duplicated data. If the similarity matching is less than 0.9 these data are consider as new data.

3.4 Hash Key Verification

The hash key verification, the user stores the encrypted data, if data are not similar to any data then data is stored in server

After generating hash of data. If data is similar to already stored data then the access policy is updated for each data in server. Hash is transferred from service provider to customer. Then service provider gets request from customer and gets data from server. Service provider checks the integrity of data by compare hash. Figure 3 shows the flow diagram of hash function. Initially, the encrypted data generate the hash value and the values are compared. If the hash value of the data is checked whether it is existed in the cloud if so it's sets the pointer to existing data location or else it saves a new data in the cloud.

Fig. 3 Hash function



On upload (Deduplication)*Mh1* ← message hash*Mh2* ← generate Ed.hash*Transfer hash from service provider to consumer**Fr* ← file request*Request transferred from consumer to service provider**Mh1* ← message hash*Mh2* ← generate Ed.hash**if** *Mh2==Mh1* **then** // Service provider side verification*Hash verified***else***Hash not verified***end if****//On download (Integrity)***Transfer data from service provider to consumer**Mh1* ← message hash*Mh2* ← generate Ed.hash**if** *Mh1==Mh2* **then** // Consumer side verification*Hash verified***else***Hash not verified***end if**

3.5 ECC Decryption

Here the encrypted data are decrypted by using master keys. If the secret keys are matched with encrypted key, then the user decrypt the data otherwise, the user does not retrieve the original data. An algorithm IV represents the detail description of the ECC decryption. $CT1$ denotes the cipher text 1 and Dd denotes the decrypted data. The cipher text 1 is calculated by using Eq. (11) and decrypted data is calculated by using Eq. (12)

Algorithm IV: ECC Decryption

Input: encrypted data

Output: decrypted data

User send the request to service provider

Service provider send the control information to user

User generates the CRTK

$Pr = CRTK$

Decrypted data is obtained by below steps,

$$CT1 = k * p \quad (11)$$

while Ed.data

$$Dd = Ed. data - (CRTK * CT1) \quad (12)$$

Here,

$Dd \leftarrow$ decrypted data

$Pr \leftarrow CRTK$

$k = \text{constant}$

P as point on curve

end while

Fig. 4 Encryption Time

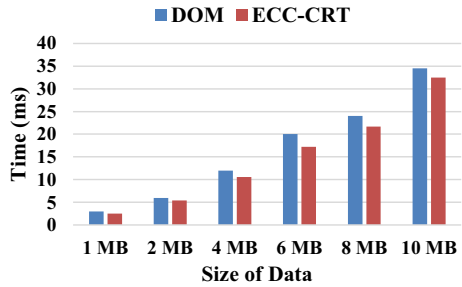
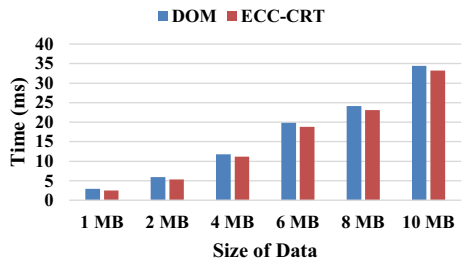


Fig. 5 Decryption



4 Performance Analysis

The performance results are compared with Data Deduplication with Dynamic Ownership Management (DOM), Convergent Encryption (CE), Leakage-Resilient (LR), Rivest Shamir Adleman (RSA), and Randomized Convergent Encryption (RCE). Here the proposed method provides the better result than existing techniques. An encryption time, decryption time, computational time, and memory consumptions are compared with existing methods.

4.1 Encryption Time

Encryption is the method of transforming any message form into unidentified scripts, for the purpose of protecting the data from unauthorized handling. The time consumed to encrypt any data is designated as encryption time. Figure 4 shows the encryption time with different data size for both existing [26] and proposed method. The X axis represents the size of the data and y axis represents the time in millisecond (ms). If the data size is 1 MB, then the existing method DOM takes 3 ms and the proposed method ECC-CRT takes only 2.5 ms. It clearly explains that the proposed method takes less time for encryption than existing technique. If data size increases, the encryption time also increases.

4.2 Decryption Time

It is the time taken by any technique to decipher or convert the encrypted data into their original format and it is termed as reverse process of encryption. The data decrypting does not require the same public key which is used encode the data. But instead, it

generates their specific private key from the attributes received from the user. Figure 5 shows the decryption with different data size for both existing [26] and proposed technique. If the data size is 1 MB, the existing method DOM takes, 2.9 ms but the proposed method takes 2.5 ms. If the data size is 10 MB, then the existing method DOM takes 34.4 ms and the proposed method takes 33.2 ms. Here, the decryption process takes less time than existing method. It is the one of the advantage of proposed technique. Decryption time increases when the data size are increased.

4.3 Computation Time Analysis

Here, the computational time represents both data uploading and downloading time. Figure 6a shows the computation time of data uploading. In x axis represents the data size in megabytes (MB) and y axis represents time in milliseconds (ms). Computation time is termed as time taken for their process (data uploading or data downloading).

If the size of data is 1 MB then the existing methods CE, LR, RCE, DOM and the proposed method ECC-CRT take 3 ms, 7 ms, 3 ms and 2 ms. If the data size is 10 MB then, the existing methods CE, LR, RCE, [27] DOM take 35 ms, 69 ms, 35 ms, 35 ms and the proposed method ECC-CRT takes 32 ms. The proposed method ECC-CRT takes minimum time then existing methods. If the data size increases the computation time also increases.

Figure 6b represents the computation time of data downloading. Here, the x axis represents the data size in megabyte (MB) and the y axis represents the time in milliseconds (ms). The data size is 10 MB then the existing methods CE, LR, RCE, DOM and the proposed method ECC-CRT takes 34.5 ms, 34.5 ms, 34.5 ms, 34.8 ms and 34.2 ms. The proposed method ECC-CRT takes minimum time for data downloading process then existing methods.

Fig. 6 a Uploading time, b Down loading time

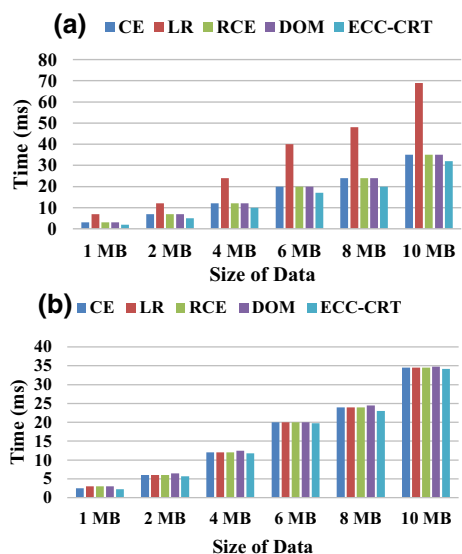


Fig. 7 Memory consumption

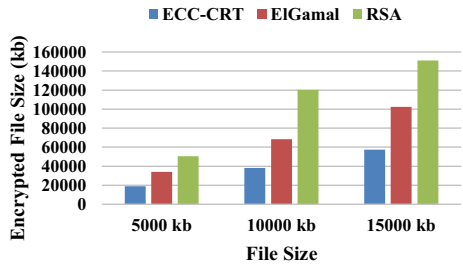
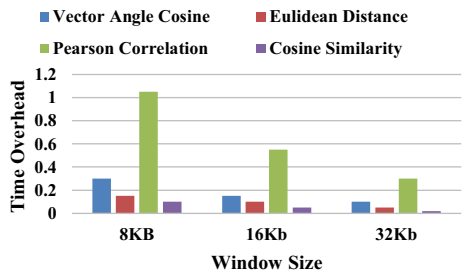


Fig. 8 Similarity comparison



4.4 Memory Consumption

Memory consumption represents the data which are occupied memory space in cloud. Figure 7 shows the memory computation of both existing ElGamal, RSA and proposed ECC-CRT. The encrypted data takes minimum storage space than existing methods of ElGamal and RSA.

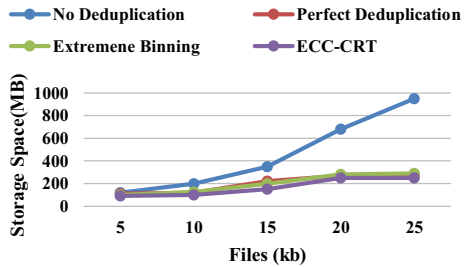
4.5 Similarity Comparison

The similarity is compared with varied time period and different window size. The proposed cosine similarity is compared with existing vector angle cosine, Euclidean [28] distance, and Pearson correlation. In X axis represents the window size in kilobyte (Kb) and Y axis represents the time. The window size increases the time also increases. The proposed Cosine similarity takes less time than existing methods (Fig. 8).

4.6 Storage Space

Figure 9 shows the storage space for different existing methods of no deduplication, perfect deduplication, extreme [29] binning and proposed ECC-CRT. In this graph, the x axis represents the files and y axis represents the storage space in megabyte (MB). The file size is 25, then the existing methods of no deduplication, perfect deduplication extreme binning and proposed ECC-CRT take 950 MB, 280 Mb, 290 MB and 250 MB storage space. The proposed ECC-CRT method takes minimum space for storage than existing methods.

Fig. 9 Storage space



5 Conclusion

This paper presented the secure data sharing and increased security of cloud data. The main contribution of the paper has considered as to provide the high security to cloud data. For achieving this high security the efficient technique like Chinese Remainder theorem applied in ECC cryptography for key generation and also the in case of de-duplication the similarity identified by cosine similarity measure. The user selected the input data and CRT has been used to generate the key and it termed as master key. Then the master key has been used to encrypt the data by using elliptical curve cryptography. Next, the cloud service provider receives the encrypted data and check the deduplication by using cosine similarity. If the data have not showing similarity then these data have stored in cloud. If the data shows similarity, then the server generated the hash and the access policy has been updated. Then the hash has transferred from service provider to customer. In decryption, the customer sends the request to the service provider. Then the service provider checks the integrity of data by comparing with hash and then customer decrypt the data. In the above experiments, the performance of the existing and proposed techniques have been analyzed and evaluated. From the result, the proposed technique provides the better result when compare to other DOM, ElGamal, RSA, vector angle cosine, Euclidean distance, and Pearson correlation techniques. For future enhancement, the various other efficient algorithm can be used which focusing on the time consumption while generating the keys and also rapid computation to achieve superior performance in case of high security required.

References

1. Arora, S., & Beri, R. (2017). Adoption and Use of Cloud by Small and Medium Businesses (SMBS). *Advances in Computational Sciences and Technology*, 10, 529–536.
2. Kawtikwar, N. P., & Joshi, M. (2017). Data Deduplication in Cloud Environment using File-Level and Block-Level Techniques. *Imperial Journal of Interdisciplinary Research*, 3(5), 1294–1298.
3. Li, J., Li, Y. K., Chen, X., Lee, P. P., & Lou, W. (2015). A hybrid cloud approach for secure authorized deduplication. *IEEE Transactions on Parallel and Distributed Systems*, 26, 1206–1216.
4. Xu, L., Pavlo, A., Sengupta, S., & Ganger, G. R. (2017). Online Deduplication for Databases. In *Proceedings of the 2017 ACM International Conference on Management of Data*, (pp. 1355–1368).
5. Yarom Y., & Falkner, K. (2014). FLUSH+RELOAD: A high resolution, low noise, L3 Cache side-channel attack. In *USENIX Security Symposium*, (pp. 719–732).
6. Ryan, M. D. (2013). Cloud computing security: The scientific challenge, and a survey of solutions. *Journal of Systems and Software*, 86, 2263–2268.
7. Kshetri, N. (2013). Privacy and security issues in cloud computing: The role of institutions and institutional evolution. *Telecommunications Policy*, 37, 372–386.

8. Wei, L., Zhu, H., Cao, Z., Dong, X., Jia, W., Chen, Y., et al. (2014). Security and privacy for storage and computation in cloud computing. *Information Sciences*, 258, 371–386.
9. Sujithra, M., Padmavathi, G., & Narayanan, S. (2015). Mobile device data security: a cryptographic approach by outsourcing mobile data to cloud. *Procedia Computer Science*, 47, 480–485.
10. Liu, J. K., Liang, K., Susilo, W., Liu, J., & Xiang, Y. (2016). Two-factor data security protection mechanism for cloud storage system. *IEEE Transactions on Computers*, 65, 1992–2004.
11. Li, M., Yu, S., Zheng, Y., Ren, K., & Lou, W. (2013). Scalable and secure sharing of personal health records in cloud computing using attribute-based encryption. *IEEE Transactions on Parallel and Distributed Systems*, 24, 131–143.
12. Jung, T., Li, X.-Y., Wan, Z., & Wan, M. (2015). Control cloud data access privilege and anonymity with fully anonymous attribute-based encryption. *IEEE Transactions on Information Forensics and Security*, 10, 190–199.
13. Li, J., Lin, X., Zhang, Y., & Han, J. (2016). KSF-OABE: outsourced attribute-based encryption with keyword search function for cloud storage. *IEEE Transactions on Services Computing*, 10, 715–725.
14. Liang, K., Au, M. H., Liu, J. K., Susilo, W., Wong, D. S., Yang, G., et al. (2015). A secure and efficient ciphertext-policy attribute-based proxy re-encryption for cloud data sharing. *Future Generation Computer Systems*, 52, 95–108.
15. Tysowski, P. K., & Hasan, M. A. (2013). Hybrid attribute-and re-encryption-based key management for secure and scalable mobile applications in clouds. *IEEE Transactions on Cloud Computing*, 1, 172–186.
16. Yang, K., & Jia, X. (2014). Expressive, efficient, and revocable data access control for multi-authority cloud storage. *IEEE Transactions on Parallel and Distributed Systems*, 25, 1735–1744.
17. Fabian, B., Ermakova, T., & Junghanns, P. (2015). Collaborative and secure sharing of healthcare data in multi-clouds. *Information Systems*, 48, 132–150.
18. Patranabis, S., Shrivastava, Y., & Mukhopadhyay, D. (2017). Provably Secure Key-Aggregate Cryptosystems with Broadcast Aggregate Keys for Online Data Sharing on the Cloud. *IEEE Transactions on Computers*, 66, 891–904.
19. Jia, X., Wang, D., Nie, D., Luo, X., & Sun, J. Z. (2019). A new threshold changeable secret sharing scheme based on the Chinese Remainder Theorem. *Information Sciences*, 473, 13–30.
20. Prasetyo, H., & Guo, J.-M. (2019). A note on multiple secret sharing using Chinese remainder theorem and exclusive-OR. *IEEE Access*, 7, 37473–37497.
21. Yan, X., Lu, Y., Liu, L., Liu, J., & Yang, G. (2018). Chinese remainder theorem-based two-in-one image secret sharing with three decoding options. *Digital Signal Processing*, 82, 80–90.
22. Wang, Q., Li, J., Xia, W., Kruus, E., Debnath, B., & Lee, P. P. (2020) Austere Flash Caching with Deduplication and Compression. In *2020 {USENIX} Annual Technical Conference ({USENIX} {ATC} 20)*, (pp. 713–726).
23. Yan, Z., Ding, W., Yu, X., Zhu, H., & Deng, R. H. (2016). Deduplication on encrypted big data in cloud. *IEEE Transactions on Big Data*, 2, 138–150.
24. Abdel-Basset, M., Mohamed, M., Elhoseny, M., Chiclana, F., & Zaied, A. E.-N. H. (2019). Cosine similarity measures of bipolar neutrosophic set for diagnosis of bipolar disorder diseases. *Artificial Intelligence in Medicine*, 101, 101735.
25. Wei, G. (2017). Some cosine similarity measures for picture fuzzy sets and their applications to strategic decision making. *Informatica*, 28, 547–564.
26. Hur, J., Koo, D., Shin, Y., & Kang, K. (2016). Secure data deduplication with dynamic ownership management in cloud storage. *IEEE Transactions on Knowledge and Data Engineering*, 28, 3113–3125.
27. Jiang, T., Chen, X., Wu, Q., Ma, J., Susilo, W., & Lou, W. (2017). Secure and Efficient Cloud Data Deduplication With Randomized Tag. *IEEE Transactions on Information Forensics and Security*, 12, 532–543.
28. Liu, J., Wang, J., Tao, X., & Shen, J. (2017). Secure similarity-based cloud data deduplication in Ubiquitous city. *Pervasive and Mobile Computing*.
29. Bhagwat, D., Eshghi, K., Long, D. D., & Lillibridge, M. (2009). Extreme binning: Scalable, parallel deduplication for chunk-based file backup. In *Modeling, Analysis & Simulation of Computer and Telecommunication Systems, 2009. MASCOTS'09. IEEE International Symposium on*, (pp. 1–9).



B. Rasina Begum Associate Professor in Department of Computer Science and Engineering at Mohamed Sathak Engineering College, Keelakarai, Tamil Nadu 623806, India. My correspondence mail address: rasinabegumphd@yahoo.com



P. Chitra Professor in Department of Computer Science and Engineering at Thiagarajar College of Engineering, Madurai, Tamil Nadu 625 015, India

A Novel Fuzzy Knowledge Based Glaucoma System for Diabetic Retinopathy using Vessel Extraction from Fundus Images

¹Dr.R.Karthikeyan, ²Mr. V.R.Sathish Kumar, ³Dr.V.Balamurugan, ⁴Ms.
M.ShanmugaPriya

^{1,3}Professor, Dept. of Computer Science and Engineering, Mohamed Sathak
Engineering College, Kilakarai, Tamilnadu, India.

^{2,4}Assistant Professor, Dept. of Computer Science and Engineering, Mohamed Sathak
Engineering College, Kilakarai, Tamilnadu, India.



ABSTRACT

The fuzzy knowledge based on the glaucoma will be designed for the working location of the private ophthalmologist. The status of various circumstances of the patient's will be implemented by a modular decision method with help of monitor detection. The modular decision technique will consist of fuzzy standards and neural classifiers. This technique can able to process the perimetry and fundus images. The diabetic retinopathy (DR) is a one mode of diabetes complication and it will have strong impact on the eyes of a human body. This disease will be caused by destruct to the blood vessels at the retina. Initially the diabetic retinopathy may not have any symptoms and it just causes a little vision issue. The diabetic retinopathy will have different treatments like intravitreal clinical treatment and sutureless standards plana vitrectomy. These treatments will provide a great relief to the disease related to eyes. The vessel extraction approach dependent on image improvement procedures and individual grouping strategies incorporate fuzzy technique. The photographic of the rear eye will be called as fundus images. The vessel extraction from retinal fundus images will able to determine the various ophthalmologic sicknesses like diabetic retinopathy, glaucoma and hypertension. It is a difficult challenge because of presence of various noises embedded with thin vessels. In this paper, the visibility issue of the eye will be detected based on fuzzy knowledge using glaucoma and will capture the fundus images with help of the process of vessel extraction.

Index terms: Fuzzy knowledge, Intravitreal, Vessel extraction, Fundus images, Diabetic retinopathy and Retina.

I. INTRODUCTION

The two diseases like glaucoma and diabetic retinopathy will become the most dangerous eye disease since they give visual deficiency. It is very important and essential function for the ophthalmologist to identify the status of the patient and proper therapy at the right time. In some developed countries like Germany the patients who are suffering with vision problems are essentially handled by the private ophthalmologists [1]. The fuzzy knowledge in fuzzy logic system represents the facts regarding the fundamental rules of fuzzy set theory. So the fuzzy knowledge will provide reasonable analysis on disease related to eye. In fuzzy logic system the fuzzy logic and fuzzy sets will be used as prominent tool for indicating the various versions of knowledge about the relevant problem and it will also be used for modeling the relations and interactions among its variables. The glaucoma is nothing but a set of rules that affect the optic nerve and the eye [2]. The eye plays a major role in the part of the human body by providing vision. This affect of the eye will be generally created due to abnormal over pressure in the eye. The glaucoma plays a major impact in way creating the blindness to the people at the age of 65. The blindness will be formed at any age but most probably quite a natural disease for older people. The glaucoma has various forms and it may not give any symptoms or some time it will give mild symptoms. The impact is continuous to the point that you may not see an adjustment in vision until the condition is at a serious stage.

Since loss of sight because of glaucoma can't be detected easily, it's critical to have ordinary eye tests that incorporate estimations of your eye pressure so a finding can be made in its beginning phases and treated with a great accuracy [3]. If the symptoms of the glaucoma will be perceived early, vision loss can be eased back or prevented. If the problem is serious then it should require treatment for life long. Diabetic retinopathy is the most well-known diabetic eye illness and a main source of visual deficiency in American old people. It is brought about by changes in the blood vessels of the retina. In certain individuals with diabetic retinopathy, blood vessels may expand and release liquid. In others, ordinary fresh blood vessels develop on the outside of the retina. In the illness's beginning phases, an individual may not see changes to their vision. However, after some time, diabetic retinopathy can deteriorate and cause vision loss. Diabetic retinopathy generally influences the two eyes. Diabetic retinopathy (DR) is vein harm in the retina that occurs because of diabetes [4]. The diabetic retinopathy will be used to retrieve the accurate images from fundus images using vessel extraction method. The major disease qualities occurred to create the problems with vision of a human body. These symptoms related to diabetic can cause a lot of problems especially in terms of deficiency in vision.

Individuals with diabetes ought to have their vision checked in any event once every year to preclude DR. There are retinal medical procedures that can calm symptoms, but controlling diabetes and overseeing early indications are the best approaches to overcome the problems related to DR. The diabetic retinopathy (DR) is having a lot of impact on the diabetes related to human body. The very significant origin of loss of visual capability of human's eye will be the surely diabetic retinopathy for entire world population. The complete protection of an eye will be prominently provided by the retina. The retina is the major body of the human that surely influence the quality of the vision. The retina will be completely dedicated to provide the light. The retina can be capable to modify the any mode of light that strike the eye of a human body into the form of signals. These signals can easily be decrypted and understood by the human's mind with

a great accuracy. The method of diabetic retinopathy will be capable to generate or create a images those are purely related to the vision of the human body. The natural eye of humans can have great capability of sight which makes the eye to capture any mode of complicated image. The diabetic retinopathy has a major drawback by means of providing dangerous defects with related to the retina. So it provide deliver the liquid in the eye of human and consequently it forms the disturbance in the quality of a vision.

II.LITERATURE SURVEY

In nowadays, there is an expanding interest for design automatic systems that screen lot of people for vision compromising illnesses like glaucoma and diabetic retinopathy and to provide a automatic detection of the sickness [3]. The image processing is currently turning out to be practical and a helpful module for screening. The ophthalmologist will be able to use fundus images and these images are created by the digital imaging technique. The digital image technique provides excellent databases of history of the fundus images. The supervising of the improvement and treatment capability will be monitored by the ophthalmologists. These advanced images can possibly be handled via automated investigation systems [5]. The fundus image analysis is a critical function, due to the fluctuation of the fundus images regarding shading or the loss in quality of images. The complicated structures that related to retina of the human will be purely controlled by the process called morphology. Based on the various exclusive features of a retina with respect to the several patients and it may lead to take faulty decisions. In present paper, various instances with utilization of the advanced picture related methods are utilized to get better quality image from fundus images. The different possible examinations to recognize the components those are related to the retinal like optic disc, optic cup and sores like hard and delicate exudates. The significant commitments to identify glaucoma and seriousness of diabetic retinopathy utilizing fundus images are depicted in this section.

Glaucoma discovery algorithms are extensively characterized into two classifications, which depend on the location of optic plate and identification of optic cup. Optic plate and optic cup discoveries are looked at dependent on the 33 localization, detection and limit extraction technique. Strategies to distinguish diabetic retinopathy are disclosed as for different extractions of features and abnormally discovery in fundus images. The inadequacies in the current algorithms are distinguished and a strategy is proposed to identify glaucoma and diabetic retinopathy at a beginning phase for screening applications. Vulnerability is a difficult part in human's regular daily existence. Since the future can't be anticipate, it is difficult to be sure about what precisely will happen every day. The fundamental driver of vulnerability is the lack of data [6]. The data might be inadequate, fragmentary, not completely solid, unclear, opposing or insufficient in some other way. These different data inadequacies may bring about various kinds of vulnerability. The three significant kinds of vulnerabilities are fuzzyness (or ambiguity), which results from the imprecise limits of fuzzy sets, non-particularity (or imprecision), which is associated with sizes (cardinalities) of relevant sets of options and hardship (or friction), which communicates clashes among the different arrangements of options (SaikatMaity, Jaya Sil 2009).

Anyhow, most uncertainties are negligible, reasonable or unimportant. There is a significant level of vulnerability the board in smart systems. Since human thinking and decision making is fuzzy, including a serious extent of ambiguity in proof, idea usage and mental model detailing (Wang and Elhag 2006). The collection of ocular impairments which produced in optic

nerve injury will be described with help of Glaucoma. Due to glaucoma there is a gradual loss of retinal vision. The retinopathy is simply referred to the loss of vision. According the sources related to the world health organization more than 80 million of people are suffered by the glaucoma worldwide and approximately 13 percent of the people are having a chance to get complete blindness. In developed country like United States the glaucoma was treated as the one of the major reason to cause blindness to the people. This disease will became more serious and dangerous for the elderly people when compared to the young population. The glaucoma will be attacked with mild or neglected symptoms and most of the people are even unable to identify this disease until it became sever disease [7]. If the people are failed to identify it at initial stage it may have maximum chances to cause loss of irreversible vision at huge rate of possibility. The detection of glaucoma at early stage can be possible by the two significant parameters such as recognizing the harm factors and screening. In this it is possible to detect the population who suffered with glaucoma at an early stage before affecting of irreversible damage. In this paper, it is focused on the how the glaucoma will be identified at an early so that the loss will be reduced to a great extent. The fundus images are extracted with great quality by using the Glaucoma System for Diabetic Retinopathy using Vessel Extraction (GSDRVE) and fuzzy logic.

III. GSDRVE SYSTEM

The fundus photography will be used to take the fundus images. The fundus photography will be completed by capturing a photo at a better location generally fundus. The advanced technology called intricate microscope will be incorporated with a model cameras and these type of cameras have flash with them. The peripheral retina, optic disc and macula are the major available designs of the fundus photos. The designs are very useful designs of the retina. The original image will be applied as an input and generally it consists of three regions such as Red, Green and Blue in the fundus images.

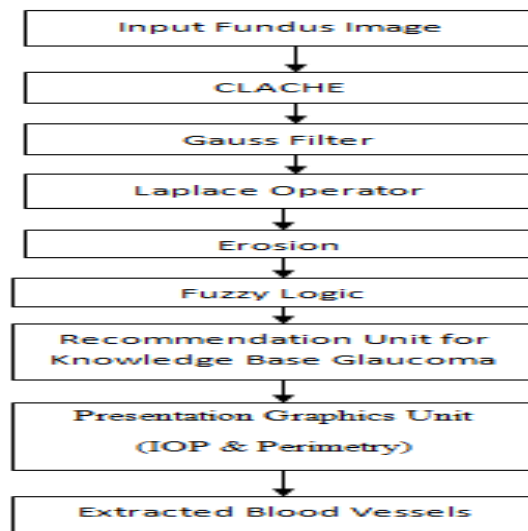


Fig. 1: Flowchart for Vessel Extraction in GSDRVE System.

The CLACHE and image enhancement will be done based on the histogram of an image. The OpenCV1(Open Computer Vision) method uses a adaptive histogram equalization. The technique called OpenCV1 will be performed to the derived images. The boundaries of the

image will be determined based on the boundaries of the fundus images and they can also used to get the width of the vessels. The retina's vessels will be derived by improve the quality of the image that can be extracted from fundus image. The entire process how the fundus images are extracted from clinical images by using vessel extraction and fuzzy logic will be described in as shown in fig.1. The Laplace operator is used to get the required portion of the image from the fundus image as shown in fig. 2(a). The wanted vessels can be possible to get by using thresholding of the image. This can also isolate the undesired part of the vessel. The technique of Erosion is much useful in the process of isolating the faulty vessels and generally these faulty vessels are developed due to thresholding process. It is very important to isolate the vessels those are broken into smaller pieces so that it can have only required width of the vessels. In this way the operation of the vessel extraction will be achieved. Based on the various derived features of the diabetic retinopathy such as domain, shape and color the automatic detection will be possible. Due to this process some abnormalities will be formed by capturing the fundus images at different positions and this will be shown in fig.2 (b). The abnormal fundus image will be improved its contrast after performing photo coagulation and it will show in fig.2(c). The major form availability of vessels in this method is in the mode of RGB. The effective method which is called as ISODATA iteration method will be used to extract or derive the Gauss filter from the fundus images. In a Gauss filter there is a possibility of presenting huge number of vessels so the extraction is very important. The output of the gauss filter will be shown in fig.3. There are two approaches to determine the abnormalities of the fundus images such as direct approach. The direct approach involves only screening whereas indirect approach contains both screening and monitoring. All vital information and data will be used in the process of discovery of crucial circumstances has provided by information of patient. The derived information can be transformed to a desired form so that the data preparing is takes place easily. The advanced techniques called intraocular pressure (IOP) and perimetry will be helpful in the analysis of Glaucoma. The type of genuine numbers will be determined based on IOP and the perimetry is used to provide the output of software. This software is used to determine sensitivity loss of information.

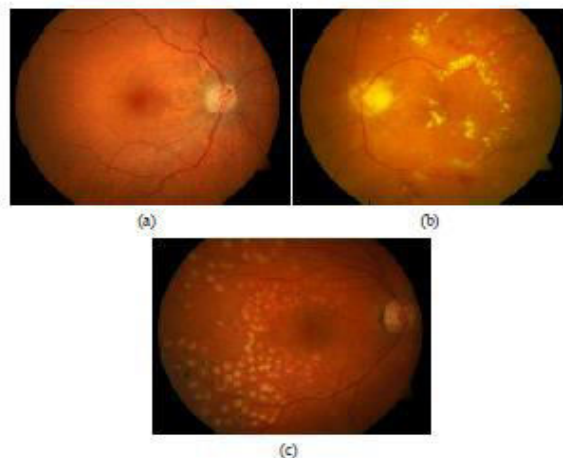


Fig. 2: (a) The normal fundus image, (b) The abnormal fundus image and (c) The abnormal fundus image

The fuzzy based knowledge is useful to know the status of the IOP method. The direct prediction results of the medical information are determined by using fuzzy sets. The analysis of the perimetry information classification has two methods. The first method is used to find visual field of the fundus image and second method is used to find the changes in the body of the patient. The most serious disease that will be attacked to patients those who are suffering from diabetic is diabetic retinopathy and it will have immense impact on the blood vessels of the retina of the humans. The ophthalmologist can able to perform treatment and prevent the complete blindness if the patients can approach them at an early stage. The two techniques such as morphological image processing and fuzzy logic will collectively utilized to identify the complicated issues related images of retina. At very starting phase the method called morphological technique will be utilized to detect hard effusions with help of morphology. The process of morphology contains removal of the optic disc. Later in proceeding stages the complicated effusions will be extracted or derived with help of algorithms based on fuzzy logic. The fuzzy logic can utilizes the parameters in the RGB that related to the image of retina in the process of making fuzzy sets

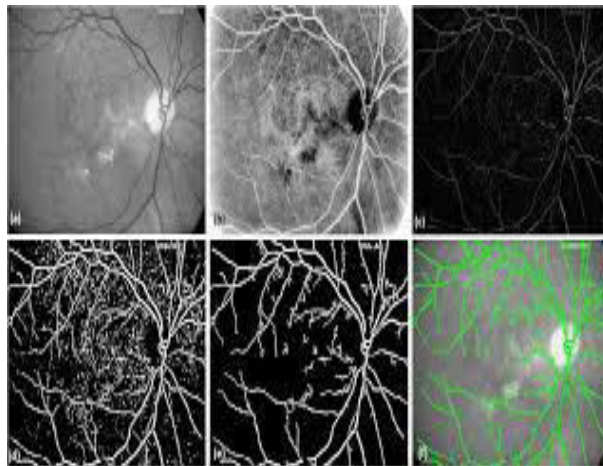


Fig.3: The Extraction of Gauss Filter.

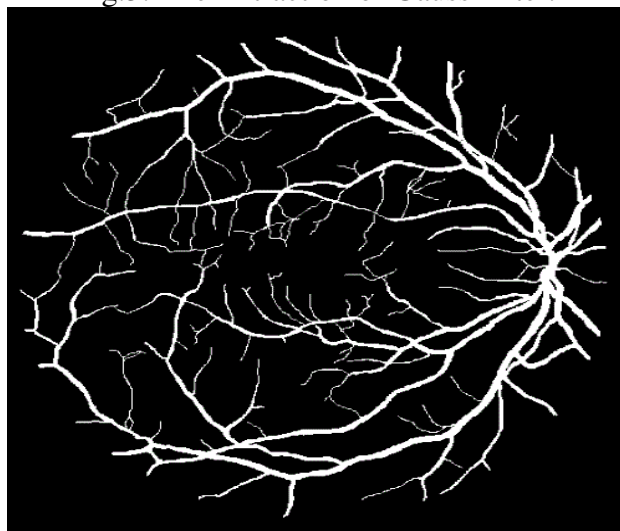


Fig. 4: The extracted blood Vessels

Depending on the input parameters applied to a processor such as red, green and blue mediums of a pixel in effusions process. The derived output of fuzzy logic which was calculated for complicated effusions based on its related area. The improvement of the diabetic retinopathy can achieved by the ophthalmologist based on the area utilized by the blood vessels of the healthy persons. In this technique the process of extraction of blood vessels will be achieved by using method of matched filtering. This method uses the preprocessing procedure in the way enhance the performance of the extracted blood vessels as shown in fig.4. The significant achievement of this technique is generating a better improved automatic Blood Vessel Extraction (BVE). The automatic blood vessels extraction will be much needful for the eye care efficient experts or professionals in the view of patient's therapy, medical study, and health research and screening. The accuracy of the GSDRVE System will be purely depends on the number of datasets used in the process. As the number of datasets increases in proportional to it the accuracy of the system will be increased. In this technique the background of the image in all its corners can be initially changed and later the efficient technique called homomorphic filter can be used to smooth the clinical images. This process can improve the brightness and contrast of the image when compared the actual images. The improvement of the signal of the blood vessels those are stay in the range below the threshold range can be possible by using fuzzy logic and blood vessel extraction methods. So by using the fuzzy knowledge based approach for glaucoma system in diabetic retinopathy the fundus images are extracted based on the blood vessel extraction.

IV. RESULTS

Table I: The Accuracy of the Extraction of the Blood Vessels.

Datasets	Existed System	GSDRVE System
10	81.6	83.4
20	83.2	85.9
40	88.7	90.2
60	91.9	93.4
80	96.1	97.8
100	97.3	98.6

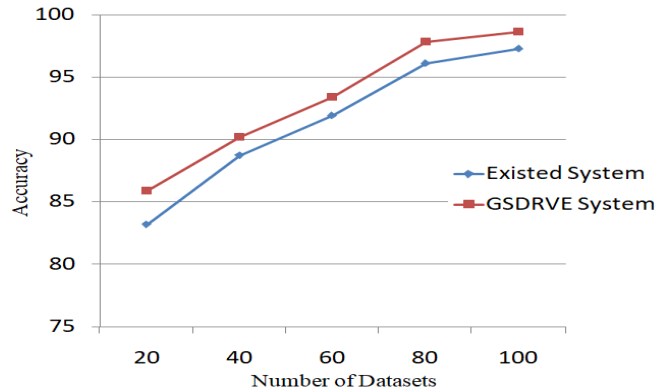


Fig. 5: The accuracy of the Existed System and GSDRVE System

The fuzzy knowledge based glaucoma system related to the diabetic retinopathy will be implemented to extract the high quality images from the available fundus images using blood vessel extraction process. This process is purely based on the number of datasets used for the deriving the image as shown in Table I. From that table it is very clear that as the number of datasets increases its obviously increases the accuracy. The accuracy was increased in a present GSDRVE System when compared to the existed system. The accuracy of the existed system and GSDRVE System will be shown in fig. 5. It shows that the accuracy of the proposed GSDRVE System will be increased as soon as the number of datasets increased. So the accuracy of the images derived from fundus images will be enhanced by using fuzzy logic and blood vessel extraction.

V. CONCLUSION

The present diabetic retinopathy (DR) technique is a one mode of diabetes complication and it has strong impact on the eyes of a human body. Initially the diabetic retinopathy may not have any symptoms and it just causes a little vision issue. The diabetic retinopathy has different treatments like intravitreal clinical treatment and sutureless standards plana vitrectomy. These treatments have provided a great relief to the disease related to eyes. The fuzzy knowledge based on the glaucoma was designed for the working location of the private ophthalmologist. The vessel extraction from retinal fundus images has determined the various ophthalmologic sicknesses like diabetic retinopathy, glaucoma and hypertension. The vessel extraction approach depended on image improvement procedures and individual grouping strategies incorporate fuzzy technique. The photographic of the rear eye is called as fundus images. In this paper, the visibility issue of the eye has detected using fuzzy knowledge based on glaucoma and it was capture the fundus images with help of the process of vessel extraction.

VI. REFERENCES

- [1]. Yaghoobi G, Heydari B, Heydari SR, Poorabdolahi F, Sharifzadeh G. Chronic Open-Angle Glaucoma and Its Association with The Cup Shape in Referral Ophthalmology Centre. *Pharmacophore*, 2018; 9(6): 65-70.

- [2].Costa, P., Galdran, A., Smailagic, A., &Campilho, A. (2018). A weaklysupervised framework for interpretable diabetic retinopathy detection on retinal images.*IEEE Access*, 6, 18747-18758.
- [3]. Jonas, Jost B, Tin Aung, Rupert R Bourne, Alain M Bron, Robert Ritch, and Songhomitra Panda-Jonas. Glaucoma. *The Lancet*, 2017; 390(10108): 2183–93. [https://doi.org/10.1016/s0140-6736\(17\)31469-1](https://doi.org/10.1016/s0140-6736(17)31469-1).
- [4].Solkar, S. D., & Das, L. (2017). Survey on retinal blood vessels segmentation techniques for detection of diabetic retinopathy.*Diabetes*.
- [5] J. Zilly, J. M. Buhmann, and D. Mahapatra, “Glaucoma detection using entropy sampling and ensemble learning for automatic optic cup and disc segmentation,” *Comput. Med. Imaging Graph.*, vol. 55, pp. 28–41, 2017.
- [6]. McMonnies CW. Glaucoma history and risk factors. *Journal of optometry*. 2017 Apr 1;10(2):71-8.
- [7]. Zhao D, Cho J, Kim MH, Friedman DS, Guallar E. Diabetes, fasting glucose, and the risk of glaucoma: a meta-analysis. *Ophthalmology*. 2015 Jan 1;122(1):72-8.
- [8]. Weinreb RN, Aung T, Medeiros FA. The pathophysiology and treatment of glaucoma: a review. *Jama*. 2014 May 14;311(18):1901- 11.
- [9]. MoriumAkter, Mohammad ShorifUddin, AhmudulHasanKhan , “Morphology Based Exudates Detection rom Color Fundus Images inDiabetic Retinopathy , “International Conference on Advance inElectronic Computer and Communication (ICAEECC),2014.
- [10]. Shon K, Wollstein G, Schuman JS, Sung KR. Prediction of glaucomatous visual field progression: pointwise analysis. *Current eye research*. 2014 Jul 1;39(7):705-10.
- [11] A. B., K. D.K., S. M.G., and J. R., “Relationshipbetween diabetes and grayscale fractal dimensions ofretinal vasculature in the Indian population,” *BMC Ophthalmol.*, vol. 14, p. 152, 2014.
- [12] L. Tang, M. Niemeijer, J.M. Reinhardt, M.K. Garvin,M.D.Abramoff, Splat feature classification with pplicationtoretinal hemorrhage detection in fundus images,*IEEE Transactions on Medical Imaging* 32 (2013) 364–375.
- [13]. Cook C, Foster P. Epidemiology of glaucoma: what's new?.*Canadian Journal of Ophthalmology*. 2012 Jun 1;47(3):223-6.
- [14]. Topouzis F, Coleman AL, Harris A, Koskosas A, Founti P, Gong G, Yu F, Anastasopoulos E, Pappas T, Wilson MR. Factors associated with undiagnosed open-angle glaucoma: the Thessaloniki Eye Study. *American journal of ophthalmology*. 2008 Feb 1;145(2):327-35.

[15]. Quigley HA, Broman AT. The number of people with glaucoma worldwide in 2010 and 2020. *British journal of ophthalmology*. 2006 Mar 1;90(3):262-7.

[16]. Rotchford AP, Kirwan JF, Muller MA, Johnson GJ, Roux P. Temba glaucoma study: a population-based cross-sectional survey in urban South Africa. *Ophthalmology*. 2003 Feb 1;110(2):376-82.

RESEARCH ARTICLE

Energy-aware and SLA-guaranteed optimal virtual machine swap and migrate system in cloud-Internet of Things

Ramamoorthy Karthikeyan  | Venkatachalam Balamurugan

Mohammed Sathak Engineering College,
Kilakarai, Ramanathapuram, India

Correspondence

Karthikeyan Ramamoorthy, Mohammed
Sathak Engineering College, Kilakarai,
Ramanathapuram, Tamil Nadu, India.
Email: karthikhonda77@gmail.com



Abstract

An emerging cloud-Internet of Things (IoT) is a novel paradigm that brings potential benefits over a variety of applications. The pervasive use of IoT devices often struggle to meet resource requirements in cloud environment. The abundant wastage or inappropriate usage of resources leads to consume larger amount of energy and delayed response. Optimization algorithms are more popular for optimal selection, the algorithms as ant colony optimization, particle swarm optimization, genetic algorithm were majorly concentrated for the purpose of load balancing. However workload is balanced in many previous research works, however it failed to mitigate SLA violations and limitations of energy consumption. In this paper, we address both energy-aware load balancing and satisfaction of SLA constraints. First, IoT devices submit tasks which are segregated into queues using policy-based SLA by taking in account of SLA constraints. Second, the tasks are allocated in accordance to dynamic threshold predicting fuzzy followed by Analytical Hierarchical Process. Third, the workload is employed for energy minimization which decides whether to perform swap or migrate virtual machines (VMs). Swapping between VMs is held by novel map and consolidates processes. Then combination of fruit fly and bird swarm hybrid optimization algorithm is enabled to select an optimal VM for workload balancing. Also, the idle physical machines (PMs) are supposed to be in OFF state for diminishing unnecessary energy consumption. The outcomes of this cloud-IoT system is experimentally evaluated and compared in terms of energy consumption, number of migrations, resource utilization, and execution time.

KEYWORDS

energy optimization, IoT devices, SLA constraints, workload balance

1 | INTRODUCTION

Nowadays IoT integrated cloud is equipped with a wide variety of advanced technologies for adapting with the growth of modern systems.¹ Queuing user tasks and processing user tasks results with better performances. Cloud offers multiple services, which is much essential to concentrate on the utilization of cloud resources. Virtual machines (VMs) in the cloud are having different resource constraints for executing incoming tasks. Cloud is enabled to be operated on any emerging technology.

Load balancing in the cloud is one of the essential processes that assist in situations of failures due to excess power consumption.² Even meta-heuristics algorithms are involved in managing load. Techniques as minimum execution time (MET), minimum compilation time (MCT), min-min, min-max, max-min, simulated annealing (SA), and other evolutionary and intelligent algorithms are studied in the cloud load balancing. Workload

balancing is achieved by VM placement which is a significant process handled for effective utilization of resources and minimization of power consumption.³ A heuristic algorithm of genetic algorithm (GA) is used for selecting a target solution for VM placement. Distribution of load for power minimization also requires the design of a task dispatching model using the queuing system.⁴ Optimal dispatching of tasks ensures the minimization of response time and power consumption. Task queuing also effects on balancing the load.

Ant colony algorithm (ACO), bat algorithm (BA) are bio-inspired algorithms that take part in balancing workload.⁵ The load is predicted using the algorithms and workflow is balanced using makespan and cost of execution. In order to balance workload, the estimation of the deciding factor plays a significant role.⁶ Load balancing is performed with the measurement of constraints (CMLB). The mathematical formulation of the deciding factor is composed of load and capacity of a particular VM. Then based on the priority, the selection factor is modeled. A combination of optimization algorithm is proposed as hybrid particle swarm optimization (HPSO) for managing load.⁷ This HPSO integrates GA into PSO and developed a dynamic load balancing procedure. Due to the frequent change in load, the dynamic operation for load balancing achieves better performances. Adjustments in the incoming number of tasks are not possible, hence dynamical load balancing is better in performances.

Load balancing is successfully obtained with VM migration which causes the problem of SLA violations.⁸ In load balancing concepts, SLA violations are also concentrated.⁹ Decreasing energy consumption should meet the requirements of SLA to minimize SLA violations. In this work deadline and budget constraints are considered as the major QoS parameters. A resampled binary PSO (RBPSO) is proposed for efficient resource utilization.¹⁰ The resources present in physical machines (PMs) are estimated to balance the load. Then using RBPSO the resource utilization is maximized along with minimization of energy consumption. SLA assured the consolidation of VM for reducing energy consumption.¹¹ Resource usages and SLA requirements are predicted for the allocation of tasks. Load balancing is majorly studied with a heuristic algorithm for obtaining an optimized energy-efficient cloud environment. So obviously, our work also concentrates on optimization algorithm for load balancing along with satisfying SLA constraints.

Contributions of this Paper: The major contributions of this paper are illustrated below,

- The problem of energy consumption and SLA violations that occur in the cloud-IoT environment is resolved by prompt task allocation and VM migration/VM swapping.
- Task are processed into queues in accordance to Policy-based SLA, which checks the SLA constraints of individual IoT device. This ensures to minimize SLA violations.
- Novel dynamic threshold estimation is presented using fuzzy logic and the task allocation is handled by Analytical Hierarchy Process (AHP).
- For faster submission and processing of tasks, broker is appointed as an intermediate. The broker updates status of load for allocating tasks according to their requirements. Broker acts a strong and supportive component for both task allocation and load balancing.
- The major problem of excess amount of power consumption is mitigated by the workload balancer which makes a decision for VM swapping or VM migration. The decision making is performed to avoid unnecessary creation of new VMs into PMs. Appropriate decision achieves effective utilization of resources by eliminating unnecessary resource wastages.
- Map and Consolidate with Levenshtein similarity is executed for VM swapping, which maps toward ideal VMs and chooses accurate matching VMs for swapping.
- Integration of Fruit fly and Bird Swarm Optimization algorithms is used to select an optimal VM for migration. The fruitfly is accurate in fitness estimation and bird swarm is faster in searching. Hence for faster selection of VMs, this combination of algorithm is proposed.
- The simultaneous monitoring of workload and reported collection builds an efficient task allocation and decision making system in cloud-IoT. Finally our proposed cloud-IoT meets the requirements of SLA and energy consumption.

Organization of this Paper: The reminder of this paper is organized as follows, Section 2 outlines the currently existing research works in cloud, Section 3 depicts problems defined in previous power optimized cloud environment, Section 4 details with the proposed design of energy-aware and SLA-guaranteed cloud, Section 5 evaluates the proposed system and presents comparative study, finally Section 6 concludes this paper along future directions.

2 | RELATED WORK

In this section, a detailed study on previous works that are focused on cloud resource utilization, load balancing and energy optimization are discussed. To hold on the SLA constraints with respect to the management of energy consumption, the measurement of workload were designed.¹² The workload at host was computed from the CPU utilization of VMs. VM migration was performed multiple times and hence it consumes a larger amount of energy. The ignorance of energy consumption during migration causes performance degradation. A Game-based method

was developed for minimizing the overall energy consumption.¹³ Load prediction involves the gathering of historical load for prediction of the future load. The PMs were split into three groups which are differentiated by varying load states. VM needs to wait for a longer time to get migrated which consequently increases task execution time. The computation of load was performed only when the overload condition was reached.

In Reference 14, a layered VM migration (LVMM) algorithm was proposed to balance the load. This work developed an inter-region VM migration and intra-region VM migration. Bandwidth utilization plays a major role for performing migration. However, the workload was balanced, it performed migration too many times while using intra-region algorithm. VM migration is not efficient due to the absence of an optimal selection of VM. An optimization algorithm was proposed for performing energy-aware load balancing.¹⁵ An energy aware load balancing algorithm was comprised of two techniques as artificial bee colony optimization (ABC) and firefly optimization (FFO) algorithm. ABC algorithm was performed in the first phase and FFO algorithm on the second phase. According to this work, loads of VMs were estimated and they are sorted into descending ordered list from which the VMs are migrated. Optimization was not used for preferring an optimal VM; hence the migration process is not recommendable.

An auction-based online algorithm was proposed¹⁶ for providing guaranteed quality of service (QoS). Cloud zones are composed of different capacities; in online algorithm priori knowledge-based bidding was undergone. Cost and load were involved in placing bidding values. Submission of the bidding values by a user will not be true at all time, hence some of the users will be served with higher response time. A modified double Q-learning algorithm (DQA) was proposed¹⁷ to perform load balancing with QoS by estimating the reward values. The cumulative reward values were maintained on Q-tables for the purpose of decision making. RAM was the only resource which was taken in account for satisfying customer's demand. DQA balances load but fails to reduce execution time.

In Reference 18, two-phase cluster-based load balancing (CLB) algorithm was proposed for constructing a graph model. Dijkstra's algorithm was used for distance estimation, using which the data centers were clustered. Then, the client cluster assignment (CCA), was existed with the major drawback of frequent updating of graph which tends to consume higher resource and longer time to response. PSO meta-heuristic algorithm was designed to perform static task scheduling.¹⁹ The resources are comprised of CPU, memory and bandwidth. PSO was enabled to compute the best position of VM to process the incoming tasks. The development of static algorithm with PSO was suitable only for stable environment, whereas the submission of tasks cannot be maintained static. Since the requirement of arriving tasks are varied dynamically. Such static algorithm also rejects certain tasks due to its limitations in resources. Swarm intelligence algorithms were widely used for load balancing. Social spider with chaotic inertia weight-based random selection was proposed.²⁰ Fitness value was computed using completion time and task execution cost for minimizing the makespan. An optimal VM was selected by broadcasting the fitness values via messages. Cost was considered as a significant parameter, which was not able to satisfy all type of tasks. A Multi-Rumen Anti-Grazing algorithm was proposed for load balancing.²¹ The two major constraints that were taken in account are task execution time and task completion time, whose aim is to reduce makespan. However this work shows better performances, it was applicable only for static cloud environment. In case of overload, this system rejects the incoming tasks.

ACO algorithm was suggested for efficient load balancing in cloud.²² The traveling salesman problem was reformulated and the load was exploited by predicting the CPU utilization. The tour in ant colony system was computed from random proportional rule with respect to the visiting VMs on PMs. Here, solving traveling salesman problems was not able to balance the load appropriately. The optimal allocation of tasks was presented by Improved PSO (IPSO).²³ The incoming tasks are categorized into batches for balancing the load. The task classification was performed using number of tasks and the task lengths. For load balancing, IPSO estimates completion time and the overloaded tasks are moved to lighter VM. Tasks are categorized based on their length, which leads to higher time for processing larger sized tasks. Energy efficient VM placement was performed by predicting the resource requirement and searching for peculiar VM.²⁴ Tasks are classified into four based on the requirements in terms of CPU-intensive, Memory-intensive, I/O-intensive and communication-intensive. Here the task's deadline was taken in account as SLA constraint. Then the VM type was determined and later the load was balanced. On considering deadline as a significant parameter fails to attain SLA and balancing of the workload with poor performances.

A SLA violation assisted load balancing system was proposed with three adaptive models.²⁵ The models are gradient descent-based regression (Gdr), maximization correlation percentage (MCP) and bandwidth-aware selection policy (Bw). The first two algorithms were enabled to compute CPU utilization and third were executed to select a VM from the overloaded PM. According to this work, the local controller was responsible to monitor the utilization of CPU resources. Once the overload is predicted, then the load will be shifted to another PM without any optimal selection. Hence this work leads to frequent load balance, even after the migration of VM. Many heuristic task scheduling algorithm was proposed for energy optimization in cloud.²⁶ Power factor was mathematically formulated using power efficiency and CPU utilization. The proposed result shows average performance due to the conventional procedure of Min-Min algorithm. Most of the previous workload balancing paper has concentrated on using optimization algorithm, task scheduling, however each work is subjected to certain limitation which are significantly concentrated in our work for better performances in energy efficient load balancing. To overwhelm the energy problem prompt migration and appropriate task allocation is proposed in this paper.

3 | PROBLEM STATEMENT

Power-aware and performance-guaranteed virtual machine placement (PPVMP) was developed in Reference 27. ACO algorithm was involved to minimize power consumption of physical machine and enhance VM performances. According to ant colony optimization, power consumption and performance degradation are computed for pheromone trails. Using ACO, initially the solutions are generated using First Fit Decreasing algorithm and further the VMS are assigned from the first PM and others. In Reference 28, ant colony system (ACS) integrated with the techniques of order exchange and migration (OEM). This combination was proposed as OEMACS to solve the problem of VM placement. Ant colony-based order exchanging operation and migration operation were performed. In case if the solution was infeasible, then OEM was executed else global pheromone was estimated and updated with optimal VM.

An energy-aware and QoS-aware multi-objective ACO (MACO) approach was also presented for solving SLA constraints during load balancing.²⁹ The proposed MACO computes pheromone factor and heuristic factor for performing VM placement and VM consolidation. These three major objectives of this paper include minimization of energy consumption, resource wastages and energy cost. Load of physical machines were determined based on the usage of CPU which includes number of requests and physical machine capacity for measuring heuristic factor. The problems existed on cloud by using ACO are elimination of migration, due to the use of static VMs, degradation of performance, higher SLA violations, consideration of minimum number of parameters for optimal VM selection and increase in execution time. The three objectives was mathematically given as,

$$\text{Objective 1 : } P_j = (P_j^{busy} - P_j^{idle}) \times U_j^p + P_j^{idle} \quad (1)$$

$$\text{Objective 2 : } \text{Min} \sum_{j=1}^M W_j^{PM} \quad (2)$$

$$\text{Objective 3 : } \text{Min} \sum_{s=1}^s P_s^{NE} \quad (3)$$

These three objectives failed to select optimal VM and also it is subjected to other performance degradations. Other optimization algorithms as GA, PSO and parallel PSO were also participate in resolving the problem of energy consumption and workload balancing.^{30,31} The problem dealt with these optimization algorithms were CPU limitations that fails to accommodate tasks, rejection of incoming tasks due to limited resources and consumption of large amount of resources. Hereby the problems stated in this section are solved with our novel energy-aware and SLA guaranteed cloud-IoT system that is detailed in next sections. Majorly, optimization algorithm was preferred for selection of VM which was not able to attain minimized power consumption and SLA constraints. The key problems to increase power consumption are infeasible VM selection, poor VM migration and rejection of SLA constraints. On taking in account of these key problematic issues, the proposed system constructs energy-aware and SLA guaranteed cloud-IoT system with optimal VM selection, satisfied SLA requirement and prompt VM migration/swapping.

4 | PROPOSED CLOUD-IOT MODEL

4.1 | System overview

The proposed cloud-IoT model is presented for energy-aware and SLA guaranteed workload balancing system. Figure 1 depicts the complete system model and the processing algorithms that are executed on each component. The proposed system is composed of IoT devices, task organizer, task allocator, broker and load balancer. The two major components are, the task organizer that manages queue based on SLA constraints and load balancer that decides activation of load balancing process. The workload in the designed cloud-IoT architecture is balanced by performing VM swapping or VM migration. Based on the predicted load status, the decision is made.

Tasks $t = \{t_1, t_2, \dots, t_k\}$ from IoT devices $D = d_1, d_2$, are submitted into task organizer, where the SLA constraints are computed and the tasks at time T_1 are split into two queues Q_1 and Q_2 respectively. Usually the IoT devices are highly energy consuming, hence the battery level of each device while submitting the tasks are also considered as a significant SLA constraint. Then task set at T_1 is allocated using PMs listed from AHP. The load at PMs are not static, hence we dynamically update threshold values with the fuzzy logic threshold prediction system. This proposed system focusing on energy consumption, maps for the appropriate VM for swapping as well as an optimal PM is preferred for migrating the tasks from one VM to another. VM swapping is performed by the novel map and consolidate procedure that operates by estimating Levenshtein similarity. For selection of an optimal PM, hybrid optimization algorithm is presented as a combination of fruit fly with bird swarm optimization algorithm. Energy aware and efficient resource utilization is achieved in this work. According to the incoming tasks, they are allotted and then simultaneously the load at PMs is balanced by appropriate decision making. Effective usage of resources minimizes the wastage of resources. In cloud, the concept of virtualization

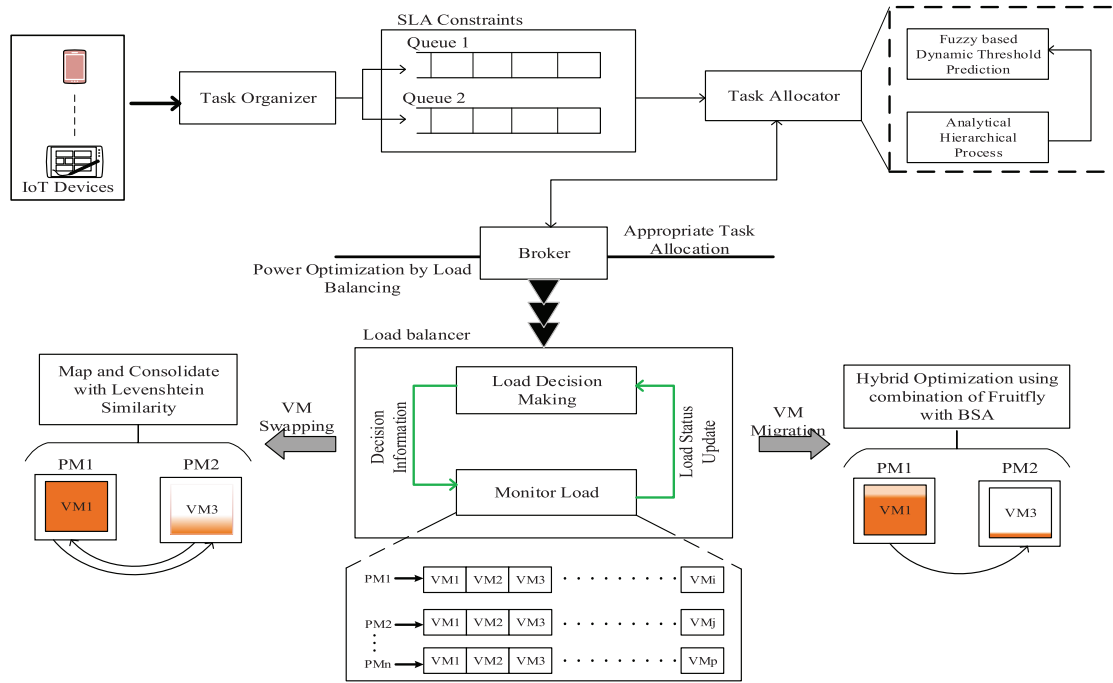


FIGURE 1 Proposed energy-aware cloud-IoT model

TABLE 1 Policy-based SLA task organizer

SLA constraints					
d_k	de_k	C_k	M_k	B_k	Action
Min	Min	Min	Min	Min	Q_1
Max	Max	Max	Max	Max	Q_2

is the key to serve users with proficient responses. As per the arrival of tasks from users, the VMs are created for processing and to meet the user's requirements.

4.2 | Task organizer

Task organizer is responsible to organize the arriving number of K tasks from IoT devices. The major parameters that are taken in account for each task are task size, task deadline, device energy, arrival time and others. A policy is applied based on these constraints to make corresponding actions. These metric are the significant SLA constraints taken in account. Based on the above mentioned constraints, each task can be described as,

$$t_k = \{Id_k, S_k, d_k, ar_k, de_k, C_k, M_k, B_k\} \quad (4)$$

The constraints $Id_k, S_k, d_k, ar_k, de_k$ denote task's identity, size, deadline, arrival time, and remaining energy at device and the other parameters include C_k, M_k, B_k as CPU, memory and bandwidth requirements for the particular task. The energy of user is considered as a significant constraint, since energy plays a major role in IoT devices. Due to this reason, energy is taken in account as a SLA constraint. Using these SLA constraints, the tasks are categorized into two queues as $Q = \{Q_1, Q_2\}$. The two queues will be composed of,

$$Q_1(T_1) = \{t_1, t_2, t_4, t_5, t_9\} \quad (5)$$

$$Q_2(T_1) = \{t_3, t_6, t_7, t_8\} \quad (6)$$

For instance a set of 10 tasks are taken at time T_1 which are split into two queues as shown in (5) and (6). From these two queues the tasks are allocated effectively. The queues are split by the policy-based SLA as depicted in Table 1.

Consider a set of tasks are arrived at time T_1 whose average waiting time, energy and deadline are estimated. Average values are estimated for submitting the tasks to appropriate VM for processing. Average is computed for d_k, C_k, M_k, B_k which maximizes the efficiency of task allocation. The average values for K tasks are estimated as follows,

$$A_{ts} = \begin{cases} \frac{\sum_{k=1}^K d_k}{K} \\ \frac{\sum_{k=1}^K C_k}{K} \\ \frac{\sum_{k=1}^K M_k}{K} \\ \frac{\sum_{k=1}^K B_k}{K} \end{cases}, \text{ at } T_1 \quad (7)$$

Let K be the total number of tasks at the time period, average values are individually computed for each queues based on the metrics for task allocation. The task organizer is equipped to collect tasks and classify based on the SLA constraints. Then average value is estimated and given to task allocator, using which the threshold value is computed.

4.3 | Task allocator

In task allocator, fuzzy-based dynamic threshold prediction is performed followed by task allocation using the ranked PMs in AHP. Fuzzy logic is equipped for determining the threshold value dynamically, since the task SLA constraints are not static. So dynamic threshold is computed and then task is assigned for appropriate PMs. Triangular fuzzifier is incorporated for predicting dynamic threshold.

Figure 2 illustrates the fuzzy logic model that uses four average values as input parameters which are computed by the task organizer for the task set at particular time period. Here the average value is computed for a set of tasks for allotting them to apt PMs. The fuzzy model is composed of the following entities,

Fuzzifier: The fuzzifier is responsible to transform crisp input values into fuzzy set using triangle shaped curves with the increasing and decreasing slopes. The converted fuzzy set is transferred for next processing. The membership functions value ranges between $[0 - 1]$.

Interference Engine: This entity identified the matched degree of the input parameter with respect to the defined fuzzy rules. Based on the fuzzy rules the control actions are made. The fuzzy rules are illustrated in "IF ... THEN" rules.

Defuzzifier: The actions taken by the engine will be converted back to crisp values by this entity. According to the obtained action, the system is adapted.

Fuzzy is used for adaptive threshold estimation, so the input constraints are varied based on the arrival of current tasks for processing into the system. The computation in fuzzy using degrees of truth is simpler and enables to obtain faster result.

Deadline of each task is one of the significant parameter that defines task's completion time, within which it should be executed on cloud. It is probably flexible to allocate tasks. Average for each queue is computed and then applied on fuzzy logic. Given, $Q_1(A_{ts}(d_k), A_{ts}(C_k), A_{ts}(M_k), A_{ts}(B_k))$ defines the threshold value for the tasks in Q_1 based on the rules given in Table 2. On the other hand AHP performs ranking by updating the load status via the broker. In general, n numbers of PMs are comprised of $\{i, j, p\}$ number of VMs as shown in Figure 1. The created VMs are supposed to have CPU, RAM, I/O, Bandwidth and other parameters which are responsible for executing tasks at faster speeds. In, AHP the load at each PM is predicted and ranked in ascending order. As per the task allocation procedure, based on the predicted threshold, the tasks are allocated to the listed PMs. AHP is a hierarchy created based on goal of the process as in Figure 3. Our goal in this section is to allocate tasks to appropriate PMs which are ranked using AHP. The three criteria chosen for ranking the PMs are CPU utilization, Memory Utilization, and Bandwidth utilization. AHP process is followed by execution the computation of weights, ratings development, and ranking.

CPU, Memory, and Bandwidth play key role in determining the affordable number of tasks in particular PM. AHP takes in account of the best alternatives for achieving best results. Usually, in cloud the PM are composed of VMs that is represented as,

$$PM_n = \{VM_i, \dots, VM_j, \dots, VM_p\} \quad (8)$$

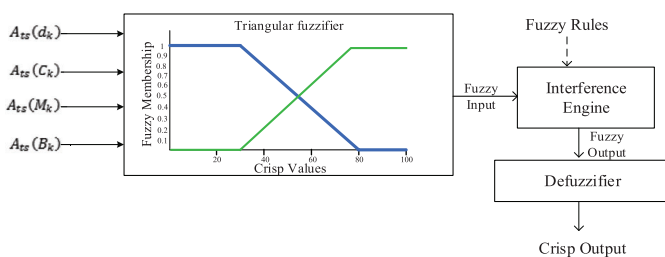
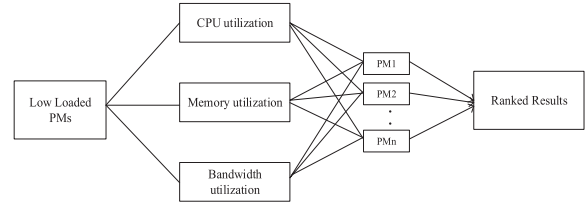


FIGURE 2 Fuzzy logic model

TABLE 2 Fuzzy logic dynamic threshold prediction

$A_{ts}(d_k)$	$A_{ts}(C_k)$	$A_{ts}(M_k)$	$A_{ts}(B_k)$	Output
Long	High	High	High	High
Long	Low	Low	Low	High
Short	High	High	High	Low
Short	Low	Low	Low	Low

FIGURE 3 AHP hierarchy structure

The terms i, j, p denote the total number of VMs present in individual PM. Each VM present in PM is composed of certain entities that are discussed previously. The specifications of VM are given in the following,

$$VM = \begin{cases} VM_i(CPU_i, MEM_i, BW_i) | i = 1, 2, \dots \\ VM_j(CPU_j, MEM_j, BW_j) | j = 1, 2, \dots \\ VM_p(CPU_p, MEM_p, BW_p) | p = 1, 2, \dots \end{cases} \quad (9)$$

The utilization of CPU, Memory, and Bandwidth is estimated by identifying difference between the total CPU, Memory, bandwidth, and the current consumption of CPU, Memory, bandwidth of the PM. This value is predicted for each PM present in the cloud. There are three steps followed in AHP process that are illustrated below,

4.3.1 | Weight computation

Weight estimation includes pairwise comparison matrix construction based on the relevance value. Single pair-wise comparison matrix is developed. Row-wise values are multiplied for determining root value. Then the values are normalized to obtain weights. The weighted value is determined mathematically using,

$$\bar{w}_m = \frac{\sum_{l=1}^N \bar{a}_{ml}}{N} \quad (10)$$

Let m and l be two different PMs, for instance two PMs are taken. The relevance score for PMs are provided according to their availability of resources for executing tasks. From Equation (7), the weight value is computed with total number of criteria N and the term \bar{a}_{ml} is the normalized value formulated as,

$$\bar{a}_{ml} = \frac{a_{ml}}{\sum_{l=1}^N a_{ml}} \quad (11)$$

4.3.2 | Development of ratings

Pairwise comparison matrix is constructed for each criteria that is taken in account. Rating for each criteria is defined according to the decision alternative. Table 3 depicts the numerical values corresponding to the importance of the criteria. For each parameter, these values are involved for predicting the pairwise comparison matrix.

This AHP is efficient in comparing each values with all the other entities, which is helpful in determining best ranking of the PMs.

4.3.3 | Ranking alternatives

Finally, average rating is computed for each decision and the values are ranking in the order of highest to lowest. The PM ranked with higher values is supposed to have larger unutilized resources for processing tasks in faster manner. The consistence check involved in AHP is supported for

Numerical value (A_{ml})	Importance
1	m and l are equally chosen
3	m is moderately chosen than l
5	m is strongly chosen l
7	m is very Strongly chosen than l
9	m is extremely chosen than l

TABLE 3 Relevance score

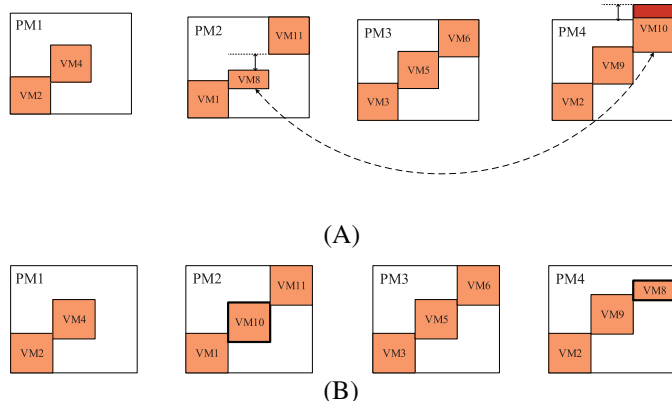


FIGURE 4 (A) Before VM swapping operation and (B) after VM swapping operation

resolving errors occurred during pairwise comparison. Consideration of multi-criteria in AHP is enabled to take three parameters for determining PMs status.

The tasks from the component task organizer are organized in queues from which a threshold value is computed using fuzzy logic. In accordance to the dynamic threshold the tasks are allotted into the PMs as ranked using the updated load information. Allocating tasks based on dynamic threshold and updated PM status ensures with good response time.

4.4 | Workload balancer

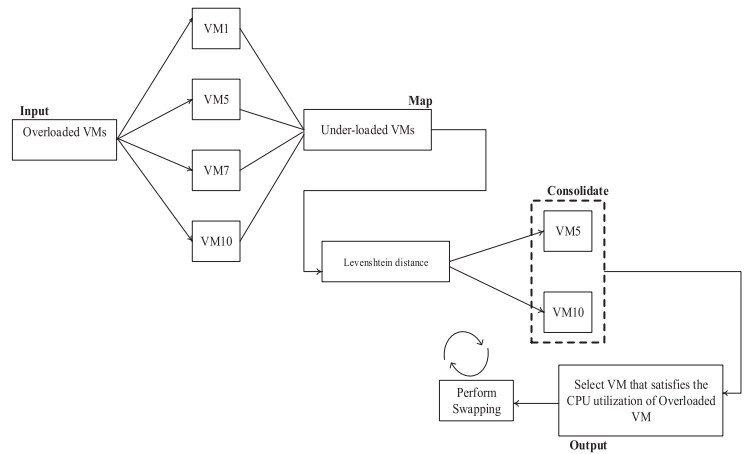
In this section, we discuss the workload balancing in cloud. An unbalanced workload in cloud leads to higher consumption of energy and wastage of resources. Workload is balanced by accurately estimating the load and make decision with respect to the computed workload. Workload at cloud is periodically updated for absolute decision making. Decision is either to perform VM swapping operation or VM migration operation, but not both at same time. The major focus of reducing energy consumption is achieved by decision making to balance the workload.

The initial step in workload balancing is the prediction of decision. For decision making, the load status from individual PMs is collected and the numbers of idle VMs are predicted. Then the estimated load is compared with respect to the threshold value, if the number of idle VMs is greater than the threshold then VM swapping operation is performed else VM migration operation.

4.4.1 | VM swapping operation

VM swapping is a process performed to operate the tasks effectively in case of overloaded condition. Swapping can be defined as exchanging of VMs between two PMs based on the load. Swapping of VMs ensures to utilize the available resources present within the deployed PMs as shown in Figure 4(A),(B). In this figure, three VMs $\{VM_1, VM_5, VM_{10}\}$ are considered to be overloaded, hence their resource utilization are estimated for mapping with the appropriate under-loaded VM. VM swapping operation is handled by map and consolidate using Levenshtein distance. Here, mapping is a simpler process of segregating all the under-loaded VMs, that is, the VMs with larger idle resources.

Initially the minimum loaded VMs are listed out, then the resources of overloaded VM is predicted and similarity measurements are determined between overloaded and under-loaded VMs. Map and Consolidate in VM swapping is performed as depicted in Figure 5. The similarity is determined using,

FIGURE 5 Map and consolidate for VM swapping

$$S_{(PM_x, PM_y)}(C_i, C_j) = \begin{cases} \max(i, j), & \text{if } \min(C_i, C_j) = 0 \\ \min \begin{cases} lev_{PM_x, PM_y}(i-1, j) + 1 \\ lev_{PM_x, PM_y}(i, j-1) + 1 \\ lev_{PM_x, PM_y}(i-1, j-i) + 1_{PM_{C_i} \neq PM_{C_j}} \end{cases} & \text{, Otherwise} \end{cases} \quad (12)$$

C_i, C_j are the CPU utilization of i th and j th VMs respectively and PM_x, PM_y denotes the x th and y th PMs in the cloud environment. Let PM_1, PM_2, PM_3, PM_4 be four PMs in the cloud, here the PM_4 is overloaded and it is not able to execute tasks present in VM_{10} , meanwhile the PM_2 is under-loaded with VM_8 . So the VM_8 from PM_2 and VM_{10} from PM_4 are exchange, that is, VM swapping is performed. Due to the utilization of resources at VM, they are enabled to be operate arriving tasks.

Measurement of similarity is efficient for choosing appropriate under-loaded VMs, based on which the VMs are swapped. Swapping of VMs in cloud, mitigates the consumption of due to overload and here, it does requires with the creation of new VM. Using the VMs present within the cloud tends to reduce the unnecessary energy consumption and also achieves better resource utilization.

4.4.2 | VM migration operation

In case, if the load at VMs is lesser than the number of idle VMs in threshold then VM migration operation is performed. Combination of optimization algorithm is used for selecting an optimal VM for migration. We have integrated fruit fly algorithm with bird swarm optimization algorithm. Initially we perform fruit fly optimization and then carryover the results into Birds swarm optimization by undergoing the following steps.

Step 1: Initialize position of each VMs present in the PMs over the cloud environment. The VMs are assumed to be fruit flies.

Step 2: Estimate distance to determine the concentration of smell of the food. Distance metric is computed using,

$$DS = \sqrt{x_i^2 + y_i^2} \quad (13)$$

The concentration is predicted from the reciprocal value of the distance metric as $1/DS$.

Step 3: the value of smell concentration for each fruit fly, that is, VM is calculated and this value is taken as fitness of each fruit fly. The maximum value of Smell is taken as best smell and then best values are given into bird swarm algorithm.

Step 4: Foraging in bird swarm optimization algorithm is performed.

Step 5: Load of VMs are determined while foraging in accordance to the tasks and VM resources. Load at individual VM can be determined using,

$$L_{VM_i} = \frac{Tk_{VM_i}}{ETk_{VM_i}} \quad (14)$$

The load at i th VM L_{VM_i} is computed with Tk_{VM_i} and ETk_{VM_i} that represents total number of tasks in i th VM and total number of tasks executed on i th VM. If the load constraint is satisfied, then proceeds with next step else compute for next VM.

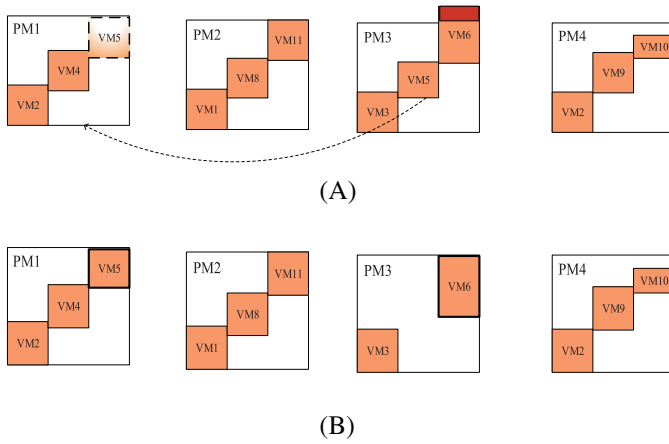


FIGURE 6 (A) Before VM migration operation and (B) after VM migration operation

Step 6: Fitness value is predicted in accordance to the capacity of VM, since only the capacity of VM is required to execute the migrated tasks from one VM to another. So fitness value is predicted based on the VM capacity that is given as,

$$Cp_{VM_i} = CPU_i, MEM_i, BW_i \quad (15)$$

The capacity of i th VM is calculated using the above Equation (15).

Step 7: Update solutions and stop when the stopping criteria is attained.

Hybrid optimization for selecting optimal VM obtains accurate selection of VM for migration. VM migration operation is execution within the created PMs, in case if need new VMs are created to balance the load. Figure 6(A),(B) depicts the migration operation. From the four PMs, one of it is considered to be overloaded, that is, PM_3 with VM_6 is overload and so the VM_5 is migrated to the optimally selected PM_1 to balance the load. On the other hand, we also shut down the unnecessarily executing PMs. If only a fewer number of tasks are involved in a PM, then the task from that particular PM is migrated and then turned off to minimize power consumption.

5 | EXPERIMENTAL EVALUATION

In this section, we analyze the proposed cloud environment to measure the efficiency and the betterments in terms of significant performance metrics. This section is categorized into two as implementation environment and comparative analysis. Each sub-section details about the proposed experimental analysis and comparison with previous research works.

5.1 | Implementation environment

The proposed energy efficient and SLA guaranteed cloud environment is implemented using CloudSim toolkit. In this work, number of tasks is received from IoT users and configurations for VMs are defined. CloudSim is a proficient tool that is extensively enabled to undergo modeling of VM allocation, dynamic workload balancing and energy consumption monitoring. Due to these special functionalities, we have preferred this CloudSim tool for our work and we have applied the proposed novel algorithms and method for mitigating power consumption as well as satisfying the SLA constraints.

Table 4 shows the major parameters that are used for executing our proposed work over the simulation tool. The specifications listed in the above table are not limited to this. The number of tasks can be varied and the results are evaluated.

5.2 | Comparative analysis

In this section, we present a comparative study to analyze the better efficiencies that are achieved in this proposed Cloud-IoT environment. In this discussion, we highlight the performances in terms of energy efficiency. Since task allocation and workload balancing proposed in this paper are the major contributions to obtain lesser energy consumption. The major parameters that are taken in account are concentrated in measurements of energy and resources. The key goal of this proposed Cloud-IoT environment is to achieve reduction of energy consumption and enhancement

TABLE 4 Experimental setup

Configuration parameter		Specification/value
Virtual machine	MIPS	500–2000
	RAM	128–2048 GB
	Bandwidth	500–1000 kbps
	Storage	11 TB
Number of VMs on each PM		12–15
Number of Tasks		1000–2000
Number of PMs		10–30
File size		500
Bird swarm parameters	Probability	[0.8,1]
	Frequency of birds	3

TABLE 5 Comparison on proposed and existing works

Works	Criteria considered	VM placement	Operations performed	Problematic issue
RBPSO ¹⁰	CPU, Memory, and Network Bandwidth	No broker	Computation of criteria	Overhead occurs due to the absence of centralized broker
First fit decreasing–PPVMP ²⁷	Power consumption and VM performance degradation	No broker	Computation of hybrid heuristic information	Utilization of larger memory
OEMACS ²⁸	CPU and memory	No broker	Computation of pheromone	Frequent computations due to infeasible solution
MACO ²⁹	CPU resources	No broker	Computation of available VMs and set of resources	SLA violations and Performance Degradation
GA ³⁰	CPU Utilization, Turn-around time and waiting time	Broker-based VM placement	Selection, crossover, and mutation	Consumes larger resources for processing
Proposed	<i>Task Constraints</i> —task's identity, size, deadline, arrival time and remaining energy at device, CPU, memory and bandwidth <i>VM Constraints</i> —CPU, Memory and Bandwidth	Broker-based VM placement	<ul style="list-style-type: none"> • Weight computation for task allocation. • Fitness value computation for VM 	Nil

of resource utilization with the satisfaction of SLA constraints. The parameters compared are energy consumption, resource utilization, migrations and execution time. Each comparative plot is detailed in the following sections.

Table 5 depicts the existing works that are considered for comparison to our proposed. From our literature, most of the previous works were concentrated on bio-inspired optimization algorithms. Hereby, the major part of our comparison also deals with the prior optimization that defines different constraints of VM. Among these works, ignorance of SLA constraints and task requirements was the significant issues that lead to poor performances. In order to overwhelm this, the proposed cloud-IoT model is developed with assured SLA and task allotment. Broker is the intermediate entity that is appointed to allot appropriate VMS for the tasks, since the current status of VMS are consecutively updated by the broker.

5.2.1 | Energy consumption

The main aim of the proposed workload balancing system in cloud-IoT is to minimize the energy consumption. Energy consumption is one of the challenging research issue in the cloud which is focused on several works. However the previous works have considerably reduce energy consumption, still it was challenging in efficient utilization of the resources. So reducing the energy consumption reflects over the performance on cloud which requires to be concentrated.

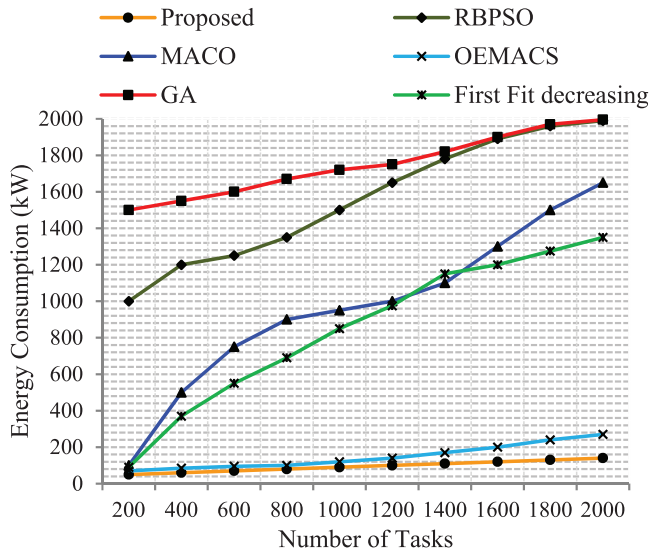


FIGURE 7 Comparative results on energy consumption

Technique	Energy consumption
MACO	44%
First fit decreasing	43%
OEMACS	8%
GA	87%
RBPSO	78%
Proposed	5%

TABLE 6 Average energy consumption

The amount of energy consumed by a PM is computed as summation of the VMs energy constraint.²⁷ Let PM_1 be composed of i number of VMs whose energy consumption is given as follows,

$$E(PM_1) = \sum_1^i E \{VM_1, VM_2, VM_3, \dots, VM_i\} \quad (16)$$

For each VM,

$$E(VM_1) = \omega_1 \cdot U_i + \omega_2 \cdot U_i^2 \quad (17)$$

The energy consumption $E(VM_1)$ is estimated from the amount of CPU utilized by the VM, that is, U_i and ω_1, ω_2 are the nonlinear model parameters included as constants. The energy consumption of PMs also includes the energy consumed by idle VMs.

Minimization of energy consumption in cloud environment brings improvements in computing capacity, storage management, bandwidth utilization, and workload balancing. Figure 7 demonstrates the energy consumption with respect to the increasing order of number of tasks. Tasks from users play a major role which is the major cause to increase the workload in cloud. From the comparison, the algorithms like MACO, GA, RBPSO, OEMACS, First Fit Decreasing have consumed larger amount of energy when compared with our proposed cloud-IoT environment. The OEMACS work have nearly reached energy consumption of our work, however the deployment of static VMs cannot perform well for increasing number of tasks. Other optimization algorithms also consumed higher energy consumption.

The proposed energy aware cloud-IoT has reduced upto 50%–75% of the energy consumption than the previous research algorithms. Table 6 shows the average value of energy consumption of each algorithm. In the comparison table, GA and RBPSO yields higher energy consumption where, the MACO and first fit decreasing algorithm better, but it also consumes certain amount of energy. Our proposed cloud-IoT is best among the other algorithm and hence the contribution of the proposed work is achieved. Most of the previous works have involved with VM migration only.

5.2.2 | Resource utilization

Resource utilization is a significant parameter that is essential in evaluating results of workload balancing. Resources play a major role in executing tasks over VMs that are present in cloud environment. The utilized resources depend on the processing speed of the VMs.²³ Here the PMs resource utilization is collectively computed with respect to the specifications of VMs. The resource utilized by each VM is expressed as,

$$R = \sum_1^i \frac{VM_i(MIPS)}{i} \quad (18)$$

MIPS is the million instructions per second by which the tasks are handled in each VM. i denote the total number of VMs present in the particular PM. Resource utilization is computed from Equation (14). CPU and memory are two major resources that are defined for validating proposed system.

The comparison of resource utilization in accordance to the number of PMs is depicted in the Figure 8. Appropriate utilization of resource causes unnecessary consumption of energy. The increased number of user tasks requires increased number of resources for processing. Resources are the key to execute hundreds and thousands of requests from users. Hereby this comparative plot shows that our proposed work utilizes larger amount of resources.

The proposed work uses almost 98% of the available resources whereas the previous work has utilized upto 90%. So minimum of 10%–60% of resources were wasted in previous research works. Unnecessary VM migrations, random allocation of tasks, SLA violations are the major reasons to cause wastage of resources. In our proposed work, the tasks are allotted with the monitored PM status which eliminates the wastage of resources. Also the decision making for workload balancing also enhances the utilization of resources. Appropriate VM for swapping and optimal VM for migration achieves efficient resource utilization.

Resources in VM include CPU and RAM, that is, Memory which defines the processing fastness of the tasks. Table 7 illustrates the measured idle and utilized CPU and memory resources. This comparison is predicted for the allocated number of tasks in VMs. The idle CPU in ACO, MACO, GA, PSO, Round Robin and First Fit Decreasing algorithms are high, which increases the energy consumption due to the idle CPU and memory processed without any tasks. In our work the perfect processing of workload balancing enriches the resource utilization as well as minimizes idle resource which consumes unnecessary energy.

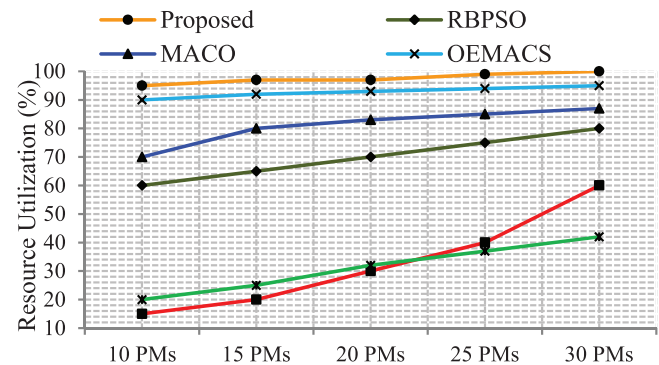


FIGURE 8 Comparative results on resource utilization

TABLE 7 Comparison on resource utilization

Technique	Utilized CPU (%)	Idle CPU (%)	Utilized memory (%)	Idle memory (%)
GA	5	95	5	95
PSO	6	94	6	94
Round Robin	12	88	61	39
First fit decreasing	28	72	75	25
ACO	31	69	80	20
MACO	70	30	90	10
OEMACS	90	10	90	10
Proposed	98	2	97	3

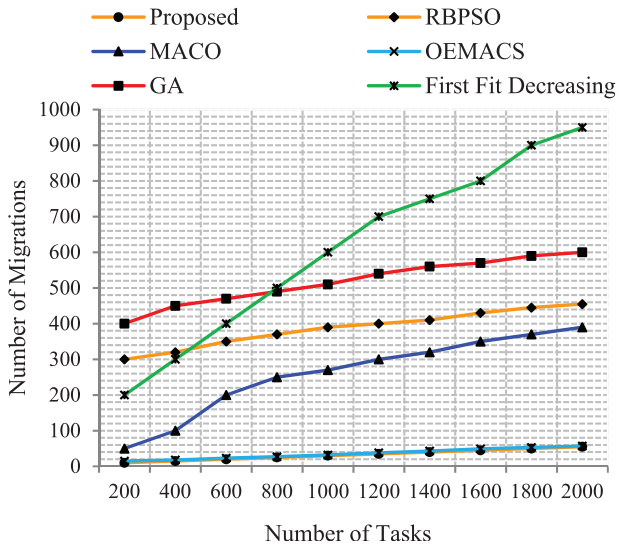


FIGURE 9 Comparative results on number of VM migrations

5.2.3 | VM migration

VM migration is an important process performed for balancing the workload. However the increased number of migrations in a cloud environment reflects over the increase in energy consumption. Migration of VMs over PMs also impacts the results on resource consolidation. To minimize the VM migration, an appropriate task allocation is essential. The VM migration is validated with the number of counts that the particular task is migrated due to load at PM. Using Equation (11), the load at individual VM is computed. If the load value is beyond threshold, then VM migration takes place else remains same. According to the load, tasks are migrated from one VM to another. The number of Migration takes place when,

$$L_{VM_i} > L_T \quad (19)$$

L_T is the load threshold of VM, if the load exceeds beyond threshold then the migration if performed and the migration count is increased. On behalf of the estimated load, the migration count is predicted for increasing number of tasks.

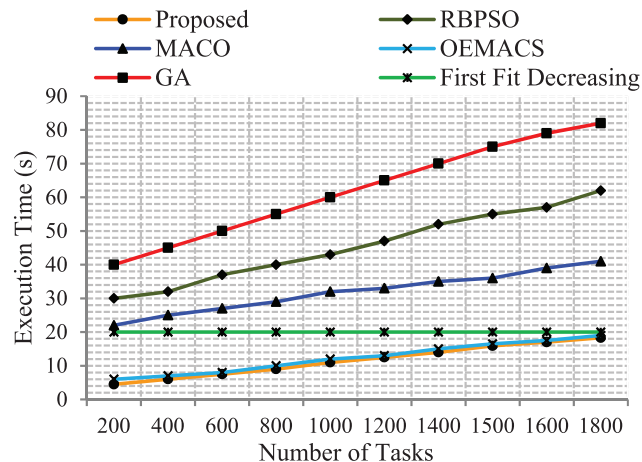
The performance comparison metric used in Figure 9 is the evaluation result for number of migrations. Our simulation results depicts that the proposed cloud-IoT having lesser number of migrations when compared with other research works as MACO, GA, OEMACS, RBPSO, and first fit decreasing. As per the proposed work, workload decision is made based on the availability of VMs. Hence VM migration is not often performed, this operation is handled only when the idle VMs are not able to tolerate the load. The minimized number of migrations is also a key point to reduce the unnecessary energy consumption. In all the previous research works, either only migration is performed or migration is performed with random selection. The impact of VM migration on energy consumption is also concentrated in our work by decision making which minimizes number of VM migrations as well as reduces energy consumption. Approximately 30%–80% of the unnecessary VM migration is eliminated in our proposed work with respect to the previous works.

5.2.4 | Execution time

Execution time is defined as the time taken to execute the number of incoming tasks. According to the arrival of tasks and management of workload at cloud are the major constraints that either increase or decrease the execution time. The execution time is mathematically computed by the following,

$$ET = \sum_{1}^k (TA_t - TC_t) \quad (20)$$

The execution time ET is determined from the task arrival time TA_t , that is, the time at which a particular task is allotted into VM and TC_t is the time during which the particular task completes its processing. The execution time is determined for k number of tasks which is varied from 200 to 1800 for analyzing the efficiency the system to cope up with the increase in the number of tasks.

FIGURE 10 Comparative results on execution time

The execution time plot in Figure 10 is drawn across the increasing number of tasks. In algorithms as GA, RBPSO, MACO and first fit decreasing, the execution is high for minimum number of tasks and it keeps on increasing double the time for increase in number of tasks. An unbalanced workload in cloud also increases the execution time, that is, tends higher response time for the user's tasks. The proposed energy aware and SLA guaranteed system in cloud-IoT is subjected to have reduced execution time due to workload balancing and faster task allocation based on dynamic threshold. In our proposed work, the range of 100–2000 tasks are executed within 7–20s, which is almost reached only in OEMACS algorithm. Hereby the increase in number of tasks are also processed at higher speed and tolerates for a large scale environment.

From these comparative results, the performance of OEMACS attains marginal variations with respect to the proposed work. Since, the authors have performed both VM swapping and VM migration. But the limitation was, they have not made decision on whether to perform VM swapping or VM migration. Due to this reason the resource utilization was higher than the proposed. The proposed work focuses to minimize the energy consumption by performing proper task allocation based on the cloud status.

5.2.5 | Efficiencies

In cloud, energy is one of the major challenging topic that are been studied with many solutions. The maintenance of load at VMs enables to minimize energy consumption. As a solution, many authors have proposed optimization algorithms to resolve energy problem with optimal selection of VMs and placement. Those optimization algorithms were subjected with (1) frequent migration, (2) SLA violations and (3) larger resource consumption for processing. On taking in account of these three problems the proposed work is designed with the following process,

- (i) SLA-based task queuing to solve SLA violations.
- (ii) AHP-based task allocation using dynamic threshold that is determined from the current status to cope with the present task's requirements.
- (iii) Decision making to activate VM swapping or VM migration for load balancing which ignores unnecessary creation of VMs that also consumes excess power in case of lesser number of task arrival.
- (iv) Map and consolidate for VM swapping which maps with perfect matching VM to which the tasks can be exchanged, so that it does not effect on execution time.
- (v) Hybrid Fruit fly with bird swarm optimization algorithm for faster selection of a VM to be migrated.

The proposed contributions of this work are attained modeling the cloud environment with the above mentioned processes. The potentiality of each process is highlighted, based on which the results of the proposed system are better than the previous research works.

6 | CONCLUSION

In this paper, the major contribution is to minimize the unnecessary consumption of energy that reflects on efficient and faster response time. The selection of workload balancing operation and switching off the idle PMs are ensured to reduce energy consumption. This paper's contribution is to satisfy SLA constraints based on which the tasks are split into two queues. The tasks are arrived from IoT devices are highly energy consuming and so the battery level is also considered as one of the SLA constraint. Then the tasks in the queues are allotted to PMs using dynamic threshold estimation

with fuzzy logic and AHP for selecting the best available PM with lesser workload. Due to the varying requirements of the task, the threshold value is computed dynamically.

Once the tasks are allotted to the cloud, they are processed in the corresponding PM. On the other hand, the workload status is monitored and if overload is predicted then the decision on load balancing is made. Here, we perform VM swapping operation or VM migration operation for balancing the workload, that is, only one at a time. VM swapping operation is handled by Map and consolidate procedure whereas VM migration operation is performed by hybrid Fruit fly with bird swarm optimization algorithm. The decision making for balancing the workload is one of the main contributions for reducing the energy. If there is sufficient number of PMs then, it is better to perform swapping operation else migration operation will be performed. Optimal selection of PM for swapping and migration assures with efficient resource utilization and energy consumption. This cloud-IoT applied on CloudSim toolkit and the comparative results are evaluated from which the proposed energy-aware and SLA-guaranteed cloud-IoT shows better performance.

In future, we have planned to extend the proposed cloud-IoT system along with the radio access network for workload balancing.

ORCID

Ramamoorthy Karthikeyan  <https://orcid.org/0000-0002-7128-5969>

REFERENCES

- Filip I-D, Pop F, Serbanescu C, Choi C. Microservices scheduling model over heterogeneous cloud-edge environments as support for IoT applications. *IEEE Internet Things J.* 2018;5(4):2672-2681.
- Mishra SK, Sahoo B, Parida PP. Load balancing in cloud computing: a big picture. *J King Saud Univ Comput Inform Sci.* 2018;32(2):149-158.
- Chen Y-H, Chen C-Y. Service oriented cloud VM placement strategy for internet of things. *IEEE Access.* 2017;5:25396-25407.
- Li K. Optimal Tash dispatching on multiple heterogeneous multiserver systems with dynamic speed and power management. *IEEE Trans Sustain Comput.* 2017;2(2):167-182.
- Kaur A, Kaur B, Singh D. Meta-heuristic based framework for workflow load balancing in cloud environment. *Int J Inform Technol.* 2018;1-7.
- Polepally V, Chatrapati KS. Dragonfly optimization and constraint measure-based load balancing in cloud computing. *Cluster Comput.* 2017;11:1-13.
- Eswaran S, Rajakannu M. Multiservice load balancing with hybrid particle swarm optimization in cloud-based multimedia storage system with QoS provision. *Mobile Netw Appl.* 2017;22(4):760-770.
- Babu KRR, Samuel P. Service-level agreement-aware scheduling and load balancing of tasks in cloud. *J Softw Pract Exp.* 2019;49(6):995-1012.
- Kamran BN. QoS-aware VM placement and migration for hybrid cloud infrastructure. *J Supercomput.* 2018;74(9):4623-4646.
- Wang X, Haoran G, Yue YX. The optimization of virtual resource allocation in cloud computing based on RBPSO. *Concurr Comput Pract Exp.* 2018;32:e5113.
- Cao G. Topology-aware multi-objective virtual machine dynamic consolidation for cloud datacenter. *Sustain Comput Informat Syst.* 2019;21:179-188.
- Chang K, Park S, Kong H, Kim W. Optimizing energy consumption for a performance-aware cloud data center in the public sector. *Sustain Comput Informat Syst.* 2018;20:34-45.
- Guo L, Hu G, Dong Y, Luo Y, Zhu Y. A game based consolidation method of virtual machines in cloud data centers with energy and load constraints. *IEEE Access.* 2017;6:4664-4676.
- Fu X, Chen J, Deng S, Wang J, Zhang L. Layered virtual machine migration algorithm for network resource balancing in cloud computing. *Front Comp Sci.* 2018;12(1):75-85.
- Kansal NJ, Chana I. An empirical evaluation of energy-aware load balancing technique for cloud data center. *Cluster Comput.* 2018;21(2):1311-1329.
- Gharaibeh A, Khreishah A, Mohammadi M, Al-Fuqaha A, Khalil I. Online auction of cloud resources in support of Internet of Things. *IEEE Internet Things J.* 2017;4(5):1583-1596.
- Tennakoon D, Chowdhury M, Luan TH. Cloud-based load balancing using double Q-learning for improved quality of service. *Wirel Netw.* 2018;177:1-8.
- Kanniga Devi R, Murugaboopathi G. An efficient clustering and load balancing of distributed cloud data centers using graph theory. *Int J Commun Syst.* 2019;32:1-17.
- Ebadifard F, Babamir SM. A PSO-based task scheduling algorithm improved using a load-balancing technique for the cloud computing environment. *Cloud Comput Big Data Technol Appl.* 2018;12:30.
- Arul Xavier VM, Annadurai S. Chaotic social spider algorithm for load balance aware task scheduling in cloud computing. *Cluster Comput.* 2018;22:1-11.
- Sharma SCM, Rath AK. Multi-rumen anti-grazing approach of load balancing in cloud network. *Int J Inform Technol.* 2017;9(2):129-138.
- Moussaddaq C, Ezzati A, Elharti R. A new reformulation of the load balancing problem in cloud computing based on TSP and ACO. *Proc Int Conf Big Data Cloud Appl.* 2017;54:1-4.
- Saleh H, Nashaat H, Saber W, Harb HM. IPSO task scheduling algorithm for large scale data in cloud computing environment. *IEEE Access.* 2019;7:5412-5420.
- Mishra SK, Puthal D, Sahoo B, et al. Energy-efficient VM-placement in cloud data center. *Sustain Comput Informat Syst.* 2018;20:48-55.
- Rahul Yadav, Weizhe Zhang, Omprakash Kaiwartya, PR Singh Elgendy, IA Tian, YC, "Adaptive energy-aware algorithms for minimizing energy consumption and SLA violation in cloud computing", *IEEE Access*, Vol 6, pp. 55923-55936, 2018.
- Lin W, Wang W, Wu W, Pang X, Liu B, Zhang Y. A heuristic task scheduling algorithm based on server power efficiency model in cloud environments. *Sustain Comput Informat Syst.* 2018;20:56-65.
- Zhao H, Wang J, Liu F, Wang Q, Zhang W, Zheng Q. Power-aware and performance-guaranteed virtual machine placement in the cloud. *IEEE Trans Parallel Distri Syst.* 2018;29(6):1385-1400.
- Liu XF, Zhan ZH, Deng JD, Li Y, Gu T, Zhang J. An energy efficient ant colony system for virtual machine placement in cloud computing. *IEEE Trans Evol Comput.* 2018;22(1):113-128.
- Malekloo M-H, Kara N, El Barachi M. An energy efficient and SLA complaint approach for resource allocation in cloud computing environments. *Sustain Comput Informat Syst.* 2018;17:9-24.

30. Elhoseny M, Abdelaziz A, Ahmed S, Salama AMR, Muhammad K, Sangaiah AK. A hybrid model of Internet of things and cloud computing to manage big data in health services applications. *Future Gener Comput Syst.* 2018;86:1383-1384.
31. Zhang X, Wu T, Chen M, et al. Energy-aware virtual machine allocation for cloud with resource reservation. *J Syst Softw.* 2019;147:147-161.

How to cite this article: Karthikeyan R, Balamurugan V. Energy-aware and SLA-guaranteed optimal virtual machine swap and migrate system in cloud-Internet of Things. *Concurrency Computat Pract Exper.* 2021;33:e6171. <https://doi.org/10.1002/cpe.6171>



Contents lists available at ScienceDirect

Materials Today: Proceedings

journal homepage: www.elsevier.com/locate/matpr

Enhanced security in IOT environment using Blockchain: A survey

S. Ramamoorthi^a, B. Muthu Kumar^{b,*}, M. Mohamed Sithik^a, T. Thinesh Kumar^a, J. Ragaventhiran^b, M. Islabudeen^b^a Department of Computer Science and Engineering, Mohamed Sathak Engineering College, Kilakarai, Tamilnadu, India^b Department of Computer Science and Engineering, Syed Ammal Engineering College, Ramanathapuram, Tamilnadu, India

ARTICLE INFO

Article history:

Received 20 February 2021

Accepted 12 March 2021

Available online xxx

Keywords:

Blockchain
Internet of Things (IoT)
Cryptography
Security
Communication
Industrial applications.

ABSTRACT

Blockchain (BC) methods is one of the best technologies in the Internet of Things (IoT) environments, it is a distributed sharing mechanism and communicate the IoT devices with secure manner. A blockchain is a connection of blocks and each block is linked to its earlier blocks. All block has the security hash code, previous block hash, and its data. The transaction between the BlockChain are the data is transfer between one IoT block nodes to another IoT Block node. The IoT device nodes are various types of physical devices like smart devices with embedded sensors, actuators, and capable of be in touch with other IoT device nodes. The responsibility of BlockChain in IoT is to grant a method to provide protected data transmission through IoT device nodes. In this paper discussed about the blockchain technology is how to secure the IoT transmission data and what are the challenges comes into these technologies. BlockChain is a safe method that can be used widely. IoT needs this type of skill to permit protected communication among IoT device nodes in mixed atmosphere.

© 2021 Elsevier Ltd. All rights reserved.

Selection and peer-review under responsibility of the scientific committee of the Emerging Trends in Materials Science, Technology and Engineering.

1. Introduction

The blockchain is a chain of consecutive blocks, which connecting an all list of transaction records like predictable user data. Figure 1 shows an example of a blockchain. Each block is point to previous block with hash code and point to next block with another hash code. The each block contain the timestamp, nonce and transaction history. The first block have no parent block that is called genesis block. We can create the block structure, digital signature mechanism and blockchain taxonomy. The blockchain is like a linked list in data structure architecture. The each and every node is connected by reference point value. The starting node containing the next block node reference point address, the second block node contain the previous node reference point address and next block node reference point address value. The last block node contains the previous block node address only. This is the structure of blockchain architecture which consists of a continuous sequence of blocks Fig. 1.1. [1]. Fig. 3.1. Fig. 3.2. Fig. 4.1.

The decentralization is main concept in blockchain technology. The computer or other organization network is not form a chain. As

an alternative, the circulated user data ledger via the nodes connected to the chain [2–5]. The block Nodes is one type of electronic device that stores user data in the secure manner.

1.1. Block

A block contains block header and the block body as shown in Fig. 1.2.

In exacting the block header contains:

Parent block hash: it denotes the previous block hash value (256-bit hash value).

- Merkle tree root hash: all transaction in the block hash value.
- Timestamp: it denotes the current transaction value.
- nBits
- Nonce: it normally starts with 0 and increases for every hash value calculation(16-bits field,)

2. Literature survey

The authors **Sujit Biswas, Kashif Sharif, Fan Li, Sabita Maharjan, Saraju P. Mohanty, and Yu Wang** represents that many of the business organization relies on IoT. These include educational

* Corresponding author.

E-mail address: muthu122@gmail.com (B. Muthu Kumar).

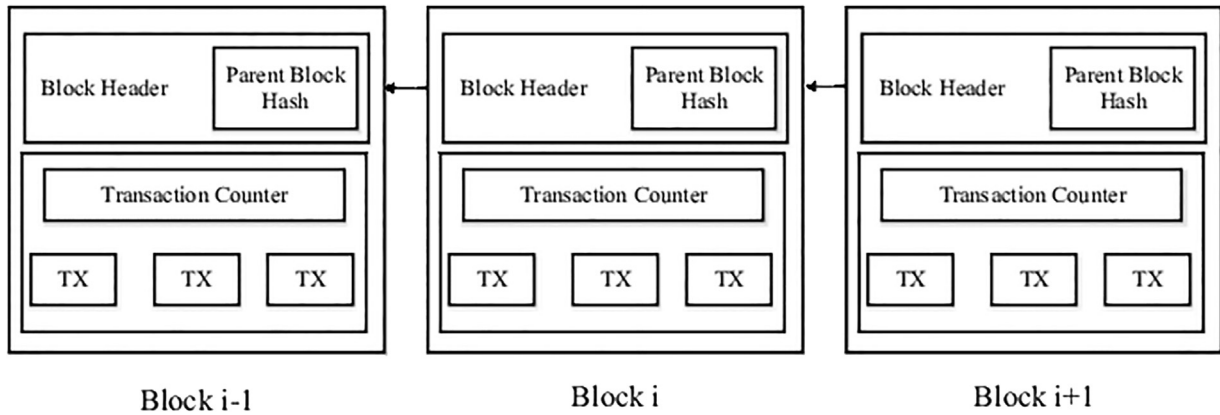


Fig. 1.1. An example of blockchain which consists of a continuous sequence of blocks.

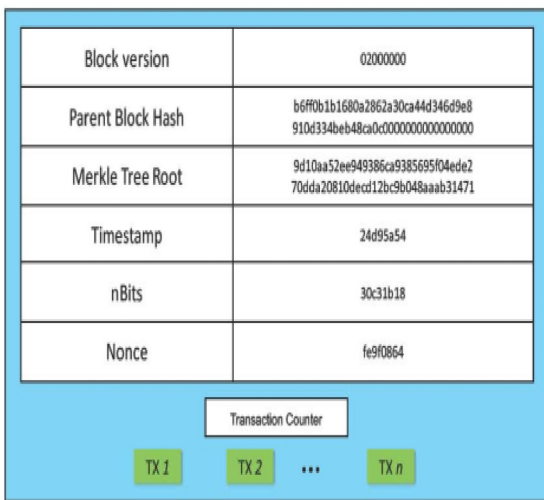


Fig. 1.2. Block structure.

organization, manufacturing organization, medicine and other organization. All the above mentioned organization uses dissimilar networks for complete their task [6–8]. This leads to many security challenges in the respective field. Already we have been using blockchain for providing security but this method is not sufficient due to dynamic challenges arises with respect to the security. So they are proposing PoBT algorithm for enhancing security as well as coping dynamic challenges in security. This method allows us to verify any blocks with in the short span. Also they were proposing ledger distribution mechanism for less memory utilization. End of their analysis process they have concluded that this mechanisms enhance the security level in IoT based application.

The author **Tanweer Alam** represents that IoT has been used for storing the node information including each and every transaction states. Blockchain is made by using normal chain mechanism where each part of the chain is associated with its previous and next part. In blockchain contains message digest function; previous part hash value and the information. IoT consist of dissimilar node includes sensors, actuators and any other physical devices and machines. Blockchain allows IoT to verify each and every process which is taking place within the environment. Author discusses about blockchain opportunities and challenges in IoT.

The authors **Hong-Ning Dai, Zibin Zheng and Yan Zhang** represents that IoT drives the industry towards smart devices based dissimilar network for their development process. Internal features

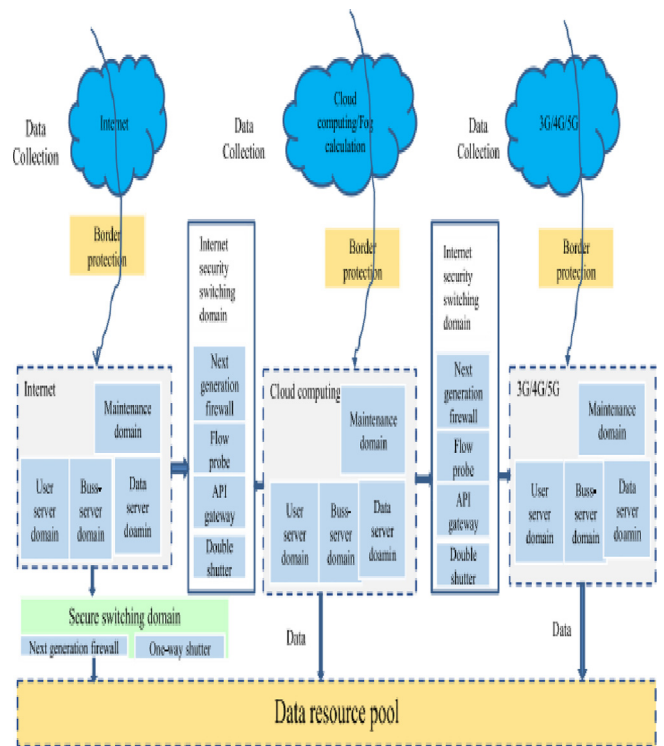


Fig. 3.1. Blockchain IoT information security structure.

of IoT leads to many difficulties like interoperability, security related issues and optimization issues. In this paper they analyze about the blockchain method integration with IoT. Blockchain with IoT is shortly denoted as BCOT by the authors. Also the list out the challenges of integrating BC with IoT. Finally they were proposing BCOT architecture for combining BC with IoT [9].

The authors **Riya, Raj Chintan and Nishant** represents that Blockchain and IoT are two distinguished technology ruling the digital world. IoT make each and every physical as smart enabled one. SO this actually helps us to have the link between any two things. And exchange of information between those linked things possible. But the problem is who is going to take care of connecting and disconnecting those things when required. If we don't have verifier security will become very complicated one to achieve. Blockchain provide security for any IoT things and its network by verifying. Author proposes BIoT architecture for all issues related to integrating IoT with BC [10].



Fig. 3.2. Security Framework for information Sharing in IoT.

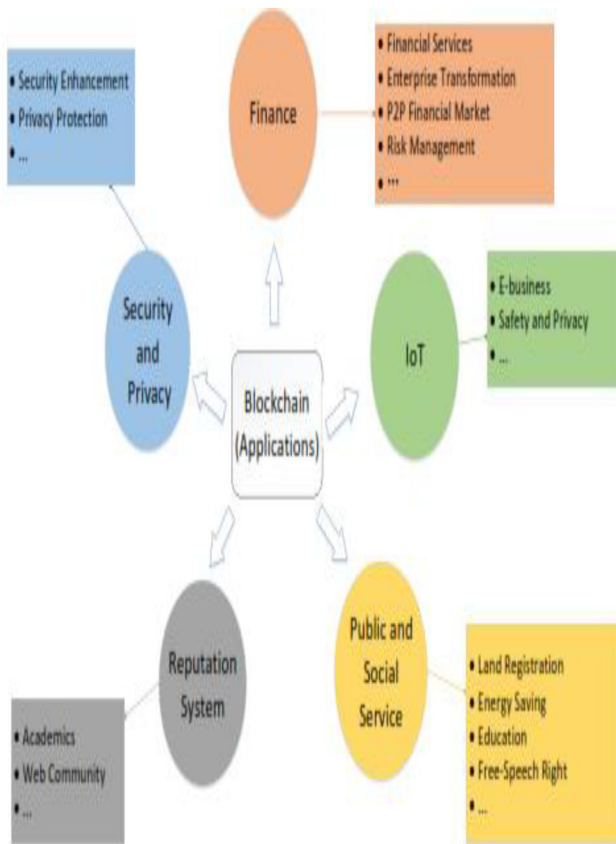


Fig. 4.1. Representative application domains of Blockchain.

The authors **Mohamed Amine Ferrag , Lei Shu, Abdelouahid Derhab and Leandros Maglaras** represents that challenges are more in IoT field with respect to provide security. Describe about

4 tier green IoT model for managing smart agri. They suggest method for classifying security related matters in smart agri based IoT. How IoT is adapted for agri has been discussed by the authors. They analyze how blockchain can be used for green IoT most effectively. Finally they concluded that challenges and research directions in green IoT field.

The authors **Haiping Si, Changxia Sun, Yanling Li, Hongbo Qiao and Lei Shi** represents that blockchain is the first distributed security related mechanism. It achieves reliability for peer to peer environment. In this paper they proposed a lightweight IoT security framework based on BC. Method includes both data blockchain and transaction blockchain. Distributing the information and integrity of the information is achieved by practical Byzantine fault-tolerant. Security mainly depends on partial blind signature algorithms. They proposed a dynamic game method for node cooperation. Hidden node state is predicted by institutional reputation value. Malicious node can be managed by high-trust reference report. They conclude that this framework is most effectively and feasibly work against intruder activities.

3. IoT information sharing based on blockchain

The successful secure sharing method in the IoT is very difficult. There are many issues and a problem comes in the connectivity of data. The security difficulty comes in IoT information sharing has become important point and a complicated point in the information security. The information sharing is the user device data will be viewed by another secure IoT device. The method of information sharing is more important in the cryptographic algorithms [11–13]. The data may be off line or cloud based data in the Internet of Things. These technologies have many shortcut and methods: Facing a massive IoT information network Fig 3.1

Simplified Payment Verification (SPV) is one of the payment methods in digital transactions. In blockchain mechanism, it can be achieved by The Merkle tree algorithms.

3.1. Double-chain mode based on blockchain technology

The blockchain method was collects all data from IoT node and form the data book for private agreement mechanism. The IoT source data is reliable and the data is stored by centralized network systems. In IoT sensors devices, infrared sensor and other IoT devices are used to storage, transmission and computing the frequency of sensors. The blockchain methodology having capabilities of reduce the redundancy and improve the efficiency of the IoT devices. The IoT data is necessary to categorize, combine data expression and allocate storage operations.

3.2. Time stamp method for blockchain structure

Data blocks and chain structure used to store data in blockchain. Every block contains block header and block body. In each block is assigned by unique address value and pointer reference value. The current block is stored the previous block address and next block address. Each block is denoted by timestamp. The timestamp contains the address value of block node and time of executions in the transactions [14].

3.3. IoT information security by blockchain

The combinations of information and IoT devices are main characteristic of blockchain IoT. The important basic operation contains real-time monitoring The real time program of blockchain IoT is that enables the energy information system to be altered by particular network [15]. The standard protocol of blockchain is provide

the technical support of smart electronic IoT device sensor and information system. It solves the network security problems.

4. Applications of blockchain

Applications of blockchain technology classified into various aspects like finance, IoT, public and social services, reputation system, security and privacy. **Figure No: 4.1**

4.1. Finance

In established financial and business activities, Bitcoin and hyperledger has bring massive role. In banking sector blockchain is the prospective to affect the world. Blockchain knowledge is very much useful in financial activities and IT industries. Blockchain is used in Microsoft Azure and IBM service sector..

4.2. Internet of things (IoT)

IoT is the most potential area of ICT and its planned to combine the effects into the various services like Atzori, Miorandietal, logistic management with RFID, smart systems, online health services,

4.3. Public and social services

Different public and social aspects like Land registration, Energy saving, Education, Free-speech right are developed by Blockchain. It also involved in municipal services such as marriage registration, patent management and Income Tax systems.

4.4. Reputation system

In community confident, Reputation is the essential computation. The reputation of a human being computed on before business communications with the society. Reputation involved major role in academics and web community.

5. Conclusion

The block chains extremely appraised and authorized for its decentralized structure and peer-to-peer nature. In more developer and researchers find out the blockchain are secured by Bitcoin. But blockchain is used to a different fields far beyond Bitcoin. Blockchain has different personality like decentralisation, persistency, ambiguity and audit ability. In this paper, we present a broad survey on the blockchain. We describe an overview of blockchain technology like blockchain architecture and main blockchain characteristics. We discuss various blockchain algorithms. We list the different characters and various applications are used in blockchain IoT security. We explain the problems and

problems of blockchain implementation. In future we will develop a smart blockchain for enhanced security in the block node of IoT devices.

CRedit authorship contribution statement

S. Ramamoorthi: Conceptualization, Methodology, Writing - original draft. **B. Muthu Kumar:** Visualization, Writing - review & editing. **M. Mohamed Sithik:** Software. **T. Thinesh Kumar:** Investigation. **J. Ragaventhiran:** Supervision. **M. Islabudeen:** Validation.

Declaration of Competing Interest

The authors declare that they have no known competing financial interests or personal relationships that could have appeared to influence the work reported in this paper.

References

- [1] H. Si, C. Sun, Y. Li, H. Qiao, L. Shi, *Future Generation Computer Systems* 101 (2019) 1028–1040.
- [2] Sujit Biswas, Kashif Sharif, Fan Li, Sabita Maharjan, Saraju P. Mohanty, and Yu Wang "PoBT: A Light Weight Consensus Algorithm for Scalable IoT Business Blockchain" *IEEE Internet of Things Journal* 2019
- [3] D. Li, Z. Cai, L. Deng, X. Yao, H.H. Wang, *Information security model of block chain based on intrusion sensing in the IoT environment*, *Cluster Comput.* 22 (S1) (2019) 451–468.
- [4] P.K. Sharma, S. Singh, Y.S. Jeong, *DistBlockNet: A distributed blockchains-based secure SDN architecture for IoT networks*, *IEEE Commun. Mag.* 55 (9) (2017) 78–85.
- [5] A. Ouaddah, A. Abou Elkalam, A. Ait Ouahman, *FairAccess: a new Blockchain-based access control framework for the IoT*, *Secur. Commun. Netw.* 9 (18) (2016) 5943–5964.
- [6] W. He, *Computational neuroscience applied in surface roughness fiber optic sensor*, *Trans. Neurosci.* 10 (1) (2019) 70–75, <http://dx.doi.org/10.1515/tnsci-2019-0012>.
- [7] M.H. Miraz, M. Ali, *Blockchain enabled enhanced iot ecosystem security*, *Soc. Sci. Electron. Publ.* 9 (3) (2018) 38–46.
- [8] P.K. Sharma, M.-Y. Chen, J.H. Park, *A software defined fog node based distributed blockchain cloud architecture for IoT*, *IEEE Access* 6 (2018) 115–124.
- [9] P. Alfonso, T. Nachiket, M. Giovanni, L. Francesco, P. Antonio, *Blockchain and iot integration: a systematic survey*, *Sensors* 18 (8) (2018) 2575.
- [10] Z. Yu, J. Wen, *The IoT electric business model: Using blockchain technology for the IoT*, *Peer-to-Peer Netw. Appl.* 10 (4) (2017) 983–994.
- [11] O. Novo, *Blockchain meets IoT: An architecture for scalable access management in IoT*, *IEEE IoT J.* 5 (2) (2018) 1184–1195.
- [12] K.R. Ozyilmaz, A. Yurdakul, *Designing a blockchain-based IoT with ethereum, swarm, and LoRa: The software solution to create high availability with minimal security risks*, *IEEE Consum. Electron. Mag.* 8 (2) (2019) 28–34.
- [13] M.-C. Chen, S.-q. Lu, Q.-L. Liu, *Global regularity for a 2D model of electrokinetic fluid in a bounded domain*, *Acta Math. Appl. Sin. Engl. Ser.* 34 (2) (2018) 398–403.
- [14] A. Reyna, C. Martín, J. Chen, E. Soler, M. Díaz, *On blockchain and its integration with IoT, challenges and opportunities*, *Future Gener. Comput. Syst.* 88 (2018) 173–190.
- [15] M.A. Ferrag, M. Dardour, M. Mukherjee, *Blockchain technologies for the IoT: Research issues and challenges*, *IEEE IoT J.* 6 (2) (2018) 2188–2204. [14] G. Feng, L. Zhu, S. Meng, *A blockchain-based privacy-preserving payment mechanism for vehicle-to-grid networks*, *IEEE Netw.* 32 (6) (2018) 184–192..



Contents lists available at ScienceDirect

Materials Today: Proceedings

journal homepage: www.elsevier.com/locate/matpr

Effective adaptive routing for Lossy networks using enhanced RPL in the heterogeneous network

M Mohamed Sithik^a, B Muthu Kumar^{b,*}, S. Ramamoorthi^a, R. Karthikeyan^a, J. Ragaventhiran^b, M. Islabudeen^b

^aDepartment of Computer Science and Engineering, Mohamed Sathak Engineering College, Kilakarai, Tamilnadu, India

^bDepartment of Computer Science and Engineering, Syed Ammal Engineering College, Ramanathapuram, Tamilnadu, India *Corresponding author at: Syed Ammal Engineering College.

ARTICLE INFO

Article history:

Received 11 February 2021

Accepted 12 March 2021

Available online xxxx

Keywords:

Objective function

Internet of Things

RPL

Routing and LLN



ABSTRACT

In this network environment, the different applications of sensor have to generate a huge data traffic which includes basic sensing methods such as air pollution or environment checking. In this huge congested network, the two-standard objective methods, that are objective method 0 (OM0) and objective method 1 OM1 for Congested Networks that has to perform deprived routing paths by picking an already congested parental node and a greater number of retransmissions happened between the networks. So, it is required that to design a new effective Routing Protocol for various congested environments. In our paper, I observe the RPL protocol for various congested networks and developed a new routing protocol technique (QWL-RPL) related with information of queue and node-wise workload. Objective of our developed Routing protocol has to attain an Optimum shortest path in challengeable performance. Our proposed Objective method has to consider connectivity capacity and also representing status of congestion in particular node or device using information of queue in data or packet. Our proposed routing technique was implemented in Cooja environment for comparing with the existing techniques. The results of simulation are shown through Queue status information and balanced Workload routing protocol of RPL that can reduce the data traffic of a various networks as related with OM0 and OM1, exactly specified terms of average delay, ratio of packets transmission and reception, jitter delay and header overhead information. At last, the results shown as on average, 30%–50% reduced header overhead information, 15%–30% reduced in average throughput delay, 10%–30% improvement in PRR and 25%–40% reduced in jitter delay.

© 2021 Elsevier Ltd. All rights reserved.

Selection and peer-review under responsibility of the scientific committee of the Emerging Trends in Materials Science, Technology and Engineering.



1. Introduction

1.1. Traffic issues on IoT networks

The Internet of Things is the more collection of networks involved with the sensor devices that can sense many physical environments and transfer the information that was sensed. Each and every sensor device senses neighborhood and conveys their identified information to the particular destination node through its neighboring devices using multiple node communication. The example of the IoT system that includes industrial and building automation, smart cities, smart grid, disaster management and smart healthcare.

Many IoT sensor devices are in open environment and it is possible to defect this by various natural factors. Therefore, it is quit complex job for designing enhanced routing protocol technique because of the shortage of memory, very restricted resources in these devices, restricted processing power and restricted energy. We consider there are two communicating nodes, an accurate objective of routing protocol is to increase communication activities among all the nodes and also maintain low level energy consumption. Though, achieving this objective it requires proper attention of the fluctuating traffic patterns, Lossy congestion type of the network, routing loops, convergence time and varying link qualities.

A sensor determines its successive path, that constructs the topology through which identified information can be sent. An Internet of Things needs an effective and interactive technique to

E-mail address: muthu122@gmail.com (B Muthu Kumar)

<https://doi.org/10.1016/j.matpr.2021.03.350>

2214-7853/© 2021 Elsevier Ltd. All rights reserved.

Selection and peer-review under responsibility of the scientific committee of the Emerging Trends in Materials Science, Technology and Engineering.

control the congestion among interconnected routing paths. There are many effective routing techniques for controlling the congestion and load balancing.

1.2. Routing protocols for congested networks

Many routing protocol techniques are developed for these congested Network devices. Best routing protocol among them has to offer IPv6 address to the Lossy and congested devices called as the enhanced routing protocol techniques (RPL) for congested Networks, as developed by IETF working members. An enhanced RPL protocol is developed on IPv6 Congested wireless personal area network (6LoCWpan) then it is linked to IPV6 network via the neighborhood devices (Fig. 1). We developed an enhanced routing protocol for multiple networking areas for instance architecture and building, safe home system, urban routing, networking in industrial side, and machine learning. We developed an enhanced RPL used as economically in smart grids (CG-Mesh) and Cisco for the Neighborhood area network (NAN) to enhance the advanced meter infrastructure (AMI).

1.3. An enhanced routing protocol (RPL)

An enhanced routing (RPL) protocol is an effective distance vector routing protocol that has to create a tree-like structured routing path called as (DODAG) destination oriented directed acyclic graph, created the path towards a greater number of neighborhood devices from source to destination. We create a general objective method (OM) using (DAGs) directed acyclic graphs. OM defines a function to determine the optimum path from available paths for every node in congested network. There are two Initial Objective Methods (OMO) and (MRHOM) reduced rank with hysteresis objective method defined IETF's working members Fig. 1

Initially we use OMO that is to determine best route from source to all destination devices by choosing low-cost neighborhood device to reach on successive devices. MRHOM determines accurate shortest paths through all sensor devices with lowest cost

value. If the cost of the corresponding path is lesser than the cost of currently occurred path then it has to select newly generated shortest path. This is called as 'hysteresis.' MRHOM effectively takes Predictable Transmission Count (PTC) then it has to determine quality of link. Then, PTC predicts occurrence of node level congestion. An efficient enhanced load balancing solution has not considered quality of link and least hop count in a heterogeneous congestion environment for finding an optimum routing path. The neighborhood nodes of the sink node are affected from loss of packets because of high delay in congested networking. Then selected parent node of enhanced routing protocol is having many numbers of child nodes; therefore, the highly burdened ideal parent node becomes failure because its energy drained quickly rather than any other nodes. Inaccurate OMs have built an irregular routing structure that is experiencing extremely imbalanced energy distribution.

Lot of applications for resolving congested network that include starting from measuring the temperature to multimedia application services these require effective and good network communication without any congestion. The worst congestion in networking that mostly affect many LLN heterogeneous networks and it causes loss of packets and it could not use full network bandwidth. Unbalanced load, limited resources and high relay burden gradually went to device failure. PTC-related device distributes control packets at proper time intervals for evaluating quality of link.

Receiving device again redistributes same control packet then it is one of the reasons to increase congestion in networks. If any device failure found in the network, RPL proposes 2 types of resolutions: global resolution and local resolution. In local resolution, child device has to transfer many packets via its the neighborhood device to reach its destination. Sink node or gateway introduced global resolution. From two above types, the overall network experiences additional control overhead the it causes huge delay, due to this finally it reduces performance of whole networks. If the number of failed devices increased accordingly, there is possible to occur many numbers of separated networks in this way it is not possible to communicate with sink device through any of the possible paths and it affects overall result as failure network.

1.4. Balancing the load in various heterogeneous networks

The general meaning of heterogeneity is an absence of uniformity or homogeneity. Any of the devices in network are to increase congestion while other nodes have generated congestion with less transfer rate in heterogeneous network load. In normal case, the sensor devices have transferred data in the direction of root device based on tree topology. Flow of data is regular with constant time. In this scenario, we expect traffic method and not possible to expect its load imbalance. Data transmission capacity and also time interval in data transmission have been differed in each and every node of heterogeneous scenario; thus, the traffic oscillates randomly causing problem of load imbalance.

There is no any load imbalance in heterogeneous network due to its subtree's size represented in Fig. 2, in which a node number 5 has possible choices to pick the node (device) number 3 or node number (device) 2 to consider as parent node (device). If a node (device) number 3 contains any of child node (device), then node (device) number 5 is expected to choose node (device) number 3 as parent node (device). In this case, it is possible to happen again and again in heterogeneous networks scenario. From this figure, overall traffic workload of node number 3 is larger than traffic load of node number 2 because of huge packet transmission rate at node number 6, that means it took 60 number of packets per minutes. Thus, if we are having some additional nodes (devices) in subtree of the routing should not imply that huge network data streams in a different traffic network. From this diagram we learnt

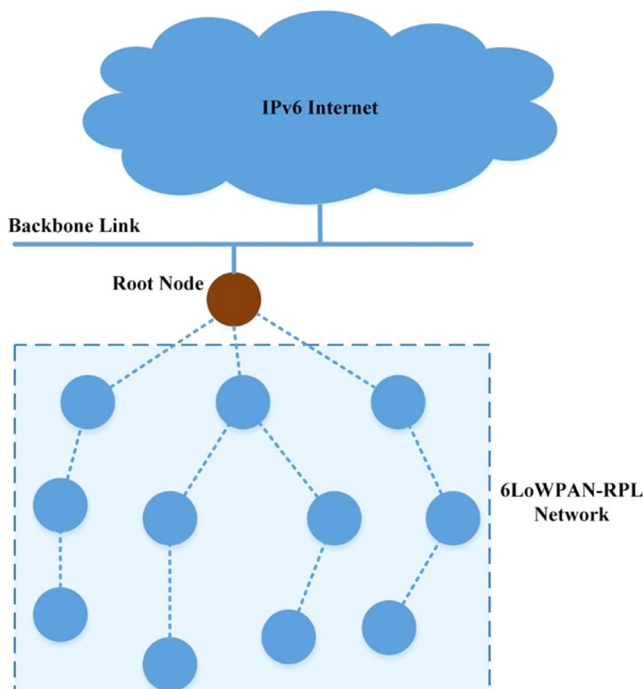


Fig. 1. The 6LoCWpan Enhanced Routing protocol for IoT based Network.

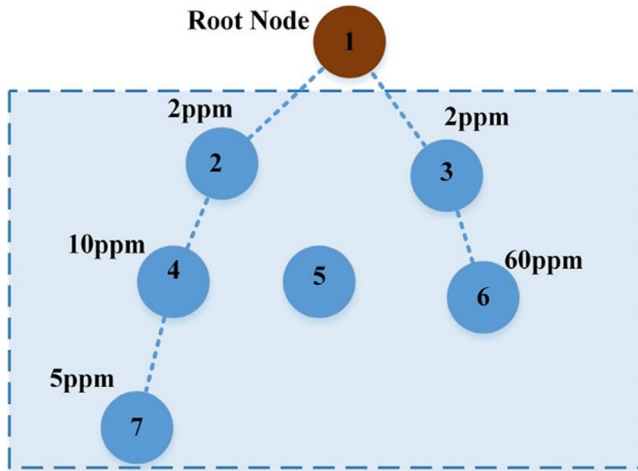


Fig. 2. Representing problem of load traffic imbalance in heterogeneous network environment.

that large sized subtree with a parent node (device) that has to imply maximum losses in queue. Anyway, in heterogeneous networks, we can't say that large sized subtree with parent node (device) will have always maximum losses in queue. In this heterogeneous network, queue losses and imbalanced loads could be the primary concern because of the unbalanced network traffic is comparing with size of imbalanced subtree. PTC could not generate Packet losses in node (device) level but it affects link level. In this, hop (node) count is total number of devices or nodes regardless of any losses in queue and network traffic load. We cannot consider queue size as important decision metric to imitate the traffic loads. We consider workload of every node (device) is a significant (parameter) term in heterogeneous network traffic. In this same way, we must consider average node to node delay or latency and the total amount of huge workload as a significant performance parameter in the design of protocol. Thus, it is compulsory to design new routing protocol technique that can solve problem of load traffic imbalance in a heterogeneous network environment.

There are many numbers of routing techniques available for homogeneous traffic loads. But in nature of IoT, there are many numbers of heterogeneous networks involved in traffic then it may cause congestion due to imbalance load in heterogeneous network. We propose a new routing technique (QWL-RPL) which can resolve majority issues happened in choosing optimum path among the heterogeneous network nodes. This technique is going to be discussed in next successive sections.

2. Related work

The RPL is implemented for Lossy and congested networks as an active routing protocol technique that works on the (MAC) medium access control and (PHY) physical 802.15.4 layers (Fig. 3). We know that sensor nodes are smaller in size and typically contain a restricted battery energy source, the network protocol sensor nodes or RDC (radio duty cycling) protocol such as Contiki MAC, NullRDC, and X-MAC.

NullRDC does not utilize transmission or reception of the data continuously to or from physical layer respectively and its framer methods. Contiki MAC utilizes continuously wakeups that is ready to listen for packet transmissions or reception to or from its neighborhood though X-MAC protocol does not switch off this whole network after some packet reception or transmission. The Cooja simulator of Contiki OS implements all RDC protocol. This RDC protocol has to gradually maximize its efficient and dominant

Application	Websocket, HTTP, COAP
Transport	UDP, TCP
Network	RPL
Adaptation	6LoWPAN
MAC	CSMA
Radio Duty Cycling	NullRDC, ContikiMAC, X-MAC
Physical	IEEE 802.15.4

Fig. 3. Network stack of Sensor node or device (Contiki OS).

energy level after sleeping the network if sensing behavior is not found. Routing Protocol RPL utilizes particular OM that has to define particular technique for calculating the rank (weight value) to create best routing path. And also, it creates tree-like structured routing technique called as DO-DAG. Main purposes of RPL routing protocol have to make a perfect DO-DAG graph and agree with its current topology with respect to heterogeneous networks. For managing different routing issues, the routing techniques must consider lot of conditions, then it needs to reduce the Lossy and congestion in heterogeneous network. This Routing protocol RPL has not implied any of particular OM and routing techniques utilized in congested environment. Relatively, this offers major provision of flexible OM for network design and applications.

We implement Routing protocol RPL in various circumstances for different platforms; There are many protocols implemented to explain about the Routing protocol RPL. There are lot of RPL variations available based on its performance and reliability. Conventionally, VTC of MRHOM and node count of OM0 that has to provide for RPL Routing protocol implementation. OM0 has not utilized any other particular routing technique for calculating the rank (weight value) rather than node count. MRHOM has to access quality of the link among the network nodes and it has to choose ideal parent device. The above technique is to be greater eminent and efficient that is followed by many numbers of Routing protocols.

3. Analysis and implementation of routing protocol QWL-RPL

This section described about modern routing protocol called as QWL-RPL. This protocol can solve the problems of load traffic imbalance in various heterogeneous networks environment. For example, if we are taking a new network with having 2 types of network traffic and load heterogeneities. In first case it has to contain any type of traffic in any network in which nodes (sensor devices) can send data with a constant traffic rate; In another case the network can send the data with arbitrary traffic rate that can be varied based on time.

3.1. System modelling

We consider a Lossy and congested network in IoT scenario that is forming an enhanced RPL protocol as routing technique Table 1.

The network contains a multi hop heterogeneous network for traffic flow from root device (node) to child device (node), that has to form new DO-DAG acyclic graph. This network contains N number of devices (nodes) in this we have to rank all the devices

Table 1
Parameters Contiki RPL objective method and their associated files.

Contiki OS file	OMO Parameters	MRHOM Parameters
rpl-conf.h	RPL_OM_OCP RPL_OCP_OMO RPL_SUPPORTED_OMS {&rpl_om0}	RPL_OM_OCP RPL_OCP_MRHOM RPL_SUPPORTED_OMS {&rpl_mrhom} RPL_WITH_MC 1 RPL_DAG_MC_ETX (for ETX metric) RPL_DAG_MC_ENERGY (energy container) RPL_OCP_MRHOM 1
Contiki_rpl.h	RPL_OCP_OMO 1	

(nodes) from the root device (node) in increasing order. This model includes the radio transceiver that is Texas Instruments CC2420. According to these ranks, the available devices or nodes are separated into classification of child devices or nodes and parent devices or nodes that is representing through formula $N=C \cup P$, in which C denotes child devices or nodes ($c_1, c_2, c_3, \dots, c_n$) and P denotes parent devices or nodes ($p_1, p_2, p_3, \dots, p_n$). A rank is given to the candidate parent device (node) only if this was a root device or node. Then sink device or node links the all-other devices (nodes) in Lossy and congested network to the network IPv6 in connection with a WAN.

Every node transmits their actual packets or data in a finite and fixed time slots that are ($t = 2, 4, 6, \dots$). There is maximum eight retransmission only allowed for each link. Here -45 dBm is the maximum threshold limit for (CC2420_CONF_CCA_THRESH) (CCA) clear channel assessment.

3.2. Implementation of Contiki RPL and analysis with OMO and MRHOM

In this subsection we describe OMO and MRHOM objective methods that are implemented using simulation. Actually, the congested network is working with actual objective methods OMO and MRHOM. These methods are used to select a best routing path among available paths. We select either OMO or MRHOM in Contiki RPL implementation that needs to set the different parameters for this. The needed setting parameters with their information are represented in following Table 1.

Cooja utilizes only 256 units as minimum hop ranking and 255 units as maximum hop ranking for its rank system of OMO, and also Cooja utilizes a minimum unit of 128 (min_hopranking) for its rank system of MRHOF. PTC technique (parent_transmission_link_technique(p)) begins with 256 units and 128 bits LINK_STATS_PTC_DIVISOR (fixed point divisor). Then PTC can decrease or increase their value based on retransmission attempts on Physical layer. PTC is the known transmissions count and it needs retransmission technique for delivering packet or data successfully. PTC mainly imitates loss of packets when we considered channel bandwidth quality and collision of packets. In other words, less PTC means that particular device or node has attempted to transmit packet or data successfully in very fewer attempt then it consumes lesser amount of energy only. The PTC technique has not imitated bandwidth delay; If the data or packet is sent successful manner then any bandwidth delay in particular transmission has not affected any of the network.

3.3. Analysis and implementation of QWL-RPL algorithm

Enhanced algorithm of routing protocol QWL-RPL resolves problem of load traffic imbalance in various heterogeneous network environment. After observed from previous subsection, the OMO and PTC based MRHOM are not appropriate choice for resolving problem of load traffic imbalance that is affected by network

Algorithm 1: Workload measurement.

```

1.  Initialize:
2.  packet transmission (numtx)
3.  get last transmission clock time
4.  Set event timer of 10 clock seconds
5.  Workload  $\leftarrow$  workload + numtx
6.  if(event timer expired), then
7.    workload  $\leftarrow$  0
8.    reset event timer
9.  end
10. Move to step 5

```

Fig. 4. Workload measurement Algorithm.

heterogeneity. Therefore, utilizing routing topology's subtree for maintaining the load and traffic balancing, it is not applicable for various network load traffic conditions. In this case, we have to use continuous traffic workload and overhead information of every device or node. At a time, node's or device's queue can store maximum of four packets because of very lesser size of memory in the network queue. This Packet or data is significantly very lesser rather than its workload and overhead information of every devices. Workload and overhead information of every device or node contains control information and actual traffic load because of its subtree (all child nodes). In every 10-s we describe the number of traffic flow of every node and workload information. In this concept, the workload of node is found from total number of packets have transmitted in every 10-s transmission duration, it also includes the information of which packet it is received from its subtree and determine that how many packets that are generated from the parent node. The following algorithm 1 defines the workload calculation. The queue information with weight value is used with their overhead and workload information.

$$\text{Rank} = \text{Rank}(p) + \text{WLMACtx} + \alpha \text{QbufLen} \quad (1)$$

In which Rank(p) is rank of parent device or node, WLMACtx is total number of sent or transmitted packets or data at the physical layer during the final time period and Qbuf_len represented as list of data or packets in the waiting buffer queue. Then as described previously, the PTC node distributes control packets to all nodes or devices at fixed and regular time interval that has to validate quality of connectivity or link, and receiving device or node redistributes the same control or probe packet to all devices or nodes, due to this it increases the congestion in network and also increases the delay Fig. 4.

4. Simulated results and their analysis

In this section, we deliver simulated results and overall analysis of these results. Here we have used the AI software Python 3.7 version for analyzing the original data that can be attained from the simulator of Cooja. We have already studied about the behavior of routing protocols by using two different types of heterogeneous network load traffic cases then assessed the above routing protocols by updating sensor devices or nodes at regular time interval. If we increase a greater number of sensor devices or nodes then more traffic flow has happened finally that causes the congestion. It can be arranged networks maximum size of 100 nodes to study about eminent and efficient routing protocols under congested devices or nodes in huge traffic congested network.

PRR produces number of data or packets in percentage that packets are received at the destination node related with list of

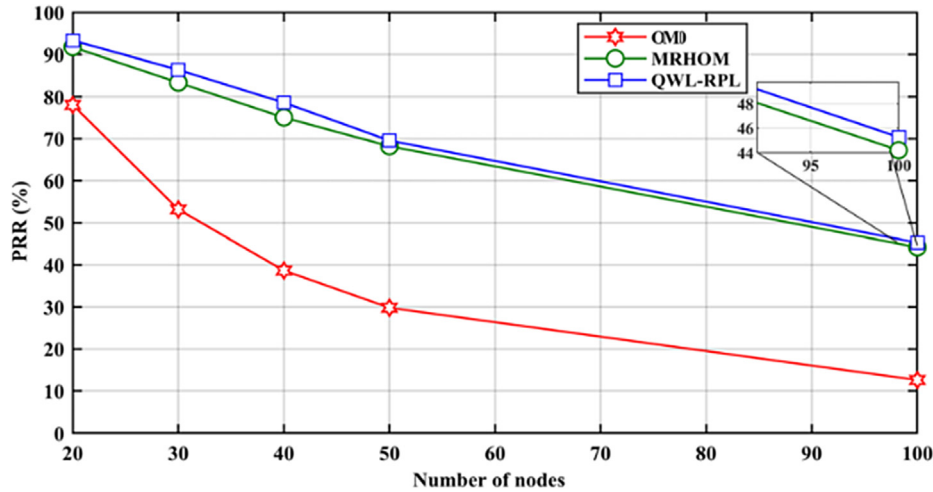


Fig. 5. OMO, MRHOM, and QWL-RPL in PRR.

data or packets transmitted from all devices or nodes to destination device or node. Finally, PRR has calculated from following formula that is $PRR = (\text{number of received data or packets} / \text{number of transmitted data or packets}) \times 100$. PRR can become best choice that can be addressed the heterogeneous unbalance load environment. Fig. 5 represents OMO, MRHOM, and QWL-RPL in PRR.

The RPL routing protocol has been analyzed in various congested network traffic data flow. In this same way, (PLR) packets or data loss ratio represented in Fig. 6. We calculate PLR from above predefined formula of Packets or data Loss Ratio = $(100 - PRR) / 100\%$. In other way, PRR represents analysis and efficiency of routing protocol that is represented by percentage of packets successfully transmitted to the destination node or device. MRHOM and QWL developed more consistent networks as compared with OMO.

5. Conclusion

Routing protocol RPL is developed to enhance all characteristics of Lossy and congested network. Lot of applications for resolving congested network that include starting from measuring the temperature to multimedia application services these require effective and good network communication without any congestion. This is mandatory to learn the enhanced routing protocol RPL technique

under different traffic load applications and it has to develop more enhanced features of routing protocol for the congested network. In our paper, we resolved problem of load traffic imbalance in the congested network traffic environment. Here we projected new innovative method for routing protocol technique and it resolves occurrence of congestion due to load traffic imbalanced network. The proposed QWL-RPL aims to resolve load imbalance heterogeneous network and also minimize the huge overhead information (control information), then raising PRR, minimizing node-to-node packets or data transmission delay, and minimizing jitter.

The enhanced RPL protocol procedure comprises an interchange of valuable control or probe packets or data. In this we can use Algorithm of Deep learning to deliver the efficient and enhanced routing protocol with balanced routing technique. Thus, in future we will focus on constraint-based routing, avoiding packets loss in communication of sensor devices using deep learning techniques.

CRedit authorship contribution statement

M. Mohamed Sithik: Conceptualization, Methodology, Writing - original draft. **B. Muthu Kumar:** Visualization, Writing - review &

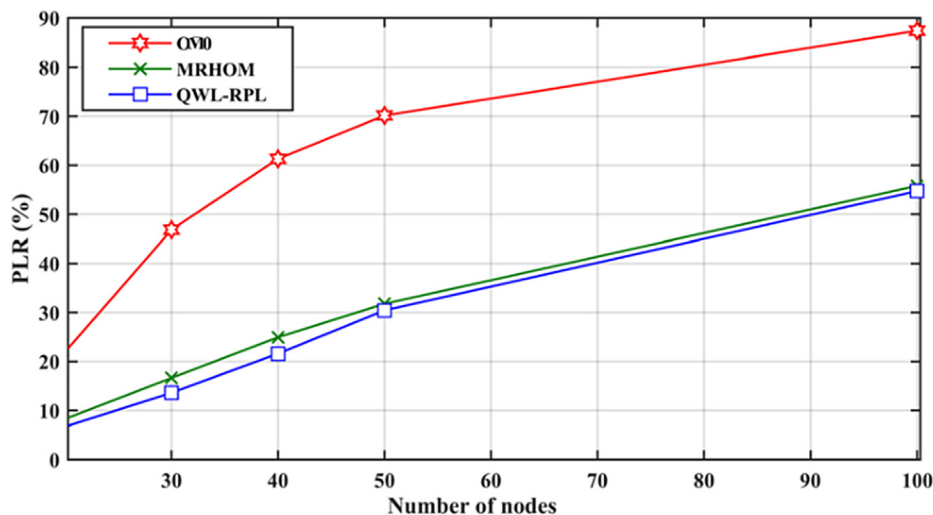


Fig. 6. (PLR) the packets loss ratio.

editing. **S. Ramamoorthi**: Software. **R. Karthikeyan**: Investigation. **J. Ragaventhiran**: Supervision. **M. Islabudeen**: Validation.

Declaration of Competing Interest

The authors declare that they have no known competing financial interests or personal relationships that could have appeared to influence the work reported in this paper.

Further Reading

[1] F. Al-Turjman, A. Malekoo, Smart parking in IoT-enabled cities: a survey, Elsevier Sustain. Cities Soc. 49 (2019) 101608.

- [2] M.Z. Hasan, F. Al-Turjman, SWARM-based data delivery in social Internet of Things, Elsevier Fut. Gener. Computer Syst. 92 (1) (2019) 821–836.
- [3] Tmote Sky Datasheet, Available: <http://www.crew-project.eu/sites/default/files/tmote-sky-datasheet.pdf>, (accessed on 20/11/2019).
- [4] M.A. Naeem, R. Ali, B.-S. Kim, S.A. Nor, S. Hassan, A periodic caching strategy solution for the smart city in information-centric Internet of Things, Sustainability 10 (7) (2018) 2576.
- [5] P. Sanmartin, A. Rojas, L. Fernandez, K. Avila, D. Jabba, S. Valle, Sigma routing metric for RPL protocol, Sensors 18 (4) (2018) 1277.
- [6] S. Taghizadeh, H. Bobarshad, CLRPL: context-aware and load balancing RPL for IoT networks under heavy and highly dynamic load, IEEE Access 6 (2018) 23277–23291.
- [7] A. Musaddiq, Y.B. Zikria, O. Hahm, H. Yu, A.K. Bashir, S.W. Kim, A survey on resource management in IoT operating systems, IEEE Access 6 (2018) 8459–8482.

IETE Journal of Research >

Latest Articles

65 0 0

Views CrossRef citations to date Altmetric

Research Article

SEEDDUP: A Three-Tier SECure Data DedUPlication Architecture-Based Storage and Retrieval for Cross-Domains Over Cloud

B. Rasina Begum & P. Chitra

Published online: 24 Feb 2021

 Download citation  <https://doi.org/10.1080/03772063.2021.1886882>
 Check for updates



Sample our
Engineering & Technology
Journals

>> Sign in here to start your access
to the latest two volumes for 14 days


 Full Article  Figures & data  References  Citations  Metrics

 Reprints & Permissions  Get access 

Abstract

Data deduplication has become a promising technique that significantly reduces space utilization of cloud storage servers and optimizes the network bandwidth. A variety of deduplication techniques have been proposed to enhance the cloud server's storage efficiency. Most of the deduplication schemes do not address global indexing and user

privacy issues. This paper elucidates a novel three-tier secure data deduplication architecture (referred to as SEEDDUP) for data storage and retrieval in the cloud.

<https://www.tandfonline.com/doi/abs/10.1080/03772063.2021.1886882>

1/6



SEEDDUP: A Three-Tier SEcurE Data DedUPlication Architecture-Based Storage and Retrieval for Cross-Domains Over Cloud

B. Rasina Begum & P. Chitra

To cite this article: B. Rasina Begum & P. Chitra (2021): SEEDDUP: A Three-Tier SEcurE Data DedUPlication Architecture-Based Storage and Retrieval for Cross-Domains Over Cloud, IETE Journal of Research, DOI: [10.1080/03772063.2021.1886882](https://doi.org/10.1080/03772063.2021.1886882)

To link to this article: <https://doi.org/10.1080/03772063.2021.1886882>



Published online: 24 Feb 2021.



Submit your article to this journal [↗](#)



Article views: 20



View related articles [↗](#)



View Crossmark data [↗](#)



SEEDDUP: A Three-Tier SEcurE Data DedUPLICATION Architecture-Based Storage and Retrieval for Cross-Domains Over Cloud

B. Rasina Begum¹ and P. Chitra²

¹Department of Computer Science and Engineering, Mohammed Sathak Engineering College, Kilakarai, Ramanathapuram District, India;

²Department of Computer Science and Engineering, Thiagarajar College of Engineering, Madurai, India

ABSTRACT

Data deduplication has become a promising technique that significantly reduces space utilization of cloud storage servers and optimizes the network bandwidth. A variety of deduplication techniques have been proposed to enhance the cloud server's storage efficiency. Most of the deduplication schemes do not address global indexing and user privacy issues. This paper elucidates a novel three-tier secure data deduplication architecture (referred to as SEEDDUP) for data storage and retrieval in the cloud. SEEDDUP provides data deduplication with proper indexing and user privacy. In this work, the optimal chunk size, for a given file size and format, is calculated using Cuckoo Search Algorithm. The chunk existence in the cloud is verified by the hash value generated via SHA3-512. To improve data deduplication speed, Merkle Hash Tree based MapReduce (MHTMR) is used for fast index lookup, which improves the performance at data storage and retrieval. In addition, data are encrypted based on its sensitivity level (low and high) using Niederreiter Public Key Cryptosystem. With this new SEEDDUP architecture, only legitimate users can request data successfully for limited times (k) and spurious data requests cannot be processed or handled in the cloud. Experiment results show that the proposed SEEDDUP can reduce latency, achieved good throughput and deduplication efficiency (chunk size variance and security measures) in data deduplication.

KEYWORDS

Access control; cloud storage; data encryption; secure data deduplication; SHA3-512; users privacy

1. INTRODUCTION

Cloud storage has attracted many Companies today [1]. Data deduplication is a compression technique to remove replicate copies of files, which has gained more interest in cloud storage. Most of cloud storage solutions, such as *Dropbox*, *Mozy*, *Google Drive*, and *Wuala*, are espoused deduplication technique to save network bandwidth and storage space of cloud [2]. According to IDC (International Data Corporation) report analysis, the size of data in the whole digital world is expected to reach 40 trillion GB in the end of 2020 [3,4]. Multimedia data files, such as images, video, audio or text documents, take around 90% of the data. There is a big problem to handle such data securely and efficiently in the cloud [5]. For data deduplication, files with various formats like *mp3*, *jpg*, *pdf*, *obb*, and *unknown* are used [6]. The computation cost for data storage, retrieval and management are rapidly increasing. Keeping Storage cost as less becomes a great challenge in the field of cloud computing [7]. Data deduplication is a popular compression technique that not only reduces space utilization but also decreases redundant data transmission in low bandwidth network environments [8]. Data deduplication can be classified into four types: file level chunking, fixed size chunking, variable size chunking, and content aware chunking [9].

Here, each file is partitioned into a number of small chunks. File level chunking can eliminate more redundant data and it is easy to remove. The fixed size chunking eliminates less redundant data and their matching probability is relatively poor. Variable size chunking can easily isolate duplication and nonduplicate information and also minimize the amount of duplicate information, but the major disadvantage is it consumes more CPU resources. The content-aware chunking algorithm determines the chunk size based on the content of the file. It can easily manage small information update and data chunking. It does not lead to large chunk size variance. It is rightly decided that content-aware chunking method is more suitable for data deduplication [10,11]. Next hash values are computed for each chunk with hashing algorithms, such as MD-5, SHA-1, and SHA-256, which are also referred to as fingerprints. With the help of hash values, chunks are identified uniquely. These hash values are transmitted to a centralized cloud for deduplication [4,12,13].

Current data deduplication systems are based on the single/centralized server for deduplication, which has limited processing capability and it is not sufficient to access petabytes/terabytes scale of data deduplication (like big

data). One possible solution to avoid limited processing capability is to use multistorage systems in which no single point of failure and also no malicious insiders to access user's sensitive data. Centralized or global index table maintenance at origin cloud server will cause single point of failure because it is burdensome due to enormous frequent requests that are processed from users. Security algorithm must be unbreakable since data can be varied according to the sensitivity level (highly sensitive, medium sensitive, and non-sensitive). Current data deduplication schemes only rely on specific application scenarios, which do not satisfy various demands of users.

Contribution. This paper proposes SEEDDUP for secure data deduplication over the cloud environment. The main goal is to develop a secure and efficient data deduplication system that achieves high deduplication ratio, low processing time, high throughput, low network traffic, and less indexing overhead. For the above objectives, the SEEDDUP takes data security and user privacy in an optimal way. The main contributions of this paper are

- Code -based Public-key Cryptosystem *Niederreiter Cryptography Algorithm* is used to generate a pair of keys, such as public and private for data owners, which have smaller keys and they can encrypt more than 1.5 million plaintexts per second.
- *Cuckoo Search Algorithm* is used for optimal divisor selection, which is based on two key attributes: *file size and file format*. *SHA3-512* is used to generate hash values for data chunks.
- An efficient multilocal server is designed to enable the original server to verify chunk existence. Three different chunks are selected to identify the chunk existence in cloud. *Merkle Hash Tree based MapReduce* algorithm is introduced for indexing hash values to different local servers.
- When data owner receives a negative response from the cloud, the whole data are uploaded in the cloud in an encrypted form and also implement data retrieval system for legitimate users, who can access data in bounded times. These services can be provided for sensitive type of data. To avoid sensitive information leakage, the plain text is split into two blocks and encrypted separately. But it is not often discussed previously for how to provide a full security for highly sensitive information.
- Finally, extensive experiment is performed that shows the deduplication efficiency and effectiveness of our SEEDDUP scheme for increasing deduplication elimination ratio, deduplication throughput and minimizing information leakage from malicious attackers.

Organization. The rest of this paper is organized as follows. Section 2 presents related work. Then Section 3 discusses the problem statement. Section 4 describes an overview of our SEEDDUP system and also gives details on secure deduplication over cloud. Section 5 demonstrates the experimental study and corresponding performance results. Finally, conclusions and some future directions are pointed in Section 6.

2. RELATED WORK

Data deduplication is a storage optimization technique that is being used to improve the storage efficiency. This section reviews some commonly used data deduplication schemes for cloud storage, such as [14–17], and identified the factors that affect storage space and also discussed various scenarios where data deduplication is used.

Daniel *et al.* [18] have presented a lightweight auditing deduplication protocol for data outsourcing in cloud, which is referred to as LDAP. In this work, data integrity is verified and symmetric encryption algorithm is proposed to satisfy two constraints, such as data storage integrity and security by the data owners. The proposed LDAP scheme decreases computational and communication overheads for integrity verification and also the storage cost minimized using combined techniques such as cuckoo filters and convergent encryption. In addition to data storage security and integrity, privacy preserved for data retrieval in cloud and search accuracy results are increases for user query. After the creation of public and private keys, input data split into a number of equal-sized chunks with the help of fixed chunk size 4KB. It is computed as follows:

$$N(C(i)) = \text{size of file } f / \text{size of chunk} \quad (1)$$

Equation (1) shows the number of chunks denoted as $N(C(i))$. It is computed using the size of file f and the chunk size. For instance, if the size of file is 40KB, then $N(C(i))$ is 10.

A new content defined chunking (CDC) method is proposed for deduplication in cloud environment [19]. CDC is a maximum data redundancy method rather than fixed-length and variable length chunks. CDC has greater advantages, including (1) Content dependent (2) Low chunk size variance (3) Ability to eliminate low entropy string and (4) High throughput and deduplication ratio. However, CDC-based deduplication requires large computation to identify cut points. Hence, Rapid Asymmetric Maximum (RAM)-based CDC algorithm is proposed, which utilizes byte values to find the cut points. This

method gives low computation overhead and also high chunking throughput, but this method comes with a major drawback: while finding duplication with big data, it requires a lot of processing time. On the other hand, bit string content-aware chunking strategy (BCCS) is proposed [20] to achieve deduplication performance. It just performs preprocessing of big data and chunking and thus time for preprocessing and chunking is calculated. The minimum chunk size is estimated as 2KB using BCCS, which avoids generation of many chunks and reduces unwanted computation and also decreases overhead in the metadata. The proposed BCCS strategy is only suitable for a small size of data.

When blocking files block or chunk size is an essential factor that should be the best to avoid chunk size variance since larger segment size and fixed-length segment size chunking methods lead to the failure of detection of data duplication. For this purpose, genetic algorithm (GA) is proposed [21] to choose optimal and single divisor value D . Then fingerprints in cloud via BST (binary search tree) construction are indexed. BST is a well-organized structure in which elements are properly arranged in the left, right, and the root. The main reason to use GA is to obtain high deduplication ratio, but it consumes more time for the selection of optimal D . Similarly binary search tree may produce partial deduplication performance for large files due to the centralized management of large index.

Mao *et al.* [22] have proposed POD (performance-oriented deduplication) scheme, which improves the primary cloud storage performance. It uses Select-Dedupe (request-based) approach for data deduplication. An iCache (intelligent cache management) is promoted in POD. This POD scheme saves a large amount of storage capacity and enhances the performance of read operation. When considering performance, POD consumes more CPU resources in fingerprint computing and thus the use of CPU resources will not be investigated in POD.

In [23] authors have proposed AR-Dedupe (Application-aware) for the cluster deduplication system. It obtained low communication overhead and high data deduplication rate via routing server. This result, due to selecting handprints, finds super-chunks based on similarity. Furthermore, the routing server chooses the best (optimal) deduplication server node, which is only used for communicating to the routing server. Finally, index is created based on application types, which have little improvement for increasing rate data deduplication. AR-Dedupe is a time-consuming process which does not handle much data owners request at a time. Xiong *et al.* [24]

have proposed RSE-PoW (Role Symmetric Encryption with Proof of Ownership) for secure deduplication. The proposed scheme uses symmetric encryption, bloom filter, and proof of ownership. After key generation, cloud server verifies the hash. If two results are the same, CS does not store the file. If they are not the same, hash of block is encrypted and stored in CS. The RSE-PoW protocol resists only against side-channel attacks, but brute force attackers may largely involve in this system by the use of wrong keys and passwords. In [25] RMD (resemblance and merge-based deduplication) is proposed, which leverages indexing and bloom filter array. Data resemblance algorithm is concentrated, which identifies and clusters segments of resemblance for data and puts resemblance segments in the same bin. In order to find duplicate data, it finds only the bin which contains same data. This process is speedup the querying process by merge strategy. When segment clustering is not accurate, it results in poor performance and increased RAM requirements. In [26] various file deduplication schemes are based on different characteristics, such as file name, file size, and partial or full content of hash value. Experiment results show that CPU usage is reduced by 25% for partial MD5 scheme and 19.3% is reduced for full MD5 scheme. MD5 is faster than other hashing algorithms, but not secure than SHA family. The proposed scheme is slight worse in data sharing, searching, and management services.

In [27] data deduplication is performed for real-world dataset, such as disk images, which save deduplication and also increase deduplication throughput and reduce computational overhead. In particular, 30%~80% of deduplication throughput is achieved, 25%~40% of RAM space saving and deduplication ratio is reduced below 5%. The deduplication work flows as follows: (1) file chunking, (2) Adaptive block stripping (3) SHA-1 hash computation for each chunk (4) Duplicate detection and (5) In-RAM metadata management for indexing. The proposed adaptive block stripping-based framework is not suitable for real-world datasets. Two major components, such as front-end deduplication application and mass storage system as backend, have been proposed for deduplication storage system (DeDu) to manage deduplication over cloud [28]. In this work, Hadoop Distributed File System (HDFS) is used on the cloud. HDFS is a mass storage system, which easily manages large amounts of data. Furthermore, VMware is used to generate in cloud for simulation. In DeDu, hash value for each chunk is computed and then transmitted to HDFS for lookup. The drawback of DeDuare is high hash generation time for single file (large size of content) and high transmission cost for lookup. In [29] Shunrong Jiang *et al.*

Table 1: Comparison between SEEDDUP with state-of-the-art approaches

Authors	Dataset type	Content-aware	Chunk size	Storage optimization
LDAP [18]	NM	No	NM	To some extent
CDC [19]	Any	Yes	Variable length	To some extent
BCCS [20]	Any	Yes	2KB	To some extent
GA [21]	NM	NM	NM	To some extent
POD [22]	Text	NM	NM	To some extent
AR-Dedupe [23]	Any	No	Optimum	To some extent
RSE-POW [24]	Any	No	Fixed	To some extent
RMD [25]	NM	No	Variable	NA
Variable File [26]	NM	NM	NM	To some extent
In-RAM [27]	Text document, PPT, mails, etc.	Yes	Fixed (10KB, 100KB, 1MB, and 10MB)	NA
DeDu [28]	.mp3, .hwp, .avi, and.xlsx	Yes	NM	NA
PoW [29]	NM	No	Fixed	NA
TPA [30]	Any	No	Fixed	To some extent
SEEDDUP	Any	Yes	Optimum	To some extent

have concentrated on secure data deduplication and PoW management. Two types of entities are used, such as data owner and cloud service provider. Credentials of user, who owns data to access cloud service provider, should be authenticated and then data encrypted and uploaded to the cloud service provider with the corresponding indexing information, which is also referred to as tag. If the file does not exist in the cloud, he/she is called an initial uploader, else called a subsequent uploader. In this work, serious issues arise in the part of key generation. A data owner generates secret keys for encryption, which can lead to information leakage. Authorized deduplication is presented in [30] to design secure cloud environment. User's privacy is an important factor to be considered before outsourcing data to the cloud. User (data owner), public cloud, and administrator (TPA) are involved in secure cloud environment. User is registered to administrator where user is authenticated by their credentials and also private keys for storing files are created. Herein user sensitive data are not secure from insider and outsider attackers. Table 1 represents the comparison between the existing works and the proposed approach.

3. PROBLEM STATEMENT

Data deduplication is an effective way to minimize the redundant data stored in the cloud. Current research involved in this topic improves the space of savings by effective data deduplication. It is achieved through various research aspects, such as Data Chunking, Data Indexing, Primary Data Access, and Storage Maintenance Operations. Security is a questioned part in previously deployed systems in particular, integrity and illegal access to access the sensitive data stored in the cloud. Hence, authentication, confidentiality, and integrity issues are addressed in the data deduplication.

To ensure the integrity of data stored in untrusted cloud environment, unique hash values are computed from the

data. Based on the hash values data, deduplication is implemented to optimize the storage of the cloud. Deduplication is at data owner's side each data is chunked and identified with unique hash value. This section summarizes the major problems in the secure data deduplication over untrusted cloud environment.

In [31] three-tiered secure data, deduplication architecture is proposed for cross domains. This is an efficient and privacy preserving big data deduplication in cloud environment and comprises key distribution center (KDC), clients, and cloud service provider (CSP) from different domains. The cross domains' local managers are represented as LMA and LMB. The trusted KDC is considered to distribute and manage private keys for the system. The CSP is a first tier which provides data storage services for clients. Deduplication is performed using decision trees, which is based on binary search tree for searching duplicate data. If any error occurs at high level, any subtree is wrong. Insertions and removals are complex when height of the tree can be N . Duplicate search time is high. In [32] two privacy aware data deduplication protocols are proposed: ZEUS and ZEUS+. ZEUS offers weaker privacy guarantees but efficient in the communication cost. Check hash first data later framework is proposed, which is based on cross-user client side fixed size chunk level data deduplication. User send duplicate check (DC) request for c_1, c_2 existence in cloud by querying hash values of $c_1(h), c_2(h)$ (hash generated using SHA-256). Herein DC request and response are verified by a centralized server, which decreases data deduplication speed. More specifically, it is not suitable when the number of users and size of data are huge and also SHA-256 is less secure.

In [33] authors have focused on encrypted data storage and management with deduplication. In this paper, heterogeneous data management approach is concentrated for data access control and deduplication for different

application scenarios. For message M , hash value is generated to verify data deduplication in cloud storage systems. Data confidentiality is achieved but user's identity privacy is neglected and also it is not applicable for practical deployment. In [34] secure data deduplication scheme is presented before data are outsourced to cloud server and thus communication cost is reduced for computation cost and communication cost. In this work, variable size block level deduplication technique is proposed which is based on the Rabin fingerprinting technique. Then users encrypt data using convergent encryption scheme which prevents attacker to access data. However, convergent encryption is the conventional encryption technique, which is 100% deterministic (users encrypt the same data will generate the same key). Variable size block level deduplication is not effective since one block size is 4KB and other block size is 512KB and hence data deduplication elimination ratio is small and it is a time-consuming process. This work uses decision tree for index construction, which consume more time. Rabin fingerprinting eliminates redundant network traffic, but it leads to low chunking throughput. In [35] PHISA (Partial Hash Information String Algorithm) is proposed for similarity evaluation on multimedia data. This finds duplicates of multimedia clips like text, image, audio, and video. PHISA uses MD5 hashing algorithm for hash value generation and hash value of each chunk is 128 bits. Then 128-bit hash value is computed and utilized for comparison instead of matching the whole hash vale (128 bits). The file digest hash values are generated by conjoining partial hash value of each chunk. Major drawbacks of PHISA are as follows: lack of security since MD5 hashing function can be easily broken and no longer used in

secure cloud systems and also execution time taken even for 200MB multimedia files.

In this paper, we are going to deal with the following problem.

$$CS \text{ or } KGC \{Verify(C, h)\} \rightarrow TRUE/FALSE \quad (2)$$

Equation (2) illustrates whether chunk C of hash h is presented in the cloud server or not. In this case, KGC has taken the responsibility to verify it. In this paper, we present an index lookup IL request, which determines the chunks' redundancy in cloud.

Two kinds of chunking are performed in general: variable chunking and fixed chunking. However, content aware chunking is preferred for effective data deduplication, which maximizes the data accuracy. Compared to the existing works, the proposed SEEDUP work has achieved 90% of deduplication and reduces the redundant copies through the servers by sending the hash requests.

4. PROPOSED WORK

In this section we first aim to present an overview of the system model. Then we present the detailed description of the proposed model.

4.1 System Overview and Threat Model

SEEDDUP system for cloud storage is depicted in Figure 1. The SEEDUP comprised of four entities: Key Generation Center (KGC), Cloud Server (CS) Data Owners (DOs), and Data Users (DUs). The KGC generates

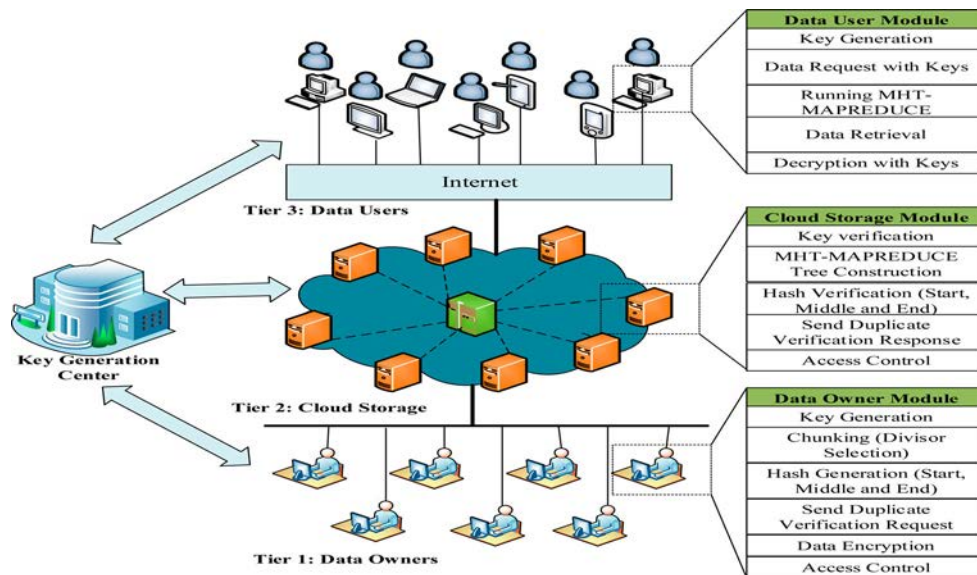


Figure 1: System architecture

key pair $\{pu_k, pr_k\}$ for data owners and users. It acts as a trusted third party, which provides auditing results. The CS consists of a set of local servers and an origin server that provides data storage and retrieval services for owners and users. When data owner wants to store file, they check duplicate in cloud (such as if the file already uploaded or not), the local server checks this duplication. If the file is stored already in cloud, local server sets pointer, instead of storing file. Otherwise the whole input file will be stored in the cloud in encrypted form. Data owner gives access control for sensitive files. In the following, we describe the threat model of the SEEDDUP system. This work focuses on various threats and particularly carried out three threat models.

Threat 1 (Account Hijacking/DoS/DDoS). This type of threat or attack is an attempt to access the cloud resources. The attackers are unauthorized parties and try to use the cloud resource. The main intention of this type of attackers is to use the cloud resources and make them unavailable to the legitimate users.

Threat 2 (Data Breaches). This type of threat attempts to overhear the user data stored in the cloud environment. This threat tries to break the authentication process and aims to breach the user data. The attacker aims to overhear, modify, and destruct the user data in cloud. This threat is vulnerable when the data security level is low.

Threat 3 (Insecure Encryption). This type of threat is launched on the encryption algorithm. The attacker tries to derive the private key of the legitimate users from their public key. This threat is severe in these three types. The main intention of the attacker is to derive the secret key of the legitimate users and to access the legitimate data in the cloud. All these threat models are considered in the proposed work. The solutions are presented to mitigate the above severe threats.

4.2 Data Deduplication

Implementation of data deduplication can differ based on variety and volume of data. To support better storage optimization, the data deduplicated storage system should decrease space utilization. The key idea behind SEEDDUP is to provide two-side privacy (*i.e.* both server and client), particularly the CS in server-side deduplication finds the additional copy only after reception of the whole file. On the other hand, user-side deduplication finds duplication through Index Lookup *ILrequest*. For example the condition Is chunk C in local server LS and *ILresponse* is used to check whether the

DO requires uploading the data. For this purpose, DO receives response from LS by *TRUEorFALSE*. Herein *Index Lookup IL* represents the chunk hash values for data deduplication. *ILrequest* is implemented in user-side by the hashing algorithm (*e.g.* SHA3-512 bits) of the data. In order to avoid the cause of hash collision avoidance, the DO may detect the existence status of c by querying the hash of cloud. Previous approaches have been proposed similar to our deduplication system (such as single chunk deduplication, double chunk deduplication, and dual side (starting and ending) file deduplication). These approaches have failed due to the incomplete deduplication exploited by the attacker. The incomplete uploading can be always exploited by the unauthorized users (*e.g.* attackers). Similarly, data may be at variety (*e.g.* audio, image, text file, and video). Hence deduplication by uploading single or double *chunks* request cannot be effective. In cloud, Sybil attacker can execute a huge number of independent duplicate checking requests on the same chunk and also attempt to propose random technique for duplicate checks. Here, we consider multi-chunk duplication verification at LS . For data deduplication optimally chosen chunk c is used instead of that chosen by the randomization technique. For that, find probability p for chunks and based on p sending *Index Lookup request* to LS .

Multi-Chunks Index Lookup. Assume that the attacker attempts to know the presence of chunks of $c_1, c_2 \dots c_n$. It requires duplicate checks thrice and thus triple *Index Lookup* is forwarded to LS which is based on the relation among the generated chunks by DO. Possibilities of *IL request* are as follows:

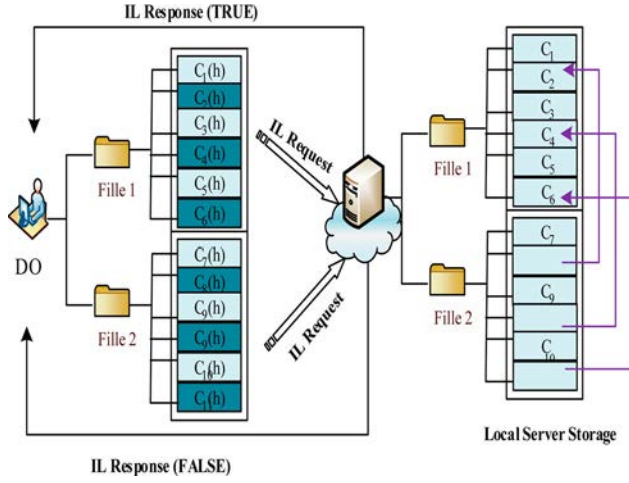
- (P_1): All *IL requests* of chunks c_1, c_2 and c_3 are unique
- (P_2): Any two chunks c_1, c_2 or c_2, c_3 and c_1, c_3 have copy of the file in LS
- (P_3): All *IL requests* of chunks c_1, c_2 , and c_3 are the same (*i.e.*) duplicated

To hide *IL requests* to attacker, we have used encodings for *IL response* and entire file to upload to the cloud. The *IL requests* of chunks, c_1, c_2 and c_3 consist of $c_1(h), c_2(h)$, and $c_3(h)$ in triple chunk uploading and the *IL response* consists of single output that represents whether chunks are presented or not.

The design of *IL request* and response for data deduplication is shown in Table 1 and the illustration of table is as follows: If all the queried chunks such as $c_1(h), c_2(h)$, and $c_3(h)$ are not in LS then DO can upload their whole file. Otherwise DO is asked to LS either two chunks or two individual chunks are existence or not. LS confirms the

Table 2: SEEDDUP table for the presence of chunk identification

IL request (hash presence)			IL response
$c_1(h)$	$c_2(h)$	$c_3(h)$	True/False
✓	✓	✓	True
✓	✗	✗	False
✗	✗	✓	False
✗	✗	✗	False
✓	✓	✗	False
✓	✗	✓	False
✗	✓	✓	False

**Figure 2: Data deduplication in local server**

index lookup requests on $c_1(h)$, $c_2(h)$, and $c_3(h)$ existence (Table 2).

Figure 2 shows data deduplication in local server where DO wants to upload two files file 1 and file 2. Herein Deduplication is performed between these two files.

In this way, data deduplication is performed in cloud. After the verification of chunks, file is encrypted by DO according to sensitive level and that forwarded to the cloud. The process of SEEDDUP interpretation is follows.

Using the multi-chunks index lookup, redundant data stored in the cloud are determined. Each chunk hash values are compared with the database. If three chunk results are true, then storage request is dropped. Otherwise, file is stored into the cloud. The benefit of using multi-chunk index lookup request is that it improves the storage optimization and also eliminates the redundant data approximately to 90%.

4.2.1 Key Generation

Initially $\{pu_k, pr_k\}$ key pairs are generated by KGC. Nieterreiter Cryptography Algorithm provides strong security. It utilizes a *syndrome* as ciphertext instead of the code word

and the plain text is an error pattern. Niederreiter encryption is ten times faster than other public cryptosystems. It can be also used to construct a digital signature algorithm. Encryption and decryption time complexity is minimum compared to traditional asymmetric algorithms such as RSA, ECC, and ECDSA. The computation of *syndrome* requires the parity check matrix as a public key instead of the generator matrix. When systematic matrices are used, then there is no effect on the size of keys. This paper presents the modern Niederreiter Cryptographic Algorithm for key generation. The procedure for key generation using *Goppa polynomial* is depicted in algorithm 1.

Algorithm 1: Niederreiter Public Cryptographic System

Input: Initialize the system parameters T, M, N, ρ

Step 1: Begin

Step 2: Choose a random *Goppa Polynomial* $G(z)$ of degree on $GF(\rho^M)$

Step 3: Select n elements arbitrarily of $GF(\rho^M)$ that are no roots of $G(z)$ as the support L

Step 4: Calculate $(n - k) \times n$ parity check matrix \hat{J} based on L and $G(z)$

Step 5: Get J to systematic form based on *Gauss – Jordan* elimination:

$$J_{\text{systematic}} = \hat{S} \times J$$

Step 6: Calculate S^{-1}

Step 7: Return $pr_k(D_{\text{goppa}(c), L, G(z), S^{-1}})$ and $pu_k(J_{\text{systematic}})$

Step 8: End

Output: pu_k, pr_k

Niederreiter cryptographic scheme utilizes a $(n \times (n - k))$ parity check matrix to serve as public key in systematic form. It uses $n - k$ bit syndrome as plaintext and it enforces less restrictions on the plaintext size which depends on the constant-weight encoding scheme and parameter sets. It concentrates plaintext blocks with a size of only 100s of bits instead of using more than 100s bits. The security parameters are selected to provide sufficient protection against security attack. For example of 80-bit security, the security parameters as follows: $M = 11, N = 2048, T = 27, k \geq 1, 751$, which leads to a public key size of 63KBytes and S^{-1} of 11 Kbytes.

4.2.2 Cuckoo Search Algorithm for Divisor Selection

In this part of the work, chunking process is carried out in the best divisor selection via cuckoo search algorithm. The size of chunk plays a significant role in data deduplication. The problem with this approach is the selection of optimum chunk size. In contrast to other chunking methods, such as fixed size and variable size, the best divisor is here selected using CS algorithm. The main advantage of using cuckoo search algorithm is that it finds the global optimal solution and solves non-smooth optimization complex issue. In cuckoo search, the number of chunks (chunk size) generated depends on the size of input file (f_s) and file format (f_f). The CS algorithm is a global optimization method that follows the behaviors of cuckoos.

The idea of this algorithm is follows: (1) How cuckoo laid their eggs in the host nests, (2) How, if not destroyed and detected, the eggs are hatched to chicks by the hosts and (3) How CS algorithm, based on such scheme, can be used to find the global optimum of a function. Due to these facts, CS algorithm is specifically suitable and favorable. However, other metaheuristic algorithms require a large number of parameters, but the CS that needs two parameters only: the total population size P_s and probability rate P_a . In this work, we take a population size of $P_s = 100$ host nests, which represents the number of candidate solutions for the method and the probability rate of $P_a = 0.25$.

Assume that data owner wants to upload a file with size MB = 1024. The number of divisors for file size is 1, 2, 4, 8, 16, 32, 64, 128, 256, 512, and 1024. The total number of divisor D for file chunking is 11, but this is possible to choose the probability of obtaining a small divisor or a larger one. However, a divisor D should be reasonable to eliminate the larger duplication elimination ratio. The steps of CS algorithm can be shown in Algorithm 2.

Algorithm 2: CS Algorithm Procedure

- Step 1:** Begin
Step 2: Objective function $f(x), x = (x_1, \dots, x_d)^T$
Step 3: Generate initial population of n host nests $x_i (i = 1, 2, \dots, n)$
Step 4: While ($t < Max_Gen$) or (stop criterion)
Step 5: Acquire a cuckoo (i) via Levyflights randomly.
Step 6: Evaluate fitness of $i(F_i)$ using equation (2)
Step 7: Select a nest j among n , randomly
Step 8: If ($F_i > F_j$)
 Replace j by the new solution;
Step 9: End if
Step 10: A fraction P_a of worse nests are abandoned and new ones are generated.
Step 11: Keep all computed solutions
Step 12: Then rank the current solutions and find the best solution/Best divisor is selected
Step 13: End while
Step 14: Implement results post processing and visualization
Step 15: End
-

The fitness value of cuckoo i can be estimated as follows:

$$F_i = w_1 \times f_s + w_2 \times f_{fs} \quad (2)$$

where w_1 and w_2 are weight values, which are constants and $w_1 + w_2 = 1$. The pictorial representation for Cuckoo Search algorithm is shown in Figure 3.

Levy flight is performed when new solutions are generated $x_i(t+1)$ for the i th cuckoo by following

$$x_i(t+1) = x_i(t) + \alpha \oplus Levy(\lambda) \quad (3)$$

where $\alpha > 0$ denotes the step size which should be related to the problem of interest. Mostly $\alpha = 1$ for all cases and

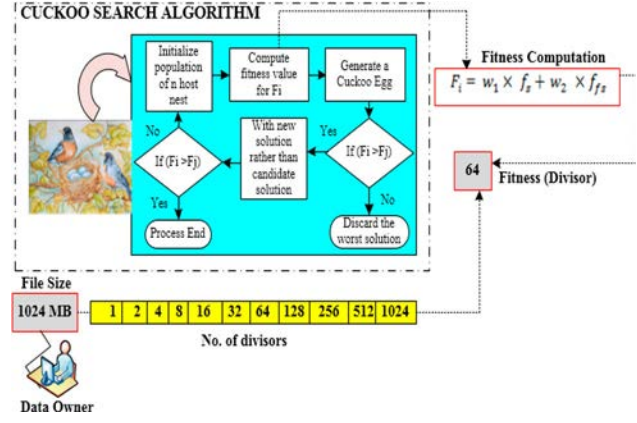


Figure 3: CS algorithm for the best divisor selection

the product \oplus refers to entrywise multiplications. This product is used in PSO, but in this work it is obtained through Levy flight which is more efficient in exploring the step length and search space. The Levy flight distribution is explored to offer the random step length in random walk.

$$Levy \sim u = t^{-\lambda} \quad (1 < \lambda \leq 3) \quad (4)$$

The Levy flight has an infinite variance with an infinite mean. The steps of a cuckoo form a random walk process which utilizes a power-law step-length distribution with a heavy tail. It is worth pointing out that in the real world and when a cuckoo's egg is very similar to a host's eggs, then the cuckoo's egg is less likely to be discovered.

4.2.3 Hash Generation (SHA3-512)

The next step after chunking is the hash generation. However, various deduplication approaches generate hashes for the total number of chunks. In this work, we create hash values for the selected chunks instead of generating the total number of chunks. Today's SHA has become a vital tool to assure the data integrity while it transfers to cloud. SHA takes as input a message of arbitrary length and output a hash or message digest. This can be represented as

$$h = H(m) \quad (5)$$

where m is the input message and h is the hash created by the hash algorithm H . However, the strong hash function has the following properties:

- (1) One-way Property:

$$H(x) = h \quad (6)$$

- (2) Weak collision resistance:

$$H(x) = H(y) \quad (7)$$

(3) Strong collision resistance:

$$H(x) = H(y) \quad (8)$$

SHA-0, SHA-1, SHA-2, and SHA-3 cryptography algorithms can be established by NIST standard. Table 3 shows various functional characteristics of hash algorithms. The security level of these hashing algorithms is managed by the size of output bits, block size of bits, word size of bits, and multiple hash rounds. These functional characteristics determine of data integrity and it finds any change in a message with high probability rate.

When compared SHA-3 with SHA-2 family, SHA-3 provides high security and SHA2 requires 64 cycles, but SHA-3 requires 24 cycles of operation. Minimum number of cycles of SHA-3 increases the speed of hash generation against SHA-2 family. The SHA-3 or Keccak is based on the sponge function, but it is not meant to replace SHA-2. The primary feature of SHA-3 is more flexible than regular hash function. It takes variable length input and produces variable length output. The parameters considered in SHA-3 are rate ($rbits$) and capacity ($cbits$) where rate defines the speed and capacity defines the security level the permutation b is defined by $r + c$. And the speed and security level defines the strength. Keccak round function is defined as

$$R = (\ddot{i}) \oplus (X) \oplus (n) \oplus (\rho) \oplus (\theta) \quad (9)$$

where \ddot{i} defines iota module which breaks up any symmetry caused by the other modules. This is estimated by XOR one of the array elements to a round constant. It has 24 round constants to choose from and these constant values are internally defined by Keccak. Without iota module, all rounds mapping would be symmetric, X defines chi module which adds a nonlinear aspect to the round of permutation. It integrates the row elements by three bitwise operators, including AND (&&), NOT (!), and XOR (\oplus). Finally it stores the result back to the state array, n defines pi module which permutes 64-bit elements where permutation works with fixed pattern assignment, ρ defines rho module that rotates 64-bit element using triangular numbers (0, 1, 3, 6, 10, 15), and θ defines theta module which renders the internal state into 5×5 array of 64-bit elements. It calculates the each column elements and combines them with an XOR operator and then it results parity to each state bit. The number of rounds defined by $12 + 2l$ and Keccak $f(r + c)$ is computed *i.e.* Keccak $f(1024 + 576)$. Finally, Keccak $f(1600)$ has 24 rounds. It utilizes byte ordering and bit numbering. The procedure for SHA-3 is as follows:

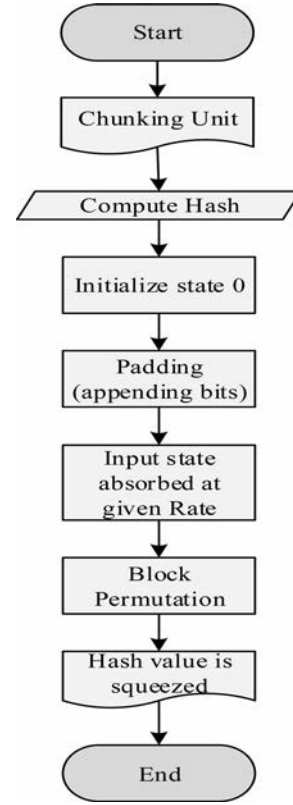


Figure 4: Flow diagram for SHA-3

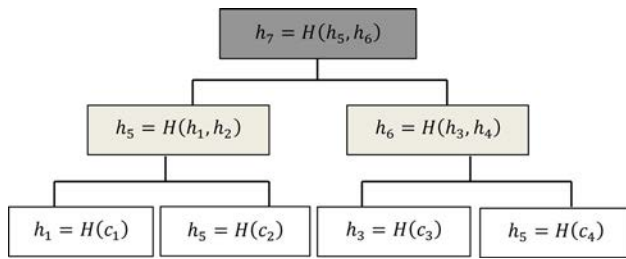
- Take the input as plain text and append the delimiter for SHA
- It uses the sponge construction where message blocks are XOR into a subset of the state. Then implement transformation to obtain the whole file
- Next implement padding (appending bits), absorb the input into the state *i.e.* for each piece XOR it into the state and then block permutation is applied.
- The hash value for given file is computed at the same rate as input file. The flowchart for SHA-3 (512bits) is depicted in Figure 4.

4.2.4 Merkle Hash Tree with MapReduce

MHT is very useful to build scalable applications. In an MHT, the master hash code is known as the Merkle Root node. Computing the root of Merkle tree is more complicated since it has multiple stages. Let's assume we have a way to split the input file into fine-grained chunks and that each chunk is identified by hash value (generated using SHA3-512 bits). For example data volume is C and it splits into four segments (c_1, c_2, c_3 , and c_4). Then we compute hash values for four chunks: $c_1(h), c_2(h), c_3(h)$, and $c_4(h)$. In the top of Merkle Hash Tree, we have the hash value roots for four chunks. Simple hash for four chunks ($c_1(h), c_2(h), c_3(h)$, and $c_4(h)$) is $h(c_1, c_2, c_3, c_4)$

Table 3: Various hash generation algorithms

Algorithm and variant	Output size (bits)	Block size (bits)	Capacity	Word size (bits)	Rounds	Operations	Security strength (bits)
MD5	124	512	0	32	4 (Each round require 16 steps)	AND, XOR, Rot, Add (mod 2^{32}), Or	≤ 18
SHA-0	160	512	0	32	80	AND, XOR, Rot, Add (mod 2^{32}), Or	< 34
SHA-1	160	512	0	32	80	AND, XOR, Rot, Add (mod 2^{32}), Or	< 63
SHA-2	224	224	512	32	64	AND, XOR, Rot, Add (mod 2^{32}), Or	112
	256	256	512	0	64	AND, XOR, Rot, Add (mod 2^{32}), Or	128
	384	384	1024	$128 \leq 384$	80	AND, XOR, Rot, Add (mod 2^{64}), Or	192
SHA-3	512	512	1024	0	80	AND, XOR, Rot, Not	256
	224	224	1152	448	24	AND, XOR, Rot, Not	112
	256	256	1088	512	24	AND, XOR, Rot, Not	128
	384	384	832	768	24	AND, XOR, Rot, Not	192
	512	512	576	1024	64	24	256

**Figure 5:** Merkle hash tree for four chunks (c_1, c_2, c_3, c_4)

and the Merkle hash for four chunks is depicted as follows:

$$MHT = h(h(c_1(h), c_2(h)), h(c_3(h), c_4(h))) \quad (10)$$

Figure 5 shows tree construction for four chunks. In order to obtain the Merkle hash tree root node, we perform indexing over chunks and their hash values. Let us assume that $n = 2^l$ for some integer l . The key idea behind the MHT function is the addition and the root will be total, which is computed by

$$Parent(root)_{total} = Left_{total} + Right_{total} \quad (11)$$

To perform data deduplication, we include all hash chunk values in tree, which becomes:

$$root_{hash} = hash(left_Hashright_Hashleft_totalright_total) \quad (12)$$

In order to achieve this performance, we design an MHT tree to organize the clusters. The blocks stored in data nodes are organized as hierarchical clusters. Let us assume that Kn -dimensional data blocks

$blk_1, blk_2, \dots, blk_K$ in the cluster and MHT is defined as follows:

$$MHT = (K, S(K), SS(K), C_{max}, andTHR) \quad (13)$$

where K is the number of data blocks, $S(K)$ is the linear sum of K vectors, $SS(K)$ is the square sum of the K vectors, and C_{max} is the maximum cluster size in blk_j . Based on the blocks in MHT, we compute the center and radius of the cluster as follows:

$$CE = \frac{S(K)}{K} \quad (14)$$

$$RA = \sqrt{\frac{\sum_{j=1}^K (blk_j - CE)^2}{K}} \quad (15)$$

According to the blocks in cluster, we redefine the radius function as follows:

$$RE = \sqrt{SS(K) - S(K)/K} \quad (16)$$

MHT is an effective hashing-based indexing scheme that introduces to effectively and securely store the data (to avoid data damage and alteration). As depicted in Fig, the construction is similar to binary tree, where the leaves are the hashes of the data blocks and the tree is valued as follows:

$$MHT_{n(i)} = H(L_c, R_c, N_{lf(n)}) \quad (17)$$

where L_c and R_c are the values of the left child node and right child node, respectively. $N_{lf(n)}$ is the dominated set of leaf nodes and it is computed as follows:

$$N_{lf(n)} = N_L + N_R \quad (18)$$

Furthermore, the Name Node may lead to central point failure or whenever loses all information in an HDFS

cluster. For this purpose, we cluster similar files and maintain η_t into Secondary Name Node. Every hour it connects to Name Node and it can make a failed Name Node and save it into η_t .

Deduplication in MHT requires large computations as long as they can be increased by height. To improve the data deduplication speed, we present MapReduce in the cloud environment. MHT-based MapReduce model provides high deduplication efficiency and ensure high integrity result of MapReduce jobs.

MHT-based MapReduce overlays on cloud environment composed of a number of local servers and one origin server. MapReduce is a distributed scalable computing model for large-scale processing. Each computation request issued by the client in MapReduce is called *Job*. In MapReduce, each job has three phases: map phase, shuffle phase, and reduce phase. MapReduce considers all data/task in the form of keys with associated values, which are performed in a Map function and in each iteration. It results a list of output values, which are performed in a Reduce function.

Map function:

$$\langle inputkey - value \rangle \rightarrow \langle intermediatekey - values \rangle$$

Reduce function:

$$\langle intermediatekey - list(value) \rangle \rightarrow \langle output \rangle$$

Each request firstly will be processed in map phase and the result of map phase will be processed in shuffle phase. Finally the result is reduced. We combine MHT with MapReduce to track left and right values of all subtrees. MHT-based MapReduce is depicted in Figure 6.

4.2.5 Data Encryption and Decryption

In encryption the message m as a constant weight encoded word of length n and hamming weight t . It uses public key pu_k encryption. Firstly data encode into initial code according to a first public key by selecting a pre-determined error vector and encoding the selected error vector into the second code through second public key. Finally it generates a ciphertext Ctx by adding the first and second codes. It is a data encryption method for normal data (*i.e.* data sensitivity level = 0.5). For high sensitivity level of data (above ≤ 0.95), dual encryption is invoked for protecting from insider and outsider attackers based on the aforementioned procedure (Figure 7).

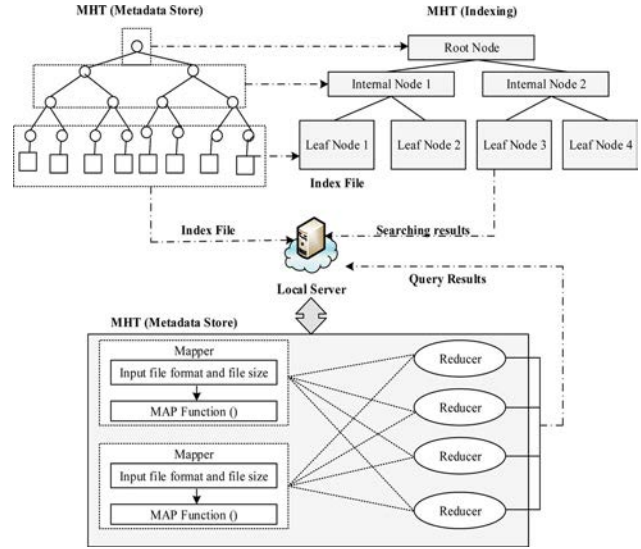


Figure 6: MHT-based MAPREDUCE

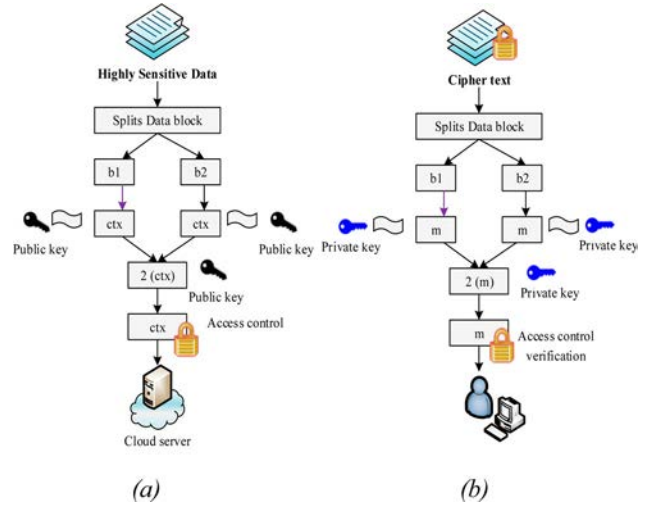


Figure 7: (a) Data encryption and (b) data decryption

Algorithm 3: Data Encryption

- Step 1:** Begin //Data sensitivity Level = 0.5 (Normal)
- Input:** pu_k and message m
- Step 2:** Define m as binary string E of length n and weight t
- //Start Encryption**
- Step 3:** Ensure $c = \hat{J}.e^T$
- Step 4:** Return Cipher text Ctx
- Step 5:** Split Ctx into two blocks $Ctx(b_1, b_2)$
- //Data sensitivity Level ≤ 0.95 (High)**
- Step 6:** Encrypt (b_1, b_2) using pu_k
- Step 7:** Return $b_1 (ctx), b_2 (ctx)$;
- Step 8:** Add $b_1 (ctx), b_2 (ctx)$;
- Step 9:** $B(ctx) = b_1 (ctx) + b_2 (ctx)$;
- Step 10:** Encrypt $B(ctx)$ using pu_k
- Step 11:** Return $B(ctx)$ and set $k = 3$ //Access control
- Step 12:** End //End Encryption

For decryption of message m , first decode the ciphertext using private key pr_k , which determines the location of errors in the result of the first decoding using a second

set of the plurality of secret keys and resolves a number of predetermined errors and determines data as a result of correcting the errors.

Algorithm 3: Data Decryption

Step 1: Begin

Input: $pr_k (D_{goppa}(c).S^{-1})$ and Cipher text Ctx

Step 2: Compute $\hat{C} = S^{-1}c$ // **Start Encryption**

Step 3: Get e from \hat{C} using the decoding algorithm $D_{goppa}(\hat{C})$ for code C

Step 4: Represent e as message m // **Data sensitivity Level = 0.5 (Normal)**

Step 5: Split m into two blocks $m (b_1, b_2)$ // **Data sensitivity Level ≤ 0.95 (High)**

Step 6: Decrypt (b_1, b_2) using pr_k

Step 7: Return $b_1(m), b_2(m)$;

Step 8: Add $b_1(m), b_2(m)$;

Step 9: $B(m) = b_1(m) + b_2(m)$;

Step 10: Decrypt $B(m)$ using pr_k

Step 11: Return $B(m)$ // **Access control**

Step 12: End // **End Decryption**

4.3 Data Retrieval

The data users request files to the cloud server, then the cloud server checks authentication from the key generation center. The main aspect of data retrieval from the cloud is “how much time does it take to download the user requested file in the protected area”. In the case of user requesting highly sensitive data, the user must be controlled by the cloud server and the cloud server checks the number of time the user accesses the particular file. After verification from KGC and time of access, the cloud server forwards the encrypted file to the user. The user can decrypt the file using the private key sent by the KGC.

5. PERFORMANCE EVALUATION

In this section, performance of the proposed SEEDDUP architecture is discussed in terms of various metrics.

5.1 Experiment Setup and Datasets Description

The proposed SEEDDUP is implemented using Hadoop framework 3.1.2 version and operating system used is Ubuntu 16.04 and the configuration of the Hadoop is depicted in Tables 4 and 5.

For performance evaluation, different datasets are used in evaluation: Traffic Signs dataset, Enron Email dataset, and the Oxford Buildings dataset [31]. In our evaluation, we believe that today data users’ demand to back up the multimedia and email contents over the cloud storage system. In our evaluation, the results will be different for several datasets.

Table 4: Experiment configuration

Operating system	Ubuntu 14.04 LTS	
System configuration	Apache Hadoop IDE Connectivity Hard disk Development toolkit	2.7.2 Netbeans 8.0 100Mbps Ethernet LAN 1TB JDK 1.8

Table 5: Hardware configuration for implementation

Specifications	N_1	N_2
Processor	Intel Core i7 – 7700	Intel Core i5 – 10500
CPU core	Quad core	6
CPU speed	3.6 GHz	3.1 GHz to 4.5 GHz
RAM	8 GB	8 GB

5.2 Performance Metrics

Our SEEDDUP scheme of data deduplication process performance has evaluated for the following metrics:

- **Deduplication Rate:** The total amount of data storage that has been optimized due to deduplication. Rate of deduplication can be varied due to chunking type and chunk size used.
- **Deduplication Speed:** The overall time taken for detecting duplicates in cloud. It can be verified due to duplicate identification algorithm.
- **Lookup Latency:** The time delay for detecting matches from given input data. It depends on the indexing for storage data.
- **Hash Collision Rate:** The amount of duplicates that detected wrongly, which is the accuracy of deduplication. It can be varied based on the hash generation algorithm.
- **Throughput:** We measure throughput of how many chunks of data will be processed in a given unit of time. The overall throughput is the total input chunks performed data deduplication in a given amount of time.
- **Security Strength Measure:** The percentage of security strength given to the user data. It depends on the type of security algorithm used and access control to authentication of user data.

5.3 Comparative Analysis

In this section, we describe the performance evaluation of our proposed SEEDDUP in terms of aforementioned performance metrics. The performance of SEEDDUP is compared with the five previous works: EPCDD [32], ZEUS & ZEUS+ [32], HDMA [33], RF [34], and PHISA [35]. The experiments were conducted on three real-life datasets that are the collection of large files downloaded from the open source projects and it is kept in

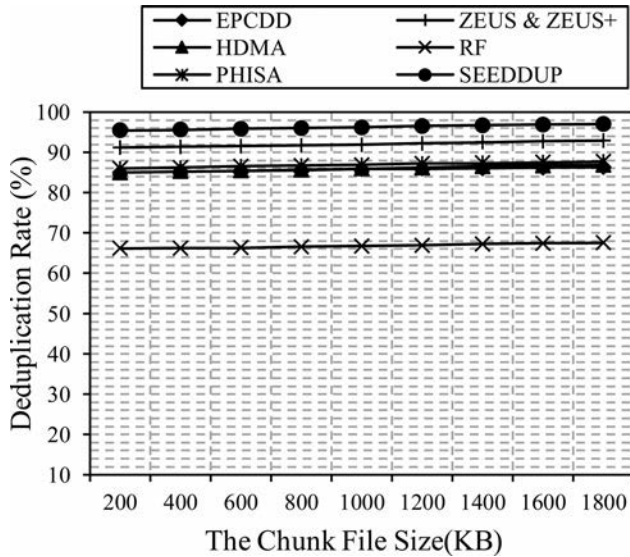


Figure 8: Comparative results on deduplication rate (%)

various file formats. The experimental results show the outcomes of different deduplication techniques. Table 6 describes the comparison between the SEEDDUP and other approaches.

5.3.1 Deduplication Rate

The data deduplication rate estimates the effectiveness of the deduplication process. Figure 8 shows the comparative results for the deduplication rate.

From Figure 2, it is observed that the proposed SEEDDUP has obtained low deduplication rate than EPCDD, ZEUS& ZEUS+, HDMA, RF, and PHISA. Generally speaking, the smaller deduplication rate shows the better data deduplication performance. With the large number of chunks generation, previous approaches obtained poor deduplication rate and also poor divisor selection. Deduplication rate increases with the file formats, file chunking, computation of fingerprints or hashes for chunks and finds matching for storing unique content in the cloud server. With variable file chunking, RF has obtained large deduplication rate and also it obtained highest overhead of I/O, and CPU and Indexing. But SEEDDUP system requires less effort to perform deduplication with the aid of optimal divisor selection, hash generation, and selection chunk types based on file formats.

5.3.2 Deduplication Speed

Deduplication speed is an important metric to measure the deduplication system performance.

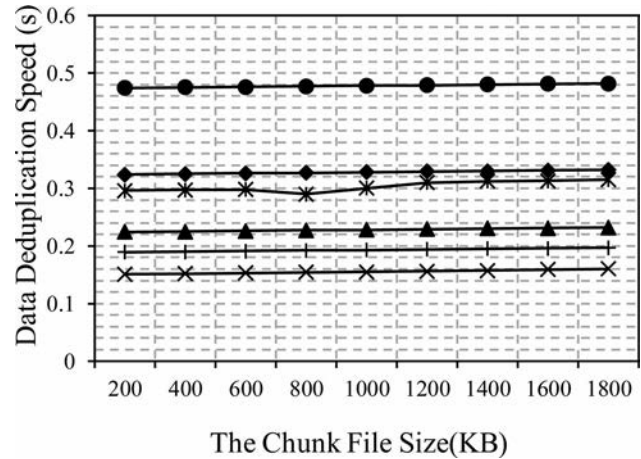


Figure 9: Comparative results on deduplication speed (s)

Figure 9 depicts the comparison results for the proposed SEEDDUP with the five previous approaches. Here, it is noted that the deduplication speed is the amount of time required for deduplication (*i.e.* find unique contents in the cloud server). Deduplication speed can be varied based on the data deduplication. EPCDD and RF was used decision tree for indexing which consumes a large amount of time for matching the contents. Hence we propose MHT with MapReduce algorithm, which takes very few seconds for deduplication. Furthermore, generate hash for triple chunks from the number of chunks, which relatively increase the deduplication speed.

5.3.3 Lookup Latency

Lookup latency plays an important role in data deduplication and eliminates redundant data at minimum delay with good duplicate removal ratio. Figure 10 demonstrates the result of lookup latency for the proposed SEEDDUP with the previous approaches.

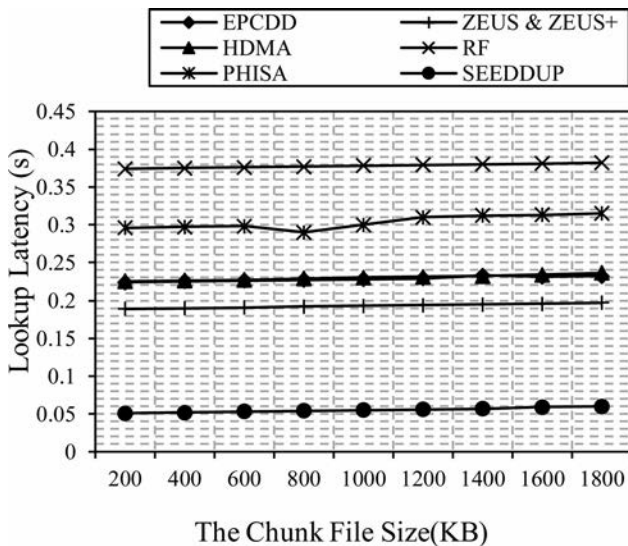
Lookup of fingerprint/hash is a bottleneck in data deduplication. Figure 10 shows that the proposed SEEDDUP system has required less lookup latency during data deduplication. Lack of indexing and fixed/variable size chunking is the major reason for large lookup latency. ZEUS & ZEUS+, PHISA, EPCDD, and HDMA require relatively large lookup latency for deduplication. MapReduce paradigm minimizes lookup latency and also periodic updates from data owners can decrease the lookup latency.

5.3.4 Hash Collision Rate

It measures the amount of contents (generated hashes) that are wrongly matched with the cloud server. The smaller hash collision rate becomes best outcome in deduplication, which means hashing technique must

Table 6: Comparison between data deduplication approaches

Algorithm	Description	Merits	Limitations	Remarks			
				Authorized deduplication	Two-side privacy	No centralized management	Trusted third party
EPCDD [31]	Privacy preserving data deduplication in big data cloud	Supports heterogeneous data deduplication in the cloud	Complex indexing (tree construction) and large time consumption in data deduplication	Yes	No	Yes	Yes
ZEUS & ZEUS+ [32]	Privacy aware data deduplication	Secure data deduplication is performed at client and server side	SHA-256 is less secure and not suitable to support for a large number of users	No	Yes	No	No
Heterogeneous data management approach [33]	Data access control and deduplication for different applications	Data confidentiality is improved since it sends input file in encrypted format to cloud	User privacy is neglected and also does not support for practical environments	No	No	Yes	No
Rabin fingerprinting [34]	Data deduplication is achieved before outsourcing data to the cloud	Efficiency of data deduplication is improved	Less scalability and high processing time for large datasets	Yes	Yes	No	No
PHISA [35]	Partial hash information verification string algorithm	Fast hash generation for multimedia files including text, audio, video, and image	Less security due to the use of MD5 hashing function	No	No	No	No
Proposed SEEDDUP	Secure data deduplication, access control before outsourcing to the cloud	High data deduplication efficiency and less lookup latency	Nil	Yes	Yes	Yes	Yes

**Figure 10:** Comparative results on lookup latency (s)

ensure 100% data integrity. High collision rate also leads to loss of data. To present such issues, accurate hashing technique is needed to ensure the file is duplicated.

Figure 11 shows the comparative results on hash collision rate for the proposed SEEDDUP with the five previous approaches. SEEDDUP system has obtained less hash collision rate rather than others.

Figure 11 shows that the proposed SEEDDUP obtained minimum hash collision rate than the other approaches. With the use of SHA3 (512 bits), minimum hash collision rate is obtained. MD5, SHA-256, and other hash generation algorithms cause large hash collision rate although the previous algorithms lead to the high chance of losing data from hash collision. The rate of hash collision between 0 and 1 and also the rate of deduplication rate is also less.

5.3.5 Throughput

It depends on the amount of file size, deduplication rate, and deduplication speed since it is a performance-dependent factor. To achieve higher throughput while deduplication, add large servers, because the single server increases overhead. Figure 12 shows the comparison results on throughput.

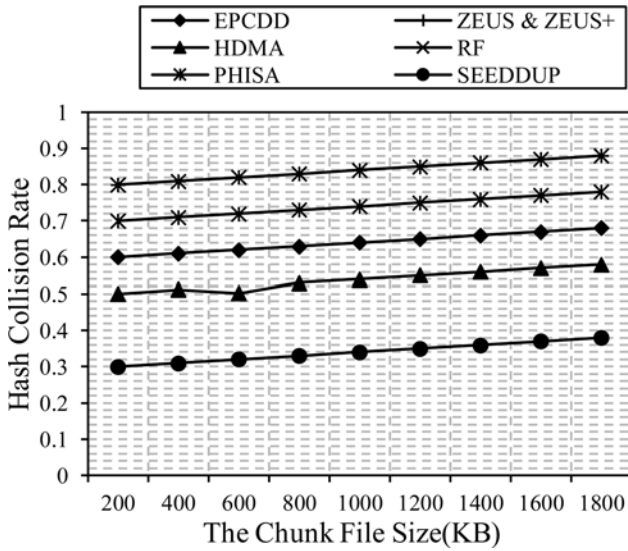


Figure 11: Comparative results on hash collision rate

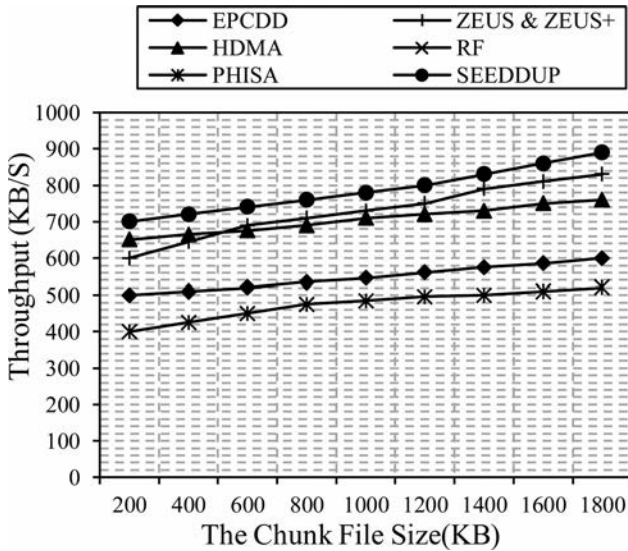


Figure 12: Comparison results on throughput

It shows that chunk size will also increase in throughput. Deduplication in centralized cloud server becomes a bottleneck and it results in more CPU and RAM utilization. An individual server increases throughput and never decreases even a large size of data uploaded for duplication verification. According to the graph, we find that the proposed SEEDDUP system increases throughput with the use of local server's deployment and also proposes novel technique for deduplication. Existing approaches, such as ZEUS& ZEUS+, RF, and PHISA, are implemented in centralized environment and HDMA and EPCDD use domain managers (*i.e.* individual servers) for executing the data deduplication.

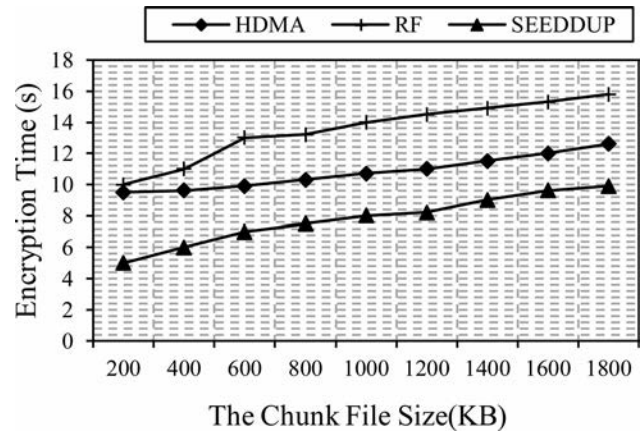


Figure 13: Comparison results on encryption time

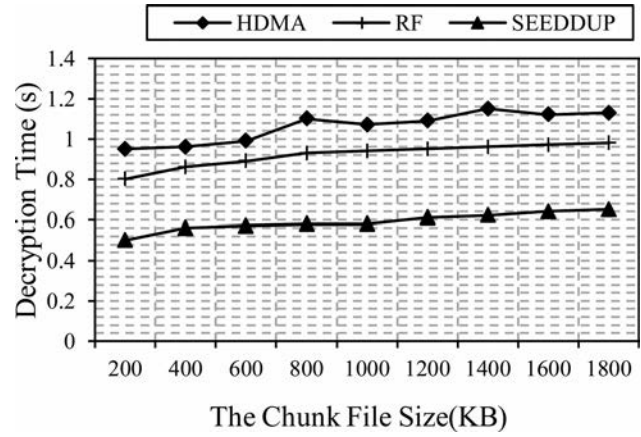


Figure 14: Comparison results on decryption time

5.3.6 Security Strength Measure

Cloud is an untrusted environment which must be important and the best possible security algorithm should be added for secure deduplication. Convergent encryption and message locked encryption are some security methods. These methods satisfy security with either client-side or server-side.

Figures 13 and 14 show the performance evaluation of encryption and decryption time, respectively. HDMA uses message locked encryption to improve the data confidentiality, whereas the RF uses convergent encryption scheme for encryption. These methods are not effective in secure data deduplication since they lack user-side privacy. The proposed SEEDDUP requires less encryption and decryption time. It can achieve its outcome due to the public key cryptosystem called code-based Niederreiter Algorithm. Table 7 shows the security strength analysis of the proposed SEEDDUP system.

Table 7: Security strength analysis

Security Strength	Security parameters				P_{U_k} size (Kbits)	Pr_k size (Kbits) [G(x) L m ⁻¹]
	N	K	T	E		
60 bit (Short-term)	1024	644	38	38	239	(0.37 10 141)
80 bit (Mid-term I)	2048	1751	27	27	507	(0.29 22 86)
128 bit (Mid-term II)	2690	2280	56	57	913	(0.38 18 164)
256 bit (Long-term)	6624	5129	115	117	7488	(1.45 84 2183)

5.3.7 Security Analysis and Results Summary

This section describes the security of the proposed system design. For the secure data deduplication achievement over the cloud, it uses several security mechanisms, and also the proposed system design works against different types of security attacks, including Duplicate Faking Attack, Erasure Attack, Impersonation Attack, Message Sniffing Attack, Man-in-the-Middle Attack, and DoS and DDoS Attack.

(a) Security mechanisms against duplicate faking attack:

In this attack, attacker can compromise the cloud server by acknowledging that he is the data owner so that he can able to replace the original file with the corrupted file. The proposed system prevents this attack by

- Sending the IL request to the cloud server, and then CS searches the lookup table for the presence of the attack. User receives the IL response from the cloud server.
- Based on that message, CS is prevented by the duplicate faking attack

(b) Security mechanisms against Erasure Attack:

Attacker behavior of this erasure attack is very similar to the duplicate faking attack and he/she behavior is to delete file in the cloud server. We prevent this attack by authenticating the user and allowed legitimate users for accessing the files stored in the cloud server. Attacker cannot insert, delete, or modify the files in the cloud server

(c) Security mechanisms against Impersonation Attack:

It is a harmful attack that uses the identity of the legitimate user and acts as legitimate user to access data from the database. This type of attack takes place only when the security credentials of the system are transferred secure to the storage. This type of attack is overwhelmed in the proposed SEEDDUP system. Niederreiter algorithm is presented to ensure secure exchange of the legitimate user's identity.

(d) Security mechanisms against Message Sniffing Attack:

This kind of attacks occurs due to the message

alteration. Integrity is ensured and hence it cannot be extracted by any data theft intermediately. The trustworthiness assured in the data transmission presents to provide integrity in the designed system. In the proposed SEEDDUP, it transmits the data in the form of hashed result; it prevents the attackers to show the original message of a data owner.

(e) Security mechanisms against Man-in-the-Middle Attack

Confidentiality are one of the major constraints in providing security to the system. This constraint denotes the state in which the secret is maintained without any changes. In this proposed SEEDDUP system, the owners and users are enabled to be assured with confidentiality. This is due to the incorporation of lightweight cryptography algorithm that encrypts and decrypts the data from one form to another that can be viewed only by the legitimate entities.

(f) Security mechanisms against DoS and DDoS Attack:

DoS is the denial of service attack which is the type of threat in which the attacker tries to breach out the resources of the cloud server through unauthorized requests and to make the particular service unavailable for authorized users. In this attack, the attacker sends unwanted requests to the victim service. Thus, the cloud server will not able to process the legitimate requests. In DDoS attack, the attacker compromises more than one number of legitimate data owners and users to launch the DoS and DDoS attacks to the multiple cloud servers. To prevent the DDoS attack, authentication is the foremost solution. When users are authorized which eliminate the unnecessary burden of processing the attacker's request.

SEEDDUP three-tier deduplication architecture achieves better performance than the previous approaches. The major benefits in the proposed system are as follows:

- Proposed system allows deduplication of any kinds of input files (multimedia files), such as movie files, documents, MP3, Images, and so on.
- Proposed system presents authorized deduplication in the cloud by registering data owners to the trusted third party. Similarly authorized data retrieval is performed by authenticating data users to the trusted third party. Data users must submit their public keys during requesting of the files to the cloud server.
- Proposed system ensures two-side privacy *i.e.* data owners firstly perform deduplication before outsourcing files to the cloud.
- Proposed system protects highly sensitive data from attackers by invoking dual encryption and also

provides access control that restricts or denies more unauthorized access to the cloud server.

- Proposed system is not application specific which can be supported for various applications and it is easy to implement in practical environment. This system obtains less lookup latency and high deduplication detection rate and also highly secured in the cloud environment.

6. CONCLUSION AND FUTURE WORK

Data deduplication is an efficient technology for eliminating data redundancy and saves large storage space. But various privacy and security issues arise in its usage. Current data deduplication scenario requires good throughput and decreases computation and communicational overheads in cloud. In this work, three-tier SEEDDUP architecture is designed to handle the problem of secure data deduplication in cloud storage. Data privacy is ensured as it only provides access to authorized users and cloud servers provide access to an encrypted file. Experimentation of SEEDDUP system, its performance evaluation with different data formats, and comparison with existing approaches are presented. The proposed SEEDDUP system uses data deduplication for storage efficiency, bandwidth efficiency of the data nodes, and saves encryption and decryption time better than the previous approaches.

In future, perform data deduplication on encrypted data over cloud will be implemented and also use real-cloud storage systems like Amazon Web Services (Amazon EC2, and S3).

REFERENCES

1. E. Bocchi, I. Drago, and M. Mellia, "Personal cloud storage benchmarks and comparison," *IEEE Trans. Cloud Comp.*, Vol. 5, no. 4, pp. 751–64, Dec 2017.
2. D. Harnik, B. Pinkas, and A. Shulman-Peleg, "Side channels in cloud services, the case of deduplication in cloud storage," *IEEE Secur. Priv. Mag.*, Vol. 8, no. 6, pp. 40–7, January 2011.
3. J. Li, X. Chen, X. Huang, S. Tang, Y. Xiang, M. Mehedi Hassan, and A. Alelaiwi, "Secure distributed deduplication systems with improved reliability," *IEEE Trans. Comput.*, Vol. 64, no. 12, pp. 3569–79, 2015.
4. J. Hur, D. Koo, Y. Shin, and K. Kang, "Secure data deduplication with dynamic ownership management in cloud storage," *IEEE Trans. Knowl. Data. Environ.*, Vol. 28, no. 1, pp. 3113–25, Jun 2016.
5. H. Kwon, C. Hahn, D. Kim, and J. Hur, "Secure deduplication system for multimedia data with user revocation in cloud storage," *Multimed. Tools Appl.*, Vol. 76, no. 4, pp. 5889–903, 2017.
6. R. N. S. Widodo, H. Lim, and M. Atiquzzaman, "SDM: smart deduplication for mobile cloud storage," *Future Gener. Comp. Sys.*, Vol. 70, pp. 64–73, 2017.
7. S. Luo, G. Zhang, C. Wu, S. U. Khan, and K. Li, "Boafft: distributed deduplication for big data storage in the cloud," *IEEE Trans. Cloud Comp.*, Vol. 61, no. 11, pp. 1–13, Dec 2015.
8. W. Xia, H. Jiang, D. Feng, and L. Tian, "DARE: A deduplication-aware resemblance detection and elimination scheme for data reduction with low overheads," *IEEE Trans. Comput.*, Vol. 65, no. 6, pp. 1692–705, 2016.
9. A. Venish, and K. Sivasankar. "Study of Chunking algorithm in data deduplication," in *Proceedings of the International Conference on Soft Computing Systems, Adv. Intell. Syst.*, Vol. 398, pp. 13–20, Jan 2016.
10. Y. Yang, X. Qin, G. Sun, Z. Yang, and Z. Zu, "Data deduplication in wireless multimedia monitoring network," *Int. J. Distrib. Sens.*, Vol. 12, 1–7, Dec 2013.
11. X. Li, J. Li, and F. Huang, "A secure cloud storage supporting privacy preserving Fuzzy deduplication," *Soft Comput.*, Vol. 20, no. 4, pp. 1437–48, Jan 2015.
12. J. R. Jane Rubel Angelina, S. Kamaraj, and V. Dharmarajan, "High-speed data deduplication using parallelized cuckoo hashing," *Turk. J. Electr. Eng. Co.*, Vol. 26, pp. 1417–29, Jun 2020.
13. Y. Allu, F. Dougli, M. Kamat, P. Shilane, H. Patterson, and B. Zhu, "Backup to the future: How workload and hardware changes continually redefine data domain file systems," *Computer*, Vol. 50, no. 07, pp. 64–72, Jul 2017.
14. J. Li, X. Chen, M. Li, P. P. C. Lee, and W. Lou, "Secure deduplication with efficient and reliable convergent key management," *IEEE Trans. Parall. Distr.*, Vol. 25, no. 6, pp. 1615–25, Jun 2014.
15. W. Xia, Y. Zhou, H. Jiang, D. Feng, Y. Hua, Y. Hu, W. Zhang, and Q. Liu. "FastCDC: a fast and efficient Content-defined chunking approach for data deduplication", *USENIX Annual Technical Conference (USENIX ATC16)*, Denver, Co, USA, June 2016.
16. R. Chen, Y. Mu, G. Yang, and F. Guo, "BL-MLE: block-level message locked encryption for secure large file deduplication," *IEEE Trans. Inf. Foren. Sec.*, Vol. 10, no. 2, pp. 2643–52, Aug 2015.
17. Y. Shin, and K. Kim, "Efficient and secure file deduplication in cloud storage," *IEICE Trans. Inf. Syst.*, Vol. E97-D, no. 2, pp. 184–97, Feb 2014.

18. E. Daniel, and N. A. Vasanthi, "LDAP: a lightweight deduplication and auditing protocol for secure data storage in cloud environment," *Cluster Comput.*, Vol. 22, 1–12, Nov 2017.
19. R. N. S. Widodo, H. Lim, and M. Atiquzzaman, "A new content defined chunking algorithm for data deduplication in cloud storage," *Fut. Gener. Comp.*, Vol. 71, pp. 145–56, Jun 2017.
20. B. Zhou, S. D. Zhang, Y. Zhang, and J. H. Tan, "A bit string content aware chunking strategy for reduced CPU energy on cloud storage," *J. Electr. Comput. Eng.*, Vol. 2015, 1–9, Aug 2015.
21. S. Singhal, A. Kaushik, and P. Sharma, "A novel approach of data deduplication for distributed storage," *Int. J. Eng. Tech.*, Vol. 7, no. 2.4, pp. 46–52, Mar 2018.
22. B. Mao, H. Jiang, S. Wu, and L. Tian, "Leveraging data deduplication to improve the performance of primary storage systems in the cloud," *IEEE Trans. Comput.*, Vol. 65, pp. 1775–1788, Jul 2015.
23. X. Y. Xuan, X. Nong, L. Fang, S. Zhen, and H. W. Hui, "AR-Dedupe: an efficient deduplication approach for cluster deduplication system," *J. Shanghai Jiaot. Univ.*, Vol. 20, no. 1, pp. 76–81, Jan 2015.
24. J. Xiong, Y. Zhang, X. Li, M. Lin, and Z. Yao, "RSE-PoW: a role symmetric encryption PoW scheme with authorized deduplication for multimedia data," *Mobile Netw. Appl.*, Vol. 23, no. 3, pp. 650–63, 2018.
25. P. Zhang, P. Huang, X. He, H. Wang, and K. Zhou, "Resemblance and merge based indexing for high performance data deduplication," *J. Syst. Softw.*, Vol. 128, pp. 11–24, Dec 2017.
26. K. W. Su, J. S. Leu, M. C. Yu, Y. T. Wu, E. C. Lee, and T. Song, "Design and implementation of various file deduplication schemes on storage devices," *Mobile Netw. Appl.*, Vol. 22, no. 1, pp. 40–50, Jan 2017.
27. B. Zhou, and J. T. Wen, "A data deduplication framework of disk images with adaptive block skipping," *J. Comput. Sci. Technol.*, Vol. 31, no. 4, pp. 820–35, Jul 2016.
28. Z. Sun, J. Shen, and J. Yong, "A novel approach to data deduplication over the engineering-oriented cloud systems, University of Wollongong Australia," *Integr. Comput. Aid. E.*, Vol. 20, no. 1, pp. 45–57, Jan 2013.
29. S. Waghmare, "Authorized deduplication: an approach for secure cloud environment," *Proc. Comput. Sci.*, Vol. 78, pp. 815–23, 2016.
30. S. Jiang, T. Jiang, and L. Wang, "Secure and efficient cloud data deduplication with ownership management," *IEEE Trans. Serv. Comput.*, Vol. 13, 1–14, Nov 2017.
31. X. Yang, R. Lu, K. K. Raymond Choo, F. Yin, and X. Tang, "Achieving efficient and privacy-preserving cross-domain big data deduplication in cloud," *IEEE Trans. Big. Data.*, 1–12, Jun 2017.
32. C. Yu, S. Prasad Gochhayat, M. Conti, and C. S. Lu, "Privacy aware data deduplication for side channel in cloud storage," *IEEE Trans. Cloud Comp.*, Vol. 8, 1–13, Jun 2018.
33. Z. Yan, L. Zhang, W. Ding, and Q. Zheng, "Heterogeneous data storage management with deduplication in cloud computing," *IEEE. Trans. Big Data.*, Vol. 5, 1–15, May 2017.
34. Y. Zhang, H. Su, M. Yang, D. Zheng, F. Ren, and Q. Zhao, "Secure deduplication based on Rabin fingerprinting over wireless sensing data in cloud computing," *Secur. Commun. Netw.*, Vol. 2018, 1–13, Sep 2018.
35. B. K. Kim, S. J. Oh, S. B. Jang, and Y. W. Ko, "File similarity evaluation scheme for multimedia data using partial hash information," *Mob. Netw. Appl.*, Vol. 76, no. 19, pp. 19649–63, Feb 2017.

AUTHORS



B. Rasina Begum received B.E degree from Madurai Kamaraj University and ME degree from Anna University, Chennai, respectively. Now she is working as an Associate Professor in the Department of Computer Science and Engineering at Mohamed Sathak Engineering College, Kilakarai. Her current research focuses on improving security in Cloud Storage. Her research interests include Cloud computing, Network security, and Deduplication. She has published over 10 technical papers in reputed Journals. She is a lifetime member of ISTE.

Corresponding author. E-mail: rasinabegumb@gmail.com



P. Chitra received PhD degree in Computer Science and Engineering from Anna University, Chennai. She received BE and ME Degree from Madurai Kamaraj University and Anna University, Chennai respectively. Now she is working as a Professor in CSE department at Thiagarajar College of Engineering, Madurai. Her current research focuses security for cloud computing systems. Her areas of specialization are High Performance Computing and Multicore processing. She has published 40 technical papers in reputed international journals and conferences. She is a lifetime member of ISTE and CSI.

Email: pccse@tce.edu



Impact of air pollution in health and socio-economic aspects: Review on future approach

R. Sivarethinamohan ^{a,*}, S. Sujatha ^b, Shanmuga Priya ^c, Sankaran ^d, Abdul Gafoor ^e, Zunaitur Rahman ^f

^a Department of Professional Studies, CHRIST (Deemed to be University), Bangalore 560 029, Karnataka, India

^b Department of Civil Engineering, K.Ramakrishnan College of Technology, Trichy 621 112, Tamil Nadu, India

^c Department of Chemical Engineering, Mohamed Sathak Engineering College, Kilakarai 623 806, Tamil Nadu, India

^d Department of Marine Engineering, Mohamed Sathak Engineering College, Kilakarai 623 806, Tamil Nadu, India

^e Department of Civil Engineering, Mohamed Sathak Engineering College, Kilakarai 623 806, Tamil Nadu, India

^f Department of Civil Engineering, Sethu Institute of Technology, Kariapatti 626 115, Tamil Nadu, India

ARTICLE INFO

Article history:

Received 7 August 2020

Accepted 20 August 2020

Available online xxxx

Keywords:

Air pollution

Impact

Psychological

Health hazards and climate

Public health

ABSTRACT

Air contamination is mainly induced by human activity and environmental pollution. Consumption of Air pollution in fewer amounts leads to a significant range of harmful effects on public safety. Nevertheless, with the accelerated pace of economic growth and modernization and the high quantity of electricity need results in huge amounts of pollutants and waste creates significant air pollution. The latest research has shown that because humans only use a tiny part of their day to drive, their constant air quality intake is primarily attributed to the commuting microenvironment. The nature of life on this planet is dependent on clean air. This article presents the literature to include a review of the effect on different facets of human existence of air emissions. The effect is narrowly classified into health and climate change. The study shows that air contamination has a broad variety of consequences, from infectious illnesses and life-threatening disorders and the breakdown of particular organ systems and psychological health. There is no question that this problem has to be addressed with the utmost focus. Such results should be used to prompt further work and to deliver clean air initiatives to officials.

© 2020 Elsevier Ltd. All rights reserved.

Selection and peer-review under responsibility of the scientific committee of the International Conference on Newer Trends and Innovation in Mechanical Engineering: Materials Science.

1. Introduction

About 91 percent of the global population resides in places where access to ambient air contamination value meets the higher than the World Health Organization prescribed guidelines [1]. However, increased use of indoor contaminants to improper cooking methods such as the usage of contaminating stoves and fossil or biomass-based fuels exacerbates these harmful effects [2,3]. The consequences of this treatment can be seen in the occurrence of multiple negative health results comprising respiratory disorders, coronary conditions that contribute to about a quarter of fatalities from stroke or ischemia and a higher risk for dementia in older adults [3]. The significant effect of both indoor and outdoor

emissions on wellbeing has established air quality as a global public health issue [4].

Depression is marked by chronic depressed health, decreased exercise motivation, fatigue, and a reduced energy level and is among the most severe psychotic illnesses [5,6]. Decreasing job efficiency, the diminished standard of living and increased likelihood of all-cause mortality is correlated with depression. Identifying the health risks for distress and designing preventive approaches is also critical in public health [7,8].

Mechanistic experiments have shown that the inhalation of air pollution can activate neurosurgery, oxidative stress, and provoke neurotoxicity of dopamine. Moreover, recent research has found that sensitivity to increased air emissions can influence individuals who were correlated with mental wellbeing and residential comfort [9]. It was thus feasibly believed that air pollution could lead to the pathogenesis of depression. Throughout the past decade, few researchers have studied the connection for both exposure and depression to long- or short-term air emissions [10]. However,

* Corresponding author.

E-mail address: mohan.dimat@gmail.com (R. Sivarethinamohan).

<https://doi.org/10.1016/j.matpr.2020.08.540>

2214-7853/© 2020 Elsevier Ltd. All rights reserved.

Selection and peer-review under responsibility of the scientific committee of the International Conference on Newer Trends and Innovation in Mechanical Engineering: Materials Science.

the findings were conflicting and contradictory; some researchers reported strong associations for air quality while depression and others reported no associations. A recent meta-analysis has found that the odds of depression have been larger, with the increased exposure to environmental fine particulate matter (PM_{2.5}), but not to inhalable particulate matter (PM₁₀) [11].

The number of cars on the streets, industrialization, inflation, urban waste burning, agricultural waste burning, and inadequate transport network, inadequate environmental legislation and much more are growing the air pollution every day [12]. According to World Health Organization statistics, nearly 91 percent of the global population resides in areas that meet the minimum air quality. Many reports regularly illustrate the impacts on public health of air pollution [13]. Therefore, air quality not only influences human wellbeing but also animal well, forestry, climate change, and more [14].

In the studies, the adverse environmental impacts of different aspects of human existence related to air contamination are illustrated, aside from the serious effects of death. Some strategies established to solve air pollution and its impacts also appear in the writings [15,16]. The article aims to incorporate these two factors into a point of reference in-depth for the analysis and research on air quality and to suggest potential steps to change the situation [17]. The air quality effect can be divided into two broad categories: safety effect and socio-economic effects, in compliance with the definition [18]. This review article mainly focused on the health effect on human and climate change due to air pollution.

2. Health impact of air pollution

Air pollution has a large number of adverse impacts on climate change, human wellbeing, wildlife, trees, and the environment. Furthermore, there is proof that air contamination is related to a decrease in people thinking, thus lowering happiness level and raising the risk of depression. Air pollutants that affect the atmosphere of the earth can be classified as primary or secondary. Main contaminants consist of particulate matter (PM_{2.5} or PM₁₀), nitrogen oxides such as carbon monoxides, sulfur oxides, arsenic, volatile organic compounds, and metals such as copper, cadmium, and mercury. Secondary toxins, on the other hand, emerge in the environment as a result of different chemical reactions between specific materials that involve nitrogen oxides which ozone [18,19]. WHO reports indicate 43% of the overall deaths from air emissions related to chronic obstructive diseases of the lung (COPD), 29% to lung cancer, 25% to dental, 24% to stroke, and 17% to pulmonary disease. Lowering air quality environmental impacts is critical in emerging as well as industrialized nations to stable growth. In this article, we examine the impact of air pollution on the lungs, eyes, pulse, blood, skin, and various human organs. The aged and infants suffer the most from air contamination [20]. Some other scholars examine the relationship between air quality with hospital admission and COPD emergency department using common additive models. Their data demonstrate a higher threat of hospitalization of the elderly the major blame is PM₁₀. The remainder of this segment classifies the research on the effect of air quality on different health measurements [12,21].

2.1. Impact on the lungs

The digestive tract is the worst impacted by air contamination by the breath inhaled. Air contamination can trigger various rates of harm to the breathing system based on intake. Through their cohort sample of 217 children living in Southern California, consider that asthma is significantly associated with intake air from traffic. Similarly, Delhi (India) as a research target zone and gather

data from 441 kids in the 7–15 age target range [22]. They notice that infants who elevated particulate pollution (because of the incidence of smoking) in their residences experience additional breathing issues including cough, sneezing, wheezing, severe cold, breathlessness, and inflammation of the mouth. Many researchers also recorded comparable findings, which create a clear correlation between respiratory morbidity and ambient pollution [23].

2.2. Impact on eyes

The environmental contaminants have a clear exposure to these ocular systems owing to frequent interaction of the ambient environment with the cornea, tear material, and conjunctive components. The research working adults at All India Medical Sciences Institute, Delhi (India), who fly by open-air vehicles [24]. They collect information over 10 years on the direction, age, sex, size, and the way we look at the eyes and other parts of the eye. This indicates that the prolonged sensitivity of diverse layers of the retina to polluted air induces itching and redness of the skin, eye diseases, and many others. Based on internal retinal shifts, analysis indicates that PM_{2.5} may represent autonomous glaucoma possible risk [25].

2.3. Impact on skin and hair

In touch with the hair of air contaminants, they are lodged and inflict inflammation and harm to the skin. The correlation among poor air quality and hair loss and weight loss is obvious from numerous studies. Another study states that air contamination sensitivity leads to scalp inflammation, hair damage, hair roots discomfort, scratching, sebaceous formation, pellicles, and even loss of hair [26]. This often affects the skin by altering the color of the skin, dimpling the hair, inducing infections of the flesh, disruption of the flesh's pH balance, and lack of nutrition [27].

2.4. Impact on liver

Particulate matter may play a major role in the development of liver damage. Several reports have shown that hepatotoxic environmental emissions are detrimental to the liver. Hepatocellular Carcinoma HCC is the predominant liver malignancy that affects primarily the liver and cirrhosis-related patients. The research shows that long-term sensitivity to contaminants contributes to HCC through persistent inflammation of the liver. Similar findings have also been recorded which provide a close bond between air pollution and hepatic cell injury, gastrointestinal, and liver cancer [28].

2.5. Impact on bones

Vitamin D deficiency and rickets are linked with air contamination. The impact on bone density is also unfavorable. For kids and teenagers, structural and biochemical bone modifications are critical. In terms of disruption to bones induced by air contamination, infants are the most impacted. The research indicates that Mexico City kids get a vitamin D deficit and elevated interleukin 6 (IL 6) levels. In bone formation, IL 6 plays a crucial function, and its higher absorption contributes to bone loss. In its research, report specific findings for the relationship with bone degradation over time likelihood of bone fracturing of black carbon and PM_{2.5} concentrations. It indicates that the amount of visits for bone fractures in hospitals by people residing in contaminated areas has risen. Numerous other tests have shown the impacts on bones due to air contamination [29].

2.6. Impact on the brain

There is growing research that demonstrates the adverse effects of air emissions on the nervous system. Air emission intake was correlated with memory impairment, reduced IQ and educational output, slower brain growth, and sometimes diminished cognitive ability [30]. Examine the impact of air quality on human actions and decision-making executive capacity. Their studies indicate that air contamination influences cognitive capacity and, very importantly, the aging brain. Several other scholars investigate the connection between long-term sensitivity to automotive pollution prooxidants of behavioral and mental impairments [31]. They create a system of automotive response to exhaust. Their research reveals that repeated sensitivity to vehicle-emitted pro-oxidants contributes to elevated stress, anxiety, and cognitive degradation [32]. Test relationship between vascular dementia (VaD) and air quality treatment. Their research shows that access to NO₂ before a pre-VaD diagnosis is substantially correlated with improved risk of VaD and that CO consumption has a higher effect on VaD incidence [33].

2.7. Impact on cancer

Research often shows a close connection between ozone and cancer emissions. Explain how lung, spine, and head cancer are linked with air exposure. To investigate the connection between lung cancer and cardiopulmonary mortality by particulate air emissions. Studies show that a rise of 10 µg/m³ air emissions from small particulates raises the probability of heart and lung cancer death by about 6% and 8% respectively. In separate research, air quality is related to multiple kinds of cancer [34].

2.8. Impact on birth weight

Newborn babies are known to have a weight of less than 2.5 kg (5 lb and 8 oz) when they are born. There is ample proof that air quality with low birth weight and other harmful effects such as early births are strongly associated. Another study arrives with reasonable findings on the relation between exposure to air pollution during childbirth and birth weight. In a community-based survey of 74,671 pregnant mothers, investigate the correlation between low birth weight and air quality. Throughway of multiple linear and regression analysis, the birth weight falls through 7.3 g and 6.9 g with a rise of 100 µg / m³ in sulfur dioxide and total suspended particles, respectively. In comparison, several other authorities emphasize the correlation between low birth weight air emissions [35].

2.9. Impact on intestines

Issues of intestinal diseases related to air contamination are often reported in the literature. The correlation of air contamination with specific intestinal conditions is observed. They claim that air contamination toxicity contributes to cancer of the digestive tract, gastrointestinal inflammation, and irritable bowel syndrome. An analysis of the effect on appendicitis of air emissions. Their data demonstrate also that short-term air contamination exposures may lead to an odds ratio (OR) of 1.14 for appendicitis. During the season, there are popular data for appendicitis: 1.32 OR for ozone exposure; 1.76 OR for nitrogen dioxide [36].

2.10. Impact on the reproductive system

Air contamination also reveals a certain relation to the weak structure of semen. Lead pollution is a significant problem because it hurts the male reproductive system and reduces the efficiency of

sperm. Research how air quality levels and sexual safety are linked. We were taking measurements of the semen content of a group of young men residing in the Czech Republic between 1993 and 1994 across the winter months. Their results suggest a clear correlation with air quality levels and weak sperm morphology. Research further shows that sensitivity to air pollutants does harm to sperm DNA and thereby raises the risk of adult infertility, pregnancy, and several complications linked to reproduction. Related findings are also documented in many other analyses that research the relation between air pollution and sperm performance changes [12].

2.11. Impact on heart

The connection regarding particulate material and cardiovascular disorders is becoming more evident. This data is in the context of an uptick in hospital visits and fatalities due to incidents of air contamination. Reports show that effect on cardiovascular death from air emissions and particulate matter using Cox's functional vulnerability correlation models they predict the mortality of particulate matter correlated with the cause of deaths. The research shows that particulate matter is closely correlated with cardiovascular disorders, contributing to cardiac attack, cardiac damage, dysrhythmia, and heart arrest. A related cohort analysis of 71,431 middle-aged Chinese men performed in 1990–91 identified a substantial correlation related to particulate air quality and cardiopulmonary disorder [37]. We note that even with a 10 mg/m³ rise in PM₁₀, the likelihood of cardiovascular and breathing mortality decreases by 1.6 percent. A few additional researches have shown a close correlation between particulate matter and cardiac issues [38].

2.12. Impact on diabetes

Research has explored the association between air quality rates and diabetes. Pollutants penetrate our bloodstream and communicate with multiple tissues and areas of the body, which change insulin development, contributing to diabetes. Research the relationship of particulate matter (PM_{2.5} in particular) with diabetes. They employed the methodology of survival simulations to investigate the relation [39]. Their study of 1,729,108 individuals over 8.5 years indicates that an improvement of 10 µg/m³ in PM_{2.5} leads to a higher incidence of diabetes of a hazard level of 1.15 with a trust rate of 95 percent [40,41].

2.13. Impact on subjective of well-being

Besides physiological effects, increased access to air emissions often influences everyday attitude changes, life satisfaction, joy, depression, and more. Their research suggests that low air performance is related to a decrease in the satisfaction that has financial consequences as well. Bad air quality often influences many facets of psychological well-being; it raises the likelihood of suicidal conditions and often decreases satisfaction. Automotive pollutants have since been reported to affect behavioral aberrations, nausea, and hypertension [42].

3. Socio-economic impact of air pollution

3.1. Air pollution impact on mortality

Several reports predict millions of deaths related to air contamination during the entire year. Air contamination has been the world's fourth-largest cause of death. Developing Poisson regression simulations to research the effect of particulate matter on death and demonstrating which a large rise in health gains can

be expected with a minor drop in air quality in clean cities, whereas only marginal health consequences are achievable from a major decline in air quality in comparatively cleaner cities [43]. Create an inclusive population composed of all patient beneficiaries in the United States and measure the probability of mortality and damage to particulate matter and ozone. We predict that a spike in PM_{2.5} and ozone between 10 µg/m³ and 10 ppb raises the likelihood of mortality by 13.6%. Some other studies have reported identical findings, which provide a positive association between mortality and air pollution degree [44]. Nevertheless, wellbeing is not the only victim of air contamination, as stated earlier. A growing body of study links air emissions to socio-economic implications. Socio-economic problems for this topic contribute to social and education results, accessibility, home costs, environment, and atmosphere [45].

3.2. Impact on social and academic outcomes

The research indicates that air contamination will contribute to negative social and educational effects as school and school involvement will decline owing to air contamination consumption. Estimate the connection between air quality and school enrollment. Using institutional details on everyday student illness and missed reports of about 3000 campuses around China, they recognize the detrimental effects of air quality on children's safety, which leads in still further absenteeism contributing to a vicious chain [46]. A similar study explores the impact of air quality on Florida student academics found that students commuting to schools on highways had poorer results of assessments, reduced participation, and a higher probability of behavioral improvements relative to others. They suggest that these results continue past their adolescence and thus influence their cumulative growth [47]. Other researchers are also exposing the connection between air quality with, life fulfillment and profits. Low ambient visibility is a significant factor that needs recognition because of its decreasing effect on socio-economic practices such as transport and living atmosphere pleasantries as well with experimental research, general knowledge confirms a clear correlation among air quality and visibility. Including natural variables such as humidity and wind direction, PM_{2.5} is a primary element liable for visibility changes. Goyal research the visibility of Delhi during the 2006 to 2011 winter period utilizing a regression-based methodology utilizing regular visibility details, certain meteorological variables, and ambient pollution data. Our study indicates a decline in the degree of air quality due to a drop in visibility. Other research has documented related results [48,49].

3.3. Impact on housing prices and economy

During 2005–2013 they concentrate on 286 cities in China and their house prices. Using a statistical model, they assume that a 10 percent rise in levels of PM_{2.5} is equal to a 2.4 percent fall in house prices. We describe this trend around the effect of air pollution and their assessment of asset worth on human resources. Numerous surveys show a correlation between air pollution and the financial markets. The correlation is largely due to air pollution-triggered mood swings, which also influence decision-making [46]. Test the relation between air quality and stock market shifts utilizing linear regression models. They find four significant events that have increased knowledge amongst the Chinese about the public climate. While people are in a favorable state of mindset due to good health, we spend more in the stock market and have more willingness to accept changes. Studies suggest an increase in the index of air quality is adversely associated with market liquidity [50].

3.4. Impact on climate

Research how air pollution deals with the environment. They show that 63.89 percent of the Earth's overall ground region has a detrimental link with air and rainfall. 69.79% of the overall land region indicates a positive association regarding air emissions and climate, which in turn contributes to a deterioration of emissions under global warming, whereas negative associations predominate in cold regimes. This ensures that increasing temperatures in cold regions disrupt the equilibrium of the environment and improve the capacity of emission sources to dispersal [51]. Evapotranspiration serves an important role in climate since it helps to estimate farm water needs, farm yields, land use management, and further. Studies the correlation of particulate matter with evapotranspiration in China's Jing-Jin-Ji area. His research indicates that air quality impacts evapotranspiration by raising the volume of field event radiation found in the environment, which is the primary force of evapotranspiration. This is also proposed that a large PM_{2.5} concentration in the environment will end in less water being sufficient for agriculture. Proof for connecting air pollution with socio-economic externalities is already important and continues to develop. The air quality issue cannot probably be ignored and therefore many measures have been introduced to tackle air pollution [52].

4. Conclusion

The ultimate focus of this article is to elaborate on the impact of air contamination on human health and future measures. This acts as a call into the action of experts and decision leaders that can be seen as a preliminary step to establish innovative air emission management approaches for businesses and public entities. Concerning these subtle measures, the encouragement and development of the usage of public transport would lead, to a decrease in pollution costs. The user experience and attitudes about the usage of public transport need to be known to enhance these implications. Furthermore, models to automate urban transit via city bus and rail will increase the access and also better fight air pollution.

Improved techniques for assessing the human susceptibility to air pollutants should be implemented and more comprehensive concepts and treatment should be introduced for depression. More rigorous mathematical methods can be used, including multi-pollutant analysis, a non-linear examination of correlations, and impact shift evaluation. Many big uncertainty variables will be gathered and modified, including meteorological conditions, vibration, and green room.

Declaration of Competing Interest

The authors declare that they have no known competing financial interests or personal relationships that could have appeared to influence the work reported in this paper.

References

- [1] J. Liu, T. Wu, Q. Liu, S. Wu, J.-C. Chen, Air pollution exposure and adverse sleep health across the life course: a systematic review. *Environ. Pollut.* 262 (2020) 114263, <https://doi.org/10.1016/j.envpol.2020.114263>.
- [2] X. Ma, I. Longley, J. Gao, J. Salmond, Assessing schoolchildren's exposure to air pollution during the daily commute - a systematic review. *Sci. Total Environ.* 737 (2020) 140389, <https://doi.org/10.1016/j.scitotenv.2020.140389>.
- [3] S. Sorte, V. Rodrigues, C. Borrego, A. Monteiro, Impact of harbour activities on local air quality: a review. *Environ. Pollut.* 257 (2020) 113542, <https://doi.org/10.1016/j.envpol.2019.113542>.
- [4] Y. Zeng, R. Liu, L. Li, Y. Liu, Y. Li, Ambient air pollution exposure and risk of depression: a systematic review and meta-analysis of observational studies. *Psychiatry Res.* 276 (2019) 69–78.

- [5] K. Rajak, A. Chattopadhyay, Short and long-term exposure to ambient air pollution and impact on health in India: a systematic review, *Int. J. Environ. Health Res.* (2019) 1–25.
- [6] Brigitte Rooney, Ran Zhao, Yuan Wang, Kelvin H. Bates, Ajay Pillarisetti, Sumit Sharma, Seema Kundu, Tami C. Bond, Nicholas L. Lam, Bora Ozaltun, Li Xu, Varun Goel, Lauren T. Fleming, Robert Weltman, Simone Meinardi, Donald R. Blake, Sergey A. Nizkorodov, Rufus D. Edwards, Ankit Yadav, Narendra K. Arora, Kirk R. Smith, and John H. Seinfeld, Impacts of Household Sources on Air Pollution at Village and Regional Scales in India, 2019.
- [7] R. Sharma, R. Kumar, D.K. Sharma, L.H. Son, I. Priyadarshini, B.T. Pham, D. Tien Bui, S. Rai, Inferring air pollution from air quality index by different geographical areas: case study in India, *Air Qual. Atmos. Health* 12 (11) (2019) 1347–1357.
- [8] K. Shehzad, M. Sarfraz, S.G.M. Shah, The impact of COVID-19 as a necessary evil on air pollution in India during the lockdown, *Environ. Pollut.* 266 (2020) 115080, <https://doi.org/10.1016/j.envpol.2020.115080>.
- [9] M.L. Cropper, S. Guttikunda, P. Jawahar, Z. Lazri, K. Malik, X.-P. Song, X. Yao, Applying benefit-cost analysis to air pollution control in the Indian power sector, *J. Benefit-Cost Anal.* 10 (S1) (2018) 185–205.
- [10] P. Govender, V. Sivakumar, Application of k-means and hierarchical clustering techniques for analysis of air pollution: a review (1980–2019), *Atmos. Pollut. Res.* 11 (1) (2020) 40–56.
- [11] J.G. Lu, Air pollution: a systematic review of its psychological, economic, and social effects, *Curr. Opin. Psychol.* 32 (2020) 52–65.
- [12] S. DeFlorio-Barker, D.T. Lobdell, S.L. Stone, T. Boehmer, K.M. Rappazzo, Acute effects of short-term exposure to air pollution while being physically active, the potential for modification: a review of the literature, *Prev. Med.* 139 (2020) 106195, <https://doi.org/10.1016/j.ypmed.2020.106195>.
- [13] D. Gautam, B.N. Bolia, Air pollution: impact and interventions, *Air Qual. Atmos. Health* 13 (2) (2020) 209–223.
- [14] S.K. Purushothaman, J. Selvam, V. Muthunayanan, Ambient indoor air pollution and its consecutive effect on environment materials and health, *Mater. Today: Proc.* (2020).
- [15] Mohammad Taleghani, Andrew Clark, William Swan, Arash Mohegh, Air pollution in a microclimate: the impact of different green barriers on the dispersion, *Sci. Total Environ.* 711 (2020) 134649, <https://doi.org/10.1016/j.scitotenv.2019.134649>.
- [16] H.R. Anderson, Air pollution and mortality: a history, *Atmos. Environ.* 43(1) (2009) 142–152. A. Sankar, J.S. Coggins, A.L. Goodkind, Effectiveness of air pollution standards in reducing mortality in India, *Resour. Energy Econ.* 62 (2020) 101188.
- [17] Daniele Sofia, Filomena Gioiella, Nicoletta Lotrecchiano, Aristide Giuliano, Mitigation strategies for reducing air pollution, *Environ. Sci. Pollut. Res.* 27 (16) (2020) 19226–19235.
- [18] Jingxin Ma, Yu Qi, Qiuli Shan, Sijin Liu, Hong He, Understanding the knowledge gaps between air pollution controls and health: impacts including pathogen epidemic, *Environ. Res.* 189 (2020) 109949, <https://doi.org/10.1016/j.envres.2020.109949>.
- [19] Charu Gangwar, Ranjana Choudhari, Anju Chauhan, Atul Kumar, Aprajita Singh, Anamika Tripathi, Assessment of air pollution caused by illegal e-waste burning to evaluate the human health risk, *Environ. Int.* 125 (2019) 191–199.
- [20] Sunil Gulia, S.M. Shiva Nagendra, Mukesh Khare, Isha Khanna, Urban air quality management—a review, *Atmos. Pollut. Res.* 6 (2) (2015) 286–304.
- [21] H.K. Suman, N.B. Bolia, Mitigation of overcrowding in buses through bus planning, *Pub. Trans.* 11 (1) (2019) 159–187.
- [22] R. Kumar, J.K. Nagar, H. Kumar, A.S. Kushwah, M. Meena, P. Kumar, et al., Indoor air pollution and respiratory function of children in Ashok Vihar, Delhi: an exposure-response study, *Asia Pac. J. Public Health* 20 (1) (2011) 36–48.
- [23] Alain Robichaud, Paul Comtois, Environmental factors and asthma hospitalization in Montreal, Canada, during spring 2006–2008: a synergy perspective, *Air Qual. Atmos. Health* 12 (12) (2019) 1495–1509.
- [24] Sharon Y.L. Chua, Anthony P. Khawaja, James Morgan, Nicholas Strouthidis, Charles Reisman, Andrew D. Dick, Peng T. Khaw, Praveen J. Patel, Paul J. Foster, The relationship between ambient atmospheric fine particulate matter (PM_{2.5}) and Glaucoma in a large community cohort, *Invest. Ophthalmol. Vis. Sci.* 60 (14) (2019) 4915, <https://doi.org/10.1167/iov.19-28346>.
- [25] Kyoung-Bok Min, Jin-Young Min, Association of ambient particulate matter exposure with the incidence of Glaucoma in childhood, *Am. J. Ophthalmol.* 211 (2020) 176–182.
- [26] R. Rajput, Understanding hair loss due to air pollution and the approach to management, *Hair. Therapy Transplant* 5 (1) (2015) 1–5.
- [27] Kyung Eun Kim, Daeho Cho, Hyun Jeong Park, Air pollution and skin diseases: adverse effects of airborne particulate matter on various skin diseases, *Life Sci.* 152 (2016) 126–134.
- [28] W.C. Pan, C. Da Wu, M.J. Chen, Y.T. Huang, C.J. Chen, H.J. Su, H.L. Yang, Fine particle pollution, alanine transaminase, and liver cancer: a Taiwanese prospective cohort study (TRIVIA-HBV), *J. Natl. Cancer Inst.* 108(12) (2016) 1–7.
- [29] Diddier Prada, Jia Zhong, Elena Colicino, Antonella Zanobetti, Joel Schwartz, Nicholas Dagnacourt, Shona C. Fang, Itai Kloog, Joseph M. Zinuda, Michael Holick, Luis A. Herrera, Lifang Hou, Francesca Dominici, Benedetta Bartali, Andrea A. Baccarelli, Association of air particulate pollution with bone loss over time and bone fracture risk: analysis of data from two independent studies, *Lancet Planetary Health* 1 (8) (2017) e337–e347.
- [30] Xin Zhang, Xi Chen, Xiaobo Zhang, The impact of exposure to air pollution on cognitive performance, *Proc. Natl. Acad. Sci. USA* 115 (37) (2018) 9193–9197.
- [31] Ankita Salvi, Gaurav Patki, Hesong Liu, Samina Salim, Psychological impact of vehicle exhaust exposure: insights from an animal model, *Sci. Rep.* 7 (1) (2017), <https://doi.org/10.1038/s41598-017-08859-1>.
- [32] Chung-Yi Li, Chien-Hsin Li, Santi Martini, Wen-Hsuan Hou, Association between air pollution and risk of vascular dementia: a multipollutant analysis in Taiwan, *Environ. Int.* 133 (2019) 105233, <https://doi.org/10.1016/j.envint.2019.105233>.
- [33] Teresa Corona-Vázquez, Jose De Jesus Flores Rivera, Mayela RodríguezViolante, Amin Cervantes-Arriaga, Air pollution, multiple sclerosis and its relevance to Mexico City, *Arch. Med. Res.* 50 (3) (2019) 111–112.
- [34] I.C.K. Wong, Y.K. Ng, V.W.Y. Lui, Cancers of the lung, head and neck on the rise: perspectives on the genotoxicity of air pollution, *Chin. J. Cancer* 33 (10) (2014) 476–480.
- [35] Stergiani Tsoli, George B. Ploubidis, Olga-Ioanna Kalantzi, Particulate air pollution and birth weight: a systematic literature review, *Atmos. Pollut. Res.* 10 (4) (2019) 1084–1122.
- [36] Leigh A. Beamish, Alvaro R. Osornio-Vargas, Eytan Wine, Air pollution: an environmental factor contributing to intestinal disease, *J. Crohn's Colitis* 5 (4) (2011) 279–286.
- [37] Maigeng Zhou, Yunning Liu, Lijun Wang, Xingya Kuang, Xiaohui Xu, Haidong Kan, Particulate air pollution and mortality in a cohort of Chinese men, *Environ. Pollut.* 186 (2014) 1–6.
- [38] Shovan Kumar Sahu, Hongliang Zhang, Hao Guo, Jianlin Hu, Qi Ying, Sri Harsha Kota, Health risk associated with potential source regions of PM_{2.5} in Indian cities, *Air Qual. Atmos. Health* 12 (3) (2019) 327–340.
- [39] Benjamin Bowe, Yan Xie, Tingting Li, Yan Yan, Hong Xian, Ziyad Al-Aly, The 2016 global and national burden of diabetes mellitus attributable to PM_{2.5} air pollution, *Lancet Planetary Health* 2 (7) (2018) e301–e312.
- [40] Gary O'Donovan, Carlos Cadena-Gaitán, Air pollution and diabetes: it's time to get active!, *Lancet Planetary Health* 2 (7) (2018) e287–e288.
- [41] Ikenna C. Eze, Lars G. Hemkens, Heiner C. Bucher, Barbara Hoffmann, Christian Schindler, Nino Künzli, Tamara Schikowski, Nicole M. Probst-Hensch, Association between ambient air pollution and diabetes mellitus in Europe and North America: systematic review and meta-analysis, *Environ. Health Perspect.* 123 (5) (2015) 381–389.
- [42] Xin Zhang, Xiaobo Zhang, Xi Chen, Happiness in the air: how does a dirty sky affect mental health and subjective well-being?, *J. Environ. Econ. Manag.* 85 (2017) 81–94.
- [43] Qian Di, Yan Wang, Antonella Zanobetti, Yun Wang, Petros Koutrakis, Christine Choirat, Francesca Dominici, Joel D. Schwartz, Air pollution and mortality in the medicare population, *N. Engl. J. Med.* 376 (26) (2017) 2513–2522.
- [44] F.W. Lipfert, An assessment of air pollution exposure information for health studies, *Atmosphere* 6(11) (2015) 1736–1752.
- [45] Ying Zhang, Xingfang Fan, Xiaoling Zhang, Pan Ma, Shigong Wang, Canjun Zheng, Moderately cold temperature associates with high cardiovascular disease mortality in China, *Air Qual. Atmos. Health* 12 (10) (2019) 1225–1235.
- [46] Shiyi Chen, Hao Jin, Pricing for the clean air: evidence from Chinese housing market, *J. Cleaner Prod.* 206 (2019) 297–306.
- [47] J. Heissel, C. Persico, D. Simon, Does pollution drive achievement? The effect of traffic pollution on academic performance, *Natl. Bureau Econ. Res.* (2019) (w25489).
- [48] Tingru Yang, Wenling Liu, Does air pollution affect public health and health inequality? Empirical evidence from China, *J. Cleaner Prod.* 203 (2018) 43–52.
- [49] P. Goyal, S. Budhiraja, A. Kumar, Impact of air pollutants on atmospheric visibility in Delhi, *Int. J. Geol. Agri. Environ. Sci.* 2 (2) (2014).
- [50] Xubiao He, Yi Liu, The public environmental awareness and the air pollution effect in Chinese stock market, *J. Cleaner Prod.* 185 (2018) 446–454.
- [51] Huihui Feng, Bin Zou, Jinyan Wang, Xiaodong Gu, Dominant variables of global air pollution-climate interaction: geographic insight, *Ecol. Ind.* 99 (2019) 251–260.
- [52] Ling Yao, Causative impact of air pollution on evapotranspiration in the North China Plain, *Environ. Res.* 158 (2017) 436–442.

- packed column. *Environ Technol* 26:267–276. <https://doi.org/10.1080/09593332608618566>
36. Smebye AB, Sparrevik M, Schmidt HP, Comelissen G (2017) Life-cycle assessment of biochar production systems in tropical rural areas: comparing flame curtain kilns to other production methods. *Biomass Bioenergy* 101:35–43. <https://doi.org/10.1016/j.biombioe.2017.04.001>
37. Lehmann J, Rillig MC, Thies J, Masiello CA, Hockaday WC, Crowley D (2011) Biochar effects on soil biota – a review. *Soil Biol Biochem* 43:1812–1836
38. Silva JP, Canchala TR, Lubberding HJ, Peña EJ, Gijzen HJ (2016) Greenhouse gas emissions from a tropical eutrophic freshwater wetland. *Int J Environ Ecol Eng* 10(5):541–547. <https://doi.org/10.5281/zenodo.1124217>

Publisher's note Springer Nature remains neutral with regard to jurisdictional claims in published maps and institutional affiliations.



Biodecolorization of Reactive Red 120 in batch and packed bed column using biochar derived from *Ulva reticulata*

Madhu Kumar¹ · Ravindiran Gokulan² · Sivarethnamohan Sujatha³ · Siva Pathanjali Shanmuga Priya⁴ · Saravanan Praveen² · Sellappan Elayaraja⁵

Received: 29 September 2020 / Revised: 28 November 2020 / Accepted: 29 December 2020

© The Author(s), under exclusive licence to Springer-Verlag GmbH, DE part of Springer Nature 2021

Abstract

A seaweed *Ulva reticulata* was used to synthesis biochar, and it was used in the removal of Reactive Red 120 (R120). The optimum thermal pyrolysis temperature was found to be 300 °C, and it was confirmed by proximate and elemental analysis of the biochar. The practical applicability of this biochar was explored by conducting the experiments in batch and continuous mode. An up-flow packed bed reactor was used to study the removal of reactive red 120 in continuous mode. The operating parameters like solution pH, contact time, biochar dosage, temperature, initial concentration were studied. A four-parameter model Fritz-Schlunder-IV and pseudo-first-order kinetic model best fitted the experimental uptake with a correlation coefficient of 0.9996 and 0.9951, respectively. The maximum removal efficiency and uptake capacity of 84.2% and 210.5 mg/g were obtained at operating conditions of pH of 2, biochar dosage of 2 g/L, temperature of 30 °C, and initial concentration of 500 mg/L. The partition coefficient was studied to overcome the limitation of the adsorption capacity, and the highest partition coefficient was obtained as 4.13 L/g at 100% breakthrough time with a removal efficiency and uptake capacity of 89.2% and 111.5 mg/g. The thermodynamic study concluded that reactions are spontaneous and endothermic. The continuous study concluded that the uptake capacity of 100.71 mg/g was obtained at operating conditions of bed depth of 25 cm, the flow rate of 0.48 L/h, and initial dye concentration of 250 mg/L.

Keywords Biochar · Modeling · Packed bed · Reactive red 120 · *Ulva reticulata*

1 Introduction

Water demand was considered as one of the emerging problems in the modern world. The usage of water has been increased from the past decade, and it was due to an increase in population and industries. This increase in population and an

increase in industries resulted in the generation of a huge quantity of water pollution, and this was considered a major concern for the environment [1]. This water pollution was having a direct impact on the environment that was having the potential of degrading the quality of the water and affects the entire ecosystem. So, special attention has to be taken

✉ Ravindiran Gokulan
gokulravi4455@gmail.com

Madhu Kumar
kumargeo_77@gct.ac.in

Sivarethnamohan Sujatha
sujalalit@gmail.com

Siva Pathanjali Shanmuga Priya
priyaa.kumaran@gmail.com

Saravanan Praveen
praveensarvan@gmail.com

Sellappan Elayaraja
elayaraja86@gmail.com

¹ Department of Civil Engineering, Government College of Technology, Coimbatore, Tamil Nadu 641013, India

² Department of Civil Engineering, GMR Institute of Technology, Rajam, Srikakulam, Andhra Pradesh 532127, India

³ Department of Civil Engineering, K. Ramakrishnan College of Technology, Trichy, Tamil Nadu 621112, India

⁴ Department of Chemical Engineering, Mohamed Sathak Engineering College, Ramanathapuram 623806, India

⁵ Department of Civil Engineering, PSG Institute of Technology and Applied Research, Coimbatore, Tamil Nadu 641062, India

Published online: 06 January 2021



PRINCIPAL
MOHAMED SATHAK ENGINEERING COLLEGE
KILAKARAI - 623 806.

Springer

towards water and wastewater pollution, since it was becoming a major issue recently. Many laws and legislation were framed at the national and international levels to reduce and dispose of this pollution, but still, the efficiency of the treatment became a major challenge in recent years [2].

Nature has its self-purification capacity, but natural phenomenon like oxidation, reduction, sunlight, and photosynthesis process can recycle and degrade the pollution to some extent, but when the pollutions are overloaded, it will result in the depletion of the dissolved oxygen in the water and destroys the self-purification process. Even a very less quantity of 1 mg/L of pollution will take more time to be entirely degraded from the ecosystem [3]. These pollutants will react with other agents and form secondary pollutants to the environment. So, pollutants that are generated from the industries are to be removed completely before it was mixing with the nearby water bodies.

Many conventional methods are adopted for the treatment of these pollutants from the industries, and it was broadly classified into physical, chemical, and biological methods [4]. Methods such as oxidation, reduction, electrochemical, ion exchange, coagulation, precipitation, membrane technology, and adsorption were effectively used for the removal of the pollutants [5, 6]. But the cost of the treatment in removing these pollutants has become the biggest challenge since it was not economical, and many industries are not able to meet the required environmental standard as framed by the environmental agencies. So, adsorption was considered as one of the cost-efficient treatment technologies, since the treatment cost associated with the adsorption was comparatively less when compared with the other treatment methods. Many materials like activated carbon, zeolite, alum, lime, and silica were used and the cost of these materials are also considerably high [7]. Recently, many research has been carried out to produce low-cost adsorbent from the biomass of plants and named as the biosorption process.

Recently, biosorption plays a very important role in the removal of pollutants namely dyes and heavy metals. The dead biomass of the plants was modified using physical, chemical, and thermal conversion, and it was used as a low-cost biosorbent. Many materials like a crab shell, coconut shell, groundnut shell, rice straw, seaweeds, and palm shell and many naturally available seeds and leaves of the plants are also used as a biosorbent [8, 9]. But the efficiency of this biosorbent was based on the functional groups and binding sites available on the surface of the adsorbent. To overcome this problem, recently, biochar, a carbon-rich material produced from biomass under slow thermal pyrolysis in the absence of oxygen, was used for the removal of heavy metals and dyes [10]. The functional groups, binding sites, and surface area of the biochar were very high when compared with the raw biosorbent, and this will enhance the uptake capacity of the biochar [11, 12].

The present study investigated the synthesis of novel biochar under slow thermal pyrolysis from marine seaweeds *Ulva reticulata*. Generally, the *Ulva* group is very rich in carboxyl, amines, and amide groups, and these are considered as the effective functional groups for the adsorption of pollutants onto the surface of the biochar. *Ulva reticulata* was commonly available in South India in the east coastal region of Andhra Pradesh and Tamil Nadu in huge quantities. Naturally, this seaweed was overgrown and synthesis of biochar from *Ulva reticulata* for the removal of reactive red 120 was not reported. Since this biomass was available in huge quantity, it will be considered as an alternate material for the treatment, and this will also result in the solution for eutrophication [13]. The adsorption mechanism of the biochar was evaluated using adsorption capacity and the partition coefficient [14].

2 Materials and methods

2.1 Chemical and biochar preparation

Reactive Red 120 (R120) and all other chemicals were procured from Sigma Aldrich, India. The structural composition of the R120 is given in Fig. 1. Reactive Red 120 was denoted by $C_{44}H_{24}C_{12}N_{14}O_{20}S_6Na_6$ as Empirical formula, 1469.98 g/mol as molecular weight, and 515 nm as wavelength. *Ulva reticulata*, a green seaweed, was collected from the eastern coastal region of south India. The collected seaweed was preliminarily treated with distilled water to remove the dirt particles and other impurities present on the surface. After washing, it was kept in an open atmosphere under sunlight for 3 days. The sun-dried biomass was shredded into small particles and kept in the hot air oven for 1 day at 103 °C, to ensure the complete removal of the moisture content. Finally, the biomass was kept in a muffle furnace under the absence of oxygen for 20 min at a pyrolysis temperature of 300 °C at a heating rate of 5 °C/min. The muffle furnace was cooled, and the obtained biochar was used for further studies [15].

2.2 Adsorption and desorption studies

The batch adsorption studies were carried out in a conical flask with a working volume of 100 mL. The conical flask was kept in a temperature-controlled rotating orbital shaker for 360 min at a rotating speed of 180 rpm. Once the equilibrium contact time was completed, the desired volume of the sample was collected and kept in a centrifuge for 5 min that was rotated at 2400 rpm. Then, the sample was taken out, the supernatant and pellet were separated, and the collected supernatant was used to measure the final concentration using UV-Visible double-beam spectrophotometer at 515 nm. Desorption studies were carried out with the same procedure

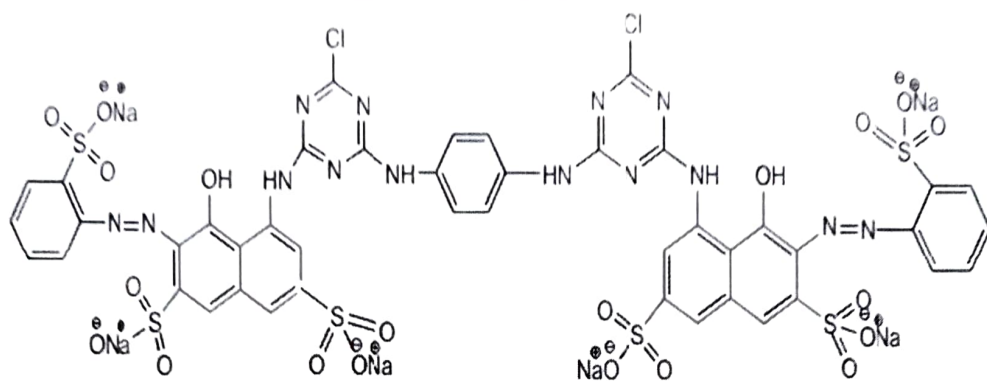


Fig. 1 The structural composition of Reactive Red 120 (R120) [16]

as followed for the adsorption studies, but the contact time was reduced to 30 min [15].

Equations 1 and 2 were used to calculate the % removal of dye and uptake capacity of biochar:

$$Q = V(C_0 - C_e) / W \quad (1)$$

$$\text{Removal efficiency} = \frac{(C_0 - C_e)}{C_0} \times 100 \quad (2)$$

where V —total volume of dye to be treated (L), C_0 —concentration before adsorption (mg/L); C_e —Concentration after adsorption (mg/L), W —total mass biochar used for adsorption (g) [3].

2.3 Partition coefficient

Commonly, the materials that were used for the removal of heavy metals or dye molecules were described based on the adsorption capacity and the removal efficiency. But, it was not meaningful without comparing it with the partition coefficient. Since, with an increase in initial concentration, the adsorption capacity of the adsorbent may increase, it was tough to consider the optimum initial concentration for the maximum removal of pollutants. In this concern, the partition coefficient was used to understand the real performance of an adsorbent in the removal of adsorbate from the aqueous solution. So, the optimum initial dye concentration was fixed using the adsorption capacity and the partition coefficient. The partition coefficient (PC) was calculated using Eq. 3 [17] or 4 [18]:

$$PC = \frac{Q_e}{C_f} \quad (3)$$

$$PC = \frac{Q_e}{\frac{C_f}{MW}} \quad (4)$$

where PC is the partition coefficient (L/g) or (mg/g/ μ mol); Q_e is adsorption capacity (mg/g); C_f is the final dye concentration (mg/L); MW is molecular weight of the dye molecules (μ Mole) [17, 18].

2.4 Biosorption isotherm models and kinetic models

The experimental uptake was compared with different isotherm models and kinetic models to understand the adsorption mechanism, optimum initial concentration and contact time required for the maximum biosorption of dye by the biochar. Different isotherm models namely the four-parameter model (Fritz-Schlunder-IV), three-parameter model (Sips, Toth, Hill, Redlich-Peterson, Radke-Prausnitz, Fritz-Schlunder-III, Vieth-Sladek, Unilin) and two-parameter model (Langmuir, Freundlich) were compared. Kinetic models namely pseudo-first-order (PFO) and pseudo-second-order (PSO) kinetic model were studied. [19].

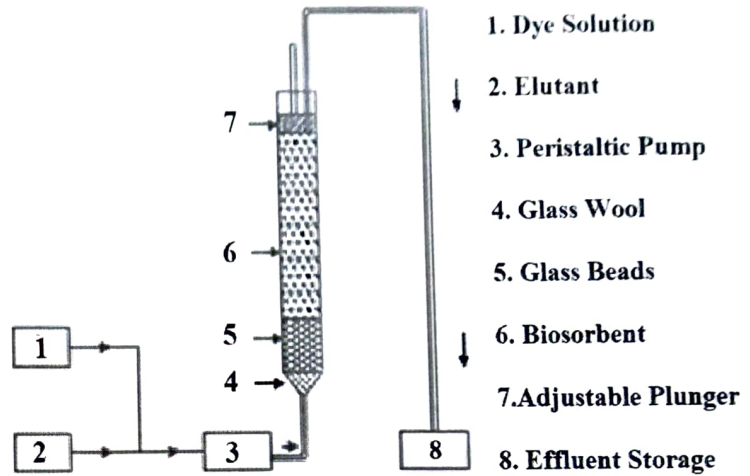
3 Biochar characterization

Characterization of biochar was analyzed using different instruments to understand the adsorption mechanism, surface morphology, chemical composition, and other characteristics of the biochar. A scanning electron micrograph (ZEISS-Gemini) was employed to understand the surface morphological changes. A Fourier transform infrared spectroscopy (Thermo Scientific Ltd., USA, and Nicolet 6700) was analyzed to confirm the presence of different functional groups of the biochar involved in dye removal. The elemental analyzer (2400 Series II-PerkinElmer) and proximate analyses were conducted to find the composition of the biochar. BELSORP mini II by Microtrac BEL Corp surface area analyzer was used to find the surface area and pore volume of the biochar.

3.1 Continuous studies

To study the practical applicability of the biochar in a real wastewater scheme, a packed bed column was designed to check the efficiency of the biochar to continuously adsorb the biochar (Fig. 2). The potential of the biochar was analyzed by varying different operating parameters namely bed height

Fig. 2 Experimental setup for continuous study [20]



(15, 20 and 25 cm), flow rate (0.3, 0.48 and 0.6 L/h), and initial dye concentration (100, 200, and 250 mg/L). The packed bed column was designed based on the recommendation given by Gokulan et al. [20].

3.2 Column data analysis

The column parameters, namely, overall sorption zone (Δt), the total treated volume of the dye (V_{eff}), the total mass of dye (m_{tot}), and the total dye removal, were calculated using Eq. 5 to 8:

$$\Delta t = t_e - t_b \quad (5)$$

$$V_{eff} = F \cdot t_e \quad (6)$$

$$m_{tot} = \frac{C_0 \cdot F \cdot t_e}{1000} \quad (7)$$

$$\text{Total dye removal (\%)} = \frac{m_{adsorb}}{m_{total}} \times 100 \quad (8)$$

where t_b —breakthrough time (h); t_e —exhaustion time (h), F —flow rate (L/h); C_0 —initial dye concentration (mg/L); m_{adsorb} —total mass of the dye adsorbed to the biochar (mg); m_{total} —total mass of the dye entered into the column (mg) [20].

3.3 Modeling of column data

The two different models as given in Eq. 9 and 10 were employed to validate the experimental uptake:

$$\begin{aligned} \text{Modified dose-response model (MDR Model)} &: \frac{C}{C_0} \\ &= 1 - \frac{1}{1 + \left(\frac{V_{eff}}{b_{mdr}}\right)^{a_{mdr}}} \quad (9) \end{aligned}$$

$$\begin{aligned} \text{Yoon-Nelson model (YN Model)} &: \frac{C}{C_0} \\ &= \frac{\exp(k_{YN}t - \tau k_{YN})}{1 + \exp(k_{YN}t - \tau k_{YN})} \quad (10) \end{aligned}$$

where V_{eff} —the volume of dye solution (L); a_{mdr} and b_{mdr} —MDR model constant; τ —YN model constant (min); k_{YN} —rate constant of the YN model (1/min), t —time (min) [20].

4 Result and discussion

4.1 Biochar characterization

Scanning electron micrographs of biochar before and after treatment is given in Fig. 3. From Fig. 3, it was clear that the surface of biochar has been modified after the adsorption of dyes onto the surface of the biochar. The raw biochar was found to have many pores and that has happened due to the thermal decomposition of the raw biomass under slow pyrolysis. These pores will act as an effective binding site that will involve in the binding of the dye molecules when it comes into contact with the biochar during adsorption. After adsorption, a considerable amount of dyes has been bounded onto the surface of the biochar, and the pores are filled with dye molecules, which resulted in the formation of a smooth biochar surface.

The adsorption of dye molecules onto the surface of the biochar will not occur only due to the presence of the binding sites or the pores, but the functional groups present on the surface of the biochar also plays a very important role in the adsorption of the dye molecules. So, to confirm the existence of different functional groups on the surface of the biochar, FT-IR analyses were conducted. The results confirmed the presence of

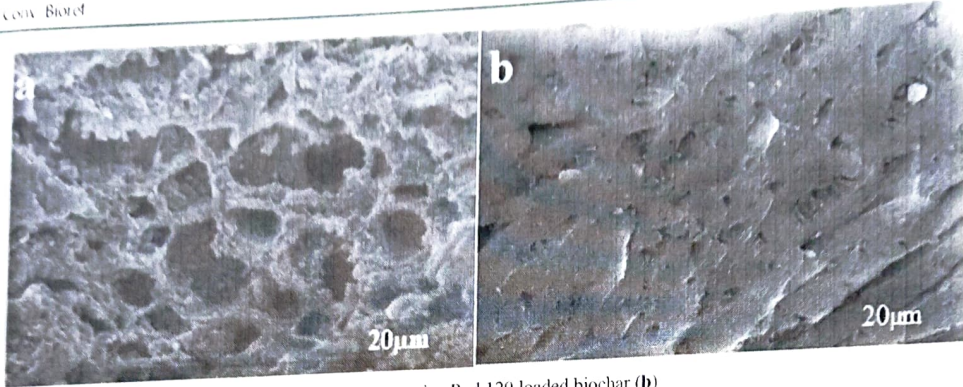


Fig. 3 Scanning electron microscope of raw biochar (a) [15]. Reactive Red 120 loaded biochar (b)

different functional groups on the surface of the biochar, and it was also confirmed that certain spectra peaks were changed or shifted to a new position, and it may happen due to the adsorption of the dye molecules to the biochar. For instance, the results confirmed the presence of the strong bands at 1121 (C–O band), 1423 (symmetric C=O), 1631 (asymmetric C=O stretch of COOH), 2984 (C–H stretch), and 3477 (–NH, –OH stretching). But after adsorption, these functional groups attained a new position at 1129 (C–O (alcohol) band), 1439 (symmetric C=O), 1635 (asymmetric C=O), 2989 (C–H stretch), and 3485 (–NH, –OH stretching) [15].

During the slow thermal pyrolysis process, the composition of the biomass will vary, and it will be confirmed by conducting the proximate and ultimate analysis. Table 1 summarizes the different composition of the biochar concerning proximate and ultimate analysis. The total carbon content of the biochar was found to be $41.2 \pm 1.2\%$, and it shows that the selected biomass was capable of producing a high content of carbon. The decreased ratio of hydrogen to carbon (H/C) confirms that the biochar was composed of aromatic structures [21]. The proximate analysis concluded that the selected biomass was having an ash content of 26.99 ± 0.26 and moisture content of 20.67 ± 0.27 . This shows that the biomass was capable of undergoing thermal decomposition and decomposed in slow thermal pyrolysis with a maximum yield.

BET analyses were conducted to find the specific surface area and average pore size of the biochar. Table 2 summarized the different parameters obtained in BET analyses. The average pore size of the biochar was found to be 0.48 nm with a specific surface area of $459.2 \text{ m}^2/\text{g}$. The pore capacity analyses confirmed that the adsorption had occurred due to the presence of micropore, mesopore, and macropore. About

60.31% of the total dye bounded was due to mesopore capacity, and 18.65 and 11.50% was due to macropore and micropore capacity. From this study, it can be concluded that the maximum removal happened due to the mesopore structure of the biochar. These results are the indication of the porous nature of the biochar and during slow thermal pyrolysis, the biomass has been broken down into several pores and resulted in the formation of binding matrixes on the surface of the biochar [22, 23]. Many researchers suggested that time and temperature during pyrolysis will increase the surface area of the biochar and pore formation [24], and this may happen due to the presence of cellulose, hemicellulose, and lignin that will breakdown and form cracking of organic compounds [25].

4.2 Effect of biochar dosage

The mass of biochar used in the removal of a dye decides the economy of the treatment. Since the cost involved in the production of the biochar was comparatively high, the optimum mass of biochar is used for the maximum removal of the dye. To study the impact of biochar dose, a varying dose from 1 to 10 mg/L was selected while other parameters were maintained as constant. Figure 4 explores the impact of dose on dye removal; it clearly shows that an increase in dose increased the dye removal and decreased the uptake of the dye molecules. For instance, the removal efficiency increased from 43 to 91% whereas the uptake capacity decreased from 215 to 45.5 mg/g when the dose was increased from 1 to 10 mg/L. The decreased uptake at increased dose may be due to the availability of excess surface area to the less concentration of the dye molecules, so not all the binding sites are utilized for the dye removal toward its less concentration [26, 27]. But at a lower

Table 1 Proximate and ultimate analysis

Elemental analysis	C (%)	H (%)	O (%)	N (%)	S (%)
	41.2 ± 1.2	2.6 ± 0.2	14.6 ± 0.8	3.4 ± 0.2	1.9 ± 0.8
Proximate analysis	Moisture	Ash	Fat	Protein	Carbohydrate
	20.67 ± 0.27	26.99 ± 0.26	0.33 ± 0.01	5.54 ± 0.02	45.52 ± 0.04

Table 2 Surface area analysis of *Ulva reticulata*-derived biochar

Parameter	Value
Size of Pore (nm)	0.48
Capacity of pore (cm ³ /g)	0.252
Capacity of micropore (cm ³ /g)	0.029
Capacity of mesopore (cm ³ /g)	0.152
Capacity of macropore (cm ³ /g)	0.047
Surface area (m ² /g)	459.2

dose, the total available binding sites are completely utilized for the adsorption of the dye molecules. Biochar dosage of 2 was considered as the optimum dosage with a removal efficiency of 84.2% and the uptake capacity of 210.5 mg/g.

4.3 Effect of pH

To study the effect of pH, a varying pH from 1.75 to 5 was selected. Figure 5 shows the impact of solution pH on dye removal, and it was concluded that an increase in pH decreased the removal efficiency and uptake capacity of biochar. For instance, the removal efficiency was decreased from 84.4 and 37%, and uptake capacity also decreased from 211 and 92.5 mg/g when pH was increased from 1.75 and 5. The increased removal efficiency at more acidic conditions may be due to the available H⁺ ions. These H⁺ ions are found to be maximum at a pH of 1.75 then at a pH of 5. Since the reactive dyes are negatively charged ions, it will move toward the positively charged ions during adsorption, and this has resulted in the maximum adsorption of the dye molecules [28]. On contrary, at increased pH, repulsive electrostatic forces may occur and decrease the adsorption of negatively charged ion onto positively charged biochar [2]. When pH is raised from 1.75 to 2, the removal efficiency was decreased from 82.4 to

84.2% and uptake capacity was decreased from 211 to 210.5 mg/g, which shows only a difference in removal efficiency of 0.2% was noticed. So, a pH of 2 was selected as optimum for further biosorption studies.

4.4 Effect of temperature

A varying temperature of 20 to 45 °C was selected to study the effect of temperature on the dye removal efficiency. From Fig. 6, it was concluded that the increase in temperature increased the removal efficiency. For instance, the removal efficiency increased from 78.2 to 86% when the temperature was raised from 20 to 45 °C. This indicates that the reactions are endothermic since in an endothermic reaction, the uptake capacity increases with an increase in temperature. An increase in temperature will result in the enlargement of the pore size and also increase the energy for the dye molecules to get interaction with the biochar, and this may result in the increased uptake capacity at higher temperatures [29]. Considering the economic aspect and average room temperature, 30 °C was considered as the optimum since the difference in removal efficiency between 30 and 45 °C was found to be only 1.8%. Thermodynamic parameters, namely, standard free energy (ΔG°), standard enthalpy (ΔH°), and standard entropy (ΔS°) were calculated by fixing the initial concentration as 0.05, 0.1, 0.25, 0.5, 0.75, and 1 mmol/L, and the study was conducted at three different temperatures 293, 303, and 313 K [3]. Standard free energy (ΔG°) was calculated as -6.28, -7.80, and -7.98 KJ/mol for temperatures of 293, 303, and 313 K, respectively. Similarly, standard enthalpy (ΔH°) of 18.86 KJ/mol and standard entropy (ΔS°) of 29.09 J/mol/K were obtained. The negative value of ΔG° and positive value of ΔH° indicates that the reactions are spontaneous and endothermic reaction [3]. These thermodynamic results are confirming the results of the batch studies. Since the ΔH° was less than 80 KJ/mol, the adsorption was favored by

Fig. 4 Influence of biochar dosage on Reactive Red 120 (R120) removal and uptake capacity

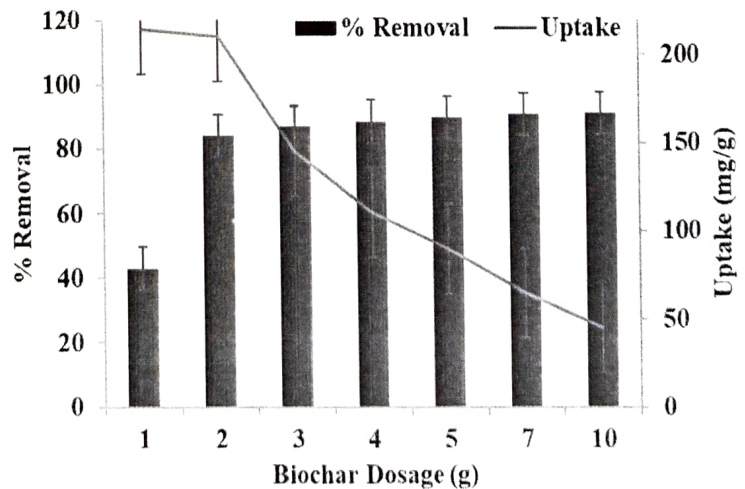
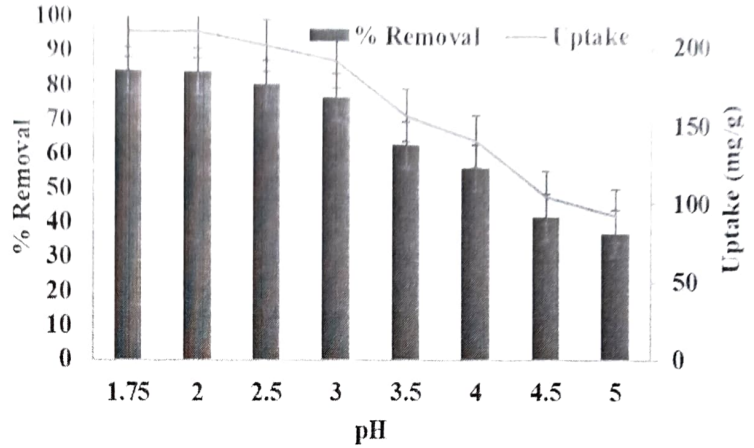


Fig. 5 Influence of pH on Reactive Red 120 (R120) removal and uptake capacity



physisorption [3]. The positive values of ΔS° also indicated the affinity of the biochar toward dye molecules and show the increased solid to liquid interface and also confirm the structural changes happened onto the biochar [3].

4.5 Biosorption isotherm studies

Table 3 and Fig. 7, demonstrate the various adsorption isotherm model constants and predicted uptakes. A varying initial concentration was selected to understand the adsorbent and dye molecule interaction, and different isotherm models were validated with the experimental uptake [30]. Figure 7 indicates that increase in dye concentration increased the uptake capacity and decreased removal efficiency. For instance, the removal efficiency was decreased from 89.4 to 53.7%, and uptake capacity was increased from 22.35 to 268.5%, when the initial dye concentration was increased from 50 to 1000 mg/L. The increased uptake at higher concentration shows the highest affinity of biochar toward the dye molecules to adsorb. The different isotherm models studied to understand the adsorption mechanism is given in Table 4. The best fit model was concluded based on the correlation coefficient

(R^2). Based on the correlation coefficient (R^2), a four-parameter model Fritz-Schlunder-IV was found to be the best-fit model with the experimental uptake, since it showed the highest correlation coefficient of 0.9996. The three-parameter model has also predicted the experimental uptake with a correlation coefficient always greater than 0.9902. But the two-parameter model predicted the experimental uptake with the lowest correlation coefficient of 0.9828. From the isotherm study, it was concluded that the correlation coefficient of different models was in the order of Fritz-Schlunder-IV (0.9996) > Sips (0.9995) > Toth (0.9995) > Hill (0.9997) > Redlich-Peterson (0.9982) > Radke-Prausnitz (0.9973) > Fritz-Schlunder-III (0.9972) > Vieth-Sladek (0.9959) > Unilin (0.9902) > Langmuir (0.9896) > Freundlich (0.9828).

4.6 Biosorption kinetic studies

Biosorption kinetic study was conducted at a different initial concentration varying from 100 to 1000 mg/L at a varying time interval from 0 to 360 min [11]. Figure 8a and b explore the experimental and predicted uptakes of different kinetic models. Table 4 summarizes the different constants of kinetic models.

Fig. 6 Influence of temperature on Reactive Red 120 (R120) removal and uptake capacity

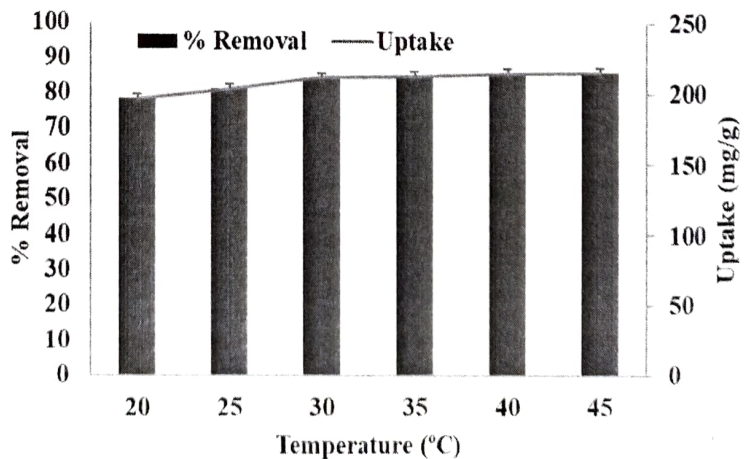


Table 3 Biosorption isotherm constants

Model	Parameter	Values	Model	Parameter	Values
Two-parameter model					
Freundlich	K_f	21.7357	Langmuir	Q_0	100
	$1/n_f$	0.47018		b	0.22607
	R^2	0.88283		R^2	0.87489
Three-parameter model					
Redlich-Peterson	K_{RP}	5.02826	Vieth-Sladek	Q_{MVS}	575.984
	α_{RP}	0.00479		B_{VS}	0.00948
	β_{RP}	1.20386		N_{VS}	1.3371
	R^2	0.99817		R^2	0.99585
Sips	K_S	1.79872	Radke-Prausnitz	Q_{MRP}	573.228
	β_S	1.41207		K_{RP}	0.00954
	a_S	0.00648		n_{RP}	1.33379
	R^2	0.9995		R^2	0.99731
Toth	Q_{max}	271.153	Fritz-Schlunder-III	Q_{MFS}	0.0048
	b_T	0.01622		K_{FS}	1048.4
	n_T	0.51526		N_{FS}	1.20383
	R^2	0.99949		R^2	0.99721
Hill	q_{mH}	282.743	Unilin	Q_{MU}	0.002
	n_H	1.37543		A_U	2315.26
	K_H	142.27		B_U	1.35001
	R^2	0.99937		R^2	0.99018
Four-parameter model					
Fritz-Schlunder-IV	A_{FS}	2.50756			
	a_{FS}	1.26732			
	B_{FS}	0.00583			
	B_{FS}	1.33859			
	R^2	0.99963			

Q_{max} in mg/g, b_T in L/mg, K_f in mg/g, (L/g)^{1/n_f}, K_S in (L/g)^{β_S}, a_S in L/mg, β_S , K_{RP1} in l/g, K_{RP2} in l/mg, q_{m1} in mg/g, q_{MRP} in mg/g, q_{MFS} in mg/g, q_{mU} in mg/g, q_{mM1} in mg/g

Fig. 7 Predicted uptakes of isotherm models

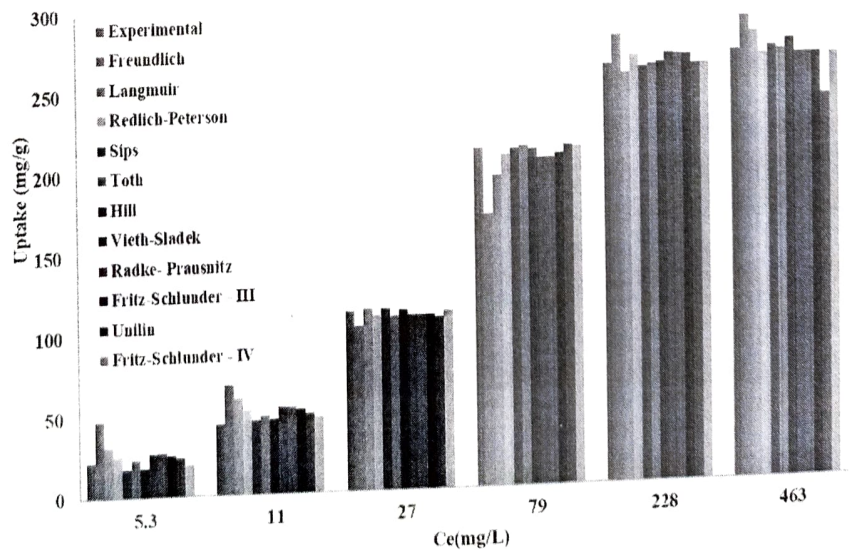


Table 4 Biosorption kinetic model constants

Kinetic model	Constant	Initial dye concentration				
		100 mg/L	250 mg/L	500 mg/L	750 mg/L	1000 mg/L
Pseudo first order	Q	43.41	109.67	210.22	256.83	261.44
	K_1	0.0552	0.0495	0.0417	0.0425	0.0538
	R^2	0.9953	0.9971	0.9986	0.9951	0.9960
Pseudo second order	Q	46.84	119.15	230.73	281.13	282.99
	K_2	0.0019	0.0006	0.0002	0.0002	0.0003
	R^2	0.9901	0.9918	0.9978	0.9916	0.9913

From the kinetic study, it was clear that uptake capacity was increased with an increase in initial concentration, and 90% of the total dye removed was obtained initially at 90 min. Initially, the adsorption was very vigorous to a contact time of 60 min, and it showed a decreased rate of removal efficiency from 60 to 90 min. Further increase in time from 90 to 360 min does not show much increase in removal efficiency, and this may be due to that the available dye molecules to the binding sites were fully utilized initially. Since the removal efficiency was increased from 0 to 85.32% when contact time was raised from 0 to 90 min and further increased from 85.2 to 88.7% when the contact time was increased from 90 to 360 min at an initial concentration of 100 mg/L. The difference in removal efficiency was only 3.5% for the last 270 min. So, the optimum contact

time for the maximum removal efficiency was fixed as 90 min. From Table 3, it was clear that both the kinetic models have the highest correlation coefficient, but PFO kinetic model predicted with the highest correlation coefficient not less than 0.9951. PSO kinetic model overpredicted the uptake capacity of the biochar than the PFO kinetic model.

4.7 Partition coefficient

Figure 8c and Table 5 summarize the partition coefficient with its corresponding experimental uptake and removal efficiency of the biochar at different breakthrough times. Generally, the partition coefficient on solid/liquid interaction describes the ratio of the analyte concentration on and in the adsorbent to the

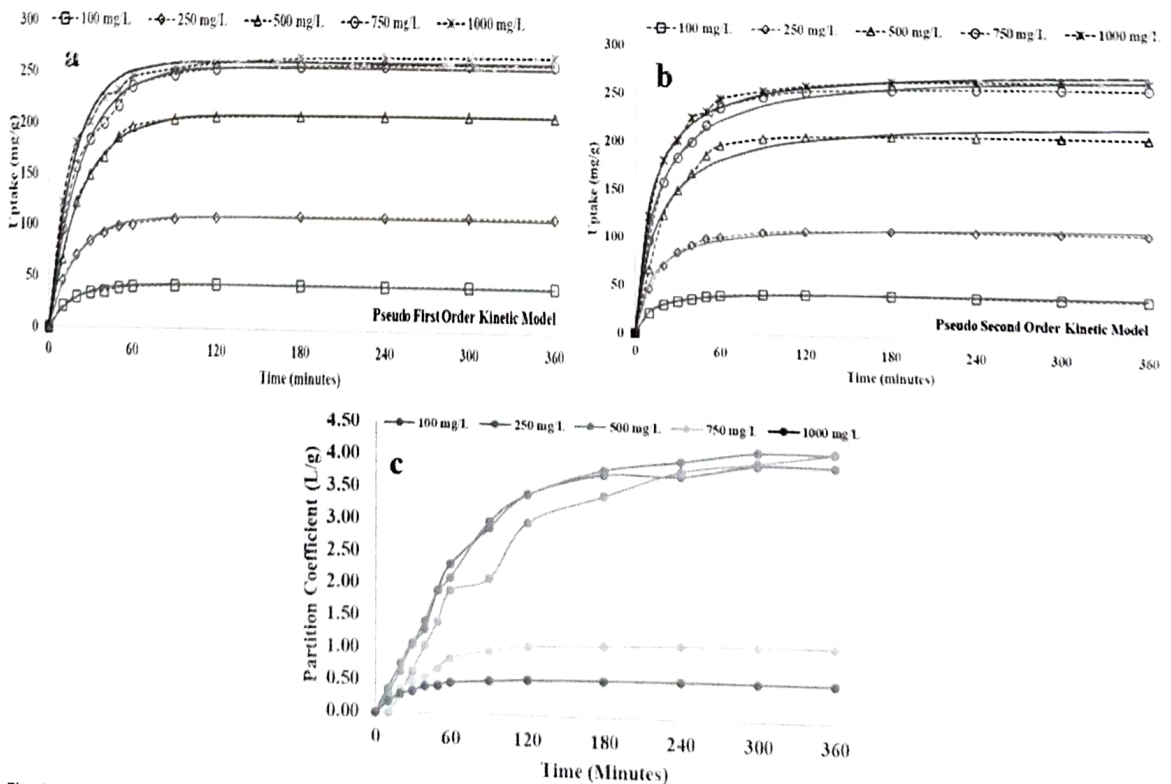


Fig. 8 Experimental and predicted uptake **a** pseudo-first-order kinetic model, **b** pseudo-second-order kinetic model, **c** partition coefficient

Table 5 Experimental uptake (Q_e), Removal Efficiency (RE), and Partition coefficient (PC) at a different breakthrough time (BT)

		Initial dye concentration (mg/L)														
		100 mg/L			250 mg/L			500 mg/L			750 mg/L			1000 mg/L		
BT (%)	Time (min)	Q_e (mg/g)	RE (%)	PC (L/g)	Q_e (mg/g)	RE (%)	PC (L/g)	Q_e (mg/g)	RE (%)	PC (L/g)	Q_e (mg/g)	RE (%)	PC (L/g)	Q_e (mg/g)	RE (%)	PC (L/g)
0.00	0.00	0.00	0.00	0.00	0.00	0.00	0.00	0.00	0.00	0.00	0.00	0.00	0.00	0.00	0.00	0.00
2.75	10.	21.10	42.20	0.37	46.00	36.80	0.29	67.00	26.80	0.18	96.50	25.73	0.17	121.50	24.30	0.16
5.5	20.	30.10	60.20	0.76	70.50	56.40	0.65	122.50	49.00	0.48	157.50	42.00	0.36	180.50	36.10	0.28
8	30.	34.10	68.20	1.07	84.50	67.60	1.04	149.50	59.80	0.74	184.00	49.07	0.48	201.50	40.30	0.34
11	40.	36.10	72.20	1.30	92.50	74.00	1.42	167.00	66.80	1.01	200.00	53.33	0.57	225.50	45.10	0.41
13	50.	39.60	79.20	1.90	99.00	79.20	1.90	186.50	74.60	1.47	218.00	58.13	0.69	232.00	46.40	0.43
16	60.	41.10	82.20	2.31	101.00	80.80	2.10	197.00	78.80	1.86	236.50	63.07	0.85	245.50	49.10	0.48
25	90.	42.60	85.20	2.88	107.00	85.60	2.97	204.50	81.80	2.25	248.50	66.27	0.98	254.00	50.80	0.52
33	120	43.60	87.20	3.41	109.00	87.20	3.41	207.50	83.00	2.44	254.50	67.87	1.06	260.00	52.00	0.54
50	180	44.10	88.20	3.74	110.50	88.40	3.81	209.00	83.60	2.55	257.50	68.67	1.10	265.50	53.10	0.57
66	240	44.10	88.20	3.74	111.00	88.80	3.96	210.00	84.00	2.63	259.50	69.20	1.12	267.00	53.40	0.57
83	300	44.35	88.70	3.92	111.50	89.20	4.13	210.50	84.20	2.66	260.50	69.47	1.14	268.00	53.60	0.58
100	360	44.35	88.70	3.92	111.50	89.20	4.13	210.50	84.20	2.66	261.00	69.60	1.14	268.50	53.70	0.58

BT breakthrough time (%), Q_e experimental uptake (mg/g), RE removal efficiency (%), PC partition coefficient (L/mg) or (mg/ μ mol)

concentration of the pollutant in the liquid phase at equilibrium solutions [31]. So, the actual potential of the biochar can be determined based on the partition coefficient rather than by removal efficiency and adsorption capacity, since these can be altered by changing the operating conditions. From Fig. 8c, it was clear that the increase in initial dye concentration decreased the partition coefficient; this may be because at high initial concentration, the surface binding sites will be easily saturated with the dye molecules and a larger number of unabsorbed dye molecules will be present in the liquid phase and result in the decreased removal efficiency and increased final concentration. Table 5 summarizes the partition coefficient with corresponding removal efficiency and experimental uptake at different breakthrough time. For instance, the partition coefficient at 100% breakthrough time (360 min) was found to be 3.92, 4.13, 2.66, 1.14, and 0.58 for the initial dye concentration of 100, 250, 500, 750, and 100 mg/L, respectively. On the other hand, the partition coefficient at 11% breakthrough time was calculated as 1.30, 1.42, 1.01, 0.57, and 0.41 for different initial dye concentrations. Based on the partition coefficient, the initial dye concentration of 250 mg/L was considered as the optimum for the maximum removal efficiency and highest uptake capacity, and these results were coinciding with the continuous study since the initial concentration of 250 mg/L was considered as the optimum.

4.8 Desorption studies

For successful adsorbent, it should have a regeneration capacity, which will, in turn, reduce the treatment cost of the dye removal. To study the desorption efficiency of biochar,

different elutants, namely, methanol, hydrochloric acid, ethylene diamine tetraacetic acid, sodium hydroxide, and sodium carbonate were used [32]. Figure 9a shows the desorption efficiency of different elutants. The highest removal efficiency of 99.3% was reported for sodium hydroxide and hydrochloric acid, and methanol showed a very less desorption efficiency of 2.4 and 1.5%. The optimum use of elutants was also an important factor since the cost associated with the chemicals was very high. So, the optimum solid to liquid ratio was also investigated. From Fig. 9b, it was concluded that the desorption efficiency was greater than 99% when the S/L ratio was maintained as 4. Further increase in the S/L ratio to 5, desorption efficiency was decreased to 94.6. The biochar was also investigated for the sorption-elution cycle. From Fig. 9c, it was evident that the biochar can be successfully used for three consecutive sorption-elution cycles.

4.9 Continuous study

The continuous study was conducted in an up-flow packed bed column under optimum conditions as concluded by batch experiments. The continuous study was investigated by varying the biochar bed depth, dye solution flow rate, and dye initial concentrations. Figure 10 explores the removal efficiency of the dye molecules at different operation conditions. The operating conditions of one parameter were investigated by fixing the other two parameters as constant such as bed depth of 25 cm, the flow rate of 0.3 L/h, and initial dye concentration of 250 mg/L.

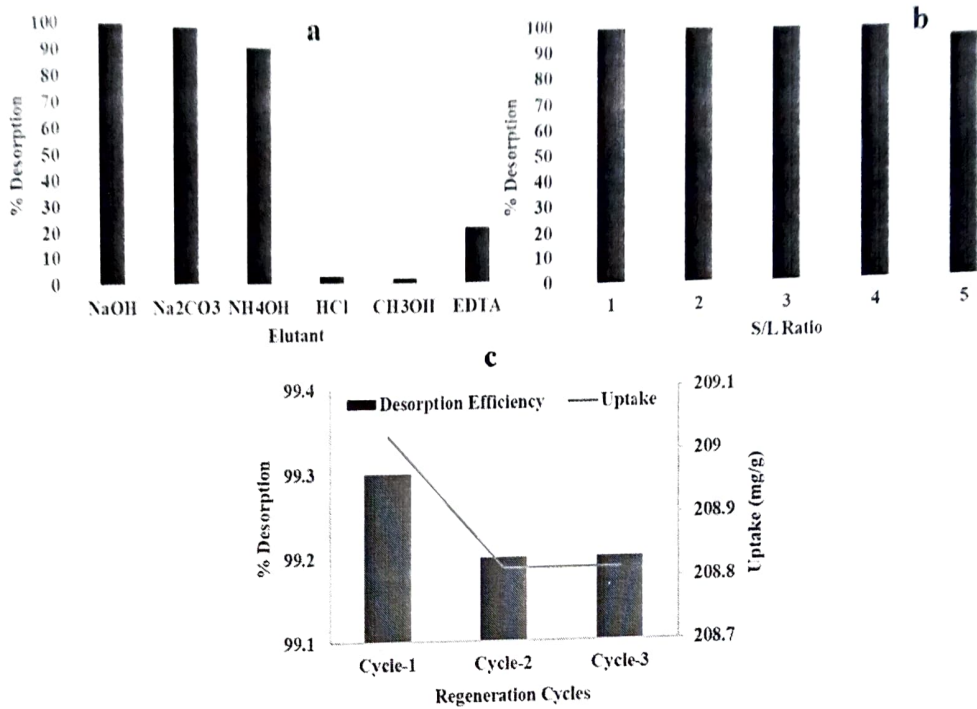


Fig. 9 Desorption efficiency of Reactive Red 120 (R120) a different elutant. b Solid/liquid ratio. c Regeneration cycles

4.10 Effect of biochar bed depth

The impact of biochar depth was studied by maintaining a bed depth of 15, 20, and 25 cm; to obtain these bed depths, a total biochar mass of 5.72, 6.32, and 6.94 g were used. From Fig. 10 and Table 6, it was concluded that an increase in bed depth increased the uptake capacity of the biochar and also increased the volume of wastewater treated. For instance, when a biochar bed depth was increased from 15 to 25 cm, the uptake capacity was increased from 96.48 to 98.94 mg/g with an increase in the volume of wastewater treated from 3.45 to 4.5 l. Other operating parameters such as breakthrough

time, exhaustion time, and overall sorption zone are summarized in Table 6. Table 6 also clearly indicates that an increase in biochar depth from 15 to 25 cm decreased the removal efficiency from 63.99 to 61.04%. But based on the practical consideration, the uptake capacity and volume of wastewater treated, a bed depth of 25 cm was considered as the optimum.

4.11 Effect of flow rate

The impact of flow rate was investigated by varying the flow rate as 0.3, 0.48, and 0.6 L/h by fixing other parameters as constant. From Fig. 11 and Table 6, it was concluded that an

Fig. 10 Effect of bed depth (BD), flow rate (F), and initial concentration (IC) on the removal of Reactive Red 120

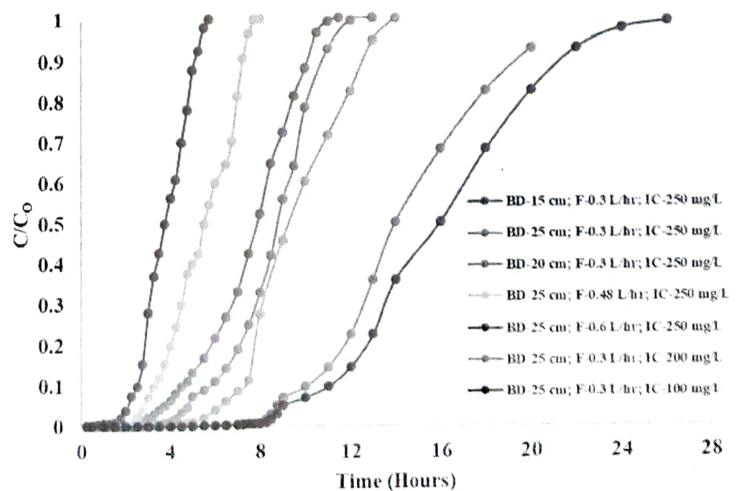


Table 6 Column parameters at various operating conditions

Bed depth (cm)	Flow rate (L/h)	Initial dye concentration (mg/L)	Uptake (mg/g)	t_b (h)	t_e (h)	Δt (h)	V_{eff} (L)	Total dye removal (%)
15	0.3	250	96.48	11.5	0.25	11.25	3.45	63.99
20	0.3	250	98.16	13	1.75	11.25	3.9	63.63
25	0.3	250	98.94	15	2.25	12.75	4.5	61.04
25	0.48	250	100.72	8	0.25	7.75	3.84	72.81
25	0.6	250	78.84	5.75	0	5.75	3.45	63.44
25	0.3	200	97.98	19	2	17	5.7	59.65
25	0.3	100	66.13	28	4.5	23.5	8.4	54.64

increase in flow rate decreased the volume of the wastewater treated and also decreased the overall sorption zone. From Table 7, it was concluded that the flow rate of 0.48 L/h was concluded as the optimum flow rate since the maximum uptake of biochar and maximum removal of dye molecules was obtained as 100.72 mg/g and 72.81%. The decreased uptake at the highest flow rate may be due to that the available residence time for the interaction of the biochar and dye molecules was not sufficient, and this resulted in the decrease in the binding between biochar and dye molecules [33]. On the contrary, at the lowest flow rate of 0.3 L/h, the available residence time was high, and the uptake capacity and removal efficiency was

less than 0.48 L/h. This may be due to the initial dye concentration having a direct impact on the flow rate, and the affinity of the biochar toward the initial concentration was high, and this resulted in maximum uptake at 0.48 L/h and a further increase in flow rate to 0.6 L/h decreased the uptake capacity.

4.12 Effect of initial dye concentration

The impact of initial dye concentration was studied by varying the initial concentration as 100, 200, and 250 mg/L by fixing other parameters as constant. Figure 10 and Table 6 explore the impact of initial concentration on dye removal. From Table 6, it

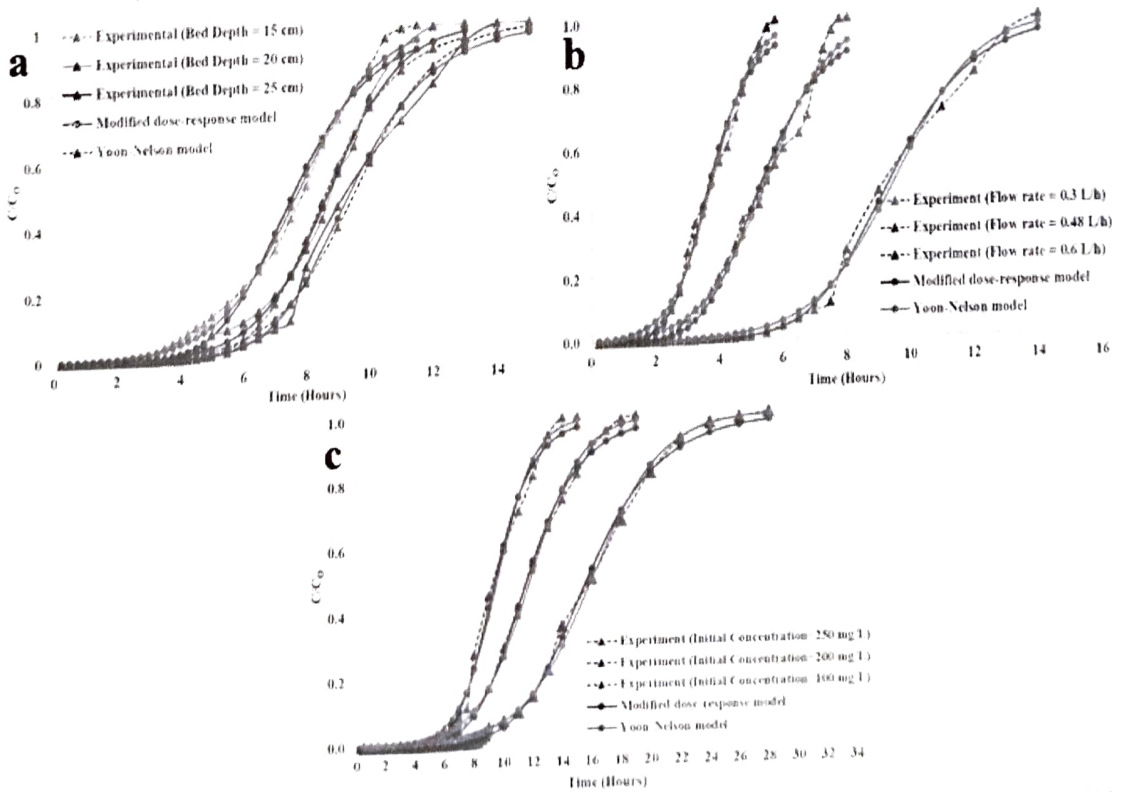


Fig. 11 Comparison of experimental and predicted uptake of different models **a** at varying bed depth, **b** at varying flow rate, **c** at varying initial concentration

Table 6 Column parameters at various operating conditions

Bed depth (cm)	Flow rate (L/h)	Initial dye concentration (mg/L)	Uptake (mg/g)	t_b (h)	t_r (h)	Δt (h)	V_{eff} (L)	Total dye removal (%)
15	0.3	250	96.48	11.5	0.25	11.25	3.45	63.99
20	0.3	250	98.16	13	1.75	11.25	3.9	63.63
25	0.3	250	98.94	15	2.25	12.75	4.5	61.04
25	0.48	250	100.72	8	0.25	7.75	3.84	72.81
25	0.6	250	78.84	5.75	0	5.75	3.45	63.44
25	0.3	200	97.98	19	2	17	5.7	59.65
25	0.3	100	66.13	28	4.5	23.5	8.4	54.64

increase in flow rate decreased the volume of the wastewater treated and also decreased the overall sorption zone. From Table 7, it was concluded that the flow rate of 0.48 L/h was concluded as the optimum flow rate since the maximum uptake of biochar and maximum removal of dye molecules was obtained as 100.72 mg/g and 72.81%. The decreased uptake at the highest flow rate may be due to that the available residence time for the interaction of the biochar and dye molecules was not sufficient, and this resulted in the decrease in the binding between biochar and dye molecules [33]. On the contrary, at the lowest flow rate of 0.3 L/h, the available residence time was high, and the uptake capacity and removal efficiency was

less than 0.48 L/h. This may be due to the initial dye concentration having a direct impact on the flow rate, and the affinity of the biochar toward the initial concentration was high, and this resulted in maximum uptake at 0.48 L/h and a further increase in flow rate to 0.6 L/h decreased the uptake capacity.

4.12 Effect of initial dye concentration

The impact of initial dye concentration was studied by varying the initial concentration as 100, 200, and 250 mg/L by fixing other parameters as constant. Figure 10 and Table 6 explore the impact of initial concentration on dye removal. From Table 6, it

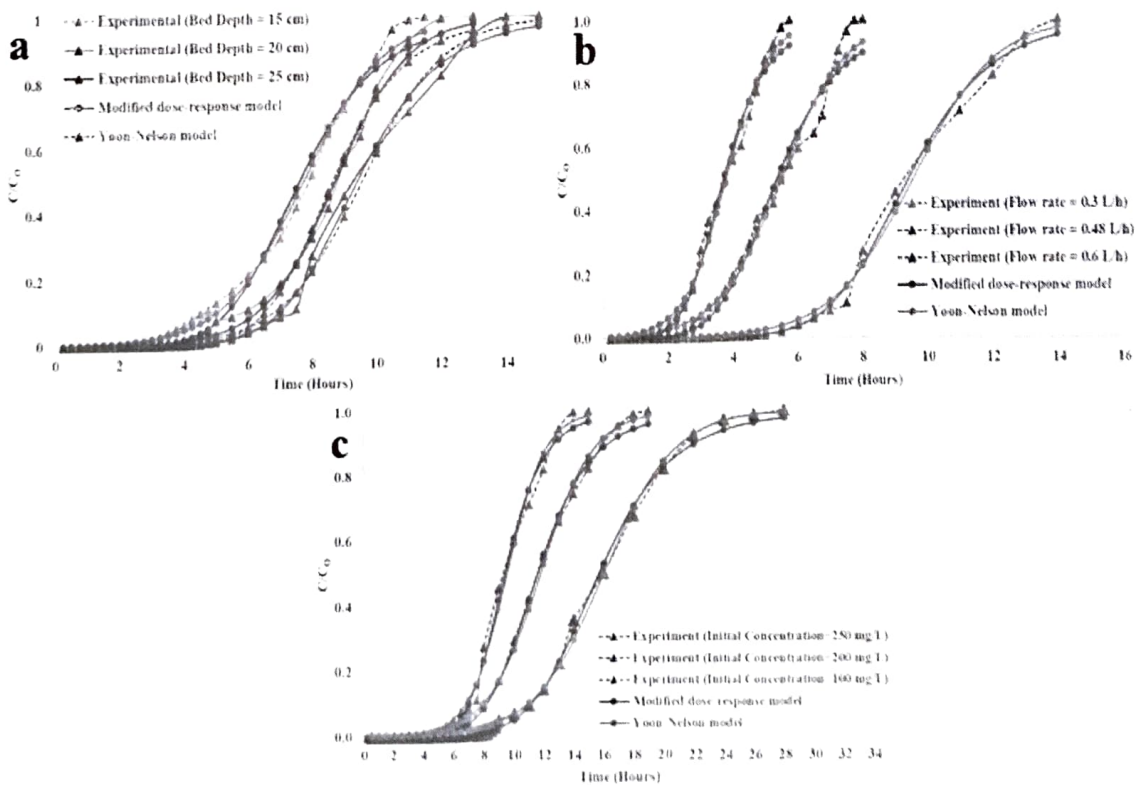


Fig. 11 Comparison of experimental and predicted uptake of different models **a** at varying bed depth, **b** at varying flow rate, **c** at varying initial concentration

Table 7 Parameters predicted by modified dose-response and Yoon-Nelson model

Bed depth (cm)	Flow rate (L/h)	Initial dye concentration (mg/L)	Modified dose-response model				Yoon-Nelson model			
			a_{mb}	b_{mb}	R^2	% error	t	k_{YN}	R^2	% error
15	0.3	250	6.1304	2.2786	0.9889	0.2091	7.7209	0.8042	0.9961	0.0779
20	0.3	250	7.6929	2.5926	0.9924	0.1925	8.7157	0.8864	0.9969	0.0807
25	0.3	250	7.3062	2.8233	0.9953	0.0325	9.5586	0.7889	0.9964	-0.0768
25	0.48	250	5.3785	2.5768	0.9819	0.0972	5.4855	1.0142	0.9881	0.0093
25	0.6	250	5.5566	2.2257	0.9903	0.0649	3.7903	1.4995	0.9929	-0.0135
25	0.3	200	6.3929	3.4686	0.9979	0.0422	11.7833	0.5667	0.9985	-0.0778
25	0.3	100	6.4268	4.7107	0.9985	0.0441	16.0168	0.4272	0.9981	-0.0943

was concluded that the increase in initial concentration increased the removal efficiency and uptake capacity. For instance, when the initial dye concentration was increased from 100 to 250 mg/L, the removal efficiency was 54.64 to 61.04%, and the uptake capacity was increased from 66.13 to 98.94 mg/g. The increased uptake and increased removal efficiency at the highest concentration proved that the biochar has the greatest affinity toward the dye adsorption at elevated concentrations [34, 35]. The biochar can be successfully applied to industries only when it was having the potential of adsorbing dye molecules at higher concentrations. These results indicate that biochar can act as a successful adsorbent which was having the high potential to adsorb the dye at higher concentration.

Further, this experimental investigation was validated with mathematical modeling to prove its application in the industrial wastewater scheme. The Yoon-Nelson model and the modified dose-response model were compared with the experiment uptake, and it was explored in Fig. 11a, b and c. Table 7 summarizes the various parameters of these two models. From Table 7, it was concluded that the Yoon-Nelson model was found to best fit with the experimental uptakes. The correlation coefficient was always higher than 0.9929. The modified dose-response model was found to have a correlation coefficient always higher than 0.9819.

4.13 Life cycle assessment

Life cycle assessment for a product investigates the effect of the product in the environment, and the assessment of a product was done with an input of reuse of the materials, health, photo-oxidation, acidification, and eutrophication [36]. In the present investigation, a marine green seaweed *Ulva reticulata* that was commonly overgrown in the eastern coastal region of south India was utilized for the production of the carbon-rich biochar. After the adsorption of the Reactive Red 120 (R120) to the biochar, the spent biochar was applied to the soil, and the microbial degradation will convert these pollutants into simpler products that can be used by the plants for the growth. Moreover, the biochar was very rich in carbon content, which will act as a fertilizer for the soil and increase the fertility of the

soil [37]. On the contrary, if these seaweeds were not used, they will grow, and these active biomasses will result in the eutrophication process and act as a cause for the greenhouse gases, so these conversions of seaweed to biochar will also act as a solution for climate mitigation measures [38].

5 Conclusion

The present research investigated the potential of a seaweed *Ulva reticulata* in the decolorization of Reactive Red 120 (R120), and the possible adsorption mechanism involved was confirmed by the characterization study of the biochar. The adsorption mechanism was based on ion exchange, complexation, and precipitation, and the presence of these complex groups was confirmed by FT-IR analysis. The batch study revealed that the removal efficiency increased with a decrease in pH and initial dye concentration, an increase in temperature and biochar dosage. The experimental uptake was best fitted with the pseudo-first-order kinetic model, and isotherm studies concluded that a four-parameter model Fritz-Schlunder-IV was best fitted. The biochar was successfully used for three consecutive sorptions—elution cycle and sodium hydroxide were used as the best elutants with a solid to liquid ratio of 4. The continuous study concluded that biochar can be effectively used in real wastewater schemes, and it was had the potential of continuous removal of dye. Further, the utilization of this seaweed will also provide a better solution for the seaweed waste management system.

Compliance with ethical standards

Conflict of interest The authors declare that they have no conflicts of interest.

References

1. Abdolali A, Guo WS, Ngo HH et al (2014) Typical lignocellulosic wastes and by-products for biosorption process in water and

- wastewater treatment: a critical review. *Bioresour Technol* 160(2014):57–66. <https://doi.org/10.1016/j.biortech.2013.12.037>
2. Felista MM, Wanyonyi WC, Ongera G (2020) Adsorption of anionic dye (Reactive black 5) using macadamia seed Husks: kinetics and equilibrium studies. *Sci African*. <https://doi.org/10.1016/j.sciaf.2020.e00283>
 3. Gokulan R, Avinash A, Prabhu GG, Jegan J (2019) Remediation of remazol dyes by biochar derived from *Caulerpa scalpelliformis* - an eco-friendly approach. *J Environ Chem Eng* 7(5):103297. <https://doi.org/10.1016/j.jece.2019.103297>
 4. Miladinova PM, Vaseva RK, Lukanova VR (2015) Synthesis and investigation of some acid azo dyes for wool. *J Chem Technol Metall* 22(2000):49–54
 5. Yagub MT, Sen TK, Afizo S, Ang HM (2014) Dye and its removal from aqueous solution by adsorption: a review. *Adv Colloid Interf Sci* 209(2014):172–184. <https://doi.org/10.1016/j.cis.2014.04.002>
 6. Salleh MAM, Mahmoud DK, Karim WAWA, Idris A (2011) Cationic and anionic dye adsorption by agricultural solid wastes: a comprehensive review. *Desalination*. 280(2011):1–13. <https://doi.org/10.1016/j.desal.2011.07.019>
 7. Fegousse A, El Gaidoumi A, Miyah Y et al (2019) Pineapple bark performance in dyes adsorption: optimization by the central composite design. *J Chem*. <https://doi.org/10.1155/2019/3017163>
 8. Franca AS, Oliveira LS, Ferreira ME (2009) Kinetics and equilibrium studies of methylene blue adsorption by spent coffee grounds. *Desalination*. <https://doi.org/10.1016/j.desal.2008.11.017>
 9. Han R, Zhang L, Song C et al (2010) Characterization of modified wheat straw, kinetic and equilibrium study about copper ion and methylene blue adsorption in batch mode. *Carbohydr Polym* 79(4):1140–1149. <https://doi.org/10.1016/j.carbpol.2009.10.054>
 10. Lehmann J, Joseph S (2012) Biochar for environmental management: an introduction. In: *Biochar for Environmental Management: Science and Technology*
 11. Liu Y, Liu YJ (2008) Biosorption isotherms, kinetics and thermodynamics. *Sep Purif Technol* 61(3):229–242. <https://doi.org/10.1016/j.seppur.2007.10.002>
 12. Beesley L, Moreno-Jiménez E, Gomez-Eyles JL et al (2011) A review of biochars' potential role in the remediation, revegetation and restoration of contaminated soils. *Environ Pollut* 159(12):3269–3282. <https://doi.org/10.1016/j.envpol.2011.07.023>
 13. Rameshkumar S, Ramakritinan C., Yokeshbabu M (2012) Proximate composition of some selected seaweeds from Palk bay and Gulf of Mannar, Tamilnadu, India. *Asian J Biomed Pharm Sci*
 14. Cui Y, Kang W, Qin L et al (2020) Magnetic surface molecularly imprinted polymer for selective adsorption of quinoline from coking wastewater. *Chem Eng J*. <https://doi.org/10.1016/j.cej.2020.125480>
 15. Gokulan R, Ganesh Prabhu G, Avinash A, Jegan J (2020) Experimental and chemometric analysis of bioremediation of remazol dyes using biochar derived from green seaweeds. *Desalin Water Treat* 184:340–353. <https://doi.org/10.5004/dwt.2020.25339>
 16. Paul J, Rawat KP, Sarma KSS, Sabharwal S (2011) Decoloration and degradation of Reactive Red-120 dye by electron beam irradiation in aqueous solution. *Appl Radiat Isot*. <https://doi.org/10.1016/j.apradiso.2011.03.009>
 17. Abdin Y, Usman A, Ok YS et al (2020) Competitive sorption and availability of coexisting heavy metals in mining-contaminated soil: contrasting effects of mesquite and fishbone biochars. *Environ Res*. <https://doi.org/10.1016/j.envres.2019.108846>
 18. Shahzad A, Jang J, Lim SR, Lee DS (2020) Unique selectivity and rapid uptake of molybdenum-disulfide-functionalized MXene nanocomposite for mercury adsorption. *Environ Res*. <https://doi.org/10.1016/j.envres.2019.109005>
 19. Sivarajasekar N, Baskar R (2014) Adsorption of basic red 9 onto activated carbon derived from immature cotton seeds: isotherm studies and error analysis. *Desalin Water Treat*. <https://doi.org/10.1080/19443994.2013.834518>
 20. Gokulan R, Ganesh Prabhu G, Jegan J (2019) A novel sorbent *Ulva lactuca*-derived biochar for remediation of Remazol Brilliant Orange 3R in packed column. *Water Environ Res* 91(7):642–649. <https://doi.org/10.1002/wer.1092>
 21. Kim WK, Shim T, Kim YS et al (2013) Characterization of cadmium removal from aqueous solution by biochar produced from a giant *Miscanthus* at different pyrolytic temperatures. *Bioresour Technol* 138:266–270. <https://doi.org/10.1016/j.biortech.2013.03.186>
 22. Jackson MB, Armstrong W (1999) Formation of aerenchyma and the processes of plant ventilation in relation to soil flooding and submergence. *Plant Biol* 1:274–287. <https://doi.org/10.1111/j.1438-8677.1999.tb00253.x>
 23. Armstrong J, Armstrong W (1991) A convective through-flow of gases in *Phragmites australis* (Cav.) Trin. ex Steud. *Aquat Bot* 39:75–88. [https://doi.org/10.1016/0304-3770\(91\)90023-X](https://doi.org/10.1016/0304-3770(91)90023-X)
 24. Mupa M, Rutsito DD, Musekiwa C (2016) Removal of methylene blue from aqueous solutions using biochar prepared from *Eichhornia crassipes* (water hyacinth)-molasses composite: kinetic and equilibrium studies. *Afr J Pure Appl Chem* 10(6):63–72. <https://doi.org/10.5897/ajpac2016.0703>
 25. Jeguirim M, Limousy L, Dutoumie P (2014) Pyrolysis kinetics and physicochemical properties of agropellets produced from spent ground coffee blended with conventional biomass. *Chem Eng Res Des*. <https://doi.org/10.1016/j.cherd.2014.04.018>
 26. Aksu Z, Çağatay ŞŞ (2006) Investigation of biosorption of Gemazol Turquoise Blue-G reactive dye by dried *Rhizopus arrhizus* in batch and continuous systems. *Sep Purif Technol* 48:24–35. <https://doi.org/10.1016/j.seppur.2005.07.017>
 27. Tangaromsuk J, Pokethitiyook P, Kruatrachue M, Upatham ES (2002) Cadmium biosorption by *Sphingomonas paucimobilis* biomass. *Bioresour Technol* 85:103–105. [https://doi.org/10.1016/S0960-8524\(02\)00066-4](https://doi.org/10.1016/S0960-8524(02)00066-4)
 28. Vijayaraghavan K, Yun YS (2008) Competition of Reactive red 4, Reactive orange 16 and Basic blue 3 during biosorption of Reactive blue 4 by polysulfone-immobilized *Corynebacterium glutamicum*. *J Hazard Mater* 153(1):478–486. <https://doi.org/10.1016/j.jhazmat.2007.08.079>
 29. Gerçel Ö, Gerçel HF (2007) Adsorption of lead(II) ions from aqueous solutions by activated carbon prepared from biomass plant material of *Euphorbia rigida*. *Chem Eng J*. <https://doi.org/10.1016/j.cej.2007.01.010>
 30. Padmash TVN, Vijayaraghavan K, Sekaran G, Velan M (2006) Application of two- and three-parameter isotherm models: biosorption of acid red 88 onto *Azolla microphylla*. *Bioremediat J* 10(1–2):37–44. <https://doi.org/10.1080/10889860600842746>
 31. Vikrant K, Kim KH (2019) Nanomaterials for the adsorptive treatment of Hg (II) ions from water. *Chem. Eng. J*
 32. Ravindiran G, Jeyaraju RM, Josephraj J, Alagumalai A (2019) Comparative desorption studies on remediation of remazol dyes using biochar (sorbent) derived from green marine seaweeds. *ChemistrySelect*. 4(25):7437–7445. <https://doi.org/10.1002/slct.201901348>
 33. Lu MC, Biel LCC, Wan MW et al (2016) Adsorption of dibenzothiophene sulfone from fuel using chitosan-coated bentonite (CCB) as biosorbent. *Desalin Water Treat* 57(11):5108–5118. <https://doi.org/10.1080/19443994.2014.996773>
 34. Ong HR, Khan MR, Yousuf A et al (2015) Effect of waste rubber powder as filler for plywood application. *Pol J Chem Technol* 17(1):41–47. <https://doi.org/10.1515/pjct-2015-0007>
 35. Vijayaraghavan K, Thilakavathi M, Palamivelu K, Velan M (2005) Continuous sorption of copper and cobalt by crab shell particles in a



Materials Today: Proceedings

journal homepage: www.elsevier.com/locate/matpr

Electrokinetic remediation: An innovation for heavy metal contamination in the soil environment

Zunaithur Rahman^a, Jagadheeswari^b, Arun Mohan^a, Tharini^c, Selvendran^d, Shanmuga Priya^{e,*}

^a Department of Civil Engineering, Sethu Institute of Technology, Kariapatti 626 115, Tamil Nadu, India

^b Department of Civil Engineering, K.Ramakrishnan College of Technology, Trichy 621 112, Tamilnadu, India

^c Department of Civil Engineering, SRM Valliammai Engineering College, Kattankulatur 603 203, Tamilnadu, India

^d Department of Civil Engineering, Vel Tech Rangarajan Dr.Saguntala R&D Institute of Science and Technology, Chennai 600 062, Tamilnadu, India

^e Department of Chemical Engineering, Mohamed Sathak Engineering College, Kilakarai 623 806, Tamil Nadu, India

ARTICLE INFO

Article history:

Received 9 August 2020

Accepted 20 August 2020

Available online xxxxx

Keywords:

Electrokinetics
Heavy metal
Contamination
Remediation
Health effects

ABSTRACT

The pollution load to the earth's crust is being added by the atmospheric deposition of heavy metals like arsenic, cadmium, lead, zinc emitted from vehicles, and several industrial plants. Numerous urban and thick urban communities with Critical Industrial waste generation were found to have contaminated Indian soil. These Heavy metals have lethal and mutagenic impacts even at a low level. Lately, numerous studies to decide hazards brought about by the disproportionate amounts of metal in the soil in terms of human well-being and forest habitats have shrunk the consideration among people groups as a result of its natural centrality. Advancements for remediation ought to be financially savvy and moderate. Most commercial enterprises use designing advances for remediation because of Physico-chemical strategies. Bioremediation techniques utilizing plant and microbial frameworks have been produced for distinguishing contamination and also for remediation. Electrokinetics is a creative innovation that is planned to isolate and separate contaminants from soaked or unsaturated soils, sludge and surface water through electro-osmosis, electro-migration, and electro-phoresis. This paper audits the different parameters required in the pragmatic uses of electrokinetics on heavy metal contaminated soils. It also discusses the completed as well as ongoing electrokinetic projects and research work all over the world.

© 2020 Elsevier Ltd. All rights reserved.

Selection and peer-review under responsibility of the scientific committee of the International Conference on Newer Trends and Innovation in Mechanical Engineering: Materials Science.

1. Introduction

Soils are essential environments in which rock, air, and water combine. Soil pollution is an equally serious issue along with air and water pollution that our world is confronted with. Common transition metals are known as heavy metals, which have the potential to cause environmental harm. Some heavy metals like zinc have eco-and phytotoxic properties, among other heavy metals such as hexavalent chrome are known carcinogens. Fertilizers, pesticides, biosolids, wastewater disposal [1] and various industrial points sources such as current and former mining operations, foundries, smelters and dispersed sources such as pipes, commodity constituents, commodity combustion, traffic, industrial and human operations are the sources of heavy metal entry into the

environment. The environmental conditions determine such heavy metals property and behavior. Extreme pH, redox, and geology depending on whether it is anionic or cationic may have a mobilizing or immobilizing impact on any specific heavy metal. Also, the presence of certain ionic species may have an immobilizing effect by rendering the unique significant metal immobile mineral species. The remediation of heavy metals needs a good understanding of the targeted heavy metals and the environmental factors they impact (Table 1).

2. Electrokinetics

Electrokinetic treatment is nearly another approach that is being researched in a Few sections of the world as a practical in situ soil remediation and treatment strategy particularly for heavy metal evacuation like lead, arsenic cadmium, and organic pollutant like ethylbenzene [10]. Different powerful

* Corresponding author.

E-mail address: priya.komaran@gmail.com (S. Priya).

<https://doi.org/10.1016/j.matpr.2020.08.541>

2214-7853/© 2020 Elsevier Ltd. All rights reserved.

Selection and peer-review under responsibility of the scientific committee of the International Conference on Newer Trends and Innovation in Mechanical Engineering: Materials Science.



PRINCIPAL

MOHAMED SATHAK ENGINEERING COLLEGE FOR

KILAKARAI - 623 806

Table 1
The industrial sources of heavy metal and its effects.

Sources	Heavy metals	Effects	References
Mining, industrial coolants, chromium salts manufacturing, leather tanning	Chromium (Cr)	Dermatitis, allergic and eczematous skin reactions, skin and mucous membrane ulceration, nasal septum perforation, allergic asthma reactions, bronchial carcinomas, gastroenteritis, hepatocellular deficiency, and renal anuric oligode deficiency	[2]
Lead-acid batteries, paints, electrical waste, smelting operations, thermal power plants focused on coal, bangle industry	Lead (Pb)	Encephalopathy [brain disorder] Peripheral nerve disorders [reduced responsiveness to the touch] Retinal degeneration Renal disease – acute nephropathy	[3,4]
Chlorinealkali plants, thermal power plants, fluorescent lamps, hospital waste (damaged thermometers, barometers, sphygmomanometers), electrical equipment, etc.	Mercury (Hg)	Symptoms of shyness, social obligation, nervousness, fatigue, cognitive loss, and lack of focus. Hearing disorder, tunnel vision, headache, tiredness, reduced sexual function and depression	[5]
Geogenic/natural systems, smelting operations, thermal power installations, fuel consumption	Arsenic (As)	melanosis, hyperkeratosis, and desquamation Anaemia and leucopenia	[6]
Mining, electroplating, smelting operations	Copper (Cu)	Liver damage, jaundice, diarrhea, anuria	[7]
Smelting operations, thermal power plants, the battery industry	Nickel (Ni)	Lung cancer, nausea, vomiting, abdominal discomfort, visual disturbance, headache, giddiness, and cough	[8]
Smelting zinc, waste batteries, E-waste, sludge paint, incineration & combustion of fuel	Cadmium (Cd)	decreased bone mineral density, a carcinogen, renal damage	[9]

strategies have been kept an eye on for the departure of overwhelming metals, for instance, substance precipitation, particle trade, switch assimilation, electrodialysis, ultrafiltration, nanofiltration, coagulation, flocculation, floatation, extraction by the addition of the biodegradable chelating agent, soil washing using chelating agent [11], bioremediation [12], etc. Anyway, these strategies have a few hindrances, for example, high reagent necessity, capricious metal particle evacuation, and age of poisonous slimes, etc. This electrokinetic system likewise can upgrade the quality and diminish the compressibility of an extensive variety of soils [13]. Electrokinetic treatment was at first depicted by F.F.

Reuss in Russia in 1808. The polluted soil was at first treated consistently by Helmholtz in 1879, which was later adjusted by Pellat in 1903 and Smoluchowski in 1921. In such way, electrochemical or electrokinetic (EK) treatment method can be used as an elective soil treatment methodology for substantial metals like cobalt, nickel, lead, arsenic, cadmium, and salts like sodium chloride [14], fluoride [15] deficiencies underneath streets, railroads or pipelines, building establishments, treatment of mechanical wastewater sludge [16] furthermore to improve the designing properties of soils by utilizing surfactants [17].

2.1. Principles of electrokinetics

The treatment methodology incorporates passing a low amperage electrical flow between a movement of cathodes and anodes implanted in the tainted soil. The nearness of a directing pore liquid in the dirt mass to be dealt with is fundamental for this remediation innovation. What's more, all together for this remediation strategy to be successful the sullied species must be solubilized by the introduction of acids or other good synthetic compounds during the treatment technique together [18].

Electro-assimilation and particle relocation are brought about by the electrical flow. This moves the watery stage contaminants in the subsurface from one cathode to the next. Contaminants in the watery stage or contaminants desorbed from the dirt surface are shipped towards discrete anodes depending upon their charge. The contaminants may then be removed to a recuperation framework or spared at the terminal. Reagents might be acquainted at the cathodes to upgrade contaminant evacuation rates. The accompanying Table 2 gives the details of the experimental results of electrokinetic remediation of different heavy metals in a different environment.

2.2. Pre-field investigations

Before going for electrokinetic treatment it is necessary to investigate the contaminated site which will be easier for applying the treatment very effectively. Field surveys for metallic objects and insulating materials like sewer and gas lines, pore water analysis, physical and chemical properties of soils and a bench-scale study are more important before starting the treatment [25].

2.3. Factors affecting electrokinetics

Previous studies have been proved that there are some parameters like soil type, history of the contaminant site, chemical and physical properties of that soils, type of electrodes, electrode configuration and spacing, the voltage applied during the treatment process will be influencing the efficiency of the electrokinetic process [19,26,27]. In most useful utilizations of electrokinetics, the anodes are iron or aluminum bars and the cathodes are steel tubes. Some of the time graphite terminals are additionally utilized for the two anodes and cathodes. It is more economical than other electrodes. In the case of nickel removal, efficiency improved from 49.3 to 57.2% when the current thickness was expanded from 4.36 to 13.1 mA/cm². Moreover, an improvement in effectiveness from 38.5 to 54.3% was seen when the voltage slope expanded from 1 to 2 V/cm. The evacuation productivity of nickel diminished definitely when the pH esteem expanded from 6.5 and demonstrated expulsion effectiveness of just 33.1% at a pH of 10. A decrease in evacuation effectiveness at higher pH of electrolyte might be credited to soluble base fronts close to the cathode which produces non-conductive encourages [27].

The same increase in efficiency was obtained for Cr, Cu, Hg, and Pb (21.87, 83.2, 62.4, and 78.06% respectively) under pulsed current supply mode replacing the traditional continuous mode [28].

Table 2
Heavy metal removal using Electrokinetics enhanced by different purging solution

Type of sample	Target contaminant	Duration	Purge solution	Removal efficiency (%)	References
Paints and fly soil	As	8 weeks	EDTA and NaOH	78.8 & 78.6	[25]
Kaolinite low permeable clay soil	Cr, Cu, and As	29 h	NaOH or NaOCl	74.4 & 78.1	[26]
Red earth	Ni, Cd, and Sr	N/A	Acetic acid and EDTA	35	[27]
Dredged harbor sediments	Cd, Cu, Pb, and Zn	7 to 15 days	Deionized water, HNO ₃ , C ₆ H ₆ O	40–50	[28]
Industrial wastewater sludge (slay)	Cr, Cu, Se, Ni, Pb, and Zn	5 days	Tap water, NaCl, H ₂ SO ₄ , C ₆ H ₆ O	1.2–60, 37.2–76.5, 43.4–78	[29]
Clay	Pb	24 to 48 hrs	C ₆ H ₆ O-NaCl	10–20	[30]
Kaolinite	Cu	4 days	C ₆ H ₆ O- Na ₂ C ₂ O ₄ -O ₂	96.6	[31]

FIRS, a novel electrokinetic technique, can be used to reduce the carcinogenic and mobile Cr (VI) to the less toxic and less mobile Cr (III), and lock up the Cr (III) in iron [25]. In this study, 50 kg soil was treated in a 700mmx300mmx300mm test cell. The initial concentration of total Cr and Cr (VI) in the soil was 9300 mg/kg soil 740 mg/kg respectively. After running the experiment for 5 weeks at 75 V the concentration of Cr (VI) was 240 mg/kg and 35 mg/kg near the anode and cathode respectively [30]. Electrokinetic remediation of cadmium contaminated soil was studied at a wide range of pH (pH 3–12) with deionized water as a purge solution in both compartments. The pH of an anodic solution is maintained by 1 N HCl and 1 N NaOH solution. The results show that there is an increase of electroosmotic flow as a gradual increase in pH in the anode compartment. However, the voltage gradient is not significantly affected by a change in pH in soil specimens [31].

To desorb contaminants sorbed on soil, some enhancement agents chelants [32] like carboxylates (EDTA), hydro carboxylates (citric acid), complexing agents like acetic acid, surfactants like sodium dodecyl sulfate, alkyl poly glucoside and oxidizing agents like hydrogen peroxide, potassium permanganate can be used [33]. In case of simultaneous removal of heavy metal (nickel) and organic pollutant polycyclic aromatic hydrocarbons from kaolinite using cyclodextrin, it was seen that nickel was encouraged inside the dirt close to cathode because of high pH condition and expulsion of PAH was low at 1% of cyclodextrin when contrasted with 10% because of the low solubility of PAH in 1% cyclodextrin [34]. The arsenic evacuation could be improved by choosing reasonable compound reagent like cetylpyridinium chloride, EDTA, citric acid, NaOH, potassium phosphate [35], etc. An examination indicated that the expulsion productivity of As(V) utilizing EDTA framework was better than that in other chemicals [36]. Additionally, As potential slope expanded from 2.0 V/cm to 3.0 V/cm, the expulsion proficiency of As (V) was expanded from 35.4% to 44.8% in framework utilizing EDTA for an upgrade. It demonstrated that the arsenic expulsion could be improved by choosing reasonable substance reagents and expanding possible slope. The serious impediment of electroosmotic flow towards the cathode caused a significant impediment of the electromigration of arsenic towards the anode.

The efficiency of electrokinetic treatment could also be improved by combing with a permeable reactive barrier such as activated carbon [24], zero-valent iron, Hydrated ferric hydroxide [37], carbon nanotubes with a metal coating, Atomizing slag [38]. When CNT coated with cobalt is used as PRB, the removal efficiency of arsenic was more than 70% using EDTA as purging solution [39]. The best results were obtained when arsenic in combination with chromium and copper ions contaminated soil was flushed with either NaOH or NaOCl (total removal efficiency 74.4% and 78.1% respectively). Relatively poor performance was observed when the contaminated soil was purged with the oxidizing agent H₂O₂, which had an initial pH of 4.6. The removal efficiency was only 16% [25].

Increased efficiency was observed in the lead-contaminated soil while increasing the duration of treatment. It was about 20% for

46 h and 10–15% for 36 h [23]. Increased time treatment enhances the migration of contaminants in kaolin like soils but the removal of contaminants was low due to adsorption or precipitation near the electrodes [40]. Unlike kaolinite, in glacial till, the increased time did not affect the removal of heavy metal due to its buffering capacity. Test results have demonstrated that ammonium citrate (pH = 9) was more successful than EDTA in antacid soil. Evacuation of lead in EDTA treatment was more than zinc and expulsion of zinc in ammonium citrate treatment was more than lead because of applying a steady voltage of 25 V [41]. Utilizing 0.1 N HNO₃ as catholyte-molding, the most extreme evacuation accomplished was 73.84% and 62.88% for cobalt and lead individually in the tainted soil [42].

Anyway, the vehicle of substantial metals towards every terminal was identified with the speciation of metals in the dirt pore arrangement and the fractionation and conveyance of the metals in the dirt framework which is because of complexation, adsorption, and precipitation [43]. The treatment time, concoction use and vitality utilization could be diminished by pretreating the dirt and by utilizing suitable electrolytes.

2.4. Merits and demerits of electrokinetics

Electrokinetic remediation has several advantages compared to other remediation technologies. It is easy to operate, cost-effective and it can be applied both in-situ and ex-situ treatment processes [27]. Soil moisture content and homogeneity of the soil in the contaminated area are the major limiting factors. It remediates faster in clays and silts when compared with gravels and sands. The availability of drilling technology to introduce the electrodes restricts the working depth of this technology. The great challenges in achieving the higher efficiency in the in-situ electrokinetic process are the metal conductors buried and the presence of non-targeted contaminants. Additionally, when the objective particle fixation is less and non-target particle focus is more, the procedure won't be effective. Erosion of the anode and acidic conditions would cause trouble in-situ endeavors. Precipitation of species near the anode is an obstruction to the procedure. At their hydroxide solvency esteem, Heavy metals can rashly accelerate near the cathode excessive warmth age during the procedure which causes breaking and age of unwanted items like chlorine gas are likewise the significant detriments [27]. An examination was directed when electrokinetic remediation is applied to diesel polluted soils. From this examination, it is found out that the pH of soil close to the anode was low about 3.5 and was extremely high close to cathode with an estimation of 10.8 following a month of remediation [35]. Even though the dirt was remediated, this has an unfavorable effect on the microbial network in the specks of dirt.

2.5. Electrokinetics in practice

The details of developers remediating the contaminated sites in the US and other countries are listed in the following Table 3.

Table 3
Developers remediating contaminated sites

Developers	Type of soil	Depth (feet)	Contaminant	Duration & cost (Month& \$)	Removal %	
					Before (ppm)	After (ppm)
Electrokinetics, Inc. (EK) - CADEX TM electrode system	Kaolinite	30x60x3	Pb	6-8 & NA	1000-5000	NA
Environmental & Technology Services (ETS)	Clay	200x200x70	VOC, BTEX, TPH	3-12 & 17-50\$ / ton	10-30, 100-2200, 3000	< 0.1, < 40, < 35
Isotron Corporation - ELECTROSORBTM Process	Sand and Kaolinite	NA	U, Hg	NA	10-20	50-99%
Geokinetics International, Inc. (GI) - Pool Process	Clay	230x10x3.3	Cd, Cu, Ni, Pb, Zn	2-18 & 300-500 \$ / Cubic yard	600, 500-1000, 860, 300-5000, 2600	< 50, < 250, < 80, < 75, < 300

3. Conclusions and future aspects

Electrokinetics is an innovation for the removal of heavy metals such as Nickel, Cobalt, Arsenic, Cadmium, Zinc, Copper, and salts like Calcium, Sodium, and Fluoride, especially in saturated soils and sediments. By utilizing appropriate electrolytes, voltage gradient furthermore combining with a permeable reactive barrier, the efficiency of Electrokinetics can be enhanced. When compared with other contamination removal process, Electrokinetics is cost-effective if suitable electrodes and electrolytes are chosen. To enhance the proficiency of contaminant removal in a wide range of soils, a considerable measure of research work and pilot studies are expected.

Declaration of Competing Interest

The authors declare that they have no known competing financial interests or personal relationships that could have appeared to influence the work reported in this paper.

References

- [1] R.A. Wuana, F.E. Okieimen, Heavy metals in contaminated soils: a review of sources, chemistry, risks and best available strategies for remediation, *ISRN Ecol.* 2011 (2011) 1-20.
- [2] F. Baruthio, Toxic effects of chromium and its compounds, *Biol. Trace Elem. Res.* 32 (1-3) (1992) 145-153.
- [3] M. Hutton, Human health concerns of lead mercury, cadmium, arsenic, John Wiley & Sons Ltd., 1987.
- [4] Vance Vella, Elizabeth O'Brien, Elisa Idris, Health impacts of lead poisoning : a preliminary listing of the health effects and symptoms of lead poisoning, *lead action news*, 6 (1998) 2.
- [5] Mark Hyman, The impact of mercury on human health and the environment, *alternative therapies*, 10 (2004) 6.
- [6] J.C. Saha, A.K. Dikshit, M. Bandyopadhyay, A review of arsenic poisoning and its effect on human health, *Critical Rev. Environ. Sci. Technol.* 29 (1999) 3.
- [7] Carl Keen, Harry J. Mcarble, The impact of copper on human health, *International Copper Association Ltd.*, 2003.
- [8] Aleksandra Duda-Chodak, Urszula B. Aszczyk, The impact of nickel on human health, *J. Elementol.* 13 (4) (2008) 685-696.
- [9] A. Bernard, Cadmium & its adverse effects on human health, *Indian J. Med. Res.* 128 (2008) 557-564.
- [10] Ching yuan, Chin-Huang Weng, Remediating ethylbenzene contaminated clayey by a surfactant -aided electrokinetic (SAEK) process, *Chemosphere* (2004) 225-232.
- [11] Meng Wei, Jiajun Chen, Xingwei Wang, Removal of arsenic and cadmium with sequential soil washing using Na2EDTA, oxalic and phosphoric acid: optimization conditions, removal effectiveness and ecological risks, *Chemosphere*, 156 (2016) 252-261.
- [12] Gosa Girma, Microbial bioremediation of some heavy metals in soils: an updated review, *Indian J. Sci. Res.* 6 (1) (2015) 147-161.
- [13] Geetha A. Megur, Kakaraddi, A study on stabilization of soil by electrokinetic method, *Int. J. Res. Eng. Technol.* 03 (06) (May-2014) 104-109.
- [14] K.R. Reddy, A.B. Shirani, Electrokinetic remediation of metal contaminated glacial tills, *Geotech. Geol. Eng.*, 15 (1997) 3-29.
- [15] Do-Hyung kim, chil sung jeon, kitae baek, sung hwan ko, jung seok yang, Electrokinetic remediation of fluoride contaminated soil:conditioning of anolyte, *J. Hazard. Mater.* 161 (2009) 565-569.
- [16] Ching yuan, Chih-huang weng, Electrokinetic enhancement removal of heavy metals from industrial waste water sludge, *Chemosphere* 65 (2006) 88-96.
- [17] Suat Akbulut, Z. Nese Kurt, Sercettin Arasan, Electrokinetics properties of surfactant modified clays, *Int. J. Civil Struct. Eng.* 1 (3) (2010).
- [18] Yalcin B. Acar, Robert J. Galeb, Akram N. Alshawabke, Robert E. Mark, Wheel Puppall, Mark Brickad, Randy Parkere, Electrokinetic remediation: Basics and technology status, *J. Hazard. Mater.* 40 (1995) 117-137.
- [19] Young-Hyun Kim, Do-Hyung Kim, Hong-Bae Jung, Bo-Ram Hwang, Sung-Hwan Ko, Kitae Baek, Pilot scale ex-situ electrokinetic remediation of arsenic contaminated soil, *Separation Sci. Technol.* 47 (2012) 14-15.
- [20] Danuta Leszczynska, Hafiz Ahmad, Toxic Elements in Soil and Groundwater: Short-Time Study on Electrokinetic Removal of Arsenic in the Presence of other Ions, *Int. J. Environ. Res. Public Health* 3 (2) (2006) 196-201.
- [21] Venkata Sivapullaiah, Sriakantappa Nagendra Prakash and Nagahanumantharao Suma, Electrokinetic removal of heavy metals from soil, *J. Electrochem. Sci. Eng.* 5 (1) (2015) 47-65.
- [22] M.T. Ammami, A. Benamar, F. Koltalo, H.Q. Wang, F. LeDerf, Heavy metals removal from dredged sediments using electro kinetics, *E3S Web of Conference*, 1 (2013) 01004.
- [23] N. Utchimuthu, K. Saravanakumar, D. Joshua Amarnath, Removal Or Reducing Heavy Metal (Lead) From Soil By Electrokinetic Process, *Int. J. Eng. Res. Appl. (IJERA)* 2 (3) (2012) 2367-2373.
- [24] Shuning Zhaoa, Li Fana, Mingyuan Zhoua, Xuefeng Zhua, Xiuli Lia, Remediation of copper contaminated kaolin by electrokinetics coupled with permeable reactive barrier, *Procedia Environ. Sci.* 31 (2016) 274-279.
- [25] Yalcin B. Acar, Akram N. Alshawabkeh, Robert J. Gales, Fundamentals of extracting species from soils by electrokinetics, *Waste Manag.* 13 (1993) 141-151.
- [26] Nasim Mosavat, Erwin Oh and Gary Chai , A Review of Electrokinetic Treatment Technique for Improving the Engineering Characteristics of Low Permeable Problematic Soils *international journal of geomate*.2012. June, 2 (2) (Si no 4) (2012) 266-272.
- [27] M. Saleem, M.H. Chakrabarti, M.F. Irfan, S.A. Hajimolana, M.A. Hussain, B.H. Diya'uddeen, W.M.A.W. Daud, Electrokinetic remediation of nickel from low permeability soil, *Int. J. Electrochem. Sci.* 6 (2011) 4264-4275.
- [28] N.D. Mu'azu, Usman A. Bukharia, H. Essam, S. Lukman, Removal of heavy metals from contaminated clay soils using pulsed electrokinetic process, *Proceedings of the 14th International Conference on Environmental Science and Technology, Athens, Greece, 2015.*
- [29] A. Hansen, L. Hopkinson, A.B. Cundy, R. Pollock, Bench scale evaluation of hexavalent chromium reduction and containment using FIRS (Ferric Iron Remediation and Stabilisation) Technology, in: 5th International Conference on Electrokinetics, 2007, pp. 31-32.
- [30] Dimple Lakherwal, Adsorption of Heavy Metals: A Review, *Int. J. Environ. Res. Devel.* 4 (1) (2014) 41-48.
- [31] Arti Alok, R.P. Tiwari, R.P. Singh, Effect of pH of Anolyte In Electrokinetic Remediation Of Cadmium Contaminated Soil, *Int. J. Eng. Res. Technol.* 1 (2012) 10.
- [32] Wei Jiang, Tao Tao, Zhuming Liao, Removal of Heavy Metal from Contaminated Soil with Chelating Agents, *Open J. Soil Sci.* 1 (2011) 70-76.
- [33] Albert T. Yeung, Ying-Ying Gu, A review on techniques to enhance electrochemical remediation of contaminated soils, *J. Hazard. Mater.* 195 (2011) 11-29.
- [34] Kianti Maturi, Krishna R. Reddy, Simultaneous removal of organic compounds and heavy metals in soils by electrokinetic remediation with a modified cyclodextrin, *Chemosphere* 63 (2006) 1022-1031.
- [35] Soon-Oh Kim, Won-Seok Kim, Kyoung-Woong Kim, Evaluation of electrokinetic remediation of arsenic-contaminated soils, *Environ. Geochem. Health* 27 (2005) 443-453.
- [36] Ching Yuan, Tzu-Shing Chiang, Enhancement of electrokinetic remediation of arsenic spiked soil by chemical reagents, *J. Hazard. Mater.* 152 (2008) 309-315.
- [37] Ching Yuan, Tzu-Shing Chiang, The mechanism of arsenic removal from soil by electrokinetic process coupled with iron permeable reaction barrier *chemosphere* 67 (2007) 1533-1542.
- [38] Ha Uk Chung, Myung Ho Lee, A new method for remedial treatment of contaminated clayey soils by electrokinetics coupled with permeable reactive barriers, *Electrochim. Acta* 52 (2007) 3427-3431.
- [39] Ching yuan, chung-hsuang hung, kun cho chen, Electrokinetic remediation of arsenate spiked soil assisted by CNT Co barrier-the effect of barrier position and processing fluid, *J. Hazard. Mater.*, 171 (2009) 563-570.
- [40] Ashraf Z. Al-Hamdan, Krishna R. Reddy, Transient behavior of heavy metals in soils during electrokinetic remediation, *Chemosphere* 71 (2008), 860-871.

- [41] Mahsa Madani Hosseini, Mohsen Farahbakhsh, Gholamreza Savaghebi, Chelate Agents Enhanced Electrokinetic Remediation for Removal of Lead and Zinc from a calcareous Soil. *Int. Conf. Environ. Sci. Eng.*, 8 (2011).
- [42] Mahdi Bahemmat, Mohsen Farahbakhsh, Catholyte-Conditioning Enhanced Electrokinetic Remediation of Co And Pb Polluted Soil. *Environ. Eng. Manag. J.*, 14 (1) (2015) 89–96.
- [43] Jung-Seok Yung, Man Jae Kwon, Jaeyoung Choi, Kitae Beak, Edward J. O'Loughlin, The transport behavior of As, Cu, Pb and Zn during electrokinetic remediation of a contaminated soil using electrolytic conditioning. *Chemosphere* 117 (2014) 79–86.

Further Reading

- [1] Farid M. Hassan, Farid R. Farahy, Electrokinetic remediation technology for in situ remediation of heavy metals. In: *16th Meeting of the Egyptian National Outdoor Action Conference and Exposition, 1996*, pp. 237–245.
- [2] Hamed Niroumand, Ramli Nazir, Khairul Anuar Kassim, The Performance of Electrochemical Remediation Technologies in Soil Mechanics. *Int. J. Electrochem. Sci.*, 7 (2012) 5708–5715.

Automatic Detection of Coronavirus Disease (COVID-19) and Viral pneumonia Using X-ray Images and Deep Convolutional Neural Network

A RIZHA UL HAQ¹, A MOHAMED IFTHIKAR ALI², I SHEIK ARAFAT³

ME(Applied Electronics), Associate Professor, Associate Professor & Head, Department of Electronics And Communication Engineering, Mohammed Sathak Engineering College Kilakarai.

Abstract—The 2019 novel coronavirus disease (COVID-19), with a starting point in China, has spread rapidly among people living in other countries, and is approaching approximately 34,986,502 cases worldwide according to the statistics of European Centre for Disease Prevention and Control. There are a limited number of COVID-19 test kits available in hospitals due to the increasing cases daily. Therefore, it is necessary to implement an automatic detection system as a quick alternative diagnosis option to prevent COVID-19 spreading among people. At the same time we are also in a urge to find the alternative methods in the detection process of viral pneumonia patients. In this study, three pre-trained convolutional neural network based models (ResNet50, ResNet101 and Densenet) have been proposed for the detection of coronavirus and pneumonia infected patients using chest X-ray radiographs. We have implemented three different binary classifications with four classes (COVID-19, normal (healthy), viral pneumonia) by using 4-fold cross validation. Considering the performance results obtained, it has seen that the pre-trained ResNet50 model provides the highest classification performance (98.3929% accuracy for Dataset-1, 98.33% accuracy for Dataset2, 97.2024% accuracy for Dataset-3 and 98.2143% accuracy for Dataset-4) among the other two used models.

I. INTRODUCTION

The coronavirus disease (COVID-19) pandemic emerged in Wuhan, China in December 2019 and became a serious public health problem worldwide. Until now, no specific drug or vaccine has been found against COVID-19. The virus that causes COVID-19 epidemic disease is called severe acute respiratory syndrome coronavirus-2 (SARS-CoV-2).

Corona viruses (CoV) is a large family of viruses that cause diseases such as Middle East Respiratory Syndrome (MERS-CoV) and Severe Acute Respiratory Syndrome (SARS-CoV). COVID-19 is a new species discovered in 2019 and has not been previously identified in humans . COVID-19 causes lighter symptoms in about 99% of cases, according to early data, while the rest is severe or critical. As of 4th October 2020, the total number of worldwide cases of Coronavirus is 35,248,330. Of these, 1,039,541 (4%) people were deaths and 26,225,235 (96%) were recovered. The number of active patients is 7,983,554. Of these, 7,917,287 (99%) had mild disease while 66,267 (1%) had more severe disease. Nowadays the world is struggling with the COVID-19 epidemic. Deaths from pneumonia developing due to the SARS-CoV-2 virus are increasing day by day.

Chest radiography (X-ray) is one of the most important methods used for the diagnosis of pneumonia worldwide. Chest X-ray is a fast, cheap and common clinical method. The chest X-ray gives the patient a lower radiation dose compared to computed tomography (CT) and magnetic resonance imaging (MRI). However, making the correct diagnosis from X-ray images requires expert knowledge and experience . It is much more difficult to diagnose using a chest X-ray than other imaging modalities such as CT or MRI . By looking at the chest X-ray, COVID-19 can only be diagnosed by specialist physicians.

The number of specialists who can make this diagnosis is less than the number of normal doctors. Even in normal times, the number of doctors per person is insufficient in countries around the world. According to data from 2017, Greece ranks first with 607 doctors per 100,000 people. In other countries, this number is much lower. In case of disasters such as COVID-19 pandemic, demanding health services at the same time, collapse of the health system is inevitable due to the insufficient number of hospital beds and health personnel.

Handwritten signature
PRINCIPAL
MOHAMED SATHAK ENGINEERING COLLEGE
KILAKARAI 623 806

Also, COVID-19 is a highly contagious disease, and doctors, nurses, and caregivers are most at risk. Early diagnosis of pneumonia has a vital importance both in terms of slowing the speed of the spread of the epidemic by quarantining the patient and in the recovery process of the patient. Doctors can diagnose pneumonia from the chest X-ray more quickly and accurately thanks to computer-aided diagnosis (CAD).

Use of artificial intelligence methods are increasing due to its ability to cope with enormous datasets exceeding human potential in the field of medical services. Integrating CAD methods into radiologist diagnostic systems greatly reduces the workload of doctors and increases reliability and quantitative analysis. CAD systems based on deep learning and medical imaging are becoming more and more research fields.

II. RELATED WORKS

Studies diagnosed with COVID-19 using chest X-rays have binary or multiple classifications. Some studies use raw data while others have feature extraction process. The number of data used in studies also varies. Among the studies, the most preferred method is convolutional neural network (CNN). Apostolopoulos and Bessiana used a common pneumonia, COVID-19-induced pneumonia, and an evolutionary neural network for healthy differentiation on automatic detection of COVID-19. In particular, the procedure called transfer learning has been adopted.

With transfer learning, the detection of various abnormalities in small medical image datasets is an achievable goal, often with remarkable results. Based on chest X-ray images, Zhang et al. aimed to develop a deep learning-based model that can detect COVID-19 with high sensitivity, providing fast and reliable scanning. Singh et al. classified the chest computed tomography (CT) images from infected people with and without COVID-19 using multiobjective differential evolution (MODE) based CNN. In the study of Chen et al, they proposed Residual Attention U-Net for automated multi class segmentation technique to prepare the ground for the quantitative diagnosis of lung infection on COVID-19 related pneumonia using CT images. Adhikari's study suggested a network called "Auto Diagnostic Medical Analysis" trying to find infectious areas to help the doctor better identify the diseased part, if any. Both X-ray and CT images were used in the study. It has been recommended DenseNet network to remove and mark infected areas of the lung. In the study by Alqudah et al., two different methods were used to diagnose COVID-19 using chest X-ray images.

The first one used AOCTNet, MobileNet and ShuffleNet CNNs. Secondly, the features of their images have been removed and they have been classified using softmax classifier, K nearest neighbor (kNN), Support vector machine (SVM) and Random forest (RF) algorithms. Khan et al. classified the chest X-ray images from normal, bacterial and viral pneumonia cases using the Xception architecture to detect COVID-19 infection. Ghoshal and Tucker used the dropweights based Bayesian CNN model using chest X-ray images for the diagnosis of COVID-19. Hemdan et al. used VGG19 and DenseNet models to diagnose COVID-19 from X-ray images.

Uçar and Korkmaz worked on X-ray images for COVID19 diagnosis and supported the SqueezeNet model with Bayesian optimization. In the study conducted by Apostolopolus et al., they performed automatic detection from X-ray images using CNNs with transfer learning. Sahinbas and Catak used X-ray images for the diagnosis of COVID-19 and worked on VGG16, VGG19, ResNet, DenseNet and InceptionV3 models. Medhi et al.

used X-ray images as feature extraction and segmentation in their study, then COVID-19 was positively and normally classified using CNN. Barstugan et al. classified X-ray images for the diagnosis of COVID-19 using five different feature extraction methods that are Grey Level Cooccurrence Matrix (GLCM), Local Directional Patterns (LDP), Grey Level Run Length Matrix (GLRLM), Grey Level Size Zone

Matrix (GLSZM), and Discrete Wavelet Transform (DWT). The obtained features were classified by SVM. During the classification process, 2-fold, 5-fold, and 10-fold cross-validation methods were used.

Punn and Agarwal worked on X-ray images and used ResNet, InceptionV3, InceptionResNet models to diagnose COVID-19. Afshar et al. developed deep neural network (DNN) based diagnostic solutions and offered an alternative modeling framework based on Capsule Networks that can process on small data sets. In our previous study in March 2020, we used ResNet50, InceptionV3 and InceptionResNetV2 models for the diagnosis of COVID-19 using chest X-ray images. However, since there was not enough data on COVID-19, we were only able to train through 50 normal and 50 COVID-19 positive cases.

In this study, we have proposed an automatic prediction of COVID-19 using a deep convolution neural network based pre-trained transfer models and chest X-ray images. For this purpose, we have used ResNet50, ResNet101, ResNet152, InceptionV3 and InceptionResNetV2 pre-trained models to obtain higher prediction accuracies for three different binary datasets including X-ray images of normal (healthy), COVID-19, bacterial and viral pneumonia patients. The novelty and originality of proposed study is summarized as follows:

- i) The proposed models have end-to-end structure without manual feature extraction, selection and classification.
- ii) The performances of the COVID-19 data across normal, viral pneumonia and bacterial pneumonia classes were significantly higher.
- iii) It has been studied with more data than many studies in the literature.
- iv) It has been studied and compared with 3 different CNN models.
- v) A high-accuracy decision support system has been proposed to radiologists for the automatic diagnosis and detection of patients with suspected COVID-19 and follow-up.

The flow of the manuscript is organized as follows: Dataset is expressed in detail in Section 3.1. Deep transfer learning architecture, pre-trained models and experimental setup parameters are described in Section 3.2 and 3.3, respectively. Performance metrics are given in detail in Section 3.4. Obtained experimental results from proposed models and discussion are presented in Section 4 and 5, respectively. Finally, in Section 6, the conclusion and future works are summarized.

1. NEED FOR THIS PROJECT

- Also, COVID-19 is a highly contagious disease, and doctors, nurses, and caregivers are most at risk.
- Early diagnosis of viral pneumonia and Covid-19 has a vital importance both in terms of slowing the speed of the spread of the epidemic by quarantining the patient and in the recovery process of the patient.
- Doctors can easily find and identify the difference between Covid patients and pneumonia patients from their respective chest X-ray images more quickly and accurately.

WHY X-Ray?:

Chest radiography (X-ray) is one of the most important methods used for the diagnosis of pneumonia worldwide. Chest X-ray is a fast, cheap and common clinical method. The chest X-ray gives the patient a lower radiation dose compared to computed tomography (CT) and magnetic resonance imaging (MRI).

III. PROPOSED SYSTEM

- The proposed models have end-to-end structure without manual feature extraction, selection and classification.
- The performances of the COVID-19 data across normal, viral pneumonia and bacterial pneumonia classes were significantly higher.
- It has been studied with more data than many studies in the literature.
- A high-accuracy decision support system has been proposed to radiologists for the automatic diagnosis and detection of patients with suspected COVID-19 and follow-up.

Dataset:

In this study, chest X-ray images of 341 COVID-19 patients have been obtained from the open source GitHub repository shared by Dr. Joseph Cohen et al. This repository is consisting chest X-ray / computed tomography (CT) images of mainly patients with acute respiratory distress syndrome (ARDS), COVID-19, Middle East respiratory syndrome (MERS), pneumonia, severe acute respiratory syndrome (SARS). 2800 normal (healthy) chest X-ray images were selected from “ChestX-ray8” database. In addition, 2772 bacterial and 1493 viral pneumonia chest X-ray images were used from Kaggle repository called “Chest X-ray Images (Pneumonia)” .

Architecture of Deep Transfer Learning:

Deep learning is a sub-branch of the machine learning field, inspired by the structure of the brain. Deep learning techniques used in recent years continue to show an impressive performance in the field of medical image processing, as in many fields. By applying deep learning techniques to medical data, it is tried to draw meaningful results from medical data.

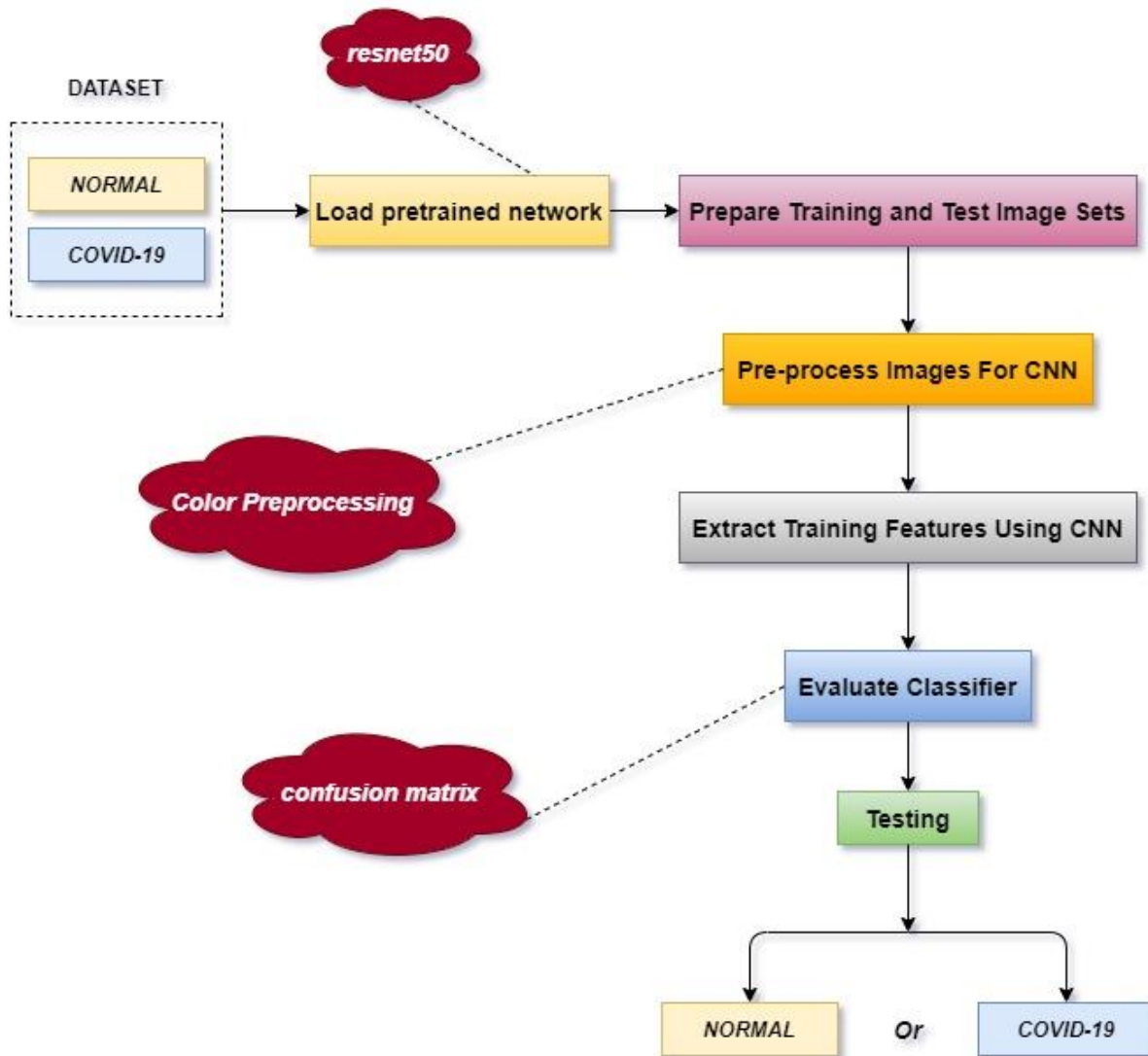
Deep learning models have been used successfully in many areas such as classification, segmentation and lesion detection of medical data. Analysis of image and signal data obtained with medical imaging techniques such as Magnetic Resonance Imaging (MRI), Computed Tomography (CT) and X-ray with the help of deep learning models. As a result of these analyzes, detection and diagnosis of diseases such as diabetes mellitus, brain tumor, skin cancer and breast cancer are provided with convenience . A convolutional neural network (CNN) is a class of deep neural networks used in image recognition problems.

Coming to how CNN works, the images given as input must be recognized by computers and converted into a format that can be processed. For this reason, images are first converted to matrix format. The system determines which image belongs to which label based on the differences in images and therefore in matrices. It learns the effects of these differences on the label during the training phase and then makes predictions for new images using them. CNN consists of three different layers that are a convolutional layer, pooling layer, and fully connected layer to perform these operations effectively.

The feature extraction process takes place in both convolutional and pooling layers. On the other hand, the classification process occurs in fully connected layer. These layers are examined sequentially in the following.

PROCESS FLOW CHART

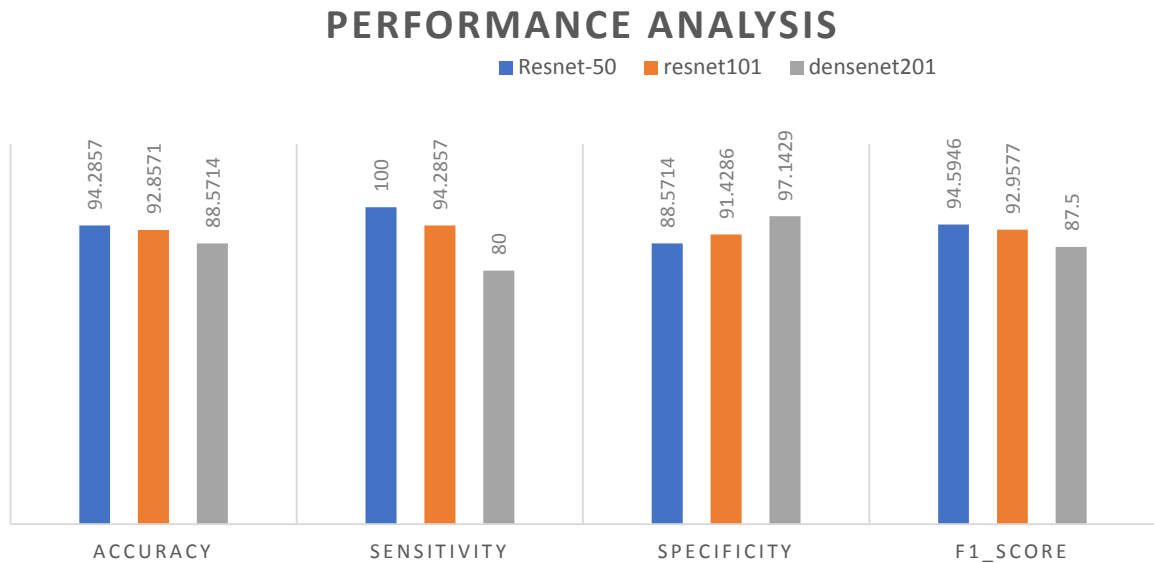
i) Binary class(Covid or not):



In the next step it is also identified whether the person is either affected by viral pneumonia or not which comes under multiple classes(Covid or viral pneumonia or normal).

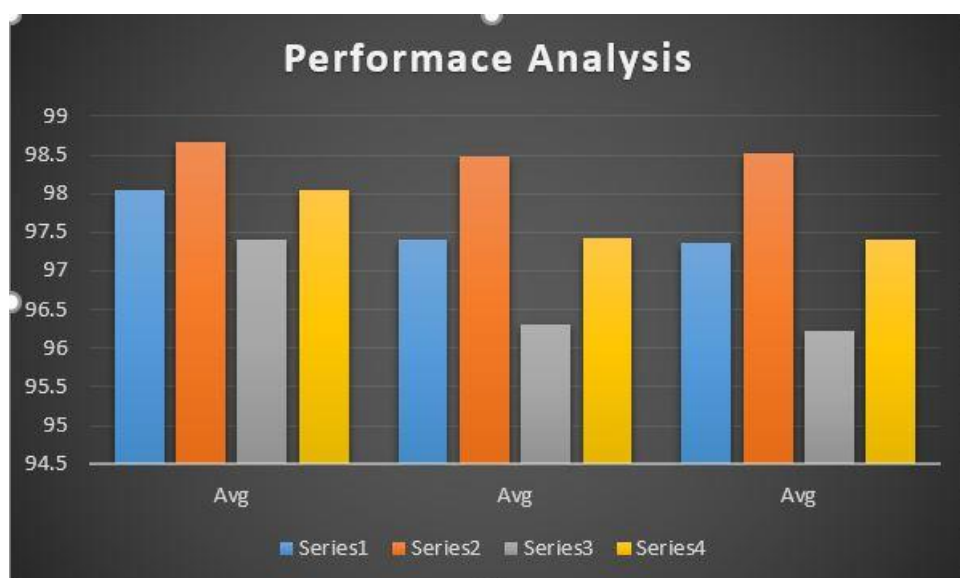
IV. PERFORMANCE ANALYSIS

2. i) *BINARY CLASS(COVID OR NOT)*:

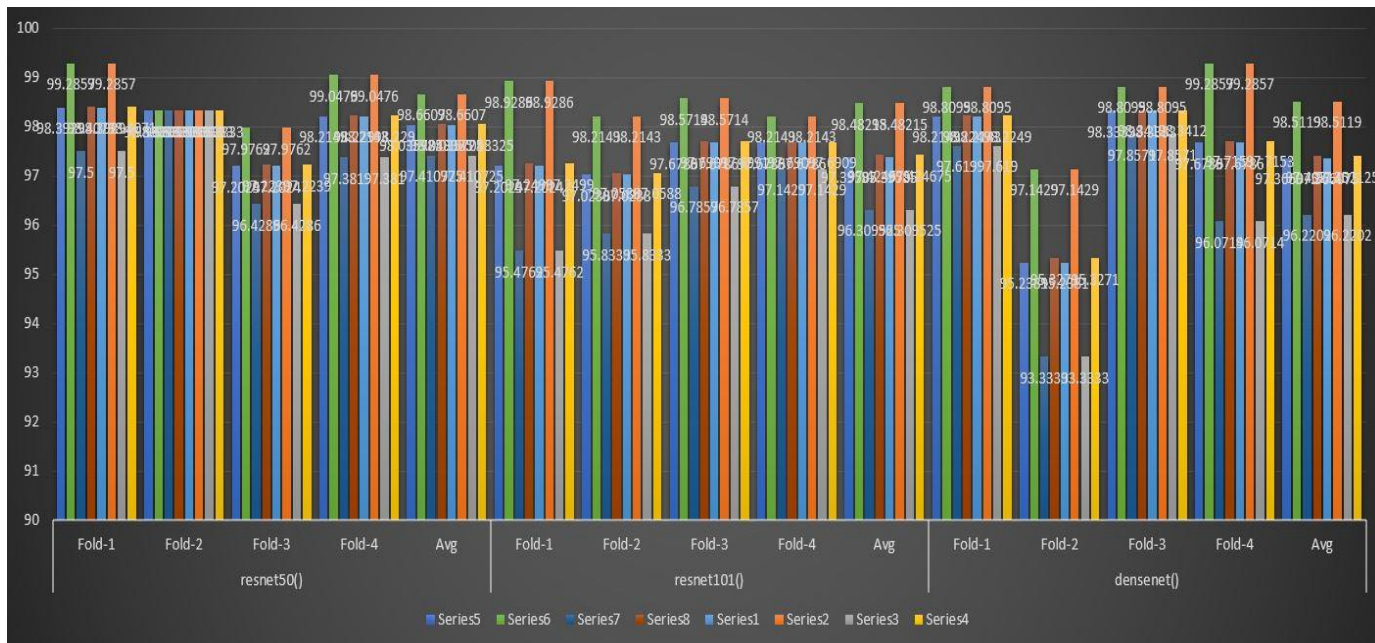


Here three types of CNN(Resne50,Resnet101,Densenet) has been compared between each other on the basis of some properties such as accuracy, sensitivity, specificity and F1_score in the graphical manner and among them Resnet50 has been found as the best alternative for the identification of covid-19 patients using their X-Ray images respectively.

ii) *MULTIPLE CLASSES(COVID OR PNEUMONIA OR NORMAL)*:



iii) MULTIPLE CLASSES BASED ON DIFFERENT ARCHITECTURES:



V.RESULTS AND DISCUSSIONS

Methods	Foldes	Accuracy	Sensitivity	Specificity	F1_Score
resnet50()	Fold-1	98.3929	99.2857	97.5	98.4071
	Fold-2	98.3333	98.3333	98.3333	98.3333
	Fold-3	97.2024	97.9762	96.4286	97.2239
	Fold-4	98.2143	99.0476	97.381	98.229
	Avg	98.035725	98.6607	97.410725	98.048325
resnet101()	Fold-1	97.2024	98.9286	95.4762	97.2499
	Fold-2	97.0238	98.2143	95.8333	97.0588
	Fold-3	97.6786	98.5714	96.7857	97.6991
	Fold-4	97.6786	98.2143	97.1429	97.6909
	Avg	97.39585	98.48215	96.309525	97.424675
densenet()	Fold-1	98.2143	98.8095	97.619	98.2249
	Fold-2	95.2381	97.1429	93.3333	95.3271
	Fold-3	98.3333	98.8095	97.8571	98.3412
	Fold-4	97.6786	99.2857	96.0714	97.7153
	Avg	97.366075	98.5119	96.2202	97.402125

Here three types of CNN(Resne50,Resnet101,Densenet) has been compared between each other on the basis of some properties such as accuracy, sensitivity, specificity and F1_score and their respective averages has been taken. Finally, among the three different architectures Resnet50 has been found as the best alternative for the identification of covid-19 and pneumonia patients using their X-Ray images respectively.

VI.CONCLUSION

Early prediction of COVID-19 and viral pneumonia patients is vital to prevent the spread of the disease to other people. In this study, we proposed a deep transfer learning based approach using Chest X-ray images obtained from normal, COVID-19 and viral pneumonia patients to predict COVID-19 patients and viral pneumonia patients automatically. Performance results show that ResNet50 pre-trained model yielded the highest accuracy among five models for used three different datasets. In the light of our findings, it is believed that it will help radiologists to make decisions in clinical practice due to the higher performance. In order to detect COVID-19 and viral pneumonia patients at an early stage, this study gives insight on how deep transfer learning methods can be used. In subsequent studies, the classification performance of different CNN models can be tested by increasing the number of COVID-19 and viral pneumonia Chest X-ray images in the dataset.



Joint intensity transformer network for gait recognition robust against clothing and carrying status

M. Amanulla Khan^a, S.M.H. Sithi Shameem Fathima^b, B. Arockia Stepnila^a, A. Mohamed Ifthikar Ali^a

Show more

Outline | Share | Cite

<https://doi.org/10.1016/j.matpr.2020.03.168>

Get rights and content

Abstract

Biometric systems are becoming increasingly important, as they provide a more reliable and efficient means of identity verification. Human identification at a distance has recently gained enormous interest among computer vision researchers. This process describes a simple but practical approach to gait recognition by detection and classification of the gait posture in image. On the other hand, background and foreground extraction maintenance model is also proposed for preventing any false information and to avoid overlapping results, poor segmentation and classification. Hence the features are extracted through the Gabor, CNN and then the classification is done by the multi SVM classifier. Index Terms— Joint intensity transformer network, joint intensity metric learning, gait recognition.

[Previous](#)

[Next](#)

Keywords

SVM; CNN; Gait recognition; Gabor filter

[Special issue articles](#)

[Recommended articles](#)

Cited by (1)

Advances in Vision-Based Gait Recognition: From Handcrafted to Deep Learning

2022, Sensors

Principal
PRINCIPAL
MOHAMED SATHAK ENGINEERING COLLEGE
KILAKARAI 623 806



Comparative Performance Analysis of Pre-Processing Techniques in CT Angiogram Images

Dr.C.Priya | Dr.I.Sheik Arafat | S.Vengateshkumar | Dr.R.Premkumar | Dr.A.Shyamala

Department of Electronics and Communication Engineering, Mohamed Sathak Engineering College, Kilakarai, Tamilnadu, India.

To Cite this Article

Dr.C.Priya, Dr.I.Sheik Arafat, S.Vengateshkumar, Dr.R.Premkumar, Dr.A.Shyamala, "Comparative Performance Analysis of Pre-Processing Techniques in CT Angiogram Images", *International Journal for Modern Trends in Science and Technology*, Vol. 07, Issue 04, April 2021, pp.:180-185.

Article Info

Received on 30-March-2021, Revised on 21-April-2021, Accepted on 25-April-2021, Published on 29-April-2021.

ABSTRACT

Cardiovascular disease is the most common killer worldwide. The technology advancement has successfully postponed someone obtaining cardiovascular disease and increased healthy life expectancy. Cardiovascular diseases are mostly caused by unhealthy life style, heredity or aging. The abnormalities of anatomy and physiology in cardiovascular system such as blood vessel blockage, valve defect, and abnormal heart muscle. The epicardial and pericardial fats presenting on the walls of the heart cause some lifethreatening diseases are typical characteristics of cardiovascular diseases. Even though manual screening is available but they are very much time consuming and inefficient. One of the best diagnosis modalities to detect the abnormalities are the medical imaging systems such as i) Ultrasound system ii) X-Ray Computer Tomography and iii) MRI. This paper discusses on seven different preprocessing methods available in literature and found the optimum technique for enhancing the coronary CT images. The performance of all the techniques has been tested on the real time images obtained.

KEYWORDS: Bottom-hat transform, CLAHE, epicardial and pericardial fats, Median filter

I. INTRODUCTION

Every 34 seconds a human being experiences a Coronary Artery Disorder, which accounts for approximately 1 out of every 6 death on the global scale. Coronary Catheter Angiography (CCA) and Coronary CT angiography (CCTA) have been used for a wide range of medical applications. CCA is invasive technique (using a large needle) to detect blocks. CCTA is non-invasive technique (using a small needle) placed in the arm or hand.

Computed Tomography (CT) is one such medical imaging method employing tomography where reconfigurable hardware can be successfully employed. Tomography refers to the process that generates a cross-sectional image of an object from a series of projections collected by scanning the object from many different directions. Among the various alternatives available for projection data

acquisition like X-rays, magnetic resonance, radioisotopes, ultrasound, our analysis pertains to two-dimensional X-ray absorption tomography.

Therefore early detection and prevention of stenosis through medical imaging is very important. For this cardiologist widely uses CCA and CT images to diagnose the heart diseases like fat deposition, soft plaque, Calcium-Score Atherosclerosis and stenosis. Preprocessing which is the fundamental step in the automatic detection of heart diseases is investigated in this paper.

The important reason for main focus on preprocessing is because the CCA images are many times degraded by several problems like noise, uneven illumination, poor contrast and variation in capturing. Preprocessing helps to remove the noise and enhance the image for early detection of the disease.

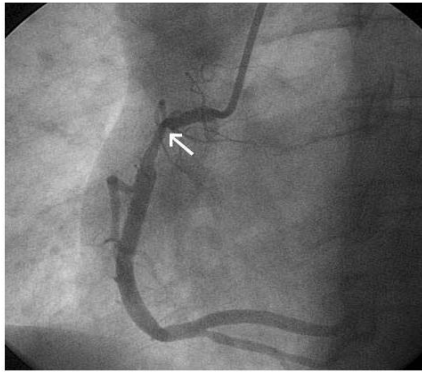


Fig. 1. CCA image with plaque

Figure 1 shows an example of CCA image. Some of the common signs of CDA which are plaque, calcium deposition and stenosis.

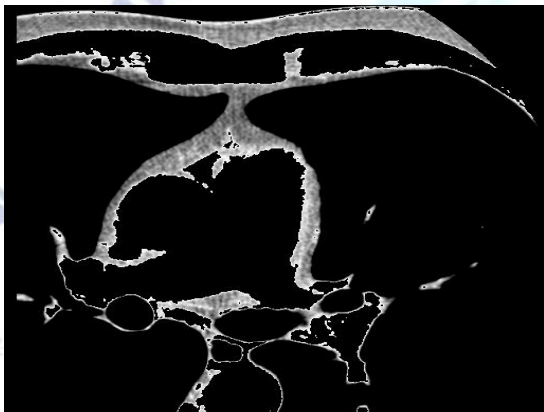


Fig 2. CCTA Image with fat deposition

The rest of this paper is organized as follows. Section II gives the study of existing approach. The materials used in this study are discussed in section III. The various preprocessing methods analyzed for the enhancement of CCA images are explained in section IV. The results are explained in section V. Finally, Section VI presents the conclusion and discussion

II. STATE OF ART

Few investigations in the past have confirmed that the good quality of CCA and CT images are required for accurate and early diagnosis of plaque. On a survey, it is predicted that nearly 12% of the images cannot be analyzed for detection because of their poor quality. Therefore an enhancement in the CCA image quality is very much essential in the diagnosis of stenosis. So to enhance the quality, preprocessing of images should be applied. In medical image registration, the utilization of external skin markers is inspired since they permit the attainment of any imaging modalities in

which the positions of markers can be accurately defined. Registration using skin markers does not vary respecting to the amendment in the image patterns, stimulated by the pathologies [6]. Skin markers must have the features like easier usage, precise attach and non-interference with the diagnostic region of the images. However, some errors occur because of the flexibility of the body, hence the chosen areas of the body must be quite stable for fixing markers. Sinha *et al* [7] endorsed the rigid cardiac MRI and PET image registration by scrutinizing the error using cardiac landmarks.

The head-and-hat algorithm [8] was initially presented by Pelizzari *et al* for brain image registration. This method demonstrates the contours of one image of the set (usually higher resolution) as a surface (head) and the contours of the remaining image set as a series of points (hat). Then the algorithm defines the optimum rigid transformation and reduces the mean squared deviation (MSD) between the elements of the hat and the surfaces of the head through the Powell minimization algorithm [9]. Dey *et al* [10] employed SPECT image as a mediator in thorax CT and SPECT image registration. Turkington *et al* [11] exploited cross-correlation measure for the firm orientation of dynamic cardiac PET images to cardiac templates. In the preprocessing stage, the authors applied Contrast Limited Adaptive Histogram Equalization technique to improve the contrast and for enhancing the plaque authors considered mean filter for image smoothing before enhancing. But mean filter does not have monotonically decreasing frequency response and it is not the best filter for image smoothing. Based on the details obtained by studying the existing works, the importance of preprocessing in CCA image was understood. The main importance of this work is to present a comparative study on various enhancement techniques available in research work. From the study and the obtained result, this work suggests a simple and efficient method for the preprocessing stage.

III. MATERIALS

To evaluate the performance of our algorithm, the CCA and CCTA images were obtained from the publicly available Databases and real time data are obtained from reputed hospitals.

IV. METHODS

In our work, various preprocessing methods have been used to enhance the digital CCA images. This work was tested with some common methodology that was introduced previously for the improvement of contrast level and removal of noise.

A. Contrast Enhancement using Bottom-hat transform

A common technique for the enhancement of contrast of an image is the use of morphological operation like bottom-hat transform. The bottom-hat transform is performed by obtaining the difference between closing of original image with the original image.

$$Bhat(f) = (f \bullet b) - f \quad (1)$$

Where $(f \bullet b)$ denotes the closing operation and f is the original image.

The closing of an image 'f' by structuring element 'b' is defined as dilation of 'f' by b, followed by erosion of the result with the structuring element b.

$$(f \bullet b) = (f \text{ dilation } b) \text{ erosion } b \quad (2)$$

A disk shaped structuring element was considered since it gives a good result for image enhancement.

B. Contrast Enhancement by Histogram Equalization

To enhance the contrast of color retinal images, histogram equalization is applied on the green channel of the color image. The Histogram equalization of image f is defined by Where floor() rounds down to the nearest integer. L denotes the number of possible intensity levels in the image f and $Pr(r_k)$ denotes the probability of occurrence of intensity level r_k .

C. Removal of Noise by median filter

Median filter is most suitable when our image is affected by impulse noise or salt and pepper noise. It involves finding the median value in a local neighborhood and it is a non-linear operation. To simultaneously reduce noise and preserves edges in color fundus images, median filtering is more effective than the convolution.

D. Enhancement using Contrast Limited Adaptive Histogram Equalization

Contrast Limited Adaptive Histogram Equalization (CLAHE) partition the green channel of the retinal image into contextual regions and

then histogram equalization is applied to each region. This equalizes the distribution of used gray levels and makes the hidden features more visible. CLAHE process on small region of image rather than the entire image itself.

V. EXPERIMENTAL RESULTS

The effect of different preprocessing techniques was evaluated on images from publicly available standard database

A. Result of Contrast Enhancement using Bottom-hat Transform

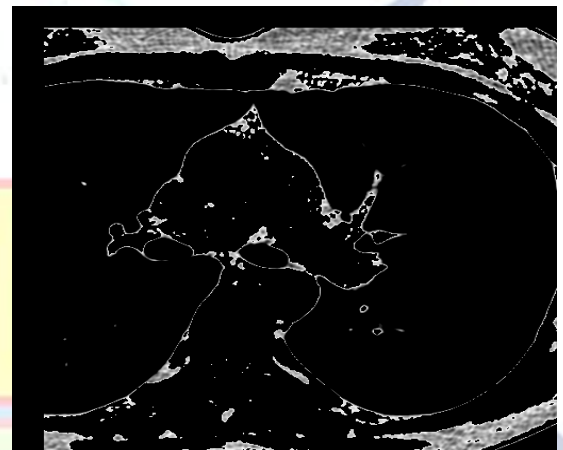


Fig. 3. Output of Bottom-hat transforms

B. Contrast Enhancement by Histogram Equalization

The image enhanced by histogram equalization is shown in figure 4.

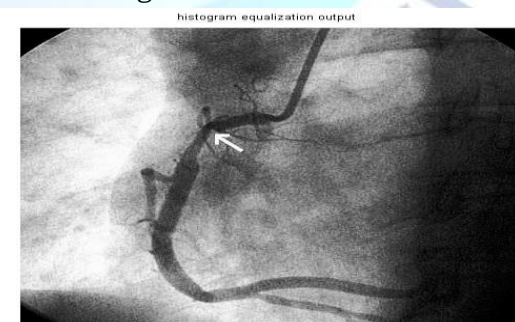


Fig. 4. Output image Enhanced image by histogramEqualization

C. Result of Removal of Noise by median filter

The CCA image which is affected by salt and pepper noise

is shown in figure 5

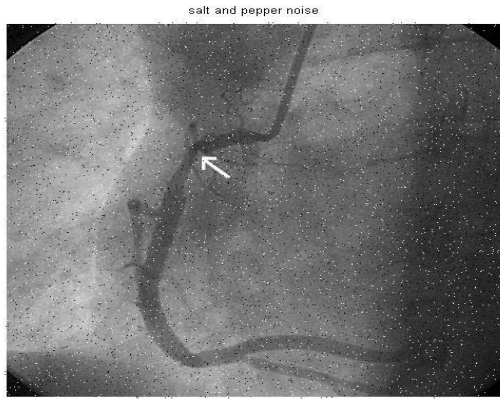


Fig. 5. Image affected by salt and pepper noise.

The output of median filtering is shown in figure 5

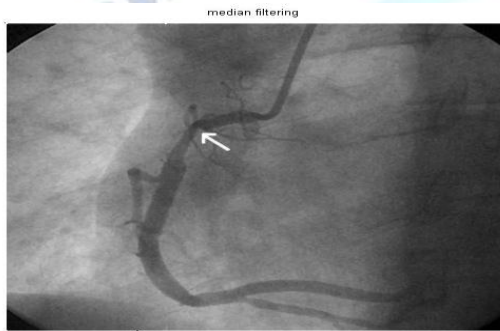


Fig. 6. Output of median filter

D. Result of Enhancement using Contrast Limited Adaptive Histogram Equalization

The resultant enhanced image by performing CLAHE on the green channel is shown in figure 6



Fig. 7. Output image enhanced by CLAHE

The CCA image which is affected by Gaussian noise is shown in figure 7

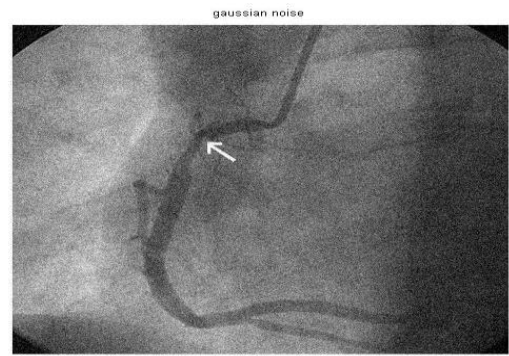


Fig. 8. Image affected by Gaussian noise
The output of Gaussian filtering is shown in figure

7

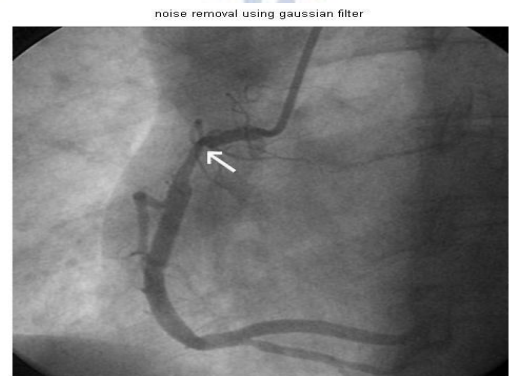


Fig. 9. Output of Gaussian filter

E. Result of Optimal preprocessing technique

The green component of the original RGB image is extracted and shown in figure 3. This image is applied to a median filter and the output obtained and the filtered image is enhanced by CLAHE and the result is shown in figure 8

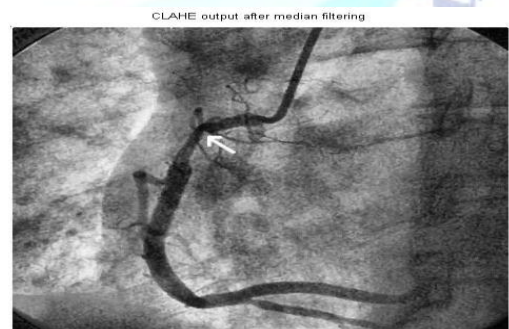


Fig. 10. Output of Optimal preprocessing technique

VI. CONCLUSION

This paper investigated and compared five different Preprocessing methods of CCA and CCTA images and found an optimum technique for preprocessing. This work evaluated the diagnostic accuracy of the proposed method in terms of

image-based criteria. Even though, the morphological top hat operation gives a good result; it failed to remove the noise completely. Median filter produces good result against noise but the features are not enhanced. Robustness and accuracy have been evaluated by our optimum technique on publicly available databases and it is found to be high when the result was consulted with an expert.

REFERENCES

- [1] Dey, Damini, et al. "Ct quantification of epicardial fat: Implications for cardiovascular risk assessment." *Current Cardiovascular Imaging Reports* 5.5 (2012): 352-359.
- [2] Rischpler, Christoph, et al. "Hybrid PET/MR imaging of the heart: potential, initial experiences, and future prospects." *Journal of Nuclear Medicine* 54.3 (2013): 402-415.
- [3] Specht, J. M., et al. "Abstract P5-01-02: Multimodality molecular imaging with dynamic 18F-fluorodeoxyglucose positron emission tomography (FDG PET) and MRI to evaluate response and resistance to neoadjuvant chemotherapy (NAC)." (2016): P5-01.
- [4] Ahmadian, Azadeh, et al. "Quantitative interpretation of FDG PET/CT with myocardial perfusion imaging increases diagnostic information in the evaluation of cardiac sarcoidosis." *Journal of nuclear cardiology* 21.5 (2014): 925-939.
- [5] Zuva, Tranos, et al. "Image segmentation, available techniques, developments and open issues." *Canadian Journal on Image Processing and Computer Vision* 2.3 (2011): 20-29.
- [6] Makela, Timo, et al. "A review of cardiac image registration methods." *IEEE Transactions on medical imaging* 21.9 (2002): 1011-1021.
- [7] Sinha, Shantanu, et al. "Noninvasive assessment of myocardial perfusion and metabolism: feasibility of registering gated MR and PET images." *AJR. American journal of roentgenology* 164.2 (1995): 301-307.
- [8] Pelizzari, Charles A., et al. "Accurate three-dimensional registration of CT, PET, and/or MR images of the brain." *J Comput Assist Tomogr* 13.1 (1989): 20-26.
- [9] Powell, M. J. D. "An iterative method for finding stationary values of a function of several variables." *The Computer Journal* 5.2 (1962): 147-151.
- [10] Dey, Damini, et al. "Automatic three-dimensional multimodality registration using radionuclide transmission CT attenuation maps: a phantom study." *The Journal of Nuclear Medicine* 40.3 (1999): 448.
- [11] T. G. Turkington, T. R. DeGrado, M. W. Hanson, and R. E. Coleman, "Alignment of dynamic cardiac PET images for correction of motion," *IEEE Trans. Nucl. Sci.*, vol. 44, pp. 235-242, Apr. 1997.
- [12] Gorter P, vanLindert A, deVos et al. A. 2008. Quantification of epicardial and peri-coronary fat using cardiac computed tomography; reproducibility and relation with obesity and metabolic syndrome in patients suspected of coronary artery disease. *Atherosclerosis* 197(2):896-903.
- [13] Dey D, Suzuki Y, et al. SS. 2008. Automated continuation of pericardial fat from noncontrast CT. *Investigative Radiology* 43(2):145-153
- [14] Bandekar, Alok N., MortezaNaghavi, and Ioannis A. Kakadiaris. "Automated pericardial fat quantification in CT data." *Engineering in Medicine and Biology Society, 2006. EMBS'06. 28th Annual International Conference of the IEEE. IEEE, 2006.*
- [15] Sicari, Rosa, Anna Maria Sironi, Roberta Petz, Francesca Frassi, Vladislav Chubuchny, Daniele De Marchi, Vincenzo Positano, Massimo Lombardi, Eugenio Picano, and Amalia Gastaldelli, "Pericardial rather than epicardial fat is a cardiometabolic risk marker: an MRI vs echo study", *Journal of the American Society of Echocardiography*, Vol.24, No. 10, pp.1156-1162, 2011.
- [16] Sacks, Harold S and John N. Fain, "Human epicardial adipose tissue: a review", *American heart journal*, Vol.153, No. 6, pp.907-917, 2007.
- [17] Ding, Xiaowei, Demetri Terzopoulos, Mariana Diaz-Zamudio, Daniel S. Berman, Piotr J. Slomka, and Damini Dey, "Automated epicardial fat volume quantification from non-contrast CT", *Journal of Medical Imaging*, pp. 90340I-9034, 2014.
- [18] Marwan, Mohamed, and Stephan Achenbach, "Quantification of epicardial fat by computed tomography: why, when and how?", *Journal of cardiovascular computed tomography*, Vol. 7, No. 1, pp. 3-10, 2013.
- [19] Pontone, Gianluca, Daniele Andreini, Erika Bertella, Maria Petullà, Eleonora Russo, Ester Innocenti, Saima Mushtaq, "Comparison of cardiac computed tomography versus cardiac magnetic resonance for characterization of left atrium anatomy before radiofrequency catheter ablation of atrial fibrillation" *International journal of cardiology*, Vol. 179, pp.114-12, 2015.
- [20] Oda, Seitaro, Daisuke Utsunomiya, Yoshinori Funama, Hideaki Yuki, MasafumiKidoh, Takeshi Nakaura, Hiroko Takaoka, "Effect of iterative reconstruction on variability and reproducibility of epicardial fat volume quantification by cardiac CT", *Journal of cardiovascular computed tomography*, Vol.10, No.2, pp.150-155, 2016.
- [21] Ling, Zhiyu, John McManigle, Vadim Zipunnikov, FarhadPashakhanloo, Irfan M. Khurram, Stefan L. Zimmerman, Binu Philips, "The association of left atrial low-voltage regions on electroanatomic mapping with low attenuation regions on cardiac computed tomography perfusion imaging in patients with atrial fibrillation", *Journal on Heart Rhythm*, Vol. 12, No. 2, pp: 857-864, 2015.
- [22] Apfaltrer, Paul, Andreas Schindler, U. Joseph Schoepf, John W. Nance, Francesco Tricarico, Ullrich Ebersberger, Andrew D. McQuiston, "Comparison of epicardial fat volume by computed tomography in black versus white patients with acute chest pain" *The American journal of cardiology*, Vol. 113, No. 3, pp.422-428, 2015.
- [23] Bucher, Andreas M., U. Joseph Schoepf, Aleksander W. Krazinski, Justin Silverman, James V. Spearman, Carlo N. De Cecco, Felix G. Meinel, Thomas J. Vogl, and Lucas L. Geyer, "Influence of technical parameters on epicardial fat volume quantification at cardiac CT", *European journal of radiology*, Vol. 84, No. 6, pp.1062-1067, 2015.
- [24] Isgum, Ivana, Marius Staring, Annemarieke Rutten, Mathias Prokop, Max A. Viergever, and Bram Van Ginneken, "Multi-atlas-based segmentation with local decision fusion—Application to cardiac and aortic segmentation in CT scans", *IEEE transactions on medical imaging*, Vol.28, No. 7, pp.1000-1010, 2009.
- [25] Rodrigues, Erick Oliveira, F. F. C. Morais, N. A. O. S. Morais, L. S. Conci, L. V. Neto, and Aura Conci, "A novel approach for the automated segmentation and volume quantification of cardiac fats on computed tomography" *Computer methods and programs in biomedicine*, Vol.123, pp.109-128, 2016.

- [26] T.E. Brinkley, Tina E., F-C. Hsu, J. Jeffrey Carr, W. Gregory Hundley, David A. Bluemke, Joseph F. Polak, and Jingzhong Ding", Pericardial fat is associated with carotid stiffness in the Multi-Ethnic Study of Atherosclerosis", *Journal on Nutrition, Metabolism and Cardiovascular Diseases*, Vol.21, No. 5, pp. 332-338, 2011.
- [27] Bandekar, Alok N., MortezaNaghavi, and Ioannis A. Kakadiaris. "Automated pericardial fat quantification in CT data", In *Engineering in Medicine and Biology Society, International Conference of the IEEE*, pp. 932-935, IEEE, 2006.
- [28] Kaus, Michael R., Jens von Berg, Jürgen Weese, WiroNiessen, and Vladimir Pekar, "Automated segmentation of the left ventricle in cardiac MRI", *Journal on Medical image analysis*, Vol.8, No. 3, pp. 245-254, 2004.
- [29] Mangili, Leonardo C., Otavio C. Mangili, Márcio S. Bittencourt, Márcio H. Miname, Paulo H. Harada, Leonardo M. Lima, Carlos E. Rochitte, and Raul D. Santos, "Epicardial fat is associated with severity of subclinical coronary atherosclerosis in familial hypercholesterolemia", *Journal on Atherosclerosis*, Vol. 254, pp.73-77, 2016.
- [30] Yang, Feng, Mingyue Ding, Xuming Zhang, Wenguang Hou, and Cheng Zhong, "Non-rigid multi-modal medical image registration by combining L-BFGS-B with cat swarm optimization", *Journal on Information sciences*, Vol.316, pp.440-456, 2015.
- [31] Champier, Jacques, Luc Cinotti, Jean-Claude Bordet, Franck Lavenne, and Jean-Jacques Mallet, "Delineation and quantization of brain lesions by fuzzy clustering in positron emission tomography", *Journal on Computerized medical imaging and graphics*, Vol.20, No. 1, pp.31-41, 2006.
- [32] Lin, Daw-Tung, Chung-Ren Yan, and Wen-Tai Chen, "Autonomous detection of pulmonary nodules on CT images with a neural network-based fuzzy system", *Journal on Computerized Medical Imaging and Graphics*, Vol.29, No. 6, pp.447-458, 2005.



Comparative Performance Analysis of Pre-Processing Techniques in CT Angiogram Images

Dr.C.Priya | Dr.I.Sheik Arafat | S.Vengateshkumar | Dr.R.Premkumar | Dr.A.Shyamala

Department of Electronics and Communication Engineering, Mohamed Sathak Engineering College, Kilakarai, Tamilnadu, India.

To Cite this Article

Dr.C.Priya, Dr.I.Sheik Arafat, S.Vengateshkumar, Dr.R.Premkumar, Dr.A.Shyamala, "Comparative Performance Analysis of Pre-Processing Techniques in CT Angiogram Images", *International Journal for Modern Trends in Science and Technology*, Vol. 07, Issue 04, April 2021, pp.:180-185.

Article Info

Received on 30-March-2021, Revised on 21-April-2021, Accepted on 25-April-2021, Published on 29-April-2021.

ABSTRACT

Cardiovascular disease is the most common killer worldwide. The technology advancement has successfully postponed someone obtaining cardiovascular disease and increased healthy life expectancy. Cardiovascular diseases are mostly caused by unhealthy life style, heredity or aging. The abnormalities of anatomy and physiology in cardiovascular system such as blood vessel blockage, valve defect, and abnormal heart muscle. The epicardial and pericardial fats presenting on the walls of the heart cause some lifethreatening diseases are typical characteristics of cardiovascular diseases. Even though manual screening is available but they are very much time consuming and inefficient. One of the best diagnosis modalities to detect the abnormalities are the medical imaging systems such as i) Ultrasound system ii) X-Ray Computer Tomography and iii) MRI. This paper discusses on seven different preprocessing methods available in literature and found the optimum technique for enhancing the coronary CT images. The performance of all the techniques has been tested on the real time images obtained.

KEYWORDS: Bottom-hat transform, CLAHE, epicardial and pericardial fats, Median filter

I. INTRODUCTION

Every 34 seconds a human being experiences a Coronary Artery Disorder, which accounts for approximately 1 out of every 6 death on the global scale. Coronary Catheter Angiography (CCA) and Coronary CT angiography (CCTA) have been used for a wide range of medical applications. CCA is invasive technique (using a large needle) to detect blocks. CCTA is non-invasive technique (using a small needle) placed in the arm or hand.

Computed Tomography (CT) is one such medical imaging method employing tomography where reconfigurable hardware can be successfully employed. Tomography refers to the process that generates a cross-sectional image of an object from a series of projections collected by scanning the object from many different directions. Among the various alternatives available for projection data

acquisition like X-rays, magnetic resonance, radioisotopes, ultrasound, our analysis pertains to two-dimensional X-ray absorption tomography.

Therefore early detection and prevention of stenosis through medical imaging is very important. For this cardiologist widely uses CCA and CT images to diagnose the heart diseases like fat deposition, soft plaque, Calcium-Score Atherosclerosis and stenosis. Preprocessing which is the fundamental step in the automatic detection of heart diseases is investigated in this paper.

The important reason for main focus on preprocessing is because the CCA images are many times degraded by several problems like noise, uneven illumination, poor contrast and variation in capturing. Preprocessing helps to remove the noise and enhance the image for early detection of the disease.

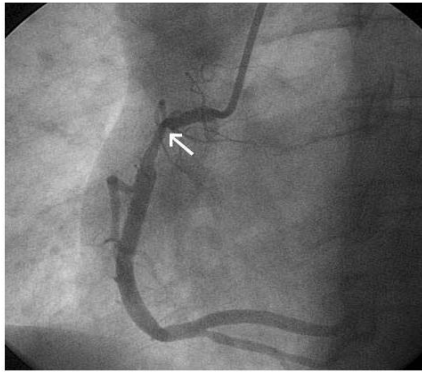


Fig. 1. CCA image with plaque

Figure 1 shows an example of CCA image. Some of the common signs of CDA which are plaque, calcium deposition and stenosis.

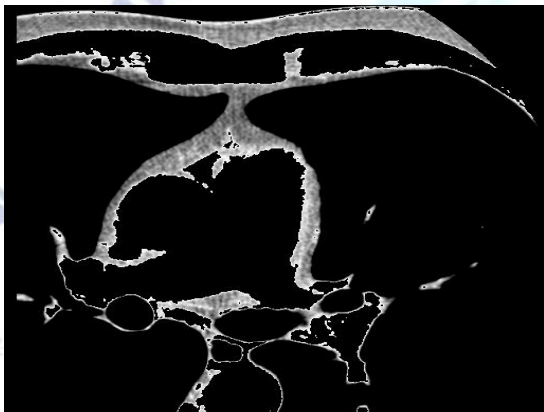


Fig 2. CCTA Image with fat deposition

The rest of this paper is organized as follows. Section II gives the study of existing approach. The materials used in this study are discussed in section III. The various preprocessing methods analyzed for the enhancement of CCA images are explained in section IV. The results are explained in section V. Finally, Section VI presents the conclusion and discussion

II. STATE OF ART

Few investigations in the past have confirmed that the good quality of CCA and CT images are required for accurate and early diagnosis of plaque. On a survey, it is predicted that nearly 12% of the images cannot be analyzed for detection because of their poor quality. Therefore an enhancement in the CCA image quality is very much essential in the diagnosis of stenosis. So to enhance the quality, preprocessing of images should be applied. In medical image registration, the utilization of external skin markers is inspired since they permit the attainment of any imaging modalities in

which the positions of markers can be accurately defined. Registration using skin markers does not vary respecting to the amendment in the image patterns, stimulated by the pathologies [6]. Skin markers must have the features like easier usage, precise attach and non-interference with the diagnostic region of the images. However, some errors occur because of the flexibility of the body, hence the chosen areas of the body must be quite stable for fixing markers. Sinha *et al* [7] endorsed the rigid cardiac MRI and PET image registration by scrutinizing the error using cardiac landmarks.

The head-and-hat algorithm [8] was initially presented by Pelizzari *et al* for brain image registration. This method demonstrates the contours of one image of the set (usually higher resolution) as a surface (head) and the contours of the remaining image set as a series of points (hat). Then the algorithm defines the optimum rigid transformation and reduces the mean squared deviation (MSD) between the elements of the hat and the surfaces of the head through the Powell minimization algorithm [9]. Dey *et al* [10] employed SPECT image as a mediator in thorax CT and SPECT image registration. Turkington *et al* [11] exploited cross-correlation measure for the firm orientation of dynamic cardiac PET images to cardiac templates. In the preprocessing stage, the authors applied Contrast Limited Adaptive Histogram Equalization technique to improve the contrast and for enhancing the plaque authors considered mean filter for image smoothing before enhancing. But mean filter does not have monotonically decreasing frequency response and it is not the best filter for image smoothing. Based on the details obtained by studying the existing works, the importance of preprocessing in CCA image was understood. The main importance of this work is to present a comparative study on various enhancement techniques available in research work. From the study and the obtained result, this work suggests a simple and efficient method for the preprocessing stage.

III. MATERIALS

To evaluate the performance of our algorithm, the CCA and CCTA images were obtained from the publicly available Databases and real time data are obtained from reputed hospitals.

IV. METHODS

In our work, various preprocessing methods have been used to enhance the digital CCA images. This work was tested with some common methodology that was introduced previously for the improvement of contrast level and removal of noise.

A. Contrast Enhancement using Bottom-hat transform

A common technique for the enhancement of contrast of an image is the use of morphological operation like bottom-hat transform. The bottom-hat transform is performed by obtaining the difference between closing of original image with the original image.

$$Bhat(f) = (f \bullet b) - f \quad (1)$$

Where $(f \bullet b)$ denotes the closing operation and f is the original image.

The closing of an image 'f' by structuring element 'b' is defined as dilation of 'f' by b, followed by erosion of the result with the structuring element b.

$$(f \bullet b) = (f \text{ dilation } b) \text{ erosion } b \quad (2)$$

A disk shaped structuring element was considered since it gives a good result for image enhancement.

B. Contrast Enhancement by Histogram Equalization

To enhance the contrast of color retinal images, histogram equalization is applied on the green channel of the color image. The Histogram equalization of image f is defined by Where floor() rounds down to the nearest integer. L denotes the number of possible intensity levels in the image f and $Pr(r_k)$ denotes the probability of occurrence of intensity level r_k .

C. Removal of Noise by median filter

Median filter is most suitable when our image is affected by impulse noise or salt and pepper noise. It involves finding the median value in a local neighborhood and it is a non-linear operation. To simultaneously reduce noise and preserves edges in color fundus images, median filtering is more effective than the convolution.

D. Enhancement using Contrast Limited Adaptive Histogram Equalization

Contrast Limited Adaptive Histogram Equalization (CLAHE) partition the green channel of the retinal image into contextual regions and

then histogram equalization is applied to each region. This equalizes the distribution of used gray levels and makes the hidden features more visible. CLAHE process on small region of image rather than the entire image itself.

V. EXPERIMENTAL RESULTS

The effect of different preprocessing techniques was evaluated on images from publicly available standard database

A. Result of Contrast Enhancement using Bottom-hat Transform

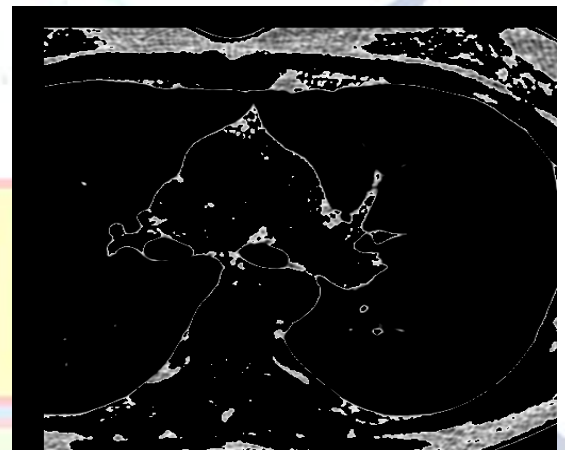


Fig. 3. Output of Bottom-hat transforms

B. Contrast Enhancement by Histogram Equalization

The image enhanced by histogram equalization is shown in figure 4.

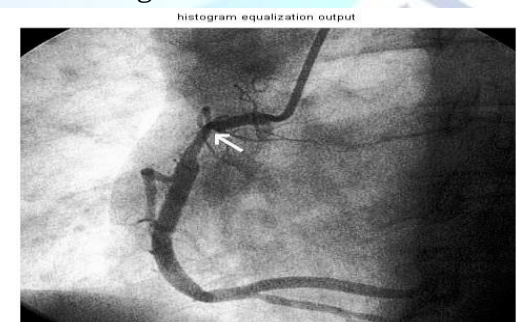


Fig. 4. Output image Enhanced image by histogramEqualization

C. Result of Removal of Noise by median filter

The CCA image which is affected by salt and pepper noise

is shown in figure 5

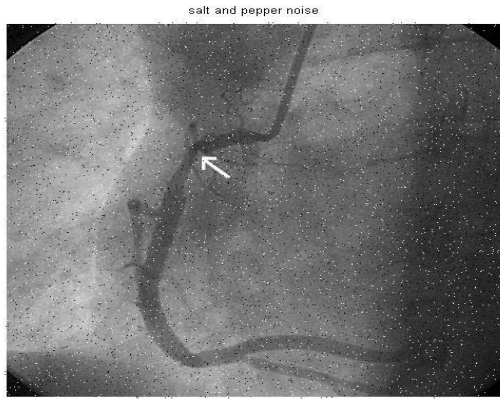


Fig. 5. Image affected by salt and pepper noise.

The output of median filtering is shown in figure 5

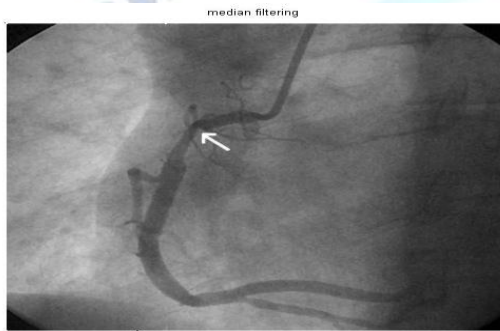


Fig. 6. Output of median filter

D. Result of Enhancement using Contrast Limited Adaptive Histogram Equalization

The resultant enhanced image by performing CLAHE on the green channel is shown in figure 6



Fig. 7. Output image enhanced by CLAHE

The CCA image which is affected by Gaussian noise is shown in figure 7

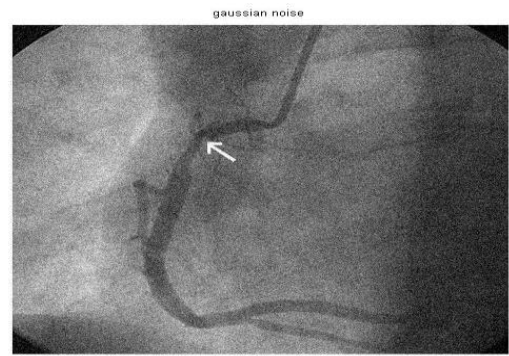


Fig. 8. Image affected by Gaussian noise
The output of Gaussian filtering is shown in figure

7

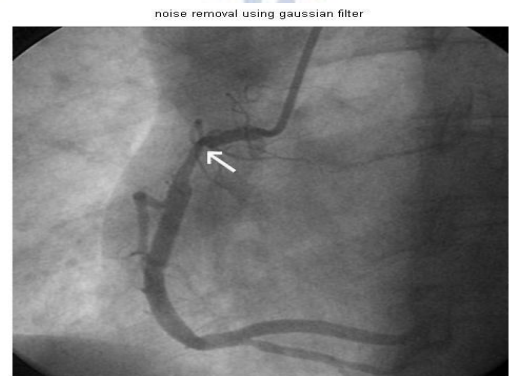


Fig. 9. Output of Gaussian filter

E. Result of Optimal preprocessing technique

The green component of the original RGB image is extracted and shown in figure 3. This image is applied to a median filter and the output obtained and the filtered image is enhanced by CLAHE and the result is shown in figure 8

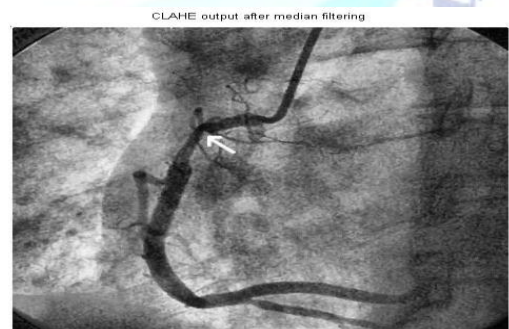


Fig. 10. Output of Optimal preprocessing technique

VI. CONCLUSION

This paper investigated and compared five different Preprocessing methods of CCA and CCTA images and found an optimum technique for preprocessing. This work evaluated the diagnostic accuracy of the proposed method in terms of

image-based criteria. Even though, the morphological top hat operation gives a good result; it failed to remove the noise completely. Median filter produces good result against noise but the features are not enhanced. Robustness and accuracy have been evaluated by our optimum technique on publicly available databases and it is found to be high when the result was consulted with an expert.

REFERENCES

- [1] Dey, Damini, et al. "Ct quantification of epicardial fat: Implications for cardiovascular risk assessment." *Current Cardiovascular Imaging Reports* 5.5 (2012): 352-359.
- [2] Rischpler, Christoph, et al. "Hybrid PET/MR imaging of the heart: potential, initial experiences, and future prospects." *Journal of Nuclear Medicine* 54.3 (2013): 402-415.
- [3] Specht, J. M., et al. "Abstract P5-01-02: Multimodality molecular imaging with dynamic 18F-fluorodeoxyglucose positron emission tomography (FDG PET) and MRI to evaluate response and resistance to neoadjuvant chemotherapy (NAC)." (2016): P5-01.
- [4] Ahmadian, Azadeh, et al. "Quantitative interpretation of FDG PET/CT with myocardial perfusion imaging increases diagnostic information in the evaluation of cardiac sarcoidosis." *Journal of nuclear cardiology* 21.5 (2014): 925-939.
- [5] Zuva, Tranos, et al. "Image segmentation, available techniques, developments and open issues." *Canadian Journal on Image Processing and Computer Vision* 2.3 (2011): 20-29.
- [6] Makela, Timo, et al. "A review of cardiac image registration methods." *IEEE Transactions on medical imaging* 21.9 (2002): 1011-1021.
- [7] Sinha, Shantanu, et al. "Noninvasive assessment of myocardial perfusion and metabolism: feasibility of registering gated MR and PET images." *AJR. American journal of roentgenology* 164.2 (1995): 301-307.
- [8] Pelizzari, Charles A., et al. "Accurate three-dimensional registration of CT, PET, and/or MR images of the brain." *J Comput Assist Tomogr* 13.1 (1989): 20-26.
- [9] Powell, M. J. D. "An iterative method for finding stationary values of a function of several variables." *The Computer Journal* 5.2 (1962): 147-151.
- [10] Dey, Damini, et al. "Automatic three-dimensional multimodality registration using radionuclide transmission CT attenuation maps: a phantom study." *The Journal of Nuclear Medicine* 40.3 (1999): 448.
- [11] T. G. Turkington, T. R. DeGrado, M. W. Hanson, and R. E. Coleman, "Alignment of dynamic cardiac PET images for correction of motion," *IEEE Trans. Nucl. Sci.*, vol. 44, pp. 235-242, Apr. 1997.
- [12] Gorter P, vanLindert A, deVos et al. A. 2008. Quantification of epicardial and peri-coronary fat using cardiac computed tomography; reproducibility and relation with obesity and metabolic syndrome in patients suspected of coronary artery disease. *Atherosclerosis* 197(2):896-903.
- [13] Dey D, Suzuki Y, et al. SS. 2008. Automated continuation of pericardial fat from noncontrast CT. *Investigative Radiology* 43(2):145-153
- [14] Bandekar, Alok N., MortezaNaghavi, and Ioannis A. Kakadiaris. "Automated pericardial fat quantification in CT data." *Engineering in Medicine and Biology Society, 2006. EMBS'06. 28th Annual International Conference of the IEEE. IEEE, 2006.*
- [15] Sicari, Rosa, Anna Maria Sironi, Roberta Petz, Francesca Frassi, Vladislav Chubuchny, Daniele De Marchi, Vincenzo Positano, Massimo Lombardi, Eugenio Picano, and Amalia Gastaldelli, "Pericardial rather than epicardial fat is a cardiometabolic risk marker: an MRI vs echo study", *Journal of the American Society of Echocardiography*, Vol.24, No. 10, pp.1156-1162, 2011.
- [16] Sacks, Harold S and John N. Fain, "Human epicardial adipose tissue: a review", *American heart journal*, Vol.153, No. 6, pp.907-917, 2007.
- [17] Ding, Xiaowei, Demetri Terzopoulos, Mariana Diaz-Zamudio, Daniel S. Berman, Piotr J. Slomka, and Damini Dey, "Automated epicardial fat volume quantification from non-contrast CT", *Journal of Medical Imaging*, pp. 90340I-9034, 2014.
- [18] Marwan, Mohamed, and Stephan Achenbach, "Quantification of epicardial fat by computed tomography: why, when and how?", *Journal of cardiovascular computed tomography*, Vol. 7, No. 1, pp. 3-10, 2013.
- [19] Pontone, Gianluca, Daniele Andreini, Erika Bertella, Maria Petullà, Eleonora Russo, Ester Innocenti, Saima Mushtaq, "Comparison of cardiac computed tomography versus cardiac magnetic resonance for characterization of left atrium anatomy before radiofrequency catheter ablation of atrial fibrillation" *International journal of cardiology*, Vol. 179, pp.114-12, 2015.
- [20] Oda, Seitaro, Daisuke Utsunomiya, Yoshinori Funama, Hideaki Yuki, MasafumiKidoh, Takeshi Nakaura, Hiroko Takaoka, "Effect of iterative reconstruction on variability and reproducibility of epicardial fat volume quantification by cardiac CT", *Journal of cardiovascular computed tomography*, Vol.10, No.2, pp.150-155, 2016.
- [21] Ling, Zhiyu, John McManigle, Vadim Zipunnikov, FarhadPashakhanloo, Irfan M. Khurram, Stefan L. Zimmerman, Binu Philips, "The association of left atrial low-voltage regions on electroanatomic mapping with low attenuation regions on cardiac computed tomography perfusion imaging in patients with atrial fibrillation", *Journal on Heart Rhythm*, Vol. 12, No. 2, pp: 857-864, 2015.
- [22] Apfaltrer, Paul, Andreas Schindler, U. Joseph Schoepf, John W. Nance, Francesco Tricarico, Ullrich Ebersberger, Andrew D. McQuiston, "Comparison of epicardial fat volume by computed tomography in black versus white patients with acute chest pain" *The American journal of cardiology*, Vol. 113, No. 3, pp.422-428, 2015.
- [23] Bucher, Andreas M., U. Joseph Schoepf, Aleksander W. Krazinski, Justin Silverman, James V. Spearman, Carlo N. De Cecco, Felix G. Meinel, Thomas J. Vogl, and Lucas L. Geyer, "Influence of technical parameters on epicardial fat volume quantification at cardiac CT", *European journal of radiology*, Vol. 84, No. 6, pp.1062-1067, 2015.
- [24] Isgum, Ivana, Marius Staring, Annemarieke Rutten, Mathias Prokop, Max A. Viergever, and Bram Van Ginneken, "Multi-atlas-based segmentation with local decision fusion—Application to cardiac and aortic segmentation in CT scans", *IEEE transactions on medical imaging*, Vol.28, No. 7, pp.1000-1010, 2009.
- [25] Rodrigues, Erick Oliveira, F. F. C. Morais, N. A. O. S. Morais, L. S. Conci, L. V. Neto, and Aura Conci, "A novel approach for the automated segmentation and volume quantification of cardiac fats on computed tomography" *Computer methods and programs in biomedicine*, Vol.123, pp.109-128, 2016.

- [26] T.E. Brinkley, Tina E., F-C. Hsu, J. Jeffrey Carr, W. Gregory Hundley, David A. Bluemke, Joseph F. Polak, and Jingzhong Ding", Pericardial fat is associated with carotid stiffness in the Multi-Ethnic Study of Atherosclerosis", *Journal on Nutrition, Metabolism and Cardiovascular Diseases*, Vol.21, No. 5, pp. 332-338, 2011.
- [27] Bandekar, Alok N., MortezaNaghavi, and Ioannis A. Kakadiaris. "Automated pericardial fat quantification in CT data", In *Engineering in Medicine and Biology Society, International Conference of the IEEE*, pp. 932-935, IEEE, 2006.
- [28] Kaus, Michael R., Jens von Berg, Jürgen Weese, WiroNiessen, and Vladimir Pekar, "Automated segmentation of the left ventricle in cardiac MRI", *Journal on Medical image analysis*, Vol.8, No. 3, pp. 245-254, 2004.
- [29] Mangili, Leonardo C., Otavio C. Mangili, Márcio S. Bittencourt, Márcio H. Miname, Paulo H. Harada, Leonardo M. Lima, Carlos E. Rochitte, and Raul D. Santos, "Epicardial fat is associated with severity of subclinical coronary atherosclerosis in familial hypercholesterolemia", *Journal on Atherosclerosis*, Vol. 254, pp.73-77, 2016.
- [30] Yang, Feng, Mingyue Ding, Xuming Zhang, Wenguang Hou, and Cheng Zhong, "Non-rigid multi-modal medical image registration by combining L-BFGS-B with cat swarm optimization", *Journal on Information sciences*, Vol.316, pp.440-456, 2015.
- [31] Champier, Jacques, Luc Cinotti, Jean-Claude Bordet, Franck Lavenne, and Jean-Jacques Mallet, "Delineation and quantization of brain lesions by fuzzy clustering in positron emission tomography", *Journal on Computerized medical imaging and graphics*, Vol.20, No. 1, pp.31-41, 2006.
- [32] Lin, Daw-Tung, Chung-Ren Yan, and Wen-Tai Chen, "Autonomous detection of pulmonary nodules on CT images with a neural network-based fuzzy system", *Journal on Computerized Medical Imaging and Graphics*, Vol.29, No. 6, pp.447-458, 2005.



Internet of Things (IoT) Based Smart Plant Monitoring System

Dr.M.Vidhyalakshmi¹ | H.Peer oli² | N.Hemakumari² | S.Bismillah Khan² | Dr.C.Priya²

¹Electronics and Communication Engineering, SRM institute of Science and Technology, Ramapuram, Tamil nadu, India.

²Electronics and Communication Engineering, Mohamed Sathak Engineering college, Kilakarai, Tamil nadu, India.

To Cite this Article

Dr.M.Vidhyalakshmi., H.Peer oli., N.Hemakumari., S.Bismillah Khan & Dr.C.Priya. Internet of Things (IoT) Based Smart Plant Monitoring System. *International Journal for Modern Trends in Science and Technology* 7, 144-146 (2021).

Article Info

Received on 18-April-2021, Revised on 11-May-2021, Accepted on 19-May-2021, Published on 22-May-2021.

ABSTRACT

In this work, we have a tendency to gift a plantation observance system supported web of Things. The system combines wireless detector network, embedded development, GPRS communication technology, net service, and automaton mobile platform. The hardware style of detector nodes, data acquisition, knowledge transmission, beside knowledge image and abnormal alarm ar mentioned well. Long-term experiment of the system shows that the theme is possible and reliable.

Keywords- *Internet of Things; surroundings monitoring; wireless detector network; net service*

I. INTRODUCTION

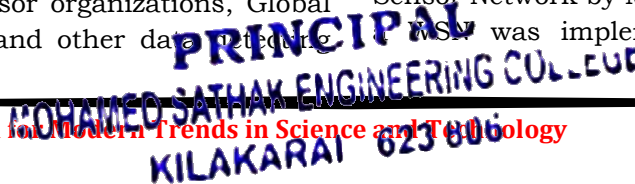
With the over-abuse of common assets, human being is confronted with progressively climate emergency, for example, energy lack, the a dangerous atmospheric devastation, deforestation, desertification and other ecological issues, so timberland ecological security turns out to be increasingly significant. Environmentalists regularly think the thickness of trees is vital for woodland development, however absence of supporting information inconveniences them. To consider the exact impacts of thickness on estate, scientists need long haul observing on an assortment of biological pointers. Notwithstanding, it is hard to gather naturally and dependably ecological observing information with conventional observing framework.

Web of things gives the specialized establishment to achieving thistask. Web of things is an organization that interfaces anything to the Internet can trade data through Radio Frequency Identification (RFID), sensor organizations, Global Situating System (GPS) and other data

gadgets, as indicated by the concurred conventions, to accomplish insightful recognize, find, track, screen and manage[1][2]. Web of Things has availability for whenever, anyplace, anybody and anything. Along these lines, focusing on the qualities of ranch, we build up an estate observing framework which dependent on Internet

II. LITREATURE SURVEY

We have studied many previous works done in this field by different researchers. Use of technology in the field of agriculture plays important role in increasing the production as well as in reducing the man power efforts. Research for improving agricultural production by utilizing different controllers like PIC microcontroller,8051 controller, ARM 7 etc or also monitoring done by different communication technology like Zigbee, Wireless sensor network(WSN),even using GSM. Greenhouse monitoring and control system based on wireless Sensor Network by Marwa Mekki et al.In this paper WSN was implemented by deployed wireless



sensor nodes in a greenhouse with temperature, humidity, moisture light, and CO2 sensors.

To control the environmental factors, the used microcontroller programmed to control the parameters according to preset values, or manually through a user interface panel. A ZigBee based energy efficient environmental monitoring alerting and controlling system by K. Lokesh Krishna et al, the paper based on paper a novel ZigBee based energy efficient environmental monitoring, alerting and controlling system for agriculture is designed and implemented. This system utilizes an ARM7 processor, various sensors and ZigBee communication module. Sensors gather various physical data from the field in real time and transmit it to the processor and to the end user via ZigBee communication. Then necessary actions are initiated to perform action on behalf of people to reduce or eliminate the need of human labor.

Embedded based Green House Monitoring system using PIC microcontroller by S. Arul Jai Singh at al ,the paper deals with a simple, easy to install, microcontroller-based circuit to monitor and record the value of temperature, humidity, soil moisture and sunlight of the natural environment that are continuously modified and controlled in order optimize them to achieve maximum plant growth and yield. The controller communicates with the various sensor modules in real-time in order to control the light, aeration and drainage process efficiently inside a greenhouse by actuating a cooler, fogger, dripper and lights respectively according to the necessary condition of the crops

III. DESIGN OF PROPOSED SYSTEM

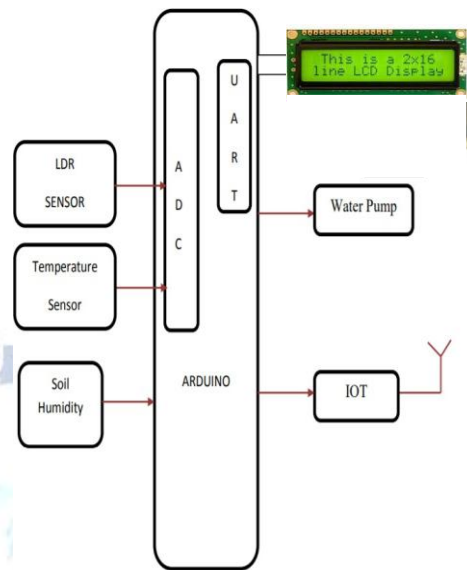
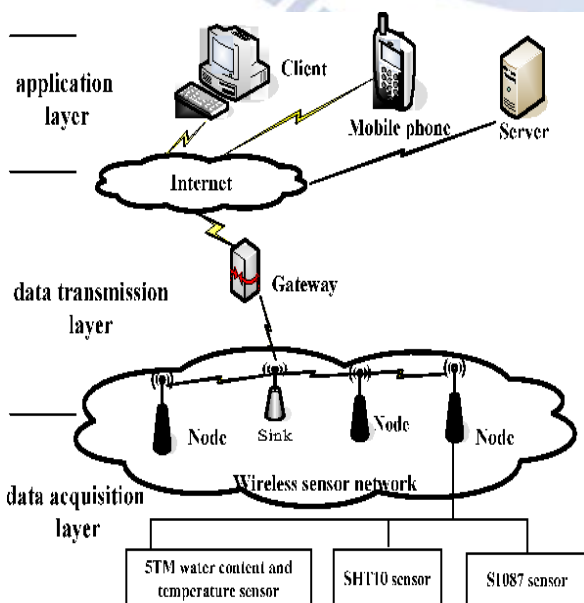


Fig. Diagram of plant monitoring system

IV. IMPLEMENTATION & WORK

Arduino is an open source computer hardware and software company, project, and user community that preassembled form, or as do-it-yourself (DIY) kits. Arduino board designs use a variety of microprocessors and controllers. The boards are equipped with sets of digital and analog input/output (I/O) pins that may be interfaced to various expansion boards (shields) and other circuits. The boards feature serial communications interfaces, including Universal Serial Bus (USB) on some models, which are also used for loading programs from personal computers.

The microcontrollers are typically programmed using a dialect of features from the programming languages C and C++. In addition to using traditional compiler tool chains, the Arduino project provides an integrated development environment (IDE) based on the Processing language project. In an industry during certain hazards is will be very difficult to monitor the parameter through wires and analog devices such as transducers. To overcome this problem we use wireless device to monitor the parameters so that we can take certain steps even in worst case. Few years back the use of wireless device was very less, but due the rapid development is technology now-a-days we use maximum of our data transfer through wireless like WiFi, Bluetooth, WI-Max,

etc. This project is designed as a plant monitoring system based on IOT.

In this project we use different modules such as IOT, arduino as controller, Temperature sensor, Moisture sensor, Humidity sensor. This project uses sensors such as a humidity sensor is also given to know about the atmospheric humidity of that place. By having knowledge of all these one can take action accordingly. Moisture sensor sense the soil is dry or wet. If soil is dry automatically water pump will get ON. the sensor values are given to ADC to get processed by arduino controller. The temperature sensor LM35 senses the temperature and converts it into an electrical (analog) signal, which is applied to the micro controller through ADC. The analog signal is converted into digital format by the analog-to-digital converter (ADC). If temp increases more than set threshold value. Automatically fan will be ON. In this project we are using ARM7, dry/wet sensor, humidity sensor and Temperature sensor. The condition of soil and the temperature maintained are being displayed on LCD and the same values are updated in the internet through IOT module interfaced to the controller. and whenever smoke sensor is detected buzzer will be ON.

The LM35 series are precision integrated-circuit temperature sensors, whose output voltage is linearly proportional to the Celsius (Centigrade) temperature. The LM35 thus has an advantage over linear temperature sensors calibrated in ° Kelvin, as the user is not required to subtract a large constant voltage from its output to obtain convenient Soil moisture sensors typically refer to sensors that estimate volumetric water content. Another class of sensors measure another property of moisture in soils called water potential; these sensors are usually referred to as soil water potential sensors and include densitometers and gypsum blocks.

V. RESULT & DISCUSSION

The performance of the system can be further improved in terms of the operating speed, memory capacity, and instruction cycle period of the microcontroller by using other high end controllers. The number of channels can be increased to interface more number of sensors which is possible by using advanced versions of controllers.

The system can be modified with the use of a data logger and a graphical LCD panel showing the measured sensor data over a period of time. A

speaking voice alarm could be used. The device can be made to perform better by providing the power supply with the help of renewable source. Time bound administration of fertilizers, insecticides and pesticides can be introduced

VI. CONCLUSION

This proposed work is made to help the ranchers and make their reap affordable by aiding them in security reason voyaging side, school and for each body and so forth. By this work, the wastage of water and the utilization of force by engine can be diminished so they are rationed for the future use. This framework gives total observing activity of sensors in fields that is exceptionally simple to control the field. It additionally give enormous security to the plants.

REFERENCES

- [1] Marwa Mekki², Osman Abdallah¹, Magdi B. M. Amin², Moez Eltayeb¹, Tafaoul Abdalfatah², Amin Babiker³, "Greenhouse monitoring and control system based on wireless sensor networks "IEEE Trans. Syst ,Man,Cybern.,Appl.Rev.,vol.37,no.3,pp.311-314,May 2007
- [2] Arul Jai Singh.S¹, Raviram.P², ShanthoshKumar.K³, "Embedded Based Green House Monitoring System Using PIC Microcontroller", IEEE Trans. Syst , Man, Cybern . A ,Systems and Humans, vol. 41, no. 6, pp.1064-1076, November 2011
- [3] K.Lokesh Krishna ,J.Madhuri and Dr.K.Anuradha, "A ZigBee based Energy Efficient Environmental Monitoring Alerting and Controlling System", IEEE Trans.g, vol.3, no.1, pp.186- 190,2009
- [4] Shiraz Pasha B.R., Dr. B Yogesha, "Microcontroller Based Automated Irrigation System", The International Journal Of Engineering And Science (IJES), Volume3, Issue 7, pp 06-09, June2014.
- [5] Venkata Naga RohitGunturi, "Micro Controller Based AutomaticPlant Irrigation System", International Journal of Advancements inResearch & Technology, Volume 2, Issue4, April-2013.
- [6] Mahir Dursun and Semih Ozden, "A wireless application of dripirrigation automation supported by soil moisture sensors", ScientificResearch and Essays, Volume 6(7), pp. 1573-1582, 4 April, 2011.
- [7] S. Harishankar, R. Sathish Kumar, Sudharsan K.P, U. Vignesh andT.Viveknath, "Solar Powered Smart Irrigation System", Advance inElectronic and Electric Engineering, Volume 4, Number 4 (2014),
- [8] Pavithra D.S, M. S .Srinath, "GSM based Automatic IrrigationControl System for Efficient Use of Resources and Crop Planning byUsing an Android Mobile", IOSR Journal of Mechanical and CivilEngineering (IOSR-JMCE) Vol 11, Issue I, Jul-Aug 2014, pp 49-55.
- [9] LaxmiShabadi, NandiniPatil, Nikita. M, Shruti. J, Smitha. P & Swati.C, "Irrigation Control System Using Android and GSM for Efficient Use of Water and Power",International Journal of AdvancedResearch in Computer Science and Software Engineering, Volume4, Issue 7, July 2014

Automatic Segmentation of Brain Tissues Using CNN in Functional MRI

¹Nandhini.S, ²A.Muthuvel

PG Student, Asst.Professor, Department of ECE, Mohamed Sathak Engineering College

Abstract: Accurate segmentation of different brain tissue types is the first step of understanding the neuronal activity in functional magnetic resonance imaging (fMRI). Due to the low spatial resolution of fMRI data and the absence of an automated segmentation approach, human experts require high resolution structural MRI images, which the fMRI data are superimposed on for analysis. The recent advent of high-resolution fMRI, along with temporal characteristic of fMRI data, suggests the possibility of segmenting fMRI image without relying on the higher resolution structural MRI image. This work proposes a patch-wise deep learning segmentation method using long-term recurrent convolution network architecture. The proposed method comprises of three stages: spatial feature extraction with convolution neural network, temporal feature extraction with long short-term memory, and brain tissue class prediction with soft max classifier. The proposed method aims to segment five classes in fMRI images, which are gray matter, white matter, blood vessel, non-brain and cerebrospinal fluid. It achieves high accuracy than conventional segmenting algorithms

I. INTRODUCTION

The idea of localisation of function within the brain has only been accepted for the last century and a half. In the early 19th century Gall and Spurzheim, were ostracised by the scientific community for their so-called science of phrenology[1]. They suggested that there were twenty-seven separate organs in the brain, governing various moral, sexual and intellectual traits. The importance of each to the individual was determined by feeling the bumps on their skull. The science behind this may have been flawed, but it first introduced the idea of functional localisation within the brain which was developed from the mid 1800's onwards by clinicians such as Jackson [2] and Broca[3]. Most of the information available on the human brain came from subjects who had sustained major head wounds, or who suffered from various mental disorders[4]. By determining the extent of brain damage, and the nature of the loss of function, it was possible to infer which regions of the brain were responsible for which function.

Patients with severe neurological disorders were sometimes treated by removing regions of their brain. For example, an effective treatment for a severe form of epilepsy involved severing the corpus callosum, the bundle of nerve fibres which connect left and right cerebral hemispheres. Following the surgery patients were tested, using stimuli presented only to the left hemisphere or to the right hemisphere[5]. If the object was in the right visual field, therefore stimulating the left hemisphere, then the subject was able to say what they saw. However if the object was in the left visual field, stimulating the right hemisphere, then the subject could not say what they saw but they could select an appropriate object to associate with that image. This suggested that only the left hemisphere was capable of speech.

II. FUNCTIONAL MRI AND MRS

Since functional magnetic resonance imaging (fMRI) is the subject of this thesis, little will be said in this section as to the mechanisms and applications of the technique, as this is covered later in the chapter. The purpose of this section is to compare fMRI to the other modalities already mentioned, and also to consider the related, but distinct technique of magnetic resonance spectroscopy (MRS). During an fMRI experiment, the brain of the subject is scanned repeatedly, usually using the fast imaging technique of echo planar imaging (EPI). The subject is required to carry out some task consisting of periods of activity and periods of rest. During the activity, the MR signal from the region of the brain involved in the task normally increases due to the flow of oxygenated blood into that region. Signal processing is then used to reveal these regions. The main advantage of MRI over its closest counterpart, PET, is that it requires no contrast agent to be administered, and so is considerably safer. In addition, high quality anatomical images can be obtained in the same session as the functional studies, giving greater confidence as to the source of the activation. However, the function that is mapped is based on blood flow, and it is not yet possible to directly map neuroreceptors as PET can. The technique is relatively expensive, although comparable with PET, however since many hospitals now have an MRI scanner the availability of the technique is more widespread.

fMRI is limited to activation studies, which it performs with good spatial resolution. If the resolution is reduced somewhat then it is also possible to carry out spectroscopy, which is chemically specific, and can follow many metabolic processes. Since fMRS can give the rate of glucose utilisation, it provides useful additional information to the blood flow and oxygenation measurements from fMRI, in the study of brain metabolism.

Nerna'
PRINCIPAL
MOHAMED SATHAK ENGINEERING COLLEGE
KILAKARAI 623 806

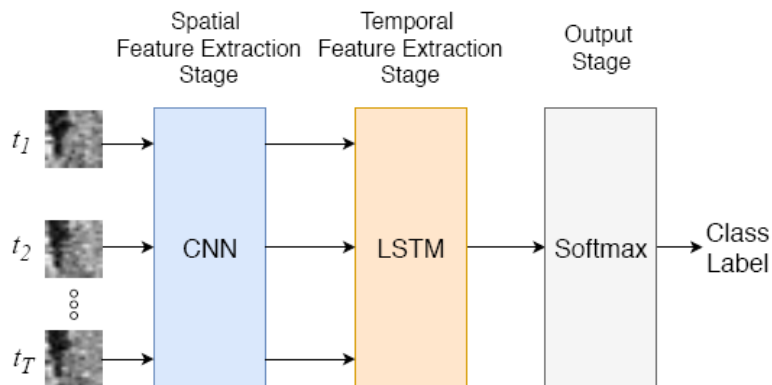


Figure 4.1: Block diagram of the proposed network.

III.RESULT AND DISCUSSION

The brain imaging techniques that have been presented in this chapter all measure slightly different properties of the brain as it carries out cognitive tasks. Because of this the techniques should be seen as complementary rather than competitive. All of them have the potential to reveal much about the function of the brain and they will no doubt develop in clinical usefulness as more about the underlying mechanisms of each are understood, and the hardware becomes more available. A summary of the strengths and weaknesses of the techniques is presented.

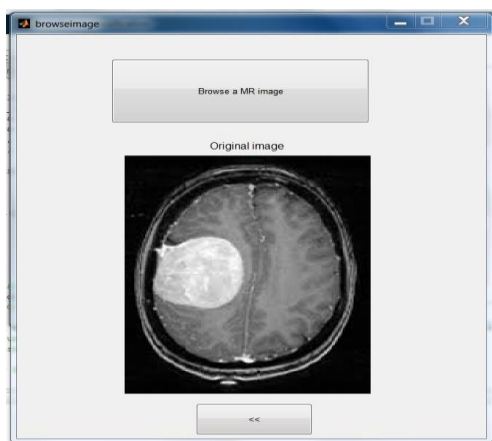


Figure 2 - Input image

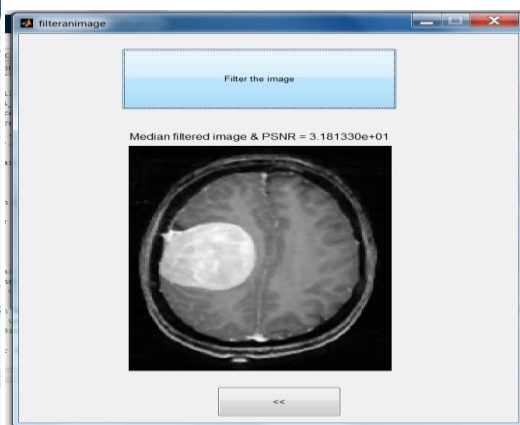


Figure 3- Filtered image

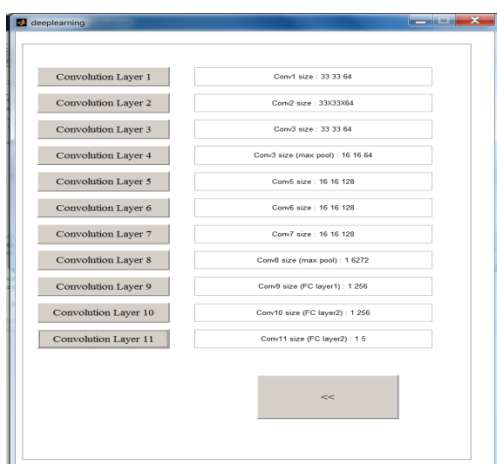


Figure 4 - Layer processing

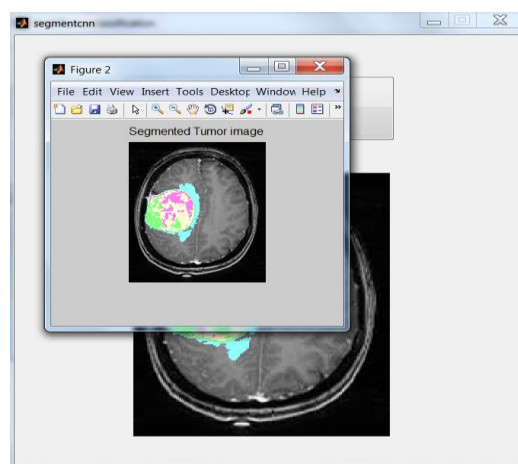
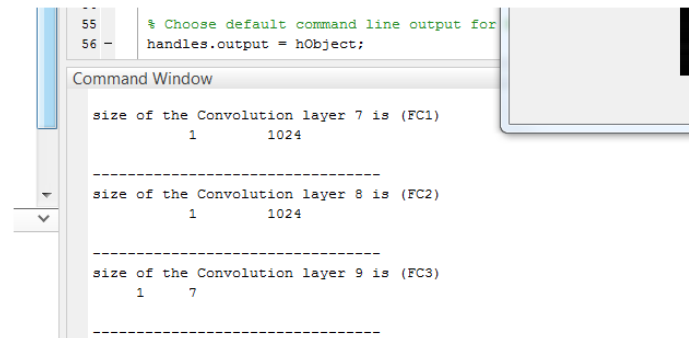


Figure 5 - Segmented result



```

55 % Choose default command line output for
56 handles.output = hObject;

Command Window

size of the Convolution layer 7 is (FC1)
      1      1024

-----
size of the Convolution layer 8 is (FC2)
      1      1024

-----
size of the Convolution layer 9 is (FC3)
      1       7
-----

```

Figure 5 - classification result

The forget gate scales the internal state of the cell before adding it back to the cell as input through self recurrent connection, therefore adaptively forgetting or resetting the cells memory. The modern LSTM architecture also contains peephole connections from its internal cells to the gates in the same cell to learn precise timing of the outputs

IV.CONCLUSION

The main objective of this research is to develop an automated approach for fMRI brain tissue segmentation proposed a novel patch-wise segmentation method based on deep learning for automatic segmentation of brain tissues in fMRI. The proposed method comprises three stages: spatial feature extraction with convolutional neural network, temporal feature extraction with long short-term memory and brain tissue class prediction with softmax classifier. The network was trained using the Adam optimizer with the categorical cross-entropy loss function. Fourth, we conducted experiments to determine the optimum hyperparameters for the proposed method. The proposed method was also compared with several temporal domain and spatial domain classifiers. The experiments were conducted using five-fold cross-validation.

References

- [1] Ambrosi.P, Costagli. M, Kuruoğlu. E. E, Biagi. L, Buonincontri. Gand Tosetti. M, (2019), "Investigating Time-Varying Brain Connectivity with Functional Magnetic Resonance Imaging using Sequential Monte Carlo," - 27th European Signal Processing Conference (EUSIPCO), A Coruna, Spain, , pp. 1-5, doi: 10.23919/EUSIPCO.2019.8902503.
- [2] Anand. K and Tayal. A, (2018), "Noise in Functional Magnetic Resonance Imaging," - International Conference on Advances in Computing, Communication Control and Networking (ICACCCN), Greater Noida (UP), India, 2018, pp. 880-882, doi: 10.1109/ICACCCN.2018.8748780.
- [3] Farias.F. S, Mendizabal.A, González-Garrido. A.A, Romo. R-Vázquez and A. Morales, (2018), "Long Short-Term Memory Neural Networks for Identifying Type 1 Diabetes Patients with Functional Magnetic Resonance Imaging," -IEEE Latin American Conference on Computational Intelligence (LA-CCI), Guadalajara, Mexico, 2018, pp. 1-4, doi: 10.1109/LA-CCI.2018.8625231.
- [4] Jiang et al. X, (2018), "Temporal Dynamics Assessment of Spatial Overlap Pattern of Functional Brain Networks Reveals Novel Functional Architecture of Cerebral Cortex," in IEEE Transactions on Biomedical Engineering, vol. 65, no. 6, pp. 1183-1192, doi: 10.1109/TBME.2016.2598728.
- [5] C.Nagarajan and M.Madheswaran - 'Stability Analysis of Series Parallel Resonant Converter with Fuzzy Logic Controller Using State Space Techniques'- Taylor & Francis, .Electric Power Components and Systems, Vol.39 (8), pp.780-793, May 2011
- [6] C.Nagarajan and M.Madheswaran - 'Performance Analysis of LCL-T Resonant Converter with Fuzzy/PID Using State Space Analysis'- Springer, Electrical Engineering, Vol.93 (3), pp.167-178, September 2011.
- [7] C. Nagarajan and M. Madhswaran, "Analysis and simulation of LCL series resonant full bridge converter using PWM technique with load independent operation", IET-UK International Conference on Information and Communication Technology in Electrical Sciences (ICTES 2007), Proc. IEEE Inf. Commun. Technol. Electr. Sci., pp. 190-195, 2007.
- [8] Liu. W, Liu. M, Yang. D, Wang. M and Tao. T, (2020) "Automatic diagnosis of autism based on functional magnetic resonance imaging and elastic net," - IEEE 5th Information Technology and Mechatronics Engineering Conference (ITOEC), Chongqing, China, pp. 104-108, doi: 10.1109/ITOEC49072.2020.9141766.
- [9] Mathieu. W, Popovich. M and Farivar. R, (2019), "Radio-Frequency Coil Array for Improved Concurrent Transcranial Magnetic Stimulation and Functional Magnetic Resonance Imaging," 2019 41st Annual International Conference of the IEEE Engineering in Medicine and Biology Society (EMBC), Berlin, Germany,pp. 6814-6817, doi: 10.1109/EMBC.2019.8857215.



Tracking the Nanoparticles using Multi Tracking Method in Human Crowds

Dr.A.Shyamala | S.Vengatesh Kumar | Dr.C.Priya | Dr.I.Sheik Arafat

Department of Electronics and Communication Engineering, Mohamed Sathak Engineering College, Kilakarai, Tamilnadu, India.

To Cite this Article

Dr.A.Shyamala, S.Vengatesh Kumar, Dr.C.Priya and Dr.I.Sheik Arafat, "Tracking the Nanoparticles using Multi Tracking Method in Human Crowds", *International Journal for Modern Trends in Science and Technology*, Vol. 07, Issue 04, April 2021, pp.:176-179.

Article Info

Received on 30-March-2021, Revised on 21-April-2021, Accepted on 25-April-2021, Published on 29-April-2021.

ABSTRACT

In our proposed we tracking the nanoparticles using multi-tracking method. The multi tracking method will help to track the multi object in single frame. In our proposed nanoparticles tracking the particles are spilt at each frame so the frames the object is increases for tracking. It is the main trajectory of the nanoparticles multi tracking. In that cause we introduce new method for our proposed to track the nanoparticles.

KEYWORDS: Nano particles, multi tracking, background modeling, track management

I. INTRODUCTION

In many applications, such as video surveillance, content based video coding, and human-computer interaction, moving object detection is an important and fundamental problem. The general technique for moving object detection is background elimination under the situation of fixed cameras. Detection of moving objects in video each individual. Crowd performance and to detect irregular activities at the crowd level rather than at the individual level.

Crowd analysis also finds applications in crowd simulation, crowd management, disaster management, outlet planning as well as other related areas. The purpose of this study is to analyses the crowd behavior in real time in order to detect abnormalities that could lead to dangerous situations using computer vision and machine learning techniques. This paper is organized as follows; motivation and related works are discussed in section II. The proposed method of abnormal crowd detection and tracking is explored in section III. Experimental results are given in section 4 and conclusion is drawn in section

5. stream is the first related step of information removal in many computer visualization applications, including video surveillance, people tracking, traffic monitoring, and semantic annotation of videos.

Video cameras are extensively used in surveillance application to examine public areas, such as train stations, airports and shopping centers. When crowds are intense, automatically tracking individuals becomes a difficult task. Anomaly detection is also known as outlier detection, which is applicable in a verity of application.

Our proposed frame work is to implement a new tracking technique. Human monitoring is tiring, expensive, and ineffective. Our approach is a real time contribution to abnormal event detection and uses the motion of computational attenuation which quantifies motion saliency. The proposed method can be applied from small group of objects to dense touching moving objects like crowded. Crowded environments are very complicated to monitor by human observer, whether live or by means of video surveillance, because the optical

patterns are highly recurring and the difficulty of the movement characterize the scene is often overpowering. Crowd finding is particularly significant in the background of intellectual and automated video surveillance systems proposed for large venues and public events, such as football games and concerts, as well as for such general environments as City Street and underground train stations during pinnacle hours.

A crowd element can be defined as a region related to more than one person who has logical and identical motion. Crowd movement tracking is quite dissimilar from tracking individuals in the crowd. When individuals are being tracked, the information is compute at the level of each individual. One purpose is to construct model of crowd performance and to detect irregular activities at the crowd level rather than at the individual level. Crowd analysis also finds applications in crowd simulation, crowd management, disaster management, outlet planning as well as other related areas. The purpose of this study is to analyses the crowd behavior in real time in order to detect abnormalities that could lead to dangerous situations using computer vision and machine learning techniques.

This paper is organized as follows; motivation and related works are discussed in section I. The proposed method of abnormal crowd detection and tracking is explored in section II. Experimental results are given in section III and conclusion is drawn in section IV. Related works the detailed literature survey of our work is presented in this section. Abnormality detection is classified into two categories; trajectory analysis and motion analysis. Trajectory analysis is based on object tracking and typically requires normal environment to operate. Motion analysis is better suitable for crowded scenes by analyzing patterns of movement rather than attempting to distinguish object. Some of the few existing works consider the relationship between pedestrians' social behaviors and their walking scenarios.

Recently, some methods [1], [2] utilize crowd flow and semantic scene knowledge to detect abnormal activity and obtained good results. But these methods can be only applied for some simple scene (e.g. single sink/source, single crowd flow). There have been attempts to model crowds based on discriminative classifiers [3].

The analysis of crowd behavior and movements are of particular In the circumstances where few operators are monitor behavioral analysis of

crowds in hundreds of cameras is useful as a very tool for video pre-screening. Activity and event detection has got more concentration in automated Recently, Mehran et al. [10] propose a method to model behaviors among a group of people.

It represents the abnormal patterns in a local region based on moving Particles. The detection of Object Put is based on dual foreground algorithm where the divergence in response is analyzed. Based on over completes set of low-level spatiotemporal features and the mining of a dense a new technique for action recognition is implemented [11]. The tracking system is a basic blob tracker described in [12].

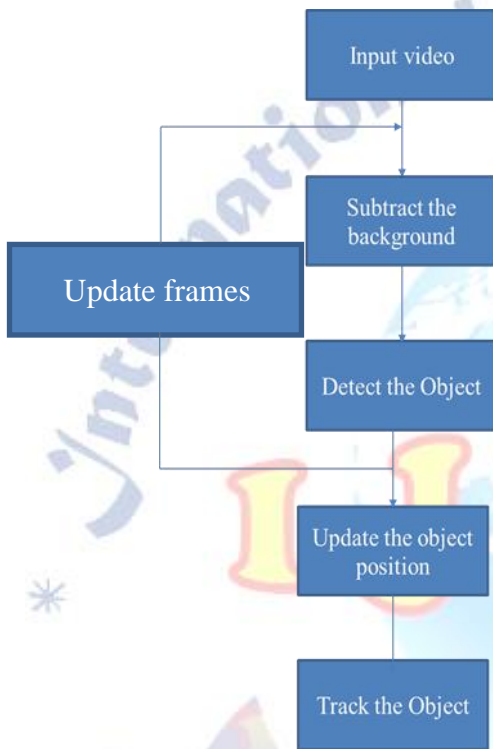
It is composed of two main components: (1) background modeling, and (2) track management. First, foreground/background segmentation is performed and then, objects are tracked with a combination of blob matching and particle filtering techniques. Ramin Mehran *et al* proposed a method to detect and focus abnormal activities in crowd videos using social force model.

This paper is tested on publicly presented dataset of normal and abnormal crowd videos. The proposed method is confining the abnormal activities in contrast to use of optical flow Louis Kratz et al a proposed new statistical framework for modeling the local spatio-temporal motion pattern behavior of extremely crowded scenes. Previous work in this paper of unusual event detection is classified into two categories; explicit and deviation methods. Deviation method is usual activity; it can detect the unusual events. Event detection approach model is each specific activity for identification in videos. The tracking-based model for extremely crowded scenes would also disregard the important correlation between pedestrians within close proximity of each other [14]. Hui Ma, et al, proposed a method is the robust descriptor for encoding the intrinsic local and global behavior signatures in crowded scenes. The crowd scenes conversion from normal to abnormal behaviors such as rush and scatter were detected.

This method is evaluating the other methods for anomaly detection in crowds with a very good detection accuracy rates. This report is not based on motion tracking.[15]. The future method a new tracker which employs a element filter tracking structure, where the state transition model is estimated by an optical-flow algorithm. The optical-flow algorithm is used to estimate the state transition. The optical-flow vector is more accurate than the fixed models. The proposed tracking

method is better than the performance is largely improved compared with state of the art trackers.

II. PROPOSED WORK



III. EXPERIMENTAL RESULTS

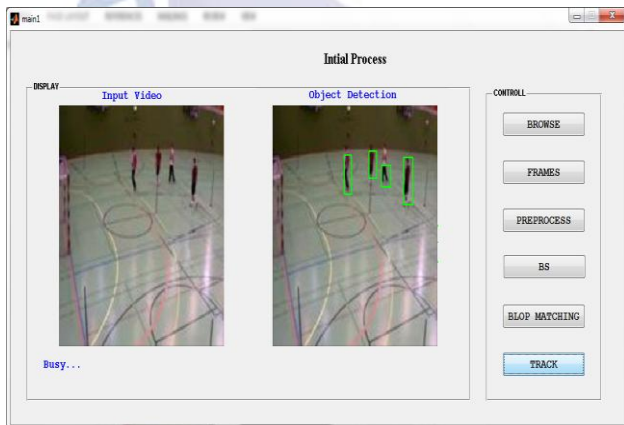


Figure 1: Object detection by tracking

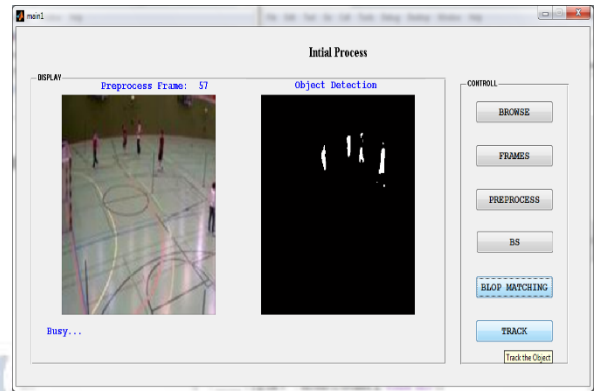


Figure 2: Preprocessing and object detection by BLOP matching

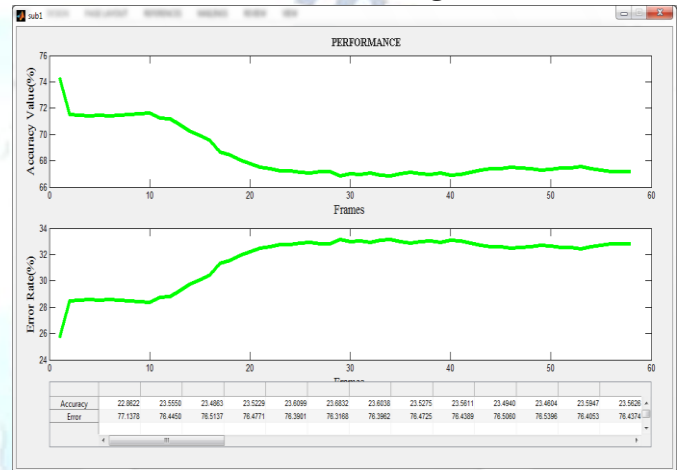


Figure 3: Performance evaluation

IV. CONCLUSION

In proposed tracking give the better tracking result compare to the existing methods. That tracking is done crowded video which tracking the spiting and merging of particles. Our proposed method is good nanoparticle tracking and that process is done in MAT lab. In feature we track anomaly in the video frames for identify the abnormal event it helps to monitor the survey line for abnormal behavior.

REFERENCES

- [1] Adam, Amit, Ehud Rivlin & Ilan Shimshoni 2006, 'Robust fragments based tracking using the integral histogram', Computer Vision and Pattern Recognition, IEEE, vol. 1.
- [2] Anand Singh Jalal & Vrijendra Singh 2012, 'The state-of-the-art in visual object tracking', International Journal of Computing and Informatics, vol. 36, no. 3, pp. 227-248.
- [3] Barnich, O & Van Droogenbroeck, M 2011, 'ViBe: A universal background subtraction algorithm for video sequences', IEEE Transactions on Image Processing, vol. 20, no. 6, pp. 1709-1724.
- [4] Barron, J, Fleet, D & Beauchemin, S 1994, 'Performance of optical flow techniques', International Journal of Computer Vision.
- [5] Besita Augustin, M, Sujitha Juliet, S & Palanikumar 2011, 'Motion and feature based person tracking in surveillance

- videos', in Proceedings of ICETECT, vol. 19, no. 7, pp. 780-785.
- [6] Bevilacqua, A & Pietro Azzari 2006, 'High-quality real time motion detection using PTZ cameras', Proceedings of the IEEE International Conference on Video and Signal Based Surveillance, P. 23.
- [7] Bhuvanewari, S & Subashini, TS 2014, 'Tracking manually selected object in videos using color histogram matching', International Journal of Theoretical and Applied Information Technology, vol. 67, no. 3, pp. 562-568.
- [8] Bilodeau, GA, Jodoin, JP & Saunier, N 2013, 'Change detection in feature space using local binary similarity patterns', in Proceedings of the International Conference on Computer & Robot Vision, vol. 10, no. 1, pp. 106-112.
- [9] Caetano, TS, McAuley, JJ, Cheng, L, Le, QV & Smola, AJ 2009, 'Learning graph matching', IEEE Trans. Pattern Anal. Mach. Intell., vol. 31, no. 6, pp. 1048-1058.
- [10] Cesar, RM, Bengoetxea, E, Bloch, I & Larrañaga, P 2005, 'Inexact graph matching for model-based recognition: Evaluation and comparison of optimization algorithms', Pattern Recognit., vol. 28, pp. 2009-2113.
- [11] Cezar, J, Silveira Jacques, Claudio Rosito Jung & Soraia Raupp Musse 2005, 'Background subtraction and shadow detection in grayscale video sequences', 18th IEEE Brazilian Symposium on Computer Graphics and Image Processing, pp. 189-196.
- [12] CIPR Dataset 2004, Available From: <http://www.cipr.rpi.edu/resource/sequences>
- [13] De Bruyne, S, Poppe, C, Verstockt, S, Lambert, P & Van de Walle, R 2009, 'Estimating motion reliability to improve moving object detection in the H.264/AVC domain', in Proc. IEEE Int. Conf. Multimedia and Expo, P. 330.
- [14] Desa, SM & Salih, QA 2004, 'Image subtraction for real time moving object extraction', in Computer Graphics, Imaging and Visualization 2004, CGIV 2004, IEEE Proceedings of International Conference on, pp. 41-45.
- [15] Gandham Sindhuja & Renuka Devi, SM 2015, 'A survey on detection and tracking of objects in video sequence', International Journal of Engineering Research and General Science, vol. 3, no. 2.
- [16] Gomila, C & Meyer 2003, 'Graph-based object tracking', Proc. Image Processing, vol. 2, pp. 41-4.
- [17] GTI Dataset, Available From: <http://www.cipr.rpi.edu/resource/sequences.html>.
- [18] Guanling Z Yuping & Nanping, D 2009, 'Graph based visual object tracking', in Proc. ISECS Int. Colloq. Computing, Communication, Control, and Management, vol. 1, pp. 99-102.
- [19] Hitesh A Patel & Darshak G Thakore 2013, 'Moving object tracking using kalman filter', International Journal of Computer Science and Mobile Computing, pp. 326-332.
- [20] Hu, WM, Tan, TN, Wang, L & Maybank, S 2004, 'A survey on visual surveillance of object motion and behaviour', IEEE Transactions on Systems, Man and Cybernetics, vol. 34, no. 3, pp. 334-352.
- [21] Joshan Athanesious, J & Suresh, P 2013, 'Implementation and comparison of kernel and silhouette based object tracking', International Journal of Advanced Research in Computer Engineering & Technology, pp. 1298-1303
- [22] Joshan Athanesious, J & Suresh, P 2012, 'Systematic survey on object tracking methods in video', International Journal of Advanced Research in Computer Engineering & Technology (IJARCET), pp. 242-247.
- [23] Joshi, KA & Thakore, DG 2012, 'A survey on moving object detection and tracking in video surveillance system', International Journal of Soft Computing and Engineering, vol. 2, no. 3.
- [24] Kalantar, B, Mansor, SB, Abdul Halin, A, Shafri, HZM & Zand, M 2017, 'Multiple moving object detection from UAV videos using trajectories of matched regional adjacency graphs', in IEEE Transactions on Geoscience and Remote Sensing, vol. 55, no. 9, pp. 5198-5213.
- [25] Kalantar, B, Mansor, SB, Abdul Halin, A, Shafri, HZM & Zand, M 2017, 'Multiple moving object detection from UAV videos using trajectories of matched regional adjacency graphs', in IEEE Transactions on Geoscience and Remote Sensing, vol. 55, no. 9, pp. 5198-5213.
- [26] Kapotas, SK & Skodras, AN 2010, 'Moving object detection in the H.264 compressed domain', in Proc. IEEE Int. Conf. Imaging Systems and Techniques (IST) 2010, pp. 325-328.
- [27] Käs, C & Nicolas, H 2009, 'An approach to trajectory estimation of moving objects in the H.264 compressed domain', in Proc. 3rd Pacific Rim Symp. Advances in Image and Video Technology (PSIVT), T. Wada, F. Huang, and S. Lin, Eds., Berlin, Germany', Springer-Verlag, pp. 318-329.
- [28] Käs, C, Brulin, M, Nicolas, H & Mailliet, C 2009, 'Compressed domain aided analysis of traffic surveillance videos', in Proc. 3rd ACM/IEEE Int. Conf. Distributed Smart Cameras 2009, pp. 1-8.
- [29] Kim, C & Hwang, JN 2002, 'Fast and automatic video object segmentation and tracking for content-based applications', Circuits and Systems for Video Technology, IEEE Transactions on, vol. 12, no. 2, pp. 122-129.
- [30] Kim, DH, Yun, ID & Lee, SU 2009, 'Attributed relational graph matching based on the nested assignment structure', Pattern Recognit., vol. 43, pp. 914-928.

An Effective Optimization and High Authenticate Feature Extraction in digital Watermarking using 2-level DWT Transform

¹Dr.A.Lakshmi ²N.Bhuvaneshwary, ³S.Jeevitha, ⁴Muthuvel Arumugam

¹Associate Professor ²Assistant Professor, Department of Electronics and Communication Engineering

Kalasalingam Academy of Research and Education, Krishnankoil-626 126

³Assistant Professor, Kalasalingam Institute of Technology, Krishnankoil- 626 126

⁴Assistant Professor, Mohamed Sathak Engineering College, Kilakarai-623 806

¹lakshmi@klu.ac.in ²bhuvaneshwary.n@klu.ac.in, ³jeevitha.ramkumar@gmail.com,
⁴muthua21@gmail.com

Received: 14 Feb 2020 Revised and Accepted: 25 March 2020

ABSTRACT

In the current scenario, the need for security in Image processing seems to be more significant. Digital watermarking is one such feature extraction. Generally PCA (Principle Component Analysis) method is used for feature extraction. A new methodology based on 'Energy Analysis' is proposed in this research work for feature extraction. Optimization techniques are used to enhance resolution and authentication of the image. The watermarked image can be hidden in the original image using 2-level DWT and as a final point watermarked image is created in wavelet domain. For a complementary watermark modulation, the perceptual lossless ratio (PLR) is initially derived in this proposed technique. From the simulation results, optimal values are calculated and compared for both Genetic Algorithm (GA) and Particle Swarm Optimization (PSO).

Keywords: Principle Component Analysis, 2-level DWT, Perceptual Lossless Ratio (PLR), Robustness, Optimal Values, Genetic Algorithm (GA), Particle Swarm Optimization (PSO).

1. INTRODUCTION

The most primitive way of hiding information is simply by means of private-key cryptography where 'key' is considered to be the knowledge of various modes being employed. Steganography books comprise numerous examples of such methods used throughout history. Greek messengers had handled different way of hiding information such as messages tattooed into their own shave head, concealing the message when their hair finally grew back. Wax tables were scraped down to bare wood where a message was scratched. Once the tables were re-waxed, the hidden message seems to be secure often. Research in primitive cryptographic techniques becomes more popular via increasing speed, capacity and highly confidential security of the transmitted information.

Technological advancement in crypto-graphical techniques in these recent days has reached the peak success in proper encrypted and secured communication for transmission of information in our daily life. In fact, it's anticipated that the most powerful algorithms using multi kilobit key lengths could not be comprised via brute force, even though all the computing worldwide power for the next 20 year focused on the attack. There is possibility of existence of vulnerabilities still or computing power breakthroughs could also arise, but in applications as per requirement of most users current cryptographic techniques are generally adequate and it is satisfactory

Information hiding is essential for several valuable reasons; the prime objective is being that "security through obscurity" isn't necessarily a bad thing, provided that it is not the only security mechanism employed. Steganography for an occasion hides encrypted information in mediums less liable to attract ones intention. A garble of random characters being transmitted among two users may tip off a watchful 3rd party that perceptive information is being transmitted.

This project will begin with a quick background on cryptography and steganography, which form the basis for a large number of digital watermarking concepts. The project will then move on to a discussion of what requirements a watermarking system must meet, as well as methods for evaluating the strengths of various algorithms.

This project focused on different watermarking techniques and its beneficial features and also its inconvenient features of all the techniques has been discussed. This project aims almost on the watermarking of digital images; however most of these similar ideas could be applicable to the watermarking of digital video and audio.

Due to the widespread of internet any Digital-contents can be easily copied, downloaded and processed. Therefore, a robust protection method of copyrights and a copy-control system are strongly required.

Watermarking is a method of embedding additional information into the digital contents that is invisible to listeners. This project investigates its techniques on data embedding, detecting, and coding also examines the difficulties concerning multimedia data hiding in the field of multimedia security and communication, addressing both theoretical and practical aspects, and tackling troubles of both design and attack. In the fundamental part, it identifies some key elements of data hiding as a layered structure. Data hiding is categorized as a communication problem since the embedded data is the required signal to be transmitted. A choice of each embedding mechanisms leads to different robustness- capacity tradeoffs. This studies trade off for two foremost categories of embedding mechanisms. In addition, irregular or random distribution of embedding capacity brings complexity in data hiding.

A comprehensive solution has been proposed to this problem, addressing the considerations for selecting constant or variable embedding rate and enhancing the algorithms for binary images, color images and grayscale, and videos, covering such applications as tamper detection annotation, copy/access control, fingerprinting, and ownership protection. The designs affords solid examples in the choice of embedding mechanisms such as the selection of modulation/multiplexing technique(s) for hiding multiple bits, and handling of random/uneven embedding capacity. Data hiding can also be used in video communication to express side information for additional functionalities or better performance.

2. AIM AND SCOPE

Prime target is to compile an introduction to the subject of image watermarking. There already exist numerous studies technically complete treatments were not common. The survey obtained from papers, journals and conference proceedings describes best.

The next target is to seek for algorithms in executing the image encoding and watermarking successfully.

In addition to this a target on performance evaluation is essential regarding to quality and compression ratio since these factors have the major impact while executing the effort.

An ultimate goal is to design and implement a watermarking encoder. This has been implemented matlab. The source code should be easily accessible and understandable so that it can serve as a standard reference for a designer which is needed to implement a watermarking.

3. DIGITAL WATERMARKING

Digital watermarking is the practice of embedding information or messages into a digital signal which may be used to verify its authenticity or the identity of its owners, in the same manner as paper bearing a watermark for visible identification. In digital watermarking, the signal may be image/pictures, audio or video. If the signal is copied, then the information also is carried with the copied signal. A single signal may carry numerous kinds of watermarks at the same time.

In visible digital watermarking, the information is visible as a picture or video. In general, if the information is assumed as text or a logo, it can be identified as the owner of the media. The image on the right side has a visible watermark. Hence if a television broadcaster adds its logo to the one corner along with the transmitted video, this logo can also be seen as a visible watermark.

In invisible digital watermarking, information is further added as digital data to any audio, picture, or video, but it cannot be perceived, although it may be possible to sense that little information is concealed in the signal). The watermark may be intended for widespread usage and thus it is made easier to retrieve or it may be in the form of steganography, where a party communicates a secret coded message embedded in the digital signal. In either case the target is to affix ownership or other descriptive information to the signal in a way that is difficult to fetch. It is also possible to use hidden embedded messages as a means of converting communication among individuals.

One best application of watermarking is in copyright protection systems, which are intended to put off in unauthorized copying of digital media. In this copyright protection the device initially fetches the watermark from the signal before copying and decides whether to copy or not by analyzing the contents enclosed in the watermark.

Another major application is in source tracing. A watermark is embedded into a digital signal at each point of distribution. If a copy of the work is found later on, then the watermark may be retrieved from the copy and the source of the distribution is identified. This technique reportedly has been used to perceive the source of illegally copied movies. Annotation of digital photographs with descriptive information is one more application of invisible watermarking.

In some file formats (.jpeg, .tiff, .png, .bmp) digital media may enclose additional information called [metadata](#), so digital watermarking is unique in the way of data carrying in the signal.

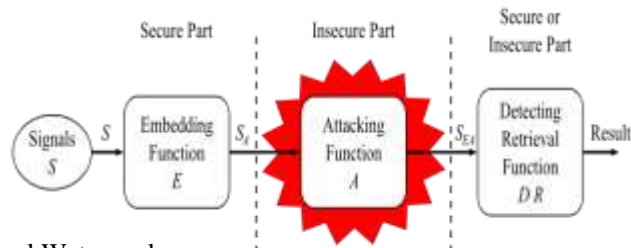


Fig. 1 - General Watermark

lifecycle

4. DISCRETE WAVELET TRANSFORM

Calculation of wavelet coefficients at each and every possible scale is a fair amount of work, and it generates an lot of data. If the scales and positions are chosen based on powers of two, the so-called dyadic scales and positions, then calculating wavelet coefficients are efficient and just as accurate. This is attained from discrete wavelet transform (DWT).

The algorithm to extract DWT coefficients is explained below: Let B be the original grey scale cover image. This image is segmented as non-overlapping using haar technique. This is denoted as, $B_k, n = 0, 1, 2, 3 \dots N-1$ (1)

A. WAVELET WATERMARKING TECHNIQUE

Wavelet domain seems to be one of the most promising watermark embedding. Separation of image into multiple components such as lower resolution approximation(LL) in addition with Horizontal(HL), vertical(LH) and diagonal(HH) components. Another possible domain for watermark embedding is that of the wavelet domain. This repetitive process is done to evaluate numerous “scale” wavelet decomposition like 2 scale wavelet transform as shown below.

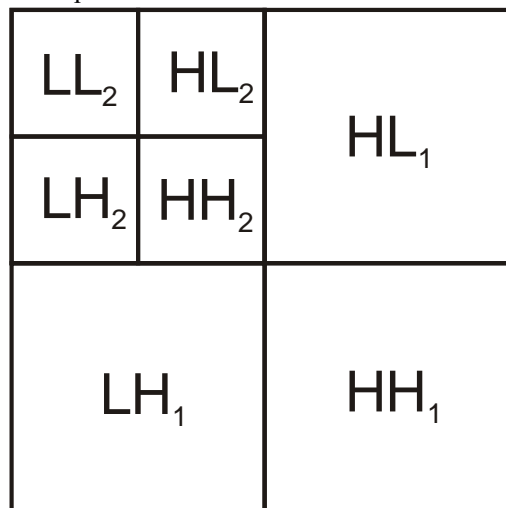


Fig. 2 - 2 Scale 2-Dimensional Discrete Wavelet Transform

The advantages of wavelet transform is trusted to be the most superior model aspects of the HVS while comparing with FFT or DCT. This beneficial feature of wavelet domain helps in

permitting higher level of watermarks in regions where the HVS is known to be less sensitive to high resolution bands (LH,HL,HH) Embedding of watermarks in these regions leads to greater increase in robustness of our watermark and besides no impact on image quality.

One such straightforward techniques is to use a identical embedding technique to that used in the DCT, the embedding of a CDMA sequence in the detail bands according to the equation given below.

$$I_{W_{u,v}} = \begin{cases} W_i + \alpha |W_i| x_i, & u, v \in HL, LH \\ W_i & u, v \in LL, HH \end{cases} \quad (2)$$

Where W_i indicates the coefficient of the transformed image, X_i denotes bit of the watermark to be embedded, and α a scaling factor. The same pseudo-random sequence used in CDMA generation is produced to perceive the watermark and estimate its correlation among two transformed detail bands. If the correlation exceeds beyond some threshold T , the watermark is predicted.

Multiple bit messages can also be easily generated by embedding multiple watermarks into the image. As in the spatial version, a separate seed is used for every PN sequence, later it is then added to the detailed coefficients. During detection, whenever the correlation exceeds T for a particular sequence a “1” is recovered; otherwise a zero. The recovery process then iterates throughout PN sequence till all the bits of the watermark have been recovered.

Moreover, the embedding process should have a certain extent to adaptability as the embedding holds the values of the transformed value in embedded which stores major watermark in larger coefficients. This claims that the embedding technique should prove resistant to JPEG compression, cropping, and other typical attacks.

The simplest example for Watermarked Lena and response of the watermark detector after JPEG-compression using 50% quality factor is clearly illustrated in the below fig.



Fig. 3 - Watermarked Lena and response of the watermark detector after JPEG-compression using 50% quality factor.

5. SINGULAR VALUE DECOMPOSITION

SVD is a numerical technique used to diagonalize matrices in numerical analysis in which this algorithm has been extends to wide range of applications. The core properties

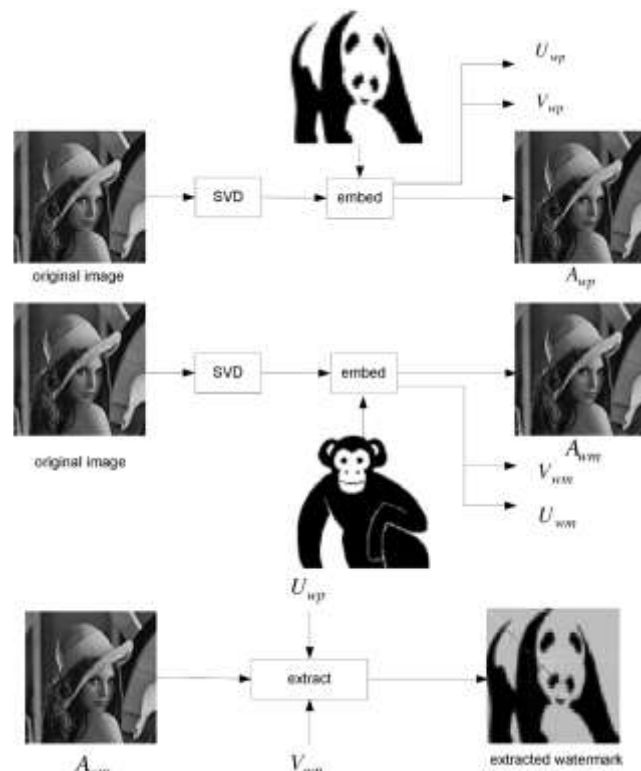


Fig. 4 - Extracted watermark is determined by the pair of SVD matrices employed in the watermark detection

of SVD in the view-point of image processing applications are:

- 1) The singular values (SVs) of an image have very fine stability, eventhough if a little undesired perturbation is included in the image its SVs do not change considerably.
- 2) SVs characterize intrinsic algebraic image properties. Based on SVD, we describe a watermark casting and detection scheme. We can examine that discrete image is considered an array matrix comprising of nonnegative scalar entries in the viewpoint of linear algebra. Let such an image be denoted by without loss of generality, we assume in the succeeding discussions that is a square image, denoted by, where depicts either the real number domain or the complex number domain. The SVD may be defined as $A=USV^T$ (3) Here U and V considered to be the orthogonal matrices ($UU^T= I, VV^T= I$) of size $m \times m$ and $n \times n$ respectively. S, with size $m \times n$, is the diagonal matrix with r (rank of A matrix) non-zero elements are known as singular values of A matrix.

U and V matrices columns are called left and right singular vectors respectively. Consider A as an image in our case, S have the luminance values of the image layers created by left and right singular vectors. Left singular vectors correspond to horizontal details while right singular vectors correspond to the vertical details of an image.

The unique aspect used in SVD based compression methods is that the SVs come in declining order which means significant fall from first SV to the last one.

Slight alteration of SVs does not cause any impact on image quality and also SVs do not seems much change even after attacks, which are the most needed pr o per ties in watermarking schemes.

In embedding stage, SVD based compression method is applied to the cover up image, watermark is further added with a gain parameter to the SV matrix S, SVD is applied just once, the resultant U and V matrices are stored and resultant SV matrix is used up with U and V matrices of the cover image to compile the watermarked image.

In extraction stage, the embedding steps are reversed: SVD is applied to watermarked image. An intermediate matrix is composed by making use of stored U and V matrices and singular matrix of watermarked image. The watermark is extracted from the intermediate matrix by subtracting singular matrix of cover image.

A. EXAMPLES

Consider a example, a 256x256 image “Lena” is taken as the host image A. “Panda” image is taken as watermark W_p and “Monkey” image is taken as watermark W_m . Both the watermarks are applied to the host image and generating two watermarked images A_{wp} and A_{wm} and also to attain the matrix S and SVD signature matrices U_{wp} and V_{wp} for the watermark W_p has also obtained.

Here the scaling parameter is $\alpha = 1/255$. At the detector end, there is no evidence for watermark whether is embedded or not. Now if we try to identify whether watermark W_p (“Panda”) is embedded in the watermarked image A_{wm} (with watermark W_m —“Monkey”).

Ideally, the extracted watermark W_{mp} must have no correlation with “Panda” because the embedded watermark is a “Monkey.” On the other hand, as predicted in Section I, the extracted watermark W_{mp} is a “Panda” in its place of the real embedded watermark “Monkey,” there are slight differences in diagonal values, as shown in Fig.

The correlation coefficient of the extracted watermark with the reference watermark “Panda” is 0.9982. It perceived “Panda” from a watermarked image along with a “Monkey” watermark using the watermarking method. The basic imperfection is that the reference watermark “Panda” is “stamped” besides at the detector end. Unlike the illustration we presented here, the true embedded watermark and the reference watermark that generates the SVD matrices employed in the detector are the alike. The correlations of the extracted watermark through a set of watermarks are then evaluated. In such cases, the “stamped” reference watermark will certainly exist at the detector end as we analysed. SVD transformation enriched with a number of attractive properties. Foremost, the matrix need not be a square, it can also be a rectangle.

Second, the singular values i, λ of an image matrix have excellent stability, i.e., when a large perturbation is added to an image, its SVs do not alter significantly. It motivates watermark embedding by modify the SVs of image slightly. Where $\lambda_i, i = 1, 2, \dots, R$ are the Eigen values of \mathbf{H} and they are satisfied $\lambda_1 \geq \lambda_2 \geq \dots \geq \lambda_R$. \mathbf{U} is $M \times M$ matrix, \mathbf{V} is $N \times N$ matrix, and they are the Eigen vectors of \mathbf{H} . The size of \mathbf{S} is $M \times N$. The upper right T is the transpose of the matrix.

6. DIGITAL WATERMARK EMBEDDING AND EXTRACTING

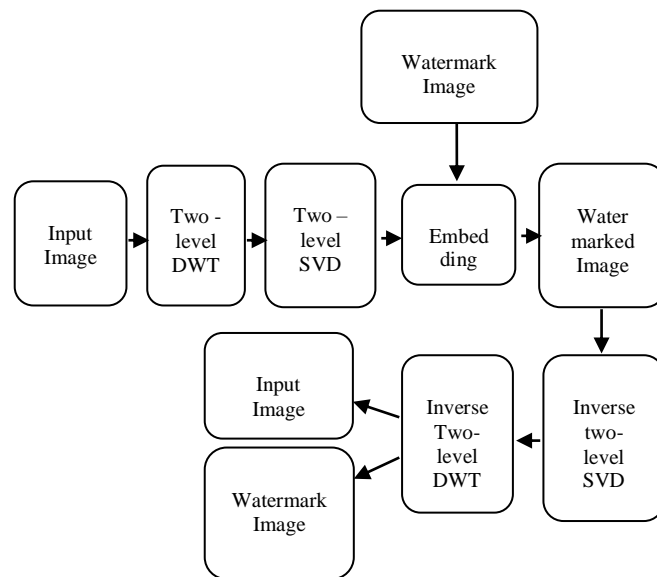


Fig. 5 - Embedding and extracting the watermark image

The proposed digital watermark embedding process is divided into 6 steps and is briefly described as below:

Step 1: The original image I (512x512) is first divided into square blocks of size 8x8 pixels, and then the DCT is applied in each block twice. Then each new block is expressed as the matrix $F_{m,n}$ ($1 \leq m \leq 64, 1 \leq n \leq 64$).

Step 2: Perform SVD on the matrix $F_{m,n}$ ($1 \leq m \leq 64, 1 \leq n \leq 64$) to get matrices $U_{f_{m,n}}$, $S_{f_{m,n}}$ and $V_{f_{m,n}}$ for each matrix $F_{m,n}$, and the $S_{f_{m,n}}(1,1)$ of every matrix $S_{f_{m,n}}$ is collected together to get a new matrix A (64×64).

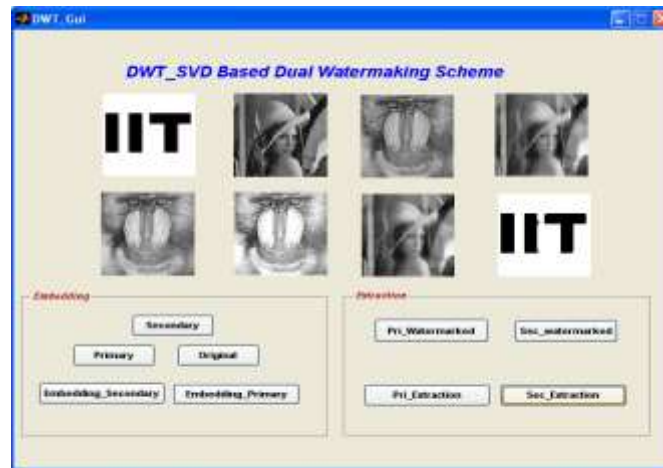
Step 3: Perform SVD on the new matrix A (64×64) and obtain U , V and S .

Step 4: Using W (32×32) to represent the grey watermark. Then according to $S + \alpha W \Rightarrow U_1 S_1 V_1^T$, obtain V_1 , U_1 and then obtain A^* (64×64) according to $A^* \leftarrow U S_1^T V$ ($\alpha = 0.1$).

Step 5: Using $A^*(m, n)$ ($1 \leq m \leq 64, 1 \leq n \leq 64$) to replace the $S_{f_{m,n}}(1,1)$ of every matrix $S_{f_{m,n}}$ to get $S^*_{f_{m,n}}$, then the $F_{m,n}$ which obtained in step 1 become $F^*_{m,n}$ according to $F^*_{m,n} \leftarrow U_{f_{m,n}} S^*_{f_{m,n}} V_{f_{m,n}}$.

Step 6: Apply inverse 8×8 block DCT and 8×8 SVD to $F^*_{m,n}$ twice to produce original image $I^*(512 \times 512)$.

7. SIMULATION RESULT



WATERMARKING	SNR	P	CC
Without Noises or Attacks	8.5300	2	$0.11003 - i2.3656e^{-017}$
With Noise(Salt & Pepper Noise)	7.4680	2	$0.11003 + i1.6177e^{-017}$
With Rotation	7.6563	5	$0.11003 - i2.4571e^{-017}$
With Cropping	1.1781	6	$0.11003 - i1.0973e^{-017}$

TABLE 1 PSNR and CC comparison for various outputs

8. CONCLUSION

The main scope of the project is to increase the authentication and the quality of the image. In this project two stages are there first stage is watermarking and the second stage is optimization. In

the first stage, watermark image is hidid into the original image in embedding process and the watermark image and original image are separated in an extraction process. The figure shows the arrangement of original image, primary image and a secondary image. And followed to that, the watermark image is embedded into the primary image and secondary image to get a primary watermarked image and Secondary watermarked image. At last the watermark image is extracted from the primary image and the secondary image. By using this dual DWT Watermarking technique, the capacity of the invisible watermarking increases and it is highly robust.

9. REFERENCES

- [1] Acken.J.M.(1998),“How watermarking adds value to digital content ” , Communications of the ACM, Vol.41, No.7, pp.74-77.
- [2] Andrews. H. C and Patterson. C. L. (1976), “Singular Value Decomposition (SVD) image coding”, IEEE Trans. on Communications, pp. 425-432.
- [3] Barni. M, Bartolini. F, Cappellini. V and Piva. A. (1998), “A DCT-domain system for robust image watermarking”, Signal Processing, Vol.66, No.3, pp. 357-372.
- [4] Cox. I. J, Kilian. J, Leighton. F. T and Shamoon. T. (1997), “Secure Spread Spectrum Watermarking for Multimedia”, IEEE Trans. on Image Processing, Vol.6, No.12, pp.1673-1687.
- [5] Craver. S, Memon. N, Yeo. B. L and Yeung. M. M. (1992), “Resolving rightful ownerships with invisible watermarking techniques: Limitations, attacks, and implications”, IEEE Journal on Selected Areas in Communications, Vol.16, No.4.
- [6] Craver. S, Memon. N, Yeo. B and Yeung. M. (1996), “Can invisible watermarks resolve rightful ownership”, Technical Report RC 20509, IBM Research Division.
- [7] Liu. R and Tan. T. (2002), ”An SVD-Based Watermarking Scheme for Protecting Rightful Ownership”, IEEE Transactions on Multimedia, Vol. 4, No. 1.
- [8] Nikolaidis. N and Pitas. I. (1996), “Copyright protection of images using robust digital signatures”, Proc. of ICASSP’96, Vol. 4, pp. 2168-2171.
- [9] Nikolaidis. N and Pitas. I. (1998), “Robust image watermarking in the spatial domain”, Signal Processing, Vol.66, No.3, pp.385-403.
- [10] Swanson. M. D, Zhu. B, Tewp. A. H. (1996), “Transparent robust image watermarking”, Proc. IEEE International Conf. on Image Processing (ICIP96), Vol. III, Lausanne, Switzerland, pp. 211-214.
- [11] Wolfgang. R. B and Delp. E. J. (1997), "A watermark technique for digital imagery: further studies", Proc. of International Conference on Imaging Science, Systems, and Technology, Las Vegas, Nevada.

Ship Detection In Medium Resolution SAR Image Via VGG NET

Madhanmani R, **Mr.K.M.Alaudeen M.E.,(Ph.d)**

Mohamed sathak engineering college, Kilakarai

Received Date: 01 April 2021

Revised Date: 07 May 2021

Accepted Date: 08 May 2021

Abstract: *In recent decades, one of the main significant applications of remote sensing is Synthetic aperture radar (SAR) technology. The SAR images on the previous method can perform with several constraints. In this paper, CNN (Convolutional Neural Network) of VGGnet (Visual Geometry Group) is proposed to detect the ship. By adopting multi-level features to improve the ship detection performance by the convolution layers. These layers are used to fit ships of different sizes. The proposed simulation results are comparable with the prior methods.*

I. INTRODUCTION

The Ship discovery in high-resolution optical satellite symbolism is an advanced field at KSAT. Convolutional neural organizations (CNNs) are the quintessential profound learning models, the primary driver of the gigantic advancement, and can be adjusted to fit different issues. When a CNN is prepared on proper preparing information, it has demonstrated to perform better compared to conventional calculations in an assortment of PC vision and picture investigation issues. Information about AI engineering and how it reacts to various information is a need and permits the chance of investigating potential wellsprings of mistakes. Edification of basic difficulties in the framework and information is wanted. One potential test in optical EO information is the appearance of little mists. These may look basically the same as boats and subsequently cause bogus cautions. Once more, this danger can be alleviated by utilizing a lot of exact preparing information for streamlining. The CNN would then be able to figure out how to overlook these bogus alerts

In this work, CNN (Convolutional Neural Network) of VG Gnet (Visual Geometry Group) is presented for the ship detection method. This method is used to improve the performance of multi-level detection systems.

The rest of the paper is organized as the related work in section 2, and section 3 illustrated the proposed work of the paper. In section 4, the experimental results are described and the conclusion in section 5, respectively.

II. RELATED WORK

Yinghua et al. introduced another various leveled conspire for distinguishing ships from high-goal engineered gap radar (SAR) pictures. The plan comprises two phases: recognition and segregation.

G.Margarit introduced a boat checking framework imagined to arrive at the past objective, SIMONS(Ship Monitoring with SAR)to identify a wide scope of boats.

Zou et al. (2020) built up an improved SSD calculation dependent on MobilenetV2 CNN for transport picture target recognition and ID.

Wang et al. (2019) outlined an improved Faster R-CNN dependent on the MSER choice rule for SAR transport discovery in the harbor in this paper.

Tao et al. (2018) carried out a worldview for engineered gap radar (SAR) perception of boat focuses adrift.

ZHANG et al. (2019) tested a rapid SAR transport identification approach by improved you're just look once form 3 (YOLOv3).

III. PROPOSED WORK

In this paper, CNN (Convolutional Neural Network) of VGGnet (Visual Geometry Group) is proposed to detect the ship. By adopting multi-level features to improve the ship detection performance by the convolution layers. These layers are used to fit ships of different sizes. It is divided into several stages. Initially, the CNN is the deep learning that is combined with the VGGnet-CNN for the detection of ships.

VGG MODEL

The VGGNet is based on a neural network (NN) that is used for the Imagenet Large Scale Visual Recognition Challenge (ILSVRC). An image localization task and the image classification task are performed well by it. The image of a certain object is described by a bounding box known as



localization, and Classification is used to detect the object in the image. The pictures utilized in the opposition are isolated into 1000 unique classes. Given a test picture, the neural organization will yield likelihood dissemination for that picture. This implies it computes a likelihood a worth somewhere in the range of 0 and 1 for every one of those 1000 classes, at that point picks the classification with the most elevated likelihood. On the off chance that the neural organization is sure about an expectation, its top decision has a high likelihood.

In the ImageNet grouping, challenge get some opportunities to anticipate the correct classification, which is the reason the demo application shows the 5 most elevated probabilities the organization figured. As the organization likewise figures, the picture might have been a library, bookshop, or comic book — however, the probabilities show that it isn't as certain about those decisions.

Among the best performing CNN models, VGG is noteworthy for its straightforwardness. We should investigate its design.

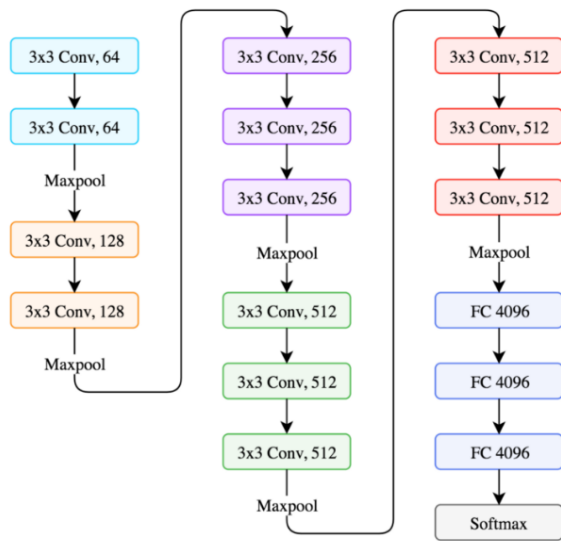


Figure VGG architecture

VGG is a 16 layer NN, not including the max pool layers and the softmax toward the end. It's additionally alluded to as VGG16. The engineering is the one we worked with above. Stacked convolution + pooling layers followed by completely associated ANN. A couple of perceptions about engineering:

It just uses 3x3 convolutions all through the organization. Note that two consecutive 3x3 convolutions have the compelling responsive field of a solitary 5x5 convolution. Furthermore, three stacked 3x3 convolutions have the open field of a solitary 7x7 one. Here's the

perception of two stacked 3x3 convolutions bringing about 5x5.

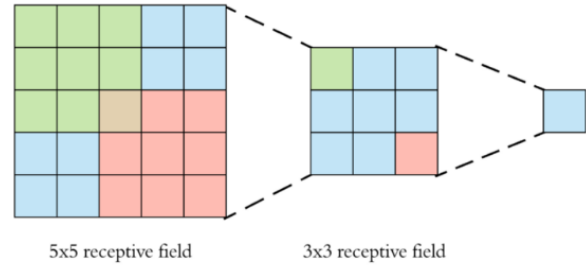


Figure 3.2 two stacked 3x3 convolutions visualization

Another benefit of stacking two convolutions rather than one is that we utilize two relu activities, and more non-linearity gives more capacity to the model. The number of channels increases as we go further into the organization. The spatial size of the component maps decline since we do pooling, yet the profundity of the volumes increment as we utilize more channels.

IV. Experimental Results

The broad trials are completed to check the viability of the proposed strategy. First, images with pixels containing ships, seawater, islands, and without ships are set up to confirm the exhibition of the proposed transport applicant extraction strategy. We tried our technique on taking the boat and no boat pictures at various occasions and areas and containing seaside landscapes. The public SAR Ship Detection Dataset (SSDD) is utilized in this work. The SSDD incorporates SAR pictures gathered from Radarsat-2, TerraSar-x, and Sentinel-1 with goals going from 1 to 15 m and polarimetric methods of HH, HV, VV, and VH. The insights concerning SAR pictures are recorded in table 1.

Table 1 Data Description

Sensors	Resolut ion	Size(p ixel)
Sentinel -1	20m	1024x1024
Radarsa t-2	1-100m	8192x8192
TerraSA R-X	10m	8891x8676

In this work, accuracy is widely used to quantitatively evaluate ship detection performance.

$$\text{Accuracy} = \frac{TP+TN}{TP+FP+FN+TN}$$

Herein, TP, FN, and FP denote true positive, false negative, and false positive, respectively. The accuracy for the input images is presented in Table 4.2.

Table 2 The accuracy of the proposed algorithm for various data set

Name of the Image	Accuracy (in %)
Image1	93.5
Image2	94.2
Image3	93.6
Image4	94.1
Image5	92.3
Image6	90.5
Image7	93.7
Image8	94.4
Image9	95.1
Image10	93.5
Image11	91.8
Image12	92.7
Image13	90.2
Image14	92.1
Image15	92.4

The simulation results of ship detection are given below

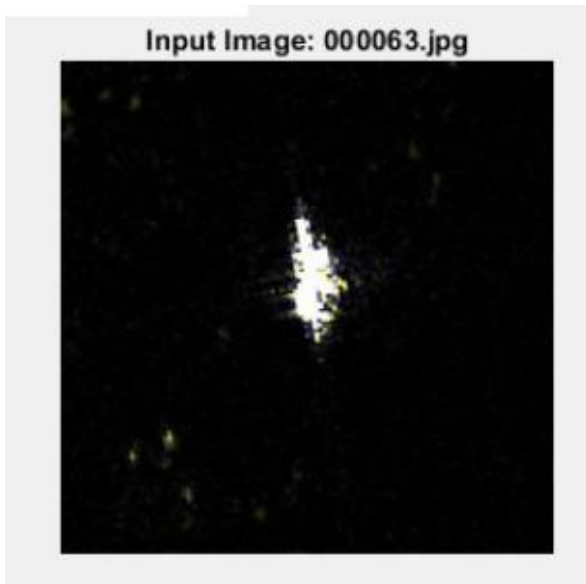


Figure Input image

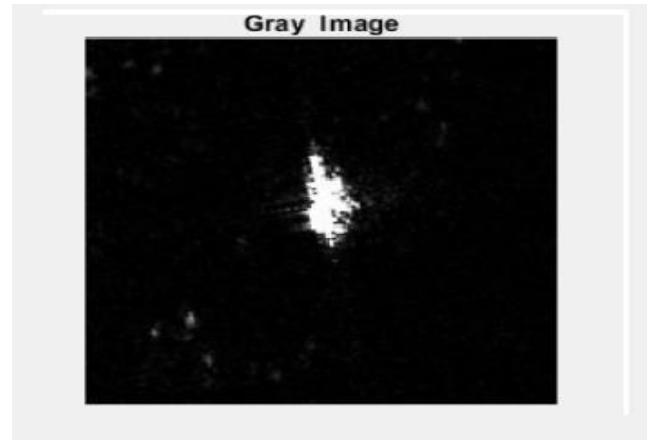


Figure Gray image

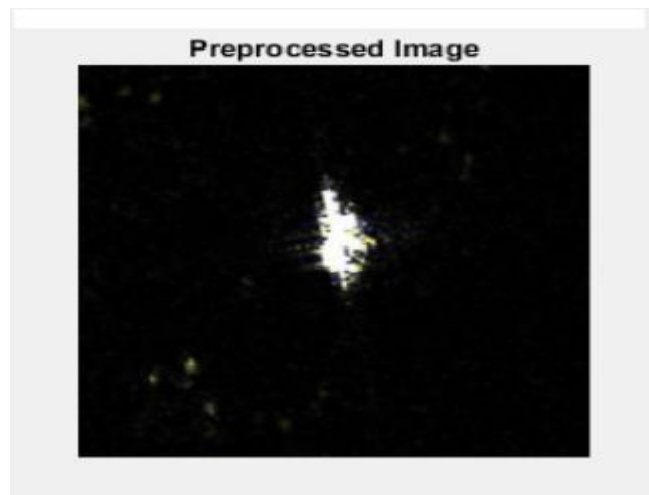


Figure Preprocessedimage

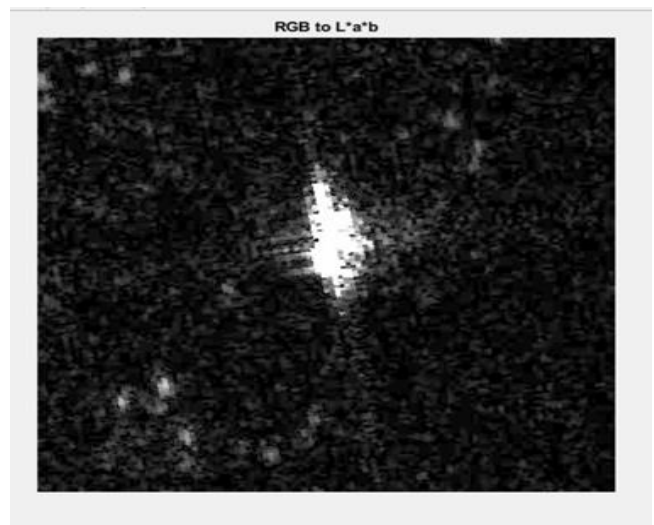


Figure RGB to L*a*b

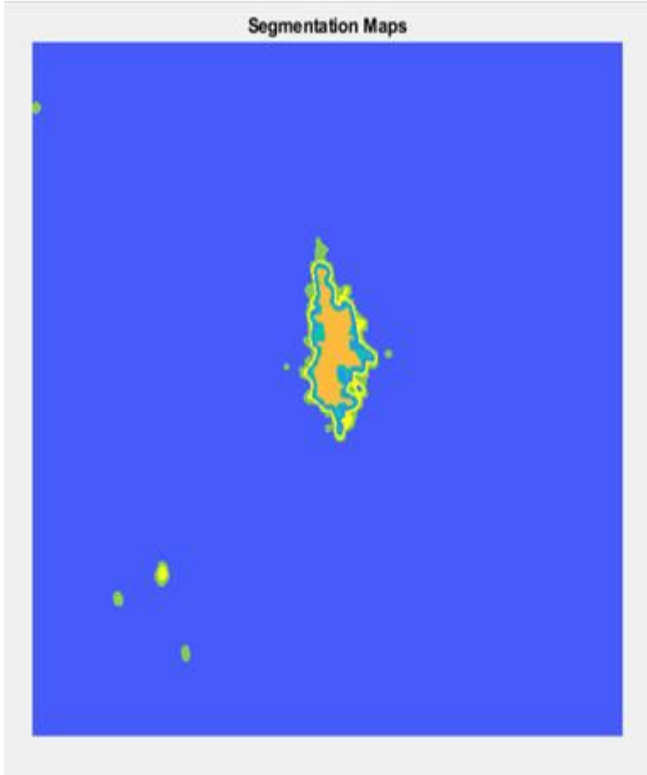


Figure Segmentation maps



Figure Classification result



Figure Layer processing



Figure Classification result

Accuracy Comparison

The accuracy of the proposed method is compared with the existing method and is illustrated in Table

Table 3 Performance comparison of the proposed method with the existing method

S.No	Method	Average Accuracy (in percentage)
1	CNN	89
2	RNet	92
3	Proposed VGGNet	92.94

V. Conclusion

This undertaking proposed a perform various tasks learning system for transport discovery in multi-goal SAR pictures. To investigate more successful element extractors, an undertaking explicit planned spine network is created roused by the VGG-Nets. The recreation results demonstrate that the proposed network is incredible to extricate discriminative portrayals for viable SAR transport grouping. The acknowledgment execution is improved by joining the trio similitude limitation joined with the softmax characterization blunder punishment framing the perform multiple tasks learning models, which can accomplish great grouping execution by pulling the profound portrayals coming from a similar class nearer to one another and pushing those of various classes far separated in the mastered inserting space. To improve the speculation execution of trio CNNs in the DML, the Fisher regularization term is forced on the profound embeddings to

exploit the trios in a preparation group. Thus, the worldwide data of the pairwise distances of the profound inserting is completely mined, and more hearty models learned are acquired.

References

- [1] Morillas, J. R. A., García, I. C., & Zölzer, U. (2015, September). Ship detection based on SVM using color and texture features. In 2015 IEEE International Conference on Intelligent Computer Communication and Processing (ICCP) 343-350 IEEE.
- [2] Liu, Y., Ma, H., Yang, Y., & Liu, Y. (2011, June). Automatic ship detection from SAR images. In Proceedings 2011 IEEE International Conference on Spatial Data Mining and Geographical Knowledge Services 386-388 IEEE.
- [3] Tanveer, H., Balz, T., & Mohamdi, B. (2019, November). Using convolutional neural network (CNN) approach for ship detection in Sentinel-1 SAR imagery. In 2019 6th Asia-Pacific Conference on Synthetic Aperture Radar (APSAR) 1-5. IEEE.
- [4] Velotto, D., Soccorsi, M., & Lehner, S. (2013). Azimuth ambiguities removal for ship detection using full polarimetric X-band SAR data. IEEE transactions on geoscience and remote sensing, 52(1) 76-88.
- [5] ZHANG, T., ZHANG, X., SHI, J., & WEI, S. (2019, December). High-speed ship detection in SAR images by improved yolov3. In 2019 16th International Computer Conference on Wavelet Active Media Technology and Information Processing 149-152 IEEE.
- [6] Jarabo-Amores, P., González-Bonilla, M. J., Mata-Moya, D., Martín-de-Nicolás, J., & Palma-Vázquez, Á. (2012, July). Demonstrator of maritime SAR applications: Automatic ship detection results. In 2012 IEEE International Geoscience and Remote Sensing Symposium 3732-3735 IEEE.
- [7] Tanveer, H., Balz, T., & Mohamdi, B. (2019, November). Using convolutional neural network (CNN) approach for ship detection in Sentinel-1 SAR imagery. In 2019 6th Asia-Pacific Conference on Synthetic Aperture Radar (APSAR) 1-5 IEEE.
- [8] Velotto, D., Soccorsi, M., & Lehner, S. (2013). Azimuth ambiguities removal for ship detection using full polarimetric X-band SAR data. IEEE transactions on geoscience and remote sensing, 52(1)76-88.
- [9] Ao, W., & Xu, F. (2018, March). Robust Ship Detection in SAR Images from Complex Background. In 2018 IEEE International Conference on Computational Electromagnetics (ICCEM) 1-2 IEEE.



Three Ways Chip to Chip Communication via a Single Photonic Structure: A Future Paragon of 3D Photonics to Optical VLSI

S. Boobalan, P. Venkatesh Kumar, K. Vinoth Kumar & G. Palai

To cite this article: S. Boobalan, P. Venkatesh Kumar, K. Vinoth Kumar & G. Palai (2021): Three Ways Chip to Chip Communication via a Single Photonic Structure: A Future Paragon of 3D Photonics to Optical VLSI, IETE Journal of Research, DOI: [10.1080/03772063.2021.1908179](https://doi.org/10.1080/03772063.2021.1908179)

To link to this article: <https://doi.org/10.1080/03772063.2021.1908179>

Published online: 18 Apr 2021.

Submit your article to this journal [↗](#)

Article views: 9

View related articles [↗](#)


View Crossmark data [↗](#)

nee mi
PRINCIPAL
MOHAMED SATHAK ENGINEERING COLLEGE
KILAKARAI 623 811a

Full Terms & Conditions of access and use can be found at
<https://www.tandfonline.com/action/journalInformation?journalCode=tjr20>



Three Ways Chip to Chip Communication via a Single Photonic Structure: A Future Paragon of 3D Photonics to Optical VLSI

S. Boobalan¹, P. Venkatesh Kumar², K. Vinoth Kumar³ and G. Palai ⁴

¹Electrical and Electronics Engineering Department, Mohamed Sathak Engineering College, Kilakarai, India; ²Department of Electrical and Electronics Engineering, Karunya Institute of Technology & Sciences, Coimbatore, Tamil Nadu, India; ³Department of Electrical and Electronics Engineering, New Horizon College of Engineering, Bengaluru, Karnataka, India; ⁴Department of Electronics and Communication Engineering, Gandhi Institute for Technological Advancement (GITA), Bhubaneswar, India

ABSTRACT

A proposal is made in this paper to realize 3-ways chip to chip communication via 3D photonic structure. The mechanism of the work is understood with the help of absorbance and reflectance of the structure. The absorbance is determined using the analytical treatment where reflectance is computed using the photonic bandgap analysis, which is found with the help of plane wave expansion method. Further the present research deals with low power input signal whose potential varies from 0.55 to 1 V because to avoid the heat generation in nanoelectronics and nanophotonic circuits where circuit comprises chip, LED and photo detector along with waveguide (3D photonic structure). The output results indicate that a proper combination of lattice spacing of silicon-based 3D photonic structure and diameter of air holes could be a right candidate to realise 3-ways communication.

KEYWORDS

3D photonic structure;
photonic integrated circuit;
Optical VLSI

1. INTRODUCTION

A set of electronic circuits is placed on one flat piece of semiconductor material is known as integrated circuit. Basically silicon is chosen as the semiconductor materials where flat piece is called chip. Further the combination of large number of tiny transistors into a small chip leads to the smaller, cheaper and faster as compared to the discrete electronic elements. The device which has ample electronic circuits in a single chip is called nano-electronics. Even though researchers from electronic community focuses on the nano-electronic devices at the present time, it has certain limitations pertaining to the excess heat generation as well as scattering effect due to the interaction of electrons with lattices. To keep away these limitations, photonic technology stands with nano-material nowadays. Even though, research on photonics is around 30 years around (staring from 1990 to 2020) the globe, many type of photonic-based devices have been explored both theoretically as well as experimentally during three decades [1,2]. For example, the devices with respect to the one dimensional photonic crystal structure have entered to the market in their physical form. Apart from this an extensive research has also been carried out using both 2D and 3D photonic structures. However, the most successful application of photonic crystal is based on 2D photonic structure; for example, photonic crystal fiber. Beside this, recently a few works have found

in the literatures [3–7]. For example; reference [3] and [4,5] deal with the sensing application where measurement of glycerol and haemoglobin in human blood is computed. Similarly, reference [6–9] discusses different application with respect to communication where solar cell, optical lock and optical demux, etc. have been found. Though the above said application deals with the different applications relating to the communication; the present work discusses a different application where three ways chip to chip communication is seen using a single photonic structure. Moreover recently a paper [9] relating to one way chip to chip communication is disclosed in the literature, where one dimensional photonic structure has been deployed. The present paper is organised as follows; section 2 deals with the operational mechanism of the work along with the structure where section 3 deals with the result and analysis to realise chip to chip communication. Finally, conclusions are indicated in the section 4.

2. PROPOSED STRUCTURE AND OPERATIONAL MECHANISM

The objective of the present work is to realize chip to chip communication through 3D photonic crystal structure. The operational mechanism for the same is understood in Figure 1.

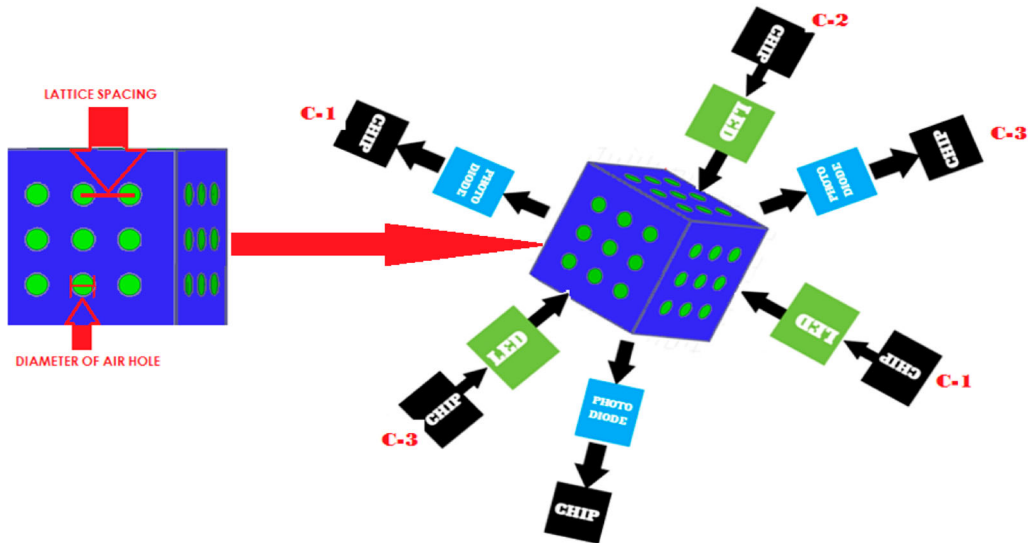


Figure 1: Operational mechanism of three ways chip to chip communication

Figure 1 explains the three ways chip to chip communication, where signals start from three chips (C-1, C-2 and C-3) simultaneously and arrives at their other sides of the chips. As far as different components in Figure 1 are concerned, each way of communication consists of chip, light emitting diode, photonic detectors aside 3D photonic structure which is acting as waveguide. Further concentrating on the signal transmission from one chip to other, it is understood that an electronic signal enters to LED from the chip and subsequently electronic signal converts into its optical counterpart. Then this light signal incidents to the silicon-based waveguide (3D photonic structure). Here the waveguide is designed in such way that it will transport the signal to the other end of the structure without making any loss. For example, when such light signal arrives at the photo detector, it will convert light energy to its electronic counterpart. Finally, the signal reaches at their respective chip of the other end. As far as electronic signal is concerned, it deals with the low power potential which varies from 0.55 to 1.0 V. The reason for choosing such potential is that these signals will create or generate a mere amount of heat in the VLSI circuit which is essential for nanoelectronic and nanophotonic communication. Again, considering the conversion of the signals from electronic to light, we use

$$\lambda = \frac{1240}{V} \text{ nm} \quad (1)$$

Here the wavelength can be obtained corresponding to the each electronic signal which varies from the 0.55 to 1.0 V. Putting the values of the potential in Equation (1), energy generated by the LED is computed. The computed results of wavelength vary from 1240 to 2250 nm corresponding to the potential which varies from 1 to 0.55 V.

Even though different components (LED, waveguide (3D structure) and photo detector) play a vital role, the inset in Figure 1 represents the operational mechanism along with three dimensional photonic crystal structure.

In this inset, the proposed structure is a three-dimensional photonic structure where silicon acts as background material and air holes have been etched on it.

In this case, photonic crystal is composed of dielectric (air) in periodic nanostructure which is etched on semiconductor material. It is designed to affect the propagation of the electromagnetic signals that create allowed and forbidden photonic energy bands. Basically it controls and manipulates light flow. Here, the proposed photonic crystal is made up lossless dielectric materials with respect to the signal ranges from 1240 to 2250 nm because both background (silicon) and column (air) materials is lossless at input signals. Here 3×3 air holes have been fixed up along three directions on the substrate material where lattice spacing and diameter of air holes is taken of 350 and 303 nm, respectively. The reason for selecting such dimensions and number of air holes is that the present structure shows a complete band gap nature at this condition with respect to the input signals. Apart from this, the structure has zero absorption at the input signals as the extinction coefficient of silicon and air materials are zero [9].

Basically, it is hard to realise more than one way communication pertaining to electronic signal simultaneously using a single device because there is an electrical interfaces between signals in the devices which creates

technical snag due to the interference. However such kind of technical snag can be avoided with respect to the optical interference because after mutual interaction of the signals in central core of waveguide, they will reach at the photo diode end without any interruption. The proposed device could be implemented in photonic integrated circuit in printed circuit board (PCB) or in VLSI (very large system of integration).

3. RESULT AND DISCUSSION

The outcomes of this research relies on the different factors such as the efficiency of the LED, coupling efficiency between LED and 3D photonic waveguide, efficiency of 3D photonic structure, coupling efficiency between 3D waveguide and photo detector, efficiency and responsivity of photo diode. Let us discuss one by one as following.

3.1 Efficiency of LED

The light emitting diode is used for the conversion of light energy from its electronic counterpart. To understand the same, various types optical sources including homo and hetero-junction have been employed. Here gallium arsenide-based semiconductor is considered to form p and n junction where silicon acts as the encapsulation or cone material. The reason for choosing such encapsulation is to fetch maximum efficiency. Basically the efficiency of the proposed light emitting diode relies on its both internal as well as external efficiency. It also depends on the different extraction efficiencies such as total internal reflection near the p-n junction of the diode, transmission efficiency at the encapsulation and transmission at the air interface. Considering simple mathematical equation, it is found that the efficiency with respect to the total internal reflection can be written as [10]

$$\eta_{\text{cone}} = \frac{1 - \sqrt{1 - \left[\frac{n_c}{n_s}\right]^2}}{2} \quad (1a)$$

Where η_{cone} , n_c and n_s be the LED efficiency at the semiconductor and cone interface, refractive index of cone and semiconductor material, respectively.

Further the transmission efficiency with respect to the semiconductor and cone interface can be written as [10]

$$\eta_{\text{SC}} = \frac{4n_s n_c}{[n_s + n_c]^2} \quad (1b)$$

The transmission efficiency at cone and air interface can be written as [10]

$$\eta_{\text{CA}} = \frac{4n_c}{[1 + n_c]^2} \quad (1c)$$

Finally, the resultant efficiency of the LED can be written as

$$\eta = \eta_{\text{cone}} \times \eta_{\text{SC}} \times \eta_{\text{CA}} \quad (1d)$$

Since LED converts light energy with having wavelength varies from 1.24 to 2.25 μm pertaining to the input potential ranges from 1 to 0.55 V, the resultant efficiency of the LED corresponding to these wavelengths is computed. The output result for the same is indicated in Figure 2(a).

Figure 2(a) represents the variation of efficiency of gallium-based light emitting diode with respect to the wavelengths. From the figure it is observed that the efficiency varies nonlinearly with respect to the wavelengths. For examples; the efficiency is 100% at some wavelengths and less than that at other signals. It is also seen that the proposed LED has minimum efficiency of 90% at some wavelengths. So it is observed that the efficiency of the LED varies from 90 to 100 %.

3.2 Coupling Efficiency between LED and Photonic Structure

Basically the optical source (LED) sends signal to the photonic structure through an interface, where interface deals with the thin thickness of air. The coupling efficiency relies on the following factors [11]

- (1) Mode of propagation from source (LED) to destination (Photonic structure),
- (2) Partial reflection at interface and transmission corresponding to the reflection
- (3) Divergence of signal from source and acceptance of signal by destination

The optical coupling between two modes relies on the effective refractive indices and it can be written as

$$\eta_{\text{coup,mode}} = \frac{n_{\text{eff},2} T_2}{n_{\text{eff},1} T_1} \quad (2a)$$

Here $n_{\text{eff},2}$, $n_{\text{eff},1}$ are called as effective refractive index and T_2 , T_1 be the transmission of mode 2 and 1, respectively.

It is understood from operational mechanism that the proposed operation deals with single mode of propagation rather dual modes because the individual signal from 0.55 to 1.0 V is considered here. So the LED transmits a single wavelength only from 1240 to 2250 nm. Therefore the $\eta_{\text{coup,mode}}$ would be '1' for single mode propagation.

As far as partial reflection at the interface is concerned, it deals with the partial reflection occurs at the interfaces due to the differences of effective refractive indices

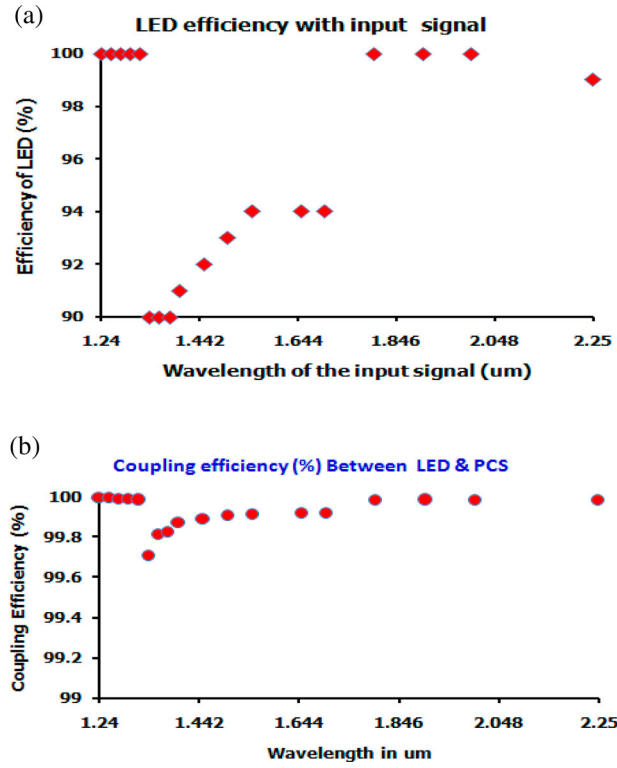


Figure 2: (a) Efficiency of LED with input signal ranges from 1.24 to 2.25 μm , (b) variation of coupling efficiency with the wavelengths

between source and destination. The expression for transmitted efficiency with respect to the same can be expressed as

$$\eta_T = \frac{2\sqrt{n_{\text{source}} \times n_{\text{structure}}}}{[n_{\text{source}} + n_{\text{structure}}]} \quad (2b)$$

Here n_{source} and $n_{\text{structure}}$ be the effective refractive index of GaAs (source) and 3D structure, respectively.

Considering the divergence of signal from source and acceptance of signal by structure, it is assumed that the size of the source is less than the photonic structure. So an entire signal generated at the source will reach at the structure. Moreover the acceptance of the signal by the structure can be expressed as

$$\eta_{\text{Acc}} = \text{Numerical Aprature of the structre} \quad (2c)$$

Here numerical aperture can be defined as the amount of the signal present in the 3D photonic structure corresponding to each signal which is generated by the LED (1240 to 2250 nm). Since the proposed 3D waveguide suffers zero loss (discussed in next section), the efficiency of acceptance is '1'. Then combining Equations 2(a)–2(c), it can be written as

$$\eta_{\text{coup}} = \eta_{\text{coup,mode}} \times \eta_T \times \eta_{\text{Acc}} \quad (2d)$$

After putting all requisite values of the information in Equation (2), the resultant coupling efficiency is computed and the same result is indicated in Figure 2(b)

Figure 2(b) represents the variation of coupling efficiency (%) between source and 3D waveguide which vary non-linear manner with respect to wavelengths ranges from 1.24 to 2.25 μm . It is observed that the minimum value of efficiency is 99.7% and maximum is 100%.

3.3 Efficiency of Photonic Structure

The efficiency of photonic structure depends on the transmitted signal of 3D photonic structure which relies on the reflection and absorption loss. The absorption loss is computed with the help of numerical treatment where reflection loss can be studied using photonic band gap analysis which is carried out plane wave expansion technique.

3.3.1 Absorption Loss

The absorption loss with respect to the silicon-based 3D photonic structure is a function of absorption coefficient of the material pertaining to the input signal and the thickness of the structure, which can be written as [12]

$$\text{Loss}_A = \left[1 - e^{-(\text{Absorption Coefficient} \times \text{thickness of structre})} \right] \quad (3a)$$

In this case absorption coefficient is due to both silicon and air material. The thickness of silicon and air

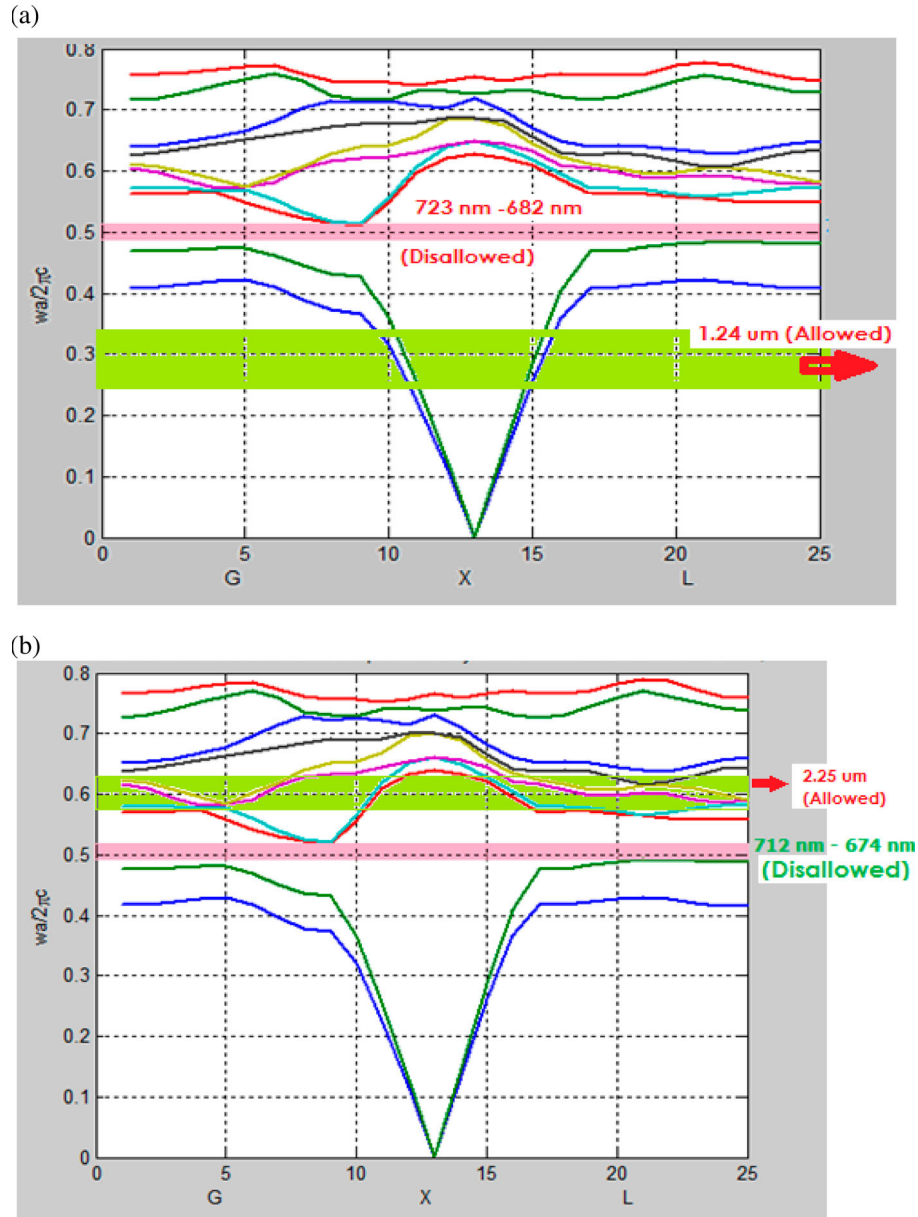


Figure 3: (a) Showing the allowance of the signal, 1.24 μm , (b) showing the allowance of the signal, 2.25 μm

material in the structure is taken of 491 nm, 909 nm, respectively. The absorption coefficient depends on the extinction coefficient of the material which relies on the imaginary part of the refractive index at the input signals. So Equation 3(a) can be modified as

$$\text{Loss}_A = \left[1 - e^{-\left(\frac{4 \times \pi \times n_{\text{imaginary}}}{\lambda} \times \text{thickness of structure} \right)} \right] \quad (3b)$$

Further putting the values of imaginary parts of refractive indices of the air and silicon materials corresponding to the input signals which range from 1240 to 2250 nm, the resultant value is found to be 'zero' at all the wavelengths. The reason for getting such 'ZERO LOSS' is that the imaginary refractive index ($n_{\text{imaginary}}$) is almost zero for the same.

3.3.2 Reflection Loss

The reflection loss of 3D photonic crystal structure depends on the photonic band gap analysis through the solution electromagnetic wave equation after solving the Maxwell's differential equation [13]. The photonic band gap of the structure is computed using plane wave expansion method. The reflected signal is a function of photonic band gap because photonic band gap corresponds to the reflection of the signal by the periodic object or structure. Even though the simulation corresponding to all input signal (1.24 μm , 1.26 μm , 1.28 μm , 1.3 μm , 1.32 μm , 1.34 μm , 1.36 μm , 1.38 μm , 1.4 μm , 1.45 μm , 1.5 μm , 1.55 μm , 1.6 μm , 1.65 μm , 1.7 μm , 1.8 μm , 1.9 μm , 2.0 μm , 2.25 μm) is done, the result for 1.24 μm and 2.25 μm is shown in Figure 3(a,b) respectively.

Figure 3 represents the photonic band gap analysis with respect to the input signals. In these figures normalised frequency and wave vector is taken along vertical and horizontal axis respectively. From Figure 3(a), it is understood that the signal of 682 nm to 713 nm is completely reflected because these band lies with the regime of complete band gap, where the green colour shows the complete allowance of 1.25 μm to 1.60 μm . It implies that allowance of the signal, 1.24 μm with respect to all directions. Similarly from Figure 3(b), it is observed that the wavelengths of 674–712 nm is getting reflected because these band lies with the regime of complete band gap, where the green colour shows the allowance of 2.15–2.40 μm . It also implies that allowance of the signal 2.25 μm . Though these two figures indicate the allowance of the signal of 1.24 and 2.25 μm only, the simulation for other wavelengths has been done. Similar type of result is also obtained for all signals. So, it is confirmed that the allowance of the signal lies with the regime of the allowed band. It indicates that such signal allowed band took place by the structure irrespective all the directions. Therefore the present structure is suitable for three ways communication because three faces of the structure will be the input end where other three faces which are just opposite faces where input signals are impinging in it.

Beside these losses (absorption and reflection), scattering loss plays a vital role in the photonic crystal structure. However the refractive index contrast of silicon-based photonic structure depends on the ratio of refractive index of background material (silicon) and column material (air). So the refractive index contrast is more than 1 for all wavelengths. It infers that the propagation is strongly guided mode and the structure is strongly guided waveguide. Further, the proposed structure is periodic, which is dictated by interference that gives existence to frequency bands where the wave propagation is allowed and disallowed band (bandgaps because no waves can propagate as a result of destructive interference). Since the structure is periodic and strongly guided waveguide, the scattering loss is feeble or null in the same.

3.4 Efficiency of Photo Diode

When the light energy arrives at the opposite faces of the structure and subsequently at the photo diode, then the light energy converts to its electronic counterpart (electrical energy). In this case we have considered p-i-n photo diode where intrinsic layer (7 μm) is large as compared to semiconductor (200 nm) bit. It is also indicated that the size of the 3D structure is less than the said p-i-n photodiode, which implies that the amount of the signal coming

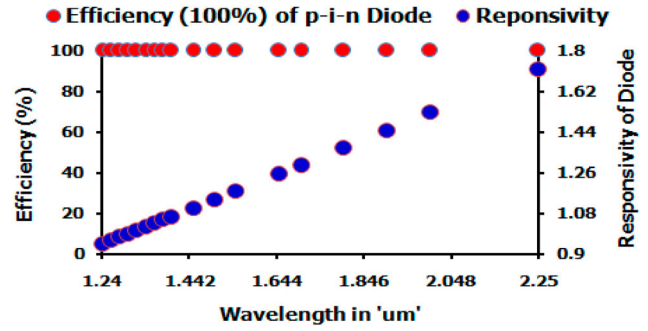


Figure 4: Variation of efficiency, responsivity with wavelength

from the structure is collected by the photo diode. Therefore no coupling loss occurs between 3D waveguide and photo detector. As far as the efficiency of the proposed diode is concerned, it is a function of absorbance of the signal in an intrinsic layer, which is expressed as [14]

$$\eta_{\text{Abs, Diode}} = e^{-[\text{absorption coefficient}_{\text{INTRINSIC}} \times \text{thickness}_{\text{INTRINSIC}}]} \quad (4a)$$

Moreover the absorption coefficient of intrinsic layer is also function of imaginary part of silicon (intrinsic) material, which is found from the literature pertaining to the input signals [15]. Moreover, it is found that the same refractive indices vary from 4.59 to 1.13 per μm . After finding the values of absorption coefficient by putting the imaginary part of the refractive indices, the absorbance of the signal by photodiode could be computed.

Apart from this, photoresponsivity of photo detector is an important parameter to realise an efficient diode. The basic formula for the same can be written as [16]

$$R = \eta_{\text{Abs, Diode}} \times \frac{\text{wavelength}}{1.24(\mu\text{m})} \quad (4b)$$

Putting the values of the input signal and efficiency of photodiode and responsivity, a graph is plotted between efficiency, responsivity and wavelengths, which is shown in Figure 4

In Figure 4, efficiency, responsivity and wavelength are taken along primary vertical, secondary vertical and primary horizontal axis, respectively. From the graph, it is found that the efficiency of the proposed p-i-n photo diode is more than 99.99%. Similarly the responsivity varies from 0.94 to 1.72 which is a significant result for any type of photo detector.

So it is realised that the proposed device is an efficient for realising the three ways chip to chip communication as the efficiency of LED is more than 90%, no coupling

loss between source and waveguide, no loss associated with the waveguide, no coupling loss between waveguide and photo diode, efficiency of photo diode is almost 100% and excellent responsivity. Finally, it can be claimed that the above said structure could be embedded with optical large scale integrated system.

4. CONCLUSION

The present article brings a proposal to realise three ways chip to chip communication using a single photonic 3D structure. The output result of LED, waveguide, photo diode is thoroughly discussed along with their coupling efficiencies. Finally it is realised that the proposed device is an efficient as the overall performance is admirable which can be introduce in an optical VLSI system.

ORCID

G. Palai  <http://orcid.org/0000-0002-9891-493X>

REFERENCES

1. J. DJoannopoulos, S. G. Johnson, J. N. Winn, and R. D. Meade. *Photonic Crystals: molding the flow of light*, University press, Princeton, Alastair D. McAulay, *Optical Computer architectures*. New York: John Wiley & Sons, 1991.
2. A. D. McAulay. *Optical Computer architectures*. New York: John Wiley & Sons, 1991.
3. G. Palai, and S. K. Tripathy, "Measurement of glycerol concentration in B-H-G solution using 3D photonic crystal structure, optik-international," *J. LightElectron Optics*, Vol. 125, no. 12, pp. 2875–2879, 2014.
4. G. Palai, and T. K. Dhir, "Theoretical model to measure the concentration of haemoglobin in human blood using 3D photonic crystal structure," *Optik. (Stuttg)*, Vol. 126, pp. 478–482, 2015.
5. K. P. Swain, and G. Palai, "Measurement of haemoglobin of human blood using 3-D photonic structure via machine learning J.K. Moharana," *Optik – International Journal for Light and Electron Optics*, Vol. 179, pp. 582–586, 2019.
6. N. D. Gupta, and V. Janyani, "Analysis of photonic crystal diffraction grating based light trapping structure for GaAs solar cell," *IETE J. Res.*, doi:10.1080/03772063.2019.1565957.
7. A. Banerjee, and B. Biswas, "Influence of time delay on pull-in behaviour of dither optical phase-lock loop," *IETE J. Res.*, Vol. 65, no. 5, pp. 679–688, 2019.
8. R. Talebzadeh, M. Soroosh, and T. Daghooghi, "A 4-channel demultiplexer based on 2D photonic crystal using line defect resonant cavity," *IETE J. Res.*, Vol. 62, no. 6, pp. 866–872, 2016.
9. I. S. Amiri, G. Palai, and J. A. Alzubi. SoumyaRanjan-Nayak; Chip to chip communication through the photonic integrated circuit: A new paradigm to optical VLSI; OptikVolume 202February 2020Article 163588.
10. G. Son, S. Han, J. Park, K. Kwon, and K. Yu, "High-efficiency broadband light coupling between optical fibers and photonic integrated circuits," *Nanophotonics.*, Vol. 7, no. 12, pp. 1845–1864, 2018.
11. E. Fred Schubert. *Light-Emitting diodes (3rd edition)*. New York: Schubert, 2018.
12. M. Vijaya, and G. Rangarajan. *Materials science*. NeDelhi: Tata McGraw-Hill Education, 2003.
13. I. A. Sukhoivanov, and I. V. Guryev. *Physics and practical modeling: photonic crystals*. Heidelberg: Springer, 2009.
14. A. K. Maini. *Lasers and optoelectronics*. Delhi: John Wiley and Sons Ltd, 2013.
15. T. Skauli, et al., "Improved dispersion relations for GaAs and applications to nonlinear optics," *J. Appl. Phys.*, Vol. 94, pp. 6447–6455, 2003.
16. S. Sharma, B. C. Bayer, V. Skakalova, G. Singh, and C. Periasam, "Structural, electrical, and UV detection properties of ZnO/Si heterojunction diodes," *IEEE Trans. Electron Devices*, Vol. 63, no. 5, pp. 1949–1956, May 2016.

AUTHORS



S. Boobalan is working as an Assistant Professor, Department of EEE, Mohamed Sathak Engineering College, Kilakarai. He has obtained his BE degree (2004) in Electronics & Communication Engineering from Madurai Kamaraj University Tamilnadu, India and ME (2010) in Power Electronics & Drives from Anna University, Tamilnadu, India. He has completed his Ph.D (2017) Degree in Electrical & Electronics Engineering from St. Peter's Institute of Higher Education and Research, Tamilnadu, India. His research areas are Nonlinear Control Systems, Internet of Things, Automation & Process Control, Soft Computing Techniques, Power Electronics, AC/DC Machine control, FACTS controllers and Power Quality Improvements. He published 34 research papers in both international and national journals as well as in conferences and also applied two Indian patents as well as guided 15 UG and 8 PG Student projects.

Email: csbhupalan@gmail.com



P. Venkatesh Kumar obtained his BE degree (2004) in Electrical and Electronics Engineering and his ME (2010) in Power Systems and PhD (2019) from Anna University, Chennai, and Tamilnadu, India. He is currently an Assistant Professor in the Department of Electrical and Electronics Engineering, Karunya University, Coimbatore, and Tamilnadu, India. He has published around 30 papers in International journals and conferences.

Email: venkat_mar@yahoo.co.in



K. Vinoth Kumar received the B.E degree in Electrical & Electronics Engineering from Anna University, India in 2006. He has completed his Master of Technology from Vellore Institute of Technology and Ph.D Degree in Electrical & Electronics Engineering from Karunya Institute of Technology and Sciences, India in 2008

and 2017 respectively. Currently, He is working as an Associate Professor in Electrical and Electronics Engineering Department at New Horizon College of Engineering, Bengaluru, India. His main research areas are intelligent control, Instrumentation, automation & process control, preventive maintenance, condition monitoring, fault analysis, Power Electronics and AC/DC Machines. He published 135 research papers in both international and national journals as well as in conferences and also published two Indian patents. He is authored the Book titled "Basic Electrical and Electronics Engineering" published by John Wiley & Sons India and Neural Networks, Soft Computing textbooks. He has delivered lectures on Energy Conservation in Industries, New techniques for Energy auditing and other related areas in various workshop and seminars as well as guided 20 UG and 16 PG Student projects and three International student projects.

Email: kvinoth_kumar84@yahoo.in



G. Palai is working as professor and head in the department of Electronics & communication Engineering in GITA, Bhubaneswar, India. He has more than 21 years of experience in teaching and research. He has published more than 150 number of research article only aside conferences, books and book chapters. His research area includes nanophotonics, photonics on machine learning and optoelectronic devices for sensing and communication application.

Corresponding author. Email: gpalai28@gmail.com

Automatic Uninterrupt Power Control System for Remotely Operated Communication System

P. Sujidha, T. Shanmuga Priya, P.Radha, A.Ush and M.Sarojini Devi

Department of Electrical and Electronics Engineering
Mohamed Sathak Engineering College, Ramanathapuram, TamilNadu, India

Abstract: Most of the Mobile base stations operate on EB power and Diesel generator based backup power. During the EB mains failure the generator is switched on manually. Once the power is restored the DG is switched off manually. This manual operation demands human presence all through the day. The proposed work involves complete automation and remote supervision for remotely operated communication stations. The purpose of the emergency diesel system is to provide reserve power, as it is essential that electricity is always available to the maintained system. In case of a black out or a power failure in the main power supply, the diesel generators can be quickly turned on to keep the necessary devices available. This work aims at identifying the best power source to be fed for the communication infra-structure, if the mains are available; this system chooses the best phase to supply the load. This is achieved by sensing the mains voltage in three phases. The phase with nearly 230v supply is chosen as best phase. If anyone phase is not available the control switches to next healthy phase. If mains fail, the system automatically switches to battery based backup power supply. When the storage battery drains a diesel generator is automatically started to provide the backup power supply. The system again checks another battery that runs the pony motor that starts the DG. If the battery has enough voltage, the DG is switched ON. The DG once switched on the system verifies whether the voltage is developed. Once the voltage is developed the system connects the load to the DG output. VI This system involve multiple PT'S for identifying the best phase and other sensors like fuel level, lubricant oil indicators, temperature sensors and battery status monitors. This system manages a constant voltage power supply from multiple power sources.

Keywords: GSM.UPS.

I. INTRODUCTION

Due to the broader applications of nonlinear loads, the degree of waveform distortion and other transients found in a power system has become increasingly serious. In order to maintain a certain high level of electric power quality, uninterruptible power supply (UPS) has emerged as a potential alternative, which was also widely applied at the customer side in order to mitigate the unexpected disturbances over the last few decades. Principally, the UPS employs the static power converter as well as batteries to supply the critical load. Its circuit structure can be categorized into three types that include off-line, on-line, and line-interactive ones. For the off-line UPS, when the utility source encounters any event that leads to the interruption of power supply, the off-line UPS circuit would supply the power to the load through the inverter, yet the load needs to shoulder the power interruption blame for about 4– 12ms. As for the on-line UPS, because of its voltage-stabilizing function, the power quality of the connected loads would be better assured. However, the resultant large heat losses through the double ac/dc operation may degrade the energy conversion efficiency. Different from the aforementioned structure, the line interactive UPS employs one inverter (dc/ac power converter) to operate in parallel with the utility grid, by which the battery charge and discharge can be both served for, hence, facilitating the mode change within a shorter time in case of power outage, while the operational losses can be controlled in a significant manner. The design of line-interactive UPS has put power quality improvement into consideration. When the mains voltage is normal, UPS serves as a shunt active power filter to curb the harmonics



Nermin
PRINCIPAL
MOHAMED SATHAK ENGINEERING COLLEGE
KILAKARAI 623 806

and compensate the power factor of loads. 2 Once encountering the loss of mains power, the line-interactive UPS will be immediately switched off-grid in order to work as an emergent power source, ensuring that the stored dc energy is converted to ac power while maintaining a reliable power to loads in spite of any loss of utility. Several technical difficulties were reported in the circuit design process. This may be attributed to the fact that the harmonic compensation as well as load voltage control are both imperative in the line-interactive UPS; therefore, the control circuit often becomes complex. Besides, the design performance is often affected because of the mode-switching transients.

II. PROPOSED TOPOLOGY

When AC is applied to the primary winding of the power transformer it can either be stepped down or up depending on the value of DC needed. In our circuit the transformer of 230v/15v is used to perform the step down operation where a 230V AC appears as 15V AC across the secondary winding. In the power supply unit, rectification is normally achieved using a solid-state diode. Diode has the property that will let the electron flow easily in one direction at proper biasing condition. As AC is applied to the diode, electrons only flow when the anode and cathode is negative. Reversing the polarity of voltage will not permit electron flow. A commonly used circuit for supplying large amounts of DC power is the bridge rectifier. A bridge rectifier of four diodes (4*IN4007) is used to achieve full wave rectification. Two diodes will conduct during the negative cycle and the other two will conduct during the positive half cycle. The DC voltage appearing across the output terminals of the bridge rectifier will be somewhat less than 90% of the applied RMS value. Filter circuits, which usually capacitor is acting as a surge arrester always follow the rectifier unit. This capacitor is also called as a decoupling capacitor or a bypassing capacitor, is used not only to 'short' the ripple with frequency of 120Hz to ground but also to leave the frequency of the DC to appear at the output. The voltage regulators play an important role in any power supply unit. The primary purpose of a regulator is to aid the rectifier and filter circuit in providing a constant DC voltage to the device. Power supplies without regulators have an inherent problem of changing DC voltage values due to variations in the load or due to fluctuations in the AC liner voltage. With a regulator connected to the DC output, the voltage can be maintained within a close tolerant region of the desired output. The regulators IC7812 and 7805 are used to provide the +12v and +5v to the circuit. 69 PIC16F877A is a 40 Pin DIP pack IC with 33 I/O pins. Out of which 9 pins can be used either as Digital I/O pins or Analog Input pins. The micro controller is having 5 ports Port A, Port B, Port C, Port D and Port E. Here Port A consists of 6Pins and can be used as Analog Pins and Digital Pins, in the same way Port E consists of 3Pins all of them can either be used as Analog Pins or Digital Pins. The Port pins of Port D are connected to LCD pins. RD0 to RD3 pins are data pins and RD5 to RD7 pins are control pins. The Pins 13 and 14 are connected to Oscillators. This Oscillator provides required clock reference for the PIC microcontroller. Either Pins 11 and 12 or 31 and 32 can be used as power supply pins. The 5v supply is given to the 11 th and 32 pin and GND is connected to the 12 th and 31 th pin of microcontroller. Pins 25 and 26 of Port C are used for serial Port communications; these pins are interfaced with MAX232 for PC based communications. Pins 39 and 40 are used for In-Circuit Debugger Operations, with which the hex code is downloaded to the Chip. Pin 33 is used as external Interrupt Pin. Pin 1 is used as Reset Pin. This Pin is connected to Vcc through a resistor. The LCD we have used in this project is HD1234. This is an alphanumeric type of LCD with 16 pins. Of which Pins 7 to 14 are used as data pins, 11 to 14 pins are connected to port D of PIC16F877A microcontroller. There are 3 control pins RS (Pin-4), RW (Pin-5) and EN (Pin-6). The RS pin is connected to the 20 th Pin of micro controller. The RW pin is usually grounded. The RW is connected to 21 th Pin. The EN pin is connected 19 th pin. The LCD has two Rows and 16 Columns. The LCD is powered up with 5V supply connected to Pins 1(GND) and 2(Vcc). The Pin 3 is connected to Vcc through a Potentiometer.

The potentiometer is used to adjust the contrast level. Here in our project we use the PIC controller in 4-bit mode. Here only 4 data pins are connected and are used as Data Port. 70 The relays are connected to microcontroller through ULN2003 relay driver IC. The ULN2003 has 16 pins. The 9 th pin of ULN2003 is Vcc and 8 th pin of the ULN2003 is GND. The 12V supply is given to the 9 th pin of the ULN2003. The ULN2003 has 7 input pins (1-7) and 7 output pins (10-16). The ULN consists of Darlington arrays. The 1 st pin of ULN2003 is connected to the 40 th pin of the

PIC16F877A microcontroller. The 16 th pin of the ULN2003 is connected to the relay, which drives the relay. A temperature sensor LM35 is interfaced to the ADC port of PIC16F877A microcontroller. The output voltage from the LM35 is linearly proportional to the measuring temperature.

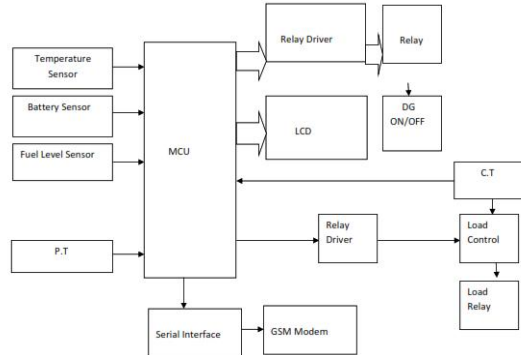


Figure 1: Block diagram of uninterrupt power control system for remotely operated communication system

The internal ADC converts the output voltages from the LM35 into digital signals, which correspond to the measured temperature. The Three pins are VCC, Output and Ground. The output voltage of the LM35 increases by 10 mV per 1° rise in temperature. This LM35 can measure temperature ranging from -55°C to 150°C. The 5V supply is given to the 1 st pin and GND is given to the 3 rd pin of LM35. The 2 nd pin (output) of LM35 is connected to the 2 nd pin of PIC16F877A microcontroller. The level sensor and battery sensor are connected to the 3 and 4 th Pin of the PIC16F877A microcontroller.

III. EXPERIMENT AND RESULT

An effective approach for the control circuit design of the line interactive UPS becomes crucial for both utility engineers and industry manufacturers. In this work, based on the paradigm of the inverter operation, a new design approach for a line-interactive UPS is proposed.

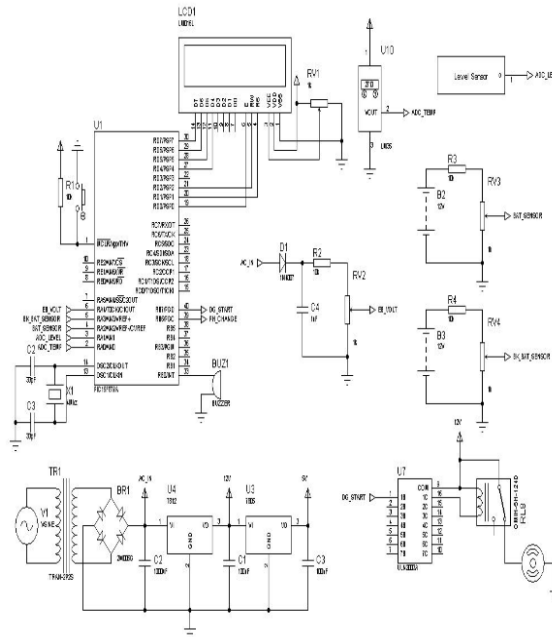


Figure 2: Main Circuit for remotely operated communication system

In the method, a unified control system associated with the special connection scheme in the inverter is developed for simplifying the system structure, where each phase only requires one current transformer (C.T.) to serve the controller for both operating schemes. In this way, the overall circuit design becomes easier to accomplish and the implementation cost can be also reduced. Besides, as this approach was aimed to minimize the mode-switching transients, the transfer time spent for the switch made between the parallel operation and the off-grid operation can thus be shortened. In this work “LCD, Microcontroller, temperature sensor, level sensor, battery sensor and relay” are chosen are proved to be more appropriate for the intended application. The project is having enough avenues for future enhancement. The project is a prototype model that fulfills all the logical requirements.

IV. CONCLUSION

The project with minimal improvements can be directly applicable for real time applications. Thus the project contributes a significant step forward in the field of “Intelligent Automation”, and further paves a road path towards faster developments in the same field. The project is further adaptive towards continuous performance and peripheral up gradations. This work can be applied to variety of industrial and commercial applications.

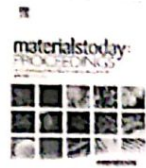
REFERENCES

- [1] Valerie A. Price, "UPS systems: Powering Up Process Performance," Intech, July 2018, pp. 38-41.
- [2] VladiBasch, "Fallacies and Facts of UPS Systems," Plant Engineering, June 3, 2018, pp. 72-74.
- [3] SAA09UP05-001, “System Assurance Analysis of the Uninterruptable Power Supply System at the Orbiter Processing Facility High Bay-3”
- [4] SAA09UP01-001, “System Assurance Analysis of the Uninterruptable Power System (Exide) UPS 2, 2A, 3, 3A at the Launch Control Center”
- [5] D.G. Hart, B. Ackerman, R. Wright, and Brian Johnson, "DA: integrated substation and feeder automation,"DistribuTech Conference Proceedings, February 2018.
- [6] D.G. Hart, W. Peterson, D. Uy, J. Schneider, D. Novosel, R.Wright, “Tapping protective relays for power quality information,”IEEE Computer Applications in Power, vol. 13, no. 1, January 2000.Modicon Modbus Protocol Reference Guide, PI-MBUS-300, Modicon, Inc., 2017



Contents lists available at ScienceDirect

Materials Today: Proceedings

journal homepage: www.elsevier.com/locate/matpr

Optimized FOPID controller for power quality enhancement between feeders using interline dynamic voltage restorer

M. Sarojini Devi^{a*}, V. Suresh Kumar^b

^a Department of EEE, Mohamed Sathak Engineering College, Kilakarai 623806, India

^b Department of EEE, Thiagarajar College of Engineering, Madurai, India

ARTICLE INFO

Article history:

Received 1 October 2020

Received in revised form 3 November 2020

Accepted 6 November 2020

Available online xxxxx

Keywords:

Power quality

Interline dynamic voltage restorer

Fractional order PID (FOPID) controller

Gravitational search algorithm (GSA)

Power quality enhancement

ABSTRACT

This paper proposes a novel control scheme for Interline dynamic voltage restorer (IDVR). The optimized fractional order PID (FOPID) controller is used in this work for power quality enhancement such as voltage regulation, harmonics distortion reduction, voltage sag and swells compensation, fault compensation etc. The gain parameters of FOPID controller are tuned by gravitational search algorithm (GSA). The performance of the suggested controller is evaluated by contrasting it with other optimization technique such as particle swarm optimization and cuckoo-search optimization algorithm. These simulation results represents that FOPID with GSA works better than the other techniques in terms of power quality enhancement.

© 2020 Elsevier Ltd. All rights reserved.

Selection and peer-review under responsibility of the scientific committee of the Emerging Trends in Materials Science, Technology and Engineering.

1. Introduction

Nowadays PQ problems are raised due to the increase in non-linear loads such as induction motor, inverter etc. In order to maintain the supply of quality power, a balanced sinusoidal voltage is needed [1]. This is achieved by compensators. Conventionally, the compensation is carried out by using bulk capacitors. But the design of capacitor values required for compensation is a critical issue when using bulk capacitor. Hence power conditioners such as STATCOM, DVR, UPFC, UPQC etc., are used [2]. A DVR compensate voltage distortion in feeder by injecting series with the voltage feeded. This is series compensation. DVR may be placed in adjacent feeders with common DC bus [3]. This is called as Interline Dynamic voltage restorer (IDVR). It controls the power flow for the entire line. IDVR comprises of two DVRs. Each DVR is connected to the separate power line through common DC link. The main objective of IDVR is reactive and real power compensation thereby mitigates voltage sag [4]. The DVR may be a current source converter (CSI) or voltage source converter (VSI). The VSI or CSI is controlled by controllers. Many literatures reports proportional integral (PI) controller as the control system for compensating

voltage [5–7]. The PI controller compares the actual load voltage with the reference voltage. The PI controller generates the required modulation index (MI) depends on error between actual and desired load voltage. This MI is then compared with PWM generation. The PWM generator produces the gate pulses as required by VSI or CSI. The inverter injects the compensation voltage from the transformer and filter. The filter is to mitigate the harmonics. The main limitations of PI controller are the tuning of gain values and design. The standard PID controller is improved to a form based on fractional order calculus called FOPID controller [8]. The FOPID controller outperforms conventional PID controller in terms of control performance. This improvement in performance is due to the introduction of fractional order term λ and μ [9]. Eventhough the FOPID controller has many advantages over conventional PID controller, the extra terms in FOPID controller makes the tuning process more difficult. The tuning of FOPID parameters is very important since it decides the steady state and transient performance, stability and robustness. To alleviate the issue of tuning FOPID controller, many researchers proposed analytical methods and optimization methods [10]. In conventional analytical methods, the process of tuning is complex for large system. Hence evolutionary based optimization algorithms like Genetic algorithm (GA), Differential Evolution (DE), Particle Swarm Optimization (PSO) algorithm, Ant colony optimization algorithm (ACO) etc. are used [11–13] Fig. 1

* Corresponding author.

E-mail addresses: devi.saro08@gmail.com (M. Sarojini Devi), vskeee@tce.edu (V. Suresh Kumar).

<https://doi.org/10.1016/j.matpr.2020.11.137>

2214-7853/© 2020 Elsevier Ltd. All rights reserved.

Selection and peer-review under responsibility of the scientific committee of the Emerging Trends in Materials Science, Technology and Engineering.

resmi
PRINCIPAL
MOHAMED SATHAK ENGINEERING COLLEGE
KILAKARAI 623 806

Please cite this article as: M. Sarojini Devi and V. Suresh Kumar, Optimized FOPID controller for power quality enhancement between feeders using interline dynamic voltage restorer, Materials Today: Proceedings, <https://doi.org/10.1016/j.matpr.2020.11.137>



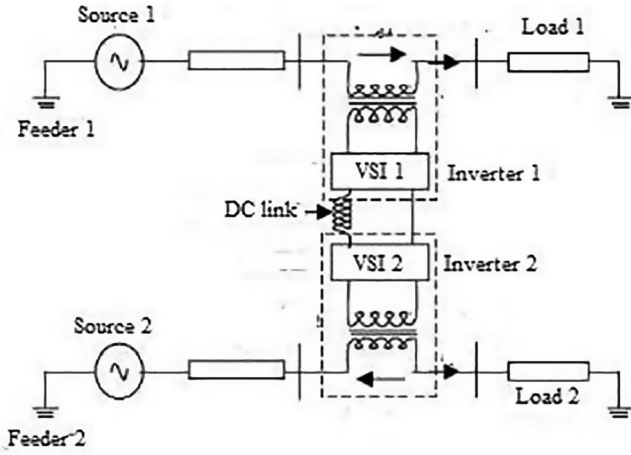


Fig. 1. Schematic diagram.

In this work, the FOPID controller is used for real and reactive power compensation using IDVR. The gravitational search algorithm is used as an optimization algorithm for tuning the FOPID controller.

2. Methodology

2.1. Idvr

IDVR is connected in series with the lines. It comprises of two DVRs connected through common DC link voltage. The voltage sag is mitigated in distribution line by real and reactive power compensation. Of two DVR, one DVR mitigates the voltage sag in the line from the DC link voltage, while other DVR stock up the consumed energy through second distribution line. Hence voltage sags of high value also able to compensate by IDVR. The schema of IDVR is shown in Figure. These IDVR consists of two DVRs that are connected to two feeders of different rating. Of the two DVR, one DVR responsible for mitigating voltage sag and the other DVR compensates the DC link voltage reduced due to real power compensation taking for mitigating voltage sag. Voltage sag is more prominent in transmission system than in the distribution system. In this proposed work, it is believed that the feeder 1 have more impact of voltage sag than feeder 2. Hence DVR1 operates for voltage sag compensation and DVR2 compensates for real power compensation.

2.2. FOPID controller

Fractional order controllers are working based on the fractional calculus. The Conventional PID controller based on fraction calculus is called FOPID controller. The integral and derivatives in PID controller may be any real number in fractional calculus. The FOPID controller is designated as $PI^\lambda D^\mu$. The function is defined as,

$$u(t) = K_p e(t) + K_i \left(\frac{de(t)}{dt} \right)^\lambda + K_d \left(\frac{de(t)}{dt} \right)^\mu \quad (1)$$

In FOPID controller, there is five degree of freedom i.e five parameters such as $(K_p, K_i, K_d, \lambda, \mu)$ needs to be designed in order to obtain reliable controller function. In those parameters, λ and μ is not an integer. Hence proper selection of those parameters is critic in controller design. In this work, the FOPID controller parameters are optimized by using GSA.

2.3. Gravitational search algorithm (GSA)

GSA is algorithm for meta heuristic optimization based on the Newtonian law of gravitation. The particles are the objects having different masses [14]. Each particle having different masses. The particle with heaviest mass is considered as an optimal solution. The force of attraction between particles is directly proportional to masses of the particles and inversely proportional to square of the distance between them. The parameters in this algorithm are position of the article, mass of inertia and the gravitational mass. The heaviest mass particle moves slowly than lighter one. The velocity of the particle is calculated by using inertial and gravitational mass. The velocity is updated using fitness function. The algorithm reaches an optimal solution by adjusting the gravitational and inertial mass. The heaviest mass particle which is the optimal solution attracted all other lighter particles in search space. These algorithm for the GSA algorithm is shown below:

3. Algorithm

3.1. Step 1

Initialization of particles i.e. masses

The position is randomly assigned as follows

$$X_n = x_n^1, x_n^2, \dots, x_n^d$$

where $n = 1, 2, 3, \dots, N_p$

X_n^d is the n^{th} particle position in d dimensional space

N_p is the Total number of particles

Step 2

Calculate the fitness function for all particles and also found the best and worst solution.

The function used in this work is minimization of error in FOPID controller. Therefore the fitness function is Integral square error (ISE). The fitness function is minimization function.

$$F = \int (e(t))^2 dt \quad (2)$$

F is the Fitness function ISE.

best (iter) = min(F), best F

worst (iter) = max(F), worst F

Step 3:

Calculation of gravitational constant $G(\text{iter})$

$$G(\text{iter}) = G_0 \exp\left(-\alpha \frac{\text{iter}}{\text{iter}_{\max}}\right) \quad (3)$$

where $G_0=100$ and $\alpha=20$

Step 4:

Calculation of mass of particles

$$S_i(\text{iter}) = \frac{F_i(\text{iter}) - \text{worst}(\text{iter})}{\text{best}(\text{iter}) - \text{worst}(\text{iter})} \quad (4)$$

$$\text{Mass}(\text{iter}) = \frac{S_i(\text{iter})}{\sum_{j=1}^N S_j(\text{iter})} \quad (5)$$

Step 5:

Calculate acceleration of particles based on law of gravity and Newton second law of motion

$$\text{acc}(\text{iter}) = \sum_{j \in \text{best}} \text{rand}_j G(\text{iter}) \frac{\text{Mass}_j(\text{iter})}{R_{ij}(\text{iter}) + \epsilon} (x_j - x_i) \quad (6)$$

$j=1, 2, \dots, N_p$

$$R_{ij} = \| X_i(\text{iter}), X_j(\text{iter}) \parallel$$

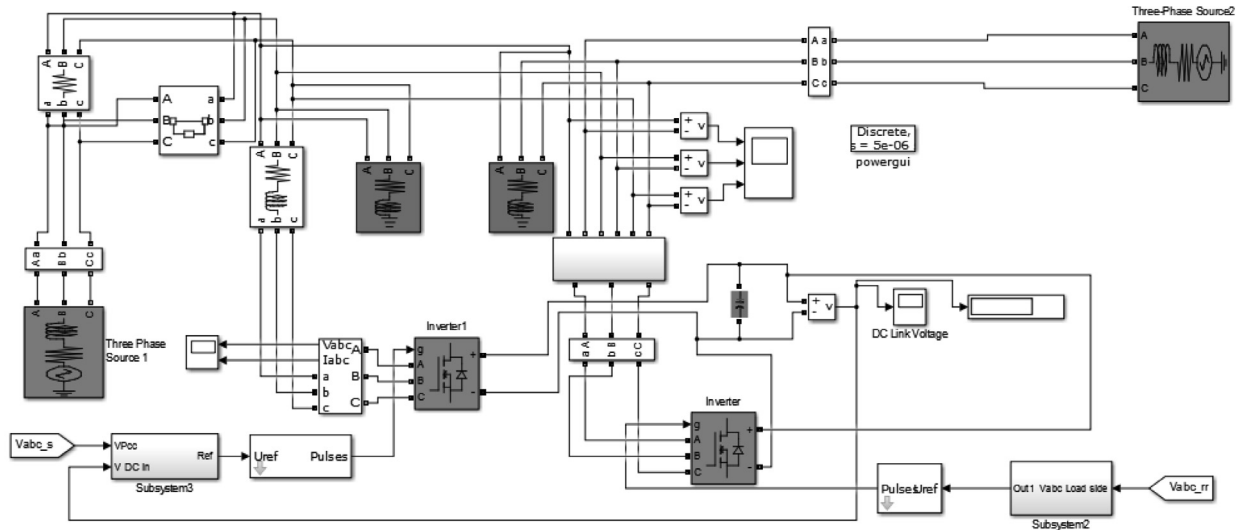


Fig. 2. Simulation diagram.

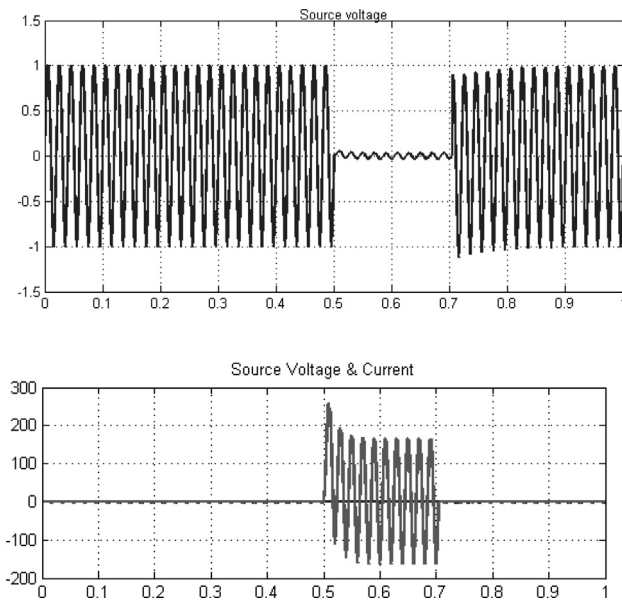


Fig. 3. Source voltage and Source current with sag.

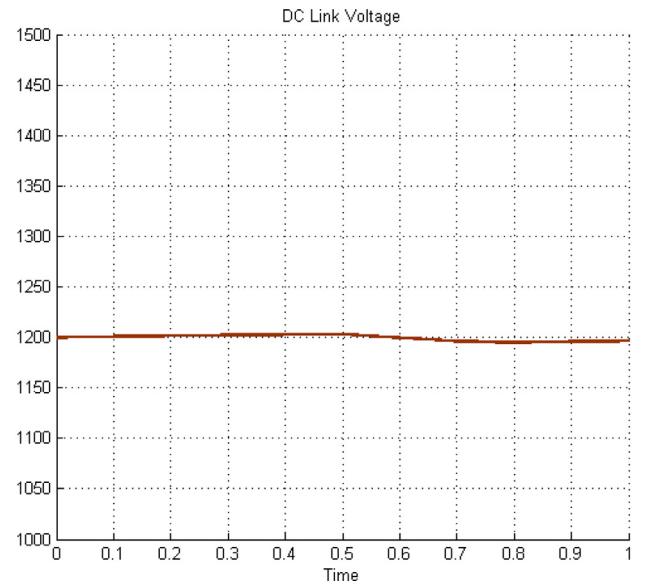


Fig. 4. DC link voltage.

where,
 acc is acceleration
 $randj$ is random variable $[0,1]$
 ϵ is the constant
 R_{ij} is the Euclidean distance
 n_{best} is the first n number of particles with best fitness
 n_{best} varies from n_0 to 1

n_0 is the initial value
 Step 6:

Table 1
 Simulation Parameters.

Parameter	Feeder 1	Feeder 2
Source Voltage	415 V	415 V
Load resistance	50 Ω	50 Ω
Load inductance	100 mH	100 mH
Filter resistance	0.5 Ω	0.5 Ω
Filter inductance	1 mH	1 mH
DC link capacitance	4700 μ F	4700 μ F
DC link voltage	1200 V	1200 V

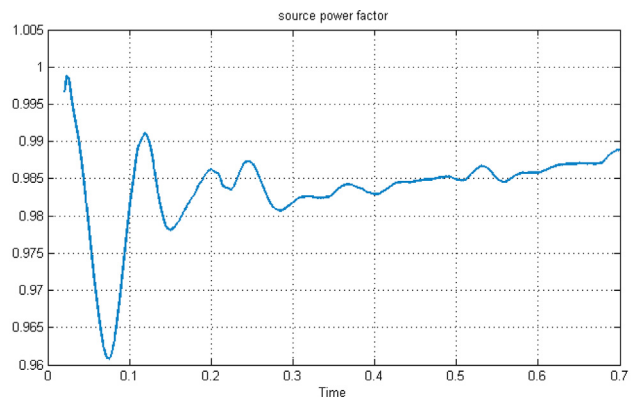


Fig. 5. Power Factor.

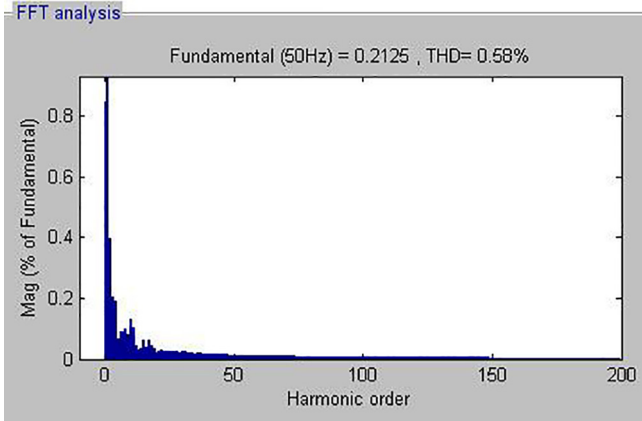


Fig. 6. THD of source current.

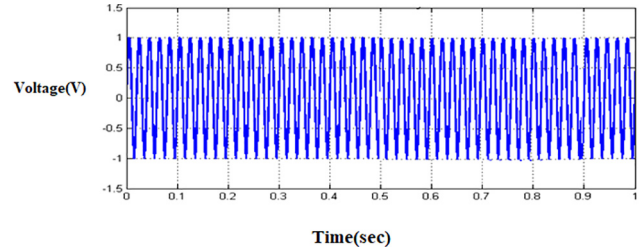


Fig. 8. Compensated load voltage.

4. Results and discussion

The two line IDVR is simulated in MATLAB/Simulink. The parameters for the simulation are shown in Table 1. The simulink diagram is shown in Fig. 2

Fig. 3 shows the source voltage and source current with 75% sag at 0.5s. The corresponding DC link compensating voltage is shown in Fig. 4. The FOPID controller compensates the load voltage at the instant voltage sag happens. The power quality is also ensured using this controller. The power factor and THD of source current is shown in Fig. 5 and Fig. 6. respectively. The power flow between the source and the load is also shown in the Fig. 7 To demonstrate the effectiveness of the proposed algorithm, a comparison is made between PSO and GSA as shown in Table 2 . From the Table 2, it clearly reveals that the GSA based FOPID controller works efficiently on the IDVR system with minimum error Fig. 8.

5. Conclusion

A novel scheme of control for Interline dynamic voltage restorer (IDVR) is proposed based on optimized FOPID controller. The IDVR is modelled using two DVR system. The FOPID controller parameters are optimized using GSA with ISE and ITSE as the performance indices. The performance of our novel controller is evaluated by comparing the performance indices based on PSO algorithm. The GSA algorithm compensates the voltage sag with power quality enhancement.

Declaration of Competing Interest

The authors declare that they have no known competing financial interests or personal relationships that could have appeared to influence the work reported in this paper.

References

- [1] Ray Arnold "Solutions to Power Quality Problems" power engineering Journal, Volume 15; Issue: 2 April 2001, pp: 65-73
- [2] A. Ghosh, G. Ledwich, Power Quality Enhancement Using Custom Power Devices, Kluwer Academic Publishers, New York, 2002.
- [3] G.J. Li, X.P. Zhang, S.S. Choi, T.T. Lie, Y.Z. Sun, Control Strategy for Dynamic Voltage Restorers to Achieve Minimum Power Injection Without Introducing Sudden Phase Shift, IEE Proceedings-Generation Transmission and Distribution 1 (5) (2007) 847–853.
- [4] D.M. Vilathgamuwa, H.M. Vijeekoon, S.S. Choi, A novel technique to compensate voltage sags in Multi-line distribution system-The interline dynamic voltage restorer, IEEE Transactions on Power Electronics 53 (5) (2006) 1603–1611.
- [5] D. Mahinda Vilathgamuwa, H.M. Wijekoon, S.S. Choi, Interline Dynamic Voltage Restorer: A Novel and Economical Approach for Multi-line Power Quality Compensation, IEEE Trans. Industry Applications, Dec. 40 (16) (2004) 1678–1685.
- [6] F.B. Ajaei, S. Afsharnia, A. Kahrobaeian, S. Farhangi, A fast and effective control scheme for the dynamic voltage restorer, IEEE Trans Power Deliv 26 (4) (2011) 2398–2406.
- [7] M. Shahabadi, H. Iman-Eini, Improving the performance of a cascaded H-bridge-based interline dynamic voltage restorer, IEEE Trans Power Deliv 31 (3) (2016) 1160–1167.

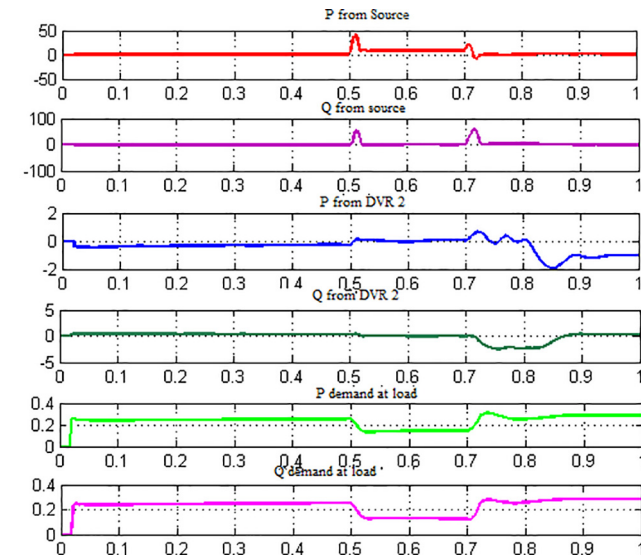


Fig. 7. Power Flow.

Table 2 Comparison between PSO and GSA.

Performance indices	PSO	GSA
$[K_p, K_i, K_d, \lambda, \mu]$	[109.7, 0.86, 1.76, 0.46, 0.97]	[101.2, 0.67, 2.32, 0.12, 0.78]
ISE	1.0868	0.7578
ITSE	2.7589	1.6289

Calculate velocity and update particles position

$$vel_{new} = rand(1) \times vel_{old} + acc(ite r) \tag{7}$$

$$x_{new} = x_{old} + vel_{new} \tag{8}$$

Repeat steps 2-6 until stopping criteria is reached

The final updated position with best fitness is the global optimal solution

The GSA and PSO both have compromise characteristics to solve the complex non linear problems. Exploitation is the major difference between PSO and GSA. PSO has exploitation based on gbest. GSA has its local exploitation capability.

- [8] M.F. Tolba, B.M. AboAlNaga, L.A. Said, A.H. Madian, A.G. Radwan, Fraction order integrator/differentiator: FPGA implementation and fopid controll application, *AUE-International Journal of Electronics and Communication* 98 (2019) 220–229.
- [9] AboBakr, L.A. Said, A.H. Madian, A.S. Elwakil, A.G. Radwan, Experimental comparison of integer/fractional-order electrical models of plant AEU-Int J Electron Commun, 80 (2017), pp. 1–9
- [10] Hybridized abc-ga optimized fractional order fuzzy pre-compensated fopid control design for 2-dof robot manipulator ,*AEU-Int J Electron Commun*, 79 (2017), pp. 219–233
- [11] O. Castillo, F. Valdez, J. Soria, L. Amador-Angulo, P. Ochoa, C. Peraza, Comparative study in fuzzy controller optimization using bee colony, differential evolution, and harmony search algorithms, *Algorithms* 12 (1) (2019) 9.
- [12] S. Singh, V.P. Singh, R.K. Dohare, S.P. Singh, S.K. Jain, Optimal PID controller design for level control of three tank system, *Int. J. Adv. Technol. Eng. Explor.* 4 (26) (2016) 1–5.
- [13] C. Singh Genetic algorithms based PID controller design *IJEDR*. 3 2015 ISSN: 2321–9939
- [14] M.B. Dowlatshahi, H. Nezamabadi-pour, Mashinchi M.A discrete gravitational search algorithm for solving combinatorial optimization problems, *Inform. Sci.* 258 (2014) 94–107.



IOT Based Home Automation Using NodeMCU and Blynk Application

P.Sujidha¹ | P.Radha² | T.Shannuga Priya³ | A.Usha² | M.Sarojini Devi¹

¹Assistant Professor, Mohamed Sathak Engineering college, kilakarai-623806, India.

²Associate Professor, Mohamed Sathak Engineering college, kilakarai-623806, India.

³Professor, Mohamed Sathak Engineering college, kilakarai-623806, India.

To Cite this Article

P.Sujidha, P.Radha, T.Shannuga Priya, A.Usha and M.Sarojini Devi, "IoT Based Home Automation Using NodeMCU and Blynk Application", *International Journal for Modern Trends in Science and Technology*, Vol. 07, Issue 03, March 2021, pp.: 151-153.

Article Info

Received on 05 February 2021, Revised on 08 March 2021, Accepted on 12 March 2021, Published on 17-March-2021.

ABSTRACT

The Internet of Things (IoT) refers to a system of interrelated, internet-connected objects that are able to collect and transfer data over a wireless network. It used to be controlled by websites and smart phone applications remotely, also, to control tools and instruments by codes and algorithms structures for artificial intelligence issues. In case we want to create advanced systems using different algorithms, Wi-Fi or Ethernet connection is connected to our tools, equipment, and devices controlling them by smart phone applications or internet websites. A smart home to operate lamps or other home-use devices, it can be used as a security system or an industrial-use system, for example, to open or close the main building gate, to operate full automatic industrial machine, or even to control internet and communication ports using IoT technology. A huge industrial facilities or governmental institutions have much of lamps. Employees sometimes forget to turn them off in the end of the day. This research suggests a solution that can save energy by letting the security to control lighting of the building with his smart home by Blynk application. The lamps can be controlled by switches distributed in the building and Blynk application at the same time with a certain electrical installation. This research presents a simple prototype of smart home, or the easy way and low cost to control loads by Wi-Fi connection generally.

KEYWORDS: Blynk, Ethernet, IOT, Wi-Fi

INTRODUCTION

Here introduce the paper, A load controlled by computer systems has many advantages compared with manual controlled loads. Nowadays there are many programs and applications help to control things better using codes or python algorithms in artificial intelligence projects. In order to save energy and make loads monitored easily, this research suggests smart home project based on IoT technology. This smart home is an Internet of Things (IoT) project that controls loads with internet connection via Wireless Fidelity WIFI

connection. A smart phone connected to internet with Blynk application as a control panel, and NodeMCU microcontroller kit in other side as a controller that receives control commands via WIFI signal. NodeMCU kit is built with ESP8266 WIFI receiver that able to process and analyze WIFI signal to input the microcontroller. The WIFI receiver and microcontroller are built in one kit to be used as IoT project. It's called NodeMCU. To connect the system to the Internet, needs a WiFi receiver. In my case I used ESP8266 that is connected as built-in in the NodeMCU board that



PRINCIPAL
MOHAMED SATHAK ENGINEERING COLLEGE
KILAKARAI 623 806

contains a firmware runs with the ESP8266. The firmware is a low-level control computer software.

II. FEATURES OF NODEMCU MODULE

NodeMCU is an open-source Lua based firmware and **development board** specially targeted for IoT based Applications. It includes firmware that runs on the ESP8266 Wi-Fi SoC from Espressif Systems, and hardware which is based on the ESP-12 module. The **NodeMCU ESP8266 development board** comes with the ESP-12E module containing ESP8266 chip having Tensilica Xtensa 32-bit LX106 RISC microprocessor. This microprocessor supports RTOS and operates at 80MHz to 160 MHz adjustable clock frequency. NodeMCU has 128 KB RAM and 4MB of Flash memory to store data and programs. Its high processing power with in-built Wi-Fi / Bluetooth and Deep Sleep Operating features make it ideal for IoT projects. NodeMCU can be powered using Micro USB jack and VIN pin (External Supply Pin). It supports UART, SPI, and I2C interface.

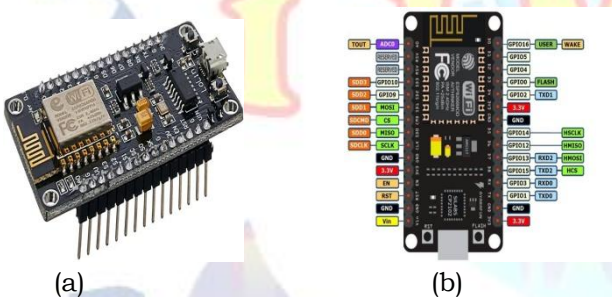


Fig. 1 - (a) NodeMCU ESP8266; (b) NodeMCU ESP8266 Pinout

III. PROPOSED METHODOLOGY

Internet of Things permits us to manage connected devices from anyplace and exchange information over the devices. The house automation system controls home appliances mechanically and once this technique is connected to the internet it becomes a locality of IoT. There is a unit of three main generations of home automation. First is, the various wireless technology with proxy servers, second is computing (AI) controlled home automation and last robots that directly communicate with humans. Our project is that the 1st generation automation. Implementing the primary generation of the house automation appliances have to connect with the web, therefore, users will manage the system from any remote place. That's why IoT has become a desire for automation.

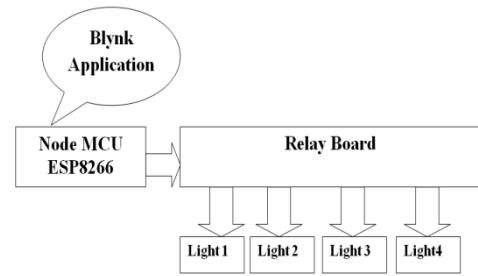


Fig. 2 - Block Diagram of Proposed Methodology

IV. IMPLEMENTATION

The home automation circuit is built around ESP8266, Blynk Android App, and a 4-channel relay board. The hardware set up should be according to the circuit diagram. AC mains appliances (Bulbs) will be connected to relays which are controlled by the ESP8266. Once Arduino IDE is installed on the computer, connect the board with the computer using the USB cable. Now open the Arduino IDE and choose the correct board by selecting Tools>Boards>NodeMCU1.0 (ESP-12E Module), and choose the correct Port by selecting Tools>Port. To get it started with the NodeMCU board and blink the built-in LED, load the example code by selecting Files>Examples>Basics>Blink. Once the example code is loaded into your IDE, click on the 'upload' button given on the top bar. Once the upload is finished, you should see the built-in LED of the board blinking. User has to install and configure the Blynk App as per the above instructions. NodeMCU to 4- Channel Relay Board Connect D0 pin of NodeMCU to D1 pin of 4- Channel Relay board, Connect D1 pin of NodeMCU to D2 pin of 4- Channel Relay board, Connect D2 pin of NodeMCU to D3 pin of 4- Channel Relay board, Connect D3 pin of NodeMCU to D4 pin of 4- Channel Relay board, Connect 3.3V of NodeMCU to Vcc pin of 4- Channel Relay board, Connect GND pin of NodeMCU to GND pin of 4- Channel Relay board. We are including ESP8266 WiFi library which provides ESP8266 specific WiFi routines and we are calling it to connect to the network. BlynkSimpleEsp8266 library establishes the communication between Blynk App and ESP8266.

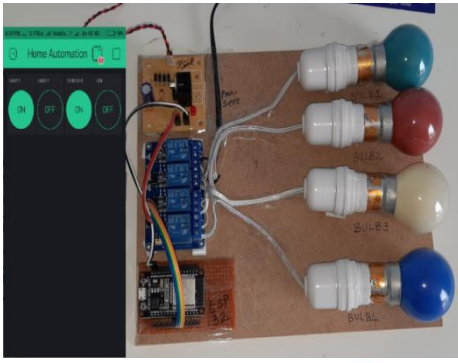


Fig. 3 Working setup of the system

V. CONCLUSION

In our planned model a high proportion of accuracy has been achieved through implementation. This method is capable of dominating the house appliances supported the user's desired mode. All the modes work with sensible accuracy that was found throughout implementation. Users solely ought to choose modes from their smartphones and our system can do the remainder of controlling the appliances. This planned project is extremely reliable. Therefore it is aforesaid that this system has higher accuracy with nice potency. This system has immense opportunities to upgrade within the future. As mentioned earlier this is often the primary generation of home automation. It might be upgraded to the second generation by storing and analyzing knowledge on the cloud servers. Then victimization machine learning algorithms, we have a tendency to even ought not to select modes from smartphones. Rather it'd be ready to switch modes with its own computer science.

REFERENCES

- [1] Vinay sagar K N and Kusuma S M, "Home automation using Internet of Things," in International Research Journal of Engineering and Technology (IRJET), Volume: 02 Issue: 03 | June-2015, e-ISSN: 2395-0056, p-ISSN: 2395-0072
- [2] Shruthi Raghavan and Girma S. Tewolde, "Cloud based low-cost home monitoring and automation system," in Proceedings of the 2015 ASEE North Central Section Conference 2015, American Society for Engineering Education
- [3] Pavithra.D and Ranjith Balakrishnan, "IoT based monitoring and control system for home automation," in Proceedings of 2015 Global Conference on Communication Technologies(GCCT 2015)
- [4] Sarthak Jain, Anant Vaibhav, and Lovely Goyal, "RaspberryPi based interactive home automation system through e-mail," in 2014 International Conference on Reliability, Optimization and Information Technology ICROIT 2014, India, Feb 6-8 2014
- [5] Mamata Khatu, Neethu Kaimal, Pratik Jadhav, and Syedali Adnan Rizvi, "Implementation of Internet of Things for

home automation," in International Journal of Emerging Engineering Research and Technology Volume 3, Issue 2, February 2015, PP 7-11 p-ISSN 2349-4395 & e-ISSN 2349-4409

- [6] Narender M and Vijayalakshmi M, "RaspberryPi based advanced scheduled home automation system through E-mail," in 2014 IEEE International Conference on Computational Intelligence and Computing Research
- [7] Pooja Patel, Mitesh Patel, Vishwa Panchal, and Vinit Nirmal, "Home automation using Internet of Things," in Imperial Journal of Interdisciplinary Research (IJIR) Vol-2, Issue-5, 2016 ISSN: 2454-1362
- [8] Dhakad Kunal, Dhake Tushar, Undegaonkar Pooja, Zope Vaibhav, and Vinay Lodha, "Smart home automation using IOT," in International Journal of Advanced Research in Computer and Communication Engineering Vol. 5, Issue 2, February 2016
- [9] Aldrich D'mello, Gaurav Deshmukh, Manali Murudkar, and Garima Tripathi, "Home automation using RaspberryPi 2," in International Journal of Current Engineering and Technology, Vol.6, No.3 (June 2016)
- [10] Silviu Folea, Daniela Bordencea, Casiana Hotea, and Honoriu Valean, "Smart home automation system using Wi-Fi low power devices,"
- [11] Rozita Teymourzadeh, Ceng, Salah Addin Ahmed, Kok Wai Chan, and Mok Vee Hoong, "Smart GSM based home automation system," in IEEE Conference on Systems, Process & Control (ICSPC 2013), 13 - 15 December 2013, Kuala Lumpur, Malaysia
- [12] Sirisilla Manohar and D. Mahesh Kumar, "E-mail interactive home automation system," in Sirisilla Manohar et al, International Journal of Computer Science and Mobile Computing, Vol.4 Issue.7, July-2015, pg. 78-87 .
- [13] Sharon Panth and Mahesh Jivani, "Home automation system (HAS) using android for mobile phone," in International Journal of Electronics and Computer Science Engineering, ISSN- 2277-1956
- [14] Renuka P. Dhage and S.P.Kharde, "A Review on home automation system (HAS)," in International Journal of Advanced Research in Electrical, Electronics and Instrumentation Engineering (An ISO 3297: 2007



Studies on *Prosopis juliflora* methyl ester production and its effect on DI diesel engine

M Rajeshwaran^{a,*}, P Marimuthu^b, V Mayilvelnathan^b & R Parthasarathi^c

^aDepartment of Mechanical Engineering, Mohamed Sathak Engineering College, Ramanathapuram, Tamil Nadu – 623 806, India

^bMNSK College of Engineering, Pudukkottai, Tamil Nadu – 622 305, India

^cDepartment of Mechanical Engineering, VSB Engineering College, Karur, Tamil Nadu – 639 111, India

*[E-mail: biorajesh2011@gmail.com]

Received 22 March 2019; revised 29 April 2019

Prosopis juliflora methyl ester (PJME) was produced from a non edible feedstock found in the arid and semi-arid regions all over the globe. The Biodiesel from this species was produced with respect to optimum transesterification process variables. An experimental investigation was done using the Methyl ester in a DI diesel engine to estimate the performance, combustion and emission characteristics at a brake power of 5.2 KW and an unvarying speed of 1500 rpm. Experimental studies on the methyl ester revealed that there was a decrease in the brake thermal efficiency by 8.34 % and increase in the emission of Carbon monoxide (CO), unburnt hydrocarbon (HC) and smoke by 10.7 %, 16 % and 11 %, respectively. PJME exhibited NO_x emission of 10.71 %, lower heat release rate (HRR) of 23 %, and 7 % peak pressure when compared to neat diesel under 100 % loading condition. From the successive experiments conducted with *Prosopis juliflora* methyl ester, B20 Biodiesel blend was found the best suitable blend for marine engines as the results almost matches with the neat diesel. Also, biodiesel from this non edible species proved that it was an inherent source for alternative fuel, with environmental benefits.

[Keywords: Biodiesel, Combustion, Emission, Performance, *Prosopis juliflora*]

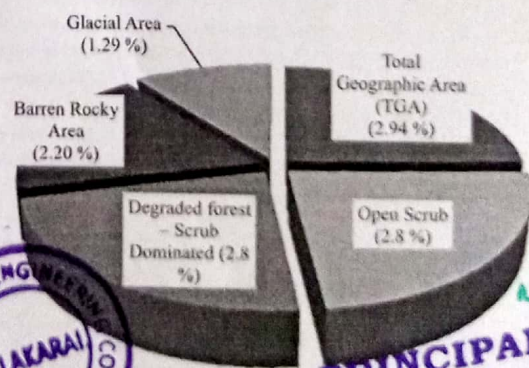
Introduction

The increase in the energy demand leads to the exhaustion of fossil fuels, price hike of oil and gas. Augmentation in environmental pollution led the researchers and scientists to propose biodiesel to be the perfect choice amongst all the available alternative fuels¹. Biodiesel can be produced from a wide variety of traditional edible and non edible oil seed crops such as ground nut, mustard, rape seed, *Jatropha*, *Pongamia*, Tobacco, Mahua, Rubber seed etc². Though there is a production of large quantity of oils, still India is not self sufficient in the production of edible oils; and the possibility of production of biodiesel from edible oil is also very less. Using non edible feedstock for Biodiesel production was found to be economical than edible feedstock and also reduces the food-fuel conflict³.

As per the Wasteland Atlas of India, 47.21 million hectare (14.92 % of total land area) are at present lying waste in India and is shown in Figure 1. The five largest wasteland are categorized as: land area with dense scrub (2.94 % of total geographic area

(TGA)), land area with open scrub (2.8 % of TGA), less utilized degraded forest – scrub dominated (2.72 % of TGA), barren rocky area (2.20 % TGA) and snow enveloped (or) glacial area (1.29 % of TGA)⁴.

As *Jatropha curcas* can grow in low rainfall areas, our Government of India has planned to plant these species in waste lands⁵. Though this species has the advantages to grow in varied climatic conditions with less water and bearing pest attack, the presence of oil



PRINCIPAL
MOHAMED SATHAK ENGINEERING COLLEGE
KILAKARAI - 623 806.



Experimental investigation on thermal behavior of graphene dispersed erythritol PCM in a shell and helical tube latent energy storage system

Mayivelnathan V.^a, Valan Arasu A.^{b,*}

^a Department of Mechanical Engineering, Mohamed Sathak Engineering College, Kilakarai, 623 806, Tamil Nadu, India
^b Department of Mechanical Engineering, Thiagarajar College of Engineering, Madurai, 623015, Tamil Nadu, India

ARTICLE INFO

Keywords:

Latent heat energy storage
 Helical coil
 Nanoparticle dispersed phase change material
 Erythritol
 Graphene nanoparticles

ABSTRACT

Thermal conductivity of the Phase Change Materials (PCMs) of latent heat storage systems is enhanced by dispersing nanoparticles in base PCM for increased heat transfer rate. Heat transfer characteristics of the newly developed erythritol PCM dispersed with 1 wt% graphene nanoparticles in a newly designed shell and helical tube storage tank during charging and discharging processes was investigated. Both melting and solidification fronts progressed from the outer wall of the shell towards the axis on either side of the shell due to the helical tube arrangement. At the middle and near the axis of the storage tank, NDPCM melting time was decreased by 21% when inlet temperature of the hot therminol oil was increased from 160 °C to 180 °C and by about 30% when the oil flow rate was increased from 0.5 kg/min to 2 kg/min. Further, NDPCM solidification time was reduced by 11% when the cold therminol oil inlet temperature was decreased from 45 °C to 30 °C and by 20% when the oil flow rate was increased from 0.5 kg/min to 2 kg/min. Complete charging and discharging periods of NDPCM was reduced respectively by 20% at an inlet temperature of 180 °C and by 6% at an inlet temperature 30 °C for 1 kg/min flow rate of therminol oil compared with pure erythritol. This research study confirmed that the helical tube flow of heat transfer oil facilitated more uniform and quicker phase transition of PCM and graphene nanoparticles dispersed erythritol (NDPCM) had superior heat transfer behavior as compared to base erythritol and it can be utilized as a potential PCM for medium temperature thermal energy storage applications.

1. Introduction

The increasing energy demand and decreasing conventional energy sources push the world to exploit new and renewable energy sources, and to conserve or store energy in every possible means; it amounts to saving equivalent amount of energy from any energy sources. Latent heat storage is one of the thermal energy storage methods which uses phase change materials (PCM) that can store/release a high amount of latent heat during the charging/discharging process [1]. The use of a latent heat storage system is an effective way for storing thermal energy and has the advantages of high-energy storage capacity with less volume and constant temperature heat storage process compared to sensible heat storage systems [2]. Solid-liquid PCMs had been widely applied in LHTES systems to store waste heat and adjust environmental temperatures. The use of solid-liquid PCMs in LHTES systems is regarded as an effective way to contribute energy efficiency solutions to solve the energy crisis [3]. Heat transfer rate is an important factor to determine the

efficiency of LHTES applications like solar energy system, buildings, cooling system, textiles and heat recovery system. The enhancement of thermal conductivity is an effective way to improve the overall performance of LHTES [4]. Studies of medium temperature latent heat thermal energy systems to be applied for hot-side thermal energy storage systems are few [5]. Though PCMs offer high energy density, they suffer from slower rates of melting and solidification due to low thermal conductivity [6]. The various techniques used to enhance the thermal performance of the LHTES system are [7] a) using extended surfaces, b) employing multiple PCM methods, c) thermal conductivity enhancement by high conductivity materials, d) micro-encapsulation of PCM. In order to design and develop energy-efficient LHTES, the nanoparticles are used to increase the thermal conductivity and heat transfer rate [8]. The temperature response in paraffin PCM with open-cell metal foam was much higher and temperature distribution was more uniform compared to pure paraffin and it also can dramatically enhance the efficiency of latent heat thermal energy storage system [9]. Embedding metal foam into phase change materials can improve the temperature

* Corresponding author.

E-mail addresses: jayaviveka@gmail.com (V. Mayivelnathan), avamech@tjce.edu.in (A. Valan Arasu).

<https://doi.org/10.1016/j.ijthermalsci.2020.106446>

Received 2 July 2019; Received in revised form 22 April 2020; Accepted 22 April 2020

Available online 29 April 2020

1290-0729/© 2020 Published by Elsevier Masson SAS.



Mohamed Sathak
 PRINCIPAL
 MOHAMED SATHAK ENGINEERING COLLEGE
 KILAKARAI - 623 806

Performance investigation of shell and helical tube heat energy storage system with graphene dispersed erythritol PCM



Running Title: Performance investigation of LHTES with graphene

V. MAYILVELNATHAN¹, A. VALAN ARASU^{2*}

¹Associate Professor, Department of Mechanical Engineering, **Mohamed Sathak**

Engineering College, Kilakarai – 623 806, Tamil Nadu, India.

^{2*}Professor, Department of Mechanical Engineering, Thiagarajar College of Engineering,
Madurai-623015, Tamil Nadu, India.

¹email: jayaviveka@gmail.com, ²email: avamech@tce.edu, contact: +919865316125

Abstract:

Experimental investigation on thermal performance of shell and helical tube latent heat thermal energy storage system for medium temperature applications is reported in the article. Commercial grade erythritol having melting temperature of 120 °C was employed as the Phase Change Material (PCM). The thermal conductivity of the erythritol had been usually very low (0.73 W/mK) and it results in low heat transfer rates during both charging and discharging processes. In the study an attempt was made this inherent limitation of erythritol, high thermal conductive graphene nanoparticles which

This article has been accepted for publication and undergone full peer review but has not been through the copyediting, typesetting, pagination and proofreading process which may lead to differences between this version and the Version of Record. Please cite this article as doi: 10.1002/est2.198

This article is protected by copyright. All rights reserved.



Kerani
PRINCIPAL
MOHAMED SATHAK ENGINEERING COLLEGE
KILAKARAI - 623.806.



Effect of mechanical properties on banana macro particle reinforced epoxy composites

Chinnapalanichamy Jayaseelan^{a*}, Palani Padmanabhan^b, Ayyanar Athijayamani^c & Kalimuthu Ramanathan^d

^aDepartment of Mechanical Engineering, Mohamed Sathak Engineering College, Kilakarai 623806, Tamilnadu, India

^bDepartment of Mechanical Engineering, V.V College of Engineering, Tisaiyanvilai 627657, Tamilnadu, India

^cDepartment of Mechanical Engineering, Government College of Engineering, Bodinayakkanur 625582, Tamilnadu, India

^dDepartment of Mechanical Engineering, A.C. College of Engineering and Technology, Karaikudi 630003, Tamilnadu, India

Received: 21 February 2017 ; Accepted: 16 January 2019

Mechanical properties of banana macro particles reinforced epoxy composites have been evaluated in this study. Composites have been prepared with 25, 30, and 35 wt % of banana macro particles using compression moulding machine. Mechanical properties (tensile, flexural, and impact) of banana macro particles reinforced epoxy composites have been obtained as a function of content of banana macro particles. The results show that the mechanical properties are found to increase substantially with increasing banana macro particles with epoxy composite. Composite with 35 wt% have the highest mechanical properties, *i.e.*, the tensile strength of 24.36 MPa; the flexural strength of 67.16 MPa; the impact strength of 0.32 J. Scanning electron microscope analysis has shown the failure mechanism and the damaged behaviors occurred in the composites after tests.

Keywords: Banana macro particles, Epoxy resin, Mechanical properties, Scanning electron microscope

1 Introduction

The increasing demand in environmental protection has confined the use of natural resources or products in the field of composite. The natural plant fibers can be a suitable replacement to synthetic fibers such as glass, carbon, and aramid¹⁻³. Nowadays, the most commonly used natural fibers as reinforcing agents in polymer composites are sisal, kenaf, hemp, roselle, flax, cotton, pineapple leaf fiber, jute, coir, flax and banana fibers. The main concept of reinforcing the polymer with natural fibers is to enhance the properties of the polymers^{4,5}. The mechanical properties of natural fiber reinforced composites, highly depend on the interface adhesion property between the fibers and the polymer matrix⁶⁻⁹. One or more discontinuous phase is embedded in a continuous phase to form a composite. The discontinuous phase is usually harder and stronger than the continuous phase and is called the reinforcement, whereas, the continuous phase is termed as matrix¹⁰⁻¹².

The matrix materials used in the preparation of composites are classified as metallic, ceramic and polymer. Among these, the polymer matrix composite is a composite material which contains polymer

resin matrix and reinforcing agents (fibers or particles). The reinforcing agents may be synthetic or bio natural materials. These composites can be prepared by a simple manufacturing methods with low cost. Fiber reinforced polymer composites consist of fibers of high strength and modulus embedded in or bonded to a matrix with a distinct interface between them. In this form, both fibers and matrix retain their physical and chemical properties. Normally, the fibers are the principal load carrying members, while the matrix keeps them at the desired location and orientation. The matrix also acts as a load transfer medium between them and protects the fiber from the environmental damage¹³⁻¹⁶.

The main parameters, which affect the physical and mechanical properties of the natural fiber-reinforced polymer composites, are fiber length, weight ratio, fiber orientation and interfacial adhesion between the fiber and the matrix¹⁷. The mechanical properties of the polymer such as impact, tensile, flexural and impact properties are enhanced by reinforcing the polymers with the fiber¹⁸. Mechanical properties of natural fiber reinforced composites are mostly based on the adhesion between the fibers and the polymer matrix^{19,20}. The mechanical properties of Agave fiber-reinforced polystyrene matrix composites have been studied based on the fiber dimensions (particle, short

* Corresponding author (E- mail: cj_seelan@y





Experimental Investigations on Microstructure, Properties and Workability Behavior of Zinc Oxide Reinforced Al–Si–Mg Matrix Composites

RM. Sakthi Sadhasivam¹ · K. Ramanathan¹ · M. Ravichandran² · C. Jayaseelan³

Received: 20 November 2020 / Accepted: 9 February 2021
© Springer Nature B.V. 2021

Abstract

Al-Si based alloy matrix composites are now broadly utilized by the industrial sectors like automobile, structural, aerospace and more practical industrial applications due to its noncompetitive economy range, good mechanical properties and less density. In order to widen its applications, it is very significant to improve its mechanical and workability behavior. So, in this work, an effort has been taken to develop a ZnO microparticles (3, 4.5 & 6 %) reinforced with Al-Si-Mg (AA6061) alloy by stir casting route. Scanning electron microscopy (SEM), energy dispersive spectroscopy (EDS) and X-ray diffraction analysis (X-RD) were employed for characterization studies of the composites. Tensile and hardness of the composites are investigated, compared and analyzed its effects. Another novel finding of the work is determining the workability behavior of the prepared samples with aspect ratio of 1 by incremental compressive loading of 25 kN through cold upsetting technique. For all developed samples, true axial stress (σ_z), hoop stress (σ), hydrostatic stress (σ_m), effective stress (σ_{eff}), formability stress index (β) and stress ratio parameters [(σ_z/σ_{eff}) , (σ/σ_{eff}) , (σ_m/σ_{eff})] were determined and the results are correlated with the axial strain (ϵ_z). The results clearly infers that increasing weight contributions of ZnO particles increase the mechanical properties, all the stresses and stress ratio parameters of the composites.

Keywords Al-Si Alloy · Zinc oxide · Composite · Stir casting · Workability behavior · Microstructure

1 Introduction

Researchers progressively exploring the work in the field of metal matrix composites (MMC) than monolithic metals and alloys for the past two decades because of the enhancing demand from the industrial side of needing the materials with economical, environmentally favorable, high wear resistance properties [1, 2]. Al-Si based alloys are principally employed in aerospace applications due to its enchanting material

properties like low weight and cost, but they declined because of the lower toughness, compressive strength and wear resistance [3]. To overcome these defects, researchers found betterment in Al-Si alloy by altering their properties through reinforcing the ceramic particles to improve as Al-Si based aluminium matrix composites (AMC). Therefore, AMC's due to their prominent mechanical strength and low density they are employed in many applications [4, 5]. Over the last two decades, AMC's were manufactured by various fabrication techniques, which can be grouped into liquid and solid-state methods. The majorly used techniques are diffusion bonding and sintering in the case of solid state based process [6]. On the other hand, liquid state processing methods include stir casting [7], squeeze casting [8], compo-casting [9], liquid metal and in-situ infiltration [10]. Among the various liquid state processing techniques, the most economical and cost-effective fabrication process adopted was stir casting method [11, 12]. Therein, particulate reinforcements are added to the molten state of matrix material and conventionally stirred with suitable speed required for the application. The disadvantages of stir casting processes are porosity and slag formation due to

✉ RM. Sakthi Sadhasivam
sakthi211193@gmail.com

¹ Department of Mechanical Engineering, Alagappa Chettiar Government College of Engineering & Technology, Karaikudi, Tamil Nadu, India

² Department of Mechanical Engineering, K. Ramakrishnan College of Engineering, Tiruchirappalli, Tamil Nadu, India

³ Department of Mechanical Engineering, Mohamed Sathak Engineering College, Kilakarai, Tamil Nadu, India

Published online: 09 March 2021



Springer
PRINCIPAL
MOHAMED SATHAK ENGINEERING COLLEGE
KILAKARAI - 623-806.



A multi-variant approach to optimize process parameters for oil extraction from non edible feedstock: *Acacia nilotica*

M. Rajeshwaran^{a,*}, R. Parthasarathi^b, J. Ganeshkumar^c, A. Ponshanmugakumar^d

^a Department of Mechanical Engineering, Mohamed Sathak Engineering College, Kilakarai, Ramanathapuram 623 806, Tamil Nadu, India

^b Department of Mechanical Engineering, VSB Engineering College, Karur, Tamil Nadu, India

^c Department of Mechanical Engineering, Mohamed Sathak Polytechnic College, Kilakarai, Ramanathapuram 623 806, Tamil Nadu, India

^d Department of Mechanical Engineering, Sai Ram Institute of Technology, Chennai, Tamil Nadu, India

ARTICLE INFO

Article history:

Received 31 July 2020

Accepted 9 August 2020

Available online xxx

Keywords:

Acacia nilotica

Response surface methodology (RSM)

D-optimal design

Soxhlet extraction

Oil extraction

Polar and Non Polar solvents

Physical and Chemical properties

ABSTRACT

The present work aims to optimize the parameters that affect the oil yield using solvent extraction technique. *Acacia nilotica* (non-edible feedstock) has been suggested as the "Miracle plant" is one of the important tree species found in the arid and semi arid zones of the world. The technique employed to extract oil from *Acacia nilotica* was Soxhlet extraction. *Acacia nilotica* due to its non-edible nature, can be converted to biodiesel there by it helps in solving the debate between food and fuel. The extraction were performed using n-Hexane as the solvent at 3:1, 5:1 and 7:1 (v/w) solid to solvent ratios and at three different extraction time periods of 4, 5 and 6 (hrs). The reaction temperature ranges between 60 °C and 70 °C. The optimization was done with the help of Response surface methodology (RSM) generated from the software Design Expert version 7.1.5 using the D-optimal design. The parameters analysed are solvent to seed ratio, reaction temperature and extraction time.

© 2020 Elsevier Ltd. All rights reserved.

Selection and peer-review under responsibility of the scientific committee of the International Conference on Nanotechnology: Ideas, Innovation and Industries.

1. Introduction

In the present industrial revolution world, developing countries like India are in the need to shift to new alternatives like biofuels. As the world is facing energy crisis due to the depletion of fossil fuels, biodiesel is found to be the best alternative source. Due to the dependence of country on petroleum and diesel for the fuels, the problem on environment, economy and energy security arise. Hence the biofuels in the form of ethanol and biodiesel is found to be best alternate to conventional fuels in the current strategy [1]. Biofuels can be produced from many plants, vegetables and animal fats. In order to reduce the dependence on imported fuels, we can make use of the oils extracted from the plants that grow in waste lands. These oils can be converted into biodiesel for further usage. The GOI has also launched a national mission on "Biofuels" with the aim of achieving a target of producing enough seed material for production of biodiesel with 20% blend, by 2012 [10].

Acacia nilotica is one of the powerful species that provides fuel wood, forage and increased fertility to the arid and semi-arid zones of India. This species can grow in highly saline areas, alkaline soils and coastal areas, sand dunes of the desert in ravines of the Indian rivers and in dry and degraded grasslands. The shrubs of drought resistant *Acacia nilotica* are recognized for sand stabilizers, soil binders, living fences, charcoal, hard timber and good animal feed [4]. The genus *Acacia nilotica* is widespread and it consists of 44 species, having mostly thorny trees and shrubs. According to the Department of land resources (DOLR), GOI about 63.9 million hectare of land is lying waste in India. The current strategy is cultivation of *Jatropha*, sweet sorghum, and castor, pongamia in these waste lands. The oils obtained from these plants are non-edible oils. Though these plants grow in diverse agro-climate conditions, withstand pest attack and drought, the yield of the seed, oil content and nutrient requirements are found to be critical. This leads to the plantation of these plants in the waste lands less viable. Hence the afforestation of the waste lands can be done with *Prosopis juliflora*, *Acacia nilotica* etc. [2]. These species require only less water and is found to be more suitable for dry and arid waste lands. *Acacia nilotica* has been suggested as the "Miracle

* Corresponding author.

E-mail address: nrajeshwaran@msec.org.in (M. Rajeshwaran).

<https://doi.org/10.1016/j.matpr.2020.08.314>

2214-7853/© 2020 Elsevier Ltd. All rights reserved.

Selection and peer-review under responsibility of the International Conference on Nanotechnology: Ideas, Innovation and Industries.



PRINCIPAL

MOHAMED SATHAK ENGINEERING COLLEGE

KILAKARAI - 623 806



Contents lists available at ScienceDirect

Materials Today: Proceedings

journal homepage: www.elsevier.com/locate/matpr

A critical evaluation of oil extraction and fatty acid composition of *Prosopis Julifera*

M. Rajeshwaran^{a,*}, S. Ramasamy^b, R. Parthasarathi^c, A. Ponshanmugakumar^d

^a Department of Mechanical Engineering, Mohamed Sathak Engineering College, Kilakarai, Ramanathapuram 623 806, Tamil Nadu, India

^b Department of Mechanical Engineering, Government Polytechnic College, Melur, Madurai, Tamil Nadu, India

^c Department of Mechanical Engineering, VSB Engineering College, Karur, Tamil Nadu, India

^d Department of Mechanical Engineering, Sai Ram Institute of Technology, Chennai, Tamil Nadu, India

ARTICLE INFO

Article history:

Received 28 July 2020

Accepted 9 August 2020

Available online xxxxx

Keywords:

Prosopis Julifera

Soxhlet extraction

Gas chromatography

Polar and non polar solvents

Physical and chemical properties of oil

ABSTRACT

The aim of the present investigation is to find a better replacement to edible oils. *Prosopis Julifera* (non-edible feedstock) is one of the important tree species in the arid and semi arid zones of the world. The fruits (Pods) of *Prosopis Julifera* were cleaned, cracked and powdered before oil extraction. Extraction of oil from *Prosopis Julifera* was carried out by soxhlet apparatus using different solvents at 3:1 to 9:1 (w/v) solid to solvent ratios and the extraction time periods were 3–10 (hrs). Polar and non-polar solvents such as Petroleum Ether, n-Pentane, Ethyl acetate, Iso-propanol, Hexane, Methanol, and Ethanol were used. Using gas chromatography (GC), Fatty acid methyl esters were separated, identified and quantified. In order to analyse the qualitative nature of the oil extracted, performance of different solvents in terms of Saponification value, Acid value, Iodine value, refractive index and free fatty acids were determined by suitable tests. The test results indicate that irrespective of the solvent used, the oil yield was found to be increasing when there is the increase in the solid to solvent ratio, reaction time period and reaction temperature. However the maximum amount of oil yield 36.9% was obtained using methanol at the solid to solvent ratio of 1: 9 (w/v), the reaction temperature of 60 °C for a time period of 9 (hrs). Hence it can be concluded that the oil produced from the non edible *Prosopis Julifera* could be a best alternate in the future days to come.

© 2020 Elsevier Ltd. All rights reserved.

Selection and peer-review under responsibility of the scientific committee of the International Conference on Nanotechnology: Ideas, Innovation and Industries.

1. Introduction

The increase in the world energy demand and due to the exhaustive nature of fossil fuels, biodiesel is found to be the suitable alternate to conventional fuels. There could be the debate between the food and fuel if edible oils were used for the production of biodiesel and this problem can be solved by utilizing non-edible oils for bio-diesel production. Naiane et al. [7] investigated Several aspects related to these feedstocks have been reviewed from various recent publications. An overview of non-edible oil resources, advantages of non-edible oils, problems in extraction of non-edible oils, fatty acid composition profiles (FAC) of non-edible oils, oil extraction techniques, technologies of biodiesel production from non-edible oils, biodiesel standards

characterization, properties and characteristic of non-edible bio-diesel and engine performance and emission were analysed and reviewed in detail. According to the Department of land resources (DOLR), GOI about 63.9 million hectare of land is lying waste in India. Rajeshwaran et al. [11] evaluated these lands are unsuitable for cultivation; they are termed as "Waste lands". Waste lands are said to be characterized by sandy soils, rocky soils, saline soils etc. The current strategy is cultivation of *Jatropha*, sweet sorghum, and castor, *Pongamia* in these waste lands. The oils obtained from these plants are non-edible oils. Though these plants grow in diverse agro-climate conditions, withstand pest attack and drought, the yield of the seed, oil content and nutrient requirements are found to be critical. This leads to the plantation of these plants in the waste lands less viable.

There is no detailed literature regarding the extraction of oil from the non edible feedstock-*Prosopis Julifera* as a potential for biodiesel Production was reported so far. *Prosopis Julifera* is one

* Corresponding author.

E-mail address: biorajesh2011@gmail.com (M. Rajeshwaran).

<https://doi.org/10.1016/j.matpr.2020.08.291>

2214-7853/© 2020 Elsevier Ltd. All rights reserved.

Selection and peer-review under responsibility of the scientific committee of the International Conference on Nanotechnology: Ideas, Innovation and Industries.

PRINCIPAL
MOHAMED SATHAK ENGINEERING COLLEGE
KILAKARAI - 623 806

Please cite this article as: M. Rajeshwaran, S. Ramasamy, R. Parthasarathi et al., A critical evaluation of oil extraction and fatty acid composition of *Prosopis Julifera*, Materials Today: Proceedings, <https://doi.org/10.1016/j.matpr.2020.08.291>



ELSEVIER



Investigations of performance and emission characteristics in diesel engine fueled with Hemp oil methyl ester

N. Bhanu Teja^{a,*}, M. Mohamed Abdul Hafeez^b, G. Surendran^c, M. Rajeshwaran^d, N. Alagumurthi^e

^a Department of Mechanical Engineering, Aditya College of Engineering, Surampalem 533437, Andhra Pradesh, India

^b Department of Mechanical Engineering, V.S.B Engineering College, Karur 639111, Tamil Nadu, India

^c Department of Chemical Engineering, KPR Institute of Engineering and Technology, Coimbatore 641407, Tamil Nadu, India

^d Department of Mechanical Engineering, Mohamed Sathak Engineering College, Kilakarai, Ramanathapuram 623 806, Tamil Nadu, India

^e Department of Mechanical Engineering, Pondicherry Engineering College, Puducherry 605014, India

ARTICLE INFO

Article history:

Received 22 October 2020

Accepted 6 November 2020

Available online xxx

Keywords:

Hemp oil methyl ester

Standard diesel: Naturally aspirated load conditions

Performance and Emissions

ABSTRACT

The depleting reserves of petrol and diesel fuels has caused the international organizations and bodies to remind the need for alternate fuel substitute on automobile manufactures which made them to rely upon biodiesel as the best possible source. The current research intended to investigate the characteristics of Hemp oilmethyl ester and compared with standard diesel. Non-edible nature of the Hemp oil favored to choose as feed stock. The Acid-catalyzed transesterification process was conducted for converting Hemp oilinto methyl ester. Experimental analysis was conducted using blends such as HOME25, HOME50, HOME75, HOME100 and standard diesel under naturally aspirated load conditions. The observations concluded that Smoke opacity, HC and CO emissions recorded significant reduction by increasing the percentage contribution of HOME in the tested fuels. The BTE has registered a slight reduction by adding HOME in standard diesel with increase in consumption of fuel. NO_x and CO₂ emissions registered higher values relative to standard diesel owing to higher O₂ concentration in the methyl ester.

© 2021 Elsevier Ltd. All rights reserved.

Selection and peer-review under responsibility of the scientific committee of the Emerging Trends in Materials Science, Technology and Engineering.

1. Introduction

Having established the relevance of biodiesels, it is pertinent to enquire into the feedstocks for biodiesel production [1–3]. Biodiesel is primarily sourced from organic entities like animal fats, algae, vegetable oils, etcetera [4,5]. Edible oil, in the majority of nations, is the predominant feedstock. This does not bode well for the food security of developing nations like India which has been characterized as a “seriously hungry” nation, as per the Global Hunger Index 2019 report released by Welthungerhilfe and Concern Worldwide. Moreover, land availability and rapidly increasing population render edible oils, unattractive, for fuel generation [6–8]. It must also be noted that animal fat cannot be considered as a major source for

the biodiesel production in these countries. This is attributed to the mixed farming practices prevalent in these nations, where animals are a major source of income support and supplementary nutrition [9–12]. Ethical concerns and the economic costs associated with harvesting animal carcasses for fuel also remain strong deterrents. Therefore, non-edible sources of biodiesel production must form the focus of scholarly and academic investigations. In addition to resolving the food-fuel conflict, the employment of non-edible feedstock sources for biodiesel production is advantageous on the front of cost-effectiveness and the cultivation of a waste to wealth culture, thus promoting a circular economy [13–18]. In the current research, *Hemp* oil was chosen as a source for producing methyl ester. The HOME is a viable source as a fuel for substituting standard diesel in evaluating engine characteristics. The blends of HOME- standard diesel were prepared in different proportions (HOME25, HOME50, HOME75, HOME100 and standard diesel in C.I Engine by varying load conditions [19–23].

* Corresponding author.

E-mail address: bhanuteja28086@gmail.com (N. Bhanu Teja).

<https://doi.org/10.1016/j.matpr.2020.11.110>

2214-7853/© 2021 Elsevier Ltd. All rights reserved.

Selection and peer-review under responsibility of the scientific committee of the Emerging Trends in Materials Science, Technology and Engineering.



Principal
MOHAMED SATHAK ENGINEERING COLLEGE
KILAKARAI - 623 806

Please cite this article as: N. Bhanu Teja, M. Mohamed Abdul Hafeez, G. Surendran et al., Investigations of performance and emission characteristics in diesel engine fueled with Hemp oil methyl ester, Materials Today: Proceedings, <https://doi.org/10.1016/j.matpr.2020.11.110>



Enzymatic Production of Biodiesel from *Acacia nilotica* oil Using NaOCH_3 as a Catalyst

M. Rajeshwaran¹, J. Ganeshkumar², V. Mayilvelnathan³, K. Niraikulasekaran⁴

¹Department of Mechanical Engineering, Mohamed Sathak Engineering College, Kilakarai, Ramanathapuram – 623 806, Tamil Nadu, India

²Department of Mechanical Engineering, Mohamed Sathak Polytechnic College, Kilakarai, Ramanathapuram – 623 806, Tamil Nadu, India,

³Department of Mechanical Engineering, Mohamed Sathak Engineering College, Kilakarai, Ramanathapuram – 623 806, Tamil Nadu, India,

⁴Department of Civil Engineering, Mohamed Sathak Engineering College, Kilakarai, Ramanathapuram – 623 806, Tamil Nadu, India.

ABSTRACT

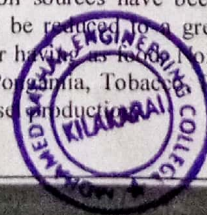
Acacia nilotica is a non edible feedstock found in the arid and semi-arid regions. Oil from *Acacia nilotica* was extracted by the method of solvent extraction. The present work mainly concentrates on the three step process of biodiesel production from *Acacia nilotica* oil. Initially the acid value of *Acacia nilotica* oil was reduced below 1% using acid catalyst 1% v/v H_2SO_4 . The second step is the esterification process of the product obtained from pretreatment using alkaline NaOCH_3 catalyst. The parameters such as methanol to *Acacia nilotica* oil molar ratio, amount of catalyst used, reaction time and reaction temperature were studied. For the efficient conversion of *Acacia nilotica* oil to methyl ester gas chromatography was used to analyse the Fatty acid methyl esters. The optimum reaction conditions of Methanol/oil molar ratio of 9:1v/v, reaction temperature of 60°C, reaction time of 2 hrs and 1% w/v of NaOCH_3 usage were determined. In the acid transesterification process, the main objective for process optimization was the reduction of acid value. The fuel properties of *Acacia nilotica* methyl ester (PJME) such as viscosity, cetane number, flash point, acid value, etc were determined. The values thus found experimentally were compared according to the ASTM standards.

Keywords: *Acacia nilotica*; Acid Esterification; Transesterification.

INTRODUCTION

As there is the increase in population, there is the rapid increase in the energy demand. The depletion of fossil fuel reserves and conventional energy sources has stimulated the interest in the alternative energy sources. While considering the environmental concerns, the alternative fuel source must be eco friendly in nature. This led the researchers to propose biodiesel to be the ideal choice among all the alternative fuels. In the recent years, world market for biodiesel has expanded rapidly. Though various research works, evaluations, tests and certifications from large number of countries, researchers have confirmed as clean alternative fuel having self combustion properties with lower carbon emission, no sulfur and no aromatics [1]. Wide ranges of traditional oil seed crops such as ground nut, mustard, rape seed, sunflower, safflower, linseed, soybean, palm etc were used for the biodiesel production. Though there is the production of large volume of oils, India is not self sufficient in producing edible oils. If the edible oils were used for biodiesel production, then there will be the world food crisis. Human rights activists and social reformers have called for a ban on the production of biodiesel from food crops for several years and hence resolved the food versus fuel conflict. Waste cooking oil, Tallow and animal fat have replaced the edible oils in the production of Biodiesel [2]. Though they can be afforded at the lowest price, the disposal of these materials constitutes a major problem.

For the production of biodiesel, non edible vegetable oil sources have become more attractive now a day. Thus the dependence of biodiesel production non edible oils can be reduced to a greater extent. Due to the presence of toxic components in the non edible oil they are not suitable for human consumption. Non edible oil can be obtained from the plants grown on unused lands. Non edible oils like Jatropha, Pongamia, Tobacco, Rubber seed, Mahua, *Camelina sativa*, Rice bran etc. are found to be the cheapest feedstock for biodiesel production.





Environmental Effect of CRDI Diesel Engine Using *Prosopis Julifera* methyl ester with Doped Nano Additives

M. Rajeshwaran¹, K. Niraikulasekaran², V. Mayilvelnathan³, J. Ganeshkumar⁴

¹Department of Mechanical Engineering, Mohamed Sathak Engineering College, Kilakarai, Ramanathapuram – 623 806, Tamil Nadu, India,

²Department of Civil Engineering, Mohamed Sathak Engineering College, Kilakarai, Ramanathapuram – 623 806, Tamil Nadu, India,

³Department of Mechanical Engineering, Mohamed Sathak Engineering College, Kilakarai, Ramanathapuram – 623 806, Tamil Nadu, India,

⁴Department of Mechanical Engineering, Mohamed Sathak Polytechnic College, Kilakarai, Ramanathapuram – 623 806, Tamil Nadu, India,

ABSTRACT

Experiments were conducted to determine engine performance, exhaust emissions and combustion characteristics of a single cylinder, common rail direct injection (CRDI) system assisted diesel engine using diesel with 25 percentage of *Prosopis Julifera* methyl ester blended fuel (PJME25). Along with this PJME25 cerium oxide nanoparticles were added as additive in mass fractions of 25 ppm (CuONP 25), 50 ppm (CuONP 50) and 75 ppm (CuONP 75) with the help of a mechanical Homogenizer and an ultrasonicator. It was observed that cerium oxide nanoparticles blended fuel exhibits a significant reduction in exhaust emissions at all operating loads. *Prosopis Julifera* methyl ester (PJME) produced under optimum transesterification process parameters was used in a DI diesel engine to evaluate the performance, combustion and emission characteristics at a brake power 5.2 kW constant speed of 3000 rpm. Results revealed that the biodiesel resulted in decreased brake thermal efficiency by 8.34% and higher Carbon monoxide (CO), unburnt hydrocarbon (HC) and smoke emission 10.7%, 16%, 11% and 15.5%. PJME exhibited lower heat release rate (HRR), oxides of nitrogen (NO_x), peak pressure. Respectively, when compared to diesel at 100% load condition.

Keywords: *Prosopis Julifera*; Biodiesel; Performance; Combustion; Emission.

INTRODUCTION

The main objective of this investigation Biodiesel derived from *Prosopis Julifera* will reduce the conflict between food and fuel as this is a non-edible feedstock. This drought resistant powerful species can be grown in the wastelands of India which will help to meet the economic needs of the poor people of our country. From the oil extracted, *Prosopis Julifera* Methyl esters were obtained. The various PJME25 cerium oxide nanoparticles were added as additive in mass fractions of 25 ppm (CuONP 25), 50 ppm (CuONP 50) and 75 ppm (CuONP 75) were tested for their performance in a common rail direct injection (CRDI) diesel engine. With the intention of improving BTE and emission characteristics of diesel engine using *Prosopis Julifera* biodiesel blend as fuel is to utilize the *Prosopis Julifera* methyl ester as an alternative fuel in a diesel engine.

The depletion of fossil fuels, price hike of oil and gas, enhancement in environmental pollution led the researchers to propose biodiesel to be the ideal choice among all the alternative fuels [1]. Wide ranges of traditional oil seed crops such as ground nut, mustard, rape seed, sunflower, safflower, linseed, soybean, palm etc were used for the biodiesel production. Though there is the production of large volume of oils, India is not self sufficient in producing edible oils and the possibility of biodiesel production from edible oil is very less. Non edible oil can be obtained from the plants grown on



Experimental analysis of solar wiper and its power estimates

A. Arjun, P. Umar Ahamed^{*}, K. Shahul Hameed, M.P.M. Mohamed Ibraheem, J. Mohammed Azharudeen, A. Muhammad Saleh

Department of Mechanical Engineering, Mohamed Sathak Engineering College, Kilakarai, Tamilnadu, India

ARTICLE INFO

Article history:

Received 26 August 2020
Received in revised form 20 September 2020
Accepted 25 September 2020
Available online xxxx

Keywords:

Solar
Wiper
Energy
Automation
Arduino microcontrol
Battery

ABSTRACT

The wipers are the most important part of the automotive components. The energy consumed for the wiper varies from vehicle operating situation and amount of energy stored in the battery. While wind rate is heavy the wiper usage is less and at the same, the rate of energy consumed during wind and rainy is more. On other hand the wind, rain water with third particle on vehicle glass is more energy required for wiper unit. In this paper, a solar panel has been designed and the wiper is modified to study the energy consumption. It has been found the movement of wiper at wind flow is control and the rate of energy consumed is reduced compared to conventional experiments.

© 2020 Elsevier Ltd. All rights reserved.

Selection and peer-review under responsibility of the scientific committee of the International Conference on Advances in Materials Research.

1. Introduction

The purpose of this project is to provide guidance for installation and operation of Solar Straight-Line Wipers which is controlled by Arduino Microcontrol system, as supplied by Solar Wiper Automatic Systems. A solar cell is an electrical device that converts the energy of light directly into electricity by the photo-voltaic effect, which is a physical and chemical phenomenon [1,2]. It is the form of photoelectric cell; define as a device whose electrical characteristics, such as current, voltage, resistance, vary when exposed to light [3]. The absorbing of light, generating either electron-hole pair or exactions. The separation of charge carriers of opposite types [4]. The wipers are mostly used to clean the glass vehicles. Mostly the wiper blades are made by rubbers, but the woolen wiper blade is made by woolen materials. It is designed for handle heat emitting glass [5]. The wipers are designed to remove the water only, but the woolen wiper is used for remove the dust which settled on the solar panel. The wiper is handled by wiper arm which is made by stainless steel [6].

Arduino is an Open Source electronic prototyping platform based on flexible easy to use hardware and software. Early micro-computers typically consisted of a half dozen (or more) circuit boards--plugged into a backplane--that implemented the central

processor unit (CPU), memory, disk controllers and serial/parallel port functions [7]. These backplane-based microcomputers were used for data acquisition, process control and R&D projects, but were generally too bulky to be used as embedded systems within devices [8].

The suspended dust in the direct optical path of incident irradiance of solar panels, and also the dust deposited on the panels, both obscure the impending solar radiation. So the panel is must cleaned every day to produce more energy per day [9–11]. The Arduino controller is control the rotation of wiper motor and water motor. By this method the solar panel can cleaned and maintained every day with minimum water and without any manual operations.

2. Design and methodology

2.1. Major mechanism used

2.1.1. Rail mounted linear slide assembly

The linear slide assembly is the linear guide motion component shown in Fig. 1, which slide on the guide pipe in forward and backward. The carriage assembly is used to handle load shifting processes. It is used to reset a device position to the beginning. Linear slide Technology handles heavy loads and excels in harsh, contaminated environments. The Plain Bearing Linear Slide Assemblies are handle a wide temperature range (-240 °C/240 °C). The Shaft

^{*} Corresponding author.

E-mail address: umarahamed@msrc.org.in (P.U. Ahamed).

<https://doi.org/10.1016/j.matpr.2020.09.589>

2214-7853/© 2020 Elsevier Ltd. All rights reserved.

Selection and peer-review under responsibility of the scientific committee of the International Conference on Advances in Materials Research.



PRINCIPAL
MOHAMED SATHAK ENGINEERING COLLEGE
KILAKARAI - 623 806



Contents lists available at ScienceDirect

Materials Today: Proceedings

journal homepage: www.elsevier.com/locate/matpr

Optimizing the process parameters for Powder metallurgy electrode in Electrical Discharge Machining

J. Mohammed Azarudeen^{a,*}, R. Kaja Bantha Navas^b, G. Vikas Reddy^b, R.S. Gowsik Saran^b, S. Prakash^b, A. Anderson^b

^a Department of Mechanical Engineering, Mohamed Sathak Engineering College, East Coast Road, Kilakarai 623 806, India

^b School of Mechanical Engineering, Sathyabama Institute of Science and Technology, Chennai 600 119, India

ARTICLE INFO

Article history:

Received 18 December 2019

Received in revised form 24 February 2020

Accepted 27 February 2020

Available online xxxxx

Keywords:

Electrical-Discharge Machining
Copper with Titanium Carbide electrode material
Copper with Tungsten Carbide electrode material
Multi response optimization
Data Envelopment Analysis based Rank Method

ABSTRACT

This paper presents a novel approach for the optimization of process parameters on new powder metallurgy electrode in Electrical Discharge Machining with multiple responses based on comparing Data Envelopment Analysis based Rank Method. These two methods have a series of steps from of proposed approach which are capable of decreasing uncertainty caused by engineering judgment in the Taguchi method. Experiments are conducted by varying the Electrical Discharge Machining parameters related to metallurgy powder proportion, current and pulse on time and optimized with the considerations of multi responses such as material removal rate (MRR) and Tool Wear Rate. Three factors and three levels were taken to conduct the experiments with the range 6–10% for proportion of powder in the combination of Copper with Titanium Carbide and Copper with Tungsten Carbide, current 3–9 A and pulse on time from 150 to 450 μ s. The two methods show a good convergence with the experimental data and the optimum process parameters combinations where maximum material removal rate (MRR) and minimum tool wear rate are obtained.

© 2020 Elsevier Ltd. All rights reserved.

Selection and Peer-review under responsibility of the scientific committee of the International Mechanical Engineering Congress 2019: Materials Science.

1. Introduction

Electrical-Discharge Machining (EDM) is widely used in tooling industry, where it is applied on materials, which are too hard to be machined with conventional techniques. In EDM, the material is removed primarily through the conversion of electrical energy into thermal energy through a series of successive sparks between the electrode and the work piece in dielectric fluid. This method is popular due to the fact that a relatively soft electrically conductive tool electrode can machine hard work piece. However, production cost increases with the complexity of the eroded cavity. And the major problem in the EDM industry is the Electrode Wear Rate. To overcome the EWR, a new electrode is developed through powder metallurgy process.

2. Literature review

Urade A.D., Deshpande V.S., (2016) carried out to improve performance measures in terms of tool wear rate by optimizing the process variables, particularly in ram electric discharge machining. Design of experimentation and ANOVA for optimization of process parameters is investigated in order to improve the responses of the machining in terms of lowering tool wear rate within work interval of semi finish machining [2]. Mathalai Sundaram et al. (2016) analysed the input parameters current and pulse on time with respect to response parameters MRR and TWR. MRR and percentage of TWR are obtained by experimental methods and by using Taguchi Techniques. In addition, the analysis of variance (ANOVA) is used to predict the significant factor affecting the responses. This research focused on fabrication of metal matrix composite (MMC) electrode by mixing copper powder Copper with Titanium Carbide and Copper with Tungsten Carbide [3]. Naveen Beri et al. (2008) attempted to correlate the usefulness of electrodes made from powder metallurgy in comparison with conventional copper electrode during electric discharge machining. Experimental

* Corresponding author.

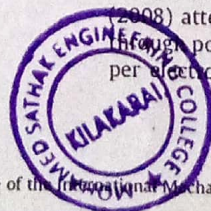
E-mail address: sumai244@gmail.com (J. Mohammed Azarudeen).

<https://doi.org/10.1016/j.matpr.2020.02.920>

2214-7853/© 2020 Elsevier Ltd. All rights reserved.

Selection and Peer-review under responsibility of the International Mechanical Engineering Congress 2019: Materials Science.

Please cite this article as: J. Mohammed Azarudeen, R. Kaja Bantha Navas, G. Vikas Reddy et al., Optimizing the process parameters for Powder metallurgy electrode in Electrical Discharge Machining, Materials Today: Proceedings, <https://doi.org/10.1016/j.matpr.2020.02.920>



PRINCIPAL
MOHAMED SATHAK ENGINEERING COLLEGE
KILAKARAI - 623 806



Structural and Optical Behavior of CuO/Ag and CuO/Ag/Au Nanocatalysts Synthesized Via a Novel Two Step Synthesis Approach for Enhancement of Catalytic Activity

A. Sankaran¹ · K. Kumaraguru² · B. Balraj³

Received: 14 May 2020 / Accepted: 30 June 2020
© Springer Science+Business Media, LLC, part of Springer Nature 2020

Abstract

In this paper, a facile two-step process of CuO/Ag and CuO/Ag/Au nanocomposites (NCs) were fabricated for the first time. The Powder X-ray Diffraction (PXRD) pattern revealed the existence of single-phase monoclinic structure of CuO and Face Centered Cubic (FCC) phase of Ag, Au and no other external phase impurities were observed from the prepared materials. In the photoluminescence (PL) studies, charge carrier trapping and fate of electron-hole pairs in CuO/Ag and CuO/Ag/Au NCs were investigated. The band-gap values of prepared CuO/Ag and CuO/Ag/Au NCs were calculated via UV-Visible Spectroscopy using Tauc's relation and found to be 2.3 eV and 2.1 eV, respectively. The flake-like morphologies were observed from the prepared CuO/Ag and CuO/Ag/Au NCs using FESEM analysis. The as-prepared CuO/Ag and CuO/Ag/Au NCs were evaluated by catalytic performances using the catalytic reduction of 4-nitrophenol (4-NP) to 4-aminophenol (4-AP) and Methylene blue (MB) to Leuco Methylene blue (LMB) with the presence of NaBH₄ in aqueous solution. Thus the result showed the synergistic effects between Ag, Au and CuO in CuO/Ag/Au NCs acted as suitable support to elevate the catalytic performance of M/CuO materials, which may be used as a potential application in industrial production.

Keywords CuO/Ag · CuO/Ag/Au NCs · Two-step process · Catalytic activity

1 Introduction

In current decade, nitroaromatic compounds are environmentally redundant materials due to outcome of the dyes from industries which are widely used in pesticides, plastics and explosives chemicals [1]. Among various nitroaromatic compounds, 4-nitrophenol (4-NP) is an example of toxic substance that exists in industrial effluents and classified as precedence pollutant by the US Environmental Protection Agency [2]. Therefore, environment friendly technique has established to remove them from waste water is the direct

reduction of 4-NP in the existence of NaBH₄ and a catalyst to 4-aminophenol (4-AP), which is one of the most valuable intermediate for antipyretic drug, manufacture of analgesic and paint industry and also can be used as the corrosion inhibitor, photographic developer, lubricant additive, anti-corrosion and hair-dyeing agent [3–6]. The NaBH₄ is the important reducing agent for catalytic activity owing to its several advantages likes easy to work at the experimental condition, safe to handle, rapid reduction, no pressure apparatus requirement and good selectivity in the reduction of nitrocompounds [7].

In the past two decades, heterostructured nanomaterials are having more attention in the area of catalysis due to their numerous functionalities and outstanding catalytic activity, selectivity and stability over monometallic nanomaterials [8]. Therefore, metal incorporated metal oxide nanostructured particles have drawn particular attention in catalytic applications due to their flexible catalytic activities, electronic properties and high surface areas [9]. Hence in the present investigation, CuO/Ag and CuO/Ag/Au nanocomposites materials were synthesized via two step approach for catalytic activity. During the catalytic reduction process, 4-NP is changed into 4-AP

✉ K. Kumaraguru
kumaraguruautt@gmail.com

¹ Department of Marine Engineering, Mohamed Sathak Engineering College, Kilakarai 623806, India

² Department of Petrochemical Technology, University College of Engineering, BIT Campus, Anna University, Tiruchirappalli 620024, India

³ Department of Electrical and Electronics Engineering, Sri Krishna College of Technology, Coimbatore 641042, India



K. Sankaran
PRINCIPAL
MOHAMED SATHAK ENGINEERING COLLEGE
KILAKARAI 623 806

as well as MB is reduction into LMB by adding NaBH_4 [10]. The semiconductor metal oxides of Cu_2O and CuO nanostructures exhibited excellent catalytic activities owing to their high oxidation–reduction potential values, low cost, non-toxicity, abundant resources and easy way to preparation in various shapes of nanosized dimensions [3]. As well as, silver (Ag) and gold (Au) act as a superior catalyst, which had exposed outstanding catalytic activity in oxygen reduction, hydrogenation and hydrogen production reaction, etc. [11]. In this connection, Zhou et al. has reported mesoporous SnO_2 decorated Ag nanostructures showed attractive multipurpose activity on 4-NP reduction [12]. Akbarzadeh et al. has fabricated Ag and Au decorated on CuO catalysts in situ formation for catalytic reduction of p-nitrophenol to p-aminophenol [13]. Guo et al. has developed core–shell structure of $\text{Cu}_2\text{O}/\text{Au}$ composites via a facile additive-assisted complex-precursor solution method for high catalytic activity toward 4-NP reduction to 4-AP at room temperature [14].

Hence, catalytic activity has been investigated by MB and 4-NP organic dyes from the developed catalyst of CuO/Ag and $\text{CuO}/\text{Ag}/\text{Au}$ NCs via a two-step approach. In synthesis process, CuO NPs were prepared by the co-precipitation approach and subsequently, CuO/Ag and $\text{CuO}/\text{Ag}/\text{Au}$ NCs were developed from the hydrothermal method. The co-precipitation method is one of the most flourishing approaches for synthesizing the materials and this technique is an effective pre-concentration technique for tracing heavy metal ions. As well as, the shape and size of the particles can be controlled by varying pH medium [10]. In addition, hydrothermal approach was used for develop the nanomaterials owing to their narrow crystallite size distribution and low aggregation level [15].

2 Experimental Procedure

2.1 Materials for Synthesizing of CuO NPs, CuO/Ag and $\text{CuO}/\text{Ag}/\text{Au}$ NCs

The Copper chloride (CuCl_2), Silver Nitrate $\text{Ag}(\text{NO}_3)$ and Tetrachloroauric acid (HAuCl_4) were used as the precursor material to develop the CuO NPs, CuO/Ag and $\text{CuO}/\text{Ag}/\text{Au}$ NCs. The sodium borohydride (NaBH_4) acted as a reducing agent. In overall experimental studies, Double Distilled (DD) water was used as a solvent. All the chemicals and organic dyes (4-nitrophenol and Methylene blue) were bought from Merck.

2.2 Synthesis Procedure of CuO/Ag and $\text{CuO}/\text{Ag}/\text{Au}$ NCs

As per previous report [10], pure CuO NPs were developed via a co-precipitation approach. To prepare CuO/Ag NCs, 0.1 gm of prepared CuO NPs was added gradually into

50 ml of DD water under sonication (15 min). Subsequently, 0.05 M of CTAB was added into the above-prepared solution under constant stirring process. Later that, 25 ml aqueous solution of 0.02 M of AgNO_3 was added into that solution. Then, 0.1 M of NaBH_4 was added to reduce $\text{Ag}(\text{NO}_3)$ to Ag. After that, the above-prepared solutions were changed into 100 ml of autoclave (Teflon-lined stainless steel) and heated at 140 °C for 12 h. Later, attained samples were collected and washed thoroughly by ethanol and DD water. After the washing process, the obtained material was heated at 90 °C and annealed at 300 °C for 2 h. The same process was followed as $\text{CuO}/\text{Ag}/\text{Ag}$ NCs. But, 25 ml aqueous solution of 0.02 M of AgNO_3 and 0.02 M of HAuCl_4 was added to the CuO and CTAB suspension solution remaining process are same. Finally, CuO/Ag and $\text{CuO}/\text{Ag}/\text{Au}$ NCs were collected for further analytical studies.

2.3 Catalytic Degradation of 4-NP and MB by CuO/Ag and $\text{CuO}/\text{Ag}/\text{Au}$ NCs

Catalytic activity of synthesized CuO/Ag and $\text{CuO}/\text{Ag}/\text{Au}$ NCs was tested for the reduction of 4-NP (1×10^{-3} M) and MB (1×10^{-5} M) solutions, which are added separately into 50 ml of DD water in the presence of NaBH_4 (1×10^{-2} M) as a reducing agent at room temperature. Without presence of nano catalyst, the blank experiment was monitored at a wavelength of 400 nm for 4-NP and 664 nm for MB, respectively. Furthermore, 2 mg of the prepared CuO/Ag and $\text{CuO}/\text{Ag}/\text{Au}$ nanocatalysts were mixed with separately into the above mentioned combination to start the reduction of dyes. At various time intervals, progress in catalytic reduction reaction was monitored by UV–Visible spectrophotometer. In this process, 4-NP and MB convert into 4-AP and LMB.

2.4 Analytical Techniques

The PXRD pattern of synthesized pure CuO/Ag and $\text{CuO}/\text{Ag}/\text{Au}$ NCs were analyzed by the Pro Penalty CAL [Cu-K α radiation (1.5406 Å)] instrument model. The UV–Visible absorption spectra of developed samples were taken from the JASCO V-670 spectrophotometer. From the Zeiss Gemini Ultra-55 instrument model, FESEM and EDAX color mapping analysis were identified.

3 Results and Discussion

3.1 Powder X-ray Diffraction (PXRD) Analysis

The PXRD pattern of CuO/Ag and $\text{CuO}/\text{Ag}/\text{Au}$ NCs were shown in Fig. 1. The primary characteristic peaks at about $2\theta = 32^\circ, 35^\circ, 38^\circ, 48^\circ, 53^\circ, 58^\circ, 61^\circ, 66^\circ, 67^\circ, 72^\circ$ and 75° correspond to the (100), (-111), (111), (-202), (020),

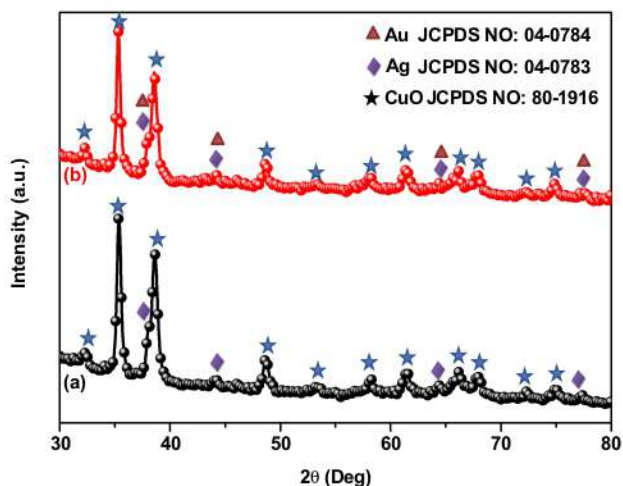


Fig. 1 PXRD pattern of a CuO/Ag NCs and CuO/Ag/Au NCs

(202), (−113), (−311), (220), (311) and (004) lattices in CuO, which were well concurred with the typical characteristic peaks for monoclinic crystal structure of CuO (JCPDS NO: 80-1916) [15]. The secondary characteristic peaks for Ag and Au NPs at 38°, 44°, 64° and 77° which belong to the Face Centered Cubic (FCC) phase of Ag (JCPDS no. 04-0783) and Au (JCPDS no. 04-0784) NPs, corresponds to reflection planes of (111), (200) (220) and (311) [16]. By using Scherrer's formula ($D = K\lambda/\beta \cos \theta$), average crystalline size was determined [15–17]. The average crystalline size was achieved to be 42 nm and 48 nm from the prepared material of CuO/Ag and CuO/Ag/Au NCs. The dislocation density (δ) was determined by the CuO/Ag and CuO/Ag/Au NCs. In dislocation density (δ), the crystal imperfection (or) defects present in the sample had been estimated from the following formula [15–17];

$$(\delta = 1/D^2)$$

The dislocation density (δ) was found to be 5.66×10^{-4} and 4.34×10^{-4} respectively for CuO/Ag and CuO/Ag/Au NCs. From the observed PXRD pattern, there were no other impurities present in the prepared material.

3.2 Photoluminescence (PL) Spectrum Analysis

The PL emission spectra had been used to study the effects of Ag and Au on CuO by the properties of immigration and transfer, charge carrier trapping, in addition to understanding the fate of electron–hole pairs in CuO/Ag and CuO/Ag/Au NCs (Fig. 2). The three emission peaks were observed by the PL spectrum. From the spectrum, PL emission peaks at 415 nm (2.98 eV) and 465 nm (2.66 eV) originated by the blue emission of Cu and luminescent excitation of Ag [15]. A green emission peak at 567 nm was attributed owing to

their recombination of photogenerated hole in the valence band with the singly ionized charge state [18]. The PL intensity of the CuO/Ag was decreased by adding Au due to the following reason (i) Radiating plasmon model which means metal nanoparticles with smaller sizes exhibited quenching by the result of small silver and gold coated onto the above surface of CuO. (ii) PL quenching happened due to exchange of electrons from the semiconductor to the metal shells [18]. During the PL measurement, the electrons were stimulated from valence to conduction band in CuO using the excitation light [18]. At the same time, nucleation formation of Ag and Au NPs may be occupy in the defects of the surface, which can trap the photo induced electrons and holes and thereby increase the charge separation in the CuO surface [18]. This was the reason for PL intensity decrement of the CuO/Ag/Au NCs than the CuO/Ag.

3.3 UV–Visible Absorption Spectroscopy

Figure 3 demonstrated UV–Vis absorption spectrum of CuO/Ag and CuO/Ag/Au NCs which was taken by the JASCO V650 instrument. From the figure, it was observed that a stronger absorption peak at 293 nm corresponded to CuO. The absorption peaks at 410 nm and 519 nm were attributed by the Ag and Au peaks [10]. The optical band gap energy (E_g) of CuO/Ag and CuO/Ag/Au NCs had been determined from Tauc's relation given below:

$$(\alpha h\nu)^2 = A (h\nu - E_g)$$

where, A is the transition probability dependent constant, α is the absorption coefficient and $h\nu$ is the incident photon energy and exponent n have values 2, 1/2 for direct and indirect allowed transitions, respectively [19]. The variation of

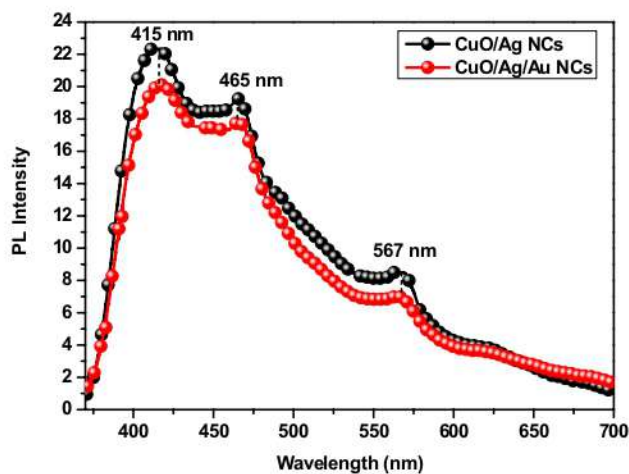


Fig. 2 PL spectrum of a CuO/Ag NCs and CuO/Ag/Au NCs

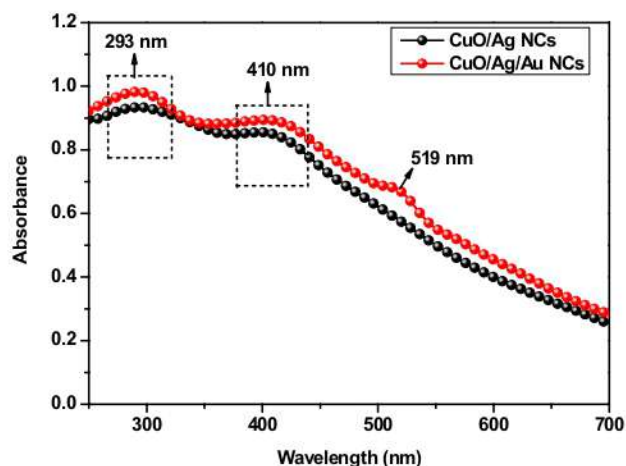


Fig. 3 UV-Visible absorption spectrum of a CuO/Ag NCs and CuO/Ag/Au NCs

$(\alpha h\nu)^2$ versus $h\nu$ in the form of Tauc plot was given in the Fig. 4a and b. Band gap energy is estimated by extending linear portion of the curve to $h\nu$ axis. The band gap of the CuO/Ag and CuO/Ag/Au NCs was found to be 2.3 eV and 2.1 eV, respectively.

3.4 Morphological Analysis

The Figs. 5a–d and 6a–d showed different magnification FESEM images of CuO/Ag and CuO/Ag/Au NCs. The attained particles of the prepared CuO/Ag and CuO/Ag/Au NCs were seemed as flake-like morphology. From the observed figure, nanoflakes had a uniform distribution of the particles and average particle size ranged around 50 to

150 nm respectively for the materials of CuO/Ag and CuO/Ag/Au NCs. The color mapping of synthesized materials (Figs. 7 and 8) demonstrated only elements of Cu, Ag, Au and O were present in the CuO/Ag and CuO/Ag/Au NCs and also results showed that there were no other impurities present in the prepared materials.

3.5 The Catalytic Reduction of 4-NP and MB by CuO/Ag and CuO/Ag/Au NCs

In catalytic process, the reduction of 4-NP and MB organic dyes from the catalysts of CuO/Ag and CuO/Ag/Au NCs using NaBH_4 reducing agent, which were monitored by UV-Visible spectrometer at every 30 s with interval of 210 s (s) shown in Fig. 9a and b. The NaBH_4 act as a strong reducing agent as well as low toxic compared to other diverse reducing agents. From UV-Visible spectra, the strong intensity peak was observed at 405 nm which is similar to earlier literature. The reduction rate of 4-NP took long time by without addition of any catalyst due to the repulsive force between negatively charged 4-NP and BH_4^- ions [20]. Then the addition of CuO/Ag and CuO/Ag/Au nanocatalysts (2 mg) in the 4-NP solution with NaBH_4 , the intensity of maximum absorbance peak at 405 nm rapidly reduces (210 s) along with the yellow colour of 4-NP solutions quickly changing to colourless owing to their conversion of 4-NP to 4-AP which revealed a new absorbance peak observed at 306 nm (Fig. 9a and b). This effect was more prominent in the occurrence of $\text{CuO}@ \text{Ag}^0 @ \text{Au}^0$, which gives support of the favorable contribution of Ag^0 and Au^0 incorporation in CuO. This reaction development must be suitable for a key-role of CuO, Ag and Au NPs in progressing the relaying electron transfer from donor BH_4^- ions to the nitro group of acceptor 4-NP [21]. Figure 10a

Fig. 4 Tauc's plot of a CuO/Ag NCs and CuO/Ag/Au NCs

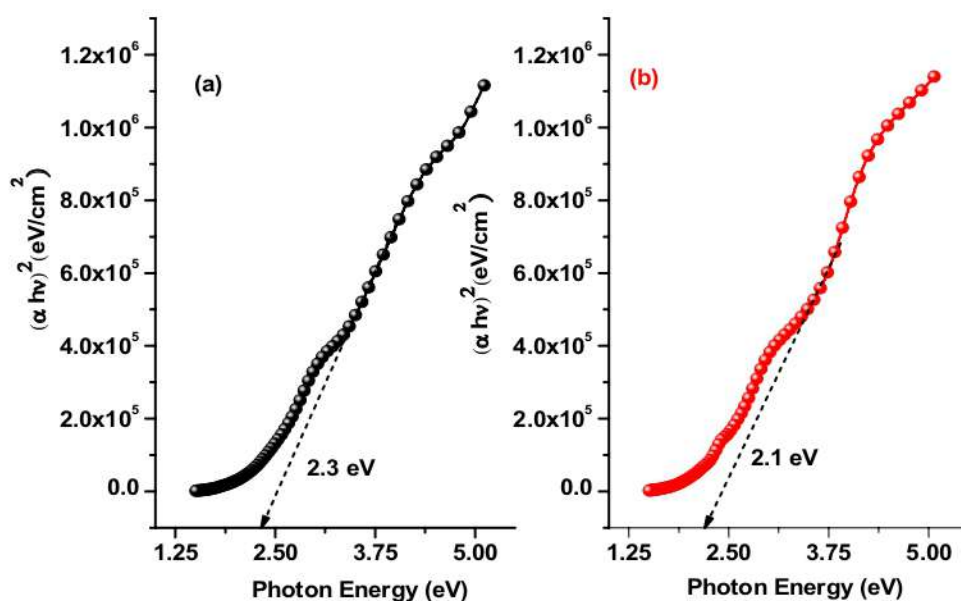


Fig. 5 Different magnification FESEM images of **a–d** CuO/Ag NCs

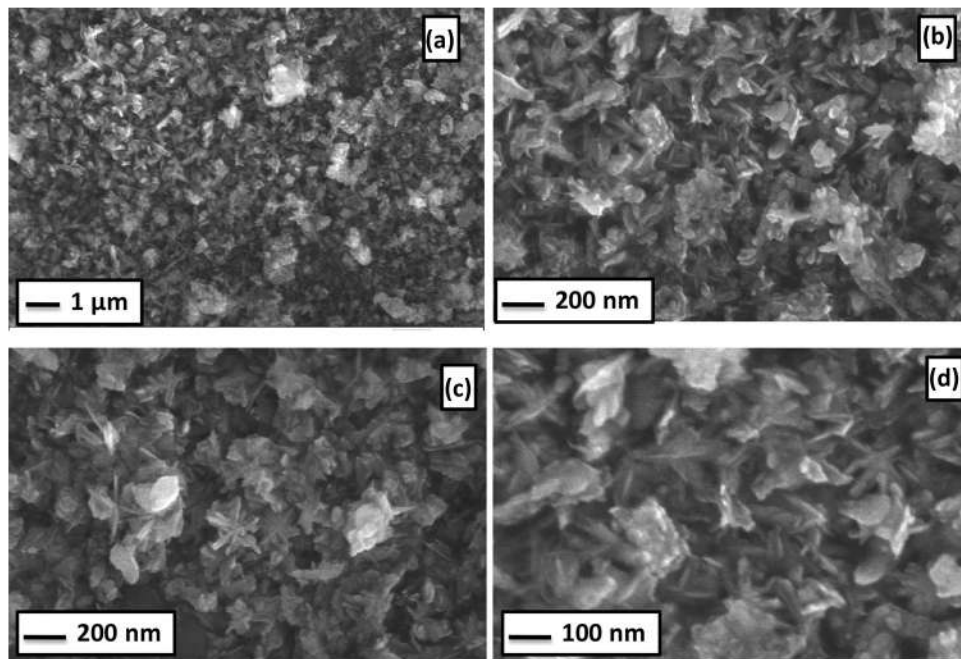
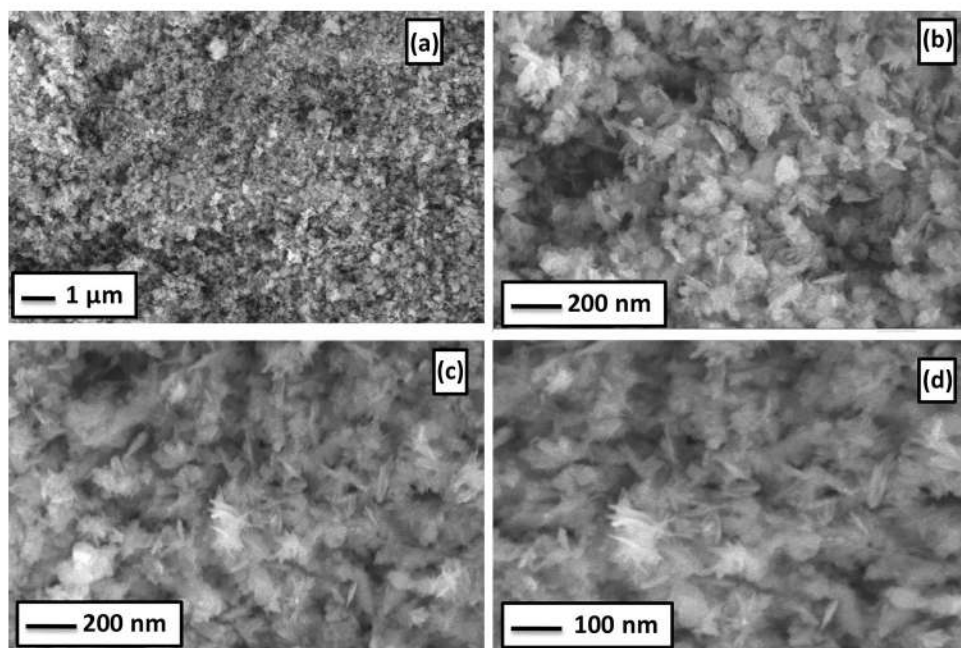


Fig. 6 Different magnification FESEM images of **a–d** CuO/Ag/Au NCs

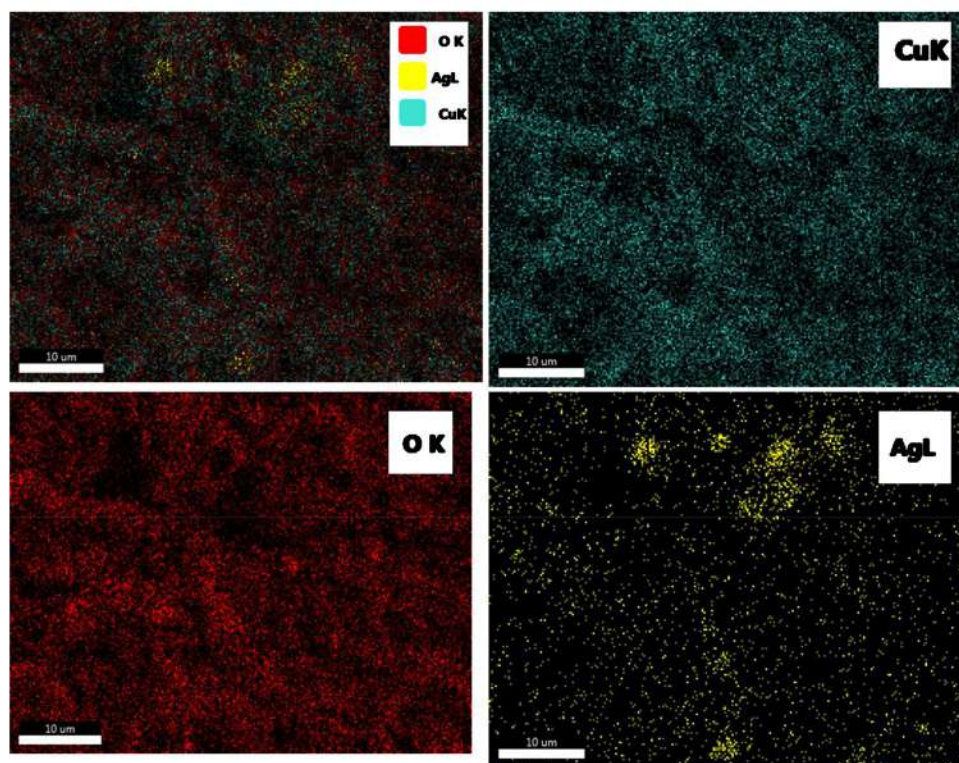


and b showed the time-dependent UV–Visible absorption spectra for the reduction of MB by CuO/Ag and CuO/Ag/Au NCs. Without presence of any catalyst, the reduction of MB was slower in presence of NaBH_4 . Addition of CuO/Ag and CuO/Ag/Au NCs catalyst (2 mg), the strong absorption peak of MB (664 nm) decreasing just 10 min and peak was shifted to 290 nm by reduction of MB (blue color) into LMB (colourless). This reaction may happen due to BH_4^- perform as an electron donor (nucleophile) at the same time MB supported as an electrophile with respect to CuO/Ag and CuO/Ag/Au

NCs catalyst [22]. The respective possible reduction mechanism of 4-NP & MB with nanocatalysts was demonstrated in Figs. 11 and 12. The deviation of C_t/C_0 versus time (t) for the degradation of 4-NP and MB by CuO/Ag and CuO/Ag/Au nanocatalysts was showed in Figs. 9c and 10c. The degradation efficiency (D) can be estimated by following relation

$$D = [(C_0 - C_t) / C_0] \times 100\%$$

Fig. 7 Elemental color mapping images of CuO/Ag NCs



where, C_0 and C_t (mg/L) are opening and last concentrations of 4-NP and MB at the time of 't' and '0', respectively. The attained degradation efficiency with time was plotted in Figs. 9d and 10d. From the Figure, the degradation efficiency of CuO/Ag and CuO/Ag/Au NCs were found to be 87% and 92% for 4-NP and 85% and 88% for MB respectively. The rate constant can be estimated by pseudo-first-order kinetics for the reduction of 4-NP and MB by CuO/Ag and CuO/Ag/Au nanocatalysts [10]. The preferred kinetic is agreed by linear plot of $\ln(C_t/C_0)$ against 't', which is demonstrated in Figs. 9e and 10e. The reaction kinetics equation is given by

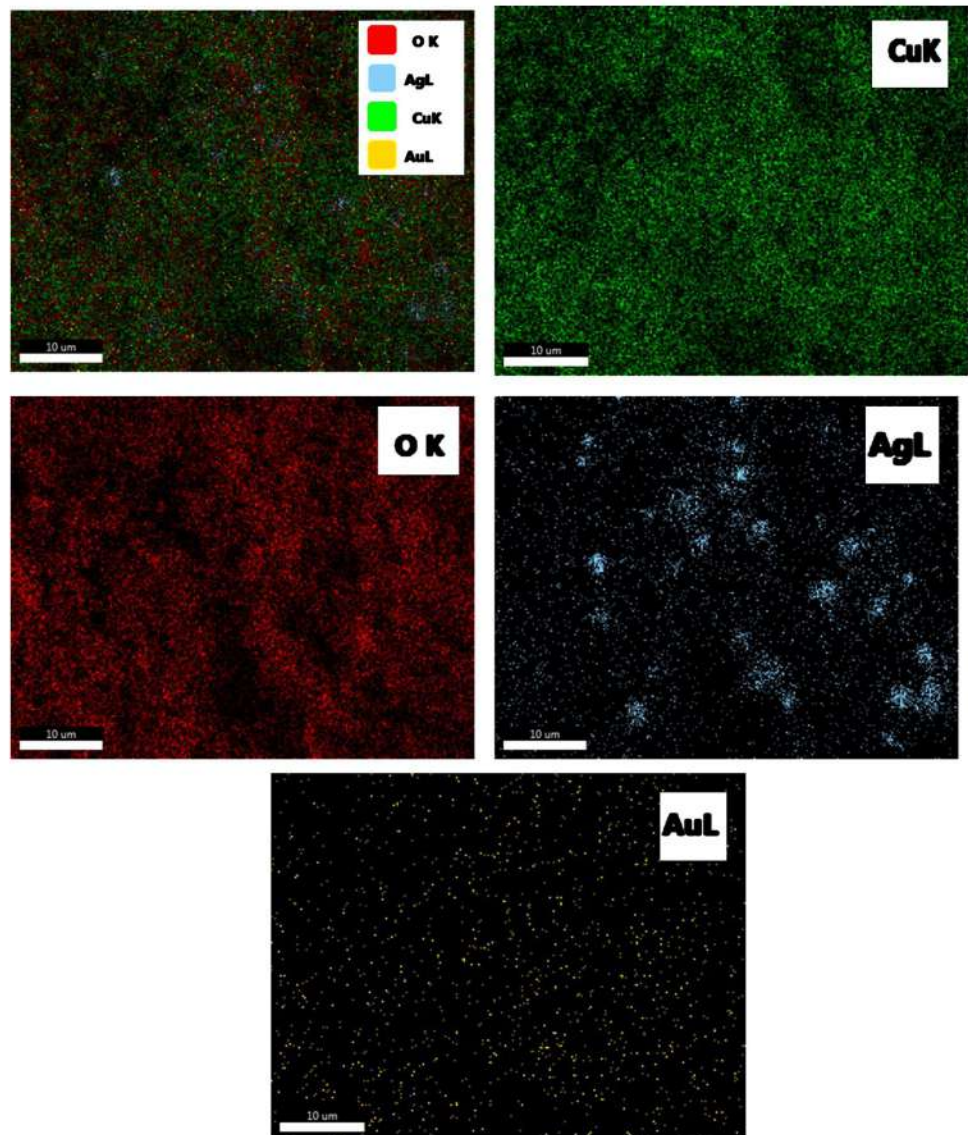
$$\ln(C_t/C_0) = kt$$

where, (k) donates the rate constant with time (t), C_0 and C_t is the concentration of 4-NP and MB at the beginning and after reaction time. The rate constant (k) of CuO/Ag and CuO/Ag/Au NCs determined from linear slope value were obtained to be $0.1055 \text{ (min}^{-1}\text{)}$ and $0.1201 \text{ (min}^{-1}\text{)}$ for 4-NP and $0.2440 \text{ (min}^{-1}\text{)}$ and $0.2914 \text{ (min}^{-1}\text{)}$ for MB respectively. The (R^2) values of CuO/Ag and CuO/Ag/Au NCs were calculated to be 0.9771 and 0.9859 for 4-NP and 0.9115 and 0.9363 for MB, respectively. The rapid catalytic reduction rate of 4-NP and MB reduction by CuO/Ag/Au nanocatalysts may be happens owing to the rate of electron transfer (or) interfacial electron transfer on the Ag and Au NPs surface, which can be influenced by the diffusion of 4-NP and MB to the metal surface. From the results exposed, addition of

noble metals significantly promote the reduction rate and demonstrate that introduction of these metals play a crucial roles in progressing the catalytic activity of CuO particles. The Tables 1 and 2 shows comparative table for previously reported catalytic reduction rate of 4-NP and MB dyes.

3.6 Catalyst Recyclability

The recycling of the catalyst is very important in industrial applications. To estimate its reusability, CuO/Ag and CuO/Ag/Au nanocatalysts were performing with successive catalytic tests (Fig. 13). After each catalytic test, the used CuO/Ag and CuO/Ag/Au nanocatalysts were washed by water and dried at room temperature. Initial three consecutive rounds, CuO/Ag/Au nanocatalyst has high recyclability than CuO/Ag nanocatalyst. After three consecutive cycles, recycling efficiency of 4-NP and MB was achieved to be 80.45% and 78.56% for CuO/Ag nanocatalyst. The presence of CuO/Ag/Au nanocatalyst, 4-NP and MB degradation recycling efficiency was attained to be 90.13% and 85.28%, respectively. Thus the result showed, degradation efficiency was rapidly reduced owing to their organic dye molecules are extremely adsorbed from the surface area [28].

Fig. 8 Elemental color mapping images of CuO/Ag/Au NCs

4 Conclusion

The CuO/Ag and CuO/Ag/Au NCs were fabricated via a facile two-step approach for enhancement of catalytic activity by the reduction of 4-NP and MB in the presence of NaBH_4 . In catalytic activity, CuO particles not only promote for Ag and Au metal nanoparticles but also play a crucial role in electron exchange from BH_4^- to organic pollutants (4-NP & MB) ions and thus enhancement of catalytic activity. The flake-like morphology was observed from the prepared CuO/Ag and CuO/Ag/Au NCs and size was found to be around 50 to 150 nm, respectively. Also, individual atoms were evenly distributed with a combined ratio throughout the composite matrix

of CuO/Ag and CuO/Ag/Au NCs which were primarily confirmed by the EDAX color mapping. In catalytic studies, degradation efficiency of CuO/Ag and CuO/Ag/Au NCs were achieved to be 87% and 92% for 4-NP and 85% and 88% for MB, respectively and noticeable rate constants of CuO/Ag and CuO/Ag/Au NCs were 0.1055 (min^{-1}), 0.1201 (min^{-1}) for the reduction of 4-NP and 0.2440 (min^{-1}), 0.2914 (min^{-1}) for the reduction of MB, respectively. From the observed results, dye degradation and rate constant of CuO/Ag/Au NCs were higher than the CuO/Ag NCs at both the dyes due to their surface electron transfer property.

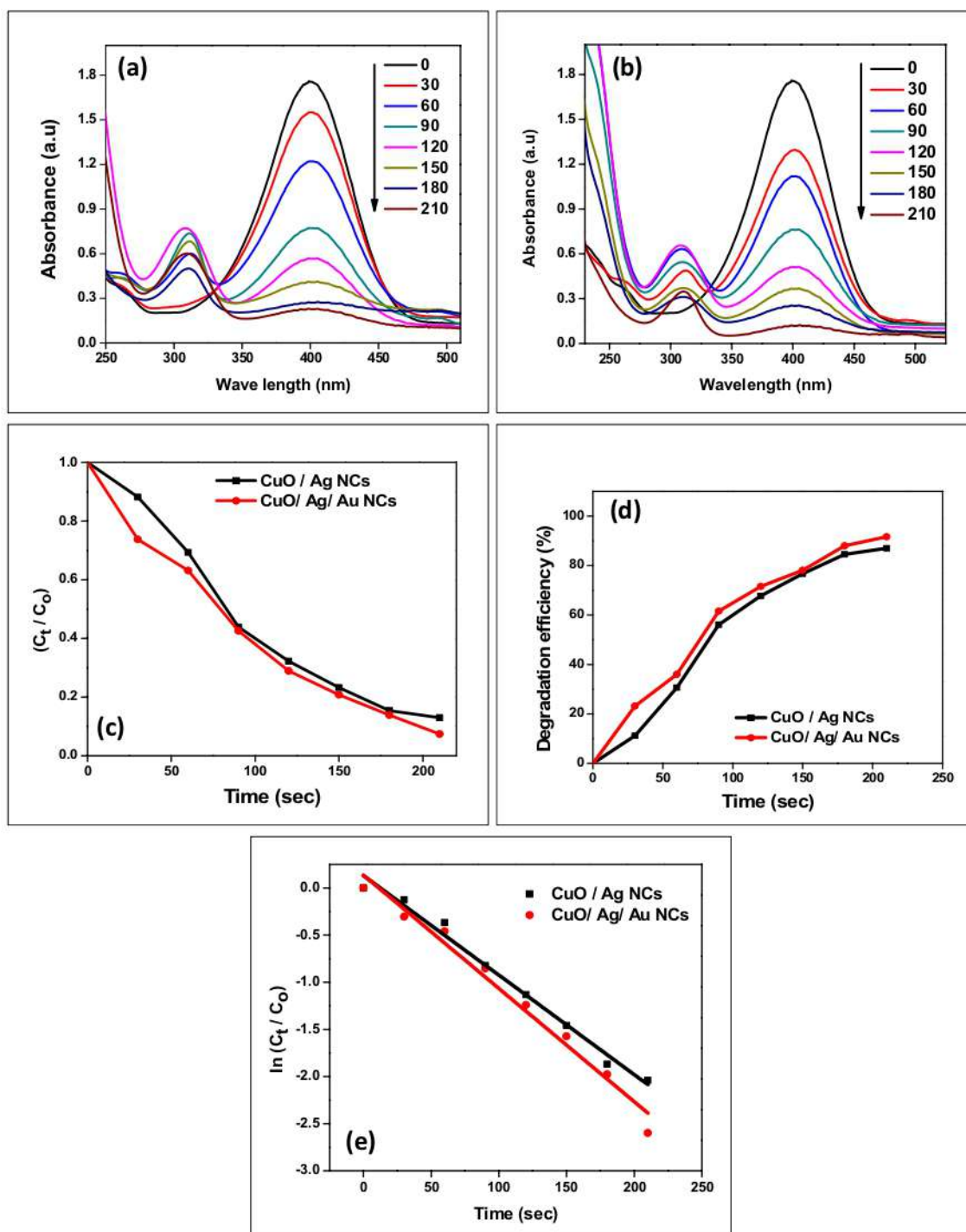


Fig. 9 Time-dependent UV-Vis absorption spectra for the reduction of 4-NP by **a** CuO/Ag NCs, **b** CuO/Ag/Au NCs, **c** Plot of C_t/C_0 versus reaction time (sec), **d** Degradation efficiency (%) versus reaction time (sec) and **e** $\ln(C_t/C_0)$ versus reaction time (sec)

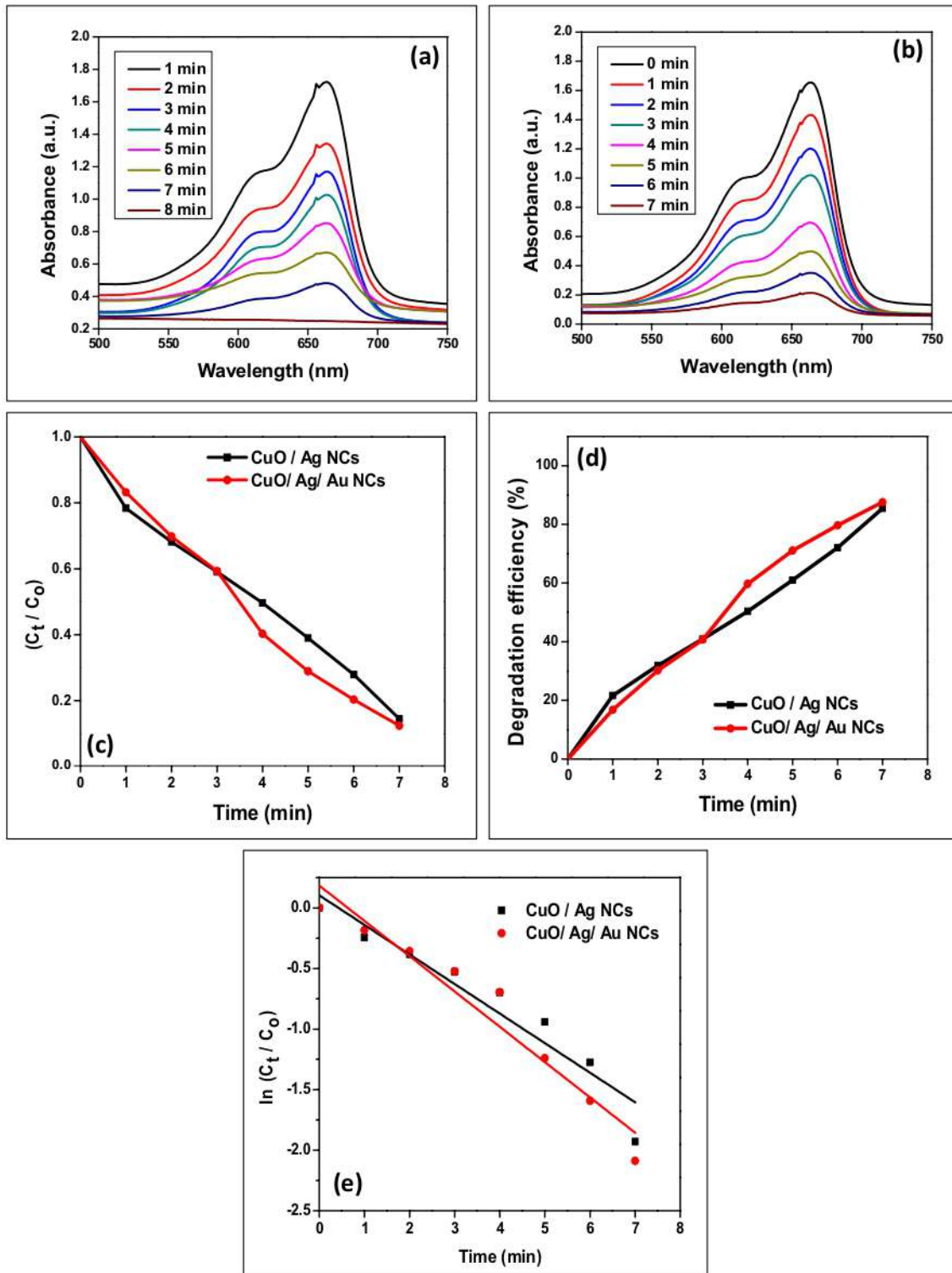


Fig. 10 Time-dependent UV-Vis absorption spectra for the reduction of MB by **a** CuO/Ag NCs, **b** CuO/Ag/Au NCs, **c** Plot of C_t/C_0 versus reaction time (sec), **d** Degradation efficiency (%) versus reaction time (sec) and **e** $\ln(C_t/C_0)$ versus reaction time (sec)

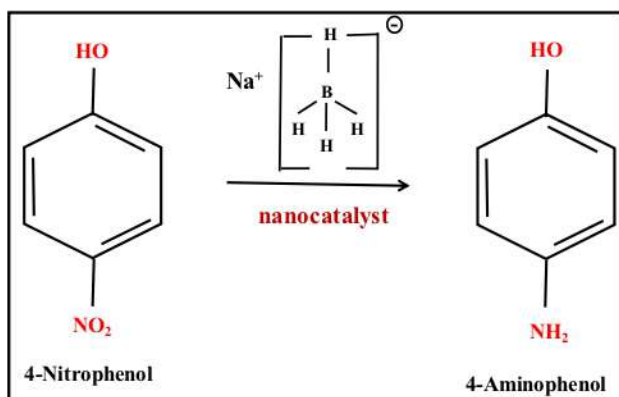


Fig. 11 Possible reduction mechanism of 4-Nitrophenol into 4-Aminophenol in presence of CuO/Ag NCs and CuO/Ag/Au nanocatalysts

Fig. 12 Possible reduction mechanism of Methylene Blue into Leuco methylene blue in presence of CuO/Ag NCs and CuO/Ag/Au nanocatalysts

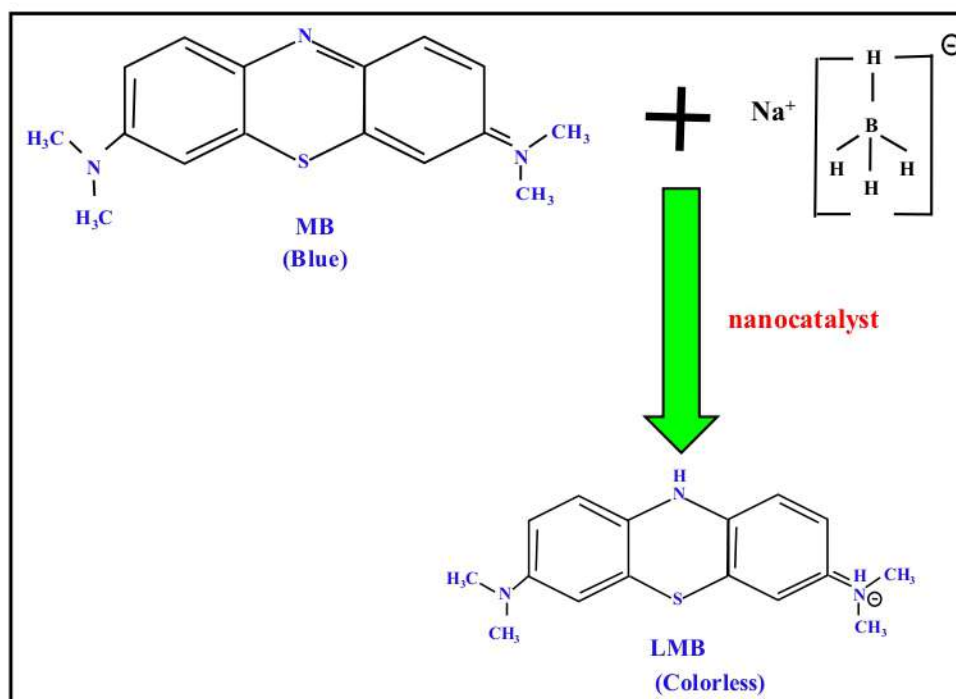
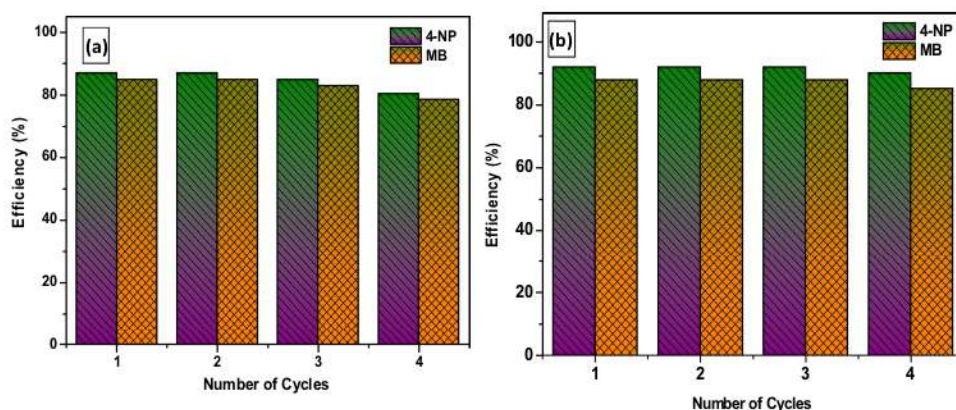


Table 1 Comparison catalytic activity of previous reported catalyst in the degradation of 4-NP

Catalyst	Quantity (mg)	4-NP (M)	Rate constant (k) (s ⁻¹)	References
CuO	1	1 ml of 10 ⁻³	0.8679 (min ⁻¹)	[10]
Cu ₂ O	1	3 ml of 10 ⁻⁴	0.5212(min ⁻¹)	[25]
Au/Fe ₂ O ₃	2	10 mM	0.63 (min ⁻¹)	[27]
Au/TiO ₂	5	5 mM	0.6326 (min ⁻¹)	[23]
CuO/Ag	5	0.20(mg/L)	0.338 (min ⁻¹)	[24]
CuO/Ag NCs	2	1 ml of 10 ⁻³	0.1055 (min ⁻¹)	[Present work]
CuO/Ag/Au NCs	2	1 ml of 10 ⁻³	0.1201 (min ⁻¹)	[Present work]

Table 2 Comparison catalytic activity of previous reported catalyst in the degradation of MB

Catalyst	Quantity (mg)	MB (M)	Rate constant (k) $\times 10^{-3}$ (s ⁻¹)	References
CuO NPs	1	1 ml of 10^{-4}	0.7368	[10]
CuOS	10	6.3×10^{-5}	0.698	[22]
Cu/MgO	10	3.1×10^{-5}	0.569	[26]
CuO/Ag NCs	2	1 ml of 10^{-4}	0.2440 (min ⁻¹)	Present work
CuO/Ag/Au NCs	2	1 ml of 10^{-4}	0.2914 (min ⁻¹)	Present work

Fig. 13 The recyclability of **a** CuO/Ag and **b** CuO/Ag/Au nanocatalysts in the reduction of 4-NB and MB dye solution with NaBH₄ at room temperature

References

- F.K. Higson, *Adv. Appl. Microbiol.* **37**, 1 (1992)
- M. Jayapriya, M. Arulmozhi, B. Balraj, *IET Nanobiotechnol.* **13**(2), 134–143 (2019)
- Z. Jin, C. Liu, K. Qi, X. Cui, *Sci. Rep.* **7**, 1 (2017)
- W. Che, Y. Ni, Y. Zhang, Y. Ma, *J. Phys. Chem. Solid.* **77**, 1 (2015)
- J.F. Corbett, *Dyes Pigment.* **41**, 127 (1999)
- C.V. Rode, M.J. Vaidya, R.V. Chaudhari, *Org. Process Res. Dev.* **3**, 465 (1999)
- P.M. Uberman, C.S. García, J.R. Rodríguez, S.E. Martín, *Green Chem.* **19**, 739 (2017)
- N. Toshimaand, T. Yonezawa, *New J. Chem.* **22**, 1179 (1998)
- C. Ray, T. Pal, *J. Mater. Chem. A* **5**, 9465 (2017)
- A. Pramothkumar, N. Senthilkumar, K.C. Mercy Gnana Malar, M. Meena, I.V. Potheher, *J. Mater. Sci.* **30**, 19043 (2019)
- Y. Liang, Z. Chen, W. Yao, P. Wang, S. Yu, X. Wang, *Langmuir* **33**, 7606 (2017)
- N. Zhou, L. Polavarapu, Q. Wang, Q. Xu, *A.C.S. Appl. Mater. Interfaces* **7**, 4844 (2015)
- E. Akbarzadeh, M. Falamarzi, M.R. Gholami, *Mater. Chem. Phys.* **198**, 374 (2017)
- X.H. Guo, J.Q. Ma, H.G. Ge, *Russ. J. Phys. Chem. A* **89**, 1374 (2015)
- B. Balraj, N. Senthilkumar, I. Vetha Potheher, M. Arulmozhi, *Mater. Sci. Eng. B* **231**, 121–127 (2018)
- N. Senthilkumar, M. Ganapathy, A. Arulraj, M. Meena, M. Vimalan, I.V. Potheher, *J. Alloys Compd.* **750**, 171 (2018)
- P. Yuvarani, B. Balraj, S. Vijayachitra, C. Siva, *Mater. Res. Express* **5**(10), 105402 (2018)
- S. Arya, P. Anoop Singh, R. Kour, *Mater. Res. Express* **6**, 116313 (2019)
- E. Nandhakumar, P. Priya, R. Rajeswari, V. Aravindhan, A. Sasi-kumar, N. Senthilkumar, *Res. Chem. Intermed.* **45**, 2657 (2019)
- J.F. Huang, S. Vongehr, S.C. Tang, H.M. Lu, X.K. Meng, *J. Phys. Chem. C* **114**, 15005 (2010)
- J. Li, C. Liu, Y. Liu, *J. Mater. Chem.* **22**, 8426 (2012)
- A.K. Abay, X. Chen, D.H. Kuo, *New J. Chem.* **41**, 5628 (2017)
- Z.H. Ren, H.T. Li, Q. Gao, H. Wang, B. Han, K.S. Xia, C.G. Zhou, *Mater. Des.* **121**, 167 (2017)
- N. Bouazizi, J. Vieillard, P. Thebault, F. Desirac, T. Clamens, R. Bargougui, N. Couvrat, O. Thoumire, N. Brun, G. Ladam, S. Morin, N. Mofaddel, O. Lesouhaitier, A. Azzouz, F. Le Derf, *Dalton Trans.* **47**, 9143 (2018)
- A.K. Sasmal, S. Dutta, T. Pal, *Dalton Trans.* **45**, 3139 (2016)
- M. Nasrollahzadeh, Z. Issaabadia, S. Mohammad Sajadi, *RSC Adv.* **8**, 3723 (2018)
- F.H. Lin, R.A. Doong, *J. Phys. Chem. C* **115**, 6591 (2011)
- M. Sundaram, S. Kalpana, S. Rafi Ahamed, V. Sivaganesan, E. Nandhakumar, *Mater. Res. Exp.* **6**, 125043 (2019)

Publisher's Note Springer Nature remains neutral with regard to jurisdictional claims in published maps and institutional affiliations.



Investigation on catalytic activity of CuO/La₂O₃, CuO/Gd₂O₃ and CuO/La₂O₃/Gd₂O₃ nanocatalysts prepared via novel two step approach

A. Sankaran^a, K. Kumaraguru^{b,*}, B. Balraj^c, A. Sridevi^d, R. Magesh^e

^a Department of Marine Engineering, Mohamed Sathak Engineering College, Kilakarai 623806, India

^b Department of Petrochemical Technology, University College of Engineering, BIT Campus, Anna University, Tiruchirappalli 620024, India

^c Department of Electrical and Electronics Engineering, K.Ramakrishnan College of Technology, Tiruchirappalli 621112, India

^d Department of Electronics and Communication Engineering, M.Kumarasamy College of Engineering, Karur 639113, India

^e Department of Chemical Engineering, Wachemo University, Hossana, Ethiopia

ARTICLE INFO

Keywords:

CuO/La₂O₃
CuO/Gd₂O₃
CuO/La₂O₃/Gd₂O₃ NCs
Two-step synthesis approach
Catalytic activity

ABSTRACT

This work was focused on facile two-step synthesis approach of CuO/La₂O₃, CuO/Gd₂O₃ and CuO/La₂O₃/Gd₂O₃ nanocomposites (NCs) that were prepared. The Powder X-ray Diffraction (PXRD) pattern demonstrated the survival of single-phase monoclinic, hexagonal and cubic phase for CuO/La₂O₃, CuO/Gd₂O₃ and CuO/La₂O₃/Gd₂O₃ NCs. The band-gap values of prepared NCs were evaluated via UV-Visible Spectroscopy using Tauc's relation and surface morphologies of the developed samples were revealed by FESEM analysis. The as-developed CuO/La₂O₃, CuO/Gd₂O₃ and CuO/La₂O₃/Gd₂O₃ NCs exhibited superior catalytic performance and high stability towards the reduction of 4-nitrophenol and methylene blue with NaBH₄ as a reducing agent, which may be due to their unique structure. The synthesized nanocomposites showed an efficient catalytic activity with a high reaction kinetic rate. Thus the result showed that the current study may be utilized for the removal of organic toxic pollutants in clearing environmental pollution and also in industrial applications.

1. Introduction

In the past decade, environmental pollution and prospective exhaustion possibility of fossil fuels has more and more attention for growth of green and renewed energy resources [1]. For that reason, the research on materials is essential for the prevention of environmental pollution via the degradation of toxic compounds [2]. Hence, nanotechnology is a promising application for wastewater treatment owing to its high surface area to volume ratio of nanomaterials [3]. There are numerous treatment processes that have been applied for pollutant removal from wastewater [4–11]. Among them, catalytic process is one of the most capable for removing organic pollutants for wastewater treatment owing to its cost-effective and environment-friendly [12]. Nowadays, nitroaromatic compounds are environmentally redundant materials owing to its consequence of the nitroaromatic contaminated dyes releases from various industries usages like plastics, pesticides and explosives chemicals [2]. Among different nitroaromatic compounds, 4-nitrophenol (4-NP) is a major class of nitroaromatic compounds in industrial effluents and has been classified as a precedence pollutant by the US Environmental Protection Agency [13]. Because, 4-NP has been

recorded as a teratogenic, carcinogenic and mutagenic element and hence is hazardous to living organisms [14]. Therefore, an environment friendly technique established to remove them from waste water is the direct reduction of 4-NP to 4-aminophenol (4-AP) in the existence of NaBH₄ and a catalyst, which is a significant intermediate in the preparation of chemical products like antipyretic, paracetamol (analgesic) and phenacetin [15–19]. In addition, 4-AP is widely used as a corrosion inhibitor, photographic developer, hair-dyeing agent and anticorrosion lubricant [15–21].

The heterostructured nanomaterials have gained increasing attention in the area of catalysis in the past two decades because they show multiple functionalities and prominent catalytic activity, selectivity, and stability over monometallic nanomaterials [8]. In recent years, lanthanide (Nd₂O₃, Y₂O₃, La₂O₃, Sm₂O₃, Gd₂O₃, Eu₂O₃, Yb₂O₃ etc.) based metal oxides incorporated with copper oxide (CuO) nanoparticles have more attention in catalytic applications by their electronic properties and flexible catalytic activities [22]. As well as, CuO NPs has demonstrated admirable catalytic activities due to their abundant resources, high oxidation–reduction potential values, non-toxicity and low cost [15]. In addition, lanthanides have been applied in different fields owing

* Corresponding author.

E-mail address: kumaraguruautt@gmail.com (K. Kumaraguru).

<https://doi.org/10.1016/j.mseb.2020.114836>

Received 25 April 2020; Received in revised form 8 September 2020; Accepted 25 September 2020

Available online 7 October 2020

0921-5107/© 2020 Elsevier B.V. All rights reserved.

PRINCIPAL
MOHAMED SATHAK ENGINEERING COLLEGE
KILAKARAI 623806



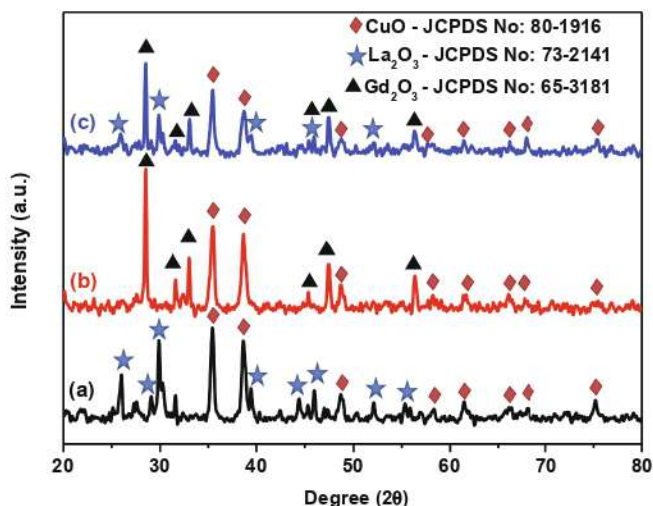


Fig. 1. PXRD pattern of (a) CuO/La₂O₃, (b) CuO/Gd₂O₃ and (c) CuO/La₂O₃/Gd₂O₃ NCs.

to their interesting magnetic, optical, electrical and therapeutic properties by their unique electronic configuration [4f electrons] [22].

Therefore, in the present work was focused to develop CuO/La₂O₃, CuO/Gd₂O₃ and CuO/La₂O₃/Gd₂O₃ nanocomposite materials from two step synthesis approach for catalytic activity. Because, Lanthanum oxide (La₂O₃) has wide band gap (4.8 eV) and lowest activation energy with the high electric constant which are the required parameters for protective coating layer against high-temperature oxidation, gas sensors, opto-electronics, photoelectrochemical cell and supercapacitor application [22]. And also, La₂O₃ nanomaterial acts as a favorable catalyst for the catalytic oxidative cracking of n-propane, ethanol oxidation and degradation of rhodamine B under visible light irradiation [22]. As well as, due to its unique properties, Gadolinium oxide (Gd₂O₃) has drawn attention in wide range of technological applications like solar cell, magnetic resonance imaging, luminescent devices, gas sensor, photocatalytic activity and energy storage devices etc. [23]. It also processes sublime catalytic properties because of its high surface area.

So, catalytic reduction had been investigated from MB and 4-NP organic dyes by the prepared CuO/La₂O₃, CuO/Gd₂O₃ and CuO/La₂O₃/Gd₂O₃ nanocatalysts via a two-step synthesis approach. In preparation of nanocomposites material, CuO NPs were developed from co-precipitation method and consequently, CuO/La₂O₃, CuO/Gd₂O₃ and CuO/La₂O₃/Gd₂O₃NCs were fabricated by hydrothermal technique.

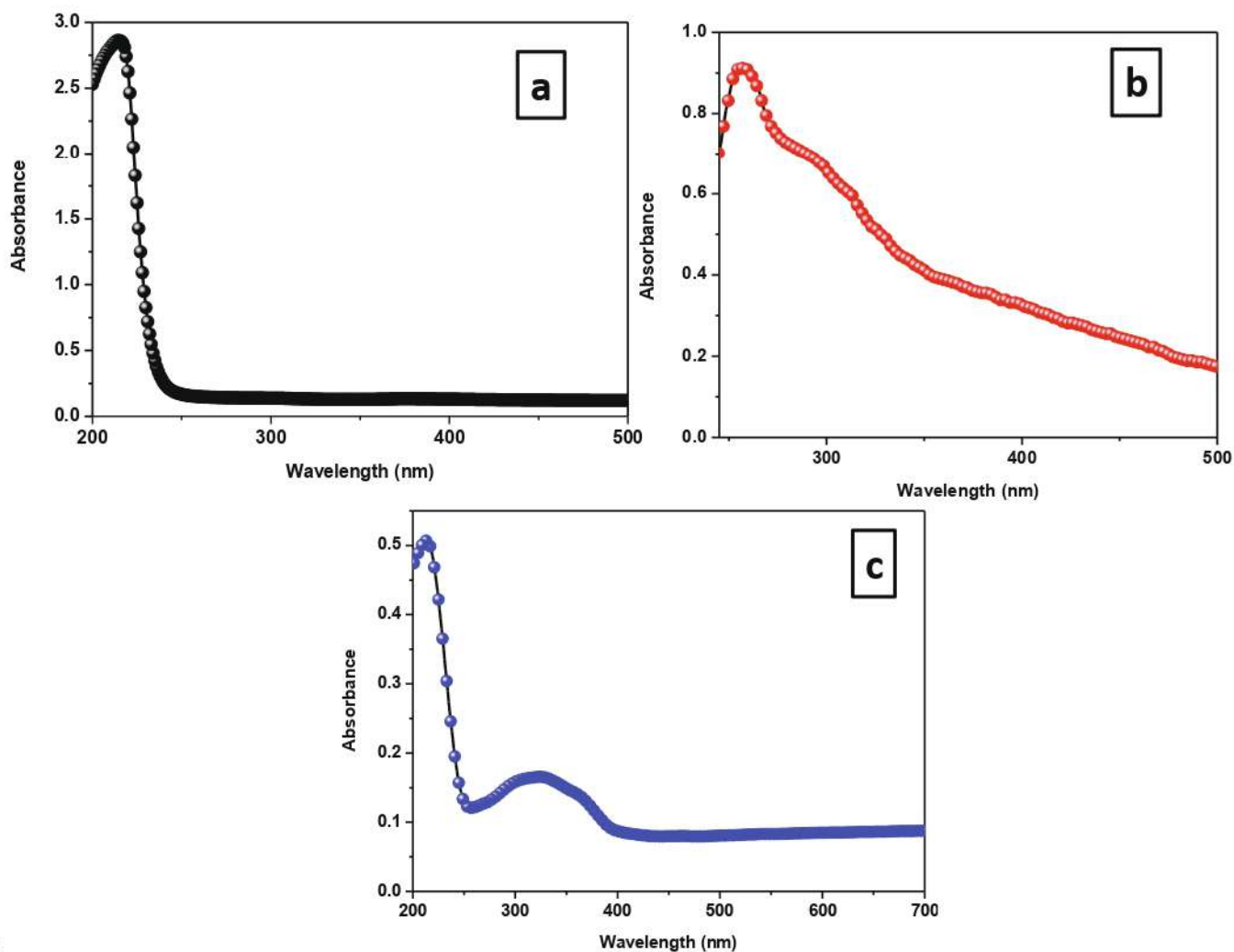


Fig. 2. UV-Visible absorption spectrum of (a) CuO/La₂O₃, (b) CuO/Gd₂O₃ and (c) CuO/La₂O₃/Gd₂O₃ NCs.

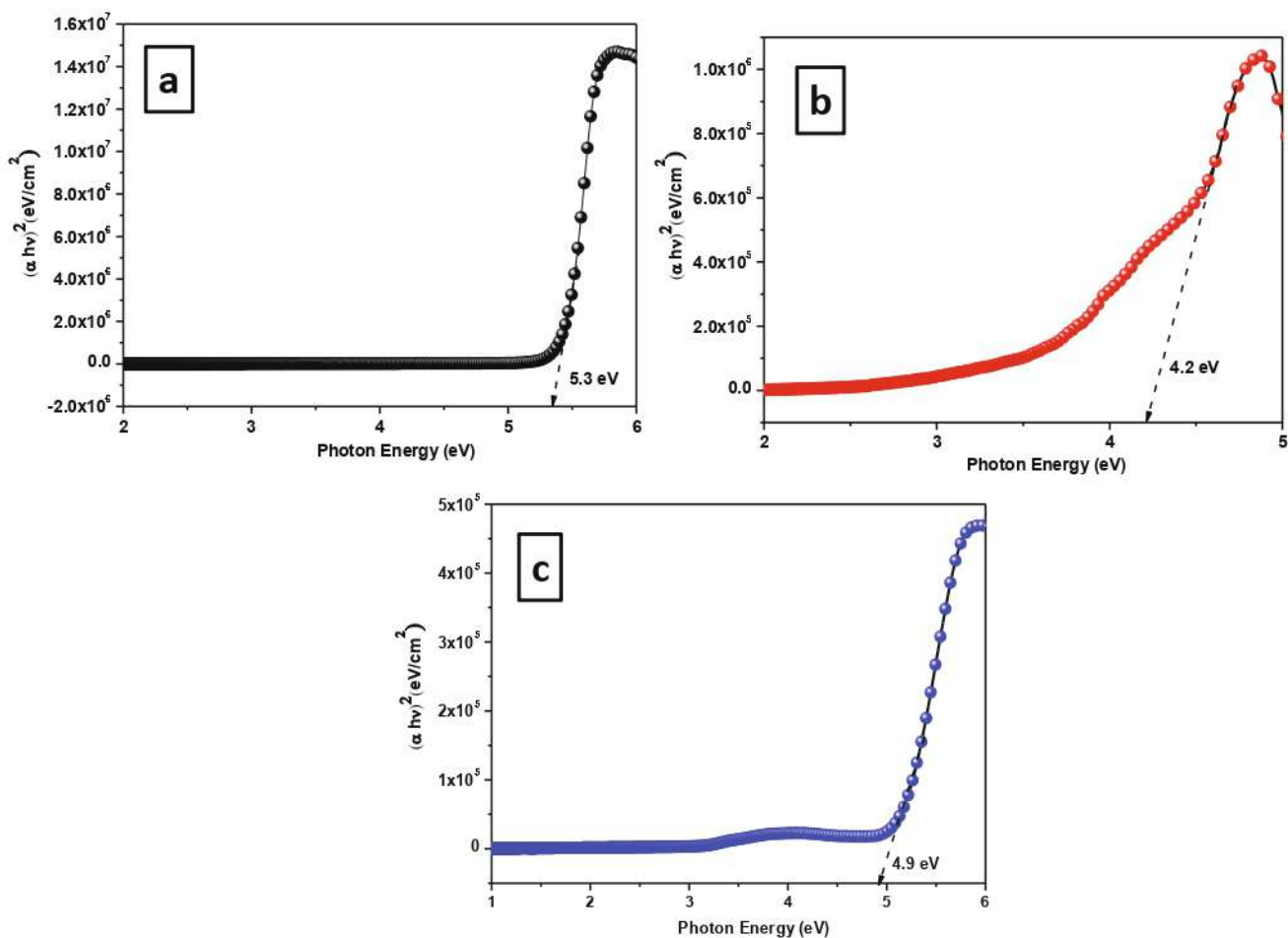


Fig. 3. Tauc's plot of (a) CuO/La₂O₃, (b) CuO/Gd₂O₃ and (c) CuO/La₂O₃/Gd₂O₃ NCs.

2. Experimental procedure

2.1. Materials

The lanthanum nitrate hexahydrate (La(NO₃)₃·6H₂O) and gadolinium nitrate hexahydrate (Gd(NO₃)₃·6H₂O) were used as the precursor material to develop the CuO/La₂O₃, CuO/Gd₂O₃ and CuO/La₂O₃/Gd₂O₃ NCs. The Double Distilled (DD) water was acts as a solvent in overall experimental studies and usage of all chemicals in the experiment was purchased from Merck.

2.2. Synthesis procedure

In co-precipitation technique, pure CuO NPs were synthesized as per the previous report [10]. To prepare CuO/La₂O₃ and CuO/Gd₂O₃ NCs, 0.2 M of CuO NPs were mixed slowly into DD water (50 ml) under sonication (15 min). Consequently, CTAB (0.05 M) was gradually mixed with above-mentioned solution under mild stirring. After that, 0.05 M of La(NO₃)₃ was dissolved into above prepared CuO mixed CTAB solution and 0.05 M of Gd(NO₃)₃ was added with another prepared CuO mixed CTAB solution. Then, the NaOH diluted solution was mixed into the each mentioned solution until pH 9 was reached. After that, prepared solutions were transferred to a 100 ml (Teflon-lined stainless steel) autoclave and then sealed. The autoclave was maintained at 140 °C for 12 h and then kept separately. Later, samples were purified with ethanol and DD water. After purification, the attained material was dried (90 °C) over night at hot air oven and annealed (300 °C) in muffle furnace for 2 h. That same procedure was followed for preparing CuO/La₂O₃/Gd₂O₃

NCs. But, each aqueous solution (50 ml) of La(NO₃)₃ (0.05 M) and Gd(NO₃)₃ (0.05 M) were mixed with the CuO and CTAB suspension solution. The remaining process was followed as same in the above prepared CuO/La₂O₃ and CuO/Gd₂O₃ NCs. Finally, collected samples of CuO/La₂O₃, CuO/Gd₂O₃ and CuO/La₂O₃/Gd₂O₃ NCs were utilized for further characterization studies.

2.3. Catalytic activity

In a catalytic activity process, 2 mg by CuO/La₂O₃, CuO/Gd₂O₃ and CuO/La₂O₃/Gd₂O₃NCs were added into 20 ml solution of 4-NP (0.2 mM) and MB (0.2 mM). Then, newly prepared solution of 2 ml of NaBH₄ (0.1 M) was added to the above mixture solution separately and was kept under stirring condition at room temperature. After that, reduction of both dyes was carried out, that is, 4-NP was reduced to 4-AP and MB to LMB. It was observed by the time dependent UV-visible absorption spectrometer with different time intervals, i.e., 210 s for 4-NP and 10 min for MB.

2.4. Analytical techniques

The PXRD measurements of prepared CuO/La₂O₃, CuO/Gd₂O₃ and CuO/La₂O₃/Gd₂O₃NCs were investigated by the instrument model of Pro Penalty CAL (Cu-Kα radiation (1.5406 Å)). The UV-Visible absorption studies of synthesized samples were carried out by JASCO V-670 spectrophotometer. The surface morphology and distribution of elemental component of the prepared CuO/La₂O₃, CuO/Gd₂O₃ and CuO/La₂O₃/Gd₂O₃NCs catalyst was analyzed by FESEM and EDAX color

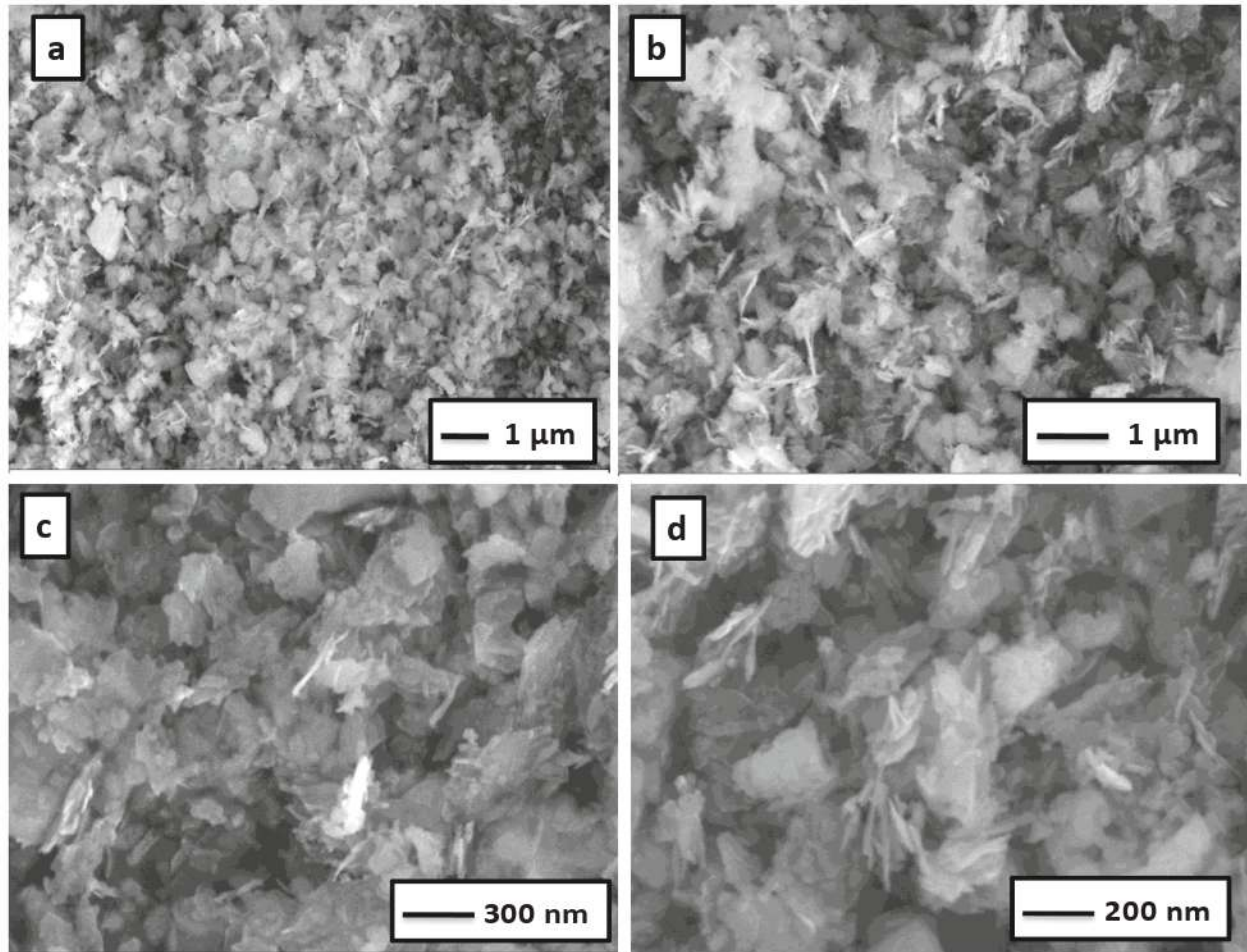


Fig. 4. Different magnification FESEM images of (a-d) CuO/La₂O₃ NCs.

mapping (Zeiss Gemini Ultra-55 model).

3. Results and discussion

3.1. Powder X-ray diffraction (PXRD) analysis

The Fig. 1 demonstrated the PXRD pattern of CuO/La₂O₃, CuO/Gd₂O₃ and CuO/La₂O₃/Gd₂O₃NCs. The strong characteristic peaks of CuO/La₂O₃, CuO/Gd₂O₃ and CuO/La₂O₃/Gd₂O₃NCs located at $2\theta = 35^\circ, 38^\circ, 48^\circ, 58^\circ, 61^\circ, 66^\circ, 68^\circ$ and 75° correspond to the $(-111), (111), (-202), (020), (-113), (-311), (220)$ and (004) lattices in CuO, which are good coherent with the standard characteristic peaks for CuO (JCPDS NO: 80-1916) [15,24]. The secondary intensity peaks for La₂O₃ and Gd₂O₃ located at $26^\circ, 29^\circ, 30^\circ, 39^\circ, 44^\circ, 46^\circ, 52^\circ, 55^\circ$ and $28^\circ, 31^\circ, 33^\circ, 45^\circ, 47^\circ, 56^\circ$ belong to the hexagonal and cubic phase of La₂O₃ and Gd₂O₃ NPs correspond to reflection planes of $(100), (002), (011), (012), (003), (110), (103), (112)$ and $(222), (123), (400), (125), (440), (622)$. The position and relative intensity of the diffraction peaks of La₂O₃ and Gd₂O₃ coincide well with the standard card pattern (JCPDS no. 73-2141) and (JCPDS no. 65-3181). The average crystalline size was determined by using the following Scherrer's formula [25,26].

$$D = K\lambda/\beta \cos \theta$$

where 'D' and 'K' is Debye-Scherrer's crystalline size and shape factor (0.94), ' λ ' represents the incident wavelength of Xray's (Cu radiation: 1.54 Å), ' β ' denotes the full-width half maximum and ' θ ' is the Bragg diffraction angle for the respective peak. The average crystalline size of

developed CuO/La₂O₃, CuO/Gd₂O₃ and CuO/La₂O₃/Gd₂O₃ NCs was attained to be 34 nm, 44 nm and 62 nm respectively. The crystal imperfection (or) defects from the prepared samples were identified by dislocation density (δ) and estimated by given formula [27,28];

$$(\delta = 1/D^2)$$

The dislocation density (δ) was found to be 8.65×10^{-4} , 5.16×10^{-4} and 2.60×10^{-4} respectively for CuO/La₂O₃, CuO/Gd₂O₃ and CuO/La₂O₃/Gd₂O₃NCs.

3.2. UV-Visible absorption Spectroscopy

The Fig. 2 (a-c) revealed the optical absorbance spectra of CuO/La₂O₃, CuO/Gd₂O₃ and CuO/La₂O₃/Gd₂O₃NCs. In the prepared nanocomposites material, maximum absorption of La₂O₃ and Gd₂O₃ occurred at 250–310 nm, respectively [22]. The optical band gap energy (E_g) of synthesized samples was estimated by following Tauc's relation:

$$(\alpha h\nu)^2 = A(h\nu - E_g)$$

where 'A' is the absorption constant that depends on transition probability, ' α ' and ' $h\nu$ ' denoted as absorption coefficient and incident photon energy [29]. From the Tauc's plot, deviation of $(\alpha h\nu)^2$ versus $h\nu$ was revealed in the Fig. 3 (a-c). The band gap of the CuO/La₂O₃, CuO/Gd₂O₃ and CuO/La₂O₃/Gd₂O₃NCs was achieved to be 5.3 eV, 4.2 eV and 4.9 eV, respectively.

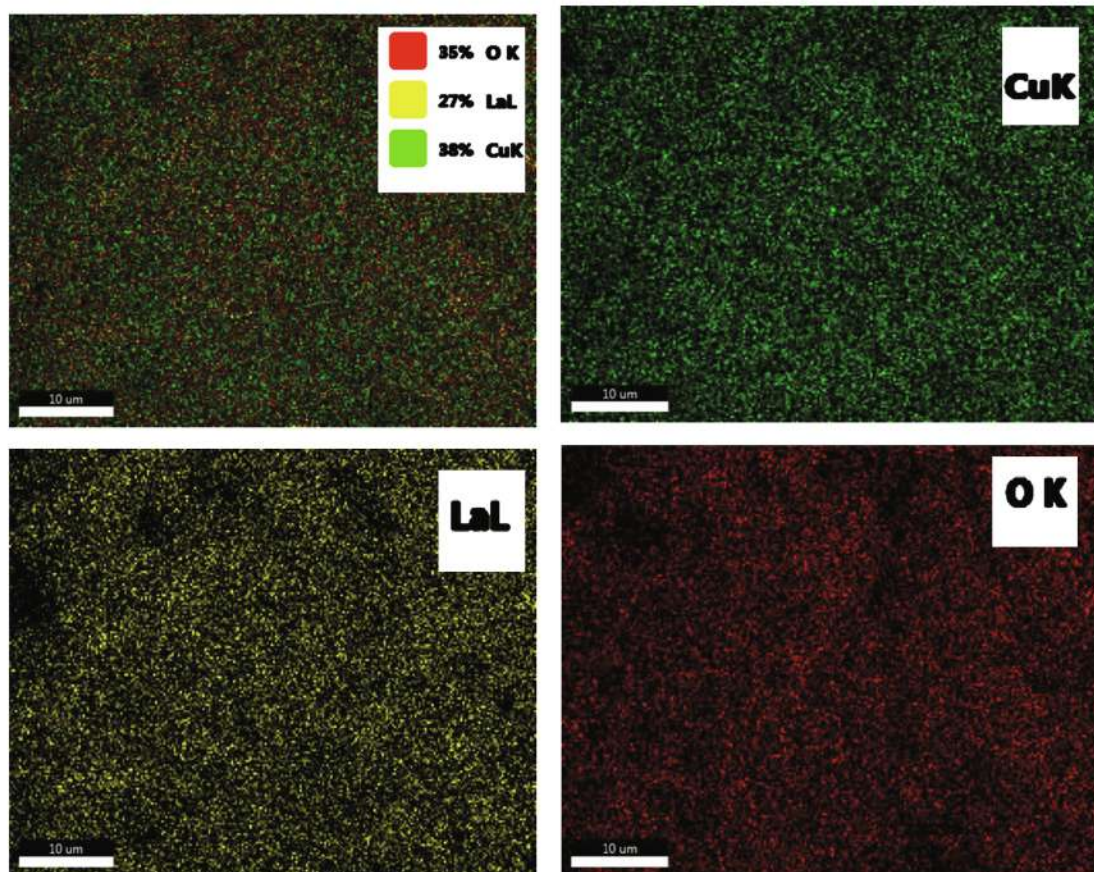


Fig. 5. Elemental color mapping images of CuO/La₂O₃ NCs.

3.3. Morphological analysis

The Figs. 4, 6 & 8 represented the different magnification FE-SEM images of CuO/La₂O₃, CuO/Gd₂O₃ and CuO/La₂O₃/Gd₂O₃NCs. The flake-like morphology was appeared from the synthesized CuO/La₂O₃NCs. From Fig. 4a–d, it was observed that the nanoflakes had a homogeneous distribution of the particles and average particle size ranged around ~ 150 nm, respectively for the materials of CuO/La₂O₃NCs. Incorporation of Gd₂O₃ in CuO (Fig. 6 a–d) resulted in the formation of composite acquiring flake-like morphology and had thickness increased few nanometers (~180 nm). The uniform composition distribution of La₂O₃ and Gd₂O₃ incorporation with CuO surface increased the size and morphology of CuO/La₂O₃/Gd₂O₃NCs due to their lanthanides material compositions (Fig. 8a–d). The EDAX elemental mapping of CuO/La₂O₃, CuO/Gd₂O₃ and CuO/La₂O₃/Gd₂O₃NCs clearly showed a homogeneous and continuous distribution of Cu, La, Gd and O elements present in the prepared nanocatalysts (Figs. 5, 7 & 9). This indicated that the prepared CuO/La₂O₃, CuO/Gd₂O₃ and CuO/La₂O₃/Gd₂O₃ nanocatalysts had high purity.

3.4. XPS analysis

The XPS analysis was used to find out the binding energies which are responsible for the La (3d), Gd (3d), Cu (2p) and O (1s) of CuO/La₂O₃, CuO/Gd₂O₃ and CuO/La₂O₃/Gd₂O₃ NCs (Fig. 10 a–c). The two strong fitting peaks are around at 959.4 and 934.4 eV for Cu²⁺ 2p_{1/2} and 2p_{3/2} peaks, which are much closer to the earlier report [20]. Two characteristic doublet peaks of La 3d are corresponding to binding energies of 827.7 eV and 870.2 eV for the La 3d_{5/2} and La 3d_{3/2} levels. Further, the

oxygen (O 1s) which is available in the nanocomposites was shows the binding energy at 531.6 eV. From the observed Fig. 10a, it is clear that the lanthanum bonded to oxygen was located at the sample surface for CuO/La₂O₃ NCs. Fig. 10b reveals the binding energy at 1147.9 and 1212 eV were originating to the Gd 3d_{3/2} and Gd 3d_{5/2} as well as oxygen (O 1 s) peak was attributed at binding energy of 544.4 eV, respectively for CuO/Gd₂O₃ NCs. The as respective peaks of Cu²⁺, La 3d, Gd 3d and O 1s are presents in CuO/La₂O₃/Gd₂O₃ NCs (Fig. 10c). The obtained results were clearly demonstrates that the observed intensity peaks of the CuO/La₂O₃/Gd₂O₃ NCs has been increased owing to the removing of impurities.

3.5. Catalytic activity of 4-nitrophenol and methylene blue for CuO/La₂O₃, CuO/Gd₂O₃ and CuO/La₂O₃/Gd₂O₃ nanocatalysts

In catalytic experiments, the degradation of 4-NP and MB dyes from CuO/La₂O₃, CuO/Gd₂O₃ and CuO/La₂O₃/Gd₂O₃nanocatalysts in the presence of NaBH₄can be monitored by UV–Visible spectrometer (wavelength 400–800) at various time intervals with respect to room temperature condition as well as the maximum intensity peaks were observed at 400 nm for 4-NP and 664 nm for MB, respectively which were shown in Fig. 11(a–c) & Fig. 12(a–c). The reduction rate mechanism of 4-NP and MB had three advantages such as: i) it can be well controlled; ii) the reaction kinetics can be investigated accurately without any difficulty; and iii) it can take place under mild conditions. The reduction rates of 4-NP and MB took much longer time in the presence of NaBH₄ due to their negative charge repulsion between BH₄⁻ ion and dyes [30]. After that, the addition of CuO/La₂O₃, CuO/Gd₂O₃ and CuO/La₂O₃/Gd₂O₃ nanocatalysts (2 mg) were added separately in

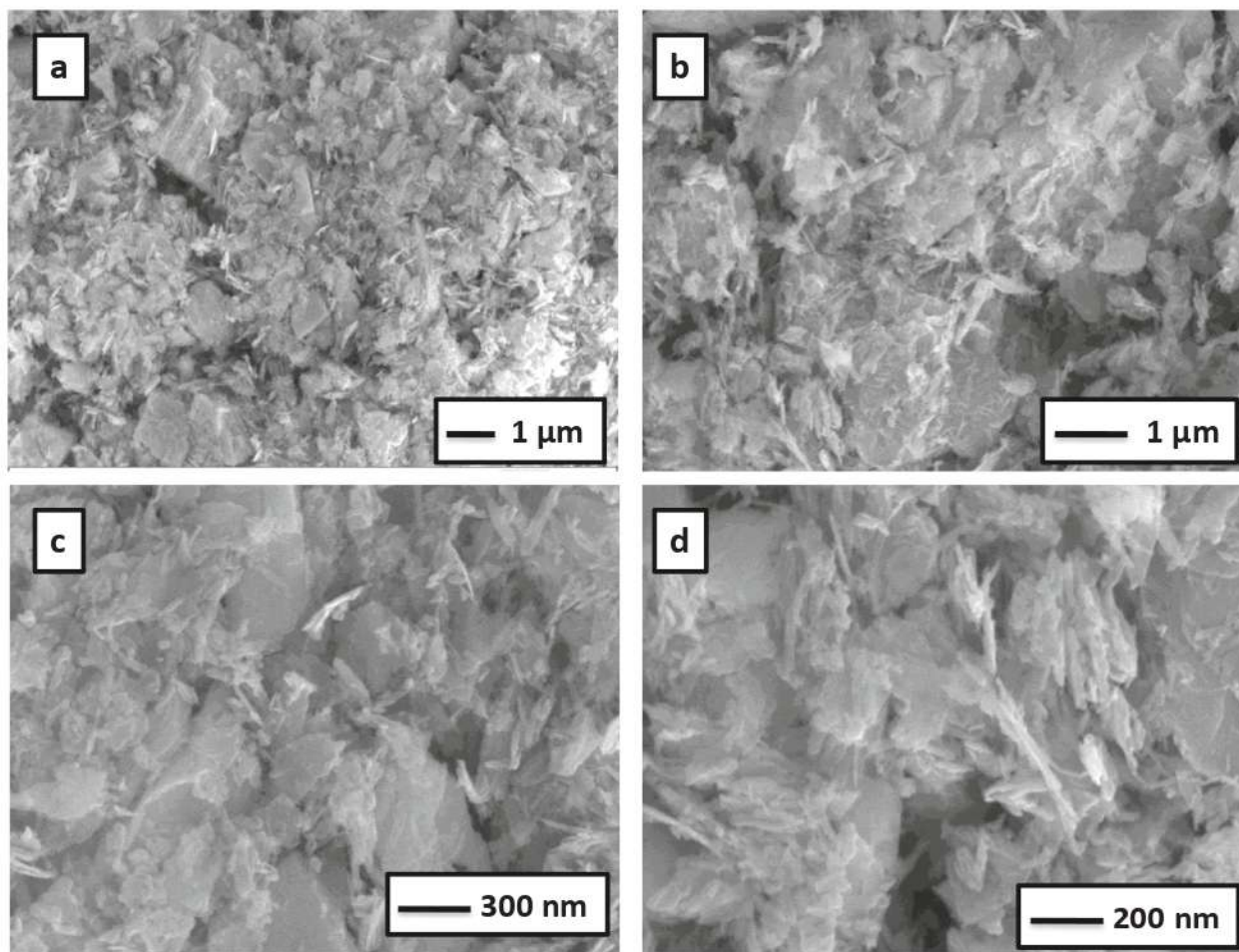


Fig. 6. Different magnification FESEM images of (a-d) CuO/Gd₂O₃ NCs.

the solution of 4-NP and MB in the presence of NaBH₄. In this process, reduction in progress took place by transmission of electron from BH₄⁻ to dyes molecules (4-NP and MB) through catalytic surface of the CuO/La₂O₃, CuO/Gd₂O₃ and CuO/La₂O₃/Gd₂O₃NCs. Hence, the reduction rate for 4-NP was very fast due to transformation of 4-NP into 4-AP along with maximum intensity peak at 400 nm just in 210 sec, which indicated the change of deep yellow color solution (4-NP) totally into colorless solution (4-AP). From the Fig. 11(a), the new absorbance peak arose at 305 nm owing to their conversion of 4-NP into 4-AP, was confirmed with previous reports [31]. The reduction of MB took place very quick due to transformation of MB into Leuco methylene blue (LMB) along with higher intensity peak at 664 nm gradually reduced in 10 min. This indicated the change of blue color solution (MB) into colorless solution (LMB). The probable reduction mechanism of 4-NP & MB with nanocatalysts was revealed in Figs. 13 and 14. During the catalytic activity, the electron transfer occurred between of dyes and NaBH₄ indicated that 4-NP and MB dyes acted as acceptor and NaBH₄ acted as donor [12]. The Fig. 11 (d) and 12 (d) showed the graph of Ct/C₀ versus time (t) for the degradation of 4-NP and MB for CuO/La₂O₃, CuO/Gd₂O₃ and CuO/La₂O₃/Gd₂O₃NCs. The conversion percentage (R) of 4-NP to 4-AP and MB to LMB was calculated by using the following relation

$$R = [(C_0 - C_t)/C_0] \times 100\%$$

where C₀ & C_t are the opening concentrations of 4-NP and MB. The plotted degradation efficiency of dyes by CuO/La₂O₃, CuO/Gd₂O₃ and

CuO/La₂O₃/Gd₂O₃NCs was found to be 86.53%, 91.64% and 93.82% for 4-NP and 72.84%, 80.56% and 87.95% for MB as shown in the Fig. 11 (e) and 12 (e). The rate constants of the developed materials were estimated by pseudo-first-order kinetics reduction of dyes [12]. The kinetics reaction were investigated via following equation,

$$\ln(C_t/C_0) = kt$$

where (k) denote the rate constant with time (t), C₀ and C_t are represents to the primary and ending concentration of 4-NP and MB. The Fig. 11 (f) and 12 (f) showed the variation of ln C_t/C₀ with time. From the observed linear slope value, the rate constant (k) of CuO/La₂O₃, CuO/Gd₂O₃ and CuO/La₂O₃/Gd₂O₃ NCs were found to be $9.27 \times 10^{-3} \text{ s}^{-1}$, $11.9 \times 10^{-3} \text{ s}^{-1}$ and $12.43 \times 10^{-3} \text{ s}^{-1}$ for 4-NP and $17.035 \times 10^{-3} \text{ s}^{-1}$, $19.99 \times 10^{-3} \text{ s}^{-1}$ and $22.81 \times 10^{-3} \text{ s}^{-1}$ for MB respectively. Also, the calculated (R²) values of CuO/La₂O₃, CuO/Gd₂O₃ and CuO/La₂O₃/Gd₂O₃ NCs were found to be 0.9406, 0.9764 and 0.9828 for 4-NP and 0.9252, 0.9454 and 0.9572 for MB respectively. From the results, the rate of constant was higher when compared with different metal oxides composites as catalyst. Rate of reaction of 4-NP and MB were previously reported in Table 1 & Table 2.

3.6. Catalyst recyclability

In industrial applications, recycling of the catalyst was act as a major role. To investigate its reusability, the as prepared CuO/La₂O₃, CuO/

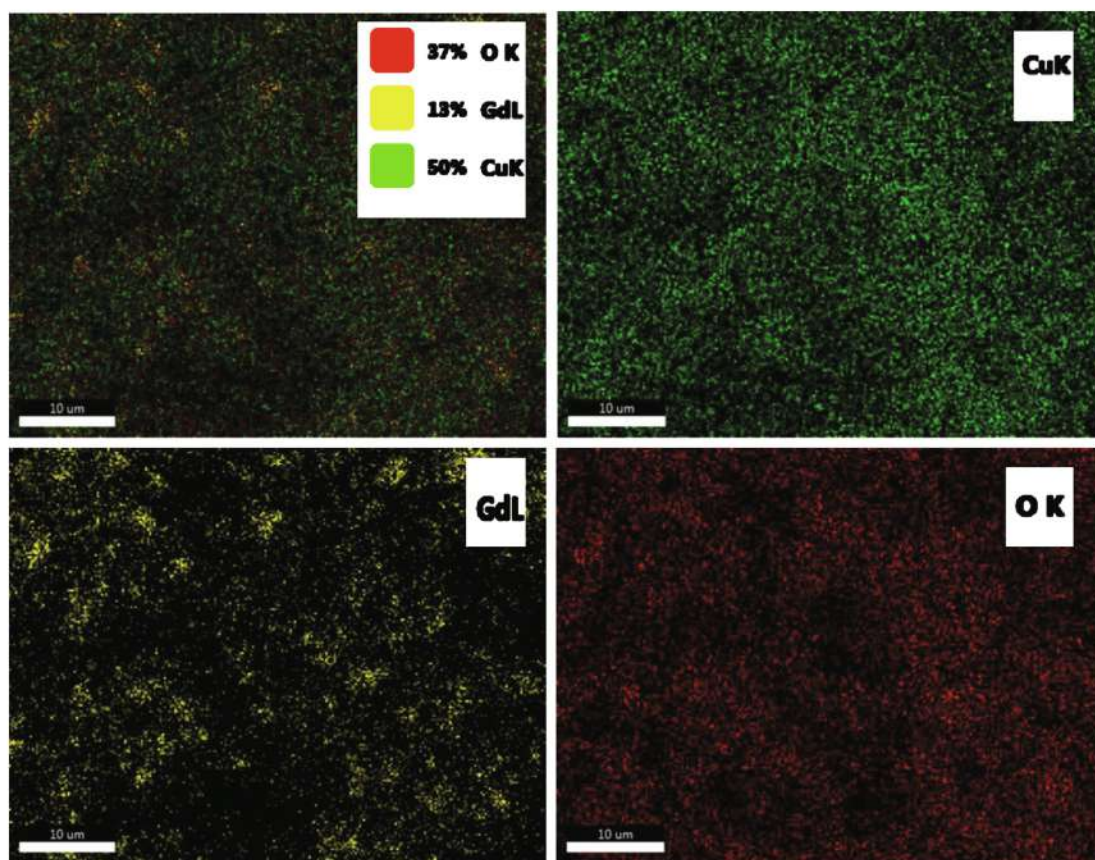


Fig. 7. Elemental color mapping images of CuO/Gd₂O₃ NCs.

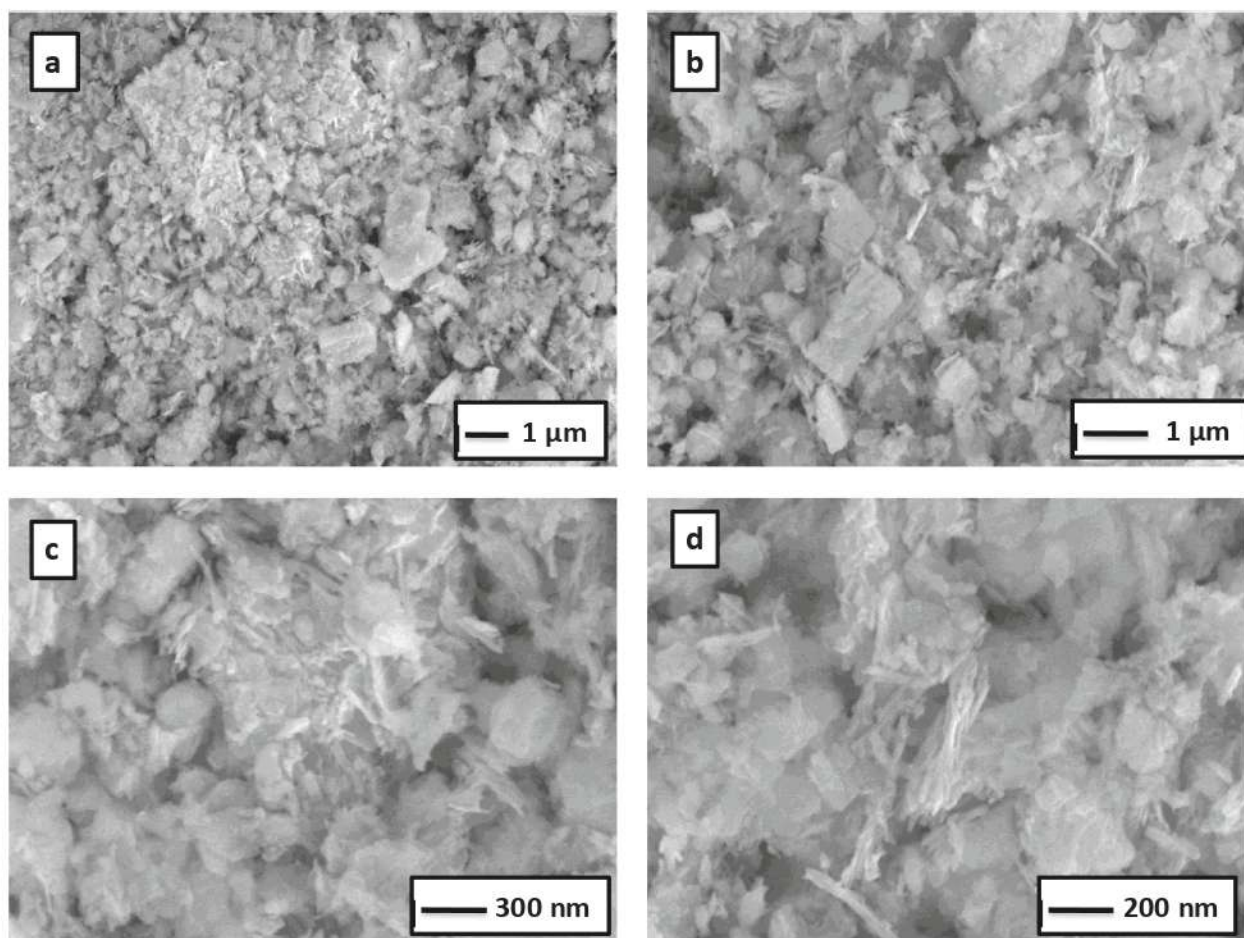


Fig. 8. Different magnification FESEM images of (a-d) CuO/La₂O₃/Gd₂O₃ NCs.

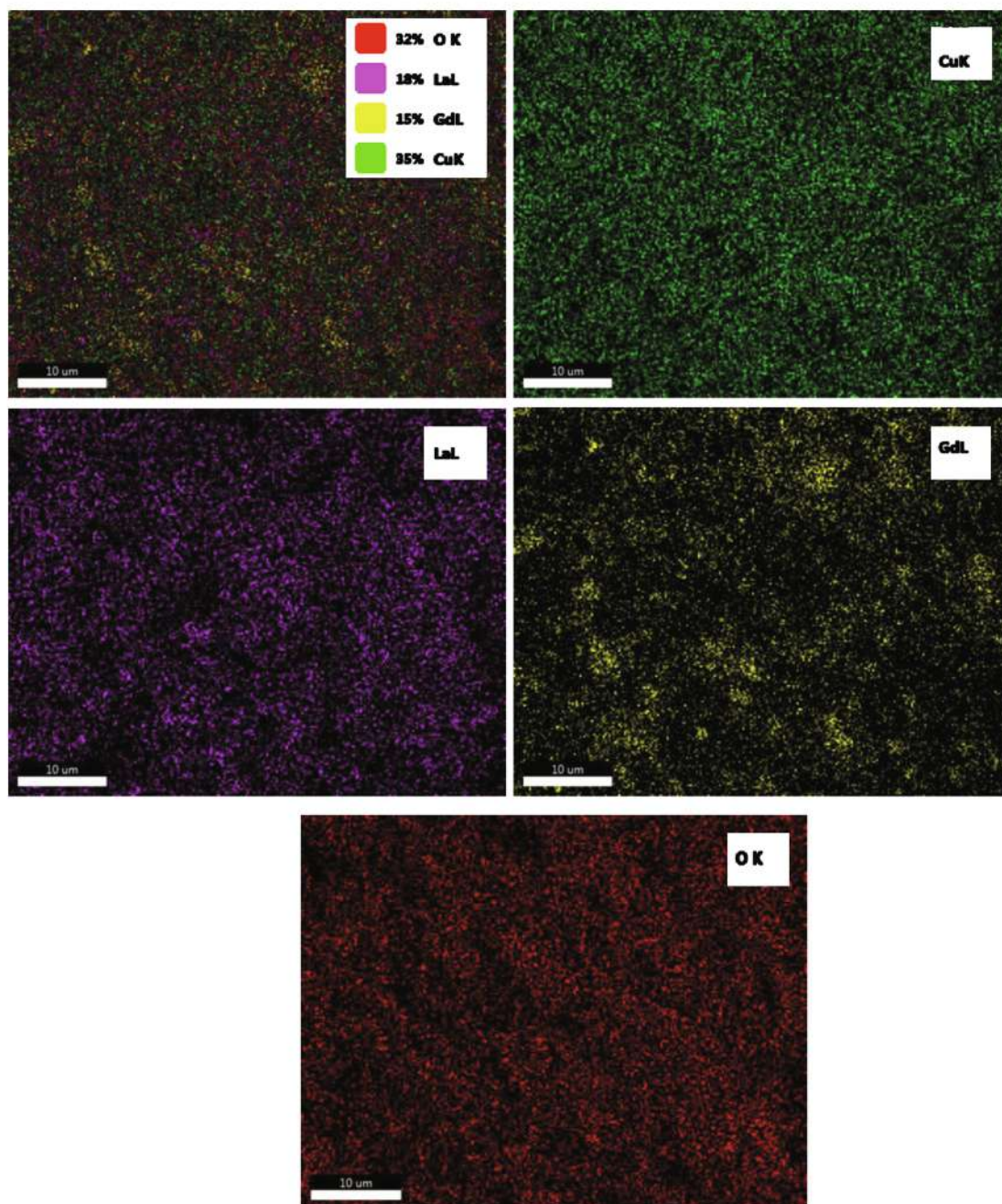


Fig. 9. Elemental color mapping images of CuO/La₂O₃/Gd₂O₃ NCs.

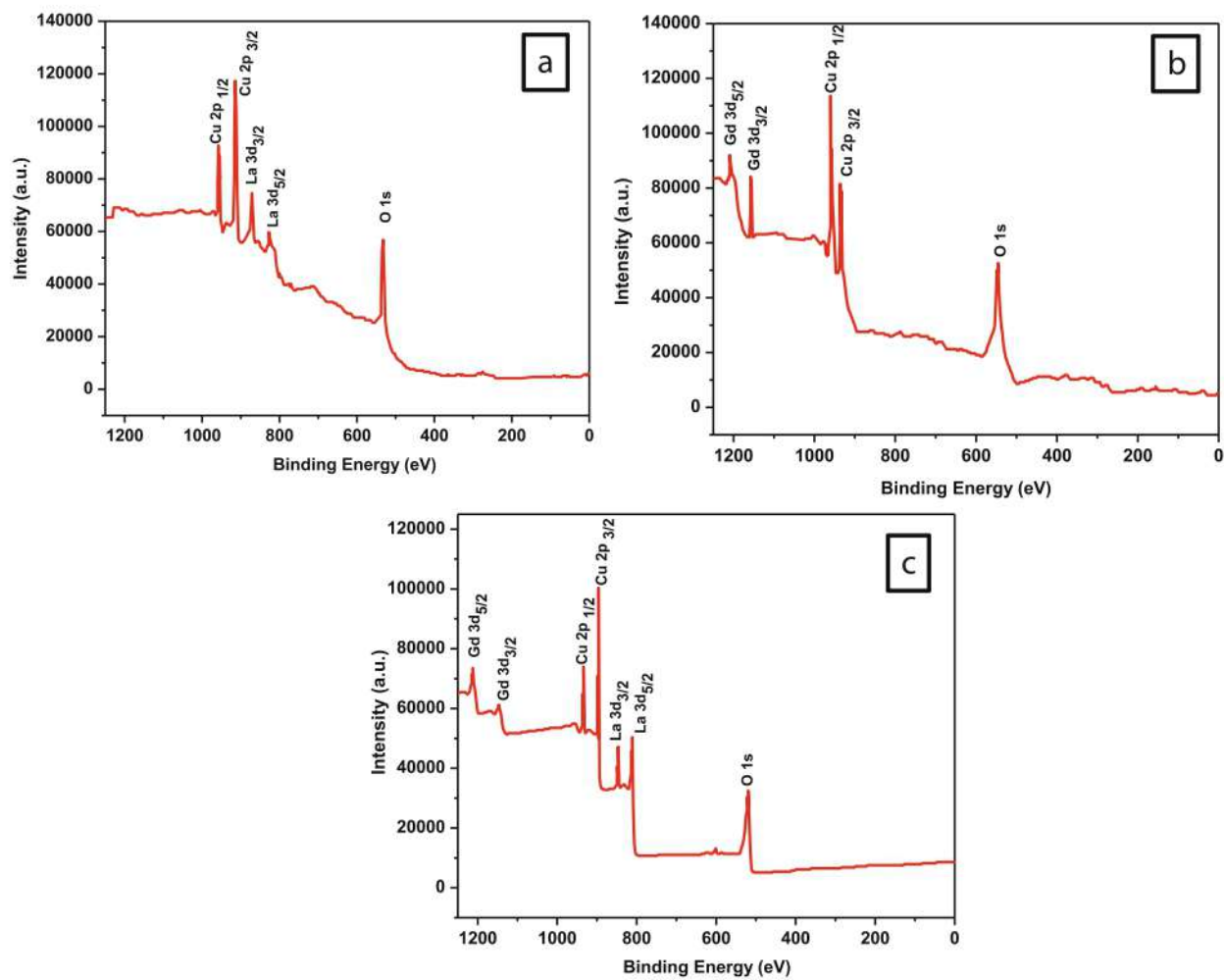


Fig. 10. XPS spectra of (a) CuO/La₂O₃, (b) CuO/Gd₂O₃ and (c) CuO/La₂O₃/Gd₂O₃ NCs.

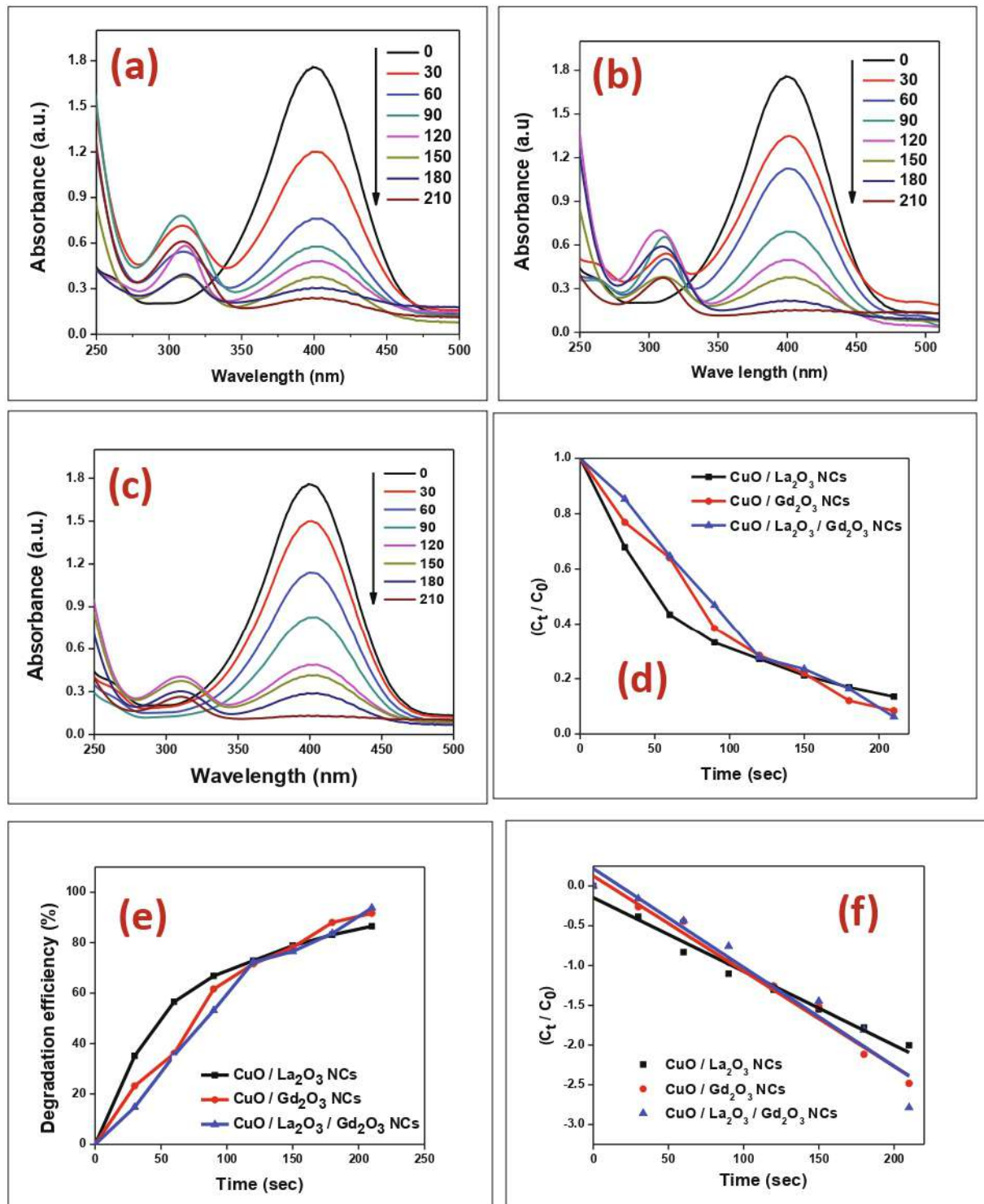


Fig. 11. Time-dependent UV-Vis absorption spectra for the reduction of 4-NP by (a) CuO/La₂O₃, (b) CuO/Gd₂O₃ and (c) CuO/La₂O₃/Gd₂O₃ NCs, (d) Plot of C_t/C₀ versus reaction time (sec), (e) Degradation efficiency (%) versus reaction time (sec) and (f) ln(C_t/C₀) versus reaction time (sec).

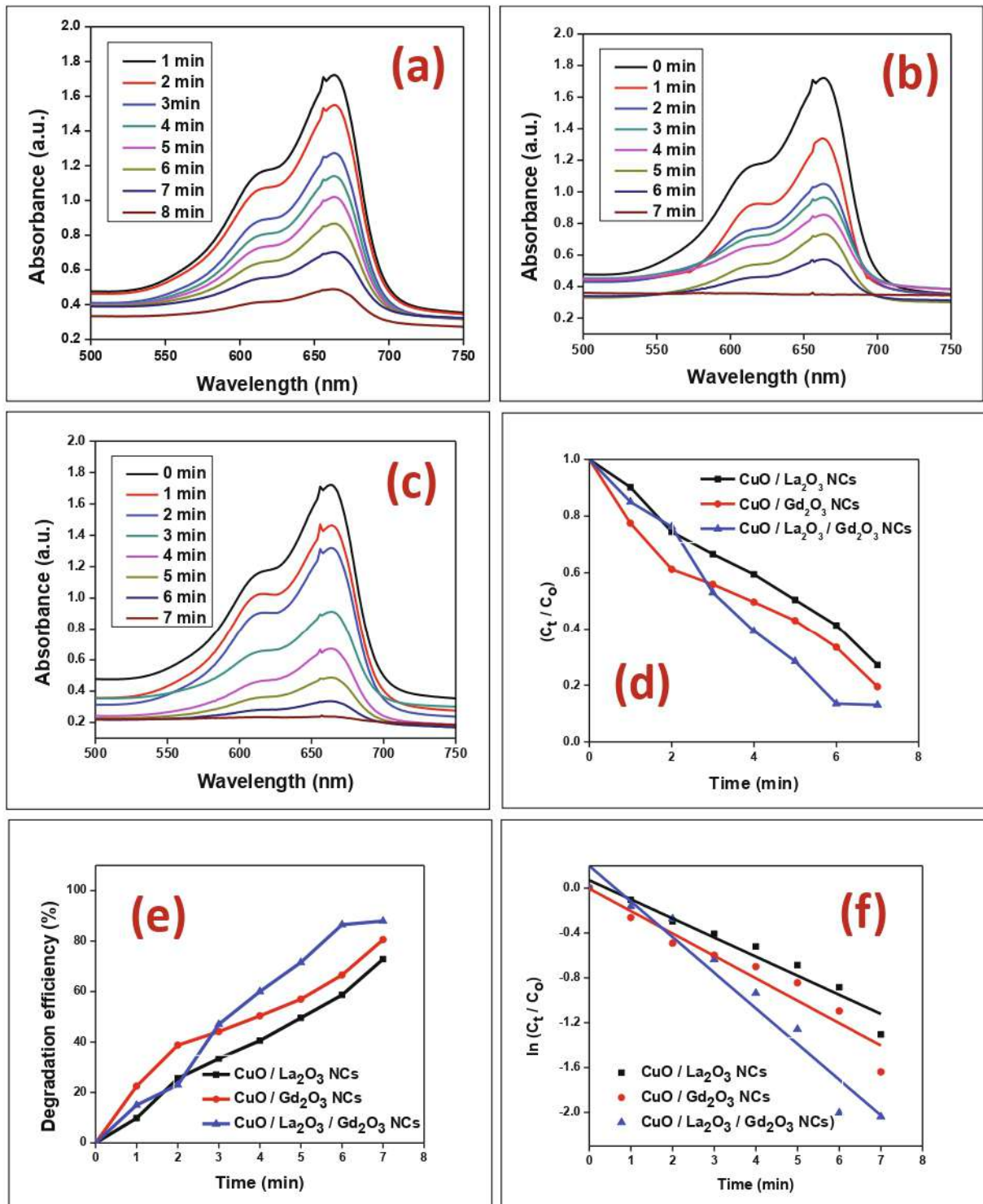


Fig. 12. Time-dependent UV-Vis absorption spectra for the reduction of MB (a) CuO/La₂O₃, (b) CuO/Gd₂O₃ and (c) CuO/La₂O₃/Gd₂O₃ NCs, (d) Plot of C_t/C₀ versus reaction time (sec), (e) Degradation efficiency (%) versus reaction time (sec) and (f) ln (C_t/C₀) versus reaction time (sec).

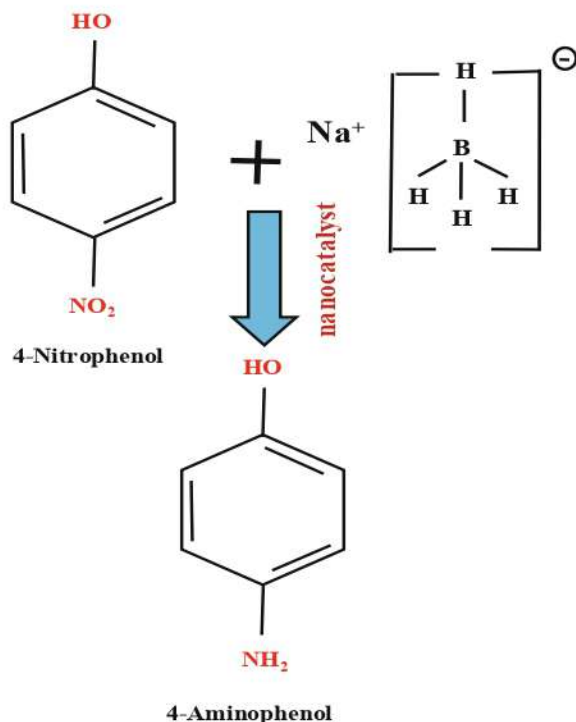


Fig. 13. Possible reduction mechanism of 4-Nitrophenol into 4-Aminophenol in presence of CuO/La₂O₃, CuO/Gd₂O₃ and CuO/La₂O₃/Gd₂O₃ nanocatalysts.

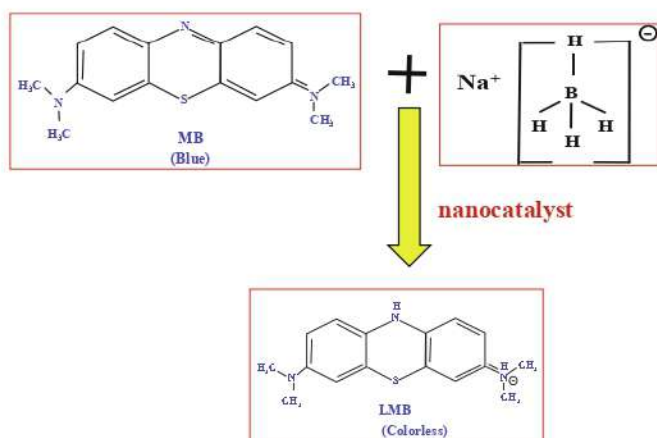


Fig. 14. Possible reduction mechanism of Methylene Blue into Leuco methylene blue in presence of CuO/La₂O₃, CuO/Gd₂O₃ and CuO/La₂O₃/Gd₂O₃ nanocatalysts. (For interpretation of the references to color in this figure legend, the reader is referred to the web version of this article.)

Gd₂O₃ and CuO/La₂O₃/Gd₂O₃ NCs were achieving consecutive catalytic tests (Fig. 15 a-c). After that, the used CuO/La₂O₃, CuO/Gd₂O₃ and CuO/La₂O₃/Gd₂O₃ nanocatalysts were purified by DD water and heated at room temperature. In the initial three consecutive rounds, CuO/La₂O₃/Gd₂O₃ NCs had high recyclability than CuO/La₂O₃ and CuO/Gd₂O₃ NCs. After three consecutive rounds, degradation efficiency was quickly reduced due to the fact that the organic dye molecules were extremely adsorbed from the surface area [31]. Recyclability efficiencies of CuO/La₂O₃, CuO/Gd₂O₃ and CuO/La₂O₃/Gd₂O₃ NCs were shown in Fig. 15 d.

Table 1

Comparison catalytic activity of previous reported catalyst in the degradation of 4-NP.

Catalyst	Quantity (mg)	4-NP (M)	Rate constant (k) (S ⁻¹)	Ref.
CuO	1	1 ml of 10 mM	0.2612 (min ⁻¹)	[32]
Au/Fe ₂ O ₃	2	10 mM	6.312 × 10 ⁻³	[33]
Au/TiO ₂	5	5 mM	0.6326 (min ⁻¹)	[34]
CuO/TiO ₂ /ZnO	5	4 ml	8.1310 ⁻³ s ⁻¹	[31]
CuO/La ₂ O ₃	2	0.2 mM	9.27 × 10 ⁻³ s ⁻¹	Present work
CuO/Gd ₂ O ₃	2	0.2 mM	11.9 × 10 ⁻³ s ⁻¹	Present work
CuO/La ₂ O ₃ /Gd ₂ O ₃	2	0.2 mM	12.43 × 10 ⁻³ s ⁻¹	Present work

Table 2

Comparison catalytic activity of previous reported catalyst in the degradation of MB.

Catalyst	Quantity (mg)	MB (M)	Rate constant (k) (S ⁻¹)	Ref.
CuO	1	1 ml of 10 mM	4.196 × 10 ⁻³	[32]
CuOS	10	6.3 × 10 ⁻⁵	6.98 × 10 ⁻³	[35]
Cu/MgO	10	3.1 × 10 ⁻⁵	5.69 × 10 ⁻³	[36]
CuO/TiO ₂ /ZnO	5	4 ml	1.35 × 10 ⁻³	[31]
CuO/La ₂ O ₃	2	0.2 mM	17.03 × 10 ⁻³	Present work
CuO/Gd ₂ O ₃	2	0.2 mM	19.99 × 10 ⁻³	Present work
CuO/La ₂ O ₃ /Gd ₂ O ₃	2	0.2 mM	22.81 × 10 ⁻³ s ⁻¹	Present work

4. Conclusion

The as developed CuO/La₂O₃, CuO/Gd₂O₃ and CuO/La₂O₃/Gd₂O₃ NCs were fabricated by two-step synthesis approach. In composite materials, CuO prepared by co-precipitation and consequently CuO/La₂O₃, CuO/Gd₂O₃ and CuO/La₂O₃/Gd₂O₃ NCs were synthesized from hydrothermal approach for catalytic activity. The flakes like morphologies were observed from the prepared composite materials and size was found to be ~200 nm. Also, individual atoms were consistently allocated with a mixed ratio during the composite matrix of CuO/La₂O₃, CuO/Gd₂O₃ and CuO/La₂O₃/Gd₂O₃ NCs which were primarily demonstrated by the EDAX color mapping. In catalytic studies, the efficiency of dye degradation and rate constant of CuO/La₂O₃/Gd₂O₃ NCs were high for both the dyes owing to their separation of charge carrier and high specific surface area. In addition, CuO/La₂O₃/Gd₂O₃ NCs could be easily recovered by centrifugation and reused for the next run of reaction and obvious loss was achieved after five successive rounds by their dye molecules were enormously adsorbed from the surface area.

Declaration of Competing Interest

The authors declare that they have no known competing financial interests or personal relationships that could have appeared to influence the work reported in this paper.

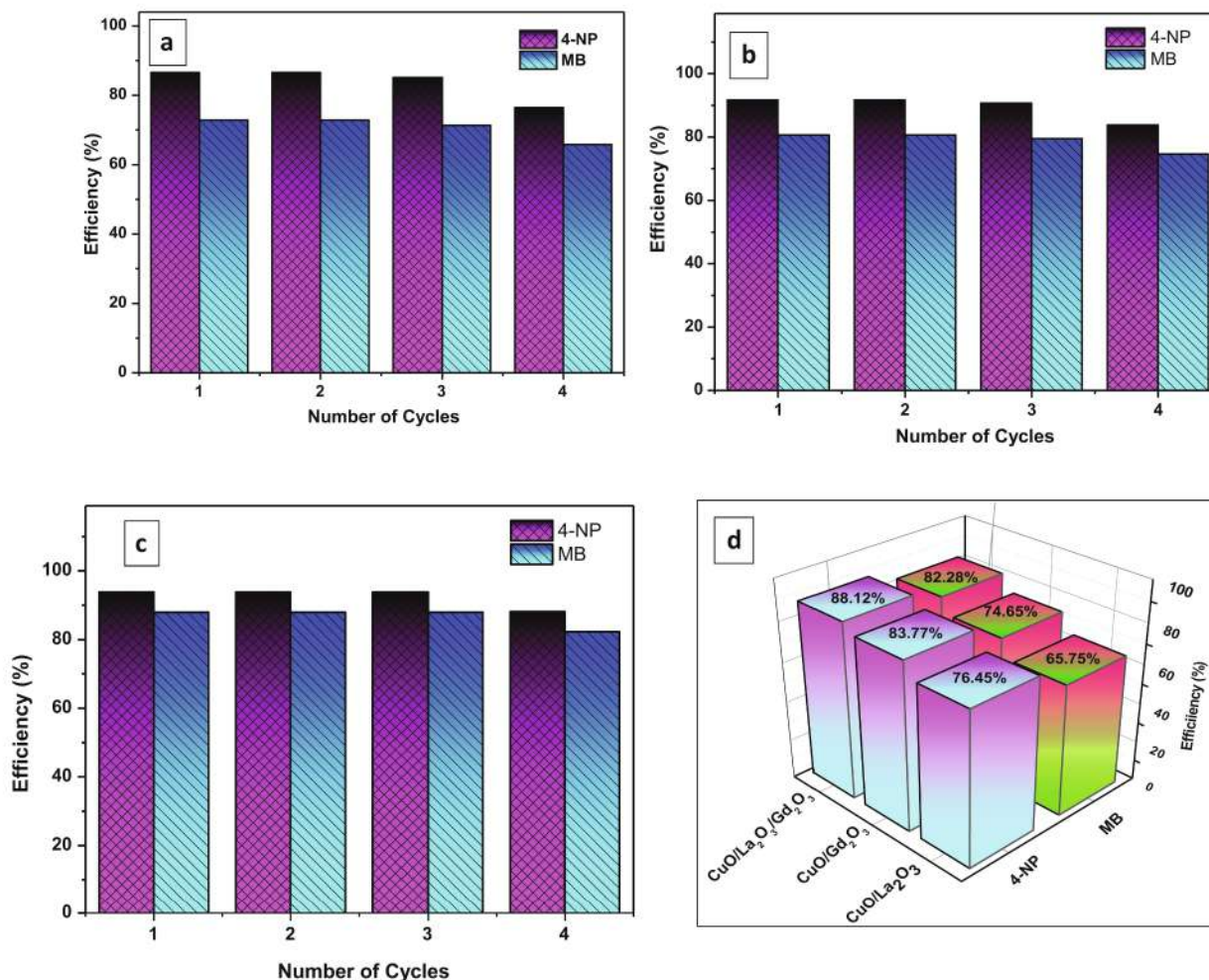


Fig. 15. The recyclability of (a) CuO/La₂O₃, (b) CuO/Gd₂O₃, (c) CuO/La₂O₃/Gd₂O₃ nanocatalysts in the reduction of 4-NB and MB dye solution with NaBH₄ at room temperature and (d) Fourth consecutive round of recyclability efficiency in the reduction of 4-NB and MB organic dyes.

References

- [1] P.A. Owusu, S. Asumadu-Sarkodie, A review of renewable energy sources, sustainability issues and climate change mitigation, *Cogent. Eng.* 3 (2016) 1167990.
- [2] F.K. Higson, Microbial degradation of nitroaromatic compounds, *Adv. Appl. Microbiol.* 37 (1992) 1–19.
- [3] V. Chandrasekaran, S. Chidambaram, M.K. Ganesan, Optical and recyclable photocatalytic properties of silica supported ZnO/Au heterostructures under sun light, *J. Mater. Sci. Mater. Elec.* 29 (2018) 667–673.
- [4] L.G. Da Silva, R. Ruggiero, P.D.M. Gontijo, et al., Adsorption of Brilliant Red 2BE dye from water solutions by a chemically modified sugarcane bagasse lignin, *Chem. Eng. J.* 168 (2011) 620–628.
- [5] A. Dabrowski, P. Podkościelny, Z. Hubicki, M. Barczak, Adsorption of phenolic compounds by activated carbon: a critical review, *Chemosphere* 58 (2005) 1049–1070.
- [6] Y. Fu, T. Viraraghavan, Fungal decolorization of dye wastewaters: a review, *Bioresour. Technol.* 79 (2001) 251–262.
- [7] A.K. Bin, S. Sobera-Madej, Comparison of the advanced oxidation processes (UV, UV/H₂O₂ and O₃) for the removal of antibiotic substances during wastewater treatment, *Ozone: Sci. Eng.* 34 (2012) 136–139.
- [8] A. Srinivasan, T. Viraraghavan, Decolorization of dye wastewaters by biosorbents: a review, *J. Environ. Manage.* 91 (2010) 1915–1929.
- [9] M. Govindaraj, R. Rathinam, C. Sukumar, M. Uthayasankar, S. Pattabhi, Electrochemical oxidation of bisphenol-A from aqueous solution using graphite electrodes, *Environ. Technol.* 34 (2013) 503–511.
- [10] K. Pirkanniemi, M. Sillanpää, Heterogeneous water phase catalysis as an environmental application: a review, *Chemosphere* 48 (2002) 1047–1060.
- [11] P.V. Suraja, Z. Yaakob, N.N. Binitha, M.R. Resmi, P.P. Siliya, Photocatalytic degradation of dye pollutant over Ti and Co doped SBA-15: comparison of activities under visible light, *Chem. Eng. J.* 176 (2011) 265–271.
- [12] A. Sankaran, K. Kumaragur, The novel two step synthesis of CuO/ZnO and CuO/CdO nanocatalysts for enhancement of catalytic activity, *J. Mol. Struct.* 1221 (2020), 128772.
- [13] R. Saranya, R.A. Raj, M.S. AlSalhi, S. Devanesan S, Dependence of catalytic activity of nanocrystalline nickel ferrite on its structural, morphological, optical, and magnetic properties in aerobic oxidation of benzyl alcohol, *J. Supercond. Nov. Magn.* 31 (2018) 1219–1225.
- [14] T. Aditya, J. Jana, N.K. Singh, A. Pal, T. Pal, Remarkable facet selective reduction of 4-nitrophenol by morphologically tailored (111) faceted Cu₂O nanocatalyst, *ACS Omega* 2 (2017) 1968–1984.
- [15] Zhao Jin, Chang Liu, Kun Qi, Xiaoqiang Cui, Photo-reduced Cu/CuO nanoclusters on TiO₂ nanotube arrays as highly efficient and reusable catalyst, *Sci. Rep.* 7 (2017) 1–9.
- [16] R. Gopalakrishnan, B. Loganathan, S. Dinesh, K. Raghu, Strategic green synthesis, characterization and catalytic application to 4-nitrophenol reduction of palladium nanoparticles, *J. Cluster Sci.* 28 (2017) 2123–2131.
- [17] J.F. Corbett, An historical review of the use of dye precursors in the formulation of commercial oxidation hair dyes, *Dyes Pig.* 41 (1999) 127–136.
- [18] C.V. Rode, M.J. Vaidya, R.V. Chaudhari, Synthesis of p-aminophenol by catalytic hydrogenation of nitrobenzene, *Org. Process Res. Dev.* 3 (1999) 465–470.
- [19] G. Wu, X. Liang, L. Zhang, Z. Tang, M.A. Mamun, H. Zhao, X. Su, Fabrication of highly stable metal oxide hollow nanospheres and their catalytic activity toward 4-nitrophenol reduction, *ACS Appl. Mater. Interfaces* 9 (2017) 18207–18214.
- [20] J. Li, C. Liu, Y. Liu, Au/graphene hydrogel: synthesis, characterization and its use for catalytic reduction of 4-nitrophenol, *J. Mater. Chem.* 22 (2012) 8426–8430.
- [21] N. Toshima, T. Yonezawa, Bimetallic nanoparticles-novel materials for chemical and physical applications, *New J. Chem.* 22 (1998) 1179–1201.
- [22] G. Ravi, M. Sarasija, D. Ayodhya, L.S. Kumari, D. Ashok, Facile synthesis, characterization and enhanced catalytic reduction of 4-nitrophenol using NaBH₄ by undoped and Sm³⁺, Gd³⁺, Hf³⁺ doped La₂O₃ nanoparticles, *Nano Converg.* 6 (2019) 12.
- [23] G.K. Das, B.C. Heng, S.C. Ng, T. White, J.S.C. Loo, L. D'Silva, Parasuraman Padmanabhan, Kishore K. Bhakoo, Subramanian Tamil Selvan, and Timothy Thatth Yang Tan, Gadolinium Oxide Ultrathin Nanorods as Multimodal Contrast Agents for Optical and Magnetic Resonance Imaging, *Langmuir* 26 (2010) 8959–8965.

- [24] A. Sankaran, K. Kumaraguru, B. Balraj, Structural and optical behavior of CuO/Ag and CuO/Ag/Au nanocatalysts synthesized via a novel two step synthesis approach for enhancement of catalytic activity, *J. Inorg. Organomet. Polym.* (2020), <https://doi.org/10.1007/s10904-020-01655-x>.
- [25] N. Senthil Kumar, M. Ganapathy, S. Sharmila, M. Shankar, M. Vimalan, I. Vetha Potheher, ZnO/Ni(OH)₂ core-shell nanoparticles: Synthesis, optical, electrical and photoacoustic property analysis, *J. Alloys Comp.* 703 (2017) 624–632.
- [26] E. Nandhakumar, P. Priya, R. Rajeswari, V. Aravindhan, A. Sasikumar, N. Senthilkumar, Studies on structural, optical and thermal properties of Fe₃O₄ (NR)/ZrO₂ CSNCs synthesized via green approach for Photodegradation applications, *Res. Chem. Intermed.* 45 (2019) 2657–2671.
- [27] N. Senthilkumar, M. Ganapathy, A. Arulraj, M. Meena, M. Vimalan, I. VethaPotheher, Two step synthesis of ZnO/Ag and ZnO/Au Core/Shell Nanocomposites: Structural, Optical and Electrical property Analysis, *J. Alloys Comp.* 750 (2018) 171–181.
- [28] N. Senthilkumar, A. Arulraj, E. Nandhakumar, M. Ganapathy, M. Vimalan, I. Vetha Potheher, Green mediated synthesis of plasmonic nanoparticle (Ag) for antireflection coating in bare mono silicon solar cell, *J. Mater. Sci: Mater. Electron.* 29 (2018) 12744–12753.
- [29] M. John Abel, A. Pramothkumar, N. Senthilkumar, K. Jothivenkatachalam, P. Fermi Hilbert Inbaraj, J. Joseph prince, Flake-like CuMn₂O₄ nanoparticles synthesized via co-precipitation method for photocatalytic activity, *Phys. B*, 572 (2019) 117–124102.
- [30] X. Liu, Q. Han, Y. Zhang, X. Wang, S. Cai, C. Wang, R. Yang, Green and facile synthesis of Rh/GO nanocomposites for high catalytic performance, *Appl. Surf. Sci.* 471 (2019) 929–934.
- [31] C. Mathalai Sundaram, S. Kalpana, S. Rafi Ahamed, V. Sivaganesan, E. Nandhakumar, Studies on the catalytic activity of CuO/TiO₂/ZnO ternary nanocomposites prepared via one step hydrothermal green approach, *Mater. Res. Exp.* 6 (2019), 125043.
- [32] N. Sreeju, Alex Rufus, Daizy Philip, Studies on catalytic degradation of organic pollutants and anti-bacterial property using biosynthesized CuO nanostructures, *J. Mol. Liq.* 242 (2017) 690–700.
- [33] F.H. Lin, R.A. Doong, Bifunctional Au-Fe₃O₄ heterostructures for magnetically recyclable catalysis of nitrophenol reduction, *J. Phys. Chem. C* 115 (2011) 6591–6598.
- [34] Z.H. Ren, H.T. Li, Q. Gao, H. Wang, B. Han, K.S. Xia, C.G. Zhou, Au nanoparticles embedded on urchin-like TiO₂ nanosphere: an efficient catalyst for dyes degradation and 4 nitrophenol reduction, *Mater. Des.* 121 (2017) 167–175.
- [35] A.K. Abay, X. Chen, D.H. Kuo, A highly efficient noble metal free copper nickel oxysulfide nanoparticles for catalytic reductions of 4-nitrophenol, Methyl blue, and Rhodamine-B organic pollutants, *New J. Chem.* 41 (2017) 5628–5638.
- [36] M. Nasrollahzadeh, Z. Issaabadia, S.M. Sajadi, Green synthesis of a Cu/MgO nanocomposite by *Cassythafiliformis* L. extract and investigation of its catalytic activity in the reduction of methylene blue, congo red and nitro compounds in aqueous media, *RSC Adv.* 8 (2018) 3723.



Structural and Optical Behavior of CuO/Ag and CuO/Ag/Au Nanocatalysts Synthesized Via a Novel Two Step Synthesis Approach for Enhancement of Catalytic Activity

A. Sankaran¹ · K. Kumaraguru² · B. Balraj³

Received: 14 May 2020 / Accepted: 30 June 2020
© Springer Science+Business Media, LLC, part of Springer Nature 2020

Abstract

In this paper, a facile two-step process of CuO/Ag and CuO/Ag/Au nanocomposites (NCs) were fabricated for the first time. The Powder X-ray Diffraction (PXRD) pattern revealed the existence of single-phase monoclinic structure of CuO and Face Centered Cubic (FCC) phase of Ag, Au and no other external phase impurities were observed from the prepared materials. In the photoluminescence (PL) studies, charge carrier trapping and fate of electron–hole pairs in CuO/Ag and CuO/Ag/Au NCs were investigated. The band-gap values of prepared CuO/Ag and CuO/Ag/Au NCs were calculated via UV–Visible Spectroscopy using Tauc’s relation and found to be 2.3 eV and 2.1 eV, respectively. The flake-like morphologies were observed from the prepared CuO/Ag and CuO/Ag/Au NCs using FESEM analysis. The as-prepared CuO/Ag and CuO/Ag/Au NCs were evaluated by catalytic performances using the catalytic reduction of 4-nitrophenol (4-NP) to 4-aminophenol (4-AP) and Methylene blue (MB) to Leuco Methylene blue (LMB) with the presence of NaBH₄ in aqueous solution. Thus the result showed the synergistic effects between Ag, Au and CuO in CuO/Ag/Au NCs acted as suitable support to elevate the catalytic performance of M/CuO materials, which may be used as a potential application in industrial production.

Keywords CuO/Ag · CuO/Ag/Au NCs · Two-step process · Catalytic activity

1 Introduction

In current decade, nitroaromatic compounds are environmentally redundant materials due to outcome of the dyes from industries which are widely used in pesticides, plastics and explosives chemicals [1]. Among various nitroaromatic compounds, 4-nitrophenol (4-NP) is an example of toxic substance that exists in industrial effluents and classified as precedence pollutant by the US Environmental Protection Agency [2]. Therefore, environment friendly technique has established to remove them from waste water is the direct

reduction of 4-NP in the existence of NaBH₄ and a catalyst to 4-aminophenol (4-AP), which is one of the most valuable intermediate for antipyretic drug, manufacture of analgesic and paint industry and also can be used as the corrosion inhibitor, photographic developer, lubricant additive, anti-corrosion and hair-dyeing agent [3–6]. The NaBH₄ is the important reducing agent for catalytic activity owing to its several advantages like easy to work at the experimental condition, safe to handle, rapid reduction, no pressure apparatus requirement and good selectivity in the reduction of nitrocompounds [7].

In the past two decades, heterostructured nanomaterials are having more attention in the area of catalysis due to their numerous functionalities and outstanding catalytic activity, selectivity and stability over monometallic nanomaterials [8]. Therefore, metal incorporated metal oxide nanostructured particles have drawn particular attention in catalytic applications due to their flexible catalytic activities, electronic properties and high surface areas [9]. Hence in the present investigation, CuO/Ag and CuO/Ag/Au nanocomposites materials were synthesized via two step approach for catalytic activity. During the catalytic reduction process, 4-NP is changed into 4-AP

✉ K. Kumaraguru
kumaraguruautt@gmail.com

¹ Department of Marine Engineering, Mohamed Sathak Engineering College, Kilakarai 623806, India

² Department of Petrochemical Technology, University College of Engineering, BIT Campus, Anna University, Tiruchirappalli 620024, India

³ Department of Electrical and Electronics Engineering, Sri Krishna College of Technology, Coimbatore 641042, India

as well as MB is reduction into LMB by adding NaBH_4 [10]. The semiconductor metal oxides of Cu_2O and CuO nanostructures exhibited excellent catalytic activities owing to their high oxidation–reduction potential values, low cost, non-toxicity, abundant resources and easy way to preparation in various shapes of nanosized dimensions [3]. As well as, silver (Ag) and gold (Au) act as a superior catalyst, which had exposed outstanding catalytic activity in oxygen reduction, hydrogenation and hydrogen production reaction, etc. [11]. In this connection, Zhou et al. has reported mesoporous SnO_2 decorated Ag nanostructures showed attractive multipurpose activity on 4-NP reduction [12]. Akbarzadeh et al. has fabricated Ag and Au decorated on CuO catalysts in situ formation for catalytic reduction of p-nitrophenol to p-aminophenol [13]. Guo et al. has developed core–shell structure of $\text{Cu}_2\text{O}/\text{Au}$ composites via a facile additive-assisted complex-precursor solution method for high catalytic activity toward 4-NP reduction to 4-AP at room temperature [14].

Hence, catalytic activity has been investigated by MB and 4-NP organic dyes from the developed catalyst of CuO/Ag and $\text{CuO}/\text{Ag}/\text{Au}$ NCs via a two-step approach. In synthesis process, CuO NPs were prepared by the co-precipitation approach and subsequently, CuO/Ag and $\text{CuO}/\text{Ag}/\text{Au}$ NCs were developed from the hydrothermal method. The co-precipitation method is one of the most flourishing approaches for synthesizing the materials and this technique is an effective pre-concentration technique for tracing heavy metal ions. As well as, the shape and size of the particles can be controlled by varying pH medium [10]. In addition, hydrothermal approach was used for develop the nanomaterials owing to their narrow crystallite size distribution and low aggregation level [15].

2 Experimental Procedure

2.1 Materials for Synthesizing of CuO NPs, CuO/Ag and $\text{CuO}/\text{Ag}/\text{Au}$ NCs

The Copper chloride (CuCl_2), Silver Nitrate $\text{Ag}(\text{NO}_3)$ and Tetrachloroauric acid (HAuCl_4) were used as the precursor material to develop the CuO NPs, CuO/Ag and $\text{CuO}/\text{Ag}/\text{Au}$ NCs. The sodium borohydride (NaBH_4) acted as a reducing agent. In overall experimental studies, Double Distilled (DD) water was used as a solvent. All the chemicals and organic dyes (4-nitrophenol and Methylene blue) were bought from Merck.

2.2 Synthesis Procedure of CuO/Ag and $\text{CuO}/\text{Ag}/\text{Au}$ NCs

As per previous report [10], pure CuO NPs were developed via a co-precipitation approach. To prepare CuO/Ag NCs, 0.1 gm of prepared CuO NPs was added gradually into

50 ml of DD water under sonication (15 min). Subsequently, 0.05 M of CTAB was added into the above-prepared solution under constant stirring process. Later that, 25 ml aqueous solution of 0.02 M of AgNO_3 was added into that solution. Then, 0.1 M of NaBH_4 was added to reduce $\text{Ag}(\text{NO}_3)$ to Ag. After that, the above-prepared solutions were changed into 100 ml of autoclave (Teflon-lined stainless steel) and heated at 140 °C for 12 h. Later, attained samples were collected and washed thoroughly by ethanol and DD water. After the washing process, the obtained material was heated at 90 °C and annealed at 300 °C for 2 h. The same process was followed as $\text{CuO}/\text{Ag}/\text{Ag}$ NCs. But, 25 ml aqueous solution of 0.02 M of AgNO_3 and 0.02 M of HAuCl_4 was added to the CuO and CTAB suspension solution remaining process are same. Finally, CuO/Ag and $\text{CuO}/\text{Ag}/\text{Au}$ NCs were collected for further analytical studies.

2.3 Catalytic Degradation of 4-NP and MB by CuO/Ag and $\text{CuO}/\text{Ag}/\text{Au}$ NCs

Catalytic activity of synthesized CuO/Ag and $\text{CuO}/\text{Ag}/\text{Au}$ NCs was tested for the reduction of 4-NP (1×10^{-3} M) and MB (1×10^{-5} M) solutions, which are added separately into 50 ml of DD water in the presence of NaBH_4 (1×10^{-2} M) as a reducing agent at room temperature. Without presence of nano catalyst, the blank experiment was monitored at a wavelength of 400 nm for 4-NP and 664 nm for MB, respectively. Furthermore, 2 mg of the prepared CuO/Ag and $\text{CuO}/\text{Ag}/\text{Au}$ nanocatalysts were mixed with separately into the above mentioned combination to start the reduction of dyes. At various time intervals, progress in catalytic reduction reaction was monitored by UV–Visible spectrophotometer. In this process, 4-NP and MB convert into 4-AP and LMB.

2.4 Analytical Techniques

The PXRD pattern of synthesized pure CuO/Ag and $\text{CuO}/\text{Ag}/\text{Au}$ NCs were analyzed by the Pro Penalty CAL [Cu-K α radiation (1.5406 Å)] instrument model. The UV–Visible absorption spectra of developed samples were taken from the JASCO V-670 spectrophotometer. From the Zeiss Gemini Ultra-55 instrument model, FESEM and EDAX color mapping analysis were identified.

3 Results and Discussion

3.1 Powder X-ray Diffraction (PXRD) Analysis

The PXRD pattern of CuO/Ag and $\text{CuO}/\text{Ag}/\text{Au}$ NCs were shown in Fig. 1. The primary characteristic peaks at about $2\theta = 32^\circ, 35^\circ, 38^\circ, 48^\circ, 53^\circ, 58^\circ, 61^\circ, 66^\circ, 67^\circ, 72^\circ$ and 75° correspond to the (100), (–111), (111), (–202), (020),

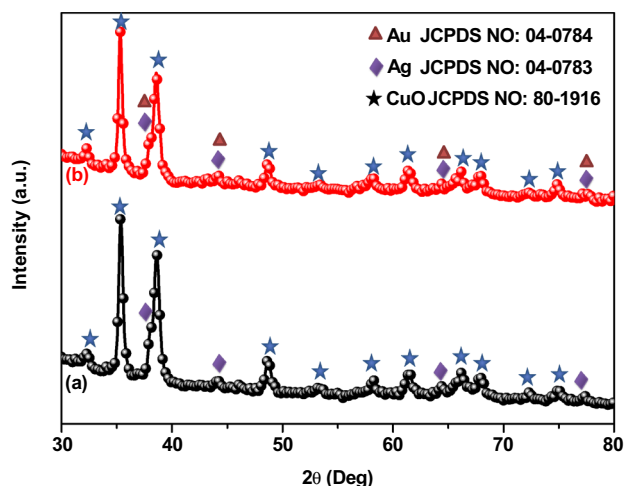


Fig. 1 PXRD pattern of a CuO/Ag NCs and CuO/Ag/Au NCs

(202), (-113), (-311), (220), (311) and (004) lattices in CuO, which were well concurred with the typical characteristic peaks for monoclinic crystal structure of CuO (JCPDS NO: 80-1916) [15]. The secondary characteristic peaks for Ag and Au NPs at 38° , 44° , 64° and 77° which belong to the Face Centered Cubic (FCC) phase of Ag (JCPDS no. 04-0783) and Au (JCPDS no. 04-0784) NPs, corresponds to reflection planes of (111), (200) (220) and (311) [16]. By using Scherrer's formula ($D = K\lambda/\beta \cos \theta$), average crystalline size was determined [15–17]. The average crystalline size was achieved to be 42 nm and 48 nm from the prepared material of CuO/Ag and CuO/Ag/Au NCs. The dislocation density (δ) was determined by the CuO/Ag and CuO/Ag/Au NCs. In dislocation density (δ), the crystal imperfection (or) defects present in the sample had been estimated from the following formula [15–17];

$$(\delta = 1/D^2)$$

The dislocation density (δ) was found to be 5.66×10^{-4} and 4.34×10^{-4} respectively for CuO/Ag and CuO/Ag/Au NCs. From the observed PXRD pattern, there were no other impurities present in the prepared material.

3.2 Photoluminescence (PL) Spectrum Analysis

The PL emission spectra had been used to study the effects of Ag and Au on CuO by the properties of immigration and transfer, charge carrier trapping, in addition to understanding the fate of electron–hole pairs in CuO/Ag and CuO/Ag/Au NCs (Fig. 2). The three emission peaks were observed by the PL spectrum. From the spectrum, PL emission peaks at 415 nm (2.98 eV) and 465 nm (2.66 eV) originated by the blue emission of Cu and luminescent excitation of Ag [15]. A green emission peak at 567 nm was attributed owing to

their recombination of photogenerated hole in the valence band with the singly ionized charge state [18]. The PL intensity of the CuO/Ag was decreased by adding Au due to the following reason (i) Radiating plasmon model which means metal nanoparticles with smaller sizes exhibited quenching by the result of small silver and gold coated onto the above surface of CuO. (ii) PL quenching happened due to exchange of electrons from the semiconductor to the metal shells [18]. During the PL measurement, the electrons were stimulated from valence to conduction band in CuO using the excitation light [18]. At the same time, nucleation formation of Ag and Au NPs may be occupy in the defects of the surface, which can trap the photo induced electrons and holes and thereby increase the charge separation in the CuO surface [18]. This was the reason for PL intensity decrement of the CuO/Ag/Au NCs than the CuO/Ag.

3.3 UV–Visible Absorption Spectroscopy

Figure 3 demonstrated UV–Vis absorption spectrum of CuO/Ag and CuO/Ag/Au NCs which was taken by the JASCO V650 instrument. From the figure, it was observed that a stronger absorption peak at 293 nm corresponded to CuO. The absorption peaks at 410 nm and 519 nm were attributed by the Ag and Au peaks [10]. The optical band gap energy (E_g) of CuO/Ag and CuO/Ag/Au NCs had been determined from Tauc's relation given below:

$$(\alpha h\nu)^2 = A (h\nu - E_g)$$

where, A is the transition probability dependent constant, α is the absorption coefficient and $h\nu$ is the incident photon energy and exponent n have values 2, 1/2 for direct and indirect allowed transitions, respectively [19]. The variation of

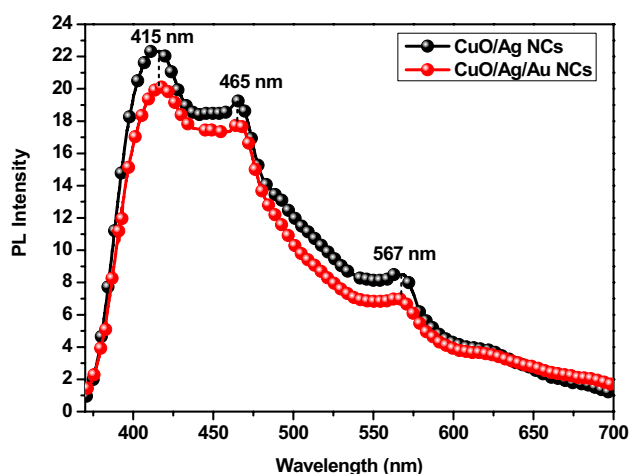


Fig. 2 PL spectrum of a CuO/Ag NCs and CuO/Ag/Au NCs

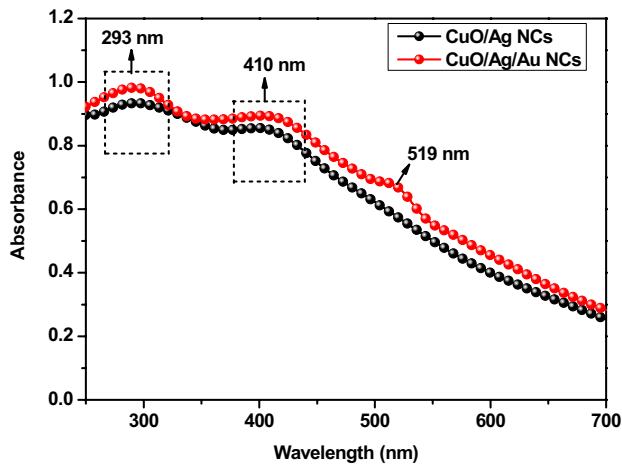


Fig. 3 UV-Visible absorption spectrum of **a** CuO/Ag NCs and CuO/Ag/Au NCs

$(\alpha h\nu)^2$ versus $h\nu$ in the form of Tauc plot was given in the Fig. 4a and b. Band gap energy is estimated by extending linear portion of the curve to $h\nu$ axis. The band gap of the CuO/Ag and CuO/Ag/Au NCs was found to be 2.3 eV and 2.1 eV, respectively.

3.4 Morphological Analysis

The Figs. 5a–d and 6a–d showed different magnification FESEM images of CuO/Ag and CuO/Ag/Au NCs. The attained particles of the prepared CuO/Ag and CuO/Ag/Au NCs were seemed as flake-like morphology. From the observed figure, nanoflakes had a uniform distribution of the particles and average particle size ranged around 50 to

150 nm respectively for the materials of CuO/Ag and CuO/Ag/Au NCs. The color mapping of synthesized materials (Figs. 7 and 8) demonstrated only elements of Cu, Ag, Au and O were present in the CuO/Ag and CuO/Ag/Au NCs and also results showed that there were no other impurities present in the prepared materials.

3.5 The Catalytic Reduction of 4-NP and MB by CuO/Ag and CuO/Ag/Au NCs

In catalytic process, the reduction of 4-NP and MB organic dyes from the catalysts of CuO/Ag and CuO/Ag/Au NCs using NaBH_4 reducing agent, which were monitored by UV-Visible spectrometer at every 30 s with interval of 210 s (s) shown in Fig. 9a and b. The NaBH_4 act as a strong reducing agent as well as low toxic compared to other diverse reducing agents. From UV-Visible spectra, the strong intensity peak was observed at 405 nm which is similar to earlier literature. The reduction rate of 4-NP took long time by without addition of any catalyst due to the repulsive force between negatively charged 4-NP and BH_4^- ions [20]. Then the addition of CuO/Ag and CuO/Ag/Au nanocatalysts (2 mg) in the 4-NP solution with NaBH_4 , the intensity of maximum absorbance peak at 405 nm rapidly reduces (210 s) along with the yellow colour of 4-NP solutions quickly changing to colourless owing to their conversion of 4-NP to 4-AP which revealed a new absorbance peak observed at 306 nm (Fig. 9a and b). This effect was more prominent in the occurrence of $\text{CuO}@ \text{Ag}^0 @ \text{Au}^0$, which gives support of the favorable contribution of Ag^0 and Au^0 incorporation in CuO. This reaction development must be suitable for a key-role of CuO, Ag and Au NPs in progressing the relaying electron transfer from donor BH_4^- ions to the nitro group of acceptor 4-NP [21]. Figure 10a

Fig. 4 Tauc's plot of **a** CuO/Ag NCs and CuO/Ag/Au NCs

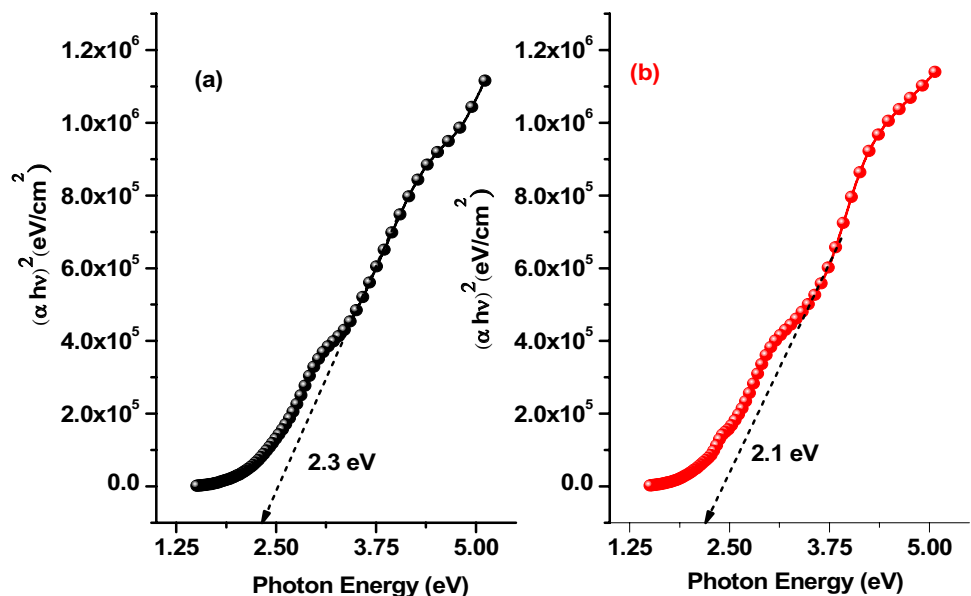


Fig. 5 Different magnification FESEM images of **a–d** CuO/Ag NCs

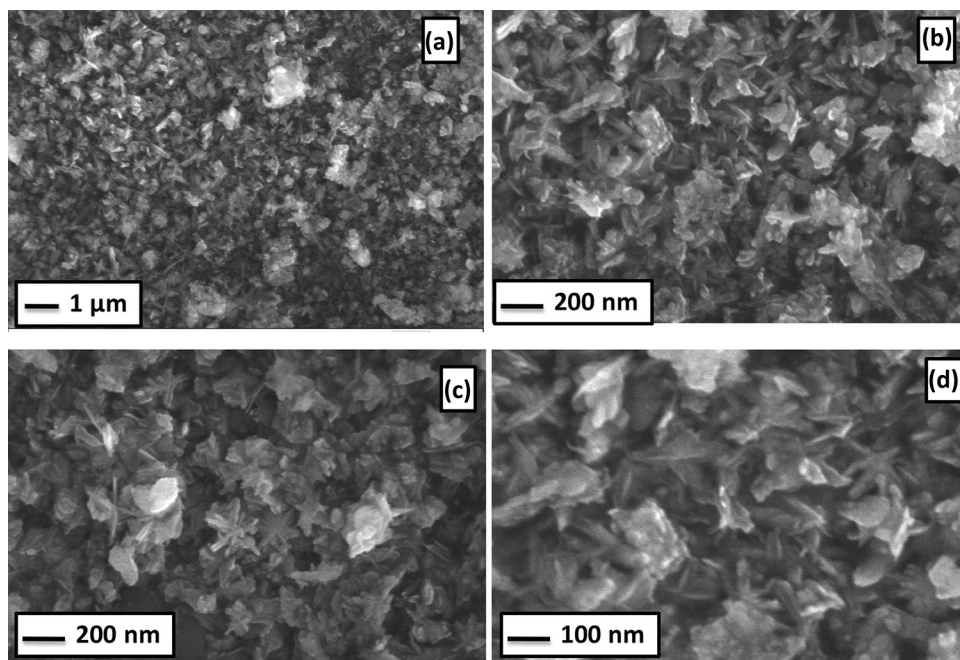
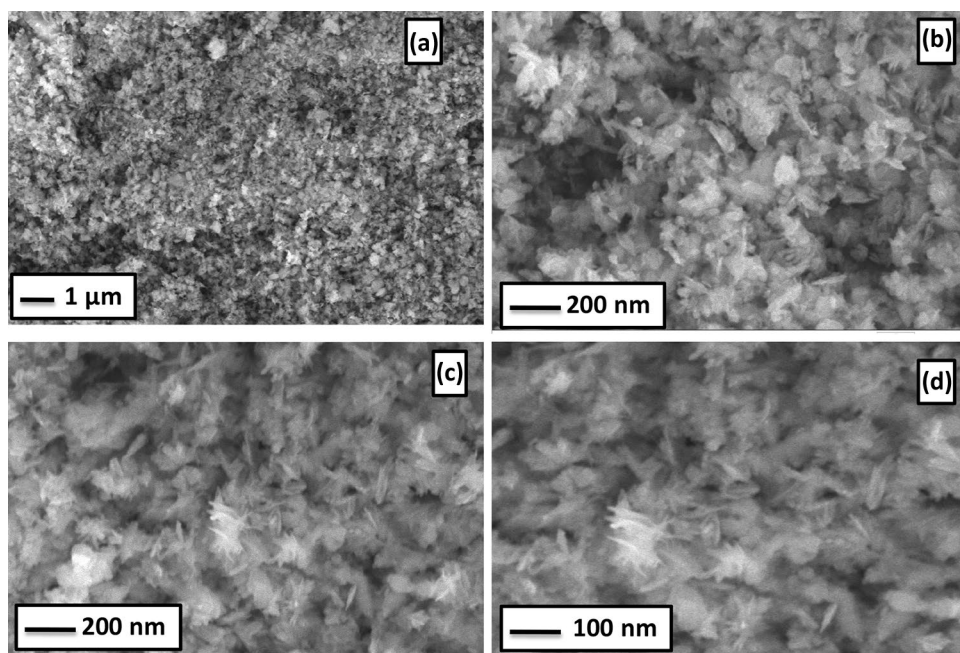


Fig. 6 Different magnification FESEM images of **a–d** CuO/Ag/Au NCs

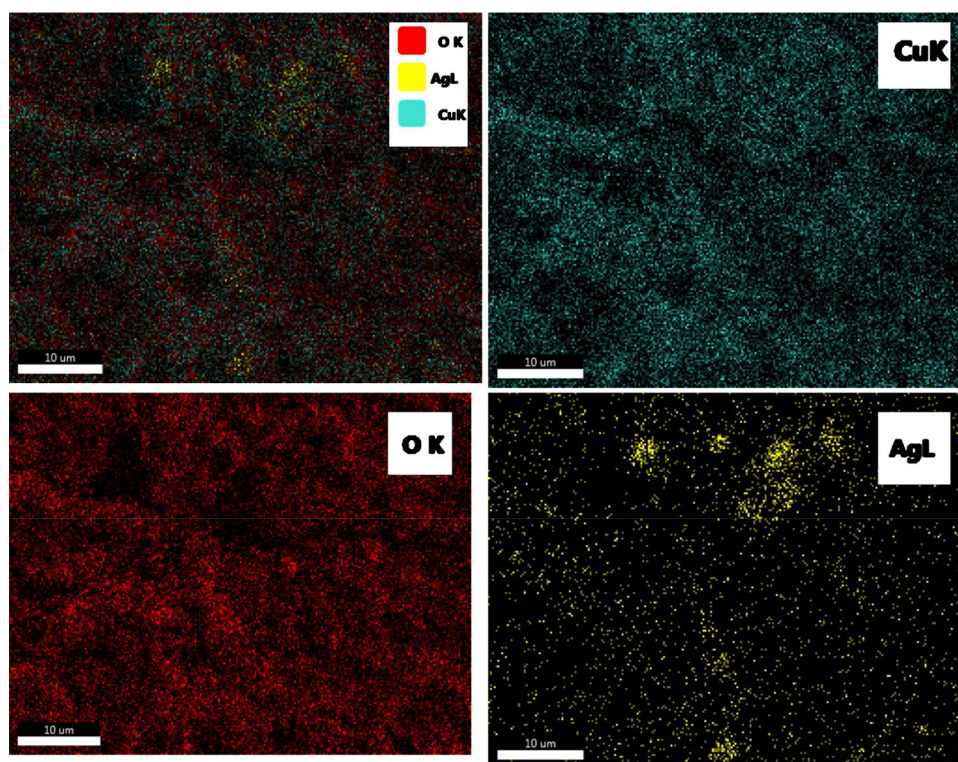


and b showed the time-dependent UV–Visible absorption spectra for the reduction of MB by CuO/Ag and CuO/Ag/Au NCs. Without presence of any catalyst, the reduction of MB was slower in presence of NaBH_4 . Addition of CuO/Ag and CuO/Ag/Au NCs catalyst (2 mg), the strong absorption peak of MB (664 nm) decreasing just 10 min and peak was shifted to 290 nm by reduction of MB (blue color) into LMB (colourless). This reaction may happen due to BH_4^- perform as an electron donor (nucleophile) at the same time MB supported as an electrophile with respect to CuO/Ag and CuO/Ag/Au

NCs catalyst [22]. The respective possible reduction mechanism of 4-NP & MB with nanocatalysts was demonstrated in Figs. 11 and 12. The deviation of C/C_0 versus time (t) for the degradation of 4-NP and MB by CuO/Ag and CuO/Ag/Au nanocatalysts was showed in Figs. 9c and 10c. The degradation efficiency (D) can be estimated by following relation

$$D = [(C_0 - C_t) / C_0] \times 100\%$$

Fig. 7 Elemental color mapping images of CuO/Ag NCs



where, C_0 and C_t (mg/L) are opening and last concentrations of 4-NP and MB at the time of 't' and '0', respectively. The attained degradation efficiency with time was plotted in Figs. 9d and 10d. From the Figure, the degradation efficiency of CuO/Ag and CuO/Ag/Au NCs were found to be 87% and 92% for 4-NP and 85% and 88% for MB respectively. The rate constant can be estimated by pseudo-first-order kinetics for the reduction of 4-NP and MB by CuO/Ag and CuO/Ag/Au nanocatalysts [10]. The preferred kinetic is agreed by linear plot of $\ln(C_t/C_0)$ against 't', which is demonstrated in Figs. 9e and 10e. The reaction kinetics equation is given by

$$\ln(C_t / C_0) = kt$$

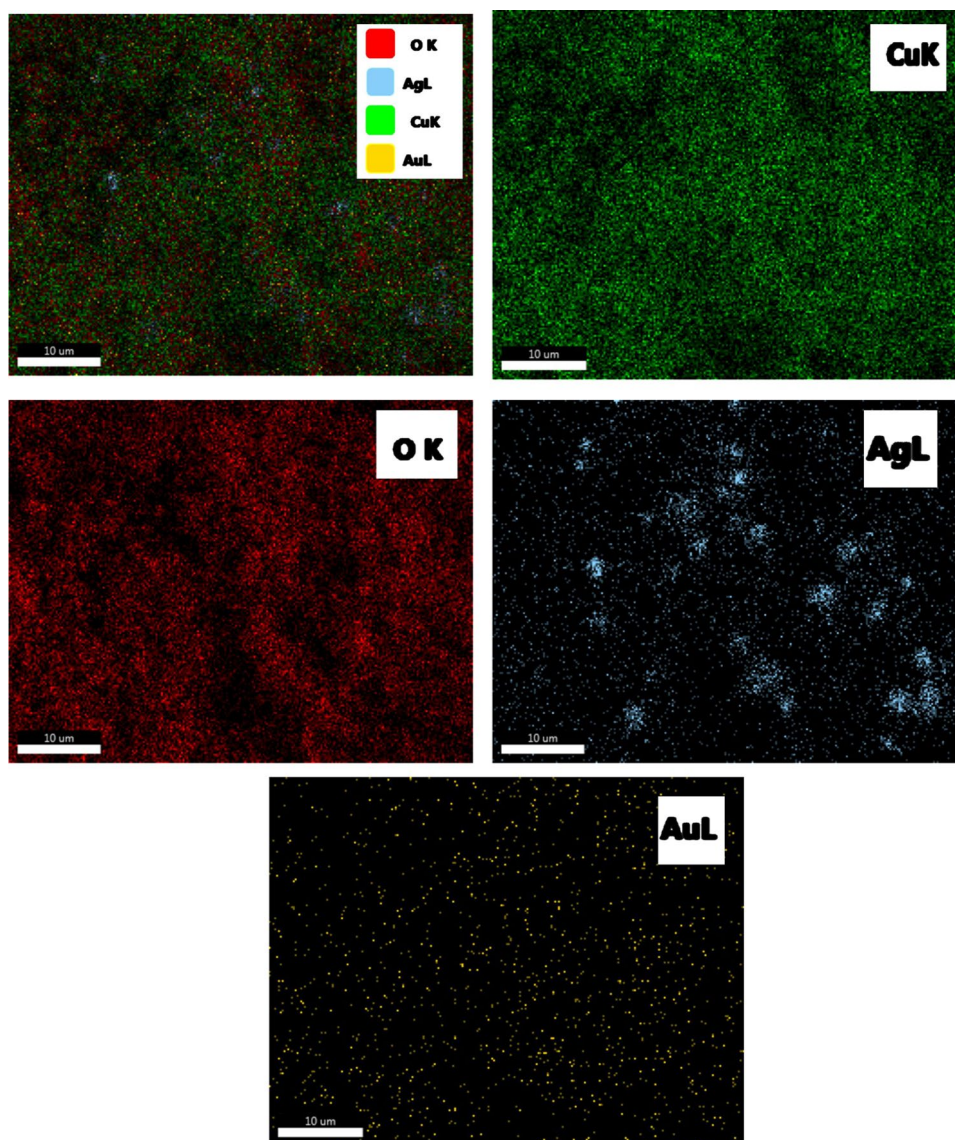
where, (k) donates the rate constant with time (t), C_0 and C_t is the concentration of 4-NP and MB at the beginning and after reaction time. The rate constant (k) of CuO/Ag and CuO/Ag/Au NCs determined from linear slope value were obtained to be $0.1055 \text{ (min}^{-1}\text{)}$ and $0.1201 \text{ (min}^{-1}\text{)}$ for 4-NP and $0.2440 \text{ (min}^{-1}\text{)}$ and $0.2914 \text{ (min}^{-1}\text{)}$ for MB respectively. The (R^2) values of CuO/Ag and CuO/Ag/Au NCs were calculated to be 0.9771 and 0.9859 for 4-NP and 0.9115 and 0.9363 for MB, respectively. The rapid catalytic reduction rate of 4-NP and MB reduction by CuO/Ag/Au nanocatalysts may be happens owing to the rate of electron transfer (or) interfacial electron transfer on the Ag and Au NPs surface, which can be influenced by the diffusion of 4-NP and MB to the metal surface. From the results exposed, addition of

noble metals significantly promote the reduction rate and demonstrate that introduction of these metals play a crucial roles in progressing the catalytic activity of CuO particles. The Tables 1 and 2 shows comparative table for previously reported catalytic reduction rate of 4-NP and MB dyes.

3.6 Catalyst Recyclability

The recycling of the catalyst is very important in industrial applications. To estimate its reusability, CuO/Ag and CuO/Ag/Au nanocatalysts were performing with successive catalytic tests (Fig. 13). After each catalytic test, the used CuO/Ag and CuO/Ag/Au nanocatalysts were washed by water and dried at room temperature. Initial three consecutive rounds, CuO/Ag/Au nanocatalyst has high recyclability than CuO/Ag nanocatalyst. After three consecutive cycles, recycling efficiency of 4-NP and MB was achieved to be 80.45% and 78.56% for CuO/Ag nanocatalyst. The presence of CuO/Ag/Au nanocatalyst, 4-NP and MB degradation recycling efficiency was attained to be 90.13% and 85.28%, respectively. Thus the result showed, degradation efficiency was rapidly reduced owing to their organic dye molecules are extremely adsorbed from the surface area [28].

Fig. 8 Elemental color mapping images of CuO/Ag/Au NCs



4 Conclusion

The CuO/Ag and CuO/Ag/Au NCs were fabricated via a facile two-step approach for enhancement of catalytic activity by the reduction of 4-NP and MB in the presence of NaBH_4 . In catalytic activity, CuO particles not only promote for Ag and Au metal nanoparticles but also play a crucial role in electron exchange from BH_4^- to organic pollutants (4-NP & MB) ions and thus enhancement of catalytic activity. The flake-like morphology was observed from the prepared CuO/Ag and CuO/Ag/Au NCs and size was found to be around 50 to 150 nm, respectively. Also, individual atoms were evenly distributed with a combined ratio throughout the composite matrix

of CuO/Ag and CuO/Ag/Au NCs which were primarily confirmed by the EDAX color mapping. In catalytic studies, degradation efficiency of CuO/Ag and CuO/Ag/Au NCs were achieved to be 87% and 92% for 4-NP and 85% and 88% for MB, respectively and noticeable rate constants of CuO/Ag and CuO/Ag/Au NCs were 0.1055 (min^{-1}), 0.1201 (min^{-1}) for the reduction of 4-NP and 0.2440 (min^{-1}), 0.2914 (min^{-1}) for the reduction of MB, respectively. From the observed results, dye degradation and rate constant of CuO/Ag/Au NCs were higher than the CuO/Ag NCs at both the dyes due to their surface electron transfer property.

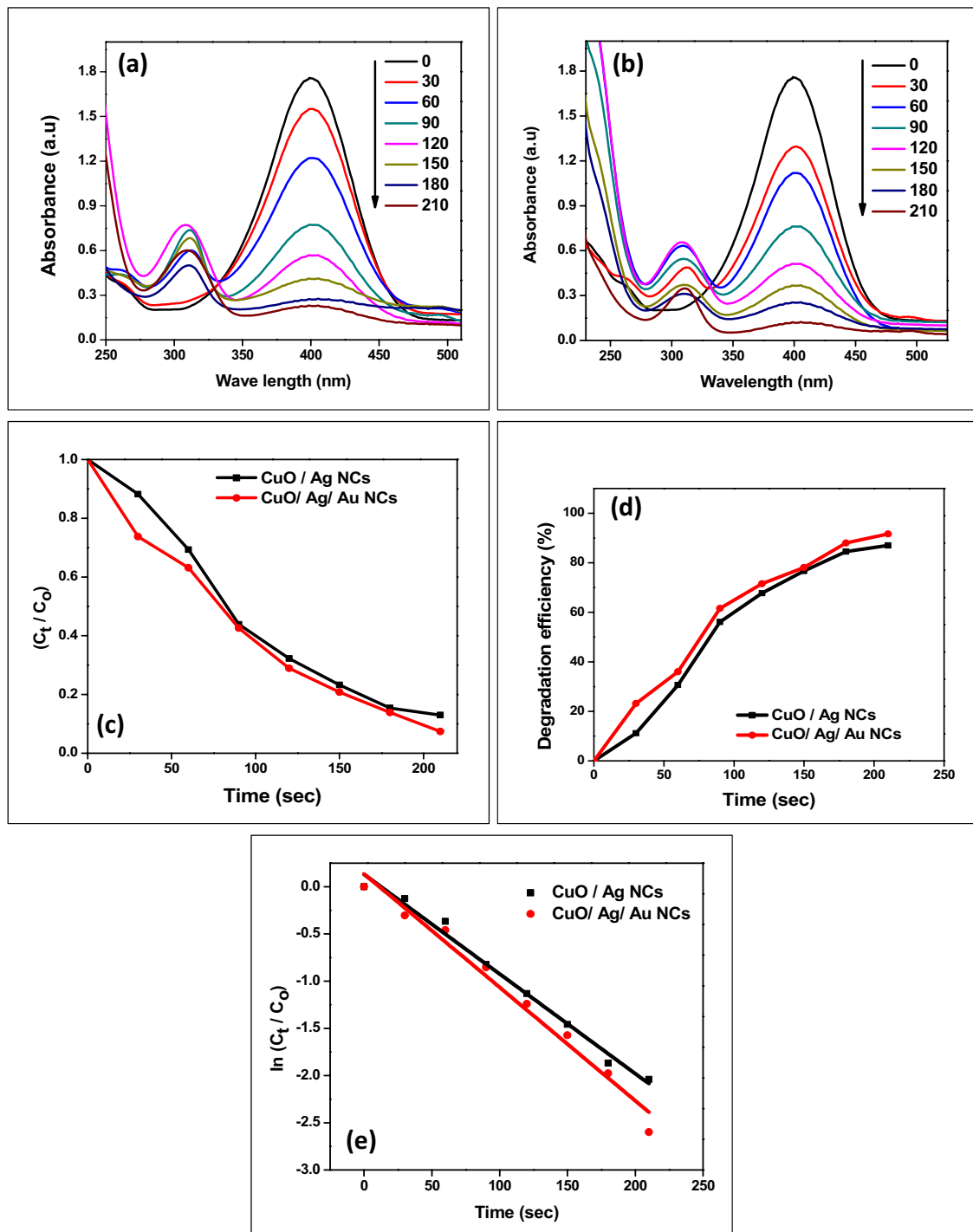


Fig. 9 Time-dependent UV-Vis absorption spectra for the reduction of 4-NP by **a** CuO/Ag NCs, **b** CuO/Ag/Au NCs, **c** Plot of C_t/C_0 versus reaction time (sec), **d** Degradation efficiency (%) versus reaction time (sec) and **e** $\ln(C_t/C_0)$ versus reaction time (sec)

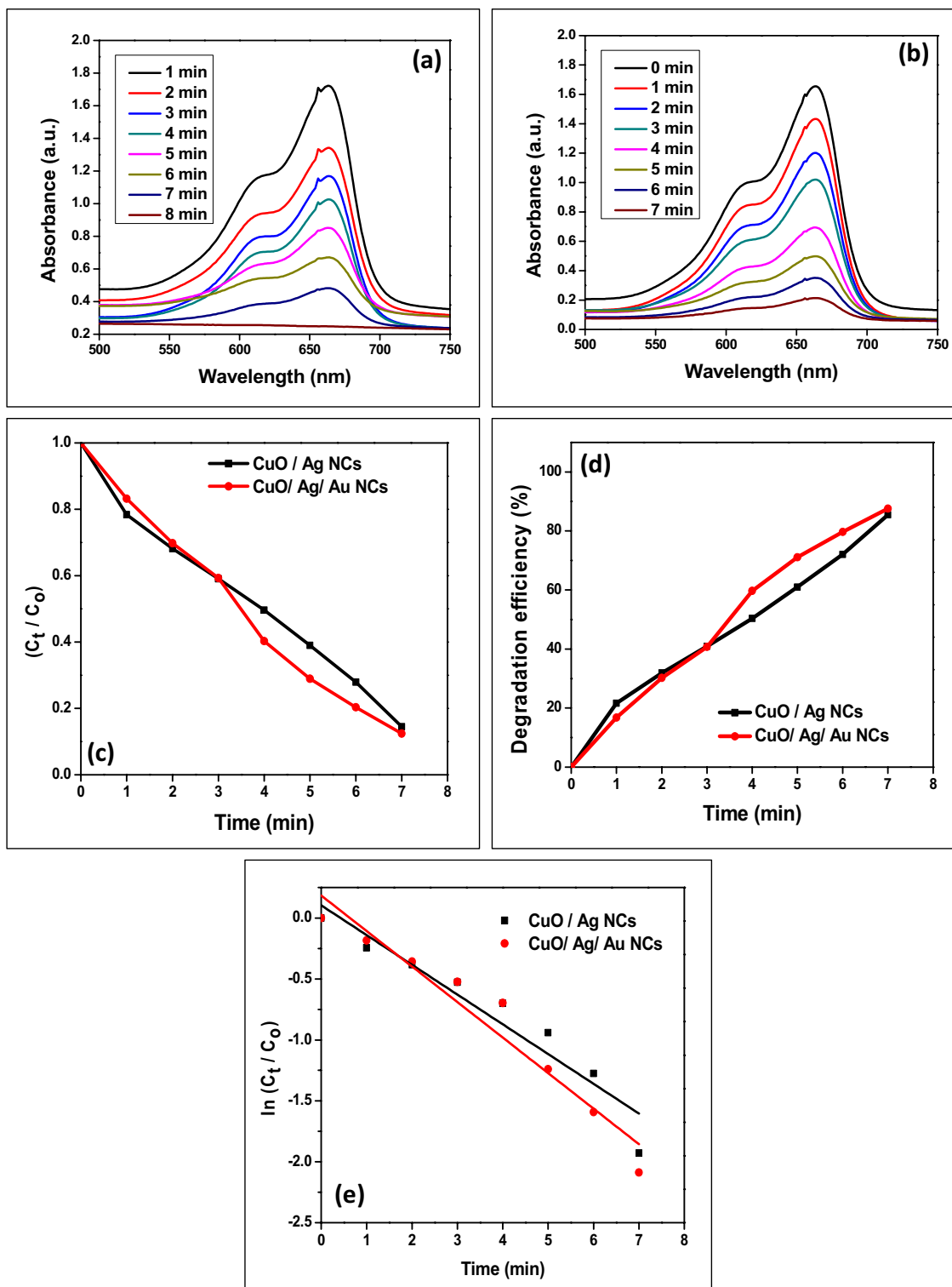


Fig. 10 Time-dependent UV-Vis absorption spectra for the reduction of MB by **a** CuO/Ag NCs, **b** CuO/Ag/Au NCs, **c** Plot of C_t/C_0 versus reaction time (sec), **d** Degradation efficiency (%) versus reaction time (sec) and **e** $\ln(C_t/C_0)$ versus reaction time (sec)

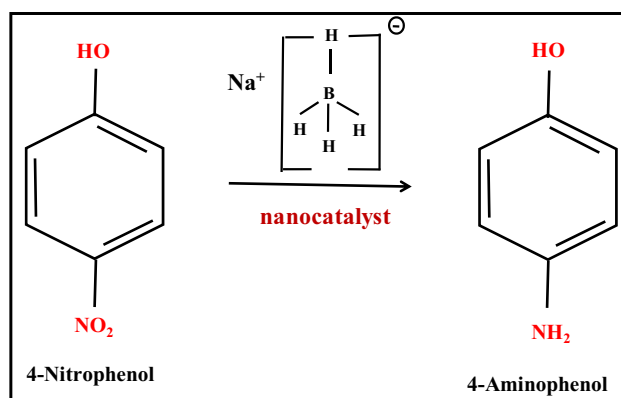


Fig. 11 Possible reduction mechanism of 4-Nitrophenol into 4-Aminophenol in presence of CuO/Ag NCs and CuO/Ag/Au nanocatalysts

Fig. 12 Possible reduction mechanism of Methylene Blue into Leuco methylene blue in presence of CuO/Ag NCs and CuO/Ag/Au nanocatalysts

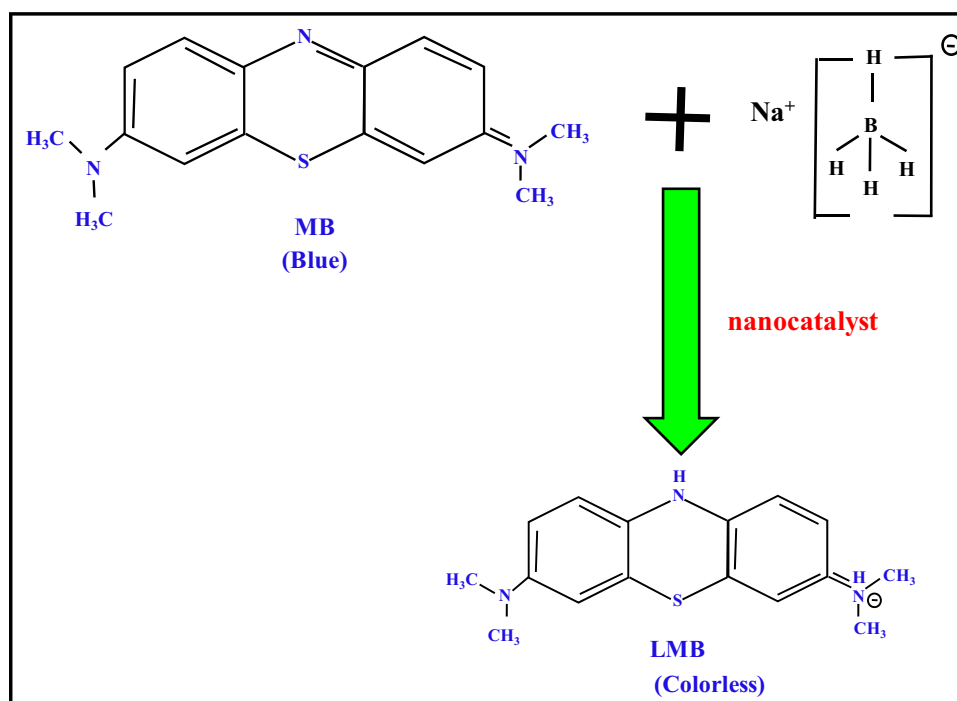
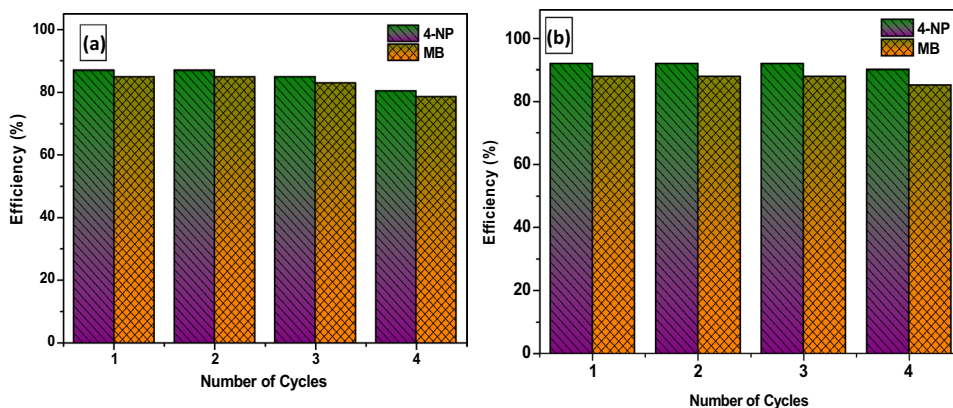


Table 1 Comparison catalytic activity of previous reported catalyst in the degradation of 4-NP

Catalyst	Quantity (mg)	4-NP (M)	Rate constant (k) (s ⁻¹)	References
CuO	1	1 ml of 10 ⁻³	0.8679 (min ⁻¹)	[10]
Cu ₂ O	1	3 ml of 10 ⁻⁴	0.5212(min ⁻¹)	[25]
Au/Fe ₂ O ₃	2	10 mM	0.63 (min ⁻¹)	[27]
Au/TiO ₂	5	5 mM	0.6326 (min ⁻¹)	[23]
CuO/Ag	5	0.20(mg/L)	0.338 (min ⁻¹)	[24]
CuO/Ag NCs	2	1 ml of 10 ⁻³	0.1055 (min ⁻¹)	[Present work]
CuO/Ag/Au NCs	2	1 ml of 10 ⁻³	0.1201 (min ⁻¹)	[Present work]

Table 2 Comparison catalytic activity of previous reported catalyst in the degradation of MB

Catalyst	Quantity (mg)	MB (M)	Rate constant (k) $\times 10^{-3}$ (s ⁻¹)	References
CuO NPs	1	1 ml of 10^{-4}	0.7368	[10]
CuOS	10	6.3×10^{-5}	0.698	[22]
Cu/MgO	10	3.1×10^{-5}	0.569	[26]
CuO/Ag NCs	2	1 ml of 10^{-4}	0.2440 (min ⁻¹)	Present work
CuO/Ag/Au NCs	2	1 ml of 10^{-4}	0.2914 (min ⁻¹)	Present work

Fig. 13 The recyclability of **a** CuO/Ag and **b** CuO/Ag/Au nanocatalysts in the reduction of 4-NB and MB dye solution with NaBH₄ at room temperature

References

- F.K. Higson, *Adv. Appl. Microbiol.* **37**, 1 (1992)
- M. Jayapriya, M. Arulmozhi, B. Balraj, *IET Nanobiotechnol* **13**(2), 134–143 (2019)
- Z. Jin, C. Liu, K. Qi, X. Cui, *Sci. Rep.* **7**, 1 (2017)
- W. Che, Y. Ni, Y. Zhang, Y. Ma, *J. Phys. Chem. Solid.* **77**, 1 (2015)
- J.F. Corbett, *Dyes Pigm.* **41**, 127 (1999)
- C.V. Rode, M.J. Vaidya, R.V. Chaudhari, *Org. Process Res. Dev.* **3**, 465 (1999)
- P.M. Uberman, C.S. García, J.R. Rodríguez, S.E. Martín, *Green Chem.* **19**, 739 (2017)
- N. Toshimaand, T. Yonezawa, *New J. Chem.* **22**, 1179 (1998)
- C. Ray, T. Pal, *J. Mater. Chem. A* **5**, 9465 (2017)
- A. Pramothkumar, N. Senthilkumar, K.C. Mercy Gnana Malar, M. Meena, I.V. Potheher, *J. Mater. Sci.* **30**, 19043 (2019)
- Y. Liang, Z. Chen, W. Yao, P. Wang, S. Yu, X. Wang, *Langmuir* **33**, 7606 (2017)
- N. Zhou, L. Polavarapu, Q. Wang, Q. Xu, *A.C.S. Appl. Mater. Interfaces* **7**, 4844 (2015)
- E. Akbarzadeh, M. Falamarzi, M.R. Gholami, *Mater. Chem. Phys.* **198**, 374 (2017)
- X.H. Guo, J.Q. Ma, H.G. Ge, *Russ. J. Phys. Chem. A* **89**, 1374 (2015)
- B. Balraj, N. Senthilkumar, I. Vetha Potheher, M. Arulmozhi, *Mater. Sci. Eng. B* **231**, 121–127 (2018)
- N. Senthilkumar, M. Ganapathy, A. Arulraj, M. Meena, M. Vimalan, I.V. Potheher, *J. Alloys Compd.* **750**, 171 (2018)
- P. Yuvarani, B. Balraj, S. Vijayachitra, C. Siva, *Mater. Res. Express* **5**(10), 105402 (2018)
- S. Arya, P. Anoop Singh, R. Kour, *Mater. Res. Express* **6**, 116313 (2019)
- E. Nandhakumar, P. Priya, R. Rajeswari, V. Aravindhan, A. Sasi-kumar, N. Senthilkumar, *Res. Chem. Intermed.* **45**, 2657 (2019)
- J.F. Huang, S. Vongehr, S.C. Tang, H.M. Lu, X.K. Meng, *J. Phys. Chem. C* **114**, 15005 (2010)
- J. Li, C. Liu, Y. Liu, *J. Mater. Chem.* **22**, 8426 (2012)
- A.K. Abay, X. Chen, D.H. Kuo, *New J. Chem.* **41**, 5628 (2017)
- Z.H. Ren, H.T. Li, Q. Gao, H. Wang, B. Han, K.S. Xia, C.G. Zhou, *Mater. Des.* **121**, 167 (2017)
- N. Bouazizi, J. Vieillard, P. Thebault, F. Desirac, T. Clamens, R. Bargougui, N. Couvrat, O. Thoumire, N. Brun, G. Ladam, S. Morin, N. Mofaddel, O. Lesouhaitier, A. Azzouz, F. Le Derf, *Dalton Trans.* **47**, 9143 (2018)
- A.K. Sasmal, S. Dutta, T. Pal, *Dalton Trans.* **45**, 3139 (2016)
- M. Nasrollahzadeh, Z. Issaabadia, S. Mohammad Sajadi, *RSC Adv.* **8**, 3723 (2018)
- F.H. Lin, R.A. Doong, *J. Phys. Chem. C* **115**, 6591 (2011)
- M. Sundaram, S. Kalpana, S. Rafi Ahamed, V. Sivaganesan, E. Nandhakumar, *Mater. Res. Exp.* **6**, 125043 (2019)

Publisher's Note Springer Nature remains neutral with regard to jurisdictional claims in published maps and institutional affiliations.

	Therapeutic Potential
	Miss. Karishma rajeshkumar Bhatt , Dr. Dipeek Kumar Mittal
1047	A Study of Corporate Social Responsibility in Mini-Ratna PSU's in India Jessica V Pillai
1048	Extraction Of A Finely Dispersed Low-Grade Iron Ore By Froth Flotation K.Prasad Babu , Mohammed Aminuddin
1049	A Critical Analysis On The Factors Of Subliminal Advertising And Its Effects On Consumer Behavior By- Dr. Shyama Charan Acharya and Ms. Sunayana Shukla
1050	Entrepreneurship For Innovation And Sustainability And Business Reengineering - Dr. N. Shankar, Dr. A. Abdul Brosekhan, Mr. M. Mohamed Naimudeen
1051	The Importance and Future of Entrepreneurship in India Vedantham Kaushik
1052	Green Marketing: Need Of The 21st Century Himani Choudhary , Prof. P. K. Agarwal
1053	IMPORTANCE OF CUSTOMER RELATIONSHIP MANAGEMENT (CRM) IN BUSINESS Sudha Anand, Dr. R. Shanmugam
1054	BLOCKCHAIN TECHNOLOGY AND ITS APPLICATION IN THE BUSINESS ENVIRONMENT Zarau Bello Baidu
1055	WORK LIFE BALANCE OF WORKING WOMEN'S IN EDUCATION INDUSTRY TAMILNADU B.Sutha, Dr.R.Viji
1056	THE EFFECT OF MACROECONOMIC VARIABLES ON EXCHANGE RATE IN GHANA Emmanuel Attah Kumah
1057	Indian Rural Market Indiscernible Boundaries with Potentials Abound S Bhavana
1058	A Study on Factors influencing the buying Behavior of Consumers K Sai Namratha



**ENTREPRENEURSHIP FOR INNOVATION AND SUSTAINABILITY AND BUSINESS
REENGINEERING**

Dr. N. SHANKAR, Associate Professor,

Dr. A. ABDUL BROSEKHAN, Associate Professor

Mr. M. MOHAMED NAIMUDEEN, Assistant Professor

Department of Management Studies, Mohamed Sathak Engineering College,
Kilakarai 623 806

Abstract

Entrepreneurial knowledge is the bedrock for entrepreneurial skills development, industrialization and sustainable national development and growth. Similarly Innovation is the key to development and contributing the advancement of economy and development of the nation. The entrepreneur as a part of his growth strategy needs to generate innovation by innovative behavior but the continuous development shall be attained by sustainability in innovation. But the question is that how to integrate innovation in entrepreneurship and sustainability. This is by Business Process Reengineering (BPR). The reengineering process is a fundamental rethinking and redesign of business process to achieve dramatic improvements in critical measures of performance like cost, quality, service and speed. This paper discusses entrepreneurship by integrating sustainability of innovation (SOI) and the concept of reengineering.



“KSA – Research” of Gap Analysis Towards Management Graduate’s Deliverables and Industry Expectations – A Contemporary Perspective of Human Resource Professionals

K S Usman Mohideen, S Helen Roselin Gracy, S Santhana Jeyalakshmi

Abstract— The object of this study is to understand the gap between the performance of management graduates and employer’s expectations from them. It is measured through KSA (Knowledge, Skills and Attitudes) approach for the services industry. The questionnaire was distributed to 210 Human Resource Professionals from different spectrum identified through convenience sampling method. Data analysed using Chi-square test, U-test and Weighted average rank. The findings indicated that to reduce a gap institute should increase an institute Industry interactions through Industrial visits, Lectures, etc., The Industry expectations are quite high so, the universities and institutes design curriculum based on the Industry expectations and review the knowledge imparting strategies.

Keywords: Attitude, HR Professionals, Industry, Knowledge, Management Institute, Skills

I. INTRODUCTION

In the last decade, the world has dramatically changed. The outlook of corporate has changed drastically with new disruptive technologies. The education industry is not fortunate enough to be updated with recent trends and demands and, the institutions have not met the requirement of the hour. Especially Indian educational institutions are blindly following an outdated educational system. Very few educational institutions which can be stated for its credibility and reliability. Majority of the educational institutions have not adopted the change. Out of millions of postgraduates or professionals, only 21% of them are fit for employability. Statistics further drops deeply to 8% in the case of engineers. This is evidence for a gap between what the industry expects and what is supplied to them.

II. NEED FOR THE STUDY

For the prospect of the country Industry and Academia should go hand in hand, but in reality, they both have a diverse obligation. Industry focus on cost and institute focus on prestige, so always there is a gap between their expectations. The bitter truth is that statistically, only 14% of

postgraduate management students have an ability to meet expectations of the industry (according to survey 2009 NSF) there is a need to tackle the problem of the gap between what industry expects and what the graduates possess. So this study is undertaken to find out the expectation of industry from management graduates.

III. OBJECTIVES OF THE STUDY

- To evaluate the level of satisfaction of recruiters.
- To assess the impact of demographic factors of HR professionals on expectation from management graduates.

IV. REVIEW OF LITERATURE

Farhad Analoui and Mirza Hassan Hosseini (2001), from the study, it is inferred that the appropriate mixture of KSA facilitates the fresh graduates to contribute more. In reality, there is an interlude between actuals and expected. They concluded that there should be more emphasis on self-development parameters.

Giannantonio and Hurley (2002), they found that the first and foremost challenge for HR professionals is “management of change.” The graduates must focus on covering the interlude, on being ready to face prospective, turbulent and dynamic opportunities.

Suchismita Bhattacharjee and Somik Ghosh (2012), the paper aims at comparing compare industry expectations from fresh graduates with student perceptions towards requisites for their professional success. The study conducted by collecting data from potential employers and graduates who are about to complete the course. The result depicts a weak correlation between expectation and requisites in the dimension of interpersonal skills.

Ana Azevedoa (2012), the study focuses on the required competencies of management students. This research found eight critical competencies for management graduates; the skills are in line with previous studies.

Revised Version Manuscript Received on 10 September, 2019.

Dr. K S Usman Mohideen, Assistant Professor, Department of Management Studies, Sri Sai Ram Engineering College, Chennai, Tamil Nadu, India

Ms. S Helen Roselin Gracy, Assistant Professor, Department of Management Studies, Sri Sairam Institute of Technology, Chennai, Tamil Nadu, India

S Santhana Jeyalakshmi, Assistant Professor, Department of Management Studies, Mohamad Sathak Engineering College, Kilakarai,



DOI: 10.23901/ijrte.B13590982S1119/2019©BEIESP
DOI: 10.23901/ijrte.B13590982S1119



V. RESEARCH METHODOLOGY

Number of respondents: 210.

Statistical Tools Applied: Chi-square, Weighted Average.

Research Design: Descriptive Study.

Sources of Data: Primary Data: Structured Questionnaire and Secondary Data: From Websites.

Sampling Design: Non-probability Convenience Sampling.

VI. RESULTS AND INTERPRETATION

Table 1: Showing Employer’s expectation management graduate’s knowledge

S. no	Knowledge	Not at all important	Not important	Neither important nor unimportant	Important	Very Important	Total
1	Industry practices	1.0	3.8	15.2	58.1	21.9	100.0
2	Organization and operations	2.9	2.9	26.7	55.2	12.4	100.0
3	Product Knowledge	1.9	4.8	24.8	55.2	13.3	100.0
4	Functional knowledge	1.9	9.5	3.5	47.6	10.5	100.0

Table 2: Showing Employer’s expectation based on attitude

S. No	Attitude	Not at all important	Not Important	Neither important nor unimportant	important	Very important	Total
1	Aptitude and willingness to learn.	1.0	1.0	7.0	53.0	38.0	100.0
2	Ethical Thinking	1.0	1.0	11.1	55.1	32.8	100.0
3	Self-discipline	1.1	1.2	5.7	48.5	43.8	100.0
4	Self-motivation	2.1	2.1	6.7	42.6	44.8	100.0
5	Commitment and Dedication	2.0	2.0	2.8	37.1	58.1	100.0

Interpretation:

From the above tables, it is inferred that 80% of the human resource professional expects various dimensions of

knowledge, skills and attitude to be qualify as successful candidates.

Table 3: Showing Performance of Management Graduates

S. no	Performance	Strongly Agree	Agree	Can't say	Disagree	Strongly Disagree	Total
1	Leadership qualities	20.0	51.4	13.3	9.5	5.7	100.0
2	Fulfilling requirements	10.5	54.3	19.0	12.4	3.8	100.0
3	High professional standards	8.6	61.0	17.1	11.4	1.9	100.0
4	Management graduates adaptable to the changing	16.2	45.7	25.7	9.5	2.9	100.0



Interpretation:

From the above tables, it is evident that nearly 70% of the human resource professionals are satisfied or delighted with the performance of fresh management graduates in all the parameters considered for the study.

To test the association between the experience and team management of fresh recruit.

H0:

There is no association between the experience and team management of fresh recruit.

H1:

There is an association between the experience and team management of fresh recruit.

Table 4: Chi-Square test between the experience and team management of fresh recruit

	Value	dof	Asymp. Sig. (2-sided)
Pearson Chi-Square	25.598	9	.002
N of Valid Cases	210		

Interpretation:

Since sig. (2-tailed) value is lesser than 0.05. H0 is rejected and H1 is accepted. Therefore, there is an association between the experience and team management of fresh recruit.

To test the association between the experience and leadership qualities of a fresh recruit.

H0:

There is no association between the experience and leadership qualities of a fresh recruit.

H1:

There is an association between the experience and leadership qualities of a fresh recruit.

Table 5: Chi-Square test between the experience and leadership qualities of a fresh recruit

	Value	dof	Asymp. Sig. (2-sided)
Pearson Chi-Square	26.045	12	.011
N of Valid Cases	210		

Interpretation:

Since sig. (2-tailed) value is lesser than 0.05. H0 is rejected and H1 is accepted. Therefore, there is an association

between the experience and leadership qualities of a fresh recruit.

Weighted average rank for Performance Indicators

Table 6: Showing frequencies for performance indicators

S.no	Indicators	Poor	Fair	Satisfactory	Good	Excellent
1	Knowledge	2	30	84	82	12
2	Skills	2	32	82	78	16
3	Attitude	6	28	70	90	16

Interpretation:

From the calculation, it is inferred that Attitude ranks first with a weighted average score of 3.39 in performance level and followed by skills and knowledge with a score of 3.35 and 3.34 respectively.

VII. SUGGESTIONS

- Industries expect management students to have adequate and appropriate knowledge, attitude and skills. So the universities and institutions design curriculum based on Industry expectations.
- To reduce a gap, the institute should increase institute industry interaction through Industrial visits, lectures.
- Management Institutes can work on case studies to enhance critical thinking.
- Fresh management graduates have to be sent to training in probation period.
- Institute can also incorporate subject knowledge from respective of practical application.

VIII. CONCLUSION

The study started to understand the reason for the gap between expectations and performance regarding knowledge, skills and attitude. It reflects in thoughts of small rewards. The aim should be to bridge the skills gap by making up and upgrading the skills of management professional students and enable them to enter the industry. The teaching methodology can incorporate case study discussions and virtual market training. Case studies will develop analytical thinking and judgement. This technique not only prepares students for technical proficiency but also to know corporate world issues. Students should be made to interact with top and middle management representatives of corporate. The curriculum should focus on technical skills and personality development. To conclude it can be stated that there is an

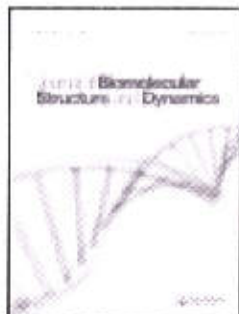


Influence of gender on the adaptability of candidates on
changing the environment and among the considered factors
Attitude of fresh management graduates matters more for
human resource professionals then followed Skills and
Knowledge.

REFERENCES

1. Alex Radermacher, Gursimran and Knudson (2014), "Investigating the skill gap between graduating students and industry expectations" ACM New York, New York, USA, pp: 291-300.
2. Ana Azevedoa Gerhard Apfelthaler (2012), "Competency development in business graduates: An industry-driven approach for examining the alignment of undergraduate business education with industry requirements" The International Journal of Management Education, Volume 10, Issue 1, April 2012, pp: 12-28.
3. Clinton Longenecker and Sonny Ariss, (2002), "Creating competitive advantage through effective management education", Journal of Management Development, Vol. 21, Issue: 9, pp: 640-654.
4. Farhad and Mirza Hassan (2001), "Management education and increased managerial effectiveness: The case of business managers in Iran", Journal of Management Development, Vol. 20 Issue: 9, pp: 785-794.
5. Neeraj Dubey, Saurabh Goyal, Ravindra Pathak, Uday Singh Rajput (2016), "An Empirical Study on Expectations of Industry from Academia" Journal of Shri Ram Institute of Information Technology, Vol. 2, Issue 1, pp: 1-99.
6. Pillai and Yusuf (2015), "Perceptions about One's Heritage Language: The Case of the Acehnese in Kampung Aceh and Malacca Portuguese" Humanities - The Asian Journal of Humanities Kemanusiaan Vol. 22, no. 2, pp: 67-92.
7. Yusof (2013), "Employers' Evaluations on Student Performance in Industrial Training: A Case of Built Environment Students in a Public University in Malaysia" School of Housing Building and Planning, Universiti Sains Malaysia, Vol.2, pp: 152-157.





Water soluble Cu(II) and Zn(II) complexes of bidentate-morpholine based ligand: synthesis, spectral, DFT calculation, biological activities and molecular docking studies

Gurusamy Sankararaj Senthilkumar , Murugesan Sankarganesh , Jeyaraj Dhaveethu Raja , Paul Raj Adwin Jose , Arumugam Sakthivel , Thayalaraj Christopher Jeyakumar & Radhakrishnan Nandini Asha

To cite this article: Gurusamy Sankararaj Senthilkumar , Murugesan Sankarganesh ; Jeyaraj Dhaveethu Raja , Paul Raj Adwin Jose , Arumugam Sakthivel , Thayalaraj Christopher Jeyakumar & Radhakrishnan Nandini Asha (2020): Water soluble Cu(II) and Zn(II) complexes of bidentate-morpholine based ligand: synthesis, spectral, DFT calculation, biological activities and molecular docking studies, Journal of Biomolecular Structure and Dynamics, DOI: [10.1080/07391102.2020.1821783](https://doi.org/10.1080/07391102.2020.1821783)

To link to this article: <https://doi.org/10.1080/07391102.2020.1821783>



Published online: 16 Sep 2020.



Submit your article to this journal [↗](#)



Article views: 19



View related articles [↗](#)




View Crossmark data [↗](#)



Usw
PRINCIPAL
MOHAMED SATHAK ENGINEERING COLLEGE
KILAKARAI - 623 806.

Water soluble Cu(II) and Zn(II) complexes of bidentate-morpholine based ligand: synthesis, spectral, DFT calculation, biological activities and molecular docking studies

Gurusamy Sankararaj Senthilkumar^{a,b}, Murugesan Sankarganesh^c, Jeyaraj Dhaveethu Raja^b, Paul Raj Adwin Jose^d, Arumugam Sakthivel^e, Thayalaraj Christopher Jeyakumar^b  and Radhakrishnan Nandini Asha^f

^aDepartment of Chemistry, Manonmanium Sundaranar University, Tirunelveli, Tamil Nadu, India; ^bDepartment of Chemistry, The American College, Madurai, Tamil Nadu, India; ^cDepartment of Chemistry, K. Ramakrishnan College of Technology, Trichy, Tamil Nadu, India; ^dDepartment of Chemistry, Mohamed Sathak Engineering College, Ramannanthapuram, Tamil Nadu, India; ^eDepartment of Chemistry, Meppo Schlenk Engineering College, Sivakasi, Tamil Nadu, India; ^fDepartment of Chemistry, Pope's College (Autonomous), Thoothukudi, Tamil Nadu, India

Communicated by Ramaswamy H. Sarma

ABSTRACT

Copper(II) and zinc(II) complexes of the type $[ML(AcO)_2 \cdot H_2O]$ were synthesized from bidentate-morpholine based Schiff base ligand (L - morpholinopropylimino)methyl)-6-methoxyphenol). The prepared ligand, copper(II) and zinc(II) complexes were characterized by elemental analysis, ESI-MS, ¹H-NMR, FT-IR, UV-Visible, ESR and spectrometric methods. The elemental and ESI-MS results have been established that the prepared ligand and complexes possess 1:1 stoichiometric ratio. ¹H-NMR and FT-IR results have been suggested that azomethine nitrogen and morpholine ring nitrogen atoms are coordinated with Cu(II) and Zn(II) metal ions. UV-Visible, ESI-MS and ESR spectroscopic results have been supported that the proposed structure of Cu(II) and Zn(II) complexes possess square pyramidal geometry. In order to confirm the proposed square pyramidal geometry of prepared complexes by DFT calculation has been studied. DNA binding ability of Cu(II) and Zn(II) complexes have been studied by electronic absorption and viscometric methods. These results reveal that Cu(II) and Zn(II) complexes interact with CT-DNA by the way of groove binding mode. Molecular docking studies result shows that synthesized compounds has better binding ability. The *in vitro* antioxidant activities of ligand, Cu(II) and Zn(II) complexes have been investigated by using the DPPH assay. The result shows that synthesized compounds have good radical scavenging activity against DPPH radical. Antimicrobial activities of synthesized ligand and its complexes have been tested against selected bacterial (gram positive & gram negative) and fungal species. The results reveal that Cu(II) and Zn(II) have good antimicrobial activity than ligand.

ARTICLE HISTORY

Received 5 August 2020
Accepted 6 September 2020

KEYWORDS

Morpholine ligand; DFT calculation; antimicrobial; DNA interaction; molecular docking

Introduction

Schiff base complexes are utilized because of the direct combination of molecular nitrogen with central metal ions and also it has been reported to possess biological properties (Sridhar et al., 2001). Since the publication of Schiff base complexes, a huge number of polydentate Schiff base complexes have been structurally characterized and extensively investigated due to their diverse chelating ability (Cotton & Wilkenson, 1988). Nowadays, researchers are involved in the development of biologically active compounds containing morpholine as a one of the substituents (War et al., 2017). Morpholine based Schiff base compounds are exclusively stable in biological systems allowing long-term applications as they compose radical re-design of DNA (Summerton, 2007). Linezolid is a familiar drug which is used in the treatment of microbial infections and restrains a morpholine ring in their structure (Senthilkumar et al., 2017). Schiff base complexes

obtained from morpholine derivatives having antitumor, anti-inflammatory, antimicrobial and anti-diabetic activities (Benítez et al., 2011; Patel et al., 2013; Sankarganesh et al., 2019). Furthermore, the groove mode of binding with metal compounds to DNA plays a significant role in applications of pharmaceutical industries (Chaurasia et al., 2019). The characterization of DNA by small redox transition metal compounds has been significantly aided by studying the DNA cleavage activity (Buldurun et al., 2020, 2020; Burrows & Muller, 1998). In our research groups constantly synthesized, characterized and evaluated the biological abilities of morpholine based ligand and its metal complexes and reported in the previous literatures (Aktas et al., 2019; Sakthikumar et al., 2018, 2018, 2019; Sankarganesh et al., 2017, 2018, 2018, 2020). The present work status from this research interest, morpholine based Schiff base ligand, Cu(II) and Zn(II) complexes have been synthesized and characterized by analytical and spectroscopic methods. DFT calculation, DNA binding, molecular



nerang
PRINCIPAL
MOHAMED SATHAK ENGINEERING COLLEGE
KILAKARAI - 623 808.

docking, antimicrobial and antioxidant activities of ligand, Cu(II) and Zn(II) complexes have been investigated.

Experimental

Materials

3-morpholinopropylamine and 2-hydroxy-3-methoxybenzaldehyde, $\text{Cu}(\text{CH}_3\text{COO})_2 \cdot \text{H}_2\text{O}$, $\text{Zn}(\text{CH}_3\text{COO})_2 \cdot 2\text{H}_2\text{O}$, deoxyribose nucleic acid from calf thymus DNA, tris-HCl, tris-buffer and sodium chloride were acquired from Sigma Aldrich and Alfa Aesar company.

Methods

The UV-Visible spectra and electronic absorption spectral titration were recorded on a UV-Visible-1800 (Shimadzu) spectrophotometer. Infrared (IR) spectra were done in KBr pellets on a FT-IR (Shimadzu, IR Affinity-1) spectrometer. The mass and $^1\text{H-NMR}$ spectra were recorded on an ESI-MS spectrometer, IIT Bombay and Bruker Avance DRX 300 FT-NMR spectrometer, IISC, Bangalore. The elemental analysis of carbon, hydrogen and nitrogen were recorded in an Elementar Vario EL III, CHNS analyser at STIC, CUSAT, India. The X-band ESR spectra of the samples in ethanol were obtained using a Varian $E_{1/2}$ spectrometer, the field being calibrated with TCNE (Tetracyanoethylene) as the g-marker.

Synthesis of ligand

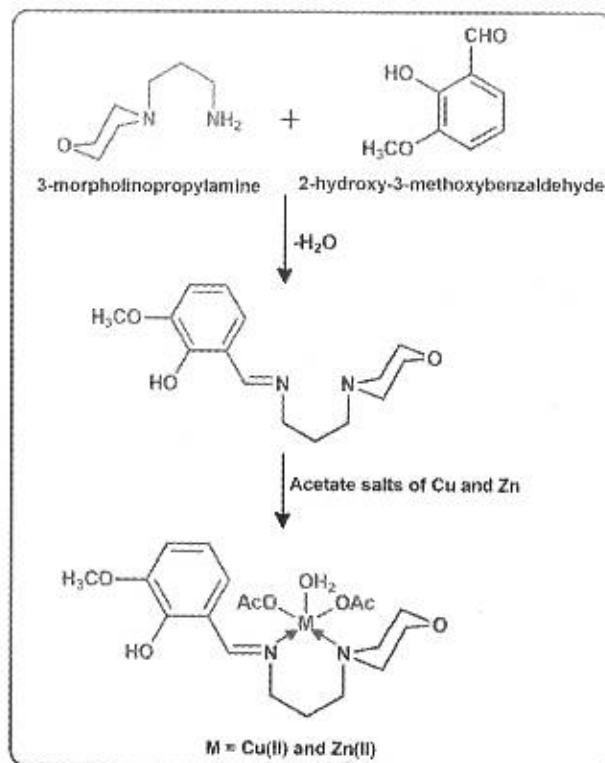
10 mmol of 2-hydroxy-3-methoxybenzaldehyde (1.52 g) and 3-morpholinopropylamine (1.44 g) was dissolved in ethanol separately. Then the mixture was stirred vigorously and refluxed for 3 h. After completion of the reaction, the above mixture was evaporated slowly on a water bath. The pale orange colored liquids was acquired and purified by column chromatography with 1:2 ratios of petroleum ether and methanol as an eluent system (Scheme 1).

Synthesis of complexes

The Cu(II) and Zn(II) acetate salts (1 mmol) were dissolved in 20 mL of ethanol and the solutions were added drop wise into 20 mL of ethanolic solution of ligand (0.278 g, 1 mmol) with constant stirring. Then the precursor solutions were refluxed for 3 h. The solvent was then reduced to one third to its volume and the resulting solution was cooled at room temperature for 48 h. The solid complexes was filtered, washed thoroughly with ethanol and dried in vacuum.

DFT calculations

Geometry of ligand, Cu(II) and Zn(II) complexes have been optimized using the density functional theory (B3LYP). The 6-31G* basis set was used to describe all the non-metal atoms and LANL2DZ basis set was used for the metal atom. Vibrational calculation has been performed on this optimized structure to ensure the global minima and no imaginary



Scheme 1. Preparation of ligand, Cu(II) and Zn(II) complexes

frequencies were found. FMO and MESP have been visualized from the optimized structure. All these calculation have been performed in the Gaussian-09 program package. All the structures were visualized using Gauss view 5.

DNA interaction

The binding behavior of ligand, Cu(II) and Zn(II) complexes with CT-DNA in Tris-HCl (50 mM)/NaCl (5 mM) buffer solution under room temperature were studied by using electronic absorption spectroscopy and viscometric measurements (Sankarganesh, et al., 2017; Sankarganesh et. al., 2019). Absorption titration experiments were performed with fixed concentration of the ligand and complexes (25 μM) with varying concentration of DNA (0–60 μM).

Molecular docking

Molecular docking analysis of ligand, Cu(II) and Zn(II) complexes with DNA double helix were studied by using Autodock Tool 4.2 software. Molecular docking procedures are followed by earlier reported literatures (Morris et. al., 2009; Trott & Olson 2010).

Antimicrobial studies

Antibacterial and antifungal activity of the ligand, Cu(II) and Zn(II) complexes were tested toward various bacterial species such as *Bacillus subtilis* (*B. subtilis*), *Enterobacter species*, *Streptococcus faecalis* (*S. faecalis*), *Escherichia coli* (*E. coli*), *Salmonella typhimurim* (*S. typhimurim*) and *Klebsiella*

Table 1. Analytical and physical properties of ligand, Cu(II) and Zn(II) complexes.

Compound	Molecular formula	Color	Yield, %	Found (Calculated), %				m_{cal} BM
				M	C	H	N	
Ligand	$C_{15}H_{22}N_2O_3$	Pale Orange	74	—	64.5 (64.7)	7.6 (7.9)	10.3 (10.1)	—
Cu(II) complex	$CuC_{19}H_{30}N_2O_8$	Green	70	13.1 (13.3)	47.9 (47.7)	6.4 (6.3)	5.8 (5.9)	1.85
Zn(II) complex	$ZnC_{19}H_{30}N_2O_8$	Yellow	61	13.7 (13.6)	47.5 (47.6)	6.2 (6.3)	5.9 (5.8)	—

pneumonia (*K. pneumonia*) and fungal species like as *Candida albicans* (*C. albicans*) and *Aspergillus niger* (*A. niger*) by disk diffusion method (Eruygur et al., 2019; Khan et al., 2020; Koksai et al., 2017; Shah et al., 2019). The standard for anti-bacterial and antifungal studies was used as streptomycin and amphotericin.

Antioxidant activity

Antioxidant of ligand, Cu(II) and Zn(II) complexes were analyzed by using DPPH scavenging method (Sukkur Saleem et al., 2017) The % inhibition was calculated according to the following formula;

(1) where, A_0 is the absorbance control and A_1 is the absorbance of sample or standard.

Results and discussion

Chemistry

The prepared Cu(II) and Zn(II) complexes are hygroscopic in nature. They are soluble in water, ethanol, methanol, chloroform and insoluble in petroleum ether, hexane. The micro-analytical data for the synthesized compounds are given in Table 1 summarized that the metal to ligand ratio is 1:1 type. The observed molar conductance of the compounds in ethanol (10^{-3} M) at room temperature is agreed with the non-electrolytic nature in the proposed structure (Scheme 1) of the metal compounds (Abd El-Wahab, 2008).

The molar conductance of Cu(II) and Zn(II) complexes are recorded in ethanol solution (10^{-3} M) at room temperature. The molar conductance values of Cu(II) complex is $20.8 \text{ ohm}^{-1} \text{ cm}^2 \text{ mol}^{-1}$ and Zn(II) complex is $26.4 \text{ ohm}^{-1} \text{ cm}^2 \text{ mol}^{-1}$ respectively. This result have been suggested that prepared complexes have non-electrolytic nature (Geary, 1971).

The ESI-MS mass spectra of ligand, Cu(II) and Zn(II) complexes were recorded in ethanol solution. The ESI-MS spectrum of ligand showed a molecular ion peak at m/z 278.05 corresponding to the $C_{15}H_{22}N_2O_3$. Similarly, the molecular ion peaks have observed at m/z 477 and 480 for the Cu(II) and Zn(II) complexes which corresponding to the $CuC_{19}H_{30}N_2O_8$ and $ZnC_{19}H_{30}N_2O_8$ respectively. These obtained molecular ion peaks clearly indicates that the prepared ligand, Cu(II) and Zn(II) complexes possess 1:1 stoichiometric ratio.

The $^1\text{H-NMR}$ spectra of ligand and Zn(II) complex were recorded in CDCl_3 solution. In ligand, azomethine ($-\text{CH}=\text{N}-$) proton signal was appeared at 8.37 ppm (s, 1H), phenyl as multiplet at 6.85-7.48 ppm (m, 3H), morpholino-O- CH_2-

proton at 3.51 ppm (t, 4H), morpholino-N- CH_2- at 2.29 (t, 4H), $-\text{CH}_2-\text{N} <$ protons at 2.48 ppm (t, 2H), $-\text{CH}_2-\text{N} =$ proton at 3.63 ppm (t, 2H) and $-\text{CH}_2-\text{CH}_2-\text{CH}_2-$ protons at 1.85 ppm (p, 2H). Further, a singlet peak is obtained at 13.6 ppm (s, 1H) is attributed to phenolic $-\text{OH}$ group. The spectrum of the Schiff base gives the methoxy peak at 3.45 ppm. The above data shows the azomethine peak at 8.37 ppm which is confirmed the formation of Schiff base ligand. $^1\text{H-NMR}$ spectra of Zn(II) complex showed the azomethine proton peak at 8.49 ppm (s, 1H) which confirms the azomethine nitrogen of ligand is coordinated to the metal(II) ions. Then, morpholino-N- CH_2- at 2.87 ppm (t, 2H) and $-\text{CH}_2-\text{N} <$ protons at 2.94 ppm (t, 2H) signals are appeared in downfield region compared to the free ligand, which is confirmed the nitrogen atom of morpholine moiety also involved in coordination of central metal(II) ions. The acetate and water molecule protons signals are appeared at 1.26 ppm (s, 3H) and 5.1 ppm (s, 2H) due to coordination of acetate and water molecules to the metal(II) ions. From the above observations, we have concluded that nitrogen from the azomethine and nitrogen from morpholine ring act as donor sites for the metal(II) complexes. This results indicate that Schiff base ligand acts as bidentate ligand for the formation of metal(II) complexes.

The FT-IR spectral data of ligand, Cu(II) and Zn(II) complexes were observed. The spectra of ligand showed the characteristic $\nu(\text{CH}=\text{N})$ band at 1602 cm^{-1} , which was shifted to lower frequencies at 1590 cm^{-1} for Cu(II) complex and 1599 cm^{-1} for Zn(II) complex indicating the participation of $-\text{CH}=\text{N}-$ nitrogen in coordination to the metal ion (Georgieva et al., 2006). Morpholine $\nu(\text{C}-\text{N})$ band of ligand was appeared at 1380 cm^{-1} , which is shifted to lower frequencies in the spectra of the complexes at 1347 cm^{-1} for Cu(II) complex and 1342 cm^{-1} for Zn(II) complex. It indicates that morpholine moiety nitrogen atom is coordinated to Cu(II) and Zn(II) metal ions. The ligand showed a broad band at 3250 cm^{-1} , assignable to the phenolic $-\text{OH}$ group, which is present in the region ($3220-3270 \text{ cm}^{-1}$) of the Cu(II) and Zn(II) complexes are suggests that phenolic groups are not involved in formation of complexes. In the Cu(II) and Zn(II) complexes, carboxylate of the acetate group is strongly observed (ν_{asy}) at 1621 cm^{-1} & 1624 cm^{-1} and (ν_{sym}) weakly at 1349 cm^{-1} & 1389 cm^{-1} . It is suggested that they are consisting of unidentate co-ordination site due to the value of differences between asymmetry and symmetry is greater than 200 cm^{-1} ($\Delta\nu_{\text{as-s}} \geq 200 \text{ cm}^{-1}$) (Ferrero, 1971). Also, methoxy group of the of ligand and its complexes were strongly observed (ν_{asy}) in the range of $1148-1145 \text{ cm}^{-1}$ and (ν_{sym}) weakly at $1084-1082 \text{ cm}^{-1}$. In IR spectra of the Cu(II)



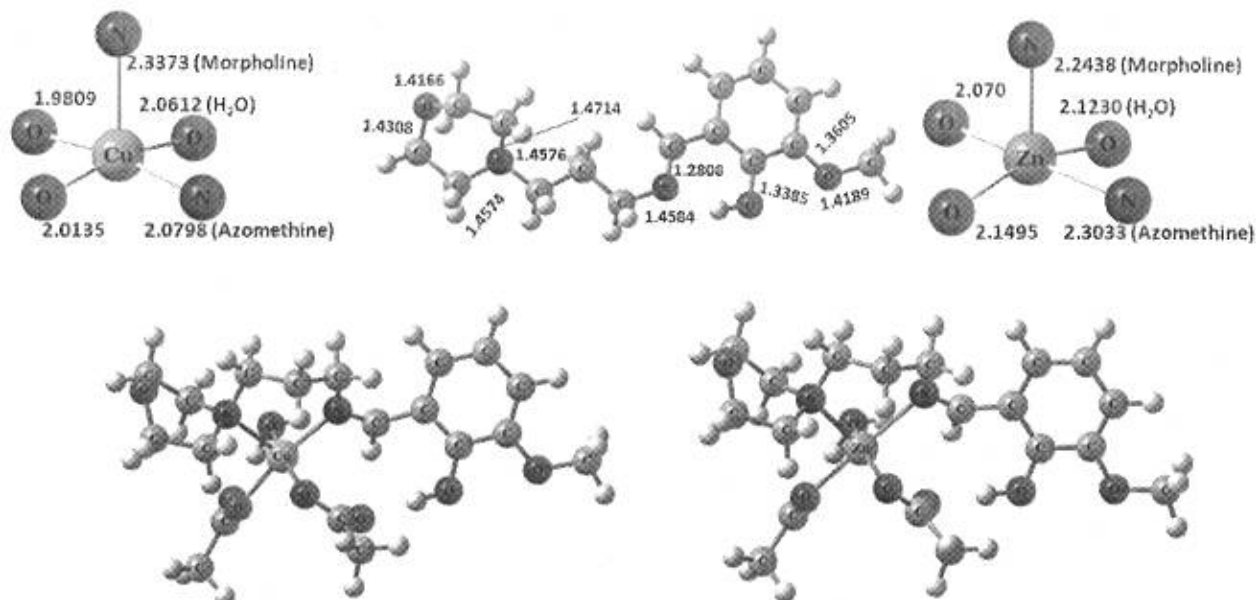


Figure 1 Optimized geometry of ligand, Cu(II) and Zn(II) complexes. All the values are in Å.

and Zn(II) complexes, a new band is observed at 674 cm^{-1} & 669 cm^{-1} due to the M-O stretching vibrations (Saif et al., 2012). Another band is observed at 561 cm^{-1} & 539 cm^{-1} due to M-N stretching vibrations (Georgieva et al., 2006). From these observations, we have concluded that metal ions possess five coordination sites like as two nitrogen atoms from $-\text{CH}=\text{N}-$ & morpholine ring, oxygen atom from H_2O and two oxygen sites from two acetate groups in metal(II) acetates.

The electronic spectra of the ligand, Cu(II) and Zn(II) complexes were recorded in ethanol solution in range of 200–800 nm. In free ligand, three bands observed at 419 nm, 331 nm and 300 nm are attributable to the intra ligand $\pi-\pi^*$, $n-\pi^*$ and $n-\pi^*$ transitions. In metal(II) complexes, bands are shifted to longer wavelengths at 312 nm and 309 nm are attributable to the intra ligand charge transitions (Elshaarawy et al., 2014) due to the donation of lone pair electron of nitrogen atom of ligand to the central metal atom. The electronic spectra of Cu(II) complex show band at 509 nm, which was attributed to ${}^2E_g \rightarrow {}^2T_{2g}$ transitions. These results favored for the proposed structure of Cu(II) complex has square pyramidal geometry (Lever et al., 1971). Zn(II) complex has d^{10} stable electronic configurations which confirms the absence of d-d transition, so the Zn(II) complex has only INCT bands at 310 cm^{-1} and 309 cm^{-1} (Lee et al., 2014).

The X-band electronic spin resonance spectrum of Cu(II) complex in frozen solution at liquid nitrogen temperature. The g tensor values of Cu(II) complex is . This is revealing that the unpaired electron lies predominantly in the orbital (Raja et al., 2012).²⁴ The calculated G value is greater than four which was implied that the local tetragonal axes are aligned parallel or slightly misaligned and the unpaired electron is presented in the orbital (Lakomska et al., 2014). The magnetic moment of the Cu(II) complex is 1.85 BM suggests that the prepared complex has mononuclear in nature (Benial et al., 2000). The co-factors of degree of geometrical

distortion cm^{-1} indicating slightly tetrahedral distortion, that is, they seemed to be square pyramidal geometry around the Cu(II) ion (Dasgupta, Khatua, Bertolasi, & Bhattacharjee, 2007). Based on the analytical and spectral results, the proposed structure of Cu(II) and Zn(II) complexes are shown in Scheme 1.

DFT calculation

The optimized structure of ligand, Cu(II) and Zn(II) complexes were shown in the Figure 1. And important bond lengths are highlighted in the structure, such as C-N, C-O, M-O and M-N. Frequency calculation was performed to ensure the optimized structure is the global minima on the potential energy surface. And functional group was confirmed by their corresponding vibrational frequencies which is very closer to the experimental values. The frontier molecular orbitals, the energy gap between the HOMO and LUMO orbitals of the ligand is 4.29 eV. The energy difference between the LUMO and HOMO for Cu(II) and Zn(II) complexes are 2.71 eV and 4.27 eV respectively. The positive lobes are shown in red color and negative phase is represented in green color, are shown in Figure 2. From this FMO analysis, LUMO of Cu(II) complex is highly stabilized when compared with ligand as well as Zn(II) complex; which indicates the Cu(II) complex will be highly reactive. The mapping of electrostatic potential onto the total electron density surface simultaneously displays electrostatic potential (electron + nuclei) distribution, molecular shape, size and dipole moments of the molecule and it useful to understand the relative polarity by visually. The MESP surfaces of the molecules are created by using B3LYP/6-31G* & LANL2DZ method. The total electron density mapped with electrostatic potential surface of ligand is shown in Figure 3. The color of MESP surface is red, it indicates that region is electron rich, partially negative charge;

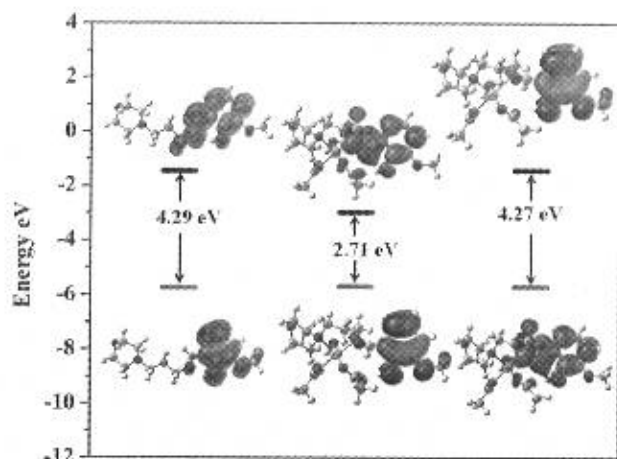


Figure 2. Optimized geometry of ligand, Cu(II) and Zn(II) complexes. All the values are in eV. (Red color lines indicates HOMO and black color line indicates LUMO).

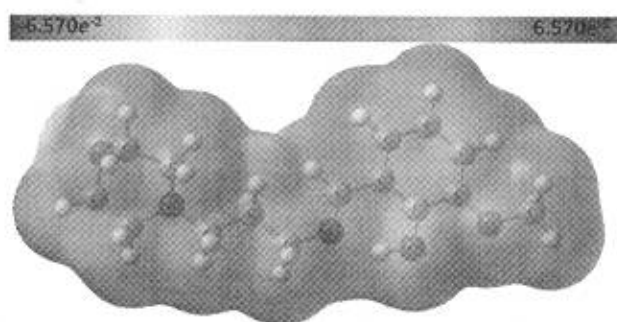


Figure 3. Molecular electrostatic potential mapping for the ligand.

blue color is indicates that electron deficient, partially positive charge; light blue means slightly electron deficient region; yellow means slightly electron rich region; green indicates the neutral; respectively. The region around the hydroxyl group and methoxy group represents the most negative potential region (red) and more positive charge around imine group. The predominance of light blue and green region in the MESP surfaces on the ligand.

DNA binding studies

Absorption titration

The absorption spectra of the Cu(II) and Zn(II) complexes with increasing concentration of CT-DNA at pH 7.0 and are shown in Figure 4 (a and b). As the concentration of DNA increases, hypochromism (52.21%, Cu(II) complex and 43.89%, Zn(II) complex) was observed in the charge transfer (CT) band of each compounds along with the red shift of about 7 and 5 nm which was suggested that the binding ability of the metal(II) complexes with DNA through groove binding (Revathi et al., 2017). The calculated intrinsic binding constant (K_b) values were shown in Table 2. These results illustrate that the Cu(II) complex exhibit more binding activity than Zn(II) complex.

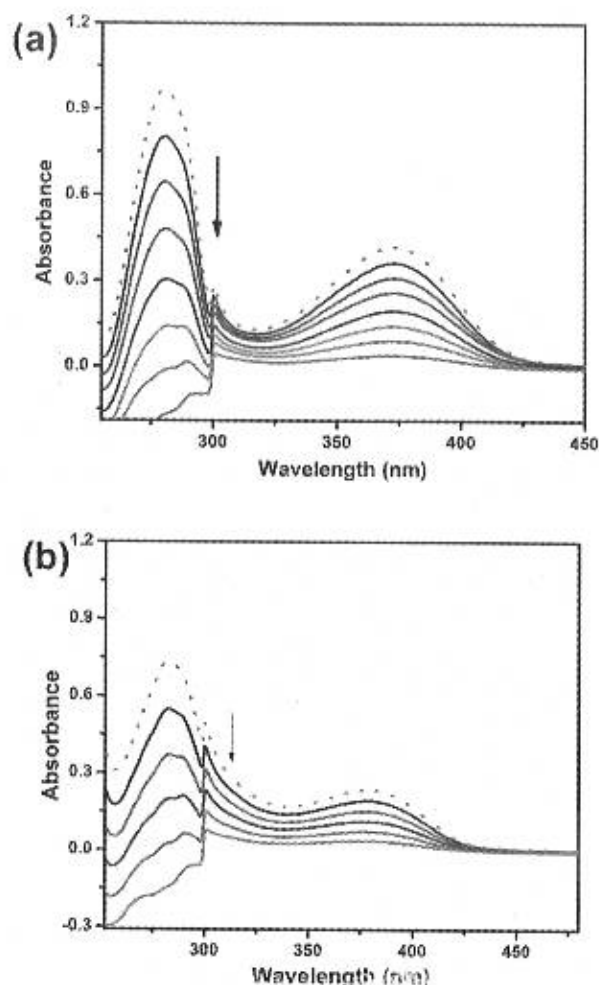


Figure 4. Absorption titration of Cu(II) (a) and Zn(II) (b) complexes in the presence and absence of CT-DNA at pH =7.0. Arrow indicate the decrease in absorption intensity upon successive addition of DNA. Dotted line indicate free complex.

Viscometric studies

Viscosity measurements were carried out on CT-DNA by varying the concentration of the added Cu(II) and Zn(II) complexes are given in Figure 5. The viscosity of DNA increased with rising ratio of compounds to DNA, also suggesting a binding of the compounds with DNA (Kelly et al., 1985). The increased degree of viscosity, which may depend on the binding affinity to DNA, follows the order EB > Cu(II) complex > Zn(II) complex. The increase in viscosity suggests that the metal(II) complexes might be bind to DNA by the groove binding nature (Arif et al., 2016).

Molecular docking

The molecular docking method was utilized to distinguish the binding abilities of ligand, Cu(II) complex and Zn(II) complex with DNA double helix. Docking studies have been demonstrated on DNA with the sequence of d(CCTCGTCC)2 in the presence of ligand, Cu(II) and Zn(II) complexes. The docking possess of prepared compounds with DNA are shown in Figure 6 (a-c). These docked poses prove the groove binding abilities of prepared compounds with DNA which is good agreement



Table 2. Absorption spectral properties of prepared complexes with CT-DNA.

Compound	max, nm			Hypochromism, %	Binding constant, $K_b \times 10^3, M^{-1}$
	Free	Bound	Red shift,		
Cu(II) complex	284	297	7	52.21	4.84
Zn(II) complex	278	283	5	43.89	3.76

with the results of electronic absorption and viscometric techniques. In free ligand, oxygen (O7, O19, and O1) atoms forms H-bond with DG10 & DG16, DG14 and DG16 in DNA double helix and the H-bond distances 1.939 Å & 2.253 Å, 2.091 Å, and 2.116 Å. Moreover, carbon atoms (C15 and C18) of ligand form H-bond with DG12 and DC15 in DNA double strand and the C-H bond distances are 3.526 Å and 3.739 Å respectively. The free binding energy values for the free ligand are found to be -6.7 kcal/mole. In Cu(II) complex, the most of the interactions are due to hydrogen bonding. In Cu(II) complex, oxygen atoms (O7, O19, O7, O1, O7, O19, O29, O7 and O1) form H-bonds with DG10, DG14, DG16, DG16, DG10, DG14, DG14, DG16 and DG16 in DNA double strands and its bond distances are 1.939 Å, 2.091 Å, 2.253 Å, 2.114 Å, 1.939 Å, 2.091 Å, 1.711 Å, 2.253 Å, 2.116 Å and 3.739 Å. And carbon atom form C-H bond with DC15 in DNA double helix and the bond distance is 3.739 Å. And hydrophobic interactions are observed between DC15 in DNA double helix with the Cu(II) complex and the bond distance is 3.739 Å. The free binding energy values for the Cu(II) complex are found to be -5.7 kcal/mole. In Zn(II) complex, oxygen atom (O7) forms H-bonding interaction with DC11, DC11 and DG14 and its bond distances are 2.708 Å, 2.634 Å and 3.036 Å. The π - π stacking interactions are observed between D13 nucleotide with the aromatic ring of the complex and the bond distance is 4.118 Å. The free binding energy values for the Zn(II) complex are found to be -5.4 kcal/mole. The binding of complexes with the DNA are stabilized by hydrogen bonding. Based on the binding energy values free ligand binds more than the metal complexes. Based on the number of interactions Cu(II) complex is higher binding than ligand and Zn(II) complex.

Antimicrobial activity

Antimicrobial activities of ligand, Cu(II) and Zn(II) complexes were tested against six pathogenic bacteria, *B. subtilis*, *E. species*, *S. faecalis*, *E. coli*, *S. typhimurim* and *K. pneumonia* using Muller Hinton nutrient agar media and two fungal *C. albicans* and *A. niger* microorganism species by well diffusion method. The zones of inhibition (mm) values of prepared compounds are summarized in Tables 3 & 4. A comparative study of the biological activities indicates that the compounds exhibit higher antimicrobial activity than the ligand and their activities are found to depend upon the size and charge distribution of metal ions, shape and redox potential of the metal chelates (Hussion Reddy, 2003). The ligand and M(II) ion formed as metal-chelates like [ML]. These complexes can bind with specific sites of microorganism to form another chelate i.e. microorganism bridged metal(II) chelates like [R-ML]. The binding property of ligand is used to transport chelates across membranes and facilitate to fix chelates to a specific site on the microorganism. Such binding capability of chelates is utilized

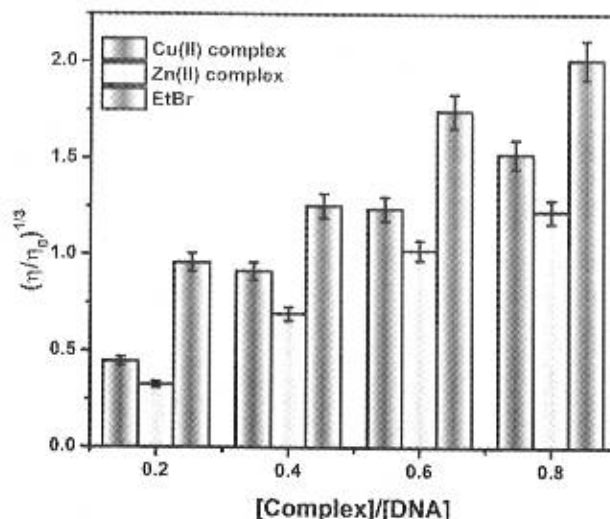


Figure 5. Effect of increasing concentrations of prepared compounds on the relative viscosity of DNA. $1/R = [\text{compound}]/[\text{DNA}]$.

to hinder the growth of bacteria. Binding of ligand with M(II) ion during the formation of metal chelates reduces the polarity of the metal ion (Chohan et al., 2006) by partial sharing of its positive charge with donor ligands within the chelate ring system. The delocalization of ligand within the chelate ring results in high lipid solubility which favors the permeation of chelates through lipid layer of the microorganism. Further, the normal cell process may also be affected by the formation of hydrogen bond through the nitrogen atom of the complexes and the active centers of cell constituent. From the zone of inhibition values, it was found that the Cu(II) and Zn(II) complexes were more potent among the ligand. The increased inhibition activity of prepared compounds can be explained on the basis of Overtone's concept (Nakajima, 2018) and Tweedy's Chelation hypothesis (Muniyandi et al., 2015). The observed zone of inhibition against these species for the compounds follows the order: Control > Cu(II) complex > Zn(II) complex > ligand. In this study, the Cu(II) and Zn(II) complexes were found to have low activities and this may due to the low lipophilicity of M(II) ion. Because of its low lipophilicity, the penetration of these compounds through the lipid membrane is diminished and consequently they could neither block nor inhibit the growth of organisms (Khan et al., 2020; Shah et al., 2019).

Antioxidant activity

The antioxidant activity of ligand and its metal(II) complexes were analyzed by using DPPH stable free radical. This method depends on the ability of the antioxidant to donate its electron to DPPH which in turn depends on the ability of DPPH to change color from purple to yellow. The measurement of the DPPH free radical scavenging activity was performed according to methodology described by Brand-Williams et al. Radical scavenging activity (RSA) was calculated as percentage of DPPH discoloration by the equation (1) (Albayrak et al., 2020)

1) where A_{control} is the absorbance of the DPPH (blank) and A_{sample} is the absorbance of the complexes. The percentage inhibition values of ligand and its metal (II) complex against DPPH radical are shown in Figure 7. The above result



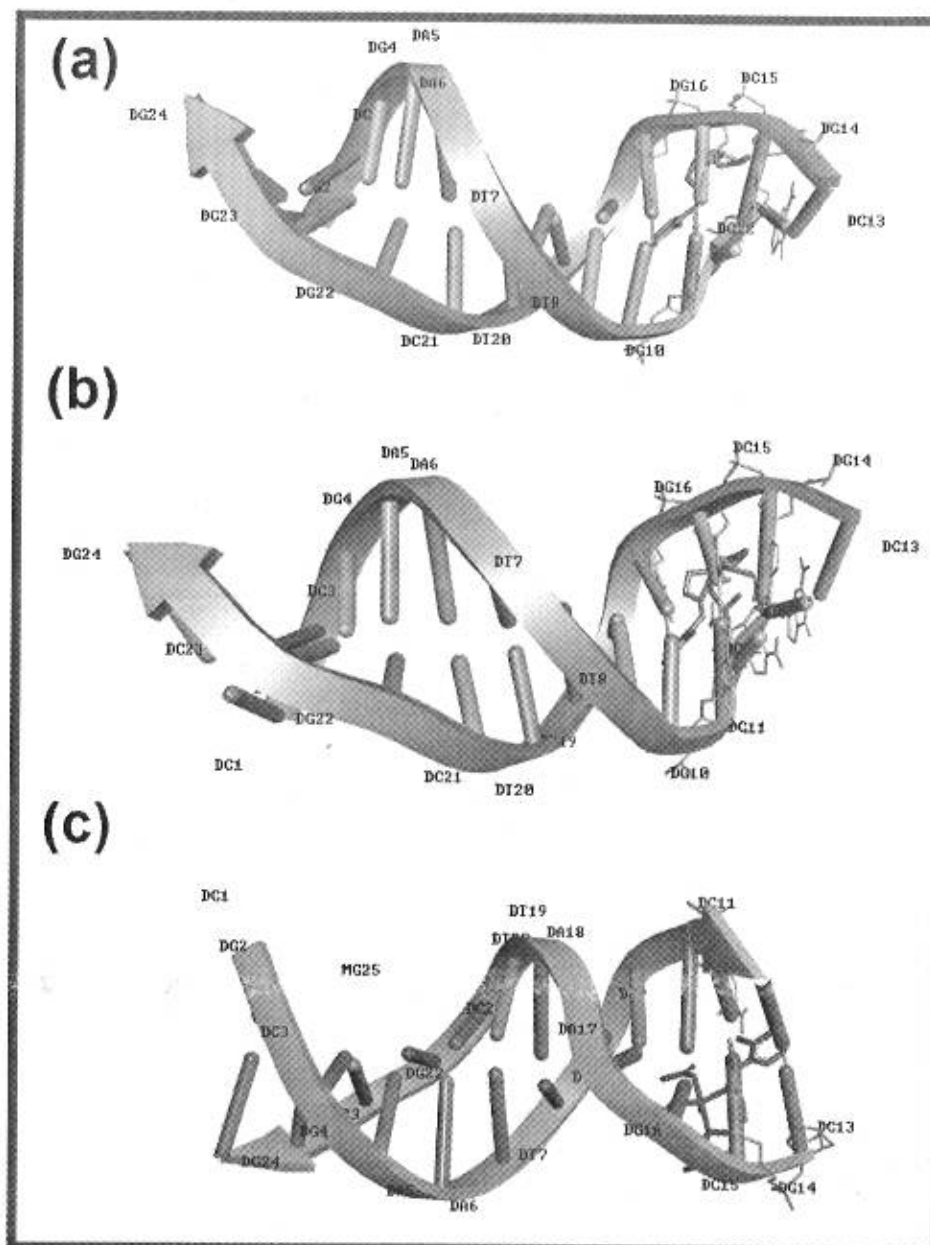


Figure 6. Molecular docking of prepared compounds with DNA (a) Ligand, (b) Cu(II) complex and (c) Zn(II) complex.

Table 3. Antibacterial activities of streptomycin, ligand, Cu(II) and Zn(II) complexes.

Gram positive bacteria, Zone of inhibition, mm			
Compounds	<i>B. subtilis</i>	<i>E. species</i>	<i>S. faecalis</i>
Ligand	8.4 ± 0.42	10.5 ± 0.53	9.2 ± 0.46
Cu(II) complex	22.3 ± 1.12	21.8 ± 1.09	23.6 ± 1.18
Zn(II) complex	19.6 ± 0.98	17.8 ± 0.89	21.5 ± 1.08
Streptomycin	28.7 ± 1.44	29.4 ± 1.47	28.7 ± 1.44
Gram negative Bacteria, Zone of inhibition, mm			
Compounds	<i>E. coli</i>	<i>S. typhimurim</i>	<i>K. pneumonia</i>
Ligand	10.5 ± 0.53	8.6 ± 0.43	14.7 ± 0.74
Cu(II) complex	24.6 ± 1.23	22.2 ± 1.11	25.4 ± 1.27
Zn(II) complex	18.1 ± 0.91	20.3 ± 1.02	21.5 ± 1.08
Streptomycin	26.1 ± 1.31	27.4 ± 1.37	25.5 ± 1.28

suggests that the compounds are having better radical scavenging ability than ligand in the following order Rutin > Cu(II) complex > Zn(II) complex > ligand

Table 4. Antifungal activities of amphotericin, ligand, Cu(II) and Zn(II) complexes.

Fungi, Zone of inhibition, mm		
Compounds	<i>C. albicans</i>	<i>A. niger</i>
Ligand	13.3 ± 0.67	11.7 ± 0.59
Cu(II) complex	23.7 ± 1.19	19.8 ± 0.99
Zn(II) complex	19.2 ± 0.96	18.5 ± 0.93
Amphotericin	28.7 ± 1.44	28.6 ± 1.43

Conclusion

Novel water soluble Cu(II) and Zn(II) complexes of bidentate-morpholine based Schiff base ligand have been synthesized and characterized by using physico-chemical, spectral and analytical techniques. These results showed that the compounds exhibit as square pyramidal geometry around the central metal ion. From the analysis, it has been concluded that the bidentate



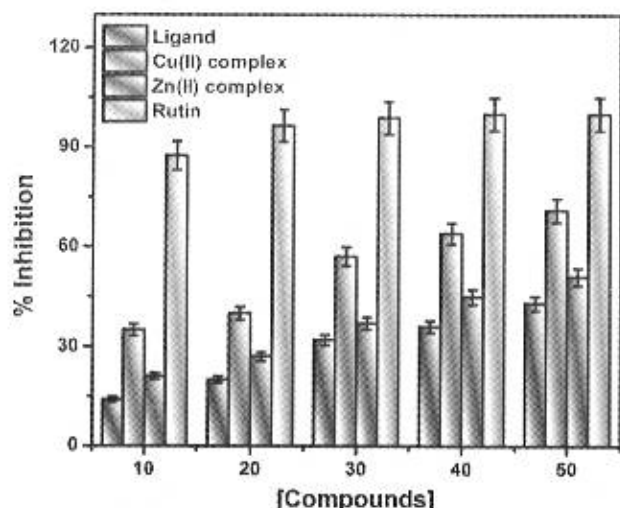


Figure 7. Antioxidant activity of ligand, Cu(II) and Zn(II) complexes against stable free radical (DPPH).

ligand bind to the Cu(II) & Zn(II) ions and their magnetic susceptibility values are revealed that prepared compounds are monomeric nature. The proposed geometry of Cu(II) and Zn(II) complexes were further confirmed by DFT calculation. The interactions of CT-DNA with Cu(II) and Zn(II) complexes were studied by electronic absorption and viscosity methods. The results revealed that the Cu(II) and Zn(II) complexes interact with DNA via groove binding. Molecular docking results suggest that the prepared ligand, Cu(II) and Zn(II) can interact with DNA double helix. Antioxidant activity of ligand, Cu(II) and Zn(II) complexes were tested against free radical DPPH and the results showed that they have good scavenging ability. The antimicrobial studies have shown that Cu(II) and Zn(II) complexes have higher potent activities than the free ligand.

Acknowledgements

The authors express their sincere and heartfelt thanks to Managing Board, Principal, Head and staff members, The American College, Madurai for providing the research facilities and their constant encouragements.

Funding

The authors acknowledge the Department of Science and Technology (DST)-Science and Engineering Research Board (SERB-Ref. No.: SR/FT/CS-117/2011 dated 29.06.2012), Government of India, New Delhi for the financial support.

ORCID

Thayalaraj Christopher Jeyakumar  <http://orcid.org/0000-0002-3568-5412>

References

Abd El-Wahab, Z. H. (2008). Complexation of 4-amino-1,3 dimethyl-2,6 pyrimidine-dione derivatives with cobalt(II) and nickel(II) ions: Synthesis, spectral, thermal and antimicrobial studies. *Journal of Coordination Chemistry*, 61(11), 1696–1709. <https://doi.org/10.1080/00958970701763076>

- Aktas, A., Barut Celepci, D., Kaya, R., Taslimi, P., Gok, Y., Aygün, M., & Gulcin, I. (2019). Novel morpholine liganded Pd-based N-heterocyclic carbene complexes: Synthesis, characterization, crystal structure, anti-diabetic and anticholinergic properties. *Polyhedron*, 159, 345–354. <https://doi.org/10.1016/j.poly.2018.11.048>
- Albayrak, S., Aksoy, A., Sagdic, O., & Hamzaoglu, E. (2020). Compositions, antioxidant and antimicrobial activities of *Helichrysum* (Asteraceae) species collected from Turkey. *Food Chemistry*, 119, 114–122. <https://doi.org/10.1016/j.foodchem.2009.06.003>
- Arif, R., Nayab, P. S., & Rahisuddin, P. (2016). Synthesis, characterization, DNA binding, antibacterial, and antioxidant activity of new bis-phthalimides. *Russian Journal of General Chemistry*, 86(6), 1374–1380. <https://doi.org/10.1134/S1070363216060232>
- Benial, A. M. F., Ramakrishnan, V., & Murugesan, R. (2000). Single crystal EPR of Cu(C₅H₅NO)₆(BF₄)₂: An example of admixed ground state. *Spectrochimica Acta Part A: Molecular and Biomolecular Spectroscopy*, 56(14), 2775–2781. [https://doi.org/10.1016/S1386-1425\(00\)00322-X](https://doi.org/10.1016/S1386-1425(00)00322-X)
- Benítez, J., Becco, L., Correia, I., Leal, S. M., Guiset, H., Pessoa, J. C., Lorenzo, J., Tanco, S., Escobar, P., Moreno, V., Garat, B., & Gambino, D. (2011). Vanadium polypyridyl compounds as potential antiparasitic and antitumoral agents: New achievements. *Journal of Inorganic Biochemistry*, 105(2), 303–312. <https://doi.org/10.1016/j.jinorgbio.2010.11.001>
- Buldurun, K., Turan, N., Bursal, E., Aras, A., Mantarci, A., Colak, N., Turkan, F., Durgun, M., & Gulcin, I. (2020). Synthesis, characterization, powder X-ray diffraction analysis, thermal stability, antioxidant properties and enzyme inhibitions of M(II)-Schiff base ligand complexes. *Journal of Biomolecular Structure & Dynamics*, 1–8. <https://doi.org/10.1080/07391102.2020.1802340>
- Buldurun, K., Turan, N., Bursal, E., Mantarci, A., Turkan, F., Taslimi, P., & Gulcin, I. (2020). Synthesis, spectroscopic properties, crystal structures, antioxidant activities and enzyme inhibition determination of Co(II) and Fe(II) complexes of Schiff base. *Research on Chemical Intermediates*, 46(1), 283–297. <https://doi.org/10.1007/s11164-019-03949-3>
- Burrows, C. J., & Muller, J. G. (1998). Oxidative Nucleobase Modifications Leading to Strand Scission. *Chemical Reviews*, 98(3), 1109–1152. <https://doi.org/10.1021/cr960421s>
- Chaurasia, M., Tomar, D., & Chandra, S. (2019). Synthesis, spectroscopic characterization and DNA binding studies of Cu(II) complex of Schiff base containing benzothiazole moiety. *Journal of Taibah University for Science*, 13(1), 1050–1059. <https://doi.org/10.1080/16583655.2019.1681724>
- Chohan, Z. H., Shaikh, A. U., Naseer, M. M., & Supuran, C. T. (2006). In-vitro antibacterial, antifungal and cytotoxic properties of metal-based furanyl derived sulfonamides. *Journal of Enzyme Inhibition and Medicinal Chemistry*, 21(6), 771–781. <https://doi.org/10.1080/14756360600829316>
- Cotton, A. F., & Wilkinson, G. (1988). *Advanced inorganic chemistry* (5th ed.) John Wiley & Sons.
- Dasgupta, S., Khatua, S., Bertolasi, V., & Bhattacharjee, M. (2007). Synthesis and characterization of copper(II) complexes containing tridentate modified amino acid ligands, [CuL(H₂O)(Pyz)] [L = {3,5-di-tert-butyl-2-hydroxybenzylamino}acetic acid and S(-)-2-(3,5-di-tert-butyl-2-hydroxy-benzylamino)-3-methyl-butyric acid; Pyz = pyrazole] and their oxidation to a copper(III) coordinated phenoxyl radical. *Polyhedron*, 26(12), 2574–2580. <https://doi.org/10.1016/j.poly.2007.01.011>
- Elshaarawy, R. F. M., Kheiralla, Z. H., Rushdy, A. A., & Janiak, C. (2014). New water soluble bis-imidazolium salts with a saldach scaffold: Synthesis, characterization and in vitro cytotoxicity/bactericidal studies. *Inorganica Chimica Acta*, 421, 110–122. <https://doi.org/10.1016/j.ica.2014.05.029>
- Eruygur, N., Kocyigit, U. M., Taslimi, P., Atas, M., Tekin, M., & Gulcin, I. (2019). Screening the in vitro antioxidant, antimicrobial, anticholinesterase and antidiabetic activities of Turkish endemic *Achillea cucullata* (Asteraceae) from ethanol extract. *South African Journal of Botany*, 120, 141–145. <https://doi.org/10.1016/j.sajb.2018.04.001>
- Ferraro, J. R. (1971). *Low-frequency Vibrations of Inorganic and Coordination Compounds*, Plenum Press.



Handwritten signature
 PRINCIPAL
 MOHAMED SATHAK ENGINEERING COLLEGE
 KILAKARAI - 623 008.

- Geary, W. J. (1971). The use of conductivity measurements in organic solvents for the characterisation of coordination compounds. *Coordination Chemistry Reviews*, 7(1), 81–122. [https://doi.org/10.1016/S0010-8545\(00\)80009-0](https://doi.org/10.1016/S0010-8545(00)80009-0)
- Georgieva, I., Trendafilova, N., & Bauer, G. (2006). Spectroscopic and theoretical study of Cu(II), Zn(II), Ni(II), Co(II) and Cd(II) complexes of glyoxalic acid oxime. *Spectrochimica Acta. Part A, Molecular and Biomolecular Spectroscopy*, 63(2), 403–415. <https://doi.org/10.1016/j.saa.2005.05.027>
- Hussion Reddy, K. (2003). *Bioinorganic chemistry*. New Age International Pvt. Ltd.
- Kelly, J. M., Tossi, A. B., McConnell, D. J., & OhUigin, C. (1985). A study of the interactions of some polypyridylruthenium (II) complexes with DNA using fluorescence spectroscopy, topoisomerisation and thermal denaturation. *Nucleic Acids Research*, 13(17), 6017–6034. <https://doi.org/10.1093/nar/13.17.6017>
- Khan, S., Singh, S., Gaikwad, S., Nawani, N., Junnarkar, M., & Pawar, S. V. (2020). Optimization of process parameters for the synthesis of silver nanoparticles from Piper beetle leaf aqueous extract, and evaluation of their antiphytofungic activity. *Environmental Science and Pollution Research International*, 27(22), 27221–27233. <https://doi.org/10.1007/s11356-019-05239-2>
- Koksal, E., Tohma, H., Kilic, O., Alan, Y., Aras, A., Gulcin, I., & Bursal, E. (2017). Assessment of Antimicrobial and Antioxidant Activities of *Nepeta trachonitica*: Analysis of Its Phenolic Compounds Using HPLC-MS/MS. *Scientia Pharmaceutica*, 85(2), 14. <https://doi.org/10.3390/scipharm85020024>
- Lakomska, I., Hoffmann, K., Wojtczak, A., Sitkowski, J., Maj, E., & Wietrzyk, J. (2014). Cytotoxic malonate platinum(II) complexes with 1,2,4-triazolo[1,5-*a*] pyrimidine derivatives: Structural characterization and mechanism of the suppression of tumor cell growth. *Journal of Inorganic Biochemistry*, 141, 188–197. <https://doi.org/10.1016/j.jinorgbio.2014.08.005>
- Lee, S. K., Tan, K. W., Ng, S. W., Ooi, K. K., Ang, K. P., & Abdah, M. A. (2014). Zinc (II) complex with a cationic Schiff base ligand: Synthesis, characterization, and biological studies. *Spectrochimica Acta. Part A, Molecular and Biomolecular Spectroscopy*, 121, 101–108. <https://doi.org/10.1016/j.saa.2013.10.084>
- Lever, A. B. P., Mantovani, E., & Donini, J. C. (1971). Temperature-dependent tetragonal distortion in some thermochromic N,N-diethylethylenediamine complexes of copper(II). *Inorganic Chemistry*, 10(11), 2424–2427. <https://doi.org/10.1021/ic50105a012>
- Muniyandi, V., Pravin, N., Mitu, L., & Raman, N. (2015). Synthesis, structural characterization, in-vitro antibiogram assay and efficient catalytic activities of transition metal(II) chelates incorporating (E)-2-((2-hydroxybenzylidene)amino)phenyl(phenyl)methanone ligand. *Journal of Molecular Structure*, 1086, 56–63. <https://doi.org/10.1016/j.molstruc.2015.01.011>
- Nakajima, M. (2018). Asymmetric Total Synthesis of Pleuromutilin. *Journal of Synthetic Organic Chemistry, Japan*, 76(3), 257–258. <https://doi.org/10.5059/yukigoseikyokaiishi.76.257>
- Patel, N. B., Purohit, A. C., Rajani, D. P., Moo-Puc, R., & Rivera, G. (2013). New 2-benzylsulfanyl-nicotinic acid based 1,3,4-oxadiazoles: Their synthesis and biological evaluation. *European Journal of Medicinal Chemistry*, 62, 677–687. <https://doi.org/10.1016/j.ejmech.2012.12.055>
- Raja, N., Ramesh, R., & Liu, Y. (2012). Paramagnetic ruthenium(III) complexes bearing O,O chelating ligands: Synthesis, spectra, molecular structure and electron transfer properties. *Polyhedron*, 31(1), 196–201. <https://doi.org/10.1016/j.poly.2011.09.019>
- Revathi, N., Sankarganesh, M., Rajesh, J., & Dhaweethu Raja, J. (2017). Biologically Active Cu(II), Co(II), Ni(II) and Zn(II) Complexes of Pyrimidine Derivative Schiff Base: DNA Binding, Antioxidant, Antibacterial and In Vitro Anticancer Studies. *Journal of Fluorescence*, 27(5), 1801–1814. <https://doi.org/10.1007/s10895-017-2118-y>
- Saif, M., Mashaly, M. M., Eid, M. F., & Fouad, R. (2012). Synthesis, characterization and thermal studies of binary and/or mixed ligand complexes of Cd(II), Cu(II), Ni(II) and Co(III) based on 2-(Hydroxybenzylidene) thiosemicarbazone: DNA binding affinity of binary Cu(II) complex. *Spectrochimica Acta. Part A, Molecular and Biomolecular Spectroscopy*, 92, 347–356. <https://doi.org/10.1016/j.saa.2012.02.098>
- Sakthikumar, K., Dhaweethu Raja, J., Sankarganesh, M., & Rajesh, J. (2018). Antimicrobial, Antioxidant and DNA Interaction Studies of Water-soluble Complexes of Schiff Base Bearing Morpholine Moiety. *Indian Journal of Pharmaceutical Sciences*, 80(4), 727–738. <https://doi.org/10.4172/pharmaceutical-sciences.1000413>
- Sakthikumar, K., Dhaweethu Raja, J., Vijay Solomon, R., & Sankarganesh, M. (2019). Density functional theory molecular modelling, DNA interactions, antioxidant, antimicrobial, anticancer and biothermodynamic studies of bioactive water soluble mixed ligand complexes. *Journal of Biomolecular Structure & Dynamics*, 37(10), 2498–2514. <https://doi.org/10.1080/07391102.2018.1492970>
- Sakthikumar, K., Sankarganesh, M., Dhaweethu Raja, J., & Mitu, L. (2018). Water Soluble Mixed Ligand Complexes Spectral, antioxidant, antimicrobial and DNA interaction studies. *Revista de Chimie*, 69(11), 3169–3177. <https://doi.org/10.37358/RC.18.11.6705>
- Sankarganesh, M., Adwin Jose, P., Dhaweethu Raja, J., Kesavan, M. P., Vadivel, M., Rajesh, J., Jeyamurugan, R., Senthil Kumar, R., & Karthikeyan, S. (2017). New pyrimidine based ligand capped gold and platinum nano particles: Synthesis, characterization, antimicrobial, antioxidant, DNA interaction and in vitro anticancer activities. *Journal of Photochemistry and Photobiology. B, Biology*, 176, 44–53. <https://doi.org/10.1016/j.jphotobiol.2017.09.013>
- Sankarganesh, M., Dhaweethu Raja, J., Adwin Jose, P. R., Vinoth Kumar, G. G., Rajesh, J., & Rajasekaran, R. (2018). Spectroscopic, Computational, Antimicrobial, DNA Interaction, In Vitro Anticancer and Molecular Docking Properties of Biochemically Active Cu(II) and Zn(II) Complexes of Pyrimidine-Ligand. *Journal of Fluorescence*, 28(4), 975–985. <https://doi.org/10.1007/s10895-018-2261-0>
- Sankarganesh, M., Dhaweethu Raja, J., Revathi, N., Solomon, R. V., & Kumar, R. S. (2019). Gold(III) complex from pyrimidine and morpholine analogue Schiff base ligand: Synthesis, characterization, DFT, TDDFT, catalytic, anticancer, molecular modeling with DNA and BSA and DNA binding studies. *Journal of Molecular Liquids*, 294, 111655. <https://doi.org/10.1016/j.molliq.2019.111655>
- Sankarganesh, M., Rajesh, J., Vinoth Kumar, G. G., Vadivel, M., Mitu, L., Senthil Kumar, R., & Dhaweethu Raja, J. (2018). Synthesis, spectral characterization, theoretical, antimicrobial, DNA interaction and in vitro anticancer studies of Cu(II) and Zn(II) complexes with pyrimidine-morpholine based Schiff base ligand. *Journal of Saudi Chemical Society*, 22(4), 416–426. <https://doi.org/10.1016/j.jscs.2017.08.007>
- Sankarganesh, M., Revathi, N., Dhaweethu Raja, J., Sakthikumar, K., Vinoth, K., Rajesh, J., Rajalakshmi, M., & Mitu, L. (2019). Computational, antimicrobial, DNA binding and anticancer activities of pyrimidine incorporated ligand and its copper(II) and zinc(II) complexes. *Journal of the Serbian Chemical Society*, 84(3), 277–291. <https://doi.org/10.2298/JSC1806090805>
- Sankarganesh, M., Vijay Solomon, R., & Dhaweethu Raja, J. (2020). Platinum complex with pyrimidine- and morpholine-based ligand: Synthesis, spectroscopic, DFT, TDDFT, catalytic reduction, in vitro anticancer, antioxidant, antimicrobial, DNA binding and molecular modeling studies. *Journal of Biomolecular Structure and Dynamics*, 1–13. <https://doi.org/10.1080/07391102.2020.1727364>
- Senthilkumar, G. S., Sankarganesh, M., Rajesh, J., Vedhi, C., & Dhaweethu Raja, J. (2017). Synthesis, spectral characterization, DNA interaction, antioxidant, and antimicrobial studies of new water soluble metal(II) complexes of morpholine based ligand. *Russian Journal of General Chemistry*, 87(11), 2654–2663. <https://doi.org/10.1134/S1070363217110214>
- Shah, S., Gaikwad, S., Nagar, S., Kulshrestha, S., Vaidya, V., Nawani, N., & Pawar, S. (2019). Biofilm inhibition and anti-quorum sensing activity of phyto-synthesized silver nanoparticles against the nosocomial pathogen *Pseudomonas aeruginosa*. *Biofouling*, 35(1), 34–49. <https://doi.org/10.1080/08927014.2018.1563686>
- Sridhar, S. K., Saravanan, M., & Ramesh, A. (2001). Synthesis and antibacterial screening of hydrazones, Schiff and Mannich bases of isatin derivatives. *European Journal of Medicinal Chemistry*, 36(7-8), 615–625. [https://doi.org/10.1016/S0223-5234\(01\)01255-7](https://doi.org/10.1016/S0223-5234(01)01255-7)



- Sukkur Saleem, S. H., Sankarganesh, M., Adwin Jose, P., Sakthikumar, K., Mitu, L., & Dhaveethu Raja, J. (2017). Investigation of Antimicrobial, Antioxidant, and DNA Binding Studies of Bioactive Cu(II), Zn(II), Co(II), and Ni(II) Complexes of Pyrimidine Derivative Schiff Base Ligand. *Journal of Chemistry*, 2017, 1–8. <https://doi.org/10.1155/2017/3831507>
- Summerton, J. E. (2007). Morpholino, siRNA, and 5-DNA compared: Impact of structure and mechanism of action on off-target effects and sequence specificity. *Current Topics in Medicinal Chemistry*, 7(7), 651–660. <https://doi.org/10.2174/156802607780487740>
- War, J. A., Srivastava, S. K., & Srivastava, S. D. (2017). Design, synthesis and DNA-binding study of some novel morpholine linked thiazolidinone derivatives. *Spectrochimica Acta, Part A, Molecular and Biomolecular Spectroscopy*, 173, 270–278. <https://doi.org/10.1016/j.saa.2016.07.054>



neeraj
PRINCIPAL
MOHAMED SATHAK ENGINEERING COLLEGE
KILAKARAI - 623 006.